VOLUME 121 NUMBER 2

THE ASTROPHYSICAL JOURNAL

AN INTERNATIONAL REVIEW OF SPECTROSCOPY AND ASTRONOMICAL PHYSICS

MARCH 1955

THE THEORY OF THE FLUCTUATIONS IN BRIGHTNESS OF THE MILKY WAY. VI . . . *Guido Münch* 291
ON THE ABUNDANCE OF INTERSTELLAR BERYLLIUM . . . *Lyman Spitzer, Jr., and George B. Field* 300
WAVE LENGTHS OF FORBIDDEN NEBULAR LINES . . . *Ira S. Bowen* 306
LINE INTENSITIES IN THE SPECTRA OF COOL CARBON STARS. II. R AND N STARS IN THE YELLOW . . . *William Buscombe* 312
THE VELOCITY AND SPECTRUM OF AC HERCULIS FROM COUDÉ SPECTROGRAMS . . . *Roscoe F. Sanford* 318
A SPECTROGRAPHIC STUDY OF BW VULPECULAE . . . *D. H. McNamara, O. Struve, and F. C. Bertiau, S.J.* 326
SPECTROGRAPHIC OBSERVATIONS OF VISUAL DOUBLE STARS . . . *Otto Struve and K. L. Franklin* 337
THE SUN'S MAGNETIC FIELD, 1952–1954 . . . *Horace W. Babcock and Harold D. Babcock* 349
ON THE CORRELATION BETWEEN RADIO-FREQUENCY RADIATION FROM THE SUN AND SOLAR ACTIVITY . . . *Einar Tandberg-Hanssen* 367
HEIGHTS OF SOLAR FLARES . . . *James W. Warwick* 376
FLARE HEIGHT AND ASSOCIATION WITH SID'S . . . *Constance S. Warwick* 385
CN BANDS IN THE CHROMOSPHERE . . . *J.-C. Pecker and R. G. Athay* 391
INVESTIGATION OF TURBULENCE IN THE SOLAR ATMOSPHERE . . . *Mahinder S. Uberoi* 400
ON BRIGHT-DARK SYMMETRY OF SOLAR GRANULATION . . . *Andrew Skumanich* 404
ON THERMAL CONVECTION IN A POLYTROPIC ATMOSPHERE . . . *Andrew Skumanich* 408

(Continued on inside page)

THE UNIVERSITY OF CHICAGO PRESS
CHICAGO, ILLINOIS, U.S.A.

March 1955 Vol. 121, No. 2

THE ASTROPHYSICAL JOURNAL

AN INTERNATIONAL REVIEW OF SPECTROSCOPY AND ASTRONOMICAL PHYSICS

Founded in 1895 by George E. Hale and James E. Keeler

Published in Collaboration with the American Astronomical Society

S. CHANDRASEKHAR
Managing Editor

GERARD P. KUIPER
Associate Editor

Yerkes Observatory of the University of Chicago

EDITORIAL BOARD

LEO GOLDBERG (1955-59)
The Observatory of the University of Michigan

H. W. BABCOCK (1953-57)
Mount Wilson Observatory of the Carnegie Institution of Washington

MARTIN SCHWARZSCHILD, JR. (1954-58)
Princeton University Observatory

G. HERZBERG (1952-56)
National Research Council, Ottawa

C. D. SHANE (1952-55)
Lick Observatory, University of California

The Astrophysical Journal is published bimonthly by the University of Chicago at the University of Chicago Press, 5750 Ellis Avenue, Chicago 37, Illinois, during January, March, May, July, September, and November. ¶Two volumes are published per year, one beginning with the January issue and the other beginning with the July issue. On all orders from the United States and its possessions the subscription price is $7.50 per volume or $15.00 per year; the price of single copies is $3.50. ¶On all orders from Canada the subscription price is $8.00 per volume or $16.00 per year; the price of single copies is $3.65. On all orders from all other countries the subscription price is $8.25 per volume or $16.50 per year; the price of single copies is $3.75. (Orders for service of less than a volume will be charged at the single-copy rate.) ¶Subscriptions are payable in advance. Please make all remittances payable to The University of Chicago Press, in United States currency or its equivalent by postal or express money orders or bank drafts. (Exception: members of The American Astronomical Society must send their subscriptions and remittances to the Treasurer of the Society.)

The following is an authorized agent:

For the British Commonwealth, except North America and Australasia: The Cambridge University Press, Bentley House, 200 Euston Road, London, N.W. 1, England. Prices of yearly subscriptions and of single copies may be had on application.

Claims for missing numbers should be made within the month following the regular month of publication. The publishers expect to supply missing numbers free only when losses have been sustained in transit, and when the reserve stock will permit.

Business correspondence should be addressed to The University of Chicago Press, Chicago 37, Illinois.

Communications for the editors and manuscripts should be addressed to: S. Chandrasekhar, Editor of THE ASTROPHYSICAL JOURNAL, Yerkes Observatory, Williams Bay, Wisconsin.

Line drawings and photographs should be made by the author, and all marginal notes such as co-ordinates, wave lengths, etc., should be included in the cuts. It will not be possible to set up such material in type.

One copy of the corrected galley proof should be returned as soon as possible to the editor, Yerkes Observatory, Williams Bay, Wisconsin. Authors should take notice that the manuscript will not be sent to them with the proof.

The cable address is "Observatory, Williamsbay, Wisconsin."

The articles in this journal are indexed in the *International Index to Periodicals*, New York, N.Y.

Applications for permission to quote from this journal should be addressed to The University of Chicago Press, and will be freely granted.

Microfilms of complete journal volumes are available to regular subscribers only and may be obtained at the end of the year. Orders and inquiries should be addressed to University Microfilms, 313 North First Street, Ann Arbor, Michigan.

Notice to subscribers: If you change your address, please notify us and your local postmaster immediately.

Entered as second-class matter, July 31, 1940, at the Post-Office at Chicago, Ill., under the Act of March 3, 1879.

Acceptance for mailing at special rate of postage provided for in United States Postal Act of October 3, 1917, Section 1103, amended February 28, 1925.

Copyright 1955 by the University of Chicago.

[PRINTED IN U.S.A.]

(Continued from front cover)

NONCOHERENT SCATTERING DUE TO COLLISIONS. I. ZANSTRA'S RATIO OF COHERENT TO UNCORRELATED NONCOHERENT SCATTERING *Frank N. Edmonds, Jr.* 418
THE GAUSSIAN QUADRATURE FORMULA FOR AN ELSASSER BAND-ABSORPTION MODEL . . . . *Jean I. F. King* 425
A MODEL FOR THE INTERNAL STRUCTURE OF THE SUN . . . *G. Ogden Abell* 430
APSIDAL MOTION FOR AN EARLY MAIN-SEQUENCE MODEL *R. Härm and J. Rogerson* 439
INHOMOGENEOUS STELLAR MODELS. IV. MODELS WITH CONTINUOUSLY VARYING CHEMICAL COMPOSITION . . . . . *R. Härm and M. Schwarzschild* 445
THE SPECTRUM-LUMINOSITY DIAGRAM FOR NGC 752 . . . . *Nancy G. Roman* 454
EFFECT OF MAGNETIC FIELDS ON GENERATION OF NOISE BY ISOTROPIC TURBULENCE . . . . *Russell M. Kulsrud* 461
MAGNETOHYDRODYNAMIC WAVES UNDER THE ACTION OF THE CORIOLIS FORCE. II . . . . *B. Lehnert* 481
THE FORMATION OF SUNSPOTS FROM THE SOLAR TOROIDAL FIELD *Eugene N. Parker* 491
THE CHARACTER OF THE INSTABILITY OF AN INCOMPRESSIBLE FLUID OF CONSTANT KINEMATIC VISCOSITY AND EXPONENTIALLY VARYING DENSITY *T. Y. Teng Fan* 508
THE PHYSICAL THEORY OF METEORS. VIII. FRAGMENTATION AS CAUSE OF THE FAINT-METEOR ANOMALY . . . . *Luigi G. Jacchia* 521
SPIN-ORBIT PARAMETERS FOR THE p^2 CONFIGURATION, WITH SPECIAL REFERENCE TO THE YELLOW CORONAL LINE . . . . *Harold Zirin* 528
INFLUENCE OF VIBRATION-ROTATION INTERACTION ON LINE INTENSITIES IN VIBRATION-ROTATION BANDS OF A ROTATING MORSE OSCILLATOR *Robert Herman and Robert J. Rubin* 533
THE *OH* BANDS IN THE INFRARED AIRGLOW *Joseph W. Chamberlain and Frederick L. Roesler* 541
THE CONCENTRATION OF CARBON DIOXIDE IN THE ATMOSPHERE OF MARS *J. Grandjean and R. M. Goody* 548

NOTES

Wide-Angle Infrared Photograph of the Southern Milky Way *A. D. Code and T. E. Houck* 553
Photometry of the Lacerta Aggregate . . . . *Daniel L. Harris III* 554
Four Faint Wolf-Rayet Stars . . . . *W. A. Hiltner and Braulio Iriarte* 556
19 Scorpii, A Luminous A Star in the Scorpio-Centaurus Association *A. Blaauw, W. W. Morgan, and F. C. Bertiau, S.J.* 557

ABSTRACTS OF ASTROPHYSICAL JOURNAL SUPPLEMENT SERIES

Numerical Integrations for the Stellar Interior . . . *R. Härm and M. Schwarzschild* 558

THE ASTROPHYSICAL JOURNAL

AN INTERNATIONAL REVIEW OF SPECTROSCOPY AND
ASTRONOMICAL PHYSICS

VOLUME 121 MARCH 1955 NUMBER 2

THE THEORY OF THE FLUCTUATIONS IN BRIGHTNESS OF THE MILKY WAY. VI

Guido Münch
Mount Wilson and Palomar Observatories
Carnegie Institution of Washington, California Institute of Technology

Received August 28, 1954

ABSTRACT

In this paper the stochastic process defined by the surface brightness of the Milky Way in the discrete cloud model is further studied. The problem of finding the probability distribution for the joint occurrence of two specified values of the surface brightness when we observe parts of the system extending to two given distances is solved. The solution is obtained in terms of a set of functions $\{\Phi_n(u, t)\}$ governing the probability distribution of the brightness u, conditioned to the occurrence of exactly n clouds in a system of extent t. The covariance of the process is shown to be of a simple exponential type, with a decay constant equal to $(1 - q)^{-1}$, q being the transparency factor of a cloud. Adopting values of q and ν (the mean number of clouds per unit distance) previously found, it is estimated that the distance over which the brightness fluctuations become effectively uncorrelated is 600 psc.

1. Introduction.—In the earlier papers of this series (Chandrasekhar and Münch 1950*a*, *b*, 1951, 1952; these papers will be referred to hereafter as Papers I, II, III, and IV) we have studied the surface brightness of the Milky Way, on the basis of Ambarzumian's model for the structure of the interstellar medium. When the interstellar dust clouds are assumed to have a constant transparency factor q, the surface brightness u is related to the extent of the system t (both u and t measured in appropriate units) through the stochastic integral

$$u(t) = \int_0^t q^{m(s)} d s , \tag{1}$$

where $m(s)$ is a chance variable representing the number of clouds between the observer and a point at a distance s. On the hypothesis that these clouds are distributed at random, independently of one another, $m(s)$ may take any integral value n with probability $p_n(s)$ given by a Poisson law with variance s,

$$p_n(s) = e^{-s} \frac{s^n}{n!} \qquad (n = 0, 1, 2, \ldots) . \tag{2}$$

The distribution function[1]

$$f(u, t) = \text{Prob}\left[\int_0^t q^{m(s)}\,ds \geq u\right], \tag{3}$$

evaluated in Paper III, has been used to study the probabilistic properties of $u(t)$. A complete description of the stochastic process underlying equation (1), however, is not provided by $f(u, t)$ alone. Rather, the knowledge of the whole set of distribution functions,

$$f_r\left(\bigcap_{k=1}^{r}\{u_k, t_k\}\right) = \text{Prob}\left[\bigcap_{k=1}^{r}\int_0^{t_k} q^{m(s)}\,ds \geq u_k\right] \qquad (r = 1, 2, 3, \ldots), \tag{4}$$

is required (Levy 1948; Wang and Uhlenbeck 1945), giving, for specified sequences $\{u_k\}$ and $\{t_k\}$, the probability for the simultaneous occurrence of all the events $u(t_k) \geq u_k$. In this paper we shall evaluate the second function $f_2(u_2, t_2; u_1, t_1)$ of sequence (4). It governs the probability distribution for the joint observation (along the same line of sight) of values u_2 and u_1 for the surface brightness, if the system extended to distances t_2 and t_1, respectively.

Although in practice it is not feasible to measure in a straightforward fashion the contribution of a limited extension of the system to the total surface brightness, indirect methods can effectively provide the required observational information. For example, the partial surface brightness resulting from stars in a fixed range of spectral type, down to two different limits of apparent magnitude, would arise in parts of the system extending to two different distances from the observer. The statistical behavior of two such partial values of the surface brightness, when compared with the predictions of the appropriate theory, would indicate how closely the interstellar dust along the direction considered follows the pure random distribution postulated in Ambarzumian's model. Considering the increasing importance of problems related to the large-scale inhomogeneities in the spatial distribution of interstellar clouds in the galactic system (spiral structure), it would appear to be of more than academic interest to provide a possible statistical basis for their discussion.

2. *Relation between the first and second probability distribution functions of the stochastic process (1).*—Let t_1 be a value of t in the interval $(0, t_2)$, and let equation (1) be written in the form

$$u(t_2) = u(t_1) + q^{m(t_1)}\int_{t_1}^{t_2} q^{m(s)-m(t_1)}\,ds. \tag{5}$$

Since, with probability 1, we have

$$m(s) - m(t_1) = m(s - t_1), \tag{6}$$

we may introduce $s - t_1$ as a new variable of integration in equation (5) and obtain

$$u(t_2) = u(t_1) + q^{m(t_1)}\int_0^{t_2-t_1} q^{m(s)}\,ds. \tag{7}$$

Now, let

$$\Phi_n(u, t) = \text{Prob}\left[\int_0^t q^{m(s)}\,ds \geq u \mid m(t) = n\right] \tag{8}$$[2]

---

[1] Probability distribution functions in this paper are defined as monotonic nonincreasing. Although unconventional, this definition conforms to the earlier papers of the series.

[2] The symbol "Prob $[A \mid H]$" means "probability of the event A conditioned to the hypothesis H."

be the conditional probability for the brightness $u(t)$ to exceed a specified value u, on the hypothesis that a fixed number n of clouds are distributed at random in $(0, t)$. Then, from the definition of conditional probabilities, it follows that

$$f_2(u_2, t_2; u_1, t_1)$$

$$= -\sum_{n=0}^{\infty} p_n(t_1) \int_u^{\infty} \text{Prob}\,[u(t_2) \geq u_2 \mid u(t_1) = u_1' \,\&\, m(t_1) = n]\, d\Phi_n(u_1', t_1)\,, \tag{9}$$

the integral being understood in the Stieltjes sense with respect to u_1', since $\Phi_n(u, t)$ may not be differentiable for all values of u. But, according to equation (7), we have

$$\text{Prob}\,[u(t_2) \geq u_2 \mid u(t_1) = u_1' \,\&\, m(t_1) = n] = f\left(\frac{u_2 - u_1'}{q^n},\ t_2 - t_1\right), \tag{10}$$

and hence equation (9) may be written in the form

$$f_2(u_2, t_2; u_1, t_1) = -\sum_{n=0}^{\infty} p_n(t_1) \int_{u_1}^{\infty} f\left(\frac{u_2 - u_1'}{q^n},\ t_2 - t_1\right) d\Phi_n(u_1', t_1)\,. \tag{11}$$

This is the required relation. It may be noticed that by setting $u_1 = 0$ in this equation, for any $t_1 \leq t_2$, we obtain

$$f_2(u_2, t_2; 0, t_1) \equiv f(u_2, t_2)$$

$$= -\sum_{n=0}^{\infty} p_n(t_1) \int_0^{\infty} f\left(\frac{u_2 - u_1'}{q^n},\ t_2 - t_1\right) d\Phi_n(u_1', t_1)\,, \tag{12}$$

a relation between the values of $f(u, t)$ for two different values of t. In the limit as t_1 approaches t_2, we further obtain

$$f(u_2, t_2) = \sum_{n=0}^{\infty} p_n(t_2)\, \Phi_n(u_2, t_2)\,, \tag{13}$$

an obvious consequence of the definition of conditional probability. The last two equations show that the set of distribution functions $\{\Phi_n\}$ completely determines the first two probability distributions of the process defined by equation (1). Quite generally one would expect that every function f_r of the sequence (4) is also determined by the functions $\Phi_n(u, t)$.

3. *The differential equation satisfied by* $\Phi_n(u, t)$.—Let us consider the random variable

$$u(t) = \int_0^t q^{m(n,\, s)}\, ds\,, \tag{14}$$

of which $\Phi_n(u, t)$ is a distribution function. The probability $p_k(n, s)$ with which $m(n, s)$ takes a value k is now given by the binomial law,

$$p_k(n, s) = \binom{n}{k}\left(\frac{s}{t}\right)^k \left(1 - \frac{s}{t}\right)^{n-k} \qquad (k = 0, 1, 2, \ldots)\,. \tag{15}$$

Suppose $\tau \epsilon (0, t)$ is an arbitrarily fixed number. Then we may write

$$\Phi_n(u, t) = \text{Prob}\left[\int^{\tau} q^{m(n,\, s)}\, ds + q^{m(n,\, \tau)} \int_{\tau}^{t} q^{m(n,\, s) - m(n,\, \tau)}\, ds \geq u\right], \tag{16}$$

and since, with probability 1,

$$m(n, s) - m(n, \tau) = m(n, s - \tau), \tag{17}$$

we may consider $s - \tau$ as a new variable of integration in the integral extending from τ to t in equation (16). We obtain

$$\Phi_n(u, t) = \text{Prob}\left[\int_0^{\tau} q^{m(n,\, s)} d s + q^{m(n,\, \tau)} \int_0^{t-\tau} q^{m(n,\, s)} d s \geq u\right]. \tag{18}$$

Now, $m(n, \tau)$ may take any value $k = 0, 1, 2, \ldots$, with probabilities given by equation (15),

$$p_0(n, \tau) = 1 - \frac{n\tau}{t} + o\left(\frac{\tau}{t}\right),$$

$$p_1(n, \tau) = \frac{n\tau}{t} + o\left(\frac{\tau}{t}\right),$$

and

$$p_k(n, \tau) = o\left(\frac{\tau}{t}\right) \qquad \text{for } k > 1. \tag{19}$$

Therefore, neglecting terms $o(\tau)$ in equation (18), we have

$$\begin{aligned} \Phi_n(u, t) = \left(1 - \frac{n\tau}{t}\right) \text{Prob}\left[\int_0^{t-\tau} q^{m(n,\, s)} d s \geq u - \tau\right] \\ + \frac{n\tau}{t} \text{Prob}\left[\int_0^{t-\tau} q^{m(n-1,\, s)} d s \geq \frac{u - \theta\tau}{q}\right], \end{aligned} \tag{20}$$

where $q \leq \theta \leq 1$. Notice that the exponent of q under the second integral sign appearing in the last equation has been written as $m(n - 1, s)$, to take into account the occurrence of only $n - 1$ clouds in (τ, t) or $(0, t - \tau)$, when it is known that $m(\tau) = 1$. From the definition (8) of $\Phi_n(u, t)$ it follows that

$$\Phi_n(u, t) = \left(1 - \frac{n\tau}{t}\right) \Phi_n(u - \tau,\ t - \tau) + \frac{n\tau}{t} \Phi_{n-1}\left(\frac{u - \theta\tau}{q},\ t - \tau\right). \tag{21}$$

Expressing the values of Φ_n appearing in the right-hand side of equation (21) as a power series in τ and neglecting terms $o(\tau)$, we find

$$\Phi_n(u, t) + \frac{t}{n}\left(\frac{\partial \Phi_n}{\partial u} + \frac{\partial \Phi_n}{\partial t}\right) = \Phi_{n-1}\left(\frac{u}{q},\ t\right), \tag{22}$$

at those points where the derivatives have a meaning. From the definition (14) of the random variable $u(t)$ it follows that

$$\Phi_n(u, t) = \begin{cases} 0 & \text{for} \quad u > t \\ 1 & \text{for} \quad u \leq q^n t \end{cases} \qquad (n = 0, 1, 2, \ldots), \tag{23}$$

and Φ_0 is thus a step function with leap unity at $u = t$. All other functions $\Phi_n(u, t)$ should be continuous for every value of u.

4. *Solution of the differential equation satisfied by* $\Phi_n(u, t)$.—We shall construct a set of functions $\{\Phi_n\}$ which satisfy the differential recurrence relations (22) and the normalizing conditions (23). They will be required, further, to be continuous for every u at all

points of the interval (0, t) open to the right. Let the u-axis be covered by the sequence of intervals $\{\Omega_k\}$ defined by the inequalities

$$q^k t < u \leq q^{k-1} t \qquad (k = 0, \pm 1, \pm 2, \ldots) . \quad (24)$$

We may then express the normalizing conditions (23) in the form

$$\Phi_n(u, t) = \begin{Bmatrix} 0 & \text{for} & u \epsilon \Omega_{k \leq 0} \\ 1 & \text{for} & u \epsilon \Omega_{k > n} \end{Bmatrix} . \quad (25)$$

It is convenient to define the auxiliary function

$$\Psi_n(u, t) = t^{-n} \Phi_n(u, t) , \quad (26)$$

which satisfies the simpler differential equation,

$$\frac{\partial \Psi_n}{\partial u} + \frac{\partial \Psi_n}{\partial t} = n \Psi_{n-1}\left(\frac{u}{q}, \ t\right) . \quad (27)$$

The normalizing conditions are

$$\Psi_n(u, t) = \begin{Bmatrix} 0 & \text{for} & u \epsilon \Omega_{k \leq 0} \\ t^n & \text{for} & u \epsilon \Omega_{k > n} \end{Bmatrix} . \quad (28)$$

Equation (27) has a meaning only at those points where $\partial \Psi_n / \partial u$ exists. But according to equation (23), Ψ_0 is discontinuous at $u = t$. From equation (27) it follows that if $\Psi_1(u, t)$ is required to be continuous for every u, then necessarily $\partial \Psi_1 / \partial u$ will be discontinuous at $u = qt$. In this case equation (27) should be replaced by two equations, one for $\Psi_1(u - 0, t)$ and the other for $\Psi_1(u + 0, t)$. For $n > 1$, every u is a point of continuity of $\Psi_n(u, t)$, and we may solve equation (27) by noticing that, when $u \epsilon \Omega_1$, $u q^{-1} \epsilon \Omega_0$. According to equations (27) and (28), we then have

$$\frac{\partial \Psi_n}{\partial u} + \frac{\partial \Psi_n}{\partial t} = 0 \qquad (u \epsilon \Omega_1) . \quad (29)$$

The arbitrary solution of this equation may be written in the form

$$\Psi_n(u, t) = \psi_n(t - u) , \quad (30)$$

ψ_n denoting any function of its argument. Equation (29) actually is valid, also, for $n = 1$, provided that the derivatives are understood to be taken only in the right-hand neighborhood of $u = qt$.

When $u \epsilon \Omega_2$, $u q^{-1} \epsilon \Omega_1$, and, according to equation (30), we have

$$\frac{\partial \Psi_n}{\partial u} + \frac{\partial \Psi_n}{\partial t} = n \psi_{n-1}(t - u q^{-1}) \qquad (u \epsilon \Omega_2) . \quad (31)$$

We may now integrate this equation formally, following the method developed in Paper III. Consider a point $S = (u, t)$ in the Ω_2 region of the $u - t$ plane, and through S a straight line PP' of unit slope,[3] $P = (q t_0, t_0)$ denoting the intersection of this straight line with the upper boundary of the Ω_2 region. Then, if s measures the length of the segment PS, oriented in the sense from P to S, we have

$$u = q t_0 - \frac{s}{\sqrt{2}} , \qquad t = t_0 - \frac{s}{\sqrt{2}} ,$$

$$t - u = t_0 (1 - q) , \qquad t - u q^{-1} = \frac{1 - q}{q} \frac{s}{\sqrt{2}} . \quad (32)$$

---

[3] See Fig. 1 of Paper III.

Further, along PP',

$$\frac{\partial}{\partial u}+\frac{\partial}{\partial t}=-\sqrt{2}\,\frac{d}{d\,s}, \tag{33}$$

and equation (31) may be expressed in terms of the variable s alone,

$$-\sqrt{2}\,\frac{d\Psi_n}{d\,s}=n\psi_{n-1}\left(\frac{1-q}{q}\,\frac{s}{\sqrt{2}}\right). \tag{34}$$

Integrating along PP' from $s = 0$, we obtain

$$\Psi_n\,(s)\;=\Psi_n\,(0)\;-n\,\frac{q}{1-q}\int_0^{s(1-q)/q\sqrt{2}}\psi_{n-1}\,(x)\,d\,x\,. \tag{35}$$

But if Ψ_n is to be continuous across the boundary between the regions Ω_1 and Ω_2, $\Psi_n(0) = \Psi_n(qt_0, t_0)$ should be given by equation (30), and then

$$\Psi_n\,(s)\;=\psi_n\,[t_0\,(1-q)\,]\,-n\,\frac{q}{1-q}\int_0^{s(1-q)/q\sqrt{2}}\psi_{n-1}\,(x)\,d\,x\,. \tag{36}$$

Reverting to the original variables u and t, according to the transformation formulae (32), we obtain

$$\Psi_n\,(u,\,t)\;=\psi_n\,(t-u)\;+nQ_1\int_0^{t-u/q}\psi_{n-1}\,(x)\,d\,x \qquad (u\epsilon\Omega_2)\,, \tag{37}$$

where, in the notation of Paper III, we have written

$$Q_j=\,(-1)^{\,j}\prod_{l=1}^{j}q^{\,l}\,(1-q^{\,l})^{\,-1} \qquad (\,j=1,\,2,\,3,\,.\,.\,.\,)\,. \tag{38}$$

Once the form of $\Psi_n(u, t)$ has been found in Ω_2, we could consider equation (27) for $u\epsilon\Omega_3$, its right-hand member being given by equation (37), and formally integrate it. Quite generally, without much difficulty it may be proved by induction that

$$\begin{aligned}\Psi_n\,(u,\,t)\;&=\psi_n\,(t-u)\\&+\sum_{j=1}^{k-1}j\binom{n}{j}Q_j\int_0^{t-u/q^j}\left(t-\frac{u}{q^j}-x\right)^{j-1}\psi_{n-j}\,(x)\,d\,x \qquad (u\epsilon\Omega_k,\;2\leq k\leq n)\,.\end{aligned} \tag{39}$$

According to the normalization conditions (23), this equation for the particular value $u = q^n t$ gives

$$t^n=\psi_n\,[t\,(1-q^n)\,]+\sum_{j=1}^{n-1}j\binom{n}{j}Q_j\int_0^{t(1-q^{n-j})}[t\,(1-q^{n-j})\,-x]^{\,j-1}\psi_{n-j}\,(x)\,d\,x\,, \tag{40}$$

a system of integral equations for the ψ_n's of a simple recursive type which may be readily solved. From equations (30) and (28) we have

$$\psi_1\,(x)\;=\frac{x}{1-q}, \tag{41}$$

and hence, by setting $n = 2$ in equation (40), we obtain

$$\psi_2\,(x)\;=\frac{x^2}{(1-q)\,(1-q^2)}\,. \tag{42}$$

Quite generally, it may be proved by induction that equation (40) implies, for any $n \geq 1$,

$$\psi_n (x) = x^n \prod_{j=1}^{n} (1 - q^j)^{-1} . \tag{43}$$

Substituting this expression in equation (39), we obtain

$$\Psi_n (u, t) = \sum_{j=0}^{k-1} Q_j \left(t - \frac{u}{q^i} \right)^n \prod_{l=1}^{n-j} (1 - q^l)^{-1} \qquad (u \epsilon \Omega_k ; \quad k = 1, 2, \ldots , n ; \quad n = 2, 3, \ldots) . \tag{44}$$

Since, according to equations (41) and (30), this equation is valid also for $n = 1$, we may finally write for our solution the general expression

$$\Phi_n (u, t) = \sum_{j=0}^{k-1} Q_j \left(1 - \frac{u}{q^i t} \right)^n \prod_{l=1}^{n-j} (1 - q^l)^{-1} \qquad (u \epsilon \Omega_k ; \quad k = 1, 2, \ldots ; \quad n = 1, 2, \ldots) . \tag{45}$$

The correctness of equation (45) may be verified by performing the summation indicated in equation (13), which leads to an expression for $f(u, t)$ identical to the one derived in Paper III.

The moment sequences,

$$\mu_i (n, t) = - \int_0^\infty u^i d\Phi_n (u, t) \tag{46}$$

of the distribution functions Φ_n, may be evaluated explicitly from equation (45) in the form

$$\mu_i (n, t) = \frac{n! \, i!}{(n+i)!} t^i \prod_{j=1}^{n} \frac{1 - q^{j+i}}{1 - q^j} \qquad (i = 0, 1, 2, \ldots) . \tag{47}$$

5. *The moments of* $f_2(u_2, t_2; u_1, t_1)$.—The explicit evaluation of the sequence of functions $\{\Phi_n(u, t)\}$ formally solves the problem formulated in the introduction. Numerical values for $f_2(u_2, t_2; u_1, t_1)$ could be computed by means of equation (11), as it does not seem likely that an expression of simpler structure could be found. However, the bivariate moments,

$$\mu_{r, s} (t_2, t_1) = \int_0^\infty u_1^r \int_0^\infty u_2^s d_{u_1 u_2} [f_2 (u_2, t_2; u_1, t_1)] \qquad (r, s = 0, 1, 2, \ldots) , \tag{48}$$

can be explicitly evaluated in terms of the moments $\mu_i(t)$ of $f(u, t)$. For, according to equation (11), we have

$$d_{u_1 u_2} [f_2 (u_2, t_2; u_1, t_1)] = \sum_{n=0}^{\infty} p_n (t_1) \, d_{u_2} \left[f \left(\frac{u_2 - u_1}{q^n} , \ t_2 - t_1 \right) \right] d_{u_1} \Phi_n (u_1, t_1) , \tag{49}$$

and equation (48) may be rewritten in the form

$$\mu_{rs} (t_2, t_1) = \sum_{n=0}^{\infty} p_n (t_1) \int_0^\infty u_1^r d_{u_1} [\Phi_n (u_1, t_1)] \int_0^\infty u_2^s d_{u_2} \left[f \left(\frac{u_2 - u_1}{q^n} , \ t_2 - t_1 \right) \right] . \tag{50}$$

If $q^{-n}(u_2 - u_1) = x$ is introduced as a new variable of integration, and $u_2^s = (u_1 + q^n x)^s$ is expressed as a polynomial, we obtain

$$\mu_{rs}(t_2, t_1) = \sum_{k=0}^{s} \binom{s}{k} \mu_{s-k}(t_2 - t_1) \sum_{n=0}^{\infty} p_n(t_1)\, q^{n(s-k)} \int_0^{\infty} u_1^{r+k} d_{u_1}\Phi_n(u_1, t_1)\,. \quad (51)$$

The summation over the index n may be carried out explicitly by noticing that $\Phi_n(u, t)$ is a homogeneous function of degree zero, and we may write

$$\sum_{n=0}^{\infty} p_n(t_1)\, q^{n(s-k)} \int_0^{\infty} u_1^{r+k} d_{u_1}\Phi_n(u_1, t_1) = e^{-(1-q^{s-k})t_1} q^{-(r+k)(s-k)} \mu_{r+k}(t_1 q^{s-k})\,. \quad (52)$$

And, accordingly, in equation (51) we have

$$\mu_{rs}(t_2, t_1) = \sum_{k=0}^{s} \binom{s}{k} \frac{e^{-(1-q^{s-k})t}}{q^{(r+k)(s-k)}} \mu_{r+k}(t_1 q^{s-k})\, \mu_{s-k}(t_2 - t_1)\,. \quad (53)$$

Of particular importance is the case $r = 1$ and $s = 1$, for equation (53) gives then the covariance of the process

$$\mu_{11}(t_2, t_1) = \mu_2(t_1) + \frac{1}{q} e^{-(1-q)t_1} \mu_1(q t_1)\, \mu_1(t_2 - t_1)\,. \quad (54)$$

Since

$$\mu_1(t) = \frac{1}{1-q}\left[1 - e^{-(1-q)t}\right], \quad (55)$$

it is readily seen that $\mu_{11}(t_2, t_1)$, for a fixed t_1, increases monotonically from the value $\mu_{11}(t_1, t_1) = \mu_2(t_1)$ to the limit

$$\mu_{11}(t_1, \infty) = \mu_2(t_1) + \frac{\mu_1(q t_1)}{q(1-q)} e^{-(1-q)t_1}. \quad (56)$$

The degree of correlation between values of the brightness arising from parts of the system extending to distances t_2 and t_1, along the same line of sight, is then measured by the quantity

$$R(t_2 - t_1) = \frac{\mu_{11}(t_1, \infty) - \mu_{11}(t_1, t_2)}{\mu_{11}(t_1, \infty) - \mu_{11}(t_1, t_1)} = e^{-(1-q)(t_2 - t_1)}, \quad (57)$$

an expression which shows that the correlation function of the stochastic process (1) has a simple exponential form, as it should be for a pure random discontinuous process.

6. *Concluding remarks.*—According to equation (57), we would expect that the correlation between the contributions to the total surface brightness of the Milky Way, arising from parts of the system extending to two different distances t_2 and t_1 would effectively disappear when

$$t_2 - t_1 = \frac{1}{1-q}\,.$$

Since t measures distances in units of ν^{-1}, ν being the mean number of clouds per unit distance, adopting the values $\nu = 8$ kpc^{-1} and $q = 0.80$ (Chandrasekhar and Münch 1950*a*), we obtain a correlation distance

$$S_0 = \frac{1}{\nu(1-q)} \simeq 600 \text{ psc}\,.$$

The order of magnitude of this distance would imply that the values of the surface brightness of the Milky Way, largely determined by absorbing clouds and stars at distances less than 500 psc, should not be correlated in the sense of equation (57), with the values of the surface density of B-type stars in the *Henry Draper Catalogue*, which extend to a mean distance of the order of 1 kpc. For, within 1 kpc from the sun, the large-scale deviations from uniformity in the distribution of B stars arising from the spiral structure are not very pronounced. The variations in the surface density of early-type stars are thus mostly due to foreground interstellar extinction. We should expect, accordingly, the color excesses of B stars to be uncorrelated to the local values of the surface brightness of the Milky Way. The observations seem to indicate such lack of correlation, as G. A. Shajn (Ambarzumian 1950) has noticed.

REFERENCES

Ambarzumian, V. A. 1950, *Trans. Internat. Astr. Union*, **7**, 452.
Chandrasekhar, S., and Münch, G. 1950*a*, *Ap. J.*, **112**, 380.
———. 1950*b*, *ibid.*, p. 393.
———. 1951, *ibid.*, **114**, 110.
Levy, P. 1948, *Processus stochastiques et mouvement Brownien* (Paris: Gauthier-Villars), p. 30.
Münch, G., and Chandrasekhar, S. 1952, *Ap. J*, **115**, 94.
Wang, M. C., and Uhlenbeck, G. E. 1945, *Rev. Mod. Phys.*, **17**, 323.

ON THE ABUNDANCE OF INTERSTELLAR BERYLLIUM*

Lyman Spitzer, Jr., and George B. Field
Princeton University Observatory

Received August 26, 1954

ABSTRACT

A search for the ultraviolet *Be* II lines on high-dispersion spectra of χ^2 Ori and ζ Per yields negative results. The resultant upper limits on *N*(*Be* II), the number of *Be* II ions in the line of sight, combined with the values of *N*(*Na* I), found from the ultraviolet *Na* doublet, yield an upper limit of about 2×10^{-3} for *N*(*Be* II)/*N*(*Na* I). To find the over-all *Be*/*Na* ratio, this upper limit must be decreased by the ratio *N*(*Na* I)/*N*(*Na* II), whose value will depend on whether the absorbing cloud is an *H* I or an *H* II region. The assumption that the ratio of gas to dust is the same in these clouds as in the Galaxy at large makes it possible to compute the number of *H* atoms in the line of sight from the observed color excess. This computed number is an order of magnitude too great for an *H* II region, in view of the absence of any interstellar Balmer emission from the neighborhood of these stars. Analysis of conditions in an *H* I region shows that *N*(*Na* I)/*N*(*Na* II) is probably about 2×10^{-2}, and the ratio *N*(*Be*)/*N*(*Na*) becomes less than about 4×10^{-5}. This low value is about an order of magnitude less than the mean of the values found in the sun or in meteorites. The ratio *N*(*Ca*)/*N*(*Na*) is also believed to be less in the interstellar gas than in the sun and in meteorites by a factor of about 40. Possibly both *Ca* and *Be* atoms, to a greater extent than *Na* atoms, may be locked up in grains.

Several years ago a search for interstellar *Li* and *Be* (Spitzer 1949) yielded negative results but led to an upper limit on the *Be*/*Na* ratio about equal to the relative abundance of these elements in meteorites. Additional observational material has now been obtained for the two stars ζ Per and χ^2 Ori with higher dispersion than was used previously. While the *Be* II lines at λ 3130.42 and λ 3131.06 were again not observed, the upper limit on the *Be*/*Na* ratio is now considerably reduced.

I. OBSERVATIONS

The plates, which were taken at the coudé focus of the 100-inch telescope, showed the *Na* I ultraviolet lines at λ 3302.34 and λ 3302.94. To determine upper limits on the ratio of *Be* to *Na*, the equivalent widths of these *Na* lines were measured in the two stars. The results are shown in Table 1. For χ^2 Ori the equivalent widths found here differ somewhat from those obtained by Dunham (1939), who found 0.060 A and 0.040 A for these two lines.

To determine an upper limit on the equivalent widths of the *Be* II lines in χ^2 Ori, the following procedure was used. A parabolic profile of about the same width as that observed for the ultraviolet *Na* lines (0.3 A) was assumed, and this profile was fitted to the tracing at the expected position of each *Be* II line and with the greatest depth consistent with the tracing. The upper limits obtained in this way were 0.018 A for λ 3131.06 and 0.015 A for λ 3130.42.

For ζ Per a different procedure was followed. On each of the two 114-inch plates a faint, sharp, presumably interstellar line could be seen some 12 A longward of the *Be* II doublet. Since this line was near the margin of visibility, its equivalent width was taken as an upper limit for the equivalent width of either of the two *Be* II lines. This procedure for determining an upper limit is perhaps more definite and less subject to criticism than the procedure used for χ^2 Ori. Measures on the tracings gave an equivalent width of 0.0052 A for this line on Plate 8410, and 0.0076 A on Plate 8418, averaging

---

* This article is based on observations made by the senior author as guest investigator at the Mount Wilson and Palomar Observatories.

0.0064 A. If the procedure used for χ^2 Ori were used for ζ Per, the upper limit found would be somewhat less than 0.0064 A.

The identification of this sharp absorption line in the spectra of ζ Per is itself a problem. The measured wave length, corrected for the earth's motion, is 3143.35 A, with virtually identical results for the two plates. If the interstellar clouds in the direction of ζ Per are assumed to have a velocity of +12.0 km/sec, the value obtained by Adams (1949) for K and H, the wave length of this line corrected for the Doppler shift of the cloud becomes 3143.22 A. An *Fe* I ultimate line at 3143.24 A might be a reasonable identification. Unfortunately, the line λ 3193.21, another ultimate line in the same multiplet, does not appear on either of the two high-dispersion plates of ζ Per. According to R. B. King and A. S. King (1938), the *f*-value of λ 3193.21 is ten times that for λ 3143.24. Failure of the stronger line to appear would seem to rule out the identification of this sharp, presumably interstellar feature as a line of neutral *Fe*. Lines of interstellar molecules are relatively strong in ζ Per, and λ 3143.2 may perhaps be a molecular feature.

TABLE 1

EQUIVALENT WIDTHS OF ULTRAVIOLET *Na* LINES

STAR	PLATE NO.	CAMERA	*W* FOR	
			λ 3302.34	λ 3302.94
χ^2 Ori	8526	73-in.	0.075 A	0.037 A
ζ Per	8348	73-in.	.030	.014
	8410	114-in.	.028	.015
	8418	114-in.	.024	.019
	Mean	....	0.027	0.017

II. NUMBER OF ABSORBING ATOMS

The observations give directly an upper limit on the ratio $N(Be\ \text{II})/N(Na\ \text{I})$, where N is the number of atoms in the line of sight, per square centimeter. For unsaturated lines the equivalent width W is given by

$$W = \frac{\pi N e^2 \lambda^2 f}{m c^2}, \tag{1}$$

where W and λ are both measured in centimeters, f is the upward oscillator strength, and other symbols have their usual meanings. Equation (1) may be applied to the *Be* II lines, and also to the ultraviolet *Na* lines in χ^2 Ori.

For the *Na* I ultraviolet lines in ζ Per, equation (1) must be modified slightly to take into account the effects of saturation, indicated by the doublet ratio less than 2.0. The theory of the equivalent width for Doppler-broadened lines has been given by Ladenburg (1930); Strömgren (1948) has given the appropriate functions in a table (Table 2 in his paper) suitable for numerical computations. With the measured value of the doublet ratio, the number of absorbing atoms may be obtained. If the true doublet ratio is substantially less than the measured value, 1.59, which might be anticipated for a single, dense, and relatively quiescent *H* I cloud, $N(Na\ \text{I})$ in the line of sight to ζ Per will exceed the value given in Table 2, and the upper limit on $n(Be)/n(Na)$ will be decreased.

The *f*-values needed have been measured, for the *Na* ultraviolet lines, by Filippov and Prokofjew (1929); they find values of 0.0094 and 0.0047 for the stronger and weaker lines, respectively, in the doublet. For the resonance lines of *Be* II no detailed computations or measures are apparently available. For the corresponding resonance lines in *Mg* II and *Ca* II the theoretical *f*-values are (Biermann 1950) 0.92 and 1.19; these values include both lines in the doublet. A similar rise in *f*-value with increasing atomic number is shown by the corresponding sequence of resonance lines of *Li* I, *Na* I, and *K* I, for which the reported *f*-values (Biermann 1950) are 0.71, 1.00, and 1.05. An *f*-value of about 0.75 for the *Be* II doublet seems reasonable; accordingly, *f* has been set equal to 0.50 for λ 3130.42 and to 0.25 for λ 3131.06. The resultant values of N are given in Table 2.

III. TOTAL NUMBER OF ATOMS

To obtain an upper limit on the ratio of beryllium to sodium in the interstellar gas, the ratios given in Table 2 must be corrected for the number of atoms in other states of ionization. The ionization equilibrium will depend on the first and second ionization potentials, which are 9.3 and 18.1 volts, respectively, for *Be;* 5.1 and 47.1 volts for *Na;* and 6.1 and 11.8 for *Ca*. We shall carry out separate analyses on the two assumptions: (*a*) the material producing the interstellar lines is an *H* I cloud (hydrogen neutral), and (*b*) the material is an *H* II region (hydrogen ionized). We shall draw heavily here on Strömgren's (1948) analysis of ionization equilibrium in the interstellar gas.

TABLE 2

NUMBER OF ATOMS IN LINE OF SIGHT

	N (*Be* II)	N(*Na* I)	N(*Be* II)/ N(*Na* I)
χ^2 Ori....	3.5×10^{11} cm^{-2}	8.2×10^{13} cm^{-2}	4.3×10^{-3}
ζ Per....	1.4×10^{11}	5.0×10^{13}	2.8×10^{-3}

a) H I CLOUD

If the hydrogen is neutral, there will be essentially no radiation shortward of 13.5 ev, and no *Be* III will be present. The ratio $n(Be\ \text{II})/n(Be\ \text{I})$ will be considerably greater than unity; it is evident from Strömgren's analysis that $n(Ca\ \text{III})/n(Ca\ \text{II})$ is usually greater than unity, and *Be* I, with a lower ionization potential and a higher *f*-value for the bound-free transition from the ground state, should be ionized more readily than *Ca* II. We shall therefore set $n(Be)$, the number of *Be* atoms per cubic centimeter, in all stages of ionization, equal to $n(Be\ \text{II})$.

The ratio of *Na* I to *Na* II may be found from the result by Strömgren (1948) for a kinetic temperature of 100° K,

$$\frac{n\ (Na\ \text{I})}{n\ (Na\ \text{II})} = 0.60 n_e . \tag{2}$$

If we assume, with Strömgren, that the relative abundances of the elements in the interstellar gas are about the same as in stars, we may set n_e equal to about 200 $n(Na\ \text{II})$. Also $N(Na\ \text{I})$, the number of neutral sodium atoms in the line of sight, may be set equal to $n(Na\ \text{I})d$, where d is the thickness of the cloud producing the observed lines. Equation (2) then yields the values in Table 3.

Since $n(H)/n_e$ is probably at least 2000 in an *H* I cloud (if *H* atoms in H_2 molecules are included in $n[H]$), a value of d as low as 0.1 parsec corresponds to a very high cloud density, at least 500 atoms/cm^3. So small a cloud seems improbable, and we may tentatively assume that d is 10 parsecs. Further evidence for this assumption will be given later. On this basis, the upper limits on $n(Be)/n(Na)$, found on combining the results in Tables 2 and 3, become 7.3×10^{-5} in χ^2 Ori and 3.9×10^{-5} in ζ Per. These values may be compared with the corresponding ratios of 6.3×10^{-4} in meteorites—according to Urey (1952)—and 1.5×10^{-4} in the sun—according to Greenstein and Tandberg-Hanssen (1954). The solar value is based on an assumed ratio of 2.5 for $n(Ca)/n(Na)$.

b) *H* II CLOUD

In this case *Be* II can be ionized to *Be* III. However, comparison with Strömgren's results for *Ca* and consideration of the 6.5-volt difference in ionization potential between *Ca* II and *Be* II indicate that, for the electron densities of interest, $n(Be\ \text{III})/n(Be\ \text{II})$ will be small. As in *H* I regions, $n(Be\ \text{I})/n(Be\ \text{II})$ will also be small, and we may again set $n(Be)$ equal to $n(Be\ \text{II})$.

TABLE 3

RELATIVE IONIZATION OF SODIUM IN *H* I REGIONS

d (PARSECS)	χ^2 ORI		ζ PER	
	n_e	$n(Na\ \text{I})/n(Na\ \text{II})$	n_e	$n(Na\ \text{I})/n(Na\ \text{II})$
0.1	2.9×10^{-1} cm^{-3}	1.7×10^{-1}	2.3×10^{-1} cm^{-3}	1.4×10^{-1}
1	9.2×10^{-2}	5.5×10^{-2}	7.3×10^{-1}	4.4×10^{-2}
10	2.9×10^{-2}	1.7×10^{-2}	2.3×10^{-2}	1.4×10^{-2}

TABLE 4

RELATIVE IONIZATION OF SODIUM IN *H* II REGIONS

d	0.1 Parsec	1 Parsec	10 Parsecs
n_e	<50 cm^{-3}	<15.8 cm^{-3}	<5.0 cm^{-3}
$n(Na\ \text{I})/n(Na\ \text{II})$	<1.0	<0.30	<0.10

The ratio of *Na* I to *Na* II in an *H* II region at 10,000° K, according to Strömgren, is

$$\frac{n\ (Na\ \text{I})}{n\ (Na\ \text{II})} = 0.019 n_e\,. \tag{3}$$

The product of n_e^2 and the thickness of the cloud, in parsecs, is called the "emission measure." According to Sharpless and Strömgren,[1] the emission measure in the line of sight to χ^2 Ori and ζ Per does not exceed 250 in either case. We thus obtain upper limits both for n_e and for $n(Na\ \text{I})/n(Na\ \text{II})$, as given in Table 4.

Again a cloud as small as 0.1 parsec in thickness seems very improbable. At a density comparable with 5cm^{-3}, such a cloud would expand at roughly the sound velocity of about 20 km/sec and would double its radius in 5000 years. Even a cloud 1 parsec across seems unlikely. We shall take 0.1 as a reasonable upper limit for $n(Na\ \text{I})/n(Na\ \text{II})$ in *H* II regions.

We see that in this case the ratio of *Be* to *Na* in the interstellar gas is less than about 3×10^{-4}, unless the clouds producing the observed lines in χ^2 Ori and ζ Per turn out to be unexpectedly dense. This upper limit is less than the value observed in meteorites but greater than the value found in the sun. In view of the many uncertainties, one may in this case conclude only that the abundance of *Be* relative to *Na* is no greater in interstellar space than it is in meteorites.

---

[1] We are much indebted to Drs. Sharpless and Strömgren for permission to use their unpublished results.

IV. RATIO OF GAS TO DUST

Evidently, a consideration only of observed equivalent widths and computed ionization conditions does not yield a very low upper limit on the *Be*/*Na* ratio, because of uncertainty as to whether or not *H* is ionized, in addition to uncertainty as to cloud size. However, the measured color excesses of χ^2 Ori and ζ Per yield additional information on the interstellar medium, which we may now take into account.

Specifically, if the ratio of gas to dust is assumed to be roughly constant throughout the Galaxy, a definite decision can be made between the assumptions of *H* I and *H* II regions in the line of sight to these stars. This assumption of uniformity is theoretically plausible and is supported, moreover, by recent measurements of *H* emission at 21 cm.

TABLE 5

DENSITY OF HYDROGEN IN χ^2 ORI CLOUD

SOURCE OF INFORMATION	$n(H)$ FOR CLOUD OF THICKNESS:		
	0.1 Parsec	1 Parsec	10 Parsecs
Color excess	7500 cm^{-3}	750 cm^{-3}	75.0 cm^{-3}
$N(Na$ I$)$, *H* I region assumed	580	180	58.0
Emission measure, *H* II region assumed	<50	<16	<5.0

Lilley (1954) has shown that regions of high 21-cm emission at galactic latitudes of −15° coincide with regions of high optical extinction. If we accept this assumption, then $N(H)$, the number of *H* atoms (including those in H_2 molecules) in the line of sight to a star, is a linear function of E_1, the photoelectric color excess of the star. According to Stebbins, Huffer, and Whitford (1940*b*), the mean increase of E_1 per kiloparsec is 0.26. Since the mean density of *H* atoms per cubic centimeter in the galactic plane is about 1, we have

$$N(H) = 1.2 \times 10^{22} E_1 . \tag{4}$$

The same value of $N(H)/E_1$ is found from the detailed correlation of extinction and 21-cm emission observed by Lilley (1954).

The density of *H* atoms per cubic centimeter in a cloud of thickness *d* equals simply $N(H)/d$. For χ^2 Ori, E_1 is 0.19, according to Stebbins, Huffer, and Whitford (1940*a*). The values of $n(H)$ found from equation (4) are shown in Table 5. Also shown are the corresponding densities computed for an *H* I cloud in the line of sight to χ^2 Ori, found from Table 3 on the assumption that $n(H)$ equals 2000 n_e, and for an *H* II cloud found from Table 4 with the obvious assumption that n_e equals $n(H)$. For ζ Per the results are closely similar, since the color excess for this star is 0.17.

While the computed densities for *H* I regions are somewhat hypothetical, relying as they do on assumed ratios of n_e to $n(Na)$ and of n_e to $n(H)$, the upper limits on the *H* densities in an *H* II region are rather direct results of the low emission measure for these regions. Evidently, the assumption of an *H* II cloud in the line of sight to these stars is grossly inconsistent with a uniform ratio of gas to grains. To reconcile the high color excess with the observed absence of Balmer emission requires a ratio of grains to gas a full order of magnitude greater than is found elsewhere in the Galaxy. Such an extreme condition seems implausible, though it cannot be excluded. Assumption of several clouds in the line of sight does not alter the situation appreciably, since most of the clouds must be H I regions, to avoid large Balmer emission, and the ultraviolet Na lines will be produced with about the strength observed.

While the assumption of an H II cloud may therefore be excluded, at least tentatively, very small H I clouds also seem ruled out by the values in Table 5. A cloud thickness of 10 parsecs, which seems most likely in any case, provides the best agreement between the different values of n (H). For this value of the cloud thickness we have already seen that the Be/Na ratio becomes less than about 5×10^{-5}, about a third of the value found in the sun and a fifteenth of the value observed in meteorites. Since the adopted upper limits are believed to be conservative, the actual Be/Na ratio in the interstellar gas is probably appreciably less than 5×10^{-5} and we may conclude that the ratio of Be to Na in the interstellar gas is probably an order of magnitude less than in the solar system and in stars generally.

V. DISCUSSION OF RESULTS

At one time it was thought likely that if the interstellar gas were primordial and had never been heated to thermonuclear temperatures, the relative abundance of Be in interstellar space might be higher than elsewhere. The present discussion suggests precisely the opposite result, with a relative Be abundance less in interstellar space than anywhere else. This unexpected conclusion cannot be regarded as established, since it rests on the assumption that the ratio of gas to dust is about the same in different clouds. In addition, uncertain assumptions as to the chemical composition of the interstellar gas enter into the precise result. However, the weight of existing evidence seems to favor the tentative conclusion that the Be/Na ratio is definitely less in the interstellar gas than in the sun and the meteorites.

This result is perhaps related to the conclusion by Strömgren (1948) that the Ca/Na ratio for the interstellar gas appears to be less by a factor of 40 than the corresponding ratio for meteorites. The atoms of Ca and Be are chemically similar, and any influence affecting one might also affect the other.

It is difficult to believe that the abundance of Ca and Be nuclei is much less in the interstellar medium as a whole than in the solar system and in the stars. Such a difference would be most difficult to account for theoretically. However, if Ca and Be are primarily concentrated in the interstellar grains, while Na atoms are mostly in the gaseous phase, the observed abundance differences are readily explained. As suggested by Spitzer (1954), surface photodissociation of atoms from grains might well be markedly different for different atoms and could perhaps account for different fractions of atoms being "locked up" in the grains. Such physical mechanisms are still somewhat speculative, but the possibility that both Be and Ca atoms are preferentially concentrated in the grains rather than in the interstellar gas would seem to offer a reasonable working hypothesis, consistent with presently known data.

REFERENCES

Adams, W. S. 1949, *Ap. J.*, **109**, 354.
Biermann, L. 1950, *Landolt-Bornstein Tables* (6th ed.), Vol. **1**, Part 1, sec. 13.181.
Brown, H. 1949, *Rev. Mod. Phys.*, **21**, 625.
Dunham, R. 1939, *Proc. Am. Phil. Soc.*, **81**, 277.
Filippov, A., and Prokofjew, W. K. 1929, *Zs. f. Phys.*, **56**, 458.
Greenstein, J., and Tandberg-Hanssen, E. 1954, *Ap. J.*, **119**, 113.
King, R. B. and A. S. 1938, *Ap. J.*, **87**, 24.
Ladenburg, R. 1930, *Zs. f. Phys.*, **65**, 200.
Lilley, A. E. 1954, *A.J.*, **59**, 327.
Spitzer, L., Jr. 1949, *Ap. J.*, **109**, 548.
———. 1954, *ibid.*, **120**, 1.
Stebbins, J., Huffer, C. M., and Whitford, A. 1940*a*, *Ap. J.*, **91**, 20.
———. 1940*b*, *ibid.*, **92**, 193.
Strömgren, B. 1948, *Ap. J.*, **108**, 242.
Urey, H. C. 1952, *Phys. Rev.*, **88**, 248.

WAVE LENGTHS OF FORBIDDEN NEBULAR LINES

IRA S. BOWEN
Mount Wilson and Palomar Observatories
Carnegie Institution of Washington, California Institute of Technology

Received November 22, 1954

ABSTRACT

With the aid of the coudé spectrograph of the Hale telescope, the wave lengths of 88 forbidden nebular lines have been measured with an accuracy substantially greater than that of the values calculated from extreme ultraviolet laboratory spectra.

With the exception of the lines of *O* I, it has not been possible to produce in the laboratory with any certainty the forbidden lines which play a prominent role in nebular spectra. The wave lengths of these lines have therefore been calculated from the differences between the levels of the terms of the ground configurations of the ions concerned. These levels have, in turn, been fixed from the wave lengths of the extreme ultraviolet lines connecting them with the high terms in the ions. An error of $\Delta\lambda$ in the wave length of these ultraviolet lines results in an error in the wave length of the calculated forbidden line of $(\Delta\lambda)(\lambda_f/\lambda_u)^2$, in which λ_f and λ_u are the wave lengths of the forbidden and ultraviolet lines, respectively. In the case of most of the forbidden lines observed in the nebulae, (λ_f/λ_u) lies between 4 and 25. Furthermore, since the ultraviolet wave lengths have been determined with relatively short-focus vacuum spectrographs, the error, $\Delta\lambda$, in λ_u is often 0.01 A or more. Uncertainties as large as a few angstroms may therefore exist in many of the calculated wave lengths of these lines.

The great light-gathering power of the Hale telescope and the high speed of its coudé spectrograph now make it possible to observe the spectra of the brighter planetary nebulae with moderately high dispersion and therefore to fix the wave lengths of the forbidden nebular lines directly with an accuracy considerably greater than that which can be obtained from the laboratory measurements. In the present investigation the stronger lines were observed with a dispersion of 9 A/mm in the ultraviolet and blue region and of 13.5 A/mm in the region of longer wave lengths. Fainter lines were measured at 18 or 38 A/mm in the shorter-wave-length range and at 27 or 57 A/mm in the visual and infrared region. Where possible, lines were observed in several nebulae, in order to decrease errors caused by differences in velocities between the ions emitting the forbidden lines and the *H* and *He* atoms producing the permitted lines used to establish the velocity corrections. The second, third, and fourth columns of Table 1 list the average wave lengths determined from these measurements, the number of plates on which each line was measured, the number of nebulae in which the line was observed, and the average deviation from the mean of the individual measurements The only previous measurements of comparable accuracy are those of several of the brightest lines made by O. C. Wilson (1950) on plates taken with the 100-inch telescope at a dispersion of 10 A/mm for the shorter-wave-length region and at 20 A/mm for the longer region. The sixth column of the table, marked "Mean λ," is an average of Wilson's measurements with the present determination, weighted according to the number and dispersion of plates used by each observer.

An indication of the accuracy of the various determinations is given in the seventh column. Results marked "A" have been obtained from measurements in several nebulae, using the highest dispersion, and can probably be depended on to 0.02 A. Those marked "B" are fainter lines and are based on fewer observations, particularly at the highest

TABLE 1

WAVE LENGTHS OF FORBIDDEN LINES

TRANSITION	λ	NO. OF PLATES	NO. OF NEBULAE	AVERAGE DEVIATION	MEAN λ (I.S.B.–O.C.W.)	ACCURACY	WAVE NO.
				N I			
$^4S-{}^2D_{5/2}$	5200.41	2	1	±0.04	....	C	19223.9
$^4S-{}^2D_{3/2}$	5197.94	2	1	±0.07	....	C	19233.1
				N II			
$^3P_2-{}^1D$	6583.37	9	5	±0.08	6583.39	B	15185.6
$^3P_1-{}^1D$	6548.06	9	5	± .05	6548.06	B	15267.5
$^1D-{}^1S$	5754.57	6	2	±0.02	....	B	17372.7
				O I			
$^3P_2-{}^1D$	6300.31	5	2	±0.04	6300.30	B	15867.9
$^3P_1-{}^1D$	6363.82	5	2	±0.02	....	B	15709.5
				O II			
$^4S-{}^2D_{5/2}$	3728.80	16	7	±0.03	3728.80	A	26810.7
$^4S-{}^2D_{3/2}$	3726.04	16	7	± .02	3726.05	A	26830.5
$^2D_{5/2}-{}^2P$	7319.92	3	1	± .08	....	C	13657.6
$^2D_{3/2}-{}^2P$	7330.19	3	1	±0.06	....	C	13638.5
				O III			
$^3P_2-{}^1D$	5006.86	11	7	±0.02	5006.85	A	19967.1
$^3P_1-{}^1D$	4958.93	11	7	± .03	4958.92	A	20160.1
$^3P_0-{}^1D$	4931.0	2	1	± .05	....	D	20274
$^1D-{}^1S$	4363.19	6	6	±0.01	4363.21	A	22912.5
				F IV			
$^3P_2-{}^1D$	4060.23	3	3	±0.03	....	D	24622.2
$^3P_1-{}^1D$	3997.40	2	2	±0.04	....	D	25009.2
				Ne III			
$^3P_2-{}^1D$	3868.76	12	6	±0.02	3868.76	A	25840.8
$^3P_1-{}^1D$	3967.47	12	6	±0.02	3967.47	A	25197.9

TABLE 1—*Continued*

Transition	λ	No. of Plates	No. of Nebulae	Average Deviation	Mean λ (I.S.B.—O.C.W.)	Accuracy	Wave No.
Ne IV							
$^2D_{5/2}-{}^2P_{3/2}$	4714.25	3	2	±0.03	....	B	21206.4
$^2D_{5/2}-{}^2P_{1/2}$	4715.61	3	2	± .06	....	B	21200.3
$^2D_{3/2}-{}^2P_{3/2}$	4724.15	3	2	± .02	....	B	21161.9
$^2D_{3/2}-{}^2P_{1/2}$	4725.62	3	2	±0.02	....	B	21155.3
Ne V							
$^3P_2-{}^1D$	3425.87	10	4	±0.05	3425.87	A	29181.3
$^3P_1-{}^1D$	3345.84	5	4	±0.01	3345.83	A	29879.4
S I							
$^1D-{}^1S$	7726.5	1	1	....	....	D	12939
S II							
$^4S-{}^2P_{3/2}$	4068.60	7	5	±0.03	4068.60	A	24571.6
$^4S-{}^2P_{1/2}$	4076.35	5	3	± .03	4076.35	A	24524.9
$^4S-{}^2D_{5/2}$	6716.42	8	4	± .08	....	B	14884.8
$^4S-{}^2D_{3/2}$	6730.78	7	4	±0.05	....	B	14853.0
S III							
$^3P_1-{}^1S$	3721.8	....	....	....	....	C	26861
$^1D-{}^1S$	6312.06	6	3	±0.05	....	B	15838.3
Cl III							
$^4S-{}^2D_{5/2}$	5517.66	3	2	±0.08	....	C	18118.6
$^4S-{}^2D_{3/2}$	5537.6	4	3	±0.24	....	D	18053
Cl IV							
$^3P_2-{}^1D$	8045.63	2	2	±0.05	....	C	12425.7
$^3P_1-{}^1D$	7530.54	2	1	± .01	....	C	13275.6
$^1D-{}^1S$	5323.29	3	1	±0.10	....	C	18780.2

TABLE 1—*Continued*

TRANSITION	λ	NO. OF PLATES	NO. OF NEBULAE	AVERAGE DEVIATION	MEAN λ (I.S.B.–O.C.W.)	ACCURACY	WAVE NO.
				A III			
${}^3P_2-{}^1D$	7135.80	5	3	±0.05	....	B	14010.0
${}^3P_1-{}^1D$	7751.06	5	3	± .15	....	C	12897.9
${}^1D-{}^1S$	5191.82	3	1	±0.03	....	C	19255.7
				A IV			
${}^4S-{}^2D_{5/2}$	4711.33	6	5	±0.02	4711.34	A	21219.5
${}^4S-{}^2D_{3/2}$	4740.20	6	5	± .02	4740.20	A	21090.3
${}^2D_{5/2}-{}^2P_{3/2}$	7237.26	2	1	± .28	....	D	13813.6
${}^2D_{3/2}-{}^2P_{3/2}$	7170.62	2	1	± .08	....	C	13942.0
${}^2D_{3/2}-{}^2P_{1/2}$	7262.76	2	1	±0.24	....	D	13765.1
				A V			
${}^3P_2-{}^1D$	7005.67	3	1	±0.09	....	C	14270.2
${}^3P_1-{}^1D$	6435.10	4	2	± .05	....	C	15535.5
${}^1D-{}^1S$	4625.54	2	1	±0.04	....	C	21613.1
				K IV			
${}^3P_2-{}^1D$	6101.83	6	3	±0.08	....	C	16384.0
${}^1D-{}^1S$	4510.9	2	2	±0.08	....	D	22162
				K V			
${}^4S-{}^2D_{5/2}$	4122.63	3	2	±0.05	....	C	24249.5
${}^4S-{}^2D_{3/2}$	4163.30	5	3	±0.05	....	C	24012.7
				Ca V			
${}^3P_2-{}^1D$	5309.18	4	1	±0.04	....	C	18830.1
${}^3P_1-{}^1D$	6086.92*	3	1	±0.11	....	C	16424.1
				Mn V			
${}^4F_{9/2}-{}^4P_{5/2}$	6393.6	1	1	....	....	E	15636
${}^4F_{7/2}-{}^4P_{5/2}$	6166.2	1	1	....	....	E	16213
${}^4F_{5/2}-{}^4P_{1/2}$	6218.6	1	1	....	....	E	16076
	6221.0	1	1	....	....	....	16070
${}^4F_{9/2}-{}^2G_{9/2}$	5891.1	2	1	±0.34	....	E	16970
${}^4F_{7/2}-{}^2G_{7/2}$	5862.3	1	1	....	....	E	17053
	5864.8	1	1	....	....	....	17046

* Blend.

TABLE 1—*Continued*

TRANSITION	λ	NO. OF PLATES	NO. OF NEBULAE	AVERAGE DEVIATION	MEAN λ (I.S.B.−O.C.W.)	ACCURACY	WAVE NO.
				Mn VI			
$^3F_2-^1D$	6518.3	1	1	....	....	E	15337
$^3F_4-^3P_2$	5894.0	1	1	....	....	E	16962
$^3F_3-^3P_1$	5776.4	1	1	....	....	E	17307
				Fe III			
$^5D_3-^3P_2$	5270.3	2	1	±0.14	....	D	18969
$^5D_3-^3F_3$	4701.5	1	1	....	....	E	21264
$^5D_2-^3F_2$	4733.7	1	1	....	....	E	21119
$^5D_4-^3F_3$	4606.5	2	1	±0.14	....	D	21702
				Fe V			
$^5D_3-^3P_2$	3895.6	1	1	....	....	D	25663
$^5D_2-^3P_1$	4072.1	2	1	±0.10	....	D	24550
$^5D_1-^3P_0$	4180.9	1	1	....	....	E	23912
$^5D_4-^3F_4$	3891.3	2	1	±0.10	....	D	25691
$^5D_3-^3F_3$	3839.6	1	1	....	....	E	26037
$^5D_3-^3F_2$	3851.8	1	1	....	....	E	25955
				Fe VI			
$^4F_{9/2}-^4P_{5/2}$	5676.96	2	1	±0.16	....	D	17610.2
$^4F_{7/2}-^4P_{5/2}$	5426.6	1	1	....	....	E	18423
$^4F_{7/2}-^4P_{3/2}$	5630.82	2	1	± .17	....	D	17754.5
$^4F_{5/2}-^4P_{3/2}$	5423.9	1	1	....	....	D	18432
$^4F_{5/2}-^4P_{1/2}$	5484.78	2	1	± .02	....	D	18227.2
$^4F_{3/2}-^4P_{1/2}$	5335.23	3	1	± .17	....	C	18738.1
$^4F_{9/2}-^2G_{9/2}$	5176.43	2	1	± .04	....	C	19313.0
$^4F_{7/2}-^2G_{7/2}$	5145.77	2	1	± .07	....	C	19428.0
$^4F_{5/2}-^2G_{7/2}$	4972.1	2	1	±0.05	....	D	20107
				Fe VII			
$^3F_4-^1D$	6598.8	1	1	....	....	E	15150
$^3F_3-^1D$	6086.92*	4	1	±0.11	....	C	16424.1
$^3F_2-^1D$	5721.11	3	1	± .10	....	C	17474.3
$^3F_4-^3P_2$	5277.67	2	1	± .28	....	D	18942.5
$^3F_3-^3P_2$	4944.0	2	1	± .27	....	D	20221
$^3F_3-^3P_1$	5158.98	2	1	± .10	....	D	19378.3
$^3F_2-^3P_1$	4893.4	2	1	±0.18	....	D	20430

dispersion. The wave lengths of these lines are therefore more uncertain and may be in error by as much as 0.04 A. Still fainter and more uncertain are the "C" and "D" classes, whose errors may range up to 0.1 and 0.3 A, respectively. The lines marked "E" are, in general, represented by a very faint line on one of the lowest-dispersion plates. In these cases the reality and identification of the line may be subject to some doubt. In two of these cases two lines are listed for a given transition, since both fall within the range of uncertainty of position as predicted from the ultraviolet laboratory measurements.

The last column of the table lists the wave number corresponding to the wave length given in the sixth column if this is present or, if not, that in the second column. The wave numbers are included, since in most cases they provide the most precise data now available for fixing the relative positions of the levels of the ground configurations of these ions.

The largest revisions in the wave lengths occur in the case of *Ne* IV. The predicted wave lengths as given in the *Revised Multiplet Table* by Charlotte E. Moore are based on the analysis of *Ne* IV by Paul and Polster (1941). A study of the wave-length table from which this analysis was made indicates that the classification of the line at $\lambda = 469.865$ should be changed from $2s^22p^{3\,2}D_{3/2}-2s2p^{4\,2}D_{5/2}$ to $2s^22p^{3\,2}D_{3/2}-2s2p^{4\,2}D_{3/2}$, while the line at $\lambda = 469.817$ should be assigned to the single transition $2s^22p^{3\,2}D_{5/2}-2s2p^{4\,2}D_{5/2}$. On the whole, the new assignments show a better agreement between observed and theoretical intensities in the lines of the multiplet concerned and also yield separations between the $2s^22p^{3\,2}P$ and ^2D terms in better agreement with those given by other extreme ultraviolet lines than the old classification. The levels of the ground configuration fixed on the basis of the new classification predict the forbidden lines at positions within a few tenths of an angstrom of the wave lengths listed in the table. As would be expected for this stage of ionization, the lines identified as *Ne* IV are observed only in high-excitation nebulae, namely, NGC 2165, 7027, and 7662. The relative intensities of the *Ne* IV nebular lines are in agreement with theory. Substantial revisions are also made in the wave lengths of the forbidden lines of several other ions, notably *F* IV, *S* I, *S* III, and *Cl* IV. The new values, in general, improve the smoothness of the progression, along an isoelectronic sequence, of the wave numbers of a given transition.

The forbidden *S* III line at 3721 A is blended in every case with the *H* line at about this wave length. In the higher-excitation nebulae the intensity of the blend is noticeably greater than that of the adjacent members of the Balmer series, and the wave length is shifted about one-tenth angstrom shortward with respect to the theoretical position of the *H* line. From these facts the position of the *S* III line is estimated to be at the wave length listed.

Several other forbidden lines have been omitted from the tables because they are blended with strong lines. These include the strongest line of *Fe* III at 4658 A, which is masked in most nebulae by a strong line of *C* IV.

REFERENCES

Paul, Fred W., and Polster, Harry D. 1941, *Phys. Rev.*, **59**, 424.
Wilson, O. C. 1950, *Ap. J.*, **111**, 279.

LINE INTENSITIES IN THE SPECTRA OF COOL CARBON STARS. II. R AND N STARS IN THE YELLOW

WILLIAM BUSCOMBE*
Mount Wilson and Palomar Observatories
Carnegie Institution of Washington, California Institute of Technology

Received February 1, 1954; revised October 21, 1954

ABSTRACT

The equivalent widths of 75 absorption lines in the region 5600–6000 A have been measured on coudé spectrograms of six R and N stars. The instrumental resolution of adjacent features on microphotometer tracings is briefly discussed. The measurements are compared with data for the sun and for typical K giants, and in a few cases with visual estimates by Sanford from spectrograms of two carbon stars. Since the lines are more intense in the later-type spectra, it is concluded that the atmospheres of these cooler stars are less opaque to continuous radiation in the yellow.

The photographic "Atlas of Spectra of Six Stars of Classes R and N" (Sanford 1950) shows clearly that a region in the yellow offers one of the few windows where unresolved band absorptions interfere least with the atomic and discrete molecular lines. The interval chosen for the present study is between the head of the $\Delta v = -1$ Swan band sequence of C_2 at λ 5635 and the (8, 3) band in the red system of *CN*, which also becomes entangled, in the spectra of the coolest N stars, with the $\Delta v = -2$ sequence of C_2.

Table 1 lists details of the spectra of six carbon stars in the yellow-green, photographed with various cameras and gratings at the coudé focus of the 100-inch Hooker telescope. The visual magnitudes of the variable stars are from A.A.V.S.O. records, kindly made available by Mrs. Margaret W. Mayall. The projected slit-width on the plate for each exposure was near 25 μ, and the variation in exposure times was required to obtain spectra of suitable density for photometry under different conditions of atmospheric transparency and "seeing." The early classification of stars in types R and N (Shane 1928) is based mainly on slitless spectrograms of dispersion about 500 A/mm in the blue-violet. Keenan and Morgan (1941) have combined these into class C from one-prism spectrograms giving 250 A/mm in the yellow and red. The decimal subclass refers to the strength of the atomic lines, and the subscript to the intensity of the C_2 bands.

Each plate was traced on the Babcock direct-intensity microphotometer with a gear ratio suitable to produce a linear dispersion on the tracing as close as possible to 1 cm/A. In order to assign the position of the fiducial continuum with greater confidence, additional spectrograms, taken on similar emulsions with the grating spectrograph[1] at the Cassegrain focus of the 60-inch reflector, giving a linear dispersion of 70 A/mm, were also traced to show the gross features of longer intervals of the spectrum of each star. The photometric procedure has been outlined in previous papers (Buscombe 1951,1953). The peaks on the tracings, chosen to represent windows of the continuum at least 0.4 A wide in the spectra of all six stars, include λλ 5457, 5505, 5596, 5704, 5779, 5828, 5845, 5882, 5985, 6072, and 6131.

Spectrograms taken with the long-focus camera were measured, to determine the effective wave lengths of the blended absorption features. The identifications were based on the usual reference sources, with interpolations from the rotational analysis of the *CN* bands (Jenkins, Roots, and Mulliken 1932). Since no analysis is available for the (6, 1) band of *CN*, it is possible that unidentified lines from this band contribute to blends near λ 5750. Hase and Shajn (1948) have discussed the spectra of N-type stars, including a detailed list of absorption features in the interval 4289–6583 A, as resolved with the former one-prism spectrograph at Simeis. The estimated strength of each group of blended lines, apart from the influence of molecular absorptions, compares very closely with the same lines in the spectra of K5–M5 stars. Ikaunieks (1952*a*, *b*) has misquoted these results, giving the misleading impression that the atomic lines are generally weaker in the spectra of carbon stars than in other stars of corresponding temperatures. My Paper I (Buscombe 1953) shows that the measured equivalent widths dispel this illusion. Shajn and Struve (1947) have stated clearly that the weakness of the lines is apparent chiefly in the violet region, where the continuous background in the spectra of the cooler carbon stars is depressed by unidentified sources of opacity.

---

* Carnegie Institution Fellow, 1950–1952. Now at Commonwealth Observatory, Canberra, Australia.

[1] Described in original form by Merrill (1931); modified in 1949.

TABLE 1

COUDÉ SPECTROGRAMS OF YELLOW REGION IN CARBON STARS

STAR NAME	HD	m_v	SPEC. TYPE		DATE (U.T.)	DISPERSION (A/MM)	EMULSION	EXPOSURE (MINUTES)
			Shane	K & M				
....	182040	7.0	R0	$C1_2$	1948 Apr. 21* 1952 June 5	9.0 20.4	103*a*-D 103*a*-E	170 180
....	156074	7.7	R1	$C1_2$	1948 Mar. 1† 1948 June 24†	20.4 9.0	103*a*-D 103*a*-D	67 365
TX Psc.......	223075	5.3	N0	$C6_2$	1950 Dec. 18 1952 July 31	4.3 20.4	103*a*-F II-F3	240 120
BL Ori.......	44984	6.7‡ 6.7‡	N0	$C6_2$	1951 Oct. 11 1951 Dec. 11	20.4 20.4	103*a*-F3 103*a*-F3	240 110
UU Aur......	46687	5.9‡ 6.1‡	N3	$C5_3$	1950 Nov. 23 1950 Dec. 18	6.7 4.3	103*a*-D 103*a*-F	480 210
Y CVn.......	110914	5.9§ 5.7§	N3	$C5_4$	1951 May 11 1952 June 5	6.7 9.0	103*a*-D II-F3	300 300

* Observer, O. C. Wilson.

† Observer, R. F. Sanford.

‡ Near mid-decline of visual light-curve.

§ Just after "secondary minima."

Several authors have recently considered the effect of instrumental resolving power on the measured equivalent widths of absorption lines. Pecker and van Regemorter (1952) have shown the effect of progressively opening the defining slit of the photometer on the profile of a sharp line in the solar spectrum, surrounded by weak lines which become less clearly resolved. It is instructive to examine their Figures 1 and 2, while bearing in mind that the interval of wave length resolved by the slit, whose projected width is narrower than the grain size, is as shown in Table 2. Most spectra are taken with the narrowest slit possible, but, in observing faint stars, one must accept lower resolution as a compromise. It is also common to use a shorter slit, with the result that the noise level from grains in the emulsion is relatively higher. In the spectra of late-type stars, very few lines are sufficiently pure to escape considerable variation in equivalent width, depending on the resolving power. Traving (1952) has also found from laboratory experiments that lines with slight blends on the wings are measured broader with lower dispersion and that the errors in equivalent width depend critically on the photographic density of the continuum, as previously pointed out (Buscombe 1951). Miss Fofanova (1950) has constructed separate curves of growth for supergiant stars, using measured equivalent widths from spectrograms and published tracings of different dispersions. Her Table 14 shows a strong dependence of turbulent velocity on the dispersion used. Miss de Strobel (1953) has shown that weak lines in the spectrum of Sirius were measured 21 per cent stronger from 40 A/mm plates than from the *Photometric Atlas of Stellar Spectra* (Hiltner and Williams 1946).

In all my work on the photometry of absorption lines, I have tried to sketch the profiles of disturbing contributors to blends. However, when tracings are to be compared, measures of blended lines are usually omitted if based on plates of lower resolution. In general, it is more difficult to identify and apportion the lines contributing to blended absorption features in the complex spectra of cool, late-type stars. Even from tracings of quite good spectrograms of the bright star TX Psc, not nearly as many lines in the violet region could be measured as for some of the early R-type stars. Provisional measures of equivalent width for a few prominent lines are compared in Table 3 with estimates from visual inspection of the original plates (Sanford 1950). Although the scatter for individual stars is rather large, the relation between the average equivalent width, *W*, of the *Na* D lines (in angstroms) and the spectral subclass, *C*, is quite similar to that obtained from spectrograms of much lower dispersion (Bouigue 1954). From the coudé plates, $\log W = 0.18C - 0.24 \pm 0.08$.

TABLE 2

RESOLVABLE INTERVALS ON SPECTROGRAMS

Dispersion (A/Mm)	$\Delta\lambda$ (A)	Type of Spectrograph	Dispersion (A/Mm)	$\Delta\lambda$ (A)	Type of Spectrograph
0.3	0.01	Solar	30.0	1.0	Cassegrain
1.0	0.03		100.0	3.0	Nebular
3.0	0.1	Coudé	300.0	10.0	Objective Prism
10.0	0.3		1000.0	30.0	

TABLE 3

ESTIMATED AND MEASURED EQUIVALENT WIDTHS IN ANGSTROMS

λ	ELEMENT	HD 156074		TX Psc	
		Sanford	Buscombe	Sanford	Buscombe
4246.83	*Sc* II	0.2	0.26	0.2	0.42
4254.35	*Cr* I	0.3	0.36	0.7	1.7:
4404.75	*Fe* I	0.7	0.70	....	1.1
4427.31	*Fe* I	0.4	0.41	0.7	0.8:
4468.49	*Ti* II	0.2	0.29	0.4	0.5:
4533.24	*Ti* I	0.3	0.28	0.2	0.6:
4554.04	*Ba* II	....	0.32	1.7	1.2:
4571.10	*Mg* I	0.2	0.31	0.5	0.59
4607.33	*Sr* I	0.1	0.1:	0.4	Blend
5183.60	*Mg* I	2.2	0.9	1.0	1.5:
5671.80	*Sc* I	0.2	0.09	0.4	0.36
5890+5896	*Na* I	3.0	1.8	15	11

In the yellow region, rather few atomic lines are sufficiently resolved to yield measur-

TABLE 4

MEASURED EQUIVALENT WIDTHS IN ANGSTROMS

	Star		182040	156074	TX Psc	BL Ori	UU Aur	Y CVn	Sun	α Boo	γ Dra
	Type (Shane) . .		R0	R1	N0	N0	N3	N3	......	......	......
	Type (K & M) . .		$C1_2$	$C1_2$	$C6_2$	$C6_2$	$C5_3$	$C5_4$	G2 V	K2 IIIp	K5 III
Atom	E.P.	λ									
Na	0.0	5889.95	1.5	1.1	6.1	3.5	5.8	2.4	0.85	1.02	2.95
		5895.92	1.0	0.7	4.7	2.5	3.8	1.6	.56	0.80	2.00
Na	2.1	5682.63	......	0.17	0.24	0.30	0.38	0.25	.13	......	......
		5688.20	0.14	0.18	0.32	0.33	0.47	0.22	.14	......	......
Si	5.0	5665.60	......	......	0.20	0.24	0.44	......	.04	......	......
		5684.52	0.11	......	0.24	0.31	0.45	0.12	.07	......	......
		5948.58	0.31	0.12	0.33	0.40	0.41	0.36	.09	......	......
Ca	4.4	5757.69	......	......	0.22	......	0.32	0.07	......	......	......
		5761.88	0.18	......	0.46:	......	0.42:	0.22:	......	......	......
Sc	1.4	5671.80	0.16	0.09	0.36	0.38	0.52	0.13	.02	......	......
		5700.14	0.21	0.11	0.25	0.31:	0.35	0.20	......	......	......
		5724.07	......	0.04	0.22	0.19	0.40	0.12	......	......	......
Ti	0.0	5913.73	0.26	0.13	0.36	0.41	0.36	0.28	......	......	......
		5944.65	0.18:	0.04	0.42	0.37	0.42	0.23	......	......	......
Ti	1.0	5814.00	0.23	0.05	0.16	0.25	0.30	0.25	......	......	......
		5866.45	0.16	0.15	0.49	0.52	0.65	0.49	.07	0.18	0.27
		5903.32	0.16	0.06:	0.26	0.29	0.40	0.23:	......	......	......
		5937.81	0.23	0.08	0.30	0.43:	......	0.28:	......	......	......
		5941.76	0.15	0.09	0.40	0.38	0.37	0.34	.02	0.14	0.24
Ti	1.9	5953.16	0.19	0.07	0.26	0.30	0.29	0.22:	.03	0.15	0.20
		5965.83	0.20	0.10	0.39	......	0.39	......	.02	0.15	0.20
		5978.54	0.19	0.09	0.30	0.34	0.32	0.34	.02	0.14	0.20
Ti	2.3	5713.90	0.11	0.05	0.26:	0.22	0.29	0.22	......	......	......
Ti	3.3	5812.83	0.12	0.05	0.28	......	0.40	0.27	......	......	......
V	1.1	5657.45	......	0.04	0.32	......	0.39	......	01	0.11	0.18
		5668.37	0.24	0.06	0.20	0.25:	0.32	......	.01	0.10	0.18
		5670.83	......	0.06	0.24	......	0.32	0.34	.02	0.17	0.15
		5698.51	0.16:	0.13	0.26	0.37	0.42	0.21	......	0.14	0.26
		5703.56	......	0.09	0.32	0.42	0.46	0.16	.03	0.18	0.26
		5706.97	0.22	......	0.41:	0.16:	0.45	0.22:	......	0.17	0.22
		5727.02	0.13	0.07	0.34	......	0.41	......	.04	0.21	0.30
		5727.66	0.12	0.13	0.31	......	0.40	0.16	.01	0.14	0.24
		5731.26	0.17	0.10	0.42	......	......	0.26	......	0.20	0.31
		5737.04	0.10	0.07	0.29	0.37	0.33	0.26	.01	0.15	0.22
		5743.44	0.13	0.07	0.32	......	0.50:	0.25:	.01	0.14	0.27
		5776.67	......	0.08	0.25	......	0.41	0.29	......	......	......
		5782.60	0.16	......	0.24	0.24	0.33	0.22:	......	......	......
		5980.75	0.12	0.04	0.28	0.26	0.31	0.25:	......	0.04	0.10
V	3.1	5830.72	......	0.06	0.26	......	0.32	0.28	......	......	......
Cr	1.0	5785.86	0.12	0.12	0.36	......	0.43	0.28:	......	......	......
Cr	3.0	5719.82	......	0.08	0.25	0.26	0.35	0.22	......	......	......
		5863.96	......	0.04	0.34	0.30	0.38	......	......	......	......
Cr	3.8	5801.14	......	0.06	0.26	......	0.46	0.27	......	......	......
Fe	2.2	5963.25	0.17	0.02	0.24	0.25:	0.32	0.25:	......	......	......
Fe	2.6	5833.93	......	0.02	0.24	0.19:	0.27	0.13	.01	......	......
Fe	3.2	5807.22	......	0.10	0.14	0.31	0.18	......	......	......	......
Fe	3.4	5658.83	0.11	0.15	0.34	0.31:	0.46	0.17:	.14	0.35	0.43
		5709.38	0.18	......	0.34	......	0.37	0.14:	.08	0.14	0.18
Fe	3.9	5809.25	0.16:	0.06	0.31	......	0.30	0.20:	.06	......	......
Fe	4.2	5638.27	0.17	0.09	......	......	......	0.21	.08	......	......
		5655.51	0.09	......	......	......	......	0.30	.08	0.10	0.10
		5705.32	0.18:	0.08	0.27	0.16:	0.37	0.11	0.04	......	......
		5826.64	0.12	0.03	0.37	0.12	0.36	0.29	......	......	......
		5959.88	0.11	0.10	0.32:	0.37:	0.32	0.33	......	......	......

TABLE 4—*Continued*

	Star		182040	156074	TX Psc	BL Ori	UU Aur	YCV n	Sun	α Boo	γ Dra
	Type (Shane)...		R0	R1	N0	N0	N3	N3	......	......	......
	Type (K & M)..		$C1_2$	$C1_2$	$C6_2$	$C6_2$	$C5_3$	$C5_4$	G2 V	K2 IIIp	K5 III
Atom	E.P.	λ									
Fe.....	4.6	5870.65	0.17	0.05	......	......	......	0.23	......	......	......
Co.....	3.6	5965.04	......	......	0.14	0.12	0.17	.16	......	......	......
Ni.....	1.9	5796.08	.16:	......	.25	.16	.42	.25:	......	......	......
Zr.....	0.0	5955.37	.22	.09	.42	.43:	.60	.28:	......	......	......
Zr.....	0.6	5664.55	.14	.07	.36	......	.45	......	......	......	......
Ba.....	1.1	5971.70	.14	.06	.23	.28	......	.23	......	......	......
Ba.....	1.6	5777.62	.12	.09	.30	.19	.53	.28:	......	......	......
CN.....	0.0	5852.4	.09	.06	.28	......	.54	......	......	......	......
		5862.0	.18	.04	.34	.19	.37	.26	......	......	......
		5864.6	.17	.07	.24	.27	.43	.25:	:......	......	......
		5869.6	......	.06	.38	.45	.51	......	......	......	......
		5871.7	......	......	.51:	.55	.61	......	......	......	......
		5873.7	.14	.07	......	......	......	.28:	......	......	......
		5875.2	......	02	.18	.16	.24	......	......	......	......
		5875.9	.09:	.04	.24	.27	.34	.27	......	......	......
		5886.1	.15:	......	.38	......	......	.28:	......	......	......
		5904.9	.20	......	.60	.68	.61	0.28:	......	......	......
		5907.8	......	.09	.36	.40	.44	......	......	......	......
		5910.0	.24	.08	......	......	......	......	......	......	......
		5917.7	0.11	0.04	0.26	0.26	0.34	......	......	......	......

able equivalent widths, because of blends with the rotational structure of the rather open bands of the *CN* red system. Quite possibly a few more blends may have to be deleted from Table 4, after the rotational structure of the (5, 0) and (6, 1) bands is analyzed. Of the 13 absorption features assigned exclusively to *CN*, many include contributions from different branches within a band, involving different quantum states which cannot be sufficiently disentangled to lead to a direct determination of rotational excitation temperature. Evidently, this parameter can be found only by matching synthetic profiles for each molecular band, computed for various temperatures, as for *TiO* in the M star β Peg (Phillips 1952). In a forthcoming publication, A. A. Wyller will discuss the determination of vibrational temperatures for several R and N stars from the integrated strengths of C_2 bands in the red and yellow. Preliminary values for early N-type stars are around 2100° K.

Equivalent widths for 75 lines are shown in Table 4, as an extension to this spectral region of the measures given in Paper I. However, less reliance has been placed here on the central absorptions, and even moderately blended lines have been generally avoided. Interpolated measures depending entirely on central absorptions are qualified by a colon (:). One line of *Ni* I, λ 5796.08, appears to be positively identified. Although he had previously questioned the presence of this element in the atmospheres of carbon stars, Dr. Sanford has recently stated in private correspondence that it is almost certainly a principal contributor to λ 5892.9 and other blends.

For comparison with the measures for carbon stars, published equivalent widths for the corresponding lines in the spectra of the sun and of two K giants are included in Table 4. The solar data were taken from the Utrecht *Atlas* (Bell 1951), in measures which cover a larger selection of the lines used in this investigation, and agree closely with other recent results (Claas 1951; Wright 1948). Wright's (1950) measures for α Boo and γ Dra are from plates taken with a Littrow grating spectrograph, which gives a dispersion of 7.0 A/mm. Although fragmentary, the comparative figures suggest that the *Ti* lines exhibit an intensity trend quite similar to *V* and other metals and that the relative abundance of *Ti* may be the same in the atmospheres of all cool stars, regardless of the formation of *TiO* in the K−M branch (cf. Buscombe and Merrill 1952).

In contrast with the violet region, where all the lines showed similar intensities in the two early R-type stars (Buscombe 1953), it is quite clear that in the yellow the lines are much stronger in HD 182040 than in HD 156074. This is consistent with previous suggestions (Bidelman 1953) that HD 182040 is deficient in hydrogen, since the continuous absorption in the yellow by H^- ions, as well as *H* atoms in the Paschen continuum, is less than in HD 156074. The general opacity in the yellow is especially low in N stars, whose extreme red color is only partially due to lower temperature.

REFERENCES

Bell, Barbara. 1951, *Harvard U. Spec. Rept.*, No. 35.
Bidelman, W. P. 1953, *Ap. J.*, **117**, 25.
Bouigue, R. 1954, *Ann. d'ap.*, **17**, 104.
Buscombe, W. 1951, *Ap. J.*, **114**, 73.
———. 1953, *ibid.*, **118**, 459.
Buscombe, W., and Merrill, P. W. 1952, *Ap. J.*, **116**, 525.
Claas, W. J. 1951, *Recherches astr. Obs. Utrecht*, Vol. **12**, No. 1.
Fofanova, T. M. 1950, *Comm. Central Astr. Obs. Pulkova*, **18**, No. 3, 68.
Hase, V. F., and Shajn, G. A. 1948, *Comm. Crimean Ap. Obs.*, **2**, 51.
Hiltner, W. A., and Williams, R. C. 1946, *Photometric Atlas of Stellar Spectra* (Ann Arbor: University of Michigan Press).
Ikaunieks, J. J. 1952*a*, *Pub. Inst. Phys. Riga*, **4**, 18.
———. 1952*b*, *A.J. USSR*, **29**, 654.
Jenkins, F. A., Roots, Y. K., and Mulliken, R. S. 1932, *Phys. Rev.*, **39**, 16.
Keenan, P. C., and Morgan, W. W. 1941, *Ap. J.*, **94**, 501.
Merrill, P. W. 1931, *Ap. J.*, **74**, 188.
Pecker, J. C., and Regemorter, H. van. 1952, *Ann. d'ap.*, **15**, 364.
Phillips, J. G. 1952, *Ap. J.*, **115**, 183.
Sanford, R. F. 1950, *Ap. J.*, **111**, 262.
Shajn, G., and Struve, O., 1947 *Ap. J.*, **106**, 86.
Shane, C. D. 1928, *Lick Obs. Bull.*, **13**, 128.
Strobel, G. de. 1953, *Mem. Soc. astr. ital.*, Vol. **23**, No. 4; *Contr. Oss. Astrofis. Asiago*, No. 31.
Traving, G. 1952, *Zs. f. Ap.*, **31**, 175.
Wright, K. O. 1948, *Pub. Dom. Ap. Obs. Victoria*, **8**, 1.
———. 1950, *ibid.*, p. 281.

THE VELOCITY AND SPECTRUM OF AC HERCULIS FROM COUDÉ SPECTROGRAMS

Roscoe F. Sanford
Mount Wilson and Palomar Observatories
Carnegie Institution of Washington, California Institute of Technology

Received October 18, 1954

ABSTRACT

The velocities from 24 coudé spectrograms of AC Herculis have been resolved into two curves; the one roughly the mirror image of the light-curve, the other, somewhat asymmetrical and with a single maximum and minimum, an amplitude of 22 km/sec, and a period of about 1240 days. Velocities from the absorption lines of *Fe* I (2v), *Fe* II, *Ti* II, and *Sr* II, respectively, differ from the *Fe* I (0v) velocities as shown in *H* and *I* of Figure 1. The systemic velocity is −31.2 km/sec from the *Fe* I (0v) velocities and −27.0 km/sec from all the enhanced lines taken together. The D lines give velocities that suggest that these lines may be blends of stellar and interstellar lines. Double absorption lines of certain metals and of hydrogen may occur in any but the last 25 days of a cycle. There are emission lines of hydrogen and of H and K of *Ca* II. The former are strongest in the phases of increase in light; $H\delta$, $H\gamma$, and $H\beta$, as well as $H\alpha$, are all bright then. $H\alpha$ is probably bright at all phases. H and K emissions were only found near phase 50 days. Velocities from the hydrogen emission lines appear to parallel the variation of the *Fe* I (0v) velocities. The emission H- and K-line velocities average 26 km/sec less algebraically than the corresponding *Fe* I (0v) velocities.

The relation of light-variation to the color index, spectral class, and velocity variations derived from the coudé spectrograms is summarized in Table 3. The results obtained from one-prism spectrograms in 1930 agree fairly well with those obtained in this paper from the much higher-dispersion coudé spectrograms, as shown in Table 4.

PHOTOMETRIC RESULTS

The RV Tauri variable, AC Herculis, was discovered by Miss Dorothy Applegate (1921). The most recent photometric observations of this variable are: visual by Pettit (1948) made in 1946 and 1947; photoelectric, Pg_p, by Eggen (1950); and visual by the American Association of Variable Star Observers (A.A.V.S.O.) (1952). Pettit derived the elements,

$$\text{Primary minimum} = \text{JD } 2432038.57 + 75\overset{\mathrm{d}}{.}44 \text{ G.M.T.},$$

from a consideration of his observations and those made within the preceding 236 cycles. These elements give the phases upon which the three curves at the top of Figure 1 are based. Only Eggen's observations are plotted in detail. Mean curves have been formed from the observations of Pettit and those of the A.A.V.S.O. The fourth curve in Figure 1 follows the plotted observations of color index, C_p, which Eggen made along with his magnitude observations. Pettit's elements give a quite similar mean representation of the maxima and minima of AC Herculis within the 17 cycles covered by these three sets of recent observations. It is, however, also obvious from Pettit's own observations, as well as from those of the A.A.V.S.O., that there are differences in the light-variation from cycle to cycle. On the other hand, Eggen's observations, all of which belong to a single cycle, show very little scatter.

SPECTROSCOPIC RESULTS

About 70 prismatic spectrograms (approximate dispersion 35 A/mm at $H\gamma$) have already been used to compare changes in velocity and spectral class with changes in the brightness of AC Herculis (Sanford 1931). These relations may now be studied with the aid of 24 spectrograms obtained in the interval from 1946 to 1950 with the coudé plane-

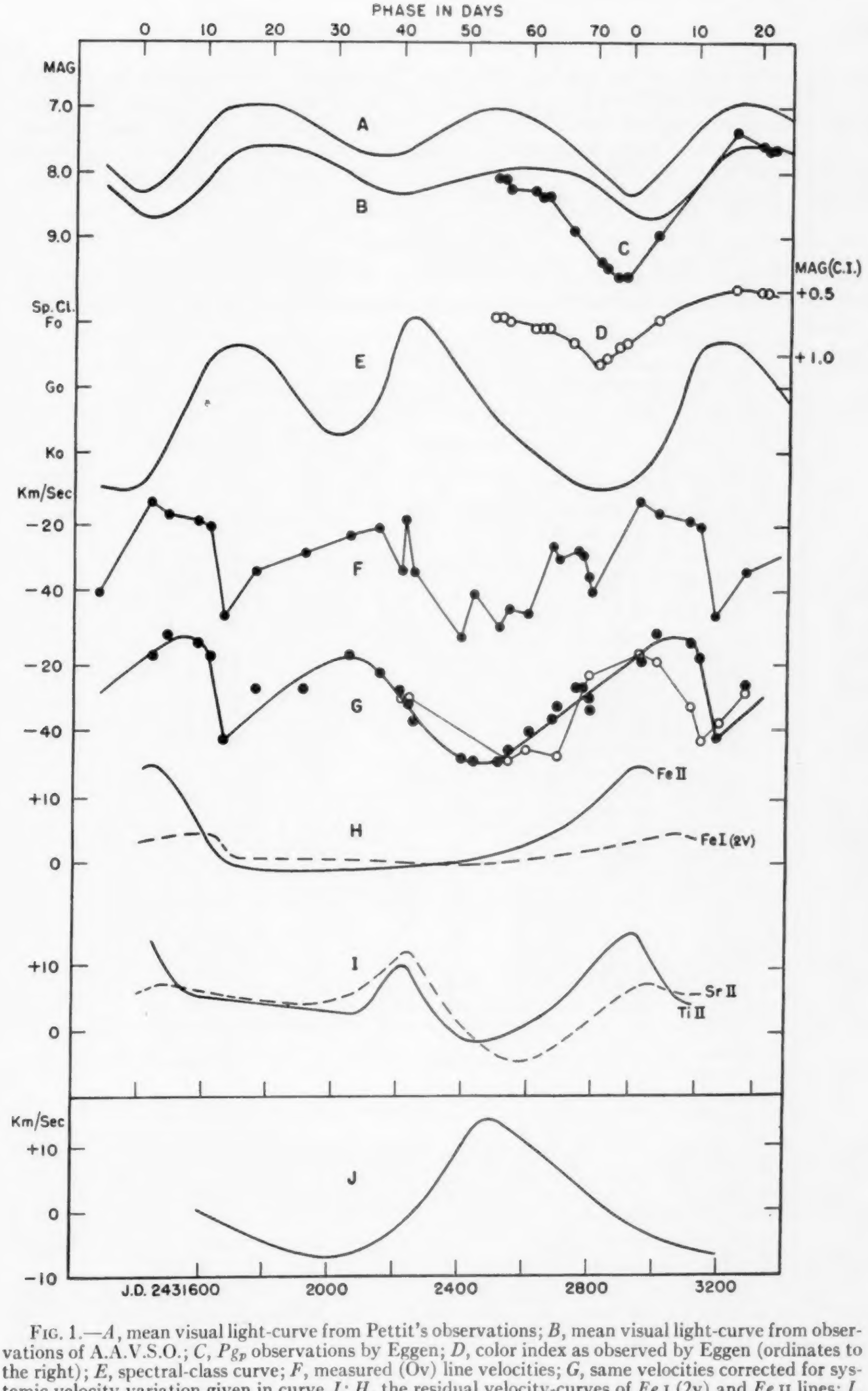

FIG. 1.—*A*, mean visual light-curve from Pettit's observations; *B*, mean visual light-curve from observations of A.A.V.S.O.; *C*, Pg_p observations by Eggen; *D*, color index as observed by Eggen (ordinates to the right); *E*, spectral-class curve; *F*, measured (Ov) line velocities; *G*, same velocities corrected for systemic velocity variation given in curve *J*; *H*, the residual velocity-curves of *Fe* I (2v) and *Fe* II lines; *I*, residual velocity-curves of *Ti* II and *Sr* II velocities. Positive residuals indicate that velocity concerned is more positive than the corresponding (Ov) line velocity.

grating spectrograph of the 100-inch telescope. Well-exposed plates extend from λ 3600 to λ 5000 in the second order with a dispersion of 10 A/mm. The region from the D lines to *Hα* was photographed in the first order (20 A/mm) on six of these spectrograms. Table 1 is a journal of these 24 observations arranged in the order of phase from primary minimum, as given by Pettit's elements. Spectral and velocity changes are compared with the changes of light and color in what follows.

SPECTRAL CHANGES

Lines of the ionized elements (enhanced lines) are prominent at all times, although they show marked changes throughout a cycle. In general, the spectrum has conspicuous enhanced lines at and near maximum light, whereas lines of the neutral elements (especially the ultimate lines) undergo marked strengthening at and near the light-minima.

TABLE 1

ABSORPTION-LINE VELOCITIES AND VELOCITY RESIDUALS

COUDÉ PLATE No.	JULIAN DAY 2430000+	PHASE (DAYS)	VELOCITIES (KM/SEC)			RESIDUAL VELOCITY (KM/SEC)				D-LINE VELOCITY (KM/SEC)
			Obs. (0v)	Long Period Corr.	Corr. (0v)	(2v)	*Fe* II	*Ti* II	*Sr* II	
4710	2342.86	2.02	−13.1	− 4.0	−17.1	+5.3	+14.1	+14.9	+ 9.5	......
4354	2043.73	4.66	−17.1	+ 7.0	−10.1	+2.9	+15.0	+ 9.3	+ 3.4	......
4195	1897.96	9.78	−18.7	+ 6.0	−12.7	+7.0	......	+ 4.6	......	......
4018	1748.65	11.34	−20.6	+ 3.2	−17.3	+3.4	......	+ 6.0	+ 3.7	......
5741	3108.74	13.48	−48.4	+ 5.5	−42.9	......	+ 0.2	......	......	......
4281	1981.96	18.33	−34.6	+ 6.7	−27.9	+0.6	− 2.5	+ 5.9	+ 8.2	−24
3900	1687.69	25.83	−29.1	+ 1.6	−27.5	−0.1	+ 0.6	+ 4.1	+ 7.3	......
4393*	2071.77	32.70	−23.6	+ 6.2	−17.4	+1.6	− 0.8	+ 2.2	+ 2.6	......
3823	1623.84	37.42	−20.8	− 1.9	−22.3	−0.6	− 0.9	+ 8.4	......	......
4223*	1927.98	39.80	......	......	......	......	......	......	......	......
4229	1928.95	40.77	−34.5	+ 6.3	−28.2	+1.9	+ 2.6	+ 7.1	+ 8.8	......
4879	2457.64	41.36	−18.2	−13.4	−31.6	−0.1	− 2.1	+12.5	+14.5	......
4665†	2307.87	42.48	−35.1	− 2.0	−37.1	−0.2	+ 0.8	......	......	......
5652	3069.90	50.09	−54.6	+ 4.8	−49.8	+0.5	+ 1.2	− 2.6	− 5.4	......
4749	2392.70	51.86	−41.5	− 9.3	−50.8	+2.4	+ 2.5	+ 1.0	− 0.4	......
3975	1717.68	55.82	−51.5	+ 1.2	−50.3	−0.3	− 2.0	− 2.2	− 3.5	......
5407†	2850.65	57.16	−46.0	− 0.5	−46.5	+0.5	+ 3.3	+ 1.3	− 2.3	−28
4347	2023.81	60.18	−47.9	+ 7.0	−40.9	+3.1	+ 3.8	+ 1.9	+ 3.9	−30
4803	2402.84	64.00	−26.5	−10.0	−36.5	+0.5	+ 4.1	+ 3.6	− 4.6	......
5284	2782.70	64.66	−30.4	− 5.0	−35.4	−1.1	+ 5.3	+ 5.2	− 5.0	−21
4624*	2258.02	68.06	−28.0	+ 0.7	−27.3	+2.3	+ 8.9	+ 9.0	+ 0.1	......
3859	1654.89	68.47	−29.6	− 0.6	−30.2	+1.5	+ 4.9	+ 5.9	− 1.4	......
4466*	2108.67	69.60	−36.2	+ 6.0	−30.2	+6.4	+ 8.9	+11.4	......	......
4275*	1957.93	69.75	−41.2	+ 6.5	−34.7	+4.1	+12.3	+10.5	+ 6.3	−24

* A weak plate.

† A very weak plate.

Estimates of spectral class have been made by comparison with spectral standards of c stars obtained with the same spectrograph. The curve of spectral-class change (*E* of Fig. 1) is based on these estimates. The spectral class has two maxima, F3 at phase 15 days and A9 at 42 days, and two minima, K5 at 2 days and G8 at 31 days.

The six spectrograms Ce 4195, 4018, 5741, 3823, 4665, and 5652 have double lines belonging to the elements indicated in the fourth to the eighth columns of Table 2. These are the strong lines of the ionized elements and a few of the very strong *Fe* I lines, such as λ 4045.82, and the *Ca* I line λ 4226.73 on Ce 5652. Abt (1953) has obtained evidence of absorption components of AC Herculis from three different sources simultaneously on some of his Lick Observatory spectrograms.

Absorption lines of *H*δ, *H*γ, *H*β, and *H*α are always present. Emission accompanies the first three of these lines on spectrograms from phase 0 to 18 days and at phase 40 days, or, in other words, hydrogen emission has its maximum strength when AC Herculis is increasing in light. However, *H*α is in emission not only at those times but also in the interval 57–69 days, which includes decreasing light. There is a strong presumption that *H*α may always be accompanied by emission. The structure of the hydrogen emission lines will be discussed later.

TABLE 2

VELOCITIES FROM SECOND COMPONENTS OF MET. LINES AND HYDROGEN LINES

Coudé Plate No.	Phase (Days)	Extra Comp. of Met. Lines						*H*-Line Velocities (Km/Sec)					
								Absorption				Emission	
		Vel. (Km/Sec)	Elements Involved					Velocity Components: Mean of δγβ			α	δγβ	α
4710..	2.02								−22	− 7		−11	
4354..	4.66								−32	− 4		−26	
4195..	9.78	−49.3	*Fe* II	*Sr* II					−48	− 9		−39	
4018..	11.34	−49.2	*Fe* II						−33	− 9		−37	
5741..	13.48	−17.2	*Fe* I	*Ti* II	*Sr* II	*Sc* II	*Ba* II		−44	− 9	− 48	−36	−50
4281..	18.33								−48	− 8	− 44	−28	−44
3900..	25.83							−102	−68	−10			
4393..	32.70									−24			
3823..	37.42	+ 3.1	*Ti* II	*Sr* II	*Sc* II				−54	+ 8			
4223..	39.80											−44	
4229..	40.77								−38	−10		−36	
4879..	41.36									− 8		−14	
4665..	42.48	+ 1.4	*Ti* II	*Sr* II	*Sc* II					− 6			
5652..	50.09	−11.0	*Ca* I	*Sr* II	*Sc* II				−34				
4749..	51.86								−29				
3975..	55.82								−46				
5407..	57.16								−30		103		(−49)
4347..	60.18								−39		− 39		−53
4803..	64.00								−24				
5284..	64.66								−28		− 78		(−46)
4624..	68.06												
3859..	68.47								−35				
4466..	69.60								−36				
4275..	69.75								−44		− 46		−38

Strong emissions appear within the broad absorption lines H and K of *Ca* II only on Ce 5652 and 4749 near phase 50 days in the second half of the cycle. Although there are spectrograms which are well enough exposed at several other phases, they fail to show these emissions.

Figure 2 reproduces microphotometer tracings of two selected 50 A regions of eight of the coudé spectrograms, and these illustrate the variations in the relative strength of enhanced and neutral lints. Examples are λ 4481.23 of *Mg* II in contrast with the blend of the two *Fe* I lines λ 4482.17 and λ 4482.26 and also the two *Fe* II lines λ 4489.18 and λ 4491.40, each in contrast with the ultimate *Fe* I line λ 4489.74. Figure 2 also shows the

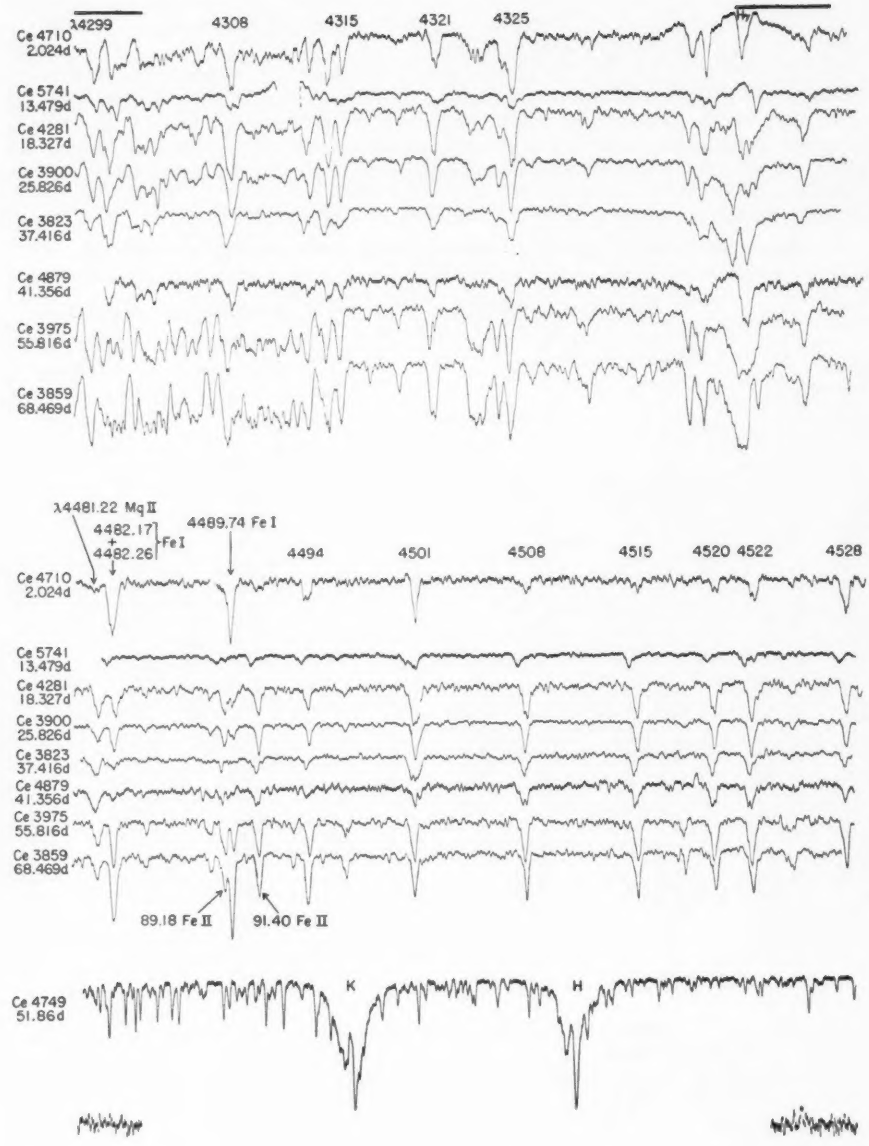

FIG. 2.—Microphotometer tracings of two 50 A regions of eight coudé spectrograms of AC Herculis. At the bottom a microphotometer tracing from Ce 4749, showing emission within the broad H and K absorption lines.

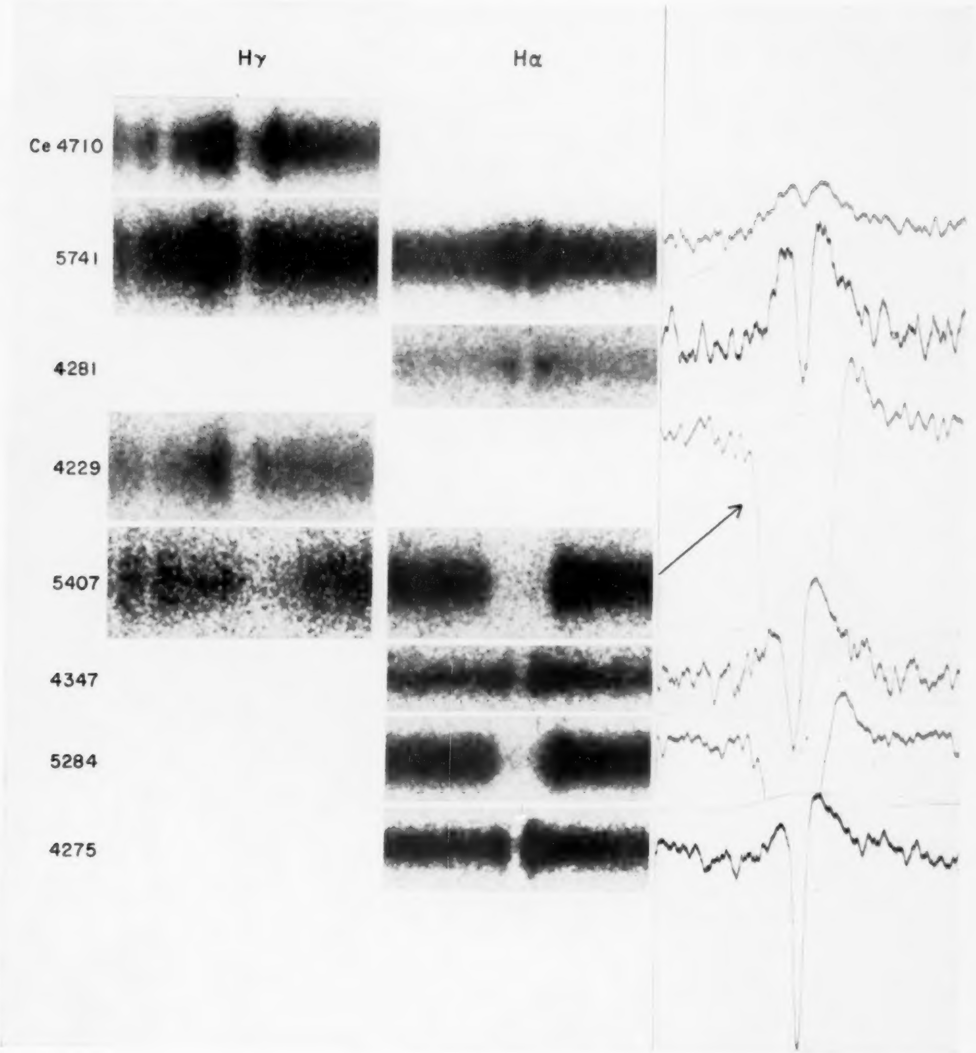

FIG. 3.—Reproductions of $H\gamma$ from four and of $H\alpha$ from six coudé spectrograms of AC Herculis and microphotometer tracings of the six $H\alpha$ lines.

varying structure of $H\gamma$ both in absorption and in emission and, at the bottom, emission within the absorption H and K on Ce 4749.

Figure 3 reproduces the $H\gamma$ line of four of the spectrograms and the $H\alpha$ of six of them. The first three $H\gamma$ and the first two $H\alpha$ lines show emission well on both sides of the absorption. On Ce 4347 and 4275 $H\alpha$ emissions are very weak on the shortward, but strong on the longward, side of the absorption. On Ce 5407 and 5284 $H\alpha$ has emission only on the longward side of the absorption, which, significantly or not, is extremely wide and strong on both spectrograms.

RADIAL VELOCITIES

The 1931 study showed a difference between the velocities from the neutral lines and those from the enhanced lines. It was feasible to make a more detailed division of the velocities with the higher dispersion of these coudé spectrograms. Hence the velocities from the low-level lines of *Fe* I (multiplets 2, 3, 4, and 5) have been made the basis of comparison with the velocities from other classes of lines. These low-level *Fe* I lines are hereafter called "(0v)" lines for short. They were chosen because they were numerous, little affected by blends, usually of good density, and never double like some of the stronger lines of higher excitation. The velocities from the (0v) lines (fourth column of Table 1) are plotted as points at the phases in the third column and connected by straight lines in curve *F* of Figure 1. A smooth curve through these points revealed large residuals, which, when plotted, defined a curve through somewhat more than a complete cycle. This curve was used to correct the measured (0v) line velocities and thus furnish another mean curve. A new residual curve was then derived, and from that a new mean curve. By such approximations the residual curve, *J*, was adopted.

This represents a variation in the systemic velocity of AC Herculis and suggests that this variable has a companion and that the two revolve about their center of mass in somewhat eccentric orbits in about 1240 days. The variable itself would have an orbital velocity at least as large as 11 km/sec, which is the semiamplitude of curve *J*. There is no spectrum of the secondary star from which to derive its orbital velocity.

The corrections in the fifth column of Table 1 are derived from curve *J* and combine with the velocities in the fourth column to give in the sixth column the (0v) line velocities freed from the long-period variation. They can now be represented by *G* of Figure 1, with quite small residuals. Curve *G* has maxima at two phases, 7 and 33 days, and minima at two phases, 13 and 54 days. They correspond to light-minima at 0 and 36 days and light-maxima at 16 and 55 days. The velocity, −30.4 km/sec, which divides curve *G* into two equal areas is one value of the systemic velocity of the variable. Another good approximation is the mean of the well-distributed velocities of the sixth column of Table 1, −32.0 km/sec. This mean and the areal value are given equal weight in deriving the adopted systemic velocity, −31.2 km/sec.

Mean velocities have been separately derived from *Fe* I lines corresponding to an interpolated excitation of 2 volts, called hereafter "(2v)" lines, as well as from *Fe* II lines, from *Ti* II lines, and from the strong *Sr* II, *Sc* II, and *Ba* II lines taken together and hereafter called "*Sr* II" lines. The residuals of these velocities from the (0v) line velocities rather than the velocities themselves are in the seventh to the tenth columns of Table 1. A positive residual means that the velocity concerned is algebraically larger than the corresponding (0v) line velocity. Plots of these residuals are in *H* and *I* of Figure 1.

The (2v) line velocities are algebraically larger than the (0v) line velocities from phase 5 to 15 days. The greatest difference is +5 km/sec near primary minimum; the difference never becomes negative. The *Fe* II velocities have positive residuals from phase 50 to about 14 days, with a maximum of +15 km/sec near primary minimum. Like the (2v) line velocities, the *Fe* II velocities seem never to be significantly less than the (0v) line velocities. The *Ti* II velocities are algebraically larger than the (0v) line velocities, except within the short phase interval 50–60 days, when they may be slightly less. The maximum of the *Ti* II velocity residual curve is +15 km/sec. The *Sr* II velocities exceed the (0v) line velocities at all phases except in the interval 52–68 days, where there are some negative residuals. The curves for *Ti* II and for *Sr* II resemble each other in having two maxima and two minima, respectively. Mean velocity-curves of the (2v), *Fe* II, *Ti* II, and *Sr* II lines can be made by adding their respective residual curves to curve *G* of Figure 1. A systemic velocity of −27.0 km/sec is obtained from the twenty-four velocities that are the means of all the enhanced lines combined.

Five of the six recorded D-line pairs could be measured for radial velocity (last column of Table 1). Their comparison with the corresponding (0v) velocities shows differences that could be explained if the D lines are blends of stellar and interstellar lines, the latter having a fixed velocity displacement of about −9 km/sec, a reasonable value.

Six spectrograms in the phase interval from 10 to 50 days have some of their metallic absorption lines double and therefore provide another velocity besides the one given in the fourth column of Table 1. The measures of these components are in the third column, and the chemical elements upon which they depend are in the fourth to eighth columns of Table 2. All but the velocities from the last two of the six spectrograms, Ce 4665 and 5652, are from the weaker of the components of the line pairs. The relation of these component velocities to those in the fourth column of Table 1 is not readily apparent.

The ninth to the twelfth columns of Table 2 contain the velocities from the absorption lines of hydrogen. There are velocities from the means of the two absorption components of $H\delta$, $H\gamma$, and $H\beta$ on most of the spectrograms during the first 40 days of a cycle; on Ce 3900 (phase 25.8 days) each of these lines has a third component, which gives a mean velocity of −102 km/sec. These hydrogen lines are single for the remainder of a cycle. The $H\alpha$ absorption lines are single on all six spectrograms and yield velocities on four of them in reasonable agreement with one of the components of the other hydrogen lines. However, the very broad absorption $H\alpha$ lines of Ce 5407 and 5284 give velocities that are very much less algebraically than the velocities derived from the other absorption hydrogen lines, as if the longward portion of the broad absorption were replaced by some of the emission, thus causing a shortward displacement. When emission is present, it seems to complicate the hydrogen absorption, so that there is no clear relation between their absorption-line velocities and those from the (0v), (2v), *Fe* II, *Ti* II, or *Sr* II absorption lines.

Rough values of the velocities from the emission hydrogen lines were obtained from the mean of settings on their extreme edges both on the original spectrograms and on their microphotometer tracings. On Ce 5407 and 5284, however, emission appears only on the longward sides of their absorption $H\alpha$ lines. Velocities were obtained from these two emission lines by decreasing the velocity displacement of their longward edges by the half-width (82 km/sec) of $H\alpha$ as measured upon the other spectrograms where both shortward and longward emission components are present. These emission-line velocities (last two columns of Table 2) have been corrected by curve *J* of Figure 1 and are plotted as circles along with curve *G*. These velocities undergo a variation as nearly parallel to that of the (0v) line velocities as could probably be expected from such crudely measured emission lines.

Ce 5652 and 4749 (phases 50.09 and 51.86 days) have emission components within their broad absorption H and K lines of *Ca* II, and the velocities from these emissions give a mean of −75 km/sec, which is 26 km/sec less algebraically than the corresponding mean from (0v) lines. Interstellar H and K may cut into these emissions on their longward edges and thus perhaps be partially responsible for their shortward shifts.

The relation of light-variation to color and spectral class has already been given. It remains to give the relation between these three variations and the variation of velocity. Table 3 condenses this by giving the phases and values of the extremes in the curves of light, color index, spectral class, and velocity.

The four curves have extremes roughly at the same phases except for the first velocity and fourth spectral-class extremes. Approximately, light-minima accompany largest color index, latest spectral class, and maximum velocity; light-maxima accompany smallest color index, earliest spectral class, and minimum velocity. However, extremes of the curve of spectral class are systematically somewhat earlier than those of the other three curves.

The conclusions drawn from the 1931 study of one-prism spectrograms are shown by Table 4 to agree fairly well with the conclusions reached here with the recent coudé spectrograms. However, the coudé velocities can be resolved into two curves of velocity variation, the one with the period and the mirror image of the light-variation; the other a somewhat eccentric curve with a period of about 1240 days. In addition, the coudé observations give velocities from the D lines, from certain component absorption lines, from the hydrogen emission lines, and from the emission lines of H and K. The velocities from the emission hydrogen lines seem to parallel the change of the (0v) line velocities. Emission H and K, found only near phase 50 days, are displaced about 26 km/sec shortward from the (0v) lines.

TABLE 3

EXTREMES OF LIGHT, COLOR INDEX, SPECTRAL CLASS AND VELOCITY-CURVES

Light	$+0^{d}(8^{m}\!.3)$	$16^{d}(7^{m}\!.0)$	$36^{d}(7^{m}\!.7)$	$55^{d}(7^{m}\!.0)$
Color index	-4 $(1^{m}\!.0)$	17 $(0^{m}\!.5)$	....	55 $(0^{m}\!.7)$
Spectral class	-2 (K5)	15 (F3)	31 (G8)	42 (A9)
Curve *G* (km/sec)	$+7$ (-11)	13 (-43)	33 (-18)	54 (-50)

TABLE 4

COMPARISON OF RESULTS FROM ONE-PRISM AND COUDÉ SPECTROGRAMS

	ONE-PRISM		COUDÉ	
	Phase (Days)	Velocity (Km/Sec)	Phase (Days)	Velocity (Km/Sec)
Maxima	5	−11	7	−11
	35	−21	33	−18
Minima	22	−30	13	−44
	57	−58	54	−50
Systemic vel.	−31.9 km/sec (arc lines) −25.0 km/sec (enh. lines)		−31.2 km/sec [(0v) lines] −27.0 km/sec (enh. lines)	
Emission *H* δγβ lines vel.	Parallel arc line vel.		Parallel (0v) vel.	
Emission *H*δγβ	During light-increase		During light-increase	
Emission *H*α	Probably at all phases		Probably at all phases	

REFERENCES

Abt, Helmut. 1953, *A.J.*, **58**, 110.
American Association of Variable Star Observers. 1952, by letter.
Applegate, Dorothy. 1921, *Harvard Circ.*, No. 225.
Eggen, O. J. 1950, by letter.
Pettit, Edison. 1948, *Pub. A.S.P.*, **60**, 66.
Sanford, Roscoe F. 1931, *Ap. J.*, **73**, 364; *Mt. W. Contr.*, No. 424.

A SPECTROGRAPHIC STUDY OF BW VULPECULAE*

D. H. McNamara, O. Struve, and F. C. Bertiau, S.J.
Berkeley Astronomical Department, University of California

Received October 11, 1954

ABSTRACT

Individual velocity-curves of this variable star were obtained from spectrograms taken at the Mount Wilson Observatory on six nights. The amplitude of the velocity-curve changes very little throughout the period of observations. The spectral lines vary in width in the same period as the velocity variation. The lines are broadest on the descending branch of the velocity-curve. They sharpen up, however, on the stillstand of the velocity-curve, which occurs about midway on the descending branch. The lines of hydrogen are found at certain phases in the cycle to give a different velocity from that of the lines of the other elements. This discrepancy persists for only short intervals of time (about 15 minutes). When the discrepancy is large, the hydrogen lines are asymmetric.

The short-period (4^h49^m) velocity variation of the star BW Vulpeculae (HD 199140) was discovered by R. M. Petrie (1937). The light-variation of the star was announced by C. M. Huffer (1938), who found an amplitude of 0.18 mag. Photometric observations have also been obtained by Eggen (1948), Nikonov and Nikonova (1952), Walker (1954), Kraft (1953), and Lynds (1954). The photometric studies have established the following facts: (1) BW Vulpeculae has a larger light-amplitude than any other star belonging to the β Canis Majoris or β Cephei group of variables, and the amplitude may vary from one cycle to another; (2) maximum light occurs when the star's velocity crosses the γ-axis from positive to negative velocities, as in the majority of the other stars of this group; (3) a stillstand occurs on the ascending branch of the light-curve; (4) the color varies with phase.

Petrie (unpublished) has recently completed a study of the spectrum and radial velocity of BW Vulpeculae, extending over a period of 28 years. The major conclusions derived by him are: (1) The total amplitude of the velocity-curve is large (about 150 km/sec in 1952) and increases at the rate of 0.7 km/sec/year; (2) the period is increasing at the rate of 3.7 seconds per century; (3) the velocity-curve shows small changes in shape from one cycle to another and exhibits a stillstand midway on its descending branch; (4) the spectral lines change in shape in the same period as does the velocity-curve (broadest on the descending branch), but they retain the same equivalent widths throughout the cycle.

Our investigation was undertaken for the purpose of studying the behavior, on consecutive nights, of the velocity-curve and of elucidating the nature of the variation in the line profiles; the latter study was made on high-dispersion spectrograms. The plates were obtained at the Mount Wilson Observatory with the 100-inch coudé spectrograph (32-inch camera) and with the 60-inch Cassegrain spectrograph. The linear dispersions are 10 and 32 A/mm (at $H\delta$), respectively. Seventy-seven spectrograms were obtained on six nights, five of which were consecutive. Table 1 lists the star lines used to determine the radial velocity, and Table 2 contains the individual plate velocities. The heliocentric phases in Table 2 have been computed from JD 2425405.000, with an assumed constant period of 0.201028 day. The preceding values were adopted from Petrie (unpublished). Zero phase falls about 0.01 day after maximum velocity.

Figure 1 shows the individual velocity-curves. An inspection of these curves reveals

---

* The spectrograms used in this work were obtained by Mr. Struve and Mr. McNamara as guest investigators at the Mount Wilson Observatory.

(*a*) the presence of a stillstand on the descending branch of the velocity-curve, which appears to change from one cycle to another, and (*b*) the total amplitude, $2K$, probably changes from one cycle to another but not through a large range of values. These results are in agreement with those obtained earlier by Petrie (unpublished); the average semi-amplitude, of 75 km/sec, is in excellent agreement with that found by him in 1952. A number of the β Canis Majoris stars show remarkable changes in the amplitudes of their velocity-curves from one cycle to another; some of these changes show a well-defined beat phenomenon (Struve 1952). Petrie (unpublished) was unable to detect a beat period in his observations, which is confirmed by the data in Figure 1. It appears likely that BW Vulpeculae displays only one pronounced oscillation ($P2$, $K2$), with small irregular changes. The possibility exists, however, that the $P1$, $K1$ variation is small and undetectable because of the irregular variations of the $P2$, $K2$ oscillation which would be superimposed over the beat-curve. In addition to the pronounced stillstand and large amplitude, another remarkable feature that sets BW Vulpeculae apart from the other β Canis Majoris stars is the rapid change of velocity just after maximum. The results obtained on May 19 show a change of velocity of the order of 80 km/sec in the short interval of only 15 minutes.

TABLE 1

LIST OF STAR LINES

Wave Length	Element	Plate*	Wave Length	Element	Plate*
3964.73	*He* I	C	4345.56	*O* II	C
3973.26	*O* II	C	4347.42	*O* II	C
4009.35	*He* I	γ	4349.43	*O* II	C
4026.18	*He* I	C, γ	4387.93	*He* I	C, γ
4069.73	*O* II	γ	4414.91	*O* II	C
4072.16	*O* II	C	4416.98	*O* II	C
4075.87	*O* II	C	4471.48	*He* I	C, γ
4101.74	*H* δ	C, γ	4481.23	*Mg* II	C, γ
4119.22	*O* II	C	4552.65	*Si* III	C
4120.81	*He* I	C, γ	4567.87	*Si* III	C
4143.76	*He* I	C, γ	4574.87	*Si* III	C
4267.14	*O* II	γ	4590.97	*O* II	C
4340.47	*H*	C, γ	4596.17	*O* II	C

* "C" = Mount Wilson coudé spectrograph on the 100-inch telescope. "γ" = Mount Wilson Cassegrain spectrograph, on the 60-inch telescope.

As was pointed out by Petrie (unpublished), the spectral lines undergo a change in shape in the same period in which the velocity and light-variations occur. This is in agreement with the behavior of the spectral lines in a number of other stars belonging to the β Canis Majoris group (Struve 1952). Figure 2 illustrates the behavior, with phase, of two *Si* III lines and two *He* I lines. The profiles of the lines are smoothed intensity tracings, and the radial velocities in the top part of the figure were measured from the corresponding coudé plates. The lines are sharpest on the ascending branch of the velocity-curve and broadest on the descending branch. A close examination of the lines on the descending branch reveals, however, some interesting details that have not previously been noticed. These lines are apparently sharper during the stillstand stage of the velocity-curve than they are above and below the stillstand. This is better illustrated in Figure 3, where the broadening is plotted as a function of phase. An objective method for measuring the line broadening is illustrated in Figure 4. The line profiles were divided into three areas, as shown; the central area is equal to the sum of the other two areas, which are located in the wings of the line. The "broadening" is then defined as the ratio

TABLE 2

Radial Velocities, 1954

Time U.T.	JD 2434+	Phase (Days)	Velocity (Km/Sec)	$V_H - V_{\mathrm{all}}$ (Km/Sec)
	Plate C			
May 17				
7:44	879.822	0.171	+51.7	− 3.6
8:09	.840	.189	+69.8	+14.2
8:31	.855	.003	+14.2	+31.8
8:54	.871	.019	+ 5.6	+ 5.0
9:15	.885	.033	− 3.9	+ 6.9
9:36	.900	.048	−67.5	+ 6.4
9:51	.910	.058	−64.8	− 3.5
10:20	.931	.079	−58.5	+ 0.3
10:42	.946	.094	−43.6	+ 2.0
11:04	.961	.109	−30.9	+ 0.9
11:26	.976	.124	−16.6	− 1.4
11:47	.991	0.139	− 0.8	− 3.2
	Plate γ			
May 18				
7:51	880.827	0.171	+52.4	+ 0.5
8:17	.845	.189	+69.9	−15.7
8:45	.865	.008	− 1.9	+21.0
9:13	.884	.027	−10.9	+ 4.8
9:40	.903	.046	−65.8	+ 7.7
10:08	.922	.065	−78.2	−11.3
10:38	.943	.086	−59.3	+ 3.6
11:13	.967	.110	−34.2	+ 2.6
11:43	.988	0.131	− 2.2	+ 2.9
	Plate C			
May 19				
7:42	881.821	0.160	+29.7	− 0.1
8:02	.835	.174	+52.9	− 0.6
8:18	.846	.185	+68.8	+ 3.8
8:33	.856	.195	+88.6	+ 2.2
8:49	.867	.005	− 2.5	+33.4
9:05	.878	.016	− 5.7	− 9.0
9:21	.890	.028	− 2.8	+ 3.9
9:36	.900	.038	−32.0	+ 1.1
9:50	.910	.048	−64.2	+ 1.0
10:10	.924	.062	−68.4	− 0.6
10:24	.933	.071	−65.3	+ 1.2
10:37	.942	.080	−61.1	− 3.9
10:50	.951	.089	−52.8	+ 2.2
11:04	.961	.099	−46.4	+ 2.3
11:17	.970	.108	−34.9	+ 1.9
11:31	.980	.118	−21.0	− 0.6
11:44	.989	.127	−13.8	+ 1.8
11:56	.997	.135	− 1.8	+ 4.3
12:08	882.006	0.144	+ 4.9	+ 1.9

TABLE 2—*Continued*

Time U.T.	JD 2434+	Phase (Days)	Velocity (Km/Sec)	$V_H - V_{all}$ (Km/Sec)
	Plate γ			
May 20				
7:28	882.811	0.145	+14.4	+16.8
7:58	.832	.166	+37.4	+ 6.4
8:25	.851	.185	+71.5	− 6.2
8:54	.871	.004	+33.6	+37.2
9:20	.889	.022	− 2.4	+ 1.2
9:46	.907	.040	−28.9	+17.8
10:12	.925	.058	−69.1	− 5.7
10:38	.943	.076	−60.1	− 0.9
11:03	.960	0.093	−51.2	− 1.7
	Plate γ			
May 21				
7:19	883.805	0.134	− 5.4	− 5.8
7:46	.824	.153	+14.5	+ 6.2
8:13	.842	.171	+45.8	+ 6.1
8:40	.861	.190	+69.7	−11.4
9:07	.880	.008	+ 4.6	+ 8.1
9:33	.898	.026	− 1.9	−11.6
9:57	.915	.043	−48.4	+16.4
10:48	.950	.078	−69.1	− 9.3
11:09	.965	.093	−50.6	+ 5.8
11:29	.978	.106	−30.6	− 6.3
11:49	.992	0.120	− 5.9	− 1.2
	Plate γ			
June 19				
6:36	912.775	0.158	+21.1	− 7.6
6:54	.788	.171	+44.2	+ 9.4
7:12	.800	.183	+68.2	− 1.2
7:29	.812	.195	+76.3	+ 6.8
7:45	.823	.005	+26.0	+35.2
8:02	.835	.017	−10.6	− 7.8
8:19	.847	.029	− 0.7	+ 5.7
8:37	.859	.041	−27.3	+11.4
8:55	.872	.054	−77.6	− 5.6
9:14	.885	.067	−71.7	− 1.2
9:28	.894	.076	−67.4	+ 3.5
9:46	.907	.089	−48.5	− 3.2
10:01	.917	.099	−42.4	+ 3.9
10:19	.930	.112	−31.0	− 0.4
10:39	.944	.126	−12.6	− 1.5
11:00	.958	.140	+ 1.4	+ 0.9
11:25	.976	0.158	+25.8	− 2.1

of the length, *ab*, to the central depth, *cd*. It is evident that this ratio will increase as the line broadens.

From an inspection of Figure 3 it is seen that the lines sharpen up during the stillstand phase of the velocity-curve. The open circles represent the computed "broadening," on the supposition that it is produced by an integration of the velocity-curve during the exposures. These computed values fall well below the observed values. There is, however, other evidence which indicates that a real physical broadening is involved rather than an integration of the velocity-curve during the exposure. For example, the lines begin to

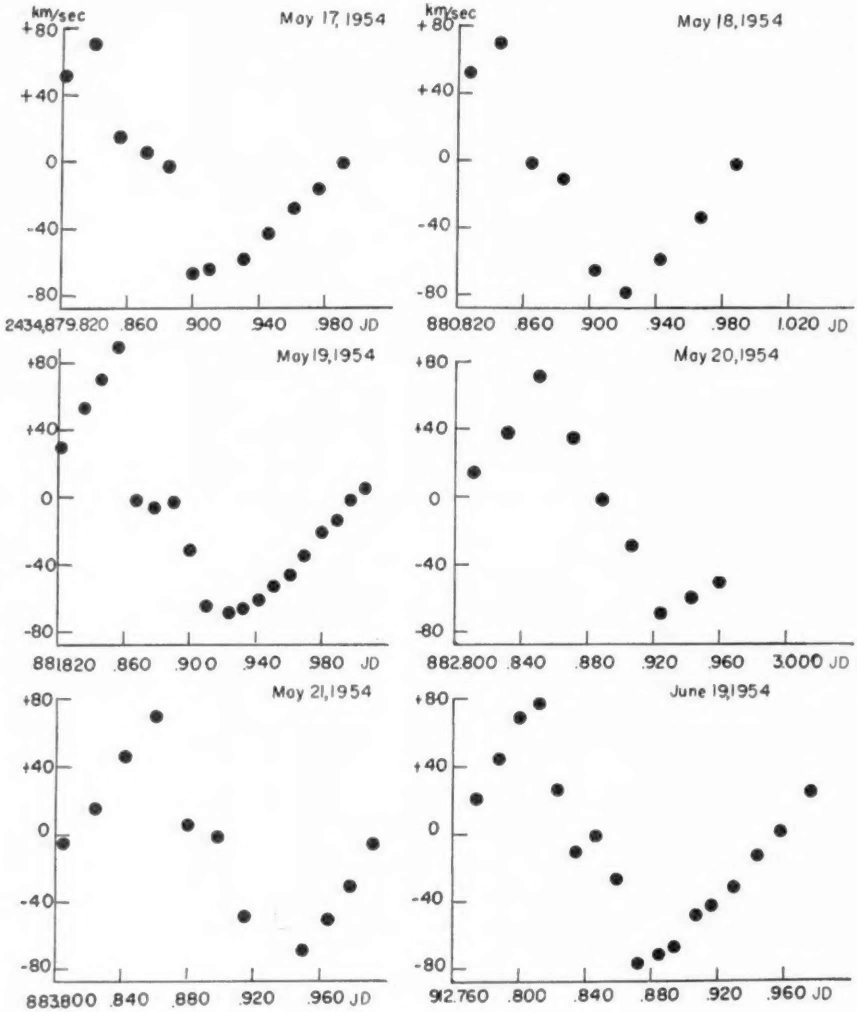

FIG. 1.—Radial velocities of BW Vulpeculae

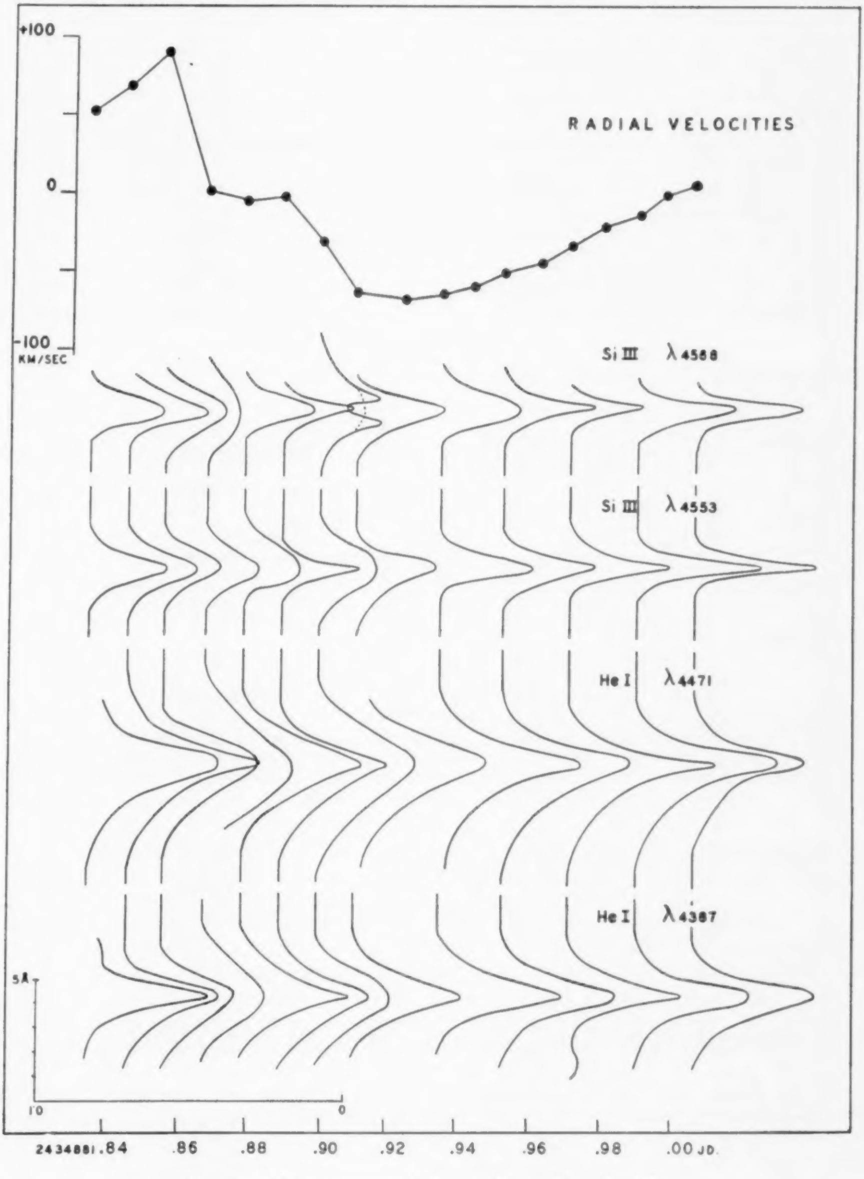

FIG. 2.—Velocity-curve and line profiles on May 19, 1954

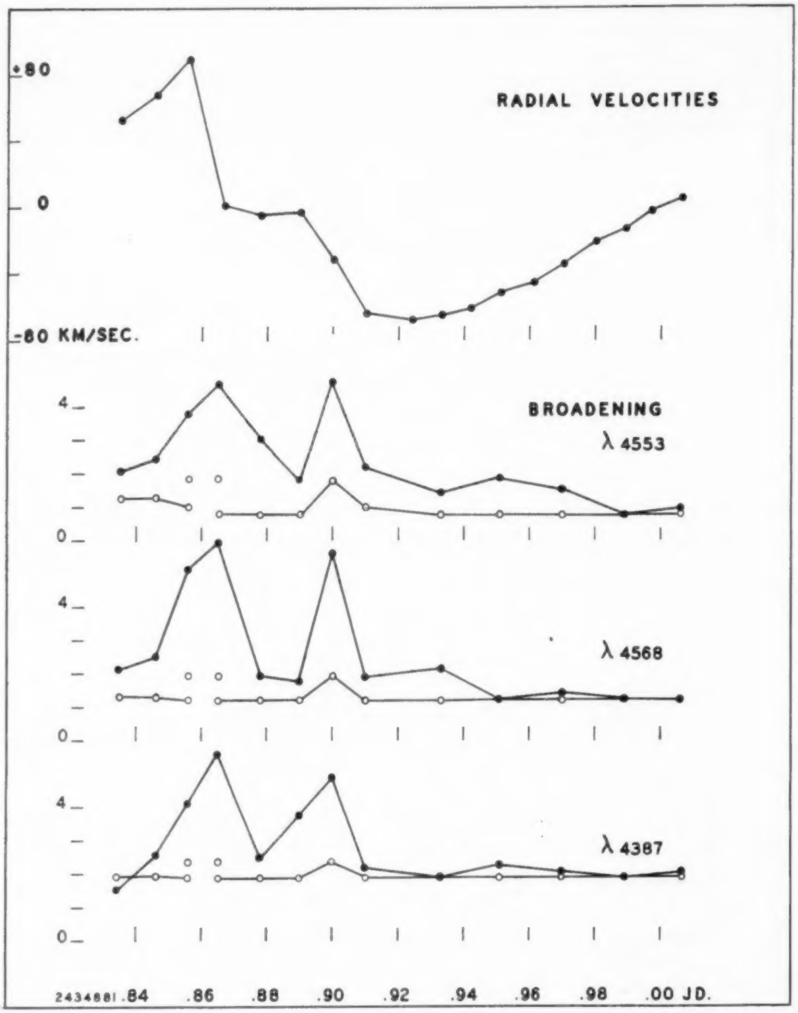

FIG. 3.—Velocity-curve and line broadening on May 19, 1954. The dots represent the observed broadening; the open circles represent the computed "broadening" on the supposition that it is produced by integration of the velocity-curve during the exposure.

broaden before maximum velocity is reached. This part of the velocity-curve shows the same change during exposure as that found from plates taken at the sharp-line stage. Furthermore, at minimum velocity the lines are broad, but the velocity-curve is nearly horizontal. An investigation was also made of the possibility that the velocity-curve is discontinuous and that the line broadening results from the merger of two lines in the spectrum. Such a phenomenon was first detected by one of us in the hydrogen absorption lines of RR Lyrae and has been confirmed by R. F. Sanford's discovery of double metallic lines in this star and in W Virginis. A complete discussion of the discontinuous velocity-curves of the latter star has recently been published by H. A. Abt (1954). In the case of BW Vulpeculae the blending of two components, having the narrow widths observed on the ascending branch of the velocity-curve and separated in radial velocity by about 150 km/sec, would produce double lines on our high-dispersion spectrograms. Such doubling is not shown on our plates, but the time resolution of our exposures (15–20 minutes per exposure) was not sufficient to investigate this question further. Shorter exposures will be obtained, to ascertain whether the steep branches of the velocity-curve are physically real or whether they are produced by a rapid change in the relative intensities of two or more component lines.

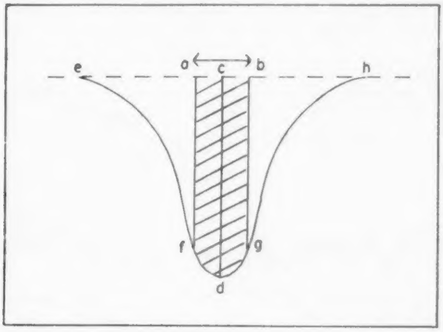

FIG. 4.—This diagram illustrates how the "broadening" of a line is determined. The line profile is divided into the three areas shown. The central area of *afdgb* is equal to the sum of the other two areas located in the wings of the line. The "broadening" is then defined as the ratio of the length, *ab*, to the central depth, *cd*.

In order to investigate whether there are velocity differences between the lines of different elements, the differences $V_H - V_{\text{all}}$ (the velocity of the H lines minus the velocity determined from all lines) were computed for all our plates. The velocity of the H lines refers to the mean of the velocities determined from $H\gamma$ and $H\delta$. The differences $V_H - V_{\text{all}}$ are given in Table 2 and are also depicted in Figure 5. An inspection of this figure reveals, just after zero phase, a distinct departure of approximately 35 km/sec between V_H and V_{all}. Since the H lines have been used in the formation of V_{all}, the departure between the H lines and the other lines is probably nearer 40 km/sec. Since the lines are broad at this phase, a considerable scatter should be expected; but there can be no doubt as to the reality of this phenomenon, because it is present on the high-dispersion as well as the lower-dispersion plates. The coudé plates were measured twice at this phase of the velocity-curve. It is surprising that the duration of this velocity difference is so short, about 15 minutes. It should be emphasized that the spectrograms were exposed for approximately 15 minutes, and therefore many details of the behavior of the H lines may have been lost. Plates taken with a greater time resolution would be useful in giving us more knowledge of this phenomenon. There is also a general tendency for the *H* lines to give larger velocities near phase 0.04 day and smaller velocities near phase 0.06 day, but they are not so pronounced as the large difference noted after zero phase. A velocity discrepancy between the *H* lines and the lines of the other elements has been found in β Canis Majoris by Van Hoof and Struve (1953) and in 16 Lacertae by Van Hoof, de Ridder, and Struve (1954). Their results are in qualitative agreement with those found for BW Vulpeculae.

Microphotometer tracings of the *H* lines, during the critical phases when they give large positive velocities, are shown in Figure 6. These tracings show that the $H\delta$ and $H\gamma$ lines of hydrogen are unsymmetrical at JD 2434881.867. This corresponds to the phase when the large positive displacements of the *H* lines are observed. The lines are unsymmetrical in the sense that they are winged shortward (i.e., sharper on the longward side).

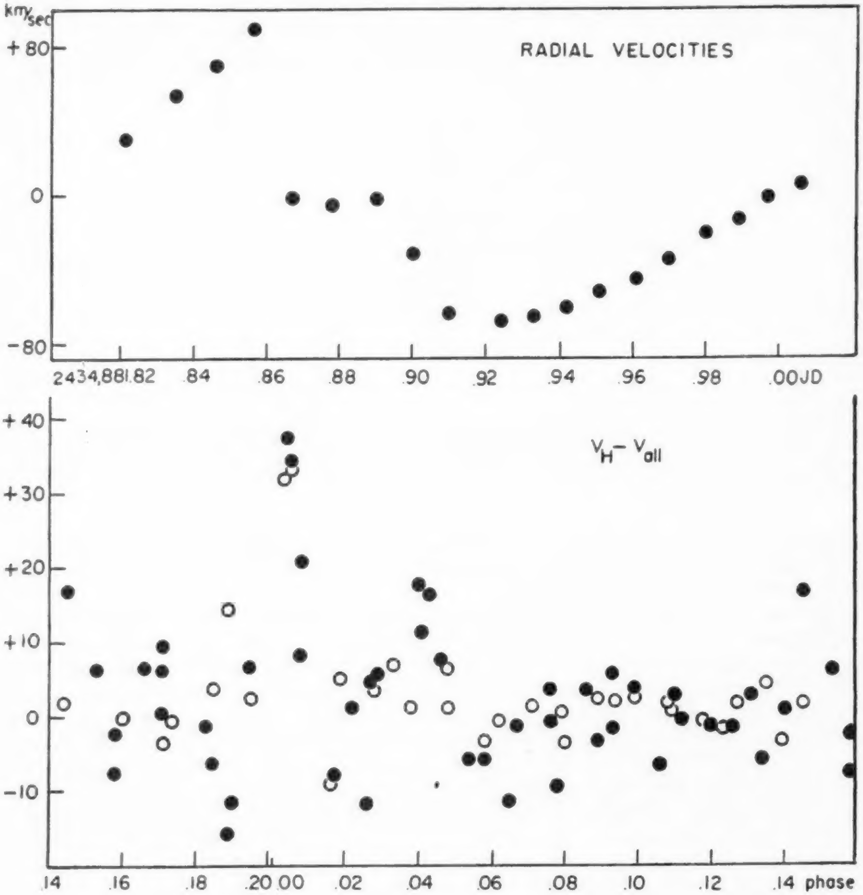

FIG. 5.—The velocity-curve on May 19, 1954, and the difference $V_H - V_{\text{all}}$ (velocity determined from the *H* lines minus the velocity determined from all lines measured) for all plates. The open circles represent coudé plate measures, and the dots Cassegrain plate measures.

This asymmetry is apparently true only for the plate taken at the time noted, since the *H* lines on the plates taken before and after this particular time show symmetrical lines. The asymmetrical *H* lines are therefore present during the same interval of time in which the large positive difference $V_H - V_{\rm all} = 35$ km/sec persists. It is interesting to note that the *H* lines are asymmetric in such a way as to give a positive displacement with respect to the other lines, since the plate measurer will set on the core of the line which is displaced to the longward side of the center of the wings.

The cores of the *H* lines, upon which settings are made for velocity measurements, are formed in the outermost layers of the atmosphere, while the wings of the *H* lines and the

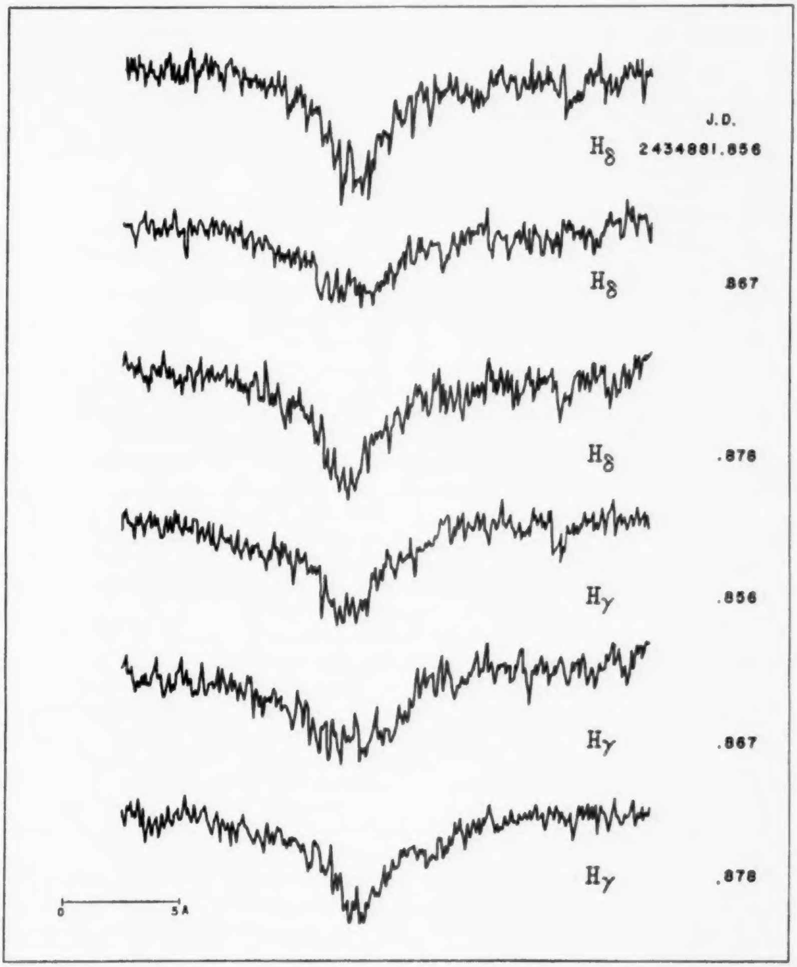

FIG. 6.—Microphotometer tracings of the hydrogen lines $H\gamma$ and $H\delta$ for three phases on May 19, 1954. Note the asymmetry of the hydrogen lines on the plate taken on JD 2434881.867. This time corresponds to the phase when the large positive displacement in the *H*-line velocity is observed.

lines of the other elements are formed at deeper layers. For example, Neven and de Jager (1954) found from their observational models of four early B-type stars that the *He* and the *H* lines are formed at different effective heights in the atmosphere. The helium lines are formed at an optical depth $\bar{\tau} \sim 1$, and the *H* lines are formed at $\bar{\tau} \sim 0.2$. Hence the asymmetric *H* lines and their departure in velocity from the lines of the other elements can be accounted for in a qualitative manner if a velocity gradient is present in the atmosphere at the appropriate phases.

We are indebted to Dr. R. M. Petrie for placing his investigation of BW Vulpeculae at our disposal in advance of publication.

REFERENCES

Abt, H. A. 1954, *Ap. J.*, Suppl. Ser., **1**, No. 3, 63–90.
Eggen, O. J. 1948, *A.J.*, **53**, 197.
Huffer, C. M. 1938, *Ap. J.*, **87**, 76.
Kraft, R. P. 1953, *Pub. A.S.P.*, **65**, 45.
Lynds, C. R. 1954, *Pub. A.S.P.*, **66**, 197.
Neven, L., and Jager, C. de. 1954, *B.A.N.*, **12**, 103.
Nikonov, V. E., and Nikonova, E. K. 1952, *Pub. Crimean Ap. Obs.*, **9**, 135.
Petrie, R. M. 1937, *Pub. A.A.S.*, **9**, 53.
———. Unpublished.
Struve, O. 1952, *Ann. d'ap.*, **15**, 157.
Van Hoof, A., Ridder, M. de, and Struve, O. *Ap. J.*, **120**, 179.
Van Hoof, A., and Struve, O. 1953, *Pub. A.S.P.*, **65**, 158.
Walker, M. F. 1954, *Ap. J.*, **119**, 631.

SPECTROGRAPHIC OBSERVATIONS OF VISUAL DOUBLE STARS*

Otto Struve and K. L. Franklin
Berkeley Astronomical Department, University of California

Received September 20, 1954

ABSTRACT

The spectral types and estimated rotational velocities of the components of visual double stars are listed in Table 1. These quantities have been plotted against the photometric values of Δ mag., taken mostly from A. Wallenquist's catalogue. The results are consistent with the hypothesis that (*a*) the binaries have different ages, but the components of each binary have the same age; (*b*) in the younger systems both components lie on the "primordial" main sequence, which differs little from the sequence defined by the single stars of luminosity class V; (*c*) in systems of intermediate age the primaries are subgiants (luminosity class IV), with rotational velocities which, on the average, exceed those of the primaries of similar spectral types; and (*d*) in the oldest systems the primaries are subgiants of later spectral types and of smaller rotational velocities than their secondaries.

The data on visual double stars, contained in *Mount Wilson Contribution*, No. 511, have been presented in a form similar to that given by F. C. Leonard in 1923. The arrangement of the primary components, according to Δ mag. and Δ color is interpreted in terms of the ratios of the radii of the components.

The observational material discussed in this paper was obtained with the coudé spectrograph of the 100-inch reflector at Mount Wilson. Most of the spectrograms have a dispersion of 10 A/mm and cover the region λλ 3600–5000, but a few were taken with dispersions of 4.5 and 2.8 A/mm, respectively. The observing program was obtained from Aitken's (1933) catalogue, and preference was given to those physical systems which either could be resolved on the slit or might be expected to show double lines, if their separations were too small for resolution. Preference was also given to those systems whose brighter components were later than about A5 and whose components were not giants or supergiants. However, these rules were not followed rigorously, so that the material contains a mixture of binaries having different characteristics.

Spectral types for all observed components have been estimated from the plates by comparison with a series of MK standard spectra at the same dispersion, chosen from the list of Johnson and Morgan (1953). The series (A7, F0, F5, F8, G2, G5, G8, all main sequence), used in accordance with the precepts of the MKK atlas (Morgan, Keenan, and Kellman 1943), allowed us to estimate spectral types in any binary system, accurate to one or two subtypes. Luminosity effects are generally too subtle for reliable estimates, without having a suitable set of standards representing the several luminosity classes. The classes appearing in Table 1 are intended only as an indication of the probable luminosity of the object, as indicated in its spectrum. The magnitude differences have been taken directly from Wallenquist's catalogue (1954), with the exception of ADS 8202 (HD), 9375 (ADS), and 14279 (Johnson 1953). The rotational broadening of the spectral lines was estimated on all spectrograms, using an arbitrary scale of 0 to 10, where 10 represents the broadening in the brighter component of ADS 8257. A rough calibration of this scale indicates an equatorial velocity of rotation $V_{\text{rot}} \sin i = 150$ km/sec for this star. Zero stands for lines of perfect sharpness, as in Procyon.

The data of Table 1 are represented in Figures 1 and 2. The co-ordinates of these figures are M_v and effective temperature. The luminosity branches III, IV, and V are plotted from Tables 1.3 and 1.5 by Keenan and Morgan, published in Hynek's *Astrophysics* (1951). In Figure 1, lines connect the same spectral types on the three branches

---

* The spectrograms used in this work were obtained by O. Struve as guest investigator at the Mount Wilson Observatory.

TABLE 1

SPECTRAL TYPE AND ROTATIONAL VELOCITIES OF DOUBLE-STAR COMPONENTS

ADS	NAME	SPECTRA		ROTATION	Δm	TYPE
		REW	Adopted			
683*	65 PSC	g F0 g F0	A9 F2 III	9 9	0.03	I
903	77 Psc	d F5 d F4	F4 F6	3 0	0.81	III
3353*	....	d F2 d F3	....	5 0	0.11	III
4849	....	d F4 d F4	F5 F4	3 0	0.59	III
5166	20 Gem	d F6 d F6	F6 F4	2 6	0.62	IV
6483*	....	d F6	....	0	....	....
6977	....	d F5 d F6	F5 F3	0 1	0.70	II
6988	ι Cnc	g G6	G5 A5	0 15	2.57	IV
7187	....	d F3 d F4	F3 V F5 V	3 1	0.39	II
7307	....	d F3 d F2	F3 V F3 V	0 0	0.24	II
8119*	ξ UMa	d G0 d G0	....	0 0	0.48	II
8148*	ι Leo	d F4	....	3	2.85	....
8202	17 Cra	d F6 d F7	F8 G0	2 2	(0.08)	II
8257	....	....	F0 III F0 III–IV	10 3	1.35	III
8406	2 Com	d A8 d F2	F0 IV–V F0 IV–V	5 2	1.44	III
8505	....	d F4 d F5	F3 V F5 V	3 0	0.39	III
8519	....	d F2 d F2	F2 F3	10 5	0.09	III
8561	....	d F8 d G2	G5p G8p	0 0	0.59	II
8627*	....	d F6 d F1	....	0 8	0.03	....

* Not plotted in Figs. 1 and 2.

TABLE 1—*Continued*

ADS	NAME	SPECTRA		ROTATION	Δ_m	TYPE
		REW	Adopted			
8630*........	γ Vir	d F0 d F0	F0 F0	3 1	0.02	II
8714........	....	....	F2p G0	6 0	0.76	III
8786........	....	d F5 d G0	F5 G0	0 0	0.47	II
8883........	....	....	K0 K2	0 0	0.30	II
8987*........	....	d A6n	A	10	....	....
9053........	....	d F7 d G1	F5 F8	5 1	0.65	III
9174*........	....	F0+A2	....	4	0.29	....
9375........	54 Hyd	d F1n d F9	F0 III G3	10 1	(1.9)	III
9413........	ξ Boo	d G5 d K5	G5 K5	0 0	2.16	II
9493........	....	F0 F0n	F1 F0	5 10	0.20	IV
9507........	....	d G5 d G5	G5 G8p	1 1	0.20	II
9535........	....	d G5 d G6	G5p G8	0 0	0.82	II
9580........	....	d F5	F5 G3	4 0	0.98	III
9617........	η CrB	d F9	G2 V G2 V	1 1	0.26	II
9728*........	....	d F6 d F6	....	1 1	0.09	....
9969........	49 Ser	d K0 d K1	K0 K0	0 0	0.09	II
10157........	ζ Her	d G0	(G0) (K0)	1 1	2.55	II
10993*........	95 Her	A1n g G3	....	10 1	0.13	....
11483........	....	d G0 d F8	G2 V G2 V	0 0	0.16	II
11639*........	ζ Lyr	d A9 A3n	....	3 15	1.38	....

TABLE 1—*Continued*

ADS	Name	Spectra		Rotation	Δ_m	Type
		REW	Adopted			
12145*	....	d G4 d K0	....	1 1	0.09	....
12169	....	d G3 d G5	G8 V G8 V	0 0	0.25	II
13868	....	d F6	F8 F8	0 0	0.79	II
14270	....	d G9 d G8	G8 K0	3 1	0.75	II
14279	γ Del	Sg K1 d F6	K2 IV F8 IV–V	1 1	(0.87)	II
14636	61 Cyg	d K6 d M0	(K5) (K7)	0 0	0.79	II
14773*	δ Equ	d F5	F5 F5	0 0	0.1	II
15971	ζ Aqr	d F2 d F1	F2 F1	6 5	0.22	I
16417*	....	d G1	....	1	....	....
16611*	....	d F d G2	....	0 0	0.63	....
16979	107 Aqr	A5	F0 IV–V F0 V	8 4	0.97	III
17149	....	d G0 d G0	F8 G1	1 1	0.19	II

NOTES TO TABLE 1

683 Both components are giants. Not plotted in Figs. 1 and 2.

903 Secondary shows very sharp lines. This system will be treated more fully in a subsequent paper.

3353 South-preceding component is a spectroscopic binary. Not plotted in Figs. 1 and 2.

4849 Spectral type of primary may be uncertain.

5166 This system will be treated more fully in a subsequent paper.

6483 Separation too small to be resolved on spectrograph slit. Not plotted in Figs. 1 and 2.

6977 Primary is clearly later than secondary.

6988 Secondary has very broad, faint features.

7307 Sharp lines in both components.

8119 Both components are spectroscopic binaries. Not plotted in Figs. 1 and 2. Secondary shows broad emission in *H* and *K*.

8148 Not resolved on spectrograph slit. Not plotted in Figs. 1 and 2.

8202 Secondary has slightly sharper lines. Δm from *HD*.

8257 Primary has very broad lines. $\lambda\,4077 \approx \lambda\,4226$. This system will be treated more fully in a subsequent paper.

8406 Primary has broader lines than secondary and shows stronger hydrogen. This system will be treated more fully in a subsequent paper.

8519 Both components show broad lines but the south-preceding component has very broad lines.

8561 Both components show fine cores in most of the lines, especially the primary. In the secondary, both hydrogen and iron lines are strong; *CN* is well developed at λ 3883.

8627 Both components are spectroscopic binaries. Not plotted in Figs. 1 and 2.

8630 The primary has slightly broader lines and may be bluer than the secondary. Not plotted in Figs. 1 and 2.

8714 *HD* remarks: "Spectrum appears to be composite. . . . The primary may be a close double." Our plates are too weak to study the peculiarities: hydrogen looks too strong; G band may be present. Note made at telescope: "m_v must be ~ 8.5 and 9.2."

8786 High-velocity object, $v_r \sim 90$ km/sec (R. E. Wilson 1953). The secondary shows more lines, stronger G band, stronger $H\delta$, but equal or weaker $H\gamma$ than primary. This system will be treated more fully in a subsequent paper.

8883 Secondary shows strong *Al* I lines.

8987 Not resolved on spectrograph slit. Not plotted in Figs. 1 and 2.

9053 Secondary shows *H* and *K* in emission; suspected in primary.

9174 Just resolvable in seeing 4/10. Secondary may have wider lines. Both are early (A or F) showing *Ca* II H and $H\epsilon$ resolved. Not plotted in Figs. 1 and 2.

9375 Primary is very similar to ADS 8257A. If ADS 9375A is placed in the position of ADS 8257A, ADS 9375B would fall about 0.3 mag. below the IV sequence at $T_e \sim 5150$. Δm from ADS.

9413 Secondary is similar to 61 CygA (=ADS 14636A); *H* and *K* show sharp emission features, stronger than the continuum. Primary also shows *H* and *K* emission.

9493 Both components have broad lines; the secondary shows very broad lines. Spectral types uncertain.

9507 Both components show emission in *H* and *K*. Hydrogen is too strong in the secondary.

9535 Hydrogen is too weak in the primary.

9580 One plate (March 13, 1954) shows in the primary a combination of sharp and also rather broad lines. A later plate (May 17, 1954), taken for confirmation, does not show this effect so clearly. The secondary has very sharp lines and shows no obvious changes in the 2 months.

9617 Clearly resolved on a night of excellent seeing. The primary is approaching, the differential radial velocity being $\cong 10$ km/sec.

9728 The primary is a spectroscopic binary. Not plotted in Figs. 1 and 2.

9969 *H* and *K* are not in emission on our plates, which are rather weak in that region.

10157 Spectral types due to Struve and Ratcliffe (1954). R. E. Wilson (1953) gives $v_r = -69.9$ km/sec; possibly a high-velocity object.

10993 All lines in the primary are very broad; only hydrogen is obvious at 4.5 A/mm. Not plotted in Figs. 1 and 2.

11483 *H* and *K* may show double emission features in both components.

11639 A multiple system. The primary is a metallic-line star. Not plotted in Figs. 1 and 2.

12145 The secondary is a close visual double. Not plotted in Figs. 1 and 2.

12169 Johnson's colors (1953) show the primary to be slightly redder than the secondary; the spectra are very nearly similar.

13868 Johnson's colors (1953) are identical for both components. Spectra are very similar.

14270 A longer exposure may show *K* in emission.

14279 Δm from Johnson (1953). Primary is clearly not a dwarf; secondary may also be somewhat above the main sequence. Jenkins (1952) gives the parallax as $+0''.022 \pm 0''.005$; therefore, $m - M = -3.3$ mag., and $M_v = +1.0$ for the primary, according to Johnson's measure, $V_A = +4.27$.

14636 Spectral types from Johnson and Morgan (1953). R. E. Wilson (1953) gives $v_r = -64$ km/sec; possibly a high-velocity object.

14773 Wehlau (thesis, University of California, 1954) finds less than one subclass difference in spectrum. He quotes $\Delta m_v = 0.1$. Not plotted in Figs. 1 and 2.

15971 The secondary may be an unresolved astrometric binary. Lines in both components are very broad; in the secondary the weak lines appear to be shifted redward with respect to the strong lines. Not plotted in Figs. 1 and 2.

16417 Not resolved on spectrograph slit. Not plotted in Figs. 1 and 2.

16611 Secondary is a spectroscopic binary. Not plotted in Figs. 1 and 2.

16979 Both spectra appear similar, although hydrogen may be too strong in the primary.

17149 The secondary may be slightly later than G1.

shown. The points of Figure 5 are the locations of the primaries after the secondaries of the observed systems have been arbitrarily placed on the main sequence drawn in the diagram. In Figure 2 the primaries and secondaries have been connected, but in both figures only the primary has been plotted. The four different symbols correspond to the four categories in which the systems have been placed: *I*, spectrum of each component shows broad (*n*) lines; *II*, spectrum of each component shows sharp (*s*) lines; *III*, spectrum of primary shows markedly broader lines than secondary; *IV*, spectrum of secondary shows markedly broader lines than primary. The symbols in the diagrams are intended to show the relative line broadening of the two components, in each system. They contain less information than is given in Table 1; nevertheless, they bring out several interesting relations:

a) There is a striking tendency for the primaries to lie above the main sequence (luminosity class V). This tendency is especially pronounced among the hotter primaries, as shown in the accompanying table. This effect is identical with that discussed by H. L. Johnson (1953). For comparison with our own results, we have replotted Johnson's data in Figure 3, showing the positions of the secondaries as they were arbitrarily placed in absolute magnitude upon the main sequence. ADS 5166 = 20 Gem and ADS 8257 have been plotted from photometric data on Johnson's system, which was supplied to us by D. L. Harris and by H. L. Johnson, respectively, at the McDonald Observatory. ADS

	No. of Primaries	
	Above V Line	Below V Line
Primaries hotter than 5700°....	17	4
Primaries cooler than 5700°....	7*	4

* Omitting one class II–III primary.

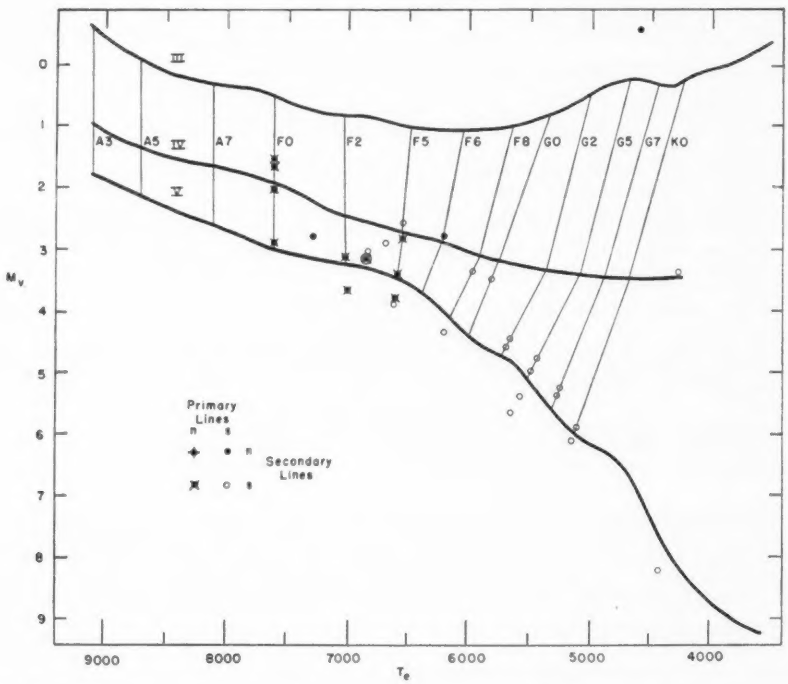

Fig. 1.—Effective temperatures derived from spectral types and luminosities of primary components of visual double stars.

5166 was also observed for us in six colors by G. E. Kron at the Lick Observatory. We have added to the diagram some systems published in the list by Johnson and Morgan (1953). The triple system is 36 UMa.

b) Only in two systems (ADS 903 and 4849) has the later component the broader lines. However, unpublished measures by H. L. Johnson show ADS 8257A to be redder than its secondary; ADS 8257 is a category *II* system. The lines in the spectrum of ADS 8257B are very similar to those of ADS 903A = 77 PscA, but the spectrum of ADS 8257A exhibits some of the broadest lines so far observed in this program. For this reason the spectral type F0 may be somewhat uncertain. With these two hypothetical exceptions (ADS 903 and 4849), the double-star components obey the general rule: the rotation, unless it is zero in both components, is larger in the one of earlier spectral type. This general rule has been known from previous investigations of single stars. But it is surprising that it should be obeyed so minutely by the double-star components. One might have expected that, since large rotations do occasionally occur among early F stars, an appreciable percentage of systems formed in a random manner out of single stars would show the narrower lines in the earlier components. But since our material is small, we cannot be certain that this peculiarity of the binaries is not due to chance or to a possible tendency of parallel orientation of the rotational axes in the two components of each system.

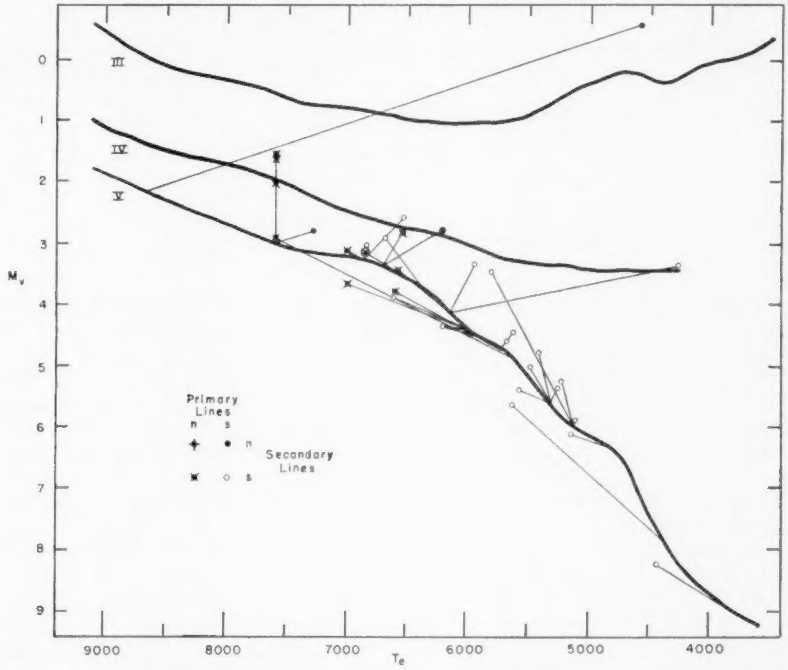

FIG. 2.—Relation between primary and secondary components in H-R diagram

c) Primaries whose temperatures are higher than 6500° K (or whose spectral types are earlier than the F7) very often have much broader lines than their secondaries. This is especially striking in the cases of ADS 8257, 8406, and 16979. ADS 9375 may also belong to this group. In these systems the primaries are subgiants (luminosity class about IV) with large rotational velocities. They are undoubtedly similar in character to the single subgiant F stars which J. L. Greenstein, G. H. Herbig, and A. Slettebak have found to possess large rotational velocities.

d) Two systems, ADS 5166 and 9493, have subgiant primaries which are redder than their secondaries and at the same time have narrower lines than the secondaries.

These results are compatible with the hypothesis that the locations of the primaries in the H-R diagram are the result of nuclear evolution, which proceeds more rapidly in the primaries than in the secondaries. According to A. Sandage (1954), M. Schwarzschild, I. Rabinowitz, and R. Härm (1953), Roy (1952), and others, unmixed stars may be expected to evolve along tracks which displace them above the main sequence and toward the right side of the diagram. Since the rate of evolution is sensitive to mass (or luminosity), it is reasonable to assume, as an approximation, that the secondaries have not had enough time to evolve appreciably off the main sequence. Hence we (and H. L. Johnson) have placed the less massive secondaries upon the main sequence (luminosity class V) in the diagrams. The primaries would then be located upon their respective evolutionary tracks appropriate to their masses, initial chemical compositions, and ages. The diagrams suggest that the binaries differ greatly in age: systems like ADS 7187 and 8505, both components of which are close to the main sequence, despite a considerable difference in luminosity, are relatively young, while systems like ADS 10157 (ζ Her), 5166 (20 Gem), 9493, and 6977 are old.

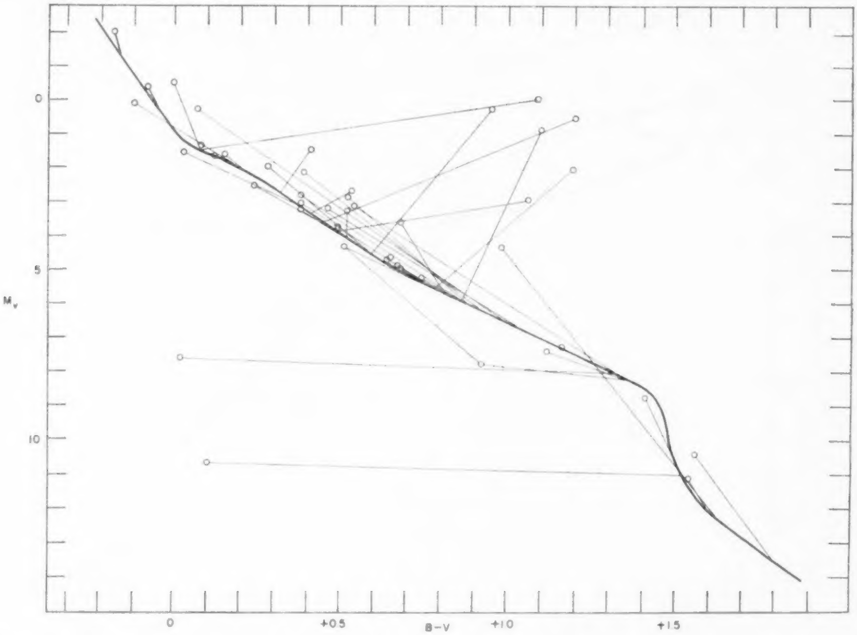

FIG. 3.—Color-magnitude diagram of visual double stars obtained mostly from H. L. Johnson's data

The observed rotational velocities of the subgiant primaries may be indicative of the law of preservation of the angular momenta of these stars. Consider, for example, three systems chosen to have roughly similar spectral types and rotations of the secondary components:

$$\text{ADS 8505}\left\{\begin{array}{ll}\text{primary} & \text{F3 rot. 3}\\ \text{secondary} & \text{F5 rot. 0}\end{array}\right\}\ \Delta m = 0.39\,,$$

$$\text{ADS 4849}\left\{\begin{array}{ll}\text{primary} & \text{F5 rot. 3}\\ \text{secondary} & \text{F4 rot. 0}\end{array}\right\}\ \Delta m = 0.59\,,$$

$$\text{ADS 6977}\left\{\begin{array}{ll}\text{primary} & \text{F5 rot. 0}\\ \text{secondary} & \text{F3 rot. 1}\end{array}\right\}\ \Delta m = 0.70\,.$$

We should regard the first as a young system, the second as of intermediate age, while the third is old. Similarly, if we compare

$$\text{ADS 8519}\left\{\begin{array}{ll}\text{primary} & \text{F2 rot. 10}\\ \text{secondary} & \text{F3 rot. \ 5}\end{array}\right\}\ \Delta m = 0.09$$

and

$$\text{ADS 5166}\left\{\begin{array}{ll}\text{primary} & \text{F6 rot. \ 2}\\ \text{secondary} & \text{F4 rot. \ 4}\end{array}\right\}\ \Delta m = 0.62\,,$$

we should conclude that the youngest systems display the original distribution of equatorial axial rotations along the main sequence. Evolutionary changes of the primaries result in an increase in their radii and, consequently, in a diminution of the observed amount of rotational broadening. But this change is slower (at least among the earlier spectral types, A to F5) than the corresponding change in spectral type. Hence in such systems as ADS 8257, where the components have similar spectral types, the subgiant primary has much broader lines than its main-sequence secondary. The primary must have been, in its youth, an A-type star of very rapid rotation.

Since we now observe the effects of evolution in the appearance of the primary, similar but less pronounced effects should be present in the secondary, and we might not be justified in placing the secondary on the main sequence. That this objection is not entirely valid may be seen when it is remembered that the presently observed main sequence is defined by stars chosen without regard to probable age, but for the purpose of defining the sequences in the co-ordinates M_v and T_e. These stars may have a wide spread in ages; therefore, the present main sequence has a certain amount of evolution already affecting it. This tends to cancel any error we might make in placing the secondaries of visual binaries on the main sequence in order to study the evolutionary effects in the primaries.

A number of primaries are below the main sequence, underluminous for the dwarf spectral types. It is tempting to suggest that these may be very young systems, with both components lying on or near the primordial main sequence. However, it must be remembered that departures from the main sequence may have other causes. A few of the overluminous primaries may themselves be undetected doubles, or the companions of underluminous primaries may be double. Another cause which should not be overlooked is the accuracy of the data used in the construction of the main sequence. A more detailed standard spectral series may show a few irregularities in the assigned spectral types.

The hypothesis which we have advanced requires the evolutionary tracks of early-type stars to carry them predominantly toward the right side in the H-R diagram. If these tracks were predominantly along vertical lines, as Sandage (1954) has convincingly shown them to be for later-type stars like ζ HerA, it would be difficult to explain the frequent occurrence of appreciable rotations among the F-type subgiants.

In order to supplement our knowledge of the physical properties of the visual binary stars, we have constructed Figure 4, similar to one employed by F. C. Leonard (1923). For each suitable pair listed in *Mount Wilson Contribution*, No. 511 (Adams *et al.* 1935), we have plotted Δm_v when available from Wallenquist's catalogue (1954) against the difference in color, ΔC_s. The colors (C_s) were obtained from the Mount Wilson spectral types by means of the conversion by Seares and Joyner (1943). The points in Figure 4 are located according to the following visualization: if the pairs are plotted in a color-magnitude diagram and the components connected by a straight line, Figure 4 is obtained by transferring the line intact to the Δm, ΔC_s co-ordinates with the secondary component placed in the origin. The plotted point is then the position of the primary.

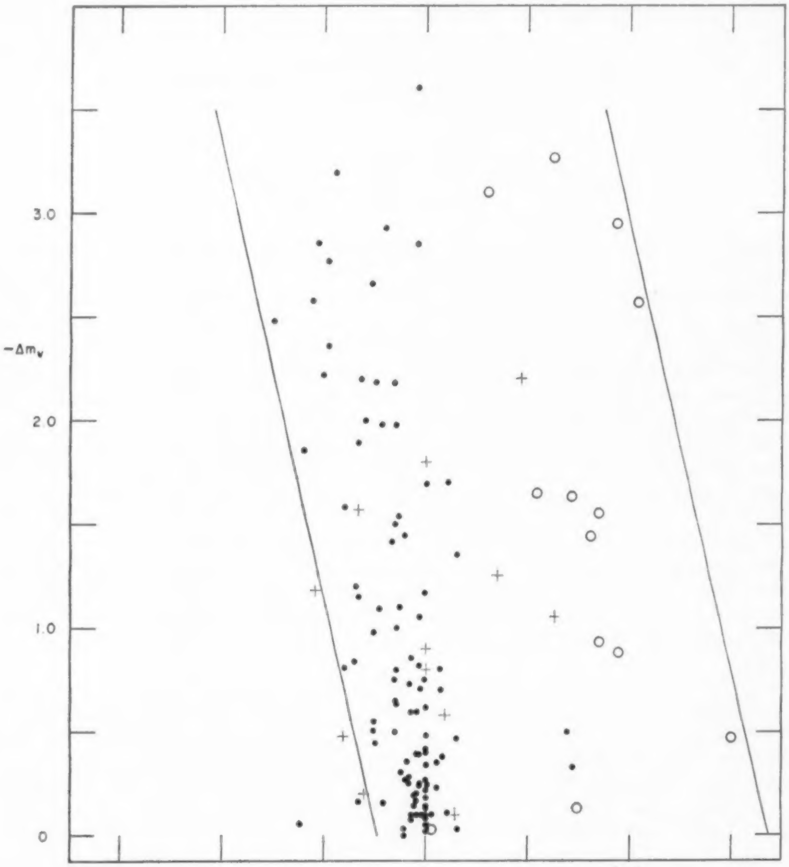

Fig. 4.—Plot of differences in magnitude and color for visual double stars

It is thus easy to understand the apparent separation in these co-ordinates of dwarf-dwarf systems (*filled circles*), giant-dwarf systems (*open circles*), and dwarf-giant systems (*triangles*). Giant-giant systems are vertical crosses.

If we assume that the stars radiate like black bodies, we may apply the formulae of Russell, Dugan, and Stewart (1938). Thus the following relation may be derived:

$$5 \log \frac{R^b}{R^f} = \Delta C \left(\frac{\lambda_2}{\lambda_1 - \lambda_2} \right) - \Delta M_{\lambda_1} + \beta ,$$

where

$$\beta = \frac{\lambda_1 \left(x^b_{\lambda_1} - x^f_{\lambda_1} \right) - \lambda_2 \left(x^b_{\lambda_2} - x^f_{\lambda_2} \right)}{(\lambda_1 - \lambda_2)} ,$$

and where b and f refer to the (visually) brighter and fainter components; R is the radius of the star; $\lambda_1 > \lambda_2$ are the effective wave lengths in centimeters at which the magnitudes are determined; ΔC is the color difference, bright *minus* faint; ΔM_{λ_1} is the absolute magnitude difference, bright *minus* faint, at λ_1; and

$$x = 2.5 \log_{10} \left(1 - 10^{-0.624/\lambda T} \right) ,$$

where T is the temperature in ° K. When the temperature difference between the components is small, β is small; any difference of the order of 1000° K may cause this term to be appreciable. If the components are hotter than approximately 10,000° K, β should be computed for differences less than 1,000° K.

Neglecting β and assuming wave lengths $\lambda_1 = 5500$ A and $\lambda_2 = 4400$ A (valid for Johnson's photometry and approximately for the International system), we find the coefficient of ΔC to be $+4.0$; thus ΔC is the most important quantity in determining the ratio of the radii of the components. The empirical limits drawn in Figure 4 represent approximately the slope of constant ratios of radii. These must be regarded as rough guides, since β may affect each system differently, depending upon the actual temperatures involved and may be either positive or negative.

By choosing a main-sequence secondary, one may find where the main sequence lies in Figure 4 by tracing out the locations of several different main-sequence primaries. Using the main sequence defined on the Mount Wilson system (Adams *et al.* 1935), we find that it has a mean slope slightly greater than $+4.0$ and that it passes through the origin of Figure 4. This mean line, however, passes on the left of the line one would draw as an average among all the main-sequence primaries shown in Figure 4. This indicates that most of the systems available for discussion show primaries whose radii are larger than they would be if they were lying on the main sequence. This is just the effect one would expect to find if these stars had undergone appreciable evolution, with consequent increase in radiating area. The evidence of Figure 4 supports the general relations already noted and is in agreement with the observation that many primaries are too luminous for their masses, as determined by Hertzsprung (1923), Strand (unpublished), and van de Kamp (1954).

REFERENCES

Adams, W. S., Joy, A. H., Humason, M. L., and Brayton, A. M. 1935, *Ap. J.*, **81**, 187.

Aitken, R. G. 1933, *New General Catalogue of Double Stars within 120° of the North Pole* (Washington: Carnegie Institution of Washington).

Hertzsprung, E. 1923, *B.A.N.*, **2**, No. 43, 15.

Hynek, J. A. (ed.) 1951, *Astrophysics* (New York: McGraw-Hill Book Co., Inc.), pp. 20 and 23.

Jenkins, Louise F. 1952, *General Catalogue of Trigonometric Stellar Parallaxes* (New Haven: Yale University Observatory).

Johnson, Harold L. 1953, *Ap. J.*, **117**, 361–365.
Johnson, H. L., and Morgan, W. W. 1953, *Ap. J.*, **117**, 313.
Leonard, F. C. 1923, *Lick Obs. Bull.*, **10**, No. 343, 169.
Morgan, W. W., Keenan, Philip C., Kellman, Edith. 1943, *An Atlas of Stellar Spectra* (Chicago: University of Chicago Press).
Roy, A. E. 1952, *M.N.*, **112**, 484.
Russell, Henry Norris, Dugan, Raymond Smith, and Stewart, John Quincy. 1938, *Astronomy*, **2** (rev. ed.; New York: Ginn & Co.), 732 ff.
Sandage, A. R. 1954, *Les Processus nucléaires dans les astres* (symposium at Liége University, 1953) (Louvain: Ceuterick).
Schwarzschild, M., Rabinowitz, I., and Härm, R. 1953, *Ap. J.*, **118**, 326.
Seares, Frederick H., and Joyner, Mary C. 1943, *Ap. J.*, **98**, 261.
Struve, O., and Ratcliffe, Edward. 1954, *Pub. A.S.P.*, **66**, No. 388, 31–32.
Van de Kamp, Peter. 1954, *A.J.*, **59**, 447.
Wallenquist, A. 1954, *Uppsala Astr. Obs. Ann.*, **4**, No. 2.
Wehlau, William H. 1954, *Ap. J.*, in press.
Wilson, Ralph Elmer. 1953, *General Catalogue of Stellar Radial Velocities* ("Carnegie Institution of Washington Publications," No. 601).

THE SUN'S MAGNETIC FIELD, 1952–1954

HORACE W. BABCOCK AND HAROLD D. BABCOCK
Mount Wilson and Palomar Observatories
Carnegie Institution of Washington, California Institute of Technology

Received November 15, 1954

ABSTRACT

More than 450 magnetograms, showing the distribution, intensity, and polarity of weak magnetic fields (> 0.3 gauss) on the sun have been obtained with the solar magnetograph over a two-year period. This interval includes the recent minimum of solar magnetic activity. The records show a pattern with a fluctuating fine structure and certain large-scale regularities.

General magnetic field.—Consistent evidence is found for a general field, predominantly dipolar, with polarity opposite to that of the earth. The mean intensity is of the order of 1 gauss. The general field is usually limited to heliographic latitudes greater than about $\pm 55°$; it has a varying fine structure and shows remarkable random fluctuations in effective intensity and extent. There seems to be no prevailing obliquity between the magnetic and rotational axes. The total flux is estimated to be nearly 10^{22} maxwells.

Bipolar magnetic (BM) regions.—In the lower latitudes the stronger magnetic effects appear as contiguous areas of opposite magnetic polarity, as if loops of a submerged toroidal field were occasionally brought to the surface by rising material. The BM regions obey Hale's laws of sunspot polarity, but spots are comparatively rare, occurring, when at all, within the BM regions while they are young. *Ca* II *plages* are observed where the field intensity is greater than about 2 gauss. Hydrogen filaments occur around the borders of BM regions or, alternatively, seem to divide the region into parts of opposite polarity. As the regions age, they generally expand, showing a decrease in field intensity, and disintegrate until lost in the background of irregular weak fields. There is much diversity in total magnetic flux, duration, area, and course of development.

Unipolar magnetic (UM) regions.—Occasional extended magnetic areas of only one outstanding polarity were recognized. The most prominent UM region of 1953 had an intensity $\overset{\sim}{<} 3$ gauss and a duration of many months; it may well have been related to a prominent sequence of 27-day-recurrent terrestrial magnetic storms. UM regions may be remnants of disintegrating BM regions. We suggest that UM regions may be identified as the heretofore hypothetical "M" regions of Bartels.

Repeated tracings of the same area of the sun at intervals of a few minutes show changes of the order of 1 gauss in the fine structure of the magnetic pattern within a half-hour.

The observations provide objective evidence for the heretofore inferential hypothesis that magnetic fields are fundamental to sunspots, *plages*, prominences, chromospheric fine structure, bright coronal emissions, and, probably, regions of strong radio emission. Several solar phenomena can be synthesized on the proposition that neutral but ionized corpuscular streams are continually being ejected from all turbulent regions of the surface characterized by coherent magnetic fields of average intensity $\frac{1}{2}$ gauss or more. A hydromagnetic model, based on chromospheric spicules, is proposed for such ejection.

INTRODUCTION

The observations of weak solar magnetic fields discussed in this paper were made in the preminimum and minimum years of the solar cycle between August, 1952, and November, 1954. They were obtained with the solar magnetograph, an instrument utilizing the Zeeman effect for the measurement and recording of weak photospheric magnetic fields, which has been described previously by one of us (H. W. Babcock 1953). The instrument measures $H \cos \gamma$, the component of the field in the line of sight, with a precision of a fraction of 1 gauss. An electo-optic analyzer for circular polarization precedes a grating spectrograph of high dispersion and resolving power; at the focus, a double-slit photoelectric detector measures the phase and amplitude of oscillation between the polarized components of the chosen spectrum line. All the results reported here were obtained with the line λ 5250.216, (0), 3 of *Fe* I.

The magnetograph scans the disk of the sun in a series of parallel traces and records conformally the location, polarity, and intensity of the photospheric magnetic fields on magnetograms, such as are reproduced in Figures 1–4. On the records, north is the top, east at the right. An upward deflection of the signal trace with respect to its fiducial line indicates that, for the region on the slit, the magnetic vector is positive in sign (toward the observer), and vice versa. The calibration of the deflections is discussed in a subsequent section, but, in general, a deflection of one trace-interval is equivalent to about 1 gauss. It should be borne in mind that the record indicates the field intensity in a strip centered on the fiducial line, not in the area under the curve. This type of recording was adopted because of its convenience from the technical standpoint. All the available information is presented, and the magnetograms can readily be interpreted. The records can be transformed into contour maps of magnetic intensity, perhaps with different colors to indicate magnetic polarity, but the process adds nothing new.

The present report is based on a sequence of 450 magnetograms, together with certain comparisons of the solar magnetic data with Mount Wilson spectroheliograms, with preliminary synoptic records of coronal line intensities published by the High Altitude Observatory, and with the geomagnetic planetary index, *K*. It has become apparent from a survey of the records that the weak fields recorded by the magnetograph provide one of the most sensitive indicators of solar activity. So much detailed information is to be found on the magnetograms that a verbal description of it is an inadequate substitute for an examination of the records themselves. A limited number of selected magnetograms and short sequences have been reproduced from the original 35-mm negatives in Figures 1–4. They are referred to by the individual dates. In almost all cases the U.T. of observation may be obtained by adding 0.8 day to the recorded calendar date.

The magnetograms reveal information of significance on the sun's general magnetic field, on hydromagnetic turbulence in the photosphere, on the development and life-history of "centers of activity" (including sunspots), and on certain solar-terrestrial phenomena. One of the chief impressions gained is that the photospheric magnetic fields have a prominent fine structure, showing fluctuations with time; this fine structure is probably closely related to turbulence of the highly conducting material with which the fields are associated. Many of the larger-scale magnetic patterns are quite complex, in spite of the fact that the general level of solar activity has been low during the years covered by these observations. Among the regular features of the weak solar magnetic fields, however, three are outstanding.

1. There has been consistent evidence, as previously reported (Babcock and Babcock 1952; Babcock 1953; Babcock and Cowling 1953), for a "general" field of the sun in high heliographic latitudes. The polarity is positive in the north, negative in the south (opposite to that of the earth's field). The intensity of the general field near the poles is of the order of 1 gauss on the average, although there are appreciable fluctuations in the intensity of the effective component and in the lower limit in latitude.
2. Bipolar magnetic (BM) regions, sometimes of vast extent, occur in and near the sunspot zones; they obey the laws of magnetic polarity established for the preceding and following sunspots in the northern and southern solar hemispheres, in a given cycle, by G. E. Hale and his associates (1919). Visible sunspots have been relatively infrequent and short-lived, but when they occur, they are within these BM regions.
3. The heliographic latitudes in the vicinity of ±45° have been, on the average, more nearly free of magnetic fields than any others.

During the period covered by the observations, various improvements have been made in the apparatus, but the principles of the instrument, including the method of recording with a cathode-ray tube and a camera, have been retained throughout. In the original form of the instrument, the parallel traces across the disk from west to east were made by allowing the sun's image to drift. Between August 1, 1952, and February 19, 1953, 101 magnetograms were obtained in this way. At the start, the analyzer incorporated a rotating quarter-wave plate, which, unless very carefully adjusted, was capable of introducing systematic errors into the records. But in October, 1952, all moving parts were eliminated from the analyzer, and the electrically excited birefringent crystal was

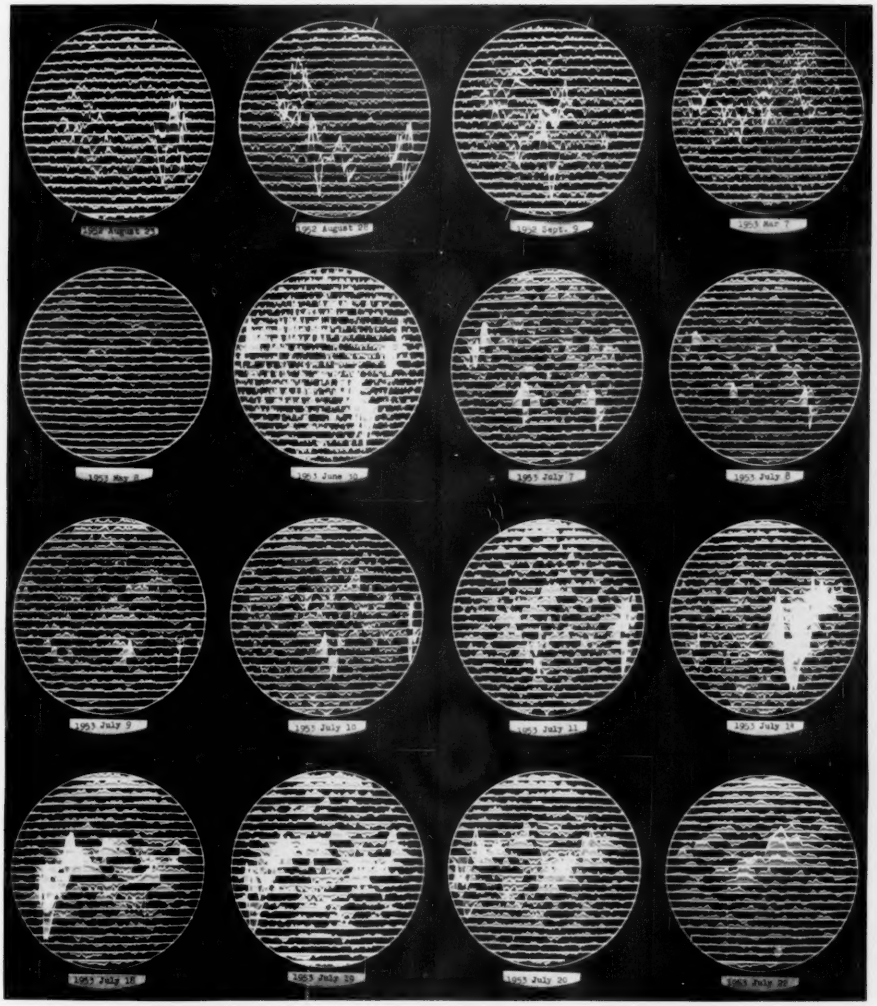

FIG. 1.—On the first three records the position of the poles of rotation is indicated. On all subsequent records the central meridian is vertical. All records were made with a time constant of about 3 seconds, except that of June 30, 1953, which was 1 second. Note the opposite characteristic polarity of BM regions in the northern and southern hemispheres; also the UM region near the c.m. on July 22. Calibration in gauss per trace-interval is: June 30, 0.9; July 7, 1.2; July 8, 1.2; and, by rows: 1.5, 1.3, 1.0, 1.0; 1.5, 1.1, 1.3, 1.4.

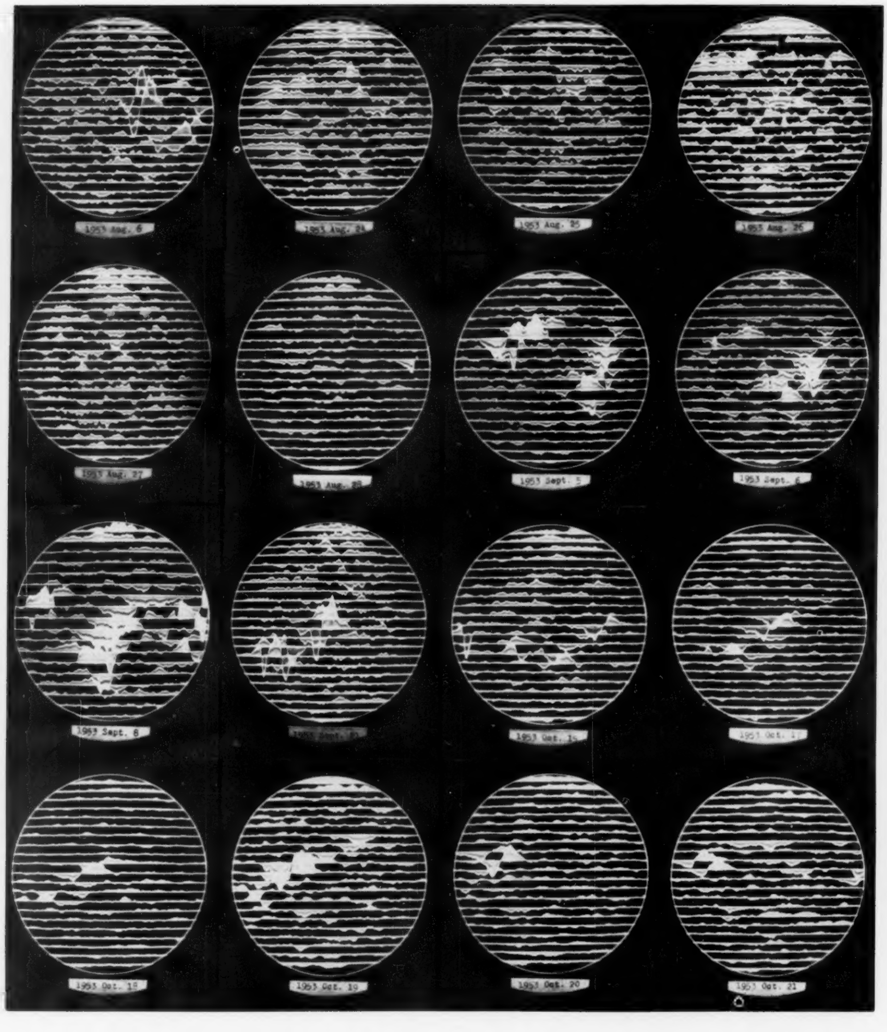

FIG. 2.—Note the unusually strong north polar field on August 26 and 27, 1953; also the UM region on September 8. Calibrations by rows are: 1.0, 1.0, 1.1, 1.1; 1.0, 1.4, 1.5, 1.4; 0.9, 1.0, 1.5, 1.3; 1.5, 0.8, 1.0, 1.3. The amplitude of the deflections is quantitative, but the degree of intensification of the trace on large deflections is arbitrary.

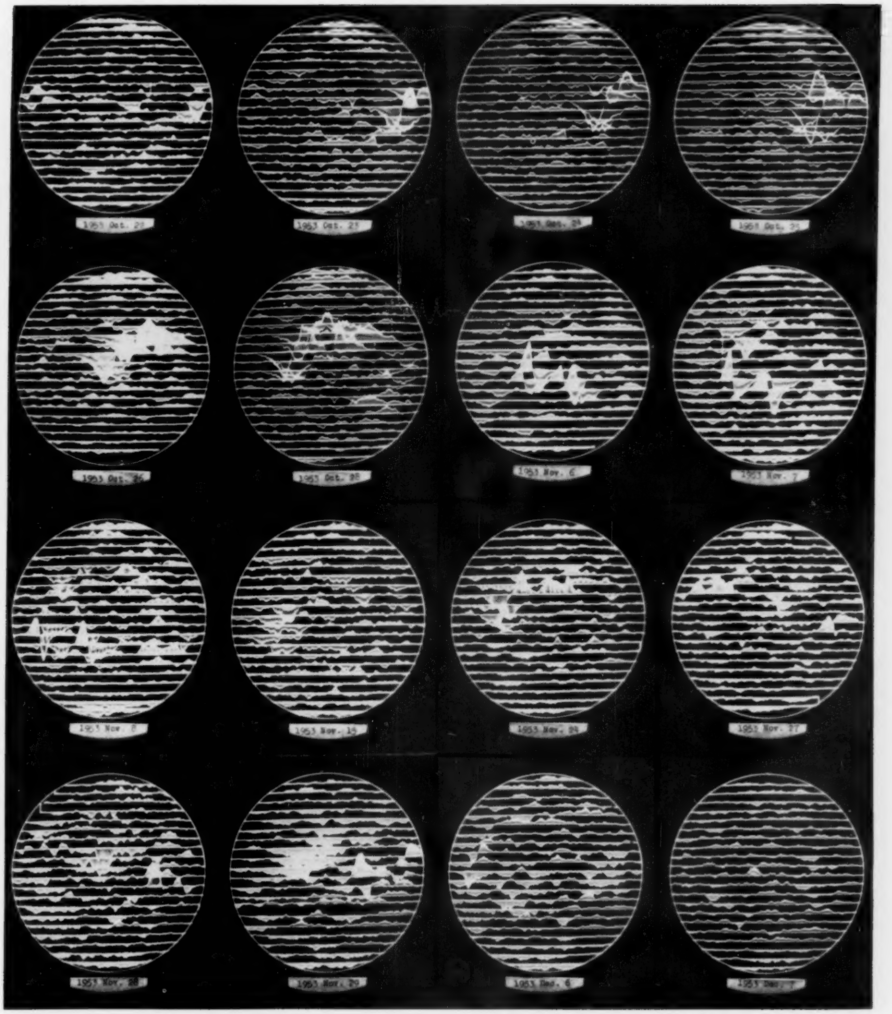

FIG. 3.—The traverse of an extended BM region is shown in the sequence of October 22 to October 28, 1953. The record of December 7 is unusually quiet, even for the months of minimum solar activity. Calibrations are: 0.9, 0.9, 1.0, 0.9; 0.9, 0.8, 1.4, 1.3; 1.1, 1.1, 1.3, 1.3; 1.3, 1.1, 1.0, 1.4.

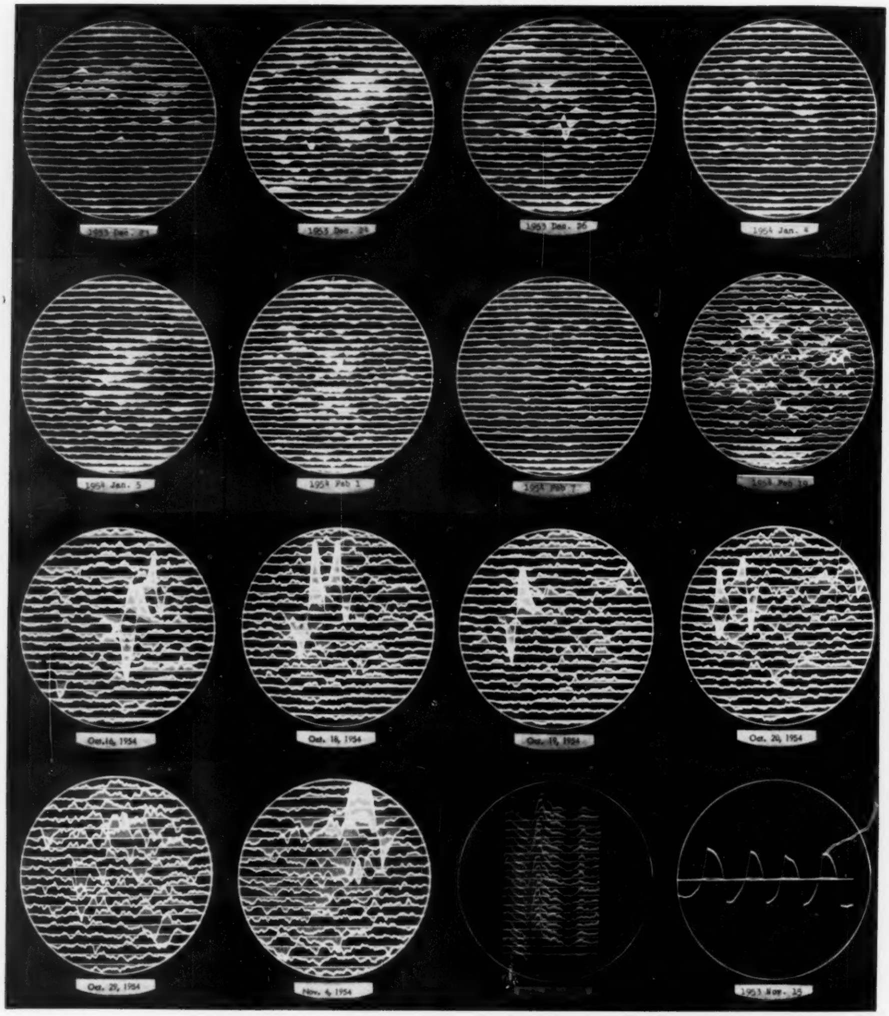

FIG. 4.—Weak but extensive UM regions are seen on December 24, 1953, and January 5, 1954. Note the "old-cycle" BM region in low north latitude on October 19, 1954, and the peculiar unbalanced BM region of "new polarity" in a high north latitude on November 4. The repeated chords of March 26, 1954, show reproducibility of deflections; minor changes are better shown in Fig. 8, *e*. The lowest trace of March 26 is "noise" alone. The record of November 15, 1953, shows calibration deflections equivalent to 5 gauss. Calibrations by rows are: 1.2, 1.0, 1.2, 1.2; 0.9, 0.9, 0.8, 0.6; 0.9, 0.9, 0.9, 0.9; 0.8, 0.8.

put into use. In the spring of 1953 the self-synchronous scanning system was placed in operation. With this system, the traces are always made perpendicular to the central meridian of the sun. Between February 19, 1953, and October 28, 1954, 350 magnetograms were obtained. During the course of these observations, occasional small improvements in sensitivity were made, the most important being the installation in February, 1954, of a superior grating that approximately doubled the available light and retained a resolving power of 600,000. All these changes resulted in a gradual improvement in the quality of the records.

Calibration.—The sensitivity was frequently checked by making calibrations according to the method of artificial deflections outlined earlier (Babcock 1953). A sample calibration record is shown in Figure 4. Also, during the course of each observation, the brightness of the solar image was measured with a simple photoelectric meter. This provided a basis for the calibration of the individual magnetograms in terms of gauss per interval between traces. Calibrations are available for 294 magnetograms taken between June 20, 1953, and October 28, 1954. One of the greatest variables is the low-level atmospheric transparency in Pasadena, where the observations were made. Records made on days of inferior transparency, when the light was reduced to a fraction of normal intensity, are recognized by the relatively low noise level and generally low deflections. On typical magnetograms, the calibration of the deflections is about 1 gauss for the interval between traces, and the noise level is about 0.1 gauss (r.m.s.). After the completion of each magnetic scan of the sun, it has been customary to make a "noise record" by switching off the exciting voltage to the birefringent crystal and permitting the instrument to make one or more traces across the disk of the sun without change of any other adjustments. Such noise traces show the small deviations due to random shot noise in the photomultipliers and would also show any systematic error or "signal bias" if such were present. There has been a satisfactory absence of systematic error on practically all magnetograms.

Heliometric resolution.—The diameter of the sun's image is about 40 cm and the length of the scanning slit is 15 mm. Thus the instrument averages the magnetic effect over 70 seconds of arc, corresponding to a distance of 52,000 km on the projected disk, in the general direction of the central meridian. In the direction of scanning (perpendicular to the central meridian) the effective resolution is determined by the time constant chosen for the electrical smoothing circuits. To obtain a suitable signal-to-noise ratio at the light-level available, the time constant is usually made about 3 seconds. At the customary rate of scanning, the motion of the slit with respect to the image is about 38 seconds of arc (28,000 km) in this interval of time. When conditions warrant, a slower rate of scanning is desirable, because there is no doubt that many of the finer details of the magnetic pattern are unresolved on the usual magnetograms. Tests with and without scanning have shown that small magnetic areas of diameter 30 seconds of arc and having an average field of 5 gauss may show on the standard magnetograms an indicated field of only 1 gauss, because of the smoothing effects mentioned. But the resolution is such that more extensive fields are recorded without serious reduction in scale, and it is these that are the first concern of this paper. The magnetogram of June 30, 1953, was made with a time constant of only 1 second and shows more fine structure, but the noise level is inevitably higher.

Studies of the position of filaments as related to magnetic areas and of the details of magnetic regions in general are limited, on the present magnetograms, by the heliometric resolution and by imperfections in the instrumental tracking on some of the records. Occasional errors of position as great as 5 per cent of the solar radius are present. Also, since alternate traces are made in opposite directions, the time constant of the smoothing circuits introduces a slight alternating asymmetry into the traces. This need for higher fidelity in recording the fine structure of the sun's magnetic pattern, as well as the desirability of a still better signal-to-noise ratio, indicates that the magnetograph is capable of much further development. The attainment of these ends is only a matter of practical design.

Sunspot fields.—The magnetograph was designed primarily for measuring and recording weak magnetic fields apart from sunspots, of intensity less than 10 gauss. In the present series of records, no attempt has been made to obtain quantitative results on the much stronger magnetic fields of sunspots themselves, although these naturally produce large deflections. Spots are small compared to the length of the slit and are dark compared to the photosphere; also the amplifier becomes saturated by signals stronger than about 10 gauss. In comparison to the very extended photospheric fields revealed by the magnetograph, sunspots may, in a certain sense, be regarded as almost incidental, being local regions in which the magnetic field is sufficiently strong, according to current ideas (Biermann 1941), to inhibit small-scale convection. This results in darkening through a diminution of energy outflow.

The photoelectric measurement of sunspot fields should be quite feasible in good seeing, however, by using a suitably short slit and by employing a spectrum line rather insensitive to the Zeeman effect, in order that the magnetic splitting of the line shall remain small relative to the half-width of the line profile and to the separation of the two exit slits.

THE GENERAL MAGNETIC FIELD

A weak field in high heliographic latitudes, of positive polarity in the north, negative in the south, has been shown almost consistently by the magnetograph since August, 1952, when good sensitivity was first obtained. Evidence for the polar fields is found on most of the records made under good atmospheric conditions. On days when low atmospheric transparency reduces the light-level and the effective sensitivity by a factor of 2 or more, the weaker fields are poorly recorded. Even under such conditions, however, the polar fields can almost invariably be detected if the scanning is stopped and the sun's image is held stationary, with the slit near the north or south pole; this permits a longer instrumental time constant to be used. In general, the polar fields are detected only in heliographic latitudes higher than about ±55°, but the lower limits in latitude are variable and irregular. When magnetograms made on days of good transparency are compared and when the calibration of all records in gauss per space is taken into account, it is found that there are appreciable fluctuations in the effective intensity of the polar fields, in the pattern of their fine structure, and in their lower limits in heliographic latitude.

Occasional small polar faculae have been seen during the interval under discussion; while these may be related to local field concentrations, they seem to have no essential bearing on the rather extensive polar fields. There appear to be no features on the usual Mount Wilson spectroheliograms in the light of *Ca* II or of hydrogen that can be related to the weak magnetic fields near the poles of the sun; but, as will be shown in a later section, there is such a relationship for the stronger localized magnetic fields found in the lower heliographic latitudes.

If due allowance is made for limb darkening, an average value for $H \cos \gamma$, the component of the field in the line of sight, is about 1 gauss near the poles. Because of the fluctuations and irregularities already mentioned, it is difficult to specify a more precise value. These small-scale fluctuations are plausibly related to turbulent convection, which is continually distorting and "bunching" the lines of force of the magnetic field in the photosphere. For the mean direction of the lines of force we have adopted here the direction of the coronal features known as "polar tufts" or "plumes," which arise from the same high-latitude regions of the sun. (This is open to some question, for, while the magnetic forces may dominate in the corona, they may not do so in the photosphere.) It is probable, then, that the mean effective value of γ is about 60°. The probable mean intensity of the general field of the sun for the last 2 years has therefore been of the order of 1 or 2 gauss near the poles.

The lines of force are most plausibly imagined as passing through the main body of the sun from the vicinity of one pole to the other; hence the field is a property of the sun as a whole, and it appears proper to speak of a general magnetic field, even though evidence for it is usually limited to the polar regions. Factors that lead to confidence in the reality of the general field, as revealed by these observations, are as follows:

1. The deflections near the heliographic poles, while small, are usually several times as great as the largest instrumental noise fluctuations (particularly with a stationary image).

2. The magnetic deflections disappear when the exciting voltage is removed from the birefringent ADP crystal of the polarizing analyzer.

3. The magnetic deflections are reversed in polarity if the azimuth of the birefringent crystal is changed by 90° from its standard position.

4. The indicated field intensity shows a fine structure, varying from point to point on the disk; and within short intervals of time the local deflections are reproducible at will as a function of position.

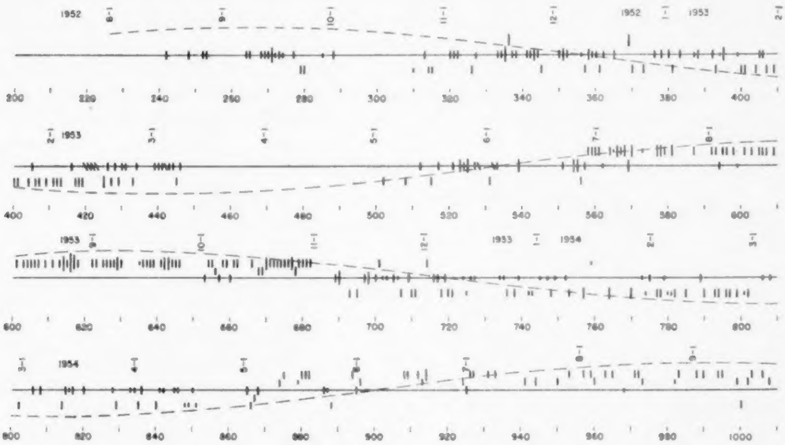

FIG. 5.—If the north polar flux appears greater than the south, a mark is placed above the horizontal axis, and vice versa. Abscissas are Julian days minus 2424000, where the first of each month is also indicated. A sine-curve indicating the heliocentric latitude of the earth, B_0 (amplitude 7°2), has been drawn in. The magnetic-flux ratio (N/S) shows a general dependence on the sign of B_0, as might be expected; but large random deviations are superposed. No evidence is found for obliquity between the magnetic and rotational axes of the sun. The B_0-curve may be used, incidentally, for estimating the heliocentric latitude of the center of any of the magnetograms of Figs. 1–4.

5. Schuster's (1892) assumption, that the polar tufts of the corona suggest the lines of force of a general magnetic field, is still plausible.

6. The ratio of the mean observable magnetic flux for the north and south poles shows an annual variation that appears to be correlated with B_0, the heliocentric latitude of the earth. This effect is discussed in the following paragraph.

On many occasions it has been found that the total apparent magnetic flux in the vicinity of one of the sun's poles is greater than that at the other by a factor of the order of 3 or more. Without at first attempting to evaluate the intensities quantitatively, the magnetograms were inspected and classified as to whether the total apparent fluxes were about equal at the two poles, or, if obviously unequal, which was the stronger. The results are displayed in Figure 5, where, if the north polar deflections were stronger than the south, a mark for the day in question was placed above the horizontal axis, and vice versa. As a matter of secondary interest, days of unusually strong or weak polar field intensity were indicated by longer or shorter marks. A definite seasonal trend appears, although this is masked in part by daily fluctuations, apparently irregular, that may be as great. For comparison, a sinusoidal line, representing B_0, the heliocentric latitude of the earth, has been drawn in. The annual variation of B_0 not only affects the ratio of the the visible areas of the respective magnetic "polar caps" of the sun above $\pm 60°$, but in the same sense it affects γ and the effective component of the field. Except for the first three months (when, in observing, little attention was given to the flux ratio at the poles), the underlying correlation between the sign of the flux ratio and the sign of B_0 appears significant. This emphasizes both the reality of the polar fields and their restriction to high heliographic latitudes.

With reference to Figure 6, we have made a rough computation of the extreme ratio to be expected for the apparent north and south polar fluxes near September 7 and March 7, when B_0 reaches its maximum of $\pm 7\overset{\circ}{.}2$. Here it is again assumed that the polar tufts of the solar corona indicate the mean direction of the lines of force of the field and, therefore, following van de Hulst (1953*a*), that they appear to be tangent to lines diverging from a point on the sun's axis about 0.6 of the way out from the center. Two examples have been considered. In the first, H, the intensity of the field, is assumed to vary linearly as $\theta - 46°$, where θ is the heliocentric latitude of the point on the surface of the sun; in the second, H is assumed to vary as $(\theta - 46°)^{1/2}$. We limit our attention to two narrow uniform strips on the central meridian, one between $+46°$ and the north limb, and the other between $-46°$ and the south limb. The effective flux is $\int H \cos\gamma \cos\theta \, d\theta$ with appropriate limits. Numerical integration shows that the ratio of the magnetic fluxes near the two poles, when B_0 has its maximum value of $7\overset{\circ}{.}2$, is 3.6:1 and 3.1:1 for the two cases. Thus there is no difficulty in accounting for the magnitude and phase of the annual variation in the smoothed mean polar flux ratio.

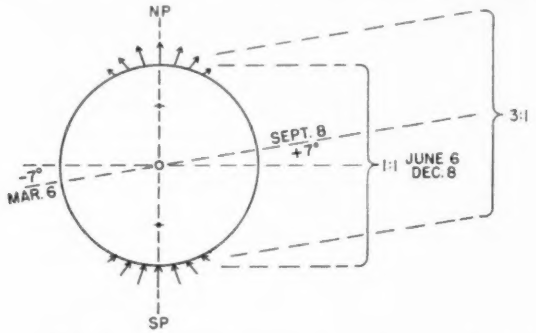

FIG. 6.—The diagram illustrates the annual variation in the magnetic-flux ratio for the north and south polar regions.

There is no evidence from the plot of Figure 5 for a periodic variation in the north and south flux ratio of the order of 30 days, which would be expected if an appreciable obliquity prevailed between the rotational and magnetic axes of the sun. The possibility of some systematic change of the polar fields with the course of the main solar magnetic cycle is not excluded; in fact, the rather limited systematic change in average obliquity of the polar coronal streamers as a function of the phase of the solar cycle (van de Hulst 1953*a*) and the systematic migration of the "polar crown" of prominences (d'Azambuja 1948) suggest the likelihood of an observable variation in the mean effective component of the polar fields.

Quite apart from the annual variation due to the changing value of B_0, the irregular fluctuations in the effective magnetic flux in the vicinity of the heliographic poles have been so large as to defy satisfactory explanation. On a few days the effective flux (usually near the north pole) has been two to three times as strong as normal. On such days not only is the effective intensity greater, but usually also the polar field seems to extend to abnormally low heliographic latitudes. The accompanying tabulation gives the dates in 1953 on which the polar fields (N or S) were observed to be unusually strong. Perhaps the most striking strong polar fields were observed in the north on August 26 and 27, 1953. On August 24 the effective north polar flux was greater than normal, but on August 25 it was about average. On these four days the magnetic activity on other parts of the visible hemisphere was unusually low, and it is by no means clear where the magnetic lines of force emanating from the north polar regions returned to the sun. In contrast to the foregoing, there have been other days on which both north and south polar fields were unusually weak, indeed barely detectable. Some of these days were: December 14, 21, 22, 23, 27, 30, 31, 1953; January 2, 9, 1954. Finally, for an interval of about 13 days, beginning on July 29, 1954, no evidence could be found for any field in the high southern latitudes, although the north polar field had nearly normal intensity; this is a result unprecedented in the 2 years of observation.

July 7	N	July 18	N	Aug. 26	NN	Sept. 22	N
9	N	19	N	27	N	Oct. 19	N
10	N	22	N	Sept. 8	N	26	N
11	N	Aug. 24	N	21	N	Nov. 8	S and N

TABLE 1

EFFECTIVE MAGNETIC FLUX OF POLAR FIELDS

		Maximum Intensity $H \cos \gamma$ (Gauss)	Average Intensity (Gauss)	Area (Disk = 1)	F_e Effective Magnetic Flux (Maxwells)
Nov. 24	N	+0.9	+0.7	0.06	$+0.56\times10^{21}$
$(B_0=+1^{\circ}.7)$	S	−0.5	− .44	.06	-0.4×10^{21}
Aug. 27	N	+1.5	+ .5	.2	$+1.6\times10^{21}$
$(B_0=+7^{\circ}.1)$	S	−0.6	−0.3	0.0002	-0.09×10^{21}

Table 1 gives, for a "normal" record (November 24, 1953) and for an exceptional record (August 27, 1953), the measurements of the effective polar fields and of F_e, the effective magnetic flux integrated over the polar regions of the disk. These measures have been corrected for limb darkening. On August 26, the effective flux was probably even greater than on August 27, but the record was slightly marred by an irregularity in the scan; on both these days the northern "polar" field showed a most unusual extension in heliographic latitude down to 15° N.

As of October, 1954, it appears that the minimum of the sunspot cycle has been passed and that the new cycle is definitely under way. The main poloidal field of the sun has shown no reversal. If it has shown any secular change, which is doubtful, it was perhaps weaker, on the average, during the extreme minimum of the cycle. The present most reasonable course seems to be to assume (for theoretical rather than observational reasons) that the total magnetic flux of the polar fields is constant and that the apparent fluctuations result from a shifting of magnetic areas and from changes in the obliquity of the lines of force.

An estimate of the order of magnitude of the total flux of the poloidal field is of some interest for comparison with the flux of local, low-latitude fields and because it may be an essentially invariant property of the sun. For this approximate calculation we start with the typical magnetogram of November 24, 1953, on which the north polar deflections are of about average intensity and extent and for which B_0 is so small ($+1^{\circ}\!.7$) that it can be neglected. Allowing for limb darkening, a measure of the average magnetic intensity and of the projected area involved for each of the three traces nearest the northern limb results in a figure of 0.56×10^{21} maxwells for the integrated component of the field in the line of sight where the sun is treated as if it were a disk; i.e., $F_e = \int H \cos \gamma \, da$ on the disk. Now to convert this to total polar flux, F_t, on the spherical sun, it is necessary to assume some distribution for H. The assumption is that the magnitude of the field is $H = (H_p/44)(\theta - 46^{\circ})$ and that the direction of the lines of force is as if they diverged from a point on the sun's axis 0.6 of the radius out from the center. The obliquity of the field to the line of sight is γ, where $\cos \gamma = \cos \phi \cos \psi$, and ϕ is the longitude of the point on the surface, while ψ is the projection angle in the meridional plane.

Now $F_e = \int H \cos \psi \cos \phi \, da$, for the polar cap ($\theta > 46^{\circ}$); and, by simple numerical methods, it is found that $H_p = 2.6$ gauss (at the pole). No special significance should be attached to this particular value of H_p, since our assumed field distribution may lead to an artificially high value at the pole. The total magnetic flux of the sun's general or poloidal field (above latitude $\pm 46^{\circ}$ on our assumed distribution) is

$$F_t = \int_{\theta=46}^{\theta=90} H \cos (\theta - \psi) \, d s \,,$$

and a numerical evaluation of this integral gives 8×10^{21} maxwells. In order of magnitude, this is five times as great as the magnetic flux of an average bipolar magnetic region or of a strong unipolar magnetic region (see next section).

LOW-LATITUDE MAGNETIC EFFECTS

In the heliographic latitudes below $\pm 50^{\circ}$ the magnetic effects are more or less localized. No consistent evidence has been found for low-latitude zonal fields that are uniform in longitude. During the months of minimum solar activity, and especially between November, 1953, and July, 1954, the greater part, and sometimes all, of the low-latitude zones have been free of observable magnetic fields. It often appears safe to place an upper limit of 0.2 gauss over considerable areas.

But, except for the extreme minimum of the solar cycle, the low-latitude fields are often numerous, as the magnetograms show. On occasion, a small-scale pattern of weak fields ($\sim$0.5 gauss) may cover nearly the whole disk (October 29, 1954). But more characteristically there are found from one to several discrete magnetic regions of greater strength that remain identifiable from day to day. The magnetic areas range in size from very small up to a considerable fraction of a hemisphere. The field intensity typically ranges from a fraction of 1 gauss in the very large regions up to several gauss in regions of moderate size (1 or 2 minutes of arc in extent) and may, of course, be far stronger in relatively small regions, such as sunspots. The magnetic regions often change appreciably in extent and in magnetic intensity from day to day; they are transient in the sense that they disappear or lose their identity in intervals from an hour for some of the smaller, weak ones up to several months for the larger. The pattern of the magnetic fine structure, like that of the polar fields, may show significant variations in a half-hour.

Most of the prominent magnetic areas may be classed as bipolar magnetic (BM) regions, although some may have to be placed in the multipolar (MM) or complex category. The records for most of the BM regions usually suggest at least approximate equality of positive and negative magnetic flux in the respective parts. In constrast, a few very interesting areas of limited intensity we have classed as "unipolar" magnetic (UM) regions. In introducing the term "unipolar," we refer to regions which on the magnetograms show deflections almost exclusively of one polarity and which are not directly accompanied by adjacent regions of opposite polarity; in most such cases it is not at all obvious where the magnetic lines of force emanating from the UM region re-enter the sun.

BM regions.—The preceding (westerly) and following parts of typical BM regions are contiguous or nearly so and are identified by their opposite magnetic polarity; in many instances the *f* part lies at a higher latitude. Several such regions appear on the magnetograms of Figures 1–4. The magnetic polarity of the *p* and *f* parts of a BM region is the same as that regularly observed in the *p* and *f* sunspots of typical groups in the same solar cycle in the same hemisphere. According to the laws of sunspot polarity, *p* spots in the northern hemisphere have negative polarity, while *f* spots have positive polarity, in the cycle that had its maximum about 1947. The reverse is true in the southern hemisphere. A few BM regions, mostly small but with high latitude and reversed polarity characteristic of the new cycle, were observed in 1954. Sunspots, when they occur, are found within BM regions, most often while these regions are quite young. In many BM regions, however, sunspots have not been seen and possibly do not occur. The regions that involve a large total magnetic flux may persist for a long time, sometimes for many months. The most extensive BM regions may cover more than a tenth of a hemisphere; in such cases, the field is usually weak, and the limits are ill defined.

Even "old-cycle" disturbances, normally originating near the equator, may extend into high latitudes such as ±50°, sometimes merging into the polar fields. Several of the BM regions with intensities of 1–2 gauss have extended over a considerable range of latitude (30°–40° across), with a tendency for the lower-latitude part to precede toward the west. The region as a whole then shows an inclination from northeast to southwest if in the northern hemisphere. Indeed, such patterns were more common in the north in 1952 and 1953. Examples are found in the magnetograms of July 20 and October 19, 1953. Sometimes there has been a less-well-defined tendency for a symmetrical portion of the pattern to appear in the southern hemisphere, the whole magnetic area suggesting in outline a large arrowhead pointing west (July 11 and October 19, 1953). While such symmetrical patterns are rare, there sometimes seem to be coherent magnetic regions that cross the equator, as in the record of September 8, 1953. It may even appear that the principal positive and negative portions of a BM region are on the same meridian on opposite sides of the equator (February 19, 1954).

Some BM regions, even those that produce visible spots, are quite small. An example is the region that crossed the central meridian on December 26, 1953, in which small spots were observed for several days (Mount Wilson group No. 11168). The area of the BM region was about 0.002 of the disk. Other small, short-lived spots, especially of the new cycle, have arisen in very small BM regions. In a few instances, such as Mount Wilson group No. 11187, which appeared very abruptly on August 9, 1954, near 24° S. latitude, no BM field was observed on the photosphere as recently as 2 days before the appearance of the spots; the *p* and *f* spots at the outset constituted almost the whole of the BM region. The spots, however, disappeared within 5 days, leaving a more extended BM field that was carried over the west limb by rotation some days later. Usually the magnetic field persists long after the disappearance of spots and *plages*.

Some of the magnetic regions are blended, indefinite, or complex, so that it is difficult or impossible to specify their relationships. Changes from day to day may be quite pronounced, although the major BM regions, which are readily identified as "centers of activity," usually remain observable for at least several days and sometimes for several solar rotations. In parallel with the decline in the number of sunspots and *plages* near the end of the sunspot cycle, the frequency of BM regions likewise declined in the interval from the beginning of our observations until the spring of 1954. Our estimate is that the average total magnetic flux of the BM regions also decreased in this interval; but, because of the rather crude intensity calibrations of the earlier magnetograms, quantitative comparisons of total flux have not been attempted. While there is a great range in the total flux of the various regions, a typical region (1953-*Hp*) had a flux of about 1×10^{21} maxwells emanating from the *f* part and returning through the *p* part.

We have compared all our magnetograms with *Ca* II spectroheliograms taken on Mount Wilson. There appears to be virtually a one-to-one correspondence between prominent regions showing calcium flocculi on the spectroheliograms and strong BM or MM regions on the magnetograms. Examples are shown in Figures 7 and 8. Only a few of the smaller bright calcium *plages* occasionally cannot be matched by deflections on the magnetograms; this may reasonably be attributed to the limited resolution of the magnetograph. Some of the weaker magnetic regions do not produce an appreciable brightening of the *Ca* II on the spectroheliograms, but every BM region of intensity greater than about 2 gauss appears to produce a calcium *plage*.

From this it appears fairly safe to infer that calcium *plages* recorded on spectroheliograms at various observatories over the past several decades represent BM areas in which the magnetic field intensity was about 2 gauss or more. Unfortunately, the calcium spectroheliograms yield no direct information as to magnetic polarity, but it may prove possible to derive some estimate of the field intensity from the brightness of the *plages*. In some well-defined bipolar sunspot groups the *p* and *f* spots lie within corresponding *p* and *f* parts of the *plage*, and the magnetic polarity of these parts may be inferred with some degree of certainty. For spot umbras observed at Mount Wilson in the last 45 years, the polarity, area, and field intensity have been recorded; hence ϕ_s^+ and ϕ_s^-, the fluxes of the spots of positive and negative (*R* and *V*) polarity, can be estimated. If we assume that in any BM region the positive flux equals the total negative flux, we can write down the identity

$$\Phi_{BM} = \phi_s^+ + a^+ \bar{H}^+ = \phi_s^- + a^- \bar{H}^- ,$$

where a and $\bar{H}$ denote the area and mean field intensity of the positive and negative parts of the *plage*, apart from the spots, as indicated. This expression must be used with caution, because the BM region may extend with low field intensity far beyond the limits of the *plage*. On this same basic assumption it has been pointed out previously (Kiele 1950; Grotrian and Künzel 1950) that, because it is an observed fact that *p* spots of a group tend to be larger and to have a longer lifetime than *f* spots, in the average spot group there will be an "uncompensated" portion of the total magnetic flux. This uncompensated flux is optically ineffective in emerging from the spot, because of the darkness of the umbra, but it is fully effective in returning through the photosphere in the unspotted *f* portion of a BM region. Thus in integrated light the intermediate latitude zones of the sun should show an average magnetic field of the order of 1 gauss, with a polarity that is opposite in the northern and southern hemispheres and that reverses every $11\frac{1}{2}$ years. The assumption as to the equality of positive and negative flux in spot groups is strengthened by the magnetograms; actual measurements of the uncompensated flux of large spotted BM regions when the solar cycle is near maximum remain to be carried out.

The magnetograms have also been compared with the preliminary charts of coronal activity circulated by the High Altitude Observatory, Boulder, Colorado. These charts show the regions over which the green and red radiations are unusually bright. Again good agreement is found, in the sense that all the stronger BM regions give rise to an observable enhancement of the coronal radiations. No coronal enhancements were reported, however, over a number of the weaker BM regions. The bright, archlike patterns of the coronal radiations, best seen on eclipse photographs at times of considerable activity, provide strong evidence, if any is needed, that the vertical extent of the BM fields

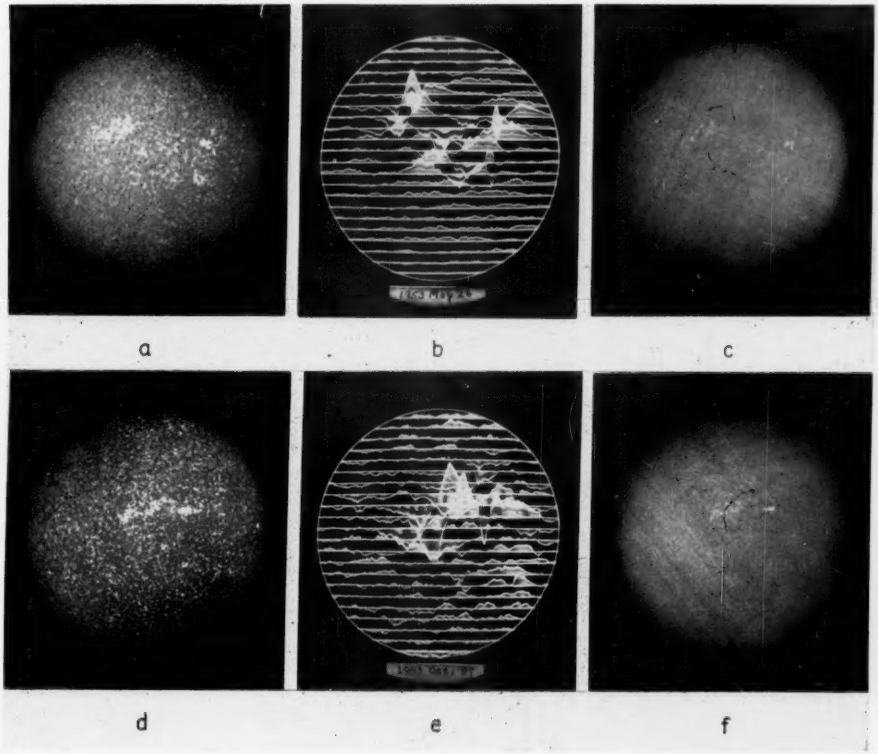

FIG. 7.—A magnetogram (*b*) is shown between (*a*) a *Ca* II and (*e*) an *H*α spectroheliogram, all for May 26, 1953. The lower row shows a similar array for October 27, 1953. Note the *Ca* II *plages* wherever $H \gtrsim 2$ gauss. Some of the dark hydrogen filaments appear to define the locus of the tops of the arching lines of force of the BM fields.

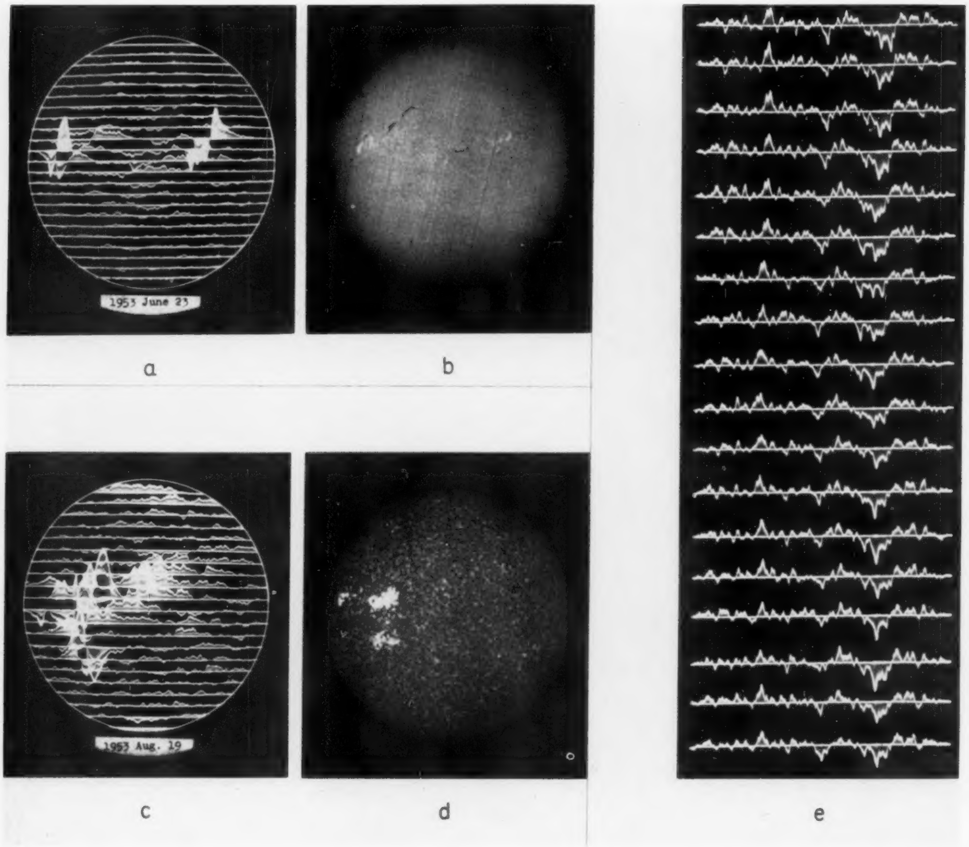

FIG. 8.—*a:* Magnetogram showing two BM regions and weak fields on June 23, 1953. *b:* $H\alpha$ spectroheliogram of the same date. The bright flocculi lie in the regions of strongest field, while the dark filaments seem to separate the areas of opposite magnetic polarity. *c:* A prominent UM region appears near the center of the disk on August 19, 1953; the connection, if any, with the two BM regions farther west is not clear. *d:* The corresponding *Ca* II spectroheliogram shows intense *plages* in the BM regions where $H \gtrsim 2$ gauss, but not in the UM region. *e:* Repeated diametral traces made with careful guiding at 10-minute intervals on June 7, 1954. The largest deflections correspond to about 2 gauss. Note the changes of detail within 20–30 minutes.

into the corona is at least of the same order as their horizontal extent, and often much greater.

UM regions.—Unipolar magnetic regions occur in the same zones of latitude as BM regions, but they are relatively rare. They are of low magnetic intensity and often cover a rather large area with ill-defined limits. They usually bear no obvious relationship to other features of the magnetic pattern. The lines of force that emanate from UM regions presumably return to the sun diffusely in areas that are far from the center of the disk. The field intensity of UM regions ranges from a few tenths of a gauss up to perhaps 3 gauss. The best example of such a region was recognizable for at least six solar rotations and is best shown on the records of July 22 and August 19, 1953. Measurements on the magnetograms yield the data on this UM region shown in Table 2.

Figure 8, *c*, shows the UM region of positive polarity centered nearly on the central meridian at about 15° N. latitude on August 19, 1953, with *d* a Mount Wilson spectroheliogram in the light of *Ca* II on the same date. Two BM regions, some 35° west of the UM region and on opposite sides of the equator, are related to the usual bright *Ca* II *plages*, but there is scarcely a trace of brightening on the spectroheliogram at the location of the UM region. Furthermore, the preliminary records of the coronagraph observers at the High Altitude Observatory indicate no coronal brightening over the UM region.

TABLE 2

1953	Max. Intensity (Gauss)	Average Intensity (Gauss)	Area (Disk = 1)	Total Flux (10^{21} Maxwells)
July 22	3.2	+0.7	0.16	+1.8
Aug. 19	2.0	+ .43	.15	+1.0
Sept. 15	1.5	+0.4	0.13	+0.8

The indications are that the UM regions revealed by the magnetograph constitute a kind of solar phenomenon not directly observable by other means. It has been noticed that the most prominent series of 27-day sequential terrestrial magnetic storms of 1953 showed its successive onsets about 2–3 days after central meridian passage (c.m.p.) of the UM region referred to earlier, which was by far the most conspicuous such region of the year. This correlation is illustrated in the diagram of Figure 9, where each horizontal row represents a sequence of 27 days, or one solar rotation. It will be recalled that magnetic storms are of two general classes: sporadic, which can be related to solar flares; and 27-day-recurrent, which have been attributed to hypothetical "M" regions on the sun (Bartels 1932; Allen 1944). Only the latter class is of interest here. The "M" regions are believed to be the sources of neutral but ionized corpuscular streams, giving rise to the terrestrial magnetic storms of the recurrent type, and they have been suggested as the roots for far-reaching coronal streamers.

We wish to propose that the newly observed UM regions may be identified with the heretofore hypothetical "M" regions. This suggestion rests mainly on the evidence of Figure 9, where the best UM sequence and the best magnetic storm sequence appear related; the delay of 2 days or more between c.m.p. of the UM region and the onset of the storm is about what had been predicted by Allen on the basis of particle speeds. It is also plausible that if corpuscular streams are to escape from the sun at all, they should do so along a coherent, nearly radial, bundle of magnetic lines of force such as one visualizes as arising from a UM region. Additional correlations of UM regions and magnetic storm sequences are much to be desired to make the identification more secure, but there have been no observations of outstanding UM regions in 1954 to date (and no outstanding storm sequences). It has been remarked that "M" regions (and also low-latitude coronal

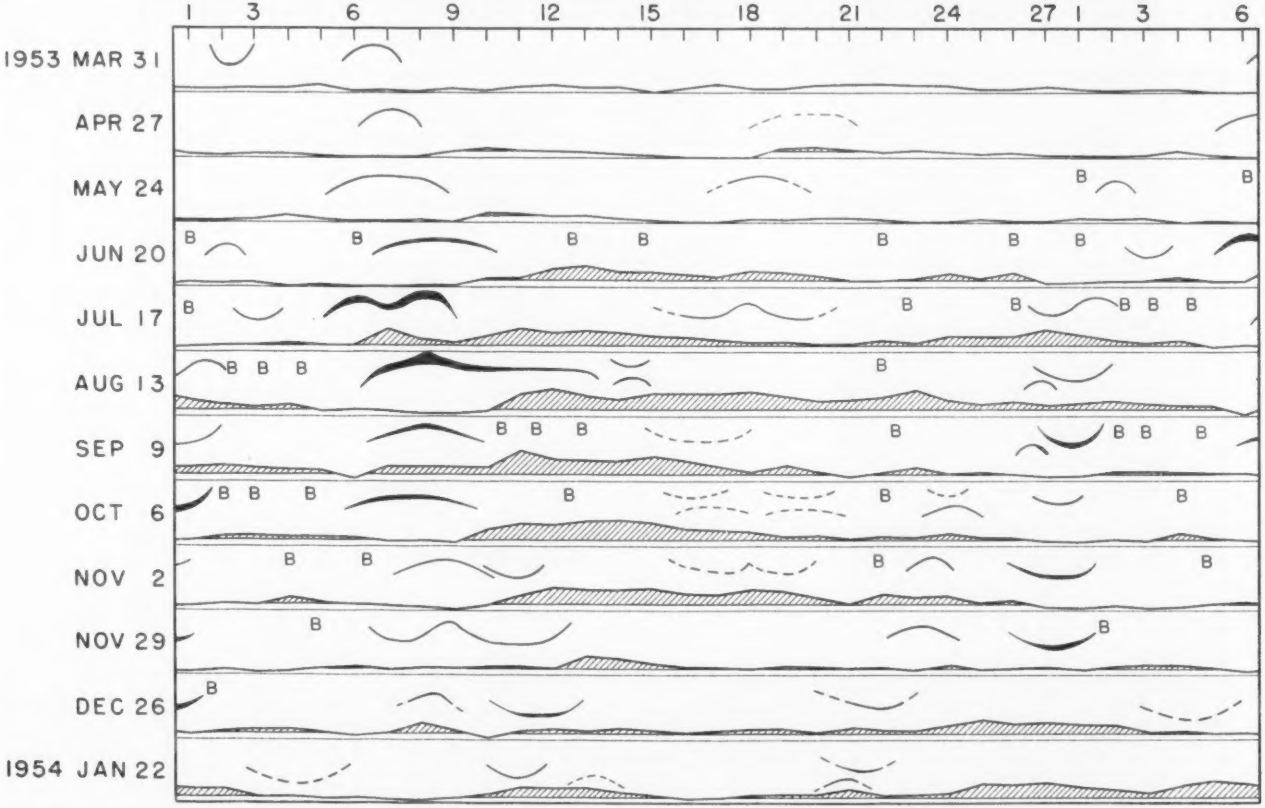

FIG. 9.—The diagram presents evidence tending to relate terrestrial magnetic storms of the sequential type to UM regions on the sun. Each row represents one solar rotation of 27 days (plus 6 repeated days). The date of the first day of each row is given at the left. For each day the *K* sum (geomagnetic planetary index) is plotted, and under the connecting curve all areas for $K > 10$ have been shaded. UM regions have been indicated, according to date of c.m.p., by **U**-shaped curves, convex upward or downward according as the magnetic polarity is positive or negative. The attempt has been made to suggest the extent of the UM regions and their relative flux. C.m.p. of the best UM region of 1953 was followed, on several successive rotations, by the onset of a 27-day sequential magnetic disturbance on the earth. A delay of 1–4 days usually occurred. Dates of c.m.p. of the stronger BM regions are indicated by the letter *B*, but these are thought not to be directly relevant.

streamers) are most numerous in the declining years of the sunspot cycle and show their greatest development 1 to 2 years before sunspot minimum. Hence 1953 was perhaps the last year in which prominent "M" or UM regions would be expected until after the next spot maximum.

It has been reported that the best 27-day sequential magnetic storms, with their inferred "M" regions, tend to occur seasonally when B_0, the heliocentric latitude of the earth, is near its maximum of $\pm 7°$ (Chapman and Bartels 1940). This is also in agreement with the proposed identification, for the UM regions are probably centered in the same latitude zones as BM regions—therefore, seldom below 6°. The probability that some UM regions will pass near the center of the apparent disk is therefore greatest in early March and September in the declining years of the sunspot cycle (and if they are remnants of BM regions, they will be more numerous in these years). If the corpuscular streams arising in UM regions emerge nearly radially or with a longitudinal lag in rotation, they will be more likely to interfere with the earth in these seasons.

It is worth pointing out that well-defined UM regions should be rather readily identifiable on magnetograms some 3 days before c.m.p. Since magnetic storms of the recurrent type commence 2–4 days after c.m.p., if our suggestion is correct, the possibility exists of strengthening the predictions of terrestrial storms and their associated effects if the solar magnetic observations are continued on a routine basis.

An effort was made to find, on $H\alpha$ spectroheliograms, some evidence of the occurrence of UM regions. Such spectroheliograms show, in general, a small-scale random pattern of light and dark chromospheric filaments. In BM regions where the field has an intensity of a few gauss (and possibly also in the best UM region) the pattern of the fine structure in the $H\alpha$ spectroheliograms assumes a larger-scale coherence. Presumably the direction and coherence of the filamentary structure are determined by the magnetic field. But this effect on the pattern of the chromospheric filaments, at least for the weaker fields, is discernible only on occasional spectroheliograms of exceptional quality. Were it not for this limitation, one could hope to identify UM regions of past decades by examining existing $H\alpha$ spectroheliograms in a search for the larger-scale coherent patterns, rejecting all those that coincide in location with *Ca* II *plages* and which are therefore presumably BM regions. An examination of a number of the older Mount Wilson $H\alpha$ spectroheliograms, preselected by picking dates preceding prominent sequential-type magnetic storms, was unsuccessful because the filamentary structure was adequately shown on so few of the plates.

Hydrogen flocculi and prominences.—Hydrogen spectroheliograms, along with magnetograms for the same dates, are shown in Figures 7 and 8. These and several other comparative observations show that bright hydrogen flocculi are found in the stronger portions of all prominent BM regions, but these bright flocculi are not so extensive as are the corresponding *Ca* II *plages;* apparently they are less sensitive as indicators of weak magnetic fields. A more sensitive indication is furnished by the alignment of the fine filamentary $H\alpha$ structure into an extended coherent pattern.

Prominences, appearing as dark hydrogen filaments, are seen on the spectroheliograms. The filaments shown are rather stable. A comparison with the magnetograms brings out some points of interest in regard to the position of the filaments. Some of them are situated on or near the borders of the magnetic regions, partly encircling them (perhaps preferentially on the high-latitude side). Other filaments seem to lie along a line dividing the BM region into two parts of opposite polarity. In the latter cases it would appear that the absorbing hydrogen has accumulated along the locus of the tops of the arching lines of force of the magnetic field. The photospheric fields in the vicinity of the filaments are of the order of 1 gauss.

The extensive observations of hydrogen filaments by M. and L. d'Azambuja (1948) show that the low-latitude filament zones migrate with the sunspot zones, remaining about 10° poleward of them; this is just what would be expected from our observation that filaments tend to delimit BM regions on the high-latitude side. The slow poleward migration of filaments (about 1° per rotation) observed by d'Azambuja may result from a gradual expansion of BM regions or perhaps in part from their proper motions. It has also been reported that long-lived prominences, in their terminal phases, drift poleward to form a "polar crown" at latitudes above 40°. This activity varies with the $11\frac{1}{2}$-year cycle. The polar crown nearly reaches the poles at sunspot maximum and thereafter disappears, to recur in about 3 years at latitudes of 40°–50°. There is a temporary decrease at spot minimum. By inference, one expects that a continuation of magnetic measurements throughout the solar cycle may disclose significant changes in the high-latitude magnetic fields of the sun. In fact, we could speculate at this stage that the polar magnetic field is the result of poleward migration of the f portions of disintegrating BM regions in the first few years of each sunspot cycle. If this were true, the main poloidal field should reverse its polarity every $11\frac{1}{2}$ years, but out of phase with the frequency-curve for sunspots. On this theory the residual p portions of BM regions should either be neutralized by merging of low-latitude fields of the northern and southern hemispheres, or there should be evidences of a general quadrupolar field. The intensity of the average low-latitude components of the quadrupolar field should be of the order of 0.3 gauss, which could hardly have escaped observation.

History of a BM region.—An attempt was made to trace the development of a prominent magnetic region from its outbreak in March, 1953, until all trace of it was lost in January, 1954. In its earlier stages this region was designated 1953-*Hp* on the charts of the High Altitude Observatory. Measurements of the area and of the magnetic flux involved were made on the magnetograms available on or near the dates of successive c.m.p.'s. The results are plotted in Figure 10. No great precision can be claimed for the measurements, but the broad features are significant.

The BM region was centered at about 10° N. Activity apparently broke out on the far side of the sun shortly before an active prominence was observed (on spectroheliograms) coming around the east limb on March 25. Two days later a *plage* and a small spot group (No. 11098) came into view. No coronal maximum was reported at the east limb at this time, but enhanced emission was observed at subsequent limb passages through August. In other BM regions it has been observed that an interval of 1 to a few days is typical between the first observation of a magnetic field and the appearance of spots. This general region showed much more activity and larger spots on the next rotation. A flare was reported on April 24. It is possible that a new and stronger disturbance broke out after the first passage while the region was out of view, for on the second passage a very conspicuous spot group (11107) was located about 15° farther east than would be expected for a return of 11098.

Because of poor weather and alterations to the equipment, no magnetograms were obtained until the third appearance of 1953-*Hp* near the end of May. However, for the first two appearances, lower limits to the magnetic flux of the region and to its area were estimated from the Mount Wilson sunspot tracings and spot field intensities, as well as from the *Ca* II spectroheliograms. The BM region probably extended beyond the limits of the *plage*. The visual measurement of the central field intensity of the principal (p) spot in 11107 was -3200 gauss (Hickox), and the flux of the umbra alone was estimated to be about 1.8×10^{21} maxwells. On the third and fourth appearances, small spots, practically all of p (negative) polarity, were observed (11118 and 11126). The BM field of spot group 11132 (10° S.) interfered somewhat with the measurement of the region in July. No correction to the total flux for the effects of small spots was attempted after the c.m.p. of April 28. No spots were observed in the region after June 22 (fourth appearance). The *Ca* II *plage* gradually faded but was observable through the c.m.p. of August.

After a high degree of activity in the first 2 months of its existence, there seems to have been a marked decrease in the total magnetic flux of the region, possibly as a result of subsidence of associated material; this was followed by a relatively stable phase, during which the region gradually expanded, with an end to coronal and *plage* activity and a decrease in maximum field intensity. The total flux of the (*p*) part of the BM region remained reasonably constant until the middle of January, 1954, after which it was lost in the random background of weak fields. No clear answer can be given as to the fate of the (*f*) part of the region. Presumably, it expanded (or migrated) more rapidly as the BM region disintegrated. The effective result is that the BM region degenerated into a UM region. As a UM region it passed considerably north of the center of the sun's disk, and for this reason may not have produced appreciable "M" region effects.

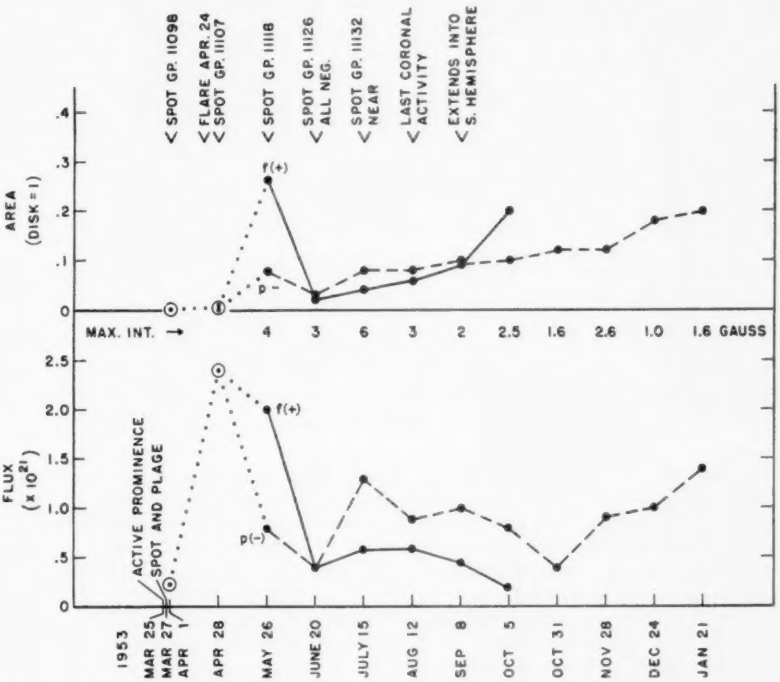

FIG. 10.—Development of the magnetic region associated with the center of activity 1953-Hp through 12 solar rotations. Measures of the area of the preceding and following parts of the BM region are plotted in the upper part of the diagram; below are estimates of the magnetic flux of the two polarities. The magnetic region was observable long after most outward signs of activity had subsided; in the final stages, only the preceding part, of negative polarity, could be identified.

While 53-*Hp* persisted as a recognizable magnetic region for the better part of a year, it has been observed that small BM regions having a flux only about one-tenth as great may appear, produce small spots, and then disappear rapidly and completely in a matter of days.

Rate of change.—A comparison of magnetograms shows that very appreciable alterations in the magnetic pattern may take place in intervals of a day; this is particularly true for the early stages of BM regions. Some of the daily changes are only apparent, because the path of the scanning slit with respect to the magnetic features is variable. But real physical variations, involving changes in the total magnetic flux in the loops that break through the surface and also changes in the mean angle between the lines of force and the line of sight are obviously present. It would be of interest to establish characteristic time constants for the magnetic fluctuations as a function of the size of the surface elements involved. A preliminary attempt in this direction is shown in Figure 8, *e*, where repeated traces, at 10-minute intervals, were made along the same diameter of the sun's image. The image was carefully guided, so that the same strip was repeated rather exactly, and the speed of scanning was about one-third that ordinarily used, so that finer detail of the magnetic pattern is shown. The slit had its usual length of 15 mm. In this special record, made on June 7, 1954, the largest deflections indicate a field of about 2 gauss. The principal features of the pattern are identifiable on all traces, but the details change within intervals of a few minutes. Note, for example, the variations in the relatively wide region showing the largest negative peaks. On the seventh trace, this region has three peaks, nearly equal; on the twelfth trace, it has only one major peak. From this and similar records, all indications are that in regions where an outstanding weak magnetic field exists, fluctuations of the order of 0.5 gauss may occur in a few minutes; this result applies, of course, to the average field over an area of the order of 5×10^8 square km. Such variations in the effective field are attributable in part to turbulence of the photosphere, which may produce a fluctuating pattern of widely separated concentrations of the magnetic lines of force, in which the field is much stronger than the mean value.

As was pointed out earlier, an upper limit of 0.2 gauss can often be placed on the effective magnetic field over very large areas of the quiet sun. This is of interest in connection with the possible fields of individual granules, considered apart from more deeply rooted coherent fields. If we assume that the granules average 1 second of arc in diameter, there may be about seventy of them along the length of the slit; and, if we assume further that each granule has a coherent field H_0 and that, because of turbulence, they are oriented at random, we see that an upper limit on H_0 is roughly 2 gauss.

CORPUSCULAR EMISSION

A number of the known facts concerning "centers of activity," prominences, localized solar radio emission, "M" regions, and other solar phenomena can be synthesized with the observations of weak solar magnetic fields on the hypothesis that electrically neutral streams of ions (mostly protons) and electrons are more or less continually ejected from the solar surface in all turbulent regions having a coherent magnetic field of average intensity $\frac{1}{2}$ gauss or more. Because of the high degree of ionization, such streams, guided by the lines of force, are essentially invisible except in so far as they excite the weak radiations of the coronal rays, fans, and arches.

The idea of outgoing corpuscular streams is not new, but we believe that the magnetic observations place it on a firmer footing. Chapman and Ferraro's (1932) theory that neutral but ionized streams of particles from the sun are responsible for terrestrial magnetic and ionospheric effects has already received good observational support. There is evidence that protons travel outward from the sun, with mean velocities of some hundreds of kilometers per second (Vegard 1939; Gartlein 1950; Meinel 1950). These observations relate to sporadic phenomena, but similar streams are supposed to proceed from "M" regions, which we suggest are identical with the newly observed UM regions.

The way in which the particles are accelerated is unknown, but hydromagnetic fluctuations in the photosphere and chromosphere, involving turbulence in the presence of a deeply rooted magnetic field, must be given strong consideration. The hope is that a way may be found in which a fraction of the energy of massive turbulence may be channeled, through the agency of local magnetic field concentrations, into the outward energy of motion of ionized streams of low density but high velocity. Such a model may be based on the observations of transient chromospheric jets or spicules, which have been summarized by van de Hulst (1953*b*).

In the layers considered, hydrogen is largely neutral, but the conductivity is sufficient that in a large element of volume the nearly vertical magnetic lines of force remain identified with the material. Owing to random motions, partly horizontal, with velocities of the order of 2–3 km/sec, occasional elements of volume will be squeezed from all sides, so that the lines of force become concentrated into concentric cylindrical tubes. The material, being free to flow along the tubes of force, escapes upward, so that a long, thin cylinder results. The upward velocity of flow at this stage, due to continuity, may be of the order of 10 or more km/sec. If the process continues until the magnetic pressure in the cylinder (which varies as the inverse fourth power of the radius) is significant in destroying the momentum of the inward-pressing material, the field H may temporarily reach values of the order of 600 gauss. This results from equating the magnetic pressure, $H^2/8\pi$, to ρv^2, where ρ, the density in the photosphere, is taken to be 4×10^{-7} gm/cm^3. After 100 seconds, the column of high field intensity will have a radius, at its base, of the order of 10 km. There has resulted a pronounced constriction in the concentric tubes of force; this generates a specialized form of hydromagnetic wave which will travel upward with a velocity $a = H/\sqrt{(4\pi\rho)}$, which is to be added to the initial jet velocity. Owing to the rapid decrease of density with height, the velocity of the constrictions will increase upward, provided that H does not decrease too rapidly and provided that the wave is not dissipated by secondary (heating) effects. If H were to retain its value of 600 gauss, the traveling-wave velocity of the constrictions would rapidly increase from 2.5 km/sec near the photosphere to 2500 km/sec at a height (somewhat above 6000 km) where the density has decreased by a factor of 10^6. The actual velocity must be less because of the direct dependence of a on H, but the nearly constant width of spicules and many coronal streamers suggests that the decrease of H with height is not so rapid as to cancel the effect of decreasing density. On this model, then, there is some expectation that wave velocities of a few hundred km/sec might be attained in the high chromosphere or inner corona. Finally, we suppose that relatively small tenuous clouds of ions and electrons are squeezed ahead of the constrictions and are thus accelerated upward with the traveling waves.

In any such process as the foregoing, the lines or tubes of force above the photosphere would be dominant in determining the disposition of the material, except perhaps for particles of very high energy. Over a BM region, particles accelerated upward from the extended areas of opposite polarity would be guided by the arching lines of force until they collided and condensed over the region at a considerable height, thus forming a prominence. The material in a prominence becomes visible by reverting partly to the neutral condition, and it begins a possibly lengthy but precarious existence under the influence of magnetic and gravitational forces. Eventually, much of the material slides back down the magnetic lines of force, or, in part, it may be thrown outward by expansion of the arching BM field.

The collision of gas clouds at relative velocities of several hundred kilometers per second has been observed in other cosmic sources to be a necessary condition for the generation of radio-frequency radiation (Baade and Minkowski 1954; Minkowski and Greenstein 1954). On this basis one could expect the fields over BM regions on the sun, but not UM regions, would be outstanding as local sources of radio noise. Through the great kindness of Dr. J. L. Pawsey and Mr. J. A. Warburton, of the Commonwealth Scientific and Industrial Research Organization, Sydney, Australia, we have been permitted to examine, before publication, records of radio observations of the sun made with a Christiansen interferometer having a resolution of about 3′ in the east-west direction. A preliminary comparison with magnetograms of 1953 shows that, in fact, there is good correspondence between "bright" radio regions and BM regions. UM regions, however, were not identifiable as radio sources on the available records. Corpuscular streams accelerated outward from UM regions would be expected to proceed more or less radially for an indefinite distance, depending upon the interaction of weak and rather irregular magnetic fields at some distance from the sun; since there is little chance of their colliding with other ion clouds before they have become very diffuse, they they are not generators of strong radio noise.

The north and south polar regions of the sun, in which the lines of force of the general field arise, may be regarded as UM regions of a special class. They are quite extensive and (at least relatively) permanent. Coronal plumes or tufts, as well as spicules, are certainly associated with the polar regions. All this suggests that if the low-latitude UM regions are, in fact, sources of corpuscular streams, then the sun's polar regions may well be even more copious sources. The lines of force of the general field presumably loop outward to great distances in the solar system and must undergo severe distortion by moving ionized clouds. These lines of force will, however, guide diffuse corpuscular streams ejected from the polar regions to the general vicinity of the equatorial plane; because of magnetic coupling, such outgoing streams will carry a share of angular momentum that is large in proportion to their mass. Since the total magnetic flux of the polar regions is probably several times as great as that or ordinary UM regions, angular momentum, as well as mass, will be carried away preferentially from the high heliographic latitudes.

We are much indebted to several of our colleagues for placing at our disposal solar data of various types, and especially to Mr. Thomas A. Cragg for assistance with the more recent magnetic observations.

REFERENCES

Allen, C. W. 1944, *M.N.*, **104,** 13.
Azambuja, M. and L., d'. 1948, *Ann. Obs. Paris, Meudon*, Vol. **6,** Fasc. VII.
Baade, W., and Minkowski, R. 1954, *Ap. J.*, **119,** 206.
Babcock, H. W. 1953, *Ap. J.*, **118,** 387.
Babcock, H. W. and H. D. 1952, *Pub. A.S.P.*, **64,** 282; also *in:* Kuiper, G. P. (ed.), *The Sun* (Chicago: University of Chicago Press, 1953), p. 704.
Babcock, H. W., and Cowling, T. G. 1953, *M.N.*, **113,** 357.
Bartels, J. 1932, *Terr. Mag. Atm. Elec.*, **37,** 48.
Biermann, L. 1941, *Vierteljahrsschr. Astr. Gesellsch.*, **76,** 194.
Chapman, S., and Bartels, J. 1940, *Geomagnetism*, **1,** 366 (Oxford).
Chapman, S., and Ferraro, V. C. A. 1930, *Nature*, **126,** 129.
Gartlein, W. 1950, *Trans. Internat. Union Geodesy and Geophys.*, Oslo Meeting, I.A.T.M.E. Bull. No. 13 (Washington), p. 491.
Grotrian, W., and Künzel, H. 1950, *Zs. f. Ap.*, **28,** 28.
Hale, G. E., Ellerman, F., Nicholson, S. B., and Joy, A. H. 1919, *Ap. J.*, **49,** 153.
van de Hulst, H. C. 1953*a*, *in:* Kuiper, G. P. (ed.), *The Sun* (Chicago: University of Chicago Press), p. 299.
———. 1953*b*, *ibid.*, p. 212.
Kienle, H. 1950, *Naturwiss.*, **37,** 37.
Meinel, A. B. 1950, *Ap. J.*, **111,** 555.
Minkowski, R., and Greenstein, J. L. 1954, *Ap. J.*, **119,** 238.
Roberts, W. O. 1945, *Ap. J.*, **101,** 136.
Schuster, A. 1892, *Report B.A.A.S.*, p. 634.
Vegard, L. 1939, *Nature*, **144,** 1089.

ON THE CORRELATION BETWEEN RADIO-FREQUENCY RADIATION FROM THE SUN AND SOLAR ACTIVITY

EINAR TANDBERG-HANSSEN
Institute of Theoretical Astrophysics, Oslo, and Mount Wilson and Palomar Observatories,
Carnegie Institution of Washington, California Institute of Technology*

Received June 22, 1953; revised September 20, 1954

ABSTRACT

An investigation is made of the correlation between radio-frequency radiation from the sun and solar activity, sunspots, prominences, and geomagnetic disturbances. The difference in observed directivity and intensity of the radiation at different frequencies is explained by the reflection conditions in the sun's atmosphere. A distinction is made between radio-noise active and radio-noise inactive sunspots.

It is known that some components of the radio-noise radiation from the sun are more or less increased during periods of sunspot activity (Wild 1951). In order to study this correlation with the best available data, the behavior of sunspots and prominences has been compared to the variation in the solar radiation at different radio frequencies. I have used the limb- and disk-spectroheliograms of the sun (in *Ca* II K and *Hα*, respectively), taken at Mount Wilson in the period January, 1950—July, 1951, to study the behavior of the "visual" sun, and the data for the 80–3000 Mc/sec radiation (as published in the I.A.U. publication, *Quarterly Bulletin on Solar Activity*) to study the "radio" sun. The material is necessarily limited, because it is difficult to use older radio data which lack sufficient calibration. The sunspot areas and sunspot numbers are those published by the U.S. Naval Observatory and the Eidgenössische Sternwarte, Zurich.

TABLE 1

RADIATION OF THE QUIET SUN (MC/SEC)

Temp. (° K)	2800	1200	600	200	81
T_{eff}	4×10^4	1×10^5	$2\times5\times10^5$	7×10^5	1×10^6
I_{quiet}	70	35	20	6	2

The observed noise level should occasionally drop to the quiet-sun noise level, when few sunspots or active regions are present. This happened around November 23 and December 20, 1950, and January 15, 1951. The corresponding temperature of the emitting region (assuming a black body) is given in Table 1, together with the mean flux of radiation, in units of 10^{-22} watts m^{-2} $(cm/sec)^{-1}$.

This thermal radiation is randomly polarized and well understood (Martyn 1948; Denisse 1950; Smerd 1950). The total radiation, I_R, can be written as follows:

$$I_R = I_{\text{quiet}} + I_{\text{active}} , \tag{1}$$

where I_{active} is the average value of the more or less steady radiation from active regions. In this paper we do not consider the different, sudden bursts which are superimposed on the more slowly varying noise level, I_R.

---

* Work done while on a Smith-Mundt/Fulbright scholarship at California Institute of Technology.

RELATION BETWEEN RADIO-NOISE INTENSITY AND SUNSPOT AREA AND NUMBER

During the occurrence of sunspots, the radio noise increases, because of I_{active}, and the radiation becomes more or less circularly polarized. The general behavior is different for different frequencies. In Table 2 are given, for the period January, 1950—July, 1951, the monthly means of sunspot area $\bar{A}$ (in millionths of the sun's hemisphere), sunspot number $\bar{S}$, and flux of radio radiation $\bar{I}_R$ in units of 10^{-22} watts m^{-2} (cm/sec)$^{-1}$. Figures 1 and 2 show the essential features of Table 2. It can be seen that, as a whole, the curves for the radiation on high frequencies follow rather closely the curve for sunspot number and area. There has been some discussion whether one should use sunspot number or sunspot area as an index of solar activity. Figures 1 and 2 seem to support Dr. Markovitz' view (1951) that one may use sunspot number and sunspot area equally well when attempting to correlate solar activity with other phenomena.

TABLE 2

OBSERVED RADIO NOISE IN UNITS OF 10^{-22} WATTS M^{-2} (CM/SEC)$^{-1}$

MONTH	MC/SEC					SUNSPOT	
	2800	1200	600	200	80*	Number $\bar{S}$	Area $\bar{A}$
Jan.	128.5	83.5	58.0	17.6	9.5	101.6	1560
Feb.	117.6	85.0	76.4	36.0	42.6	94.8	2173
Mar.	117.3	65.1	47.5	12.2	16.4	109.7	1839
Apr.	140.0	83.8	43.4	19.7	8.6	113.4	2460
May	139.0	80.9	46.3	22.2	5.0	106.2	1667
June	110.0	65.5	44.0	61.8	442	83.6	1176
July	114.7	55.2	45.0	9.2	3.0	91.0	1371
Aug.	104.0	50.9	35.0	12.3	7.8	85.2	1230
Sept.	85.4	38.0	28.2	9.1	2.3	51.3	580
Oct.	87.4	39.3	26.5	7.7	2.2	61.4	674
Nov.	89.0	39.1	27.1	10.3	3.0	54.8	900
Dec.	87.8	42.8	26.8	9.8	4.6	54.1	762
Jan.	92.6	42.1	28.0	9.6	2.9	59.8	737
Feb.	87.6	40.9	24.5	11.4	13.4	59.9	737
Mar.	87.9	35.9	24.8	9.8	2.5	55.9	943
Apr.	108.8	38.5	22.9	8.8	1.8	92.9	1611
May	141.0	42.4	29.6	17.4	4.0	108.5	2887
June	138.7	42.2	32.2	24.0	27.3	100.6	2425

* Cavendish used 80 Mc/sec in 1950, and 81 Mc/sec in 1951.

From Figure 2 we see that it is only on high frequencies, say $\nu > 600$ Mc/sec, that the curves for the variation in radio radiation follow the curve for the variation in sunspot area. This is even more pronounced when we consider *daily* median values. If we plot the monthly means of radio flux I_R against the corresponding values of $\bar{A}$, we obtain Figure 3, which shows that the higher the frequencies, the better the relation between $\bar{I}(R)$ and $\bar{A}$.

In Figure 4 the daily median values of $\bar{I}_R$ on 2800 Mc/sec are plotted against the corresponding A-values. One notices the linear relation between I_R and A; for some months (January–July, 1950) the deviations from the linear relation are more pronounced than for the rest of the period considered. The deviations from the linear relation may be explained if one assumes that the radio emission exhibits some sort of "inertia." When the sunspot area decreases (or increases) rapidly, the radiation lags behind and does not follow the straight line indicated by the linear relation. We seem to get a more area-independent emission, which does not reach the minimum value I_{quiet} when $A \rightarrow 0$.

As long as we do not know the generation mechanism which increases the radiation during the appearance of sunspots, we cannot give any physical meaning to a linear relation between I_R and A. It may be of some interest to compare radio-noise intensities from different periods and their possible correlation with the sunspot area (Blum, Denisse, and Steinberg 1952). For the 2800 Mc/sec radiation considered here, we find that the variation of I_R with A, to a good approximation, is given by

$$I_R = I_{\text{quiet}} + \text{constant} \times A\,, \tag{2}$$

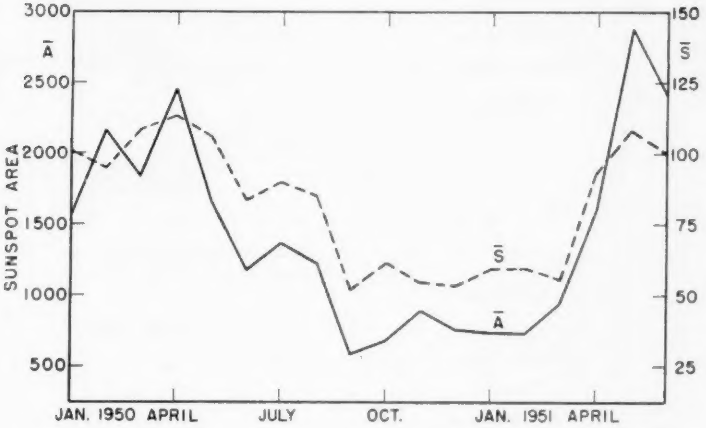

FIG. 1.—Variation of sunspot area and sunspot number in the period January, 1950—June, 1951

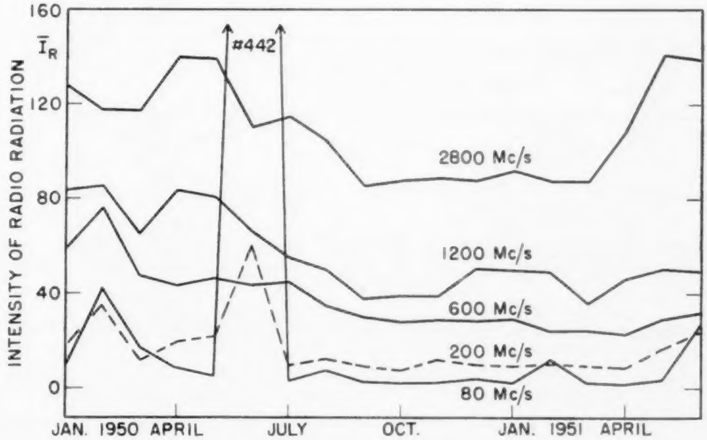

FIG. 2.—Monthly means of radio noise intensity in the period January, 1950—June, 1951

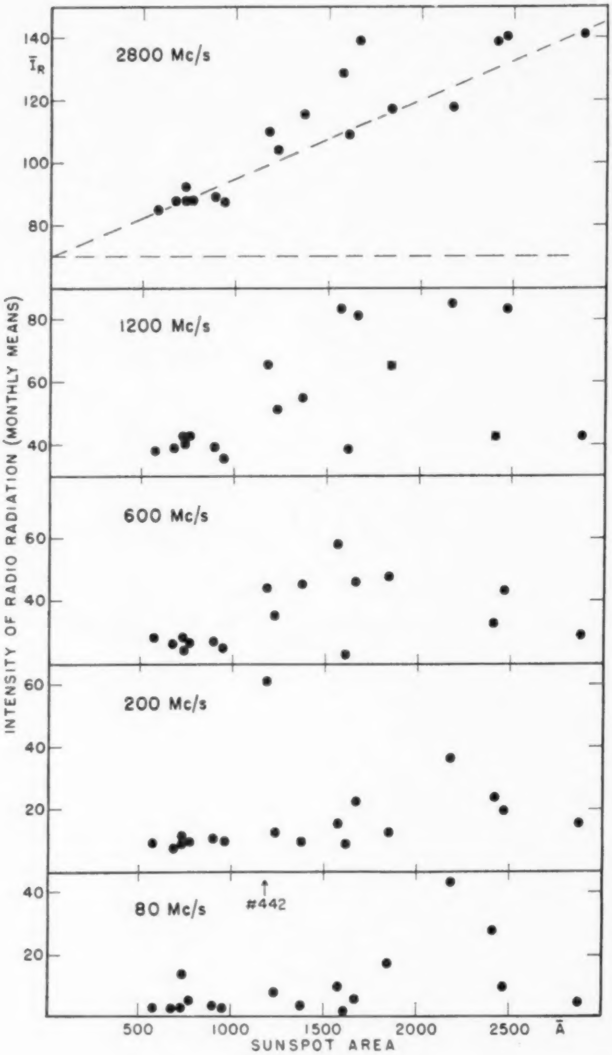

FIG. 3.—Monthly means of radio noise intensity at different frequencies as a function of sunspot area

or, with numerical constants,

$$I_R = 70 + 0.025A \,, \tag{3}$$

when A is measured in millionths of the sun's hemisphere. Similar linear relations hold (Piddington and Minnett 1951) for frequencies higher than 3000 Mc/sec but have not been observed for low-frequency radio radiation. We therefore must distinguish between high- and low-frequency radiation when dealing with sunspot activity. The separation should probably be made at approximately 600 Mc/sec.

This explains why Covington (1948), who worked on a high frequency, found a good correlation between radio noise and sunspots, while Stahr (1949), who worked on a low frequency, did not find the same good correlation. Consequently, general conclusions on solar activity cannot be drawn from the study of one, or a few, neighboring frequencies.

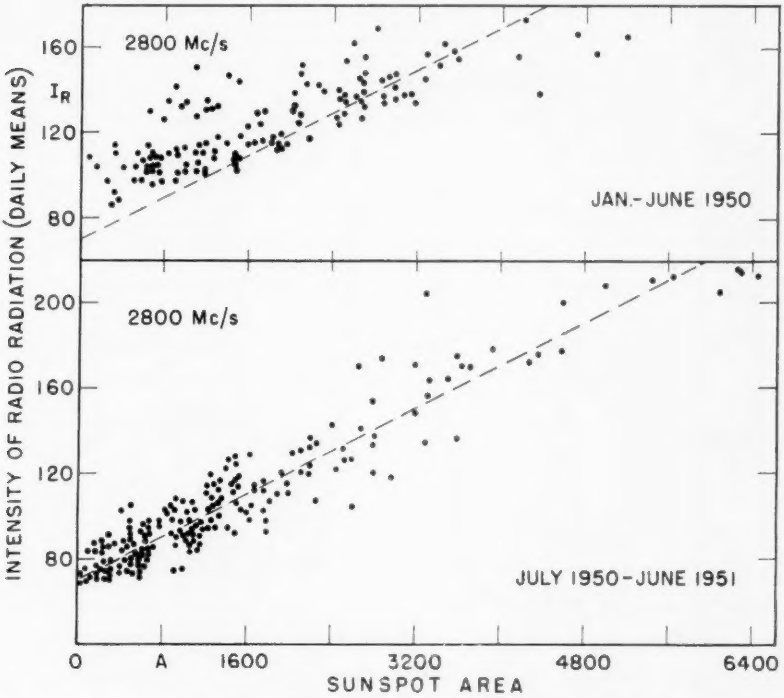

FIG. 4.—Daily means of radio noise intensity at 2800 Mc/sec as a function of sunspot area

DIRECTIVITY OF RADIO RADIATION AT LOW FREQUENCIES

For frequencies $\nu > 600$ Mc/sec, the noise level follows rather closely the sunspot-curve. Simultaneously with the appearance of spots on the sun's east limb, the noise level increases and remains high as long as the spots are visible. The corresponding black-body temperature is several times the normal thermal noise level, namely, $1\text{–}2 \times 10^5\,^\circ$K for $\nu = 2800$ Mc/sec and $\sim 5 \times 10^5\,^\circ$K for $\nu = 600$ Mc/sec.

Things behave quite differently for low frequencies, even though the noise level is somewhat increased during sunspot appearances. While the noise level for $\nu > 600$ Mc/sec remains high for about 2 weeks during the passage of a sunspot group, the noise level at low frequencies exhibits more sudden fluctuations, increasing from 10 to 100 fold, or even 1000 fold, for a few days, and then may drop nearly to the quiet noise level. Studies of the solar photographs reveal that these great increases (indicating a corresponding black-body temperature of 10^6–10^8 ° K or more) occur within a few days of the central meridian passage (C.M.P.) of a sunspot group. This points to a pronounced directivity of the radio emission, the more pronounced, the lower the frequency (Denisse 1952). See Figures 5 and 6 for some examples.

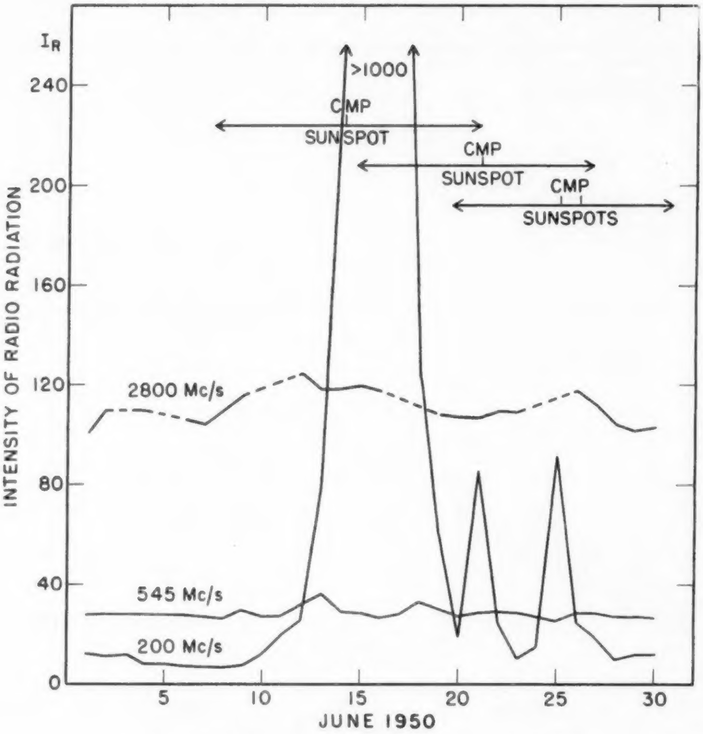

FIG. 5.—Sunspots and radio radiation in June, 1950

On special occasions one finds (July 10–13, 1950) that the radiation on high frequencies indicates decreasing activity, while the radiation on low frequencies definitely indicates an increase. This always seems to occur near the C.M.P. of a sunspot (causing the increase on lower frequencies) while the total sunspot area is decreasing because of the disappearance of a large sunspot group behind the west limb (the latter influencing only the less directive high-frequency radiation).

The difference in directivity, which requires that high-frequency radiation follow the sunspot area, while low-frequency radiation follows the C.M.P. of sunspots, may be explained by the reflection and refraction conditions in the solar atmosphere in the presence of the magnetic fields of sunspots. It may be assumed that the disturbed radiation is influenced in one way or another (or even caused) by these magnetic fields.

Figure 7 shows the levels in the chromosphere and the corona through which radiation of a given frequency cannot ordinarily penetrate (Piddington and Minnett 1951) (the full curve). Let the dotted curve be the level (and its envelope) within which the sunspot (the magnetic field) has set up conditions adequate to give disturbed radiation. It is then seen that as long as the dotted (envelope) curve is below the full curve, no radiation can escape to the earth on the frequency in question. By properly "adjusting" the heights of these levels, one can account for the difference in observed directivity. The adjustment will depend on the value of the magnetic field and electron density over sunspots. As long as the variation with height of these quantities is rather uncertain, accurate explanation of the difference in directivity can hardly be obtained.

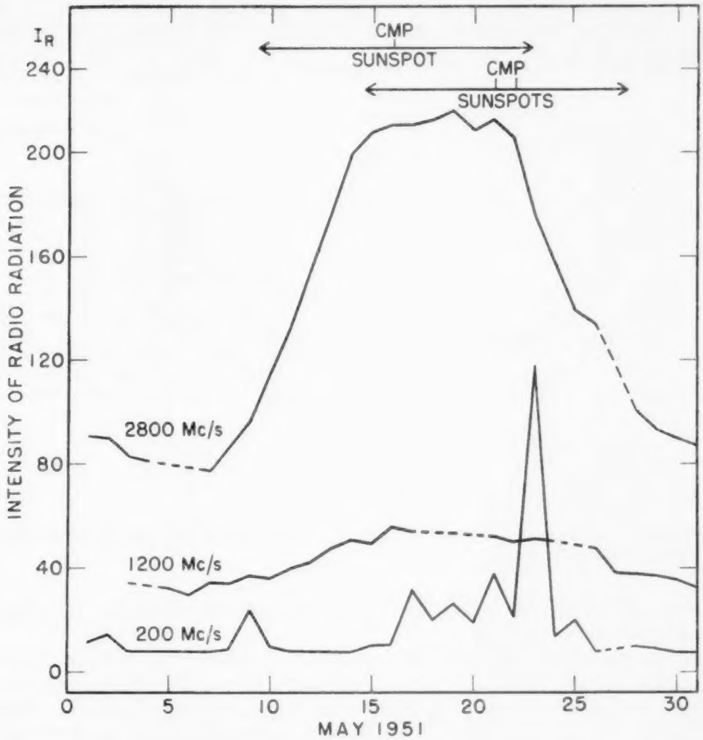

FIG. 6.—Sunspots and radio radiation in May, 1951

INTENSITY OF DISTURBED RADIATION

We have seen that the absolute intensity of the high-frequency radiation can—to a good approximation—be determined from the sunspot area. The intensity of the low-frequency radiation, on the other hand, cannot be predicted by routine inspection of the sunspot which approaches the central meridian (see Fig. 5). The C.M.P. of one sunspot often does not give rise to any increase in intensity, while another spot of the same size may cause an enormous increase. Special conditions must be present in order to increase the radiation.

On high frequencies, the ratio $I_{R,\,\max}/I_{\text{quiet}}$ varies irregularly, but with a tendency toward a 27-day period, due to the reappearance of an active region on the sun with each rotation. For the 2800 Mc/sec radiation, $I_{R,\,\max}/I_{\text{quiet}}$ is 2 to 3. At low frequencies the ratio $I_{R,\,\max}/I_{\text{quiet}}$ varies very irregularly and is of the order of 10 to 100.

Studies of the different prominences visible in the 18 months considered were undertaken in the hope of gaining some insight into the complex questions regarding the different intensities of the radio radiation from different sunspots. A qualitative comparison indicates that:

1. The presence of even huge prominences of type V (quiescent) does not presage great increases in the low-frequency radiation, except perhaps in some interesting cases where the prominence suddenly disappeared (drawn into the sun or ejected radially outward). These events seemed to be followed by increases in radio intensity; but, as they happened to occur simultaneously with the C.M.P. of the spot, it is not possible to determine the real cause of the increase.

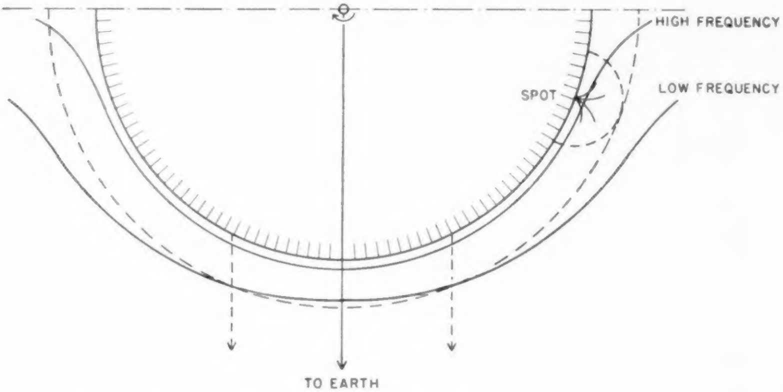

FIG. 7.—Schematic diagram of the emission and reflection levels of low and high frequency radio radiation in the solar atmosphere.

2. Active prominences—type IV—in this connection are not to be considered as a sign of great activity.

3. Things are more complicated when we consider the real sunspot prominences—type III—partly because of the refined subdivision. Generally, sunspot prominences were observed during limb passage of spots that were associated with low-frequency radio emission at the time of their central meridian passage. There is, therefore, some evidence that a great increase in radio-noise emission is seldom found without the presence of a sunspot prominence—even though the opposite seemed to take place.

RELATION BETWEEN SUNSPOTS, RADIO NOISE, AND GEOMAGNETIC ACTIVITY

For the period in question (January, 1950—July, 1951) the variation in the geomagnetic activity has been compared to the radio observations and to the behavior of the optical sun, using daily sums of the K-indices for 3-hour intervals. The indications are as follows:

A. Geomagnetic activity is often observed 1 or 2 days after the central meridian passage of a sunspot which is associated with an increase in low-frequency radio radiation.

B. Most of those sunspots which do not cause excessive radio noise on low frequencies do not cause geomagnetic disturbances either.

C. Some sunspots inactive with regard to radio noise seem to be associated with geomagnetic disturbances occurring 1 or 2 days after C.M.P.

The present analysis confirms similar results by Denisse (1952) and Owren (1954). We can distinguish between (A) radio-noise active sunspots, associated with geomagnetic disturbances, and (B) radio-noise inactive sunspots, which are not associated with magnetic disturbances. And, in addition to these types, there seems to exist a third type, C, characterized by the absence of those special conditions which must be present in order to increase the radio emission, even though they may lead to geomagnetic disturbances.

In conclusion, I should like to thank Dr. S. B. Nicholson for making available the Mount Wilson *Hα* and *Ca* II spectroheliograms, as well as the geomagnetic records. It is also a pleasure to thank Dr. J. L. Greenstein for his helpful suggestions and for reading the manuscript.

REFERENCES

Blum, E. J., Denisse, J. F., and Steinberg, J. L. 1952, *Ann. d'ap.*, **15**, 184.
Covington, A. E. 1948, *Proc. Inst. Radio Engineers*, **36**, 454.
Denisse, J. F. 1950, *Ann. d'ap.*, **13**, 181.
———. 1952, *Ann. de geophys.*, **8**, 55.
Markovitz, W. 1951, *U.S. Naval Obs. Circ.*, No. 30.
Martyn, D. F. 1948, *Proc. R. Soc. London, A*, **193**, 44.
Owren, L. 1954, thesis (unpublished).
Piddington, J. H., and Minnett, H. C. 1951, *Australian J. Sci. Research, A*, **4**, 131.
Smerd, S. F. 1950, *Australian J. Sci. Research, A*, **3**, 34.
Stahr, V. 1949, *A.J.*, **54**, 195.
Wild, J. P. 1951, *Australian J. Sci. Research, A*, **4**, 36.

HEIGHTS OF SOLAR FLARES*

JAMES W. WARWICK
Sacramento Peak Station, Harvard College Observatory, Sunspot, New Mexico

Received August 23, 1954

ABSTRACT

The observed area of a solar flare is a combination of two areas: the area of the sides of the flare as it would be seen at the limb and the area of the top of the flare as it would be seen at the center of the disk. The change in measured areas of $H\alpha$ flares observed at the center of the disk and at some distance from the center of the disk is used to derive information on heights of flares. A preliminary analysis of the raw data indicates that flares are neither flat nor needle-shaped. Explicit height distributions, functions of flare area, are derived from the smoothed data. The shape assumed here for a typical flare appears to be more realistic than that proposed by Waldmeier. The height-frequency distribution is well represented by $\exp[-\beta h]$, where β is the reciprocal of 20,300 km. Flares at the limb of the sun should therefore be visible as low, but extremely bright, prominences.

I. INTRODUCTION

Chromospheric flares are disk phenomena. But what is the appearance of a flare at the limb? The height of the flare above the point where the chromosphere becomes transparent to the flare radiation determines the answer. A disk flare gives us no direct information on its own height. However, the distribution of observed areas determined from many flares will help tell us the heights of flares in general. If flares were flat, they would tend to be larger near the center of the disk than near the limb. If they were irregular objects suspended above the chromosphere, they would appear as large near the limb as at the center. Changes in the flare-area distribution as a function of radius vector give a measure of flare heights.

This paper is a study of the areas and shapes of 419 $H\alpha$ flares observed at Sacramento Peak from February, 1951, through January, 1953. For all flares, the measurements, accurate to about 10 per cent, were carried out on photographs taken by the Sacramento Peak flare patrol camera. This camera records the sun's $H\alpha$ image, formed by a 2-inch objective through a birefringent filter, 1.25 A wide. Since the analysis is statistical, the main errors result from the small number of flares.

The flares, observed visually or as they appear on our photographs, have well-defined boundaries (to within the telescope's resolving power, say 2000 km on the surface of the sun). Also, the edge of the $H\alpha$ sun was well defined. There was no measurable difference between the diameter of the sun to the edge of the chromosphere and the diameter of the sun to the edge of the photosphere. The zero point of heights is the point at which the optical depth in the center of $H\alpha$ reaches unity. This point is sharply defined, within a possible error of 2000 km.

II. THE ANALYSIS

Table 1 shows the frequency distribution of flare areas for four annular zones of the solar disk. The area of a flare is measured on the $H\alpha$ photograph on which the flare showed maximum intensity. The photograph is projected onto a grid, and the disk area and the area of the region brighter than the disk are both determined in terms of the squares of the grid. Flares which extended partially or completely over the limb are not included in Table 1. The numbers are normalized to one hundred for each row, with the

---

* The work reported herein was accomplished under the sponsorship of the Air Force Cambridge Research Center, Geophysics Research Directorate, through Contract AF19(604)-146 with Harvard University.

actual numbers at the right of each row. The unit of area is one-millionth the area of the visible hemisphere. The zones were chosen to approximate equal areas of the disk regions in which flares occur. Eighteen flares were limb flares, omitted from the counts of the last row; two flares had no reported area. The tendency of flares to have small areas when they are observed at large radius vectors is unmistakable. The change in the distribution is apparent between all zones except between the first and second.

Table 2 shows the frequency distribution of corrected flare areas for the same four zones as before. The area of each flare has been divided by $(1 - r^2)^{1/2}$, where r is the radius vector to the position of the flare. This correction factor is the cosine of ϑ, the angle between the normal to the sun's surface and the line of sight. If flares were flat, the distribution would be the same in each zone. The corrected distributions are not equal because flare heights contribute to the observed areas.

TABLE 1

DISTRIBUTION-CURVES OF OBSERVED AREAS

RADIUS VECTORS	OBSERVED AREAS											
	0 to 49	50 to 99	100 to 149	150 to 199	200 to 249	250 to 299	300 to 349	350 to 399	400 to 449	450 to 499	≥ 500	Total Flares
0 to 0.382	27	35	19	10	5	1	0	1	0	0	2	100
0.383 to 0.706	26.3	32.5	20.1	7.0	5.4	3.9	1.6	0	0	0	3.1	129
0.707 to 0.923	35.1	40.4	20.2	3.2	1.1	0	0	0	0	0	0	94
0.924 to 0.999	44.7	34.2	13.2	4.0	2.6	1.3	0	0	0	0	0	76

TABLE 2

DISTRIBUTION-CURVES OF CORRECTED AREAS

RADIUS VECTORS	CORRECTED AREAS										
	0 to 49	50 to 99	100 to 149	150 to 199	200 to 249	250 to 299	300 to 349	350 to 399	400 to 449	450 to 499	≥ 500
0 to 0.382	27	33	18	12	6	1	0	1	0	0	2
0.383 to 0.706	17.8	35.7	17.0	10.8	6.2	5.4	2.3	0.8	0.8	0	3.1
0.707 to 0.923	14.9	27.7	21.3	21.3	5.3	5.3	0	3.2	1.1	0	0
0.924 to 0.999	2.6	11.8	19.8	10.5	10.5	6.6	7.9	6.6	2 6	7.9	13.2

If this were the only interpretation of our data, we should not be able to answer the question initially proposed. We need a numerical estimate of a flare's height in seconds of arc or kilometers. The shift in area of maximum frequency from zone to zone measures the increase in area resulting from flare height. In Table 1, for example, the area of maximum frequency in both zone 1 and zone 2 is about 75 millionths. We might expect a 20 per cent decrease in this area from zone 1 to zone 2 if flares were flat. The lack of a decrease gives information on the heights of flares.

This example is instructive, for the average projection angle for zone 2 is only 30°. The height of a flare contributes significantly to the total observed area of the flare, even when the flare is observed at angles as small as 30° from the normal. This fact implies that the edges of flares descend sharply to the level of the chromosphere, with an angle of descent greater than 60°. Flares must have clifflike edges.

A very crude estimate may now be made of the height of a flare. The area of maximum frequency in the first and second rows of Table 1 is 75 millionths. Assume that the flare is a right-circular cylinder, whose axis is perpendicular to the surface of the sun. Let l and h be the diameter and height of the flare, measured in units whose square is 10^{-6} of the area of the hemisphere. Then

$$75=\frac{\pi l^2}{4}, \tag{1}$$

for the flare as observed at the center of the disk, and

$$75=75\cos 30^\circ+lh\sin 30^\circ, \tag{2}$$

for the flare observed at 30°. In units of the solar radius, h, from equations (1) and (2), is 0.006, about 6 seconds of arc or 4800 km.

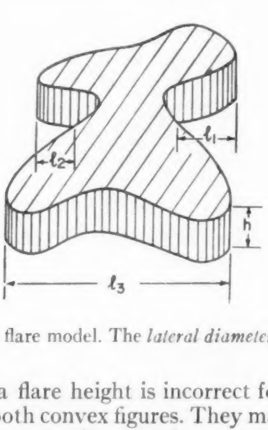

FIG. 1.—Proposed flare model. The *lateral diameter* $l = l_1 + l_2 + l_3$

The value just derived for a flare height is incorrect for several reasons. Flares are usually not circular or even smooth convex figures. They may be sinuous, with hoops and sharp curves. They sometimes appear in several separate radiating regions, which are counted together as a single flare. Flares may have any area within a large range of areas. A right-circular cylinder may be a poor approximation to the shape of the sides of the flare.

Figure 1 shows a model which meets the objections raised to the cylindrical model. We now determine the distribution of flare heights as a function of plan-areas in this model. The procedure is analogous to the crude method of equations (1) and (2).

Call the area of the top A_1, and the height, measured in units of the solar radius, h. The total area of the sides of the flare is approximately proportional to the sum $(l_1 + l_2 + l_3)$. Call this sum l, hereafter referred to as the "lateral diameter of the flare." Observe that a flare may have a shape more or less complex than Figure 1; in this case l will consist of the sum of more or less l_i than 3. Here $hrl(10^6/2\pi)$ is the projected area, in millionths of the hemispheric area, of the side of a flare observed at r. The projected area of the top of the flare is $A_1(1 - r^2)^{1/2}$. The total observed area of the flare is A_0:

$$A_0 = A_1(1-r^2)^{1/2}+hrl\left(\frac{10^6}{2\pi}\right). \tag{3}$$

The distribution of observed areas for zone 1 is essentially the distribution of A_1; and l and A_1 can be measured directly for each flare in zone 1. We measure r and A_0 for each flare in zone 2. Therefore, the distributions of all variables in equation (3) are known for zone 2, except for the distribution of h. This distribution follows from statistical theory.

The area of a flare composed of more than one distinct emitting region is reported as a single area equal to the sum of all the individual emitting areas. If one counts each separate area as an individual flare, there are 719 flares in the data. The numbers of these observed in each zone are, respectively, 193, 249, 173, and 104, in zones 1, 2, 3, and 4. The distributions of these flares over area for zones 1, 2, and 3 are shown in Figure 2.

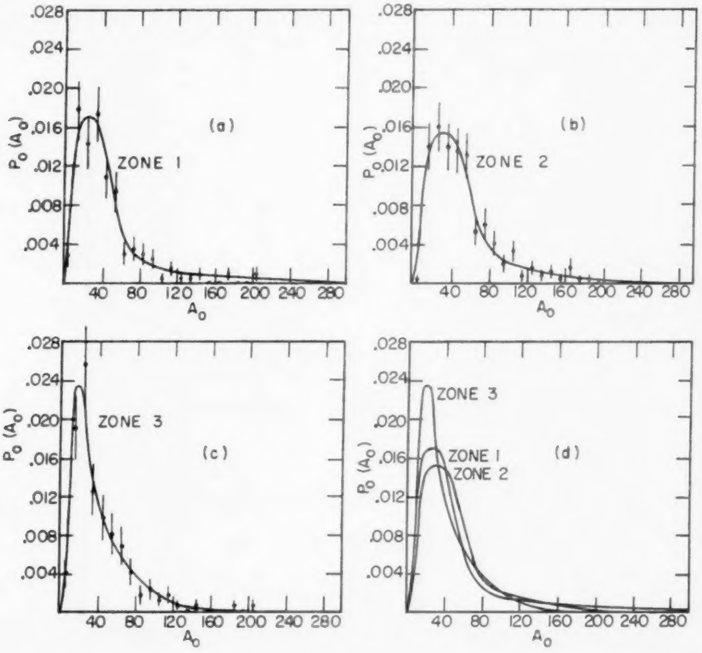

FIG. 2.—Distributions of observed areas in (*a*) zone 1, (*b*) zone 2, (*c*) zone 3, and (*d*) all zones combined. The natural uncertainty in the counts is indicated in *a*, *b*, and *c*.

These curves are undoubtedly incomplete for very small and very large areas. We assume they are reliable only for $35 \leq A_0 \leq 135$. Let

$$p_0(A_0)\,dA_0 = \text{Distribution of observed areas,}$$

$$p_1(A_1)\,dA_1 = \text{Distribution of plan-areas,}$$

$$p_2(r)\,dr = \text{Distribution of radius vectors,}$$

in which p_0 and p_1 are identical in zone 1. They are normalized over A_0 and A_1, ranging from zero to infinity; p_2 is normalized separately over each zone.

Let $q_2(A_1, l)\,dA_1dl$ equal the distribution of plan-area and lateral diameter; q_2 is observed directly in zone 1 and is shown in Figure 3. The smooth curve in Figure 3 is the relation between diameter and area for a circular flare. Flares are irregularly shaped (see Fig. 1); they are far from circular or hemispherical (Waldmeier 1948; Behr and Siedentopf 1952). To fall much below the curve for circular flares, a flare must be cigar-shaped, with axis along the radius vector.

Figure 4 shows the smoothed and normalized q_2-curves used in the analysis. These curves obey

$$p_1(A_1) = \int_0^\infty q_2(A_1, l)\, dl\,. \tag{4}$$

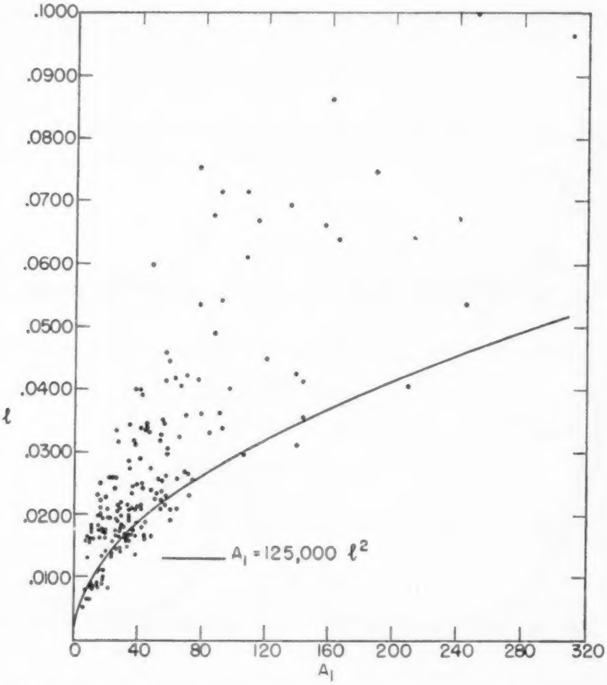

FIG. 3.—Relation of l to observed, or plan, area in zone 1. The smooth curve is the relation between diameter and area for a circular flare.

The details of the curves of Figure 4 are uncertain because of the small number of data. There are several reasons for confidence in the general trends represented there, however. Figure 3 unquestionably shows distributions which peak sharply at the circular relation for small areas and lateral diameters and taper off slowly toward increasing lateral diameters. For large areas and lateral diameters, the distributions are very flat, giving almost equal probability for us to observe a small or large lateral diameter for a given area. Even here, no flares appear below the circular relation. These features are well represented by Figure 4.

There is further reason for confidence in the smoothing. The data were far too few to give accurately the shape of each curve in Figure 4 independently of the remaining curves. Therefore, the general trends of Figure 3 were borne in mind when the sketches preparatory to Figure 4 were drawn. The size, or vertical scale, of each sketch was set by the author's judgment, based on the actual counted numbers. Each curve was drawn separately from the others. This somewhat arbitrary procedure gave surprisingly consistent results when the smooth sketches were normalized. The area under each smoothed curve was set equal to a constant *times* the corresponding ordinate of the p_1 distribution (Fig. 2, *a*). As shown by Table 3, the constants determined from the various smoothed curves agreed with one another quite satisfactorily.

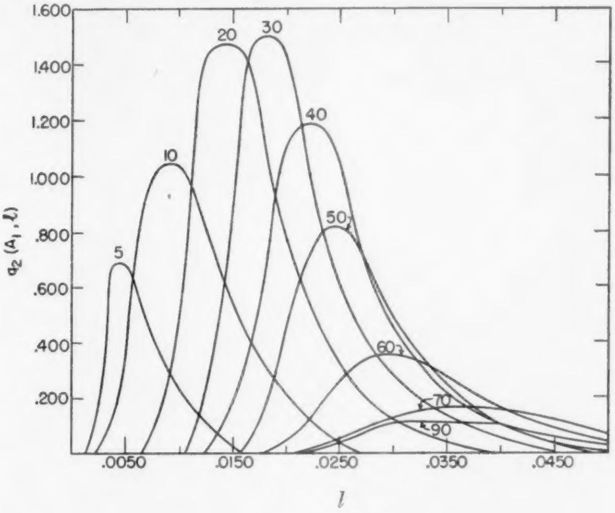

FIG. 4.—A smoothed representation of the distribution in Fig. 3

TABLE 3

NORMALIZATION OF q_2

	PLAN-AREA						
	10	30	40	50	60	70	90
Normalization constant	3.83	3.54	3.76	3.72	2.80	3.01	5.06

Let $q_1(A_1, h)\, dA_1 dh$ equal the distribution function of plan-area and height. In terms of the known functions,

$$q_1(A_1, h) = \left(\frac{10^6}{2\pi}\right) \int_{r_1}^{r_2} dr\, p_2(r)\, r \int_0^{\infty} dl\, q_2(A_1, l)\, l p_0 \left[A_1 (1 - r^2)^{1/2} + hrl \left(\frac{10^6}{2\pi}\right)\right]. \tag{5}$$

We have

$$p_1(A_1) = \int_0^\infty q_1(A_1, h)\, dh\,. \tag{6}$$

Compute q_1 for zone 2. The results of such computations are shown in Figure 5. The details of the curves for points below the lower, and to the left of the upper, dashed curves in Figure 5 are uncertain because of selection effects and small counted numbers.

The stability of the analysis was checked by a computation of q_1 from the data for zone 3. The zone-3 curves were determined only for reliable values of the p_0-curve. The agreement of the two sets of curves in Figure 6 appears satisfactory.

A further computation was necessary to check the sensitivity of the height–plan-

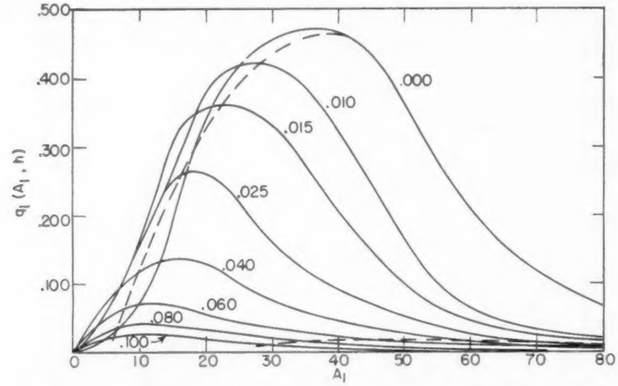

FIG. 5.—The computed plan-areas height-frequency distribution. Data from zones 1 and 2. The curves are, in detail, uncertain below the lower, and to the left of the upper, dashed curves.

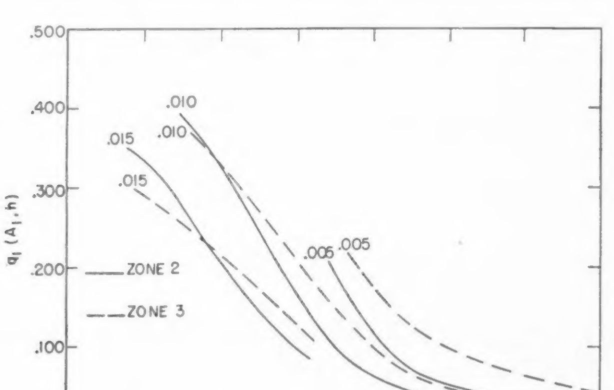

FIG. 6.—Computation of q_1 from data of zones 1 and 2 compared with similar computation from data of zones 1 and 3.

areas distribution function toward small changes in the observed areas distribution-function. Insert (incorrectly) the observed areas distribution-function from zone 2 in equation (5), written otherwise for zone 3. Figure 7 shows the three q_1-curves plotted on the same set of axes. The incorrect curves in no case fall between the correct curves. The distance between correct curves, for small areas, is of the order of one-half to one-third the distance between either correct curve and the incorrect curve.

The frequency distribution of flares over various heights is shown in Figure 8. This curve is obtained if one integrates each curve of Figure 5 over area. The dashed curve is

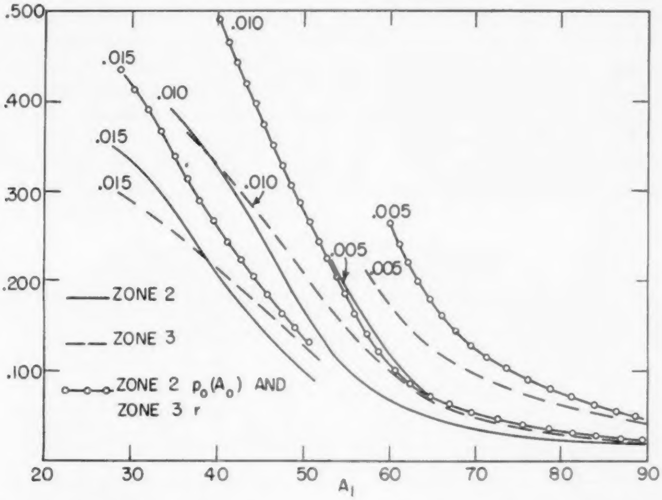

FIG. 7.—The sensitivity of the height-plan-areas distribution function toward small changes in the observed-areas distribution function (see text).

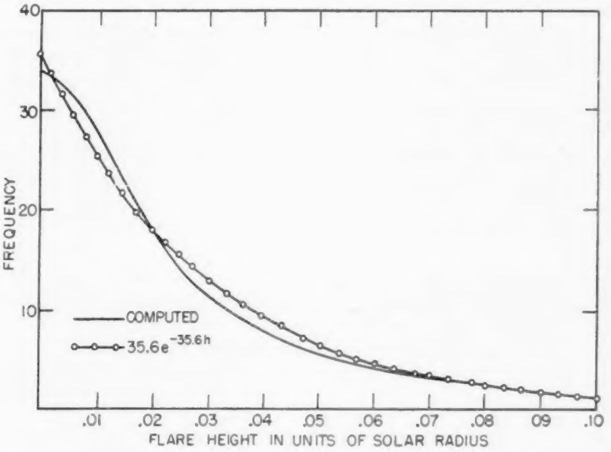

FIG. 8.—The frequency distribution of flares over height

the exponential function, with argument $-\beta h$, in which $\beta = 34.2$, in inverse solar radii, or about 20,300 km scale height.

III. CONCLUSIONS

The advantage in using the Sacramento Peak data for flares is that detailed analysis of the areas is possible. Waldmeier (1948) and Behr and Siedentopf (1952) had only numbers of flares at each *r*, arranged in three categories of "importance." Conclusions on the detailed shapes of flares are difficult or impossible to make with their kind of data. In addition to other uncertainties, no less important than in our analysis, their analysis places primary importance on the effects of observational selection in reducing the number of flares at the limb. Moreover, the decrease in counted numbers is not necessarily proportional to the projection effect for the actual shape of a flare. In the present analysis the restrictions imposed by the flare model are lessened, as compared to the earlier studies. Our knowledge of the individual flare areas and shapes allows a more rigorous analysis of flare heights than was previously possible.

The curves in Figure 5 show that large flares are generally lower than small flares. In illustration of this point, Table 4 shows the course of area and modal heights. The third row of Table 4 is the computed diameter (in units of the solar radius) for a circular flare which has the area appearing in the first row. The course of area-modal height described by Table 4 is uncertain to the extent that the uncertain small-areas range of q_1 enters the analysis.

TABLE 4

MODAL HEIGHTS AS FUNCTION OF AREA

	PLAN-AREA			
	10	20	30	40
Modal height.........	0.017	0.007	0.002	0.000
Circular flare l/R_0....	0.009	0.013	0.015	0.018

The height frequency-distribution (Fig. 8) can be fitted by an exponential function, exp $[-\beta h]$, where $\beta = 34.2$ inverse solar radii. The corresponding scale height for flares is about 20,300 km. Flares, in the disk meaning of the word, must be visible at the limb as low, exceedingly active, and bright prominences. Only their brightness separates them from the low "mounds" and surges often observed on prominence films.

In the following paper, C. Warwick analyzes the height distribution of the limb flares and shows that it is consistent with the height distribution found in this paper.

REFERENCES

Behr, A., and Siedentopf, H. 1952, *Zs. f. Ap.*, **30,** 177.
Waldmeier, M. 1948, *Astronomische Miteilungen der Eidgenössischen Sternwarte Zürich,* No. 153.

FLARE HEIGHT AND ASSOCIATION WITH SID'S*

CONSTANCE S. WARWICK
Sacramento Peak Station, Harvard College Observatory, Sunspot, New Mexico

Received August 23, 1954

ABSTRACT

The measured heights of limb flares yield a height-frequency distribution that agrees, within observational uncertainties, with that derived by J. W. Warwick from areas of disk flares. No certain case is found of an SID (sudden ionospheric disturbance) associated with a flare of height less than 15,000 km above the *Hα* limb. The existence of a minimum flare height for SID association suggests that SID's are caused by Lyman radiation rather than by soft X-rays. The observed value of 15,000 km for the minimum height above the *Hα* limb agrees fairly well with the value 11,000 km, the height above the photosphere at which optical depth becomes unity for Lyman-α radiation in Piddington's model. Values of the fraction of SID-associated flares at different distances from the center of the disk are consistent with the idea of a critical flare height for SID association.

I. THE DISTRIBUTION OF FLARE HEIGHTS

Flares within 0.01 solar radius of the limb were selected from the records of the Sacramento Peak flare and prominence patrols (February 28, 1950—December 31, 1953) and of the Boulder flare patrol (February 15–November 15, 1950). Only those objects were measured that were at least as bright as the solar disk on the *Hα* photograph. The disk diameter and radial height of the part of the flare at least as bright as the disk were measured on the projected *Hα* image. The estimated maximum error in measurement corresponds to 2000 km in flare height. Poor seeing might make bright flares appear systematically too high. On the other hand, with flare patrol pictures taken routinely at 5-minute intervals, the maximum of a fast flare might be missed, so that the measured maximum height would be too low. The measured height was converted to units of solar radius and then to kilometers, using the values of the measured disk radius and the radius of the sun in kilometers.

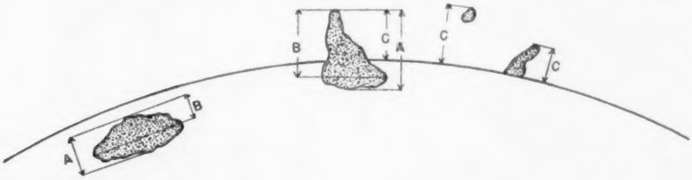

FIG. 1.—*A*, maximum height of flare; *B*, "probable height"; *C*, minimum height

More than one value of the "height" was measured for most flares, as shown in Figure 1. The largest radial diameter, *A*, is the maximum height of the flare. The radial distance, *B*, between the top of the flare and its greatest lateral diameter has been called the "probable height," and the radial distance, *C*, between the top of the flare and the limb is the minimum height. No correction has been made for projection, since the position of all flares was within 0.01 radius of the limb.

---

* The work reported herein was accomplished under the sponsorship of the Air Force Cambridge Research Center, Geophysics Research Directorate, through Contract AF19(604)-146 with Harvard University.

Figure 2 shows two height distributions. The full curve was derived by J. W. Warwick from 719 flare areas. The circles give the frequencies of measured probable heights of 39 limb flares. The length of an arrow represents the probable error of the value derived from limb flares. The frequencies for height 0.01–0.02 radius have been made equal, in order to fit the second curve to the first. The first curve is normalized; the second is not.

The only certain difference between the two distributions is the small frequency of very low limb flares. This may be explained as an effect of observational selection. Very low flares will have such small apparent areas near the limb that they will fall below the minimum area for observation (about 10 millionths the area of the solar hemisphere). We consider the agreement satisfactory and adopt the frequencies derived from disk flares as the true distribution of flare heights.

II. SID ASSOCIATION

In Table 1, limb flares are listed in the order of their probable heights. The first column gives the date and time (U.T.) of the flare. In the second column is an estimate of the intensity, made by the author from *Hα* photographs: 1, equal to disk intensity; 2, slightly greater than disk; 3, greater than disk; 4, much greater than disk. The next three columns give the measured minimum, probable, and maximum heights. The probable height, as defined above, is 0 for the first three flares listed, because the greatest lateral diameter forms the edge of the flare nearest the limb. The sixth column gives the area of the flare as measured by different observers on *Hα* photographs. In the final column a 0 appears if no SID was reported near the time of the flare in "Ionospheric Data" (National Bureau of Standards 1951–1953), while the beginning and ending times of the SID are given if one was reported near the time of the flare.

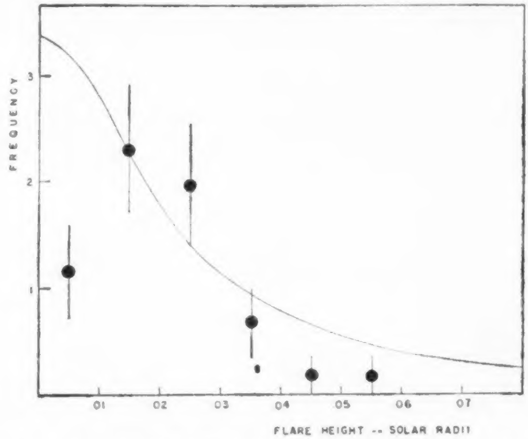

FIG. 2.—*Solid curve:* distribution derived by J. W. Warwick from flare areas; *dots:* observed distribution of 39 limb flares and bright prominences.

Among flares that did not reach a height of 15,000 km, there is only one for which an SID is reported. The probable height of this flare is 11,100 km. There was a large *plage* on the disk on this day, which was partly obscured by clouds at the time of the limb flare and SID. It is not impossible (though admittedly improbable) that a second flare, occurring on the disk at the same time but covered by clouds, was responsible for the SID.

The probability of chance occurrence of an association as large as or larger than the association observed here between flare height and SID occurrence is 1.4×10^{-4}. For these same flares the association between large area and great height has a probability of 0.16, and the association between high intensity and large height has a probability of 0.55. We cannot interpret the relation between flare height and SID occurrence as a secondary result of dependence of both height and SID occurrence on flare intensity or on flare area, since the secondary relation could not be stronger than one of the primary relations.

III. OPTICAL DEPTH FOR LYMAN RADIATION AND FOR SOFT X-RAYS

It has usually been assumed that SID's are caused by Lyman radiation, which accompanies the burst of *Hα* radiation that we call a "flare." Recent experiments in rocket flights (Tousey 1953) indicate that soft X-rays, with wave length less than 7 or 8 A, are

TABLE 1

LIMB FLARES AND THEIR PROBABLE HEIGHTS

Date (U.T.)	Int.	Height (Km)			Area	SID
		Min.	Prob.	Max.		
1951 Apr. 23, 1959	3	0	0	13,000	66	0
1952 Aug. 31, 1407	3	0	0	6,550	22	0
1951 Nov. 7, 2011	3	0	0	6,550	50	0
1951 May 9, 1520	3	4,450	4,450	> 4,450	33	0
1951 May 9, 1536	3	4,450	4,450	> 4,450	55	0
1950 Nov. 3, 1604	3	1,800	6,600	15,000	50	0
1951 May 20, 1319	3	0	6,750	6,750	91	0
1951 Aug. 7, 1620	3	0	7,650	7,650	70	0
1951 May 22, 1517	3	5,840	8,060	8,060	23	0
1952 Nov. 15, 2029	2	8,700	8,700	16,500	72	0
1952 Aug. 31, 1532	3	8,760	8,760	30,600	35	0
1951 June 28, 2315	3	9,950	9,950	> 9,950	21	0
1951 Nov. 7, 1847	2	5,200	10,400	13,900	45	0
1952 Aug. 31, 2404	3	7,800	10,900	19,700	67	0
1950 July 29, 1720	3	0	11,100	11,100	77	1720–1840*
1950 Aug. 14, 1810	1−	11,100	11,100	>11,100	34	0
1951 Nov. 7, 1740	3	8,700	11,300	11,300	....	0
1951 Mar. 11, 2255	1	11,300	11,300	>11,300	53	0
1951 May 28, 1608	3	9,000	12,500	12,500	32	0
1951 May 22, 2205	3	8,100	13,400	13,400	149	0
1951 Aug. 7, 1405	3	9,000	13,500	18,000	117	0
1951 June 24, 1630	1	9,000	13,900	13,900	....	0
1951 Oct. 8, 1506	4	11,000	13,900	17,100	34	0
1951 June 24, 1810	3	11,700	13,900	13,900	....	0
1952 Nov. 15, 2101	3	11,800	15,200	23,100	55	0
1950 July 29, 1448	1−	5,300	15,300	15,300	55	1510–1535
1950 Mar. 10, 1539	3	15,300	15,300	22,000	60	1551–1620
1951 May 22, 1534	3	15,700	15,700	>15,700	525	0
1951 June 24, 2125	3	16,100	16,100	>16,100	267	2125–2230
1951 Apr. 13, 1447	2	17,200	17,200	>17,200	45	0
1951 June 24, 1405	3	13,500	18,000	33,200	221	1405–1450
1951 Nov. 7, 1825	3	0	19,600	19,600	....	1820–1910
1953 May 4, 1640	1	20,000	20,000	>20,000	....	1625–1705
1952 Aug. 31, 2256	3	19,700	21,800	34,500	56	0
1951 June 24, 2230	1	23,100	23,100	>23,100	....	0
1951 June 24, 2205	3	23,400	23,400	>23,400	....	0
1951 May 8, 1547	3	23,500	23,500	>23,500	134	1550–1620
1951 June 19, 1745	1	29,400	29,400	>29,400	29	1750–1810
1951 May 8, 1510	3	39,600	39,600	>39,600	278	1505–1525

* No other flare reported. Large *plage* on disk; clouds at this time.

emitted by the sun only at times of disturbed solar and ionospheric conditions and suggest that this radiation might be responsible for SID's. If we accept a critical flare height in the upper chromosphere and interpret it as the height below which the optical depth becomes too great for SID-causing radiation to escape, we can show that Lyman radiation is a more probable cause of SID's than 8 A radiation.

We have used values of the temperature and electron density given by Piddington's chromospheric model (1954). The density of neutral hydrogen atoms has been computed according to the collision ionization formula given by Woolley and Allen (1950, p. 364). Let a be the absorption coefficient per atom; N the density of absorbing atoms; and τ the optical depth. Then

$$d\tau = aN dx \,, \tag{1}$$

dx being an element of path length. Let h be the height in the chromosphere (measured from the point where $\tau = 1$ for visible light), N_0 the density of absorbing atoms at height h_0, and H the scale height at h_0. Then

$$N(h) = N_0 e^{-(h-h_0)/H} \,. \tag{2}$$

Putting h, $h_0 \ll R$, the radius of the sun, we find, by integrating along the transverse path,

$$\tau = aN\sqrt{\frac{\pi R H}{2}} \,. \tag{3}$$

In the soft X-ray region and at the heights considered, photoelectric ionization was found to be the main absorbing process and neutral hydrogen the principal absorbing material. The absorption coefficient per atom was computed for various wave lengths between 5 and 140 A, from the expression given by Heitler (1944, p. 124, eq. [16]). Setting $\tau = 1$, we find, by successive approximations, values of N and H that are consistent with Piddington's model.

TABLE 2

FLARE HEIGHTS

	WAVE LENGTH (λ)								
	5 A	8 A	20 A	80 A	140 A	912 A L cont.	974 A L-γ	1028 A L-β	1216 A L-α
a_ν	4.9×10^{-22}	2.3×10^{-21}	4.1×10^{-20}	1.5×10^{-18}	1.1×10^{-17}	6.3×10^{-18}	1.8×10^{-15}	4.8×10^{-15}	2.4×10^{-14}
log N	13.0	12.4	11.1	9.6	8.7	8.0	5.4	5.0	4.2
h (km)	3,700	4,100	4,600	5,000	5,600	8,500	10,100	10,400	11,200

For the Lyman series, the line-absorption coefficient at line center was computed for L-α, L-β, and L-γ, from the expression given by Menzel (1936, p. 463, eq. [5]). The value of the absorption coefficient depends on the temperature and thus on the height. We have derived consistent values of the height, absorption coefficient, and temperature by successive approximations in equation (3), with τ set equal to unity. In Table 2 are given the values of a and log N computed here, and the corresponding values of h from Piddington's model. The value of a for the head of the Lyman continuum is quoted from an article by van de Hulst (1953).

In using Woolley and Allen's collision ionization formula, we neglect the effect of the radiation field. Computations by Giovanelli (1948) and by Thomas (1949) show that this effect is appreciable and that its inclusion raises the estimate of the number of atoms in the ground state of hydrogen. This would, of course, increase the optical depth at each height and increase the predicted critical height, bringing this value into somewhat better agreement with the observed value. On the other hand, the zero point of observed heights is at the limb as photographed through an *Hα* filter. The *Hα* limb may lie several thousand kilometers above the white-light limb, which is the zero point for heights in the model. This would mean that the gap between predicted and observed critical heights should be increased by some thousands of kilometers.

Even if these corrections were made, the predicted critical height for X-rays would lie in the lower chromosphere, while that for Lyman radiation and the observed height would lie reasonably close together in the upper chromosphere. This agreement suggests that (1) SID's are caused by Lyman radiation rather than by soft X-rays; (2) the source of the Lyman radiation coincides with the *Hα* flare; and (3) a value of the critical height for SID occurrence, based on many observations of limb flares, might be a useful observational value to be used in the construction of future chromospheric models.

IV. SID OCCURRENCE AND FLARE POSITION

If there is a critical height for the escape of the radiation causing SID's, we should expect that this height would be lower for flares viewed normally at the center of the disk than for those seen transversely at the limb. Then, if there is a distribution in flare heights, more flares would surpass the lower critical height at the center, and we should observe a larger proportion of associated SID's for central flares than for those near the limb. Table 3 shows the observed percentage of flares with SID's among all flares, and the total number of flares, within various limits of distance from the sun's center. The radius vector of the flare is the distance from the sun's center to the center of light of the flare. As we go out from the center, the proportion of SID-producing flares first decreases, as expected, but the proportion rises at the limb and beyond the limb. This can be explained as an effect of the same observational selection that caused low limb flares to be lost. Given the radius vector, flare height, and minimum flare area for observation, the minimum plan-area for observation can be computed according to J. W. Warwick's model. The fraction of flares of the given height falling below this minimum plan-area is found from his distribution-curves. This number, multiplied by the proportion of flares of that height, gives the fraction that will be lost to observation. Summing these values over the different heights, we find the fraction of flares that will be lost at each radius vector. Since all the "lost" flares will be low ones, none will have associated SID's, and the proportion of SID-associated flares among the total number will increase. The final column of Table 3 gives the corrected percentage of SID-producing flares. The value for

TABLE 3

FLARES ASSOCIATED WITH SID'S

Distance from Center of Sun (Units of Solar Radius)	Fraction of Flares with Associated SID's	Total No. of Flares	Corrected Fraction of Flares with Associated SID's	Distance from Center of Sun (Units of Solar Radius)	Fraction of Flares with Associated SID's	Total No. of Flares	Corrected Fraction of Flares with Associated SID's
0.0–0.2	0.17	23	0.17	0.8–0.9	0.09	47	0.08
.2– .4	.14	91	.14	0.9–1.00	.12	102	.10
.4– .6	.16	90	.16	>1.00	0.43	7	0.33
0.6–0.8	0.09	74	0.09				

flares with radius vector greater than 1 is still about twice too large. Here we may be adding flares that are based beyond the limb. In fact, two of the three flares with radius vector greater than 1, which had SID's, were judged to be based beyond the limb.

Considering only the flares with radius vector equal or less than 1.00, we see the suggestion of a relation between radius vector and percentage of SID's. The correlation coefficient is 0.86, and the probability of finding by chance a coefficient numerically this large is 0.03, so that we can have some confidence in its reality.

At the center of the disk, the expression for the optical depth is

$$\tau = a N H \; . \tag{4}$$

Set τ equal to its value at 15,000 km *at the limb*, according to Piddington's model. We can then find, by successive approximations, the value of the density, and so of the height, at which this value of τ occurs *at the center*. For the first three lines of the Lyman series, the height is 12,250 km; for the Lyman continuum, 11,800 km. In Table 1, we find 15 flares with height above 15,000 km, and 21 above 12,250 km. The ratio 21/15 = 1.4 should be comparable to the ratio of the fraction of SID-producing flares at the center to the fraction of SID-producing flares at the limb. A least-squares solution of the data presented in Table 2 indicates a value of 2.2 for this ratio. In view of the small number of flares, the agreement of these values seems consistent with our interpretation of a critical flare height for SID occurrence.

REFERENCES

Giovanelli, R. G. 1948, *Australian J. Sci. Res. A*, **1**, 275, 289, 305, 360.

Heitler, W. 1944, *The Quantum Theory of Radiation* (London: Oxford University Press), pp. 119–125.

van de Hulst, H. C. 1953, "The Chromosphere and the Corona," *in:* G. P. Kuiper (ed.), *The Sun* (Chicago: University of Chicago Press), pp. 207–321.

Menzel, D. H. 1936, *Ap. J.*, **84**, 462–473.

National Bureau of Standards. 1951–1953, "Ionospheric Data" (mimeographed sheets).

Piddington, J. H. 1954, *Ap. J.*, **119**, 531.

Thomas, R. N. 1949, *Ap. J.*, **109**, 480.

Tousey, R. 1953, "Solar Work at High Altitudes from Rockets," *in:* G. P. Kuiper (ed.), *The Sun* (Chicago: University of Chicago Press), pp. 658–676.

Warwick, J. W. Unpublished.

Wooley, R. v. d. R., and Allen, C. W. 1950, *M.N.*, **110**, 358–372.

CN BANDS IN THE CHROMOSPHERE*

J.-C. Pecker and R. G. Athay
High Altitude Observatory, Boulder, Colorado

Received September 7, 1954

ABSTRACT

CN bands are observed in emission in the chromosphere between the photospheric limb and a height of 750 km. Spectrograms obtained by the High Altitude Observatory at the Khartoum eclipse in 1952 showed a scale height of 210 km for the intensity of the emission in the $^2\Sigma \rightarrow {}^2\Sigma(0, 0)$ band at λ 3883. The emission spectrum at 100 km gives a rotation temperature of ∼4500°, and the photospheric absorption spectrum in the Utrecht *Atlas* gives a rotation temperature of ∼4000°. At eclipse heights other than 100 km, the data were used to determine the temperature gradient. The rotation temperature was found to increase with height. Photospheric and chromospheric models were used to predict the absolute intensity of the *CN* emission in this band. The predicted intensity was less than the observed intensity by a factor of 20. The discrepancy was accounted for by uncertainties in the absorption coefficient, which was obtained from a study of the absorption profile in the Utrecht *Atlas*.

INTRODUCTION

The presence of *CN* bands in emission in the chromospheric flash spectrum has been reported by many eclipse observers. To our knowledge, there have been no studies of the excitation conditions within the band structures. Houtgast (1953) measured the intensity of the $^2\Sigma \rightarrow {}^2\Sigma$ (0, 0) band at λ 3883 as a function of height on spectrograms obtained at the 1952 eclipse. He obtained a logarithmic emission gradient $\sim -5 \times 10^{-8}$ cm^{-1}, which is much steeper than the gradient in any of the chromospheric lines.

The molecular bands are of interest for several reasons: (1) Band emission can be observed to ∼750 km above the photosphere and is strong evidence for fairly low kinetic temperatures in these regions. (2) Molecular dissociation depends directly on the square of the density of neutral atoms, whereas line emission from atoms depends on ion and electron densities. Hence the molecular emission gradients furnish additional knowledge about the change of ionization with height. (3) Herzberg (1950, p. 205) has pointed out that thermodynamic equilibrium is much more likely to occur in molecules than in atoms, and excitation temperatures obtained from molecular lines should be closer to the kinetic temperature than excitation temperatures obtained from atomic lines. (4) A study of molecular emission bands should give values of temperature and density in the low chromosphere. If the chromospheric structure is heterogeneous, the temperatures and densities obtained by various methods (molecular and atomic lines and continuous emission) will be averaged differently, because of the different ways in which the emission depends on these parameters. Thus a study of molecular emission, combined with a study of the continuous emission, should reveal heterogeneities, if they exist on a large scale.

From a practical point of view, there are many difficulties associated with such a study of molecular emission. Molecular dissociation depends upon the numbers of free atoms. Hence we need to examine all the possibilities for removing free atoms. For example, if we are considering *CN*, we need to take account of all other molecules which affect the numbers of free *C* and *N* atoms. In many cases the dissociation energies and transition probabilities are not well known, and much uncertainty results. A further difficulty comes from a lack of good resolving power in the spectrograms.

In this paper we derive values of rotation temperature and densities in the low chro-

---

* This work was supported by the Office of Naval Research and carried out in co-operation with the Naval Research Laboratory.

mosphere from a study of the *CN* band $^2\Sigma \rightarrow {}^2\Sigma$ (0, 0) at λ 3883. The data were obtained from slitless spectrograms obtained at the 1952 eclipse by the High Altitude Observatory.

DATA

Four spectrograms were obtained in the low chromosphere, where *CN* emission was intense enough to measure. Tracings were made at four points (*a*, *b*, *c*, and *d*) on the east limb within 6° of the line of contacts. The relative heights of the four points were determined from moon-profile pictures and from the intensities of the continuous emission. Two of the points (*a* and *b*) coincided with the points where Balmer line intensities and continuum intensities were measured (Athay, Billings, Evans, and Roberts 1954; Athay, Pecker, and Thomas 1955).

Figure 1 is a reproduction of a tracing at a height of 100 km (point *b4*). The regions where the quantities of interest in the following discussion are measured are indicated in the figure. The intensities at the head of the band, E_H, and the ratios of the intensities between two fixed regions in the band, $\Delta \log E_m/A$, are given in Table 1. When the values of $\ln_e E_H$ are plotted against height, they give a straight line with a slope, -4.7×10^{-8} cm^{-1}, in good agreement with the value obtained by Houtgast (1953).

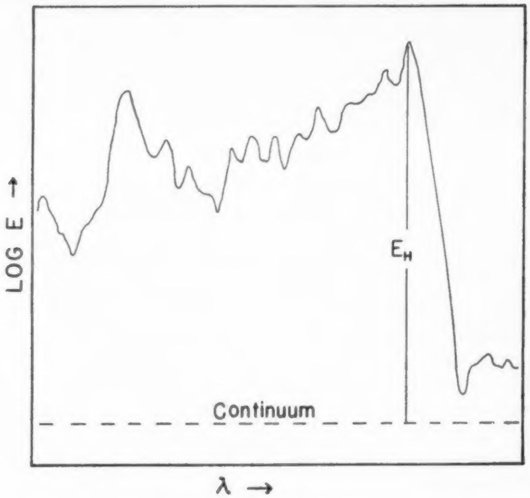

FIG. 1.—Tracing of chromospheric *CN* band, λ 3883

On one of the tracings showing the best resolving power (*b4*, $h = 100$ km) we measured the intensities at the positions of several lines in the band. These intensities are tabulated in Table 2 and will be used for an evaluation of the rotation temperature at this height. Lines are distinguished by the running number *m* (Herzberg 1950), but the negative sign of the index is not indicated. For $m \leq 13$ the lines can be identified individually.

RESOLVING POWER

Before actually computing a temperature from the data in Table 2, we need to know how the resolving power of our instruments has affected the data. The resolving power is unknown, but we can estimate its effects on our data by comparing them with the data in the Utrecht *Atlas* (Minnaert, Muldens, and Houtgast 1940). Of course, the legitimacy of this approach is questionable; the profiles of chromospheric lines are asymmetrically broadened by the fact that the spectrographs were slitless, and lines are in emission instead of absorption, and the observations refer to different layers of the atmosphere. However, the emission gradient for *CN* is very steep, and the asymmetry introduced as a result of the emission gradient is very small. In our spectrograms the profiles are almost entirely instrumental. Hence the estimation of instrumental effects by this method has some justification. We have integrated the intensity-curves in the Utrecht *Atlas* by assuming a rectangular instrumental profile of $\Delta\lambda = 0.15$, 0.25, 0.40, 0.60, and 1.00 A. Examples of the curves obtained are shown in Figure 2 on the same wave-length scale as the tracing in Figure 1. The determination of the proper resolving power may be based on (*a*) the general appearance of the band, (*b*) the ratio of intensities between line peaks and points midway between the lines, and (*c*) the wave length of the band head. Using these criteria, we obtained $0.4 \text{ A} \leq \Delta\lambda < 0.8 \text{ A}$. A value of $\Delta\lambda = 0.5$ A was chosen for the computations.

TABLE 1

INTENSITIES* VERSUS HEIGHT

Exposure	Heights (Km)	log E_H	Δ log E_m/A	Exposure	Heights (Km)	log E_H	Δ log E_m/A
b3	−10	14.27	0.03	d4	(260)	14.11	0.07
d2	(40)	14.41	.07	c4	(300)	13.97	.07
c2	(80)	14.36	.06	b5	530	13.37	.10
b4	100	14.40	.05	a2	530	13.57	.10
d3	(150)	14.02	.04	a3	640	13.22	.06
c3	(190)	14.16	0.08	a4	750	13.12	0.05

* Intensities in ergs sec^{-1} angstrom^{-1} for a slice of chromosphere 1 cm wide.

TABLE 2

INTENSITIES VERSUS *m*

m	8	9	10	11	12	13	14	15	16	17	18	19	20
log E_m . .	13.87	13.80	13.75	13.85	13.88	13.88	13.88	13.92	13.92	13.92	13.94	13.95	13.94

The foregoing method of determining resolving power has been used by Canavaggia, Chalonge, Egger Moreau, and Oziol Peltey (1950), Pecker and van Regemorter (1952), and Pecker, Billings, and Roberts (1955), with apparently reliable results. The Utrecht *Atlas* absorption profile in the *CN* band, when smoothed with a resolving power of 0.5 A, has a general appearance very similar in detail to a mirror image of our emission profile. Thus we feel we can use it with some confidence.

The curves in Figure 2 show an interesting phenomenon, pointed out by Pecker and van Regemorter (1952). With low resolving power, the peak intensities do not necessarily coincide with individual lines, and some care must be used in identifying the lines. Actually, only the general slope of the intensities in the band can be used as a measure of excitation.

This last point raises a further question about the effect of resolving power, viz., how does the resolving power affect the intensities within the band? Again we have answered this question by smoothing the band structure in the Utrecht *Atlas* with different resolving powers. The results are shown in Figure 3. When the resolving power is moderately good, as in the Utrecht *Atlas*, the slope of the band is not too sensitive to changes in

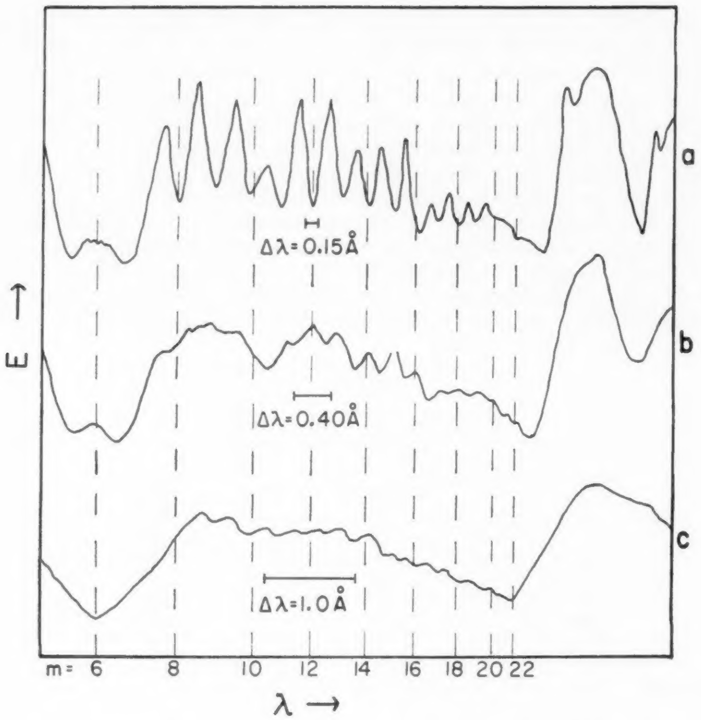

FIG. 2.—Photospheric *CN* band, λ 3883, modified with various resolving powers

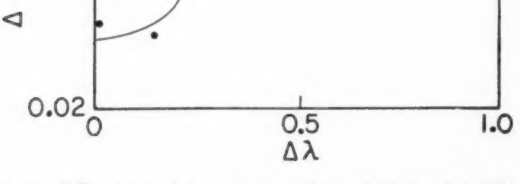

FIG. 3.—Effect of resolving power on slope of *CN* band, λ 3883

resolving power. When the resolving power is comparable to the separation between lines, ~0.25 A, the slope begins to increase strongly. However, at still lower resolving power the slope again becomes practically independent of resolving power. Thus either a low or a moderately good resolving power is better for determining the excitation conditions in the band. The resolving power of our instruments, fortunately, occurs in a favorable position on the curve in Figure 3.

ROTATION TEMPERATURES

On spectrograms of resolving power high enough that each line from the K levels may be identified and measured, the rotation temperature is determined by (Herzberg, 1950, p. 205)

$$\log \frac{E_M}{K'+K''+1} = \begin{cases} A' - \dfrac{h\nu B'_v}{2.3kT_r} K'(K'+1) & \text{(emission)} \\[2ex] A'' - \dfrac{h\nu B''_v}{2.3kT_r} K''(K''+1) & \text{(absorption)}\,. \end{cases} \tag{1}$$

Figure 4 contains a plot of log $[E_m/(K'+K''+1)]$ versus $K''(K''+1)$ from the data of the Utrecht *Atlas*. According to equation (1), this should be a straight line. However, there is a marked curvature to the best curve through the points, and no single value of T_r can be given. The slopes corresponding to $2000° \leq T \leq 5000°$ are given in Figure 4 for comparison. In plotting Figure 4, we were forced to use the peak estimates of the lines rather than the total intensities, because of insufficient resolving power. This is permissible only if the profiles are the same for all lines. However, this is not likely to be the case for this band in the Utrecht *Atlas*. The separation of the two intense J components of each K line increases as K increases (Herzberg 1950, p. 247). Thus, if the resolving power is of the same order as the splitting between the J components, as it is in the Utrecht *Atlas*, the peak intensities will be relatively too high for low values of K. This explains the change of slope shown in Figure 4. If the resolving powers were low enough that the profiles were instrumental, this difficulty would not be so pronounced. Hence we have smoothed the data in the Utrecht *Atlas* with a resolving power of 0.6 A, which puts the data in a favorable part of the curve in Figure 3. The results are shown in Figure 4, and, as was expected, a straight line was obtained. The straight line has a slope corresponding to $T_r \sim 4000°$.

The values of log $[E_m/(K'+K''+1)]$ obtained from the chromospheric data in Table 2 are plotted in Figure 5. The scattering of the points about a straight line is quite large. A least-squares fit of a straight line to these points gives $T_r = 4500° \pm 750°$. The probable errors determined in this way perhaps give too optimistic an estimate of the true uncertainty, because of the small number of data.

A further application of equation (1) may be used to give a lower limit to T_r. The maximum intensity in the band occurs at a value of K' (or K'') such that

$$K' = 0.43\,(T_r)^{1/2} - 0.5\,. \tag{2}$$

In both the photospheric and the chromospheric spectra the maximum intensity occurs for K' (or K'') ≥ 23, and equation (2) gives $T_r \geq 3000$. Unfortunately, there is no improvement in the limits of T_r.

We cannot apply these same methods directly to most of the chromospheric data because of the difficulty of identifying the individual lines. Instead, we have plotted the intensity profile of each tracing of the band and drawn a straight line through the upper envelope of the band, trying to use the same criteria for determining the line on each tracing. These straight lines gave the values of $\Delta \log E_m/\text{A}$ in Table 1. This value can be

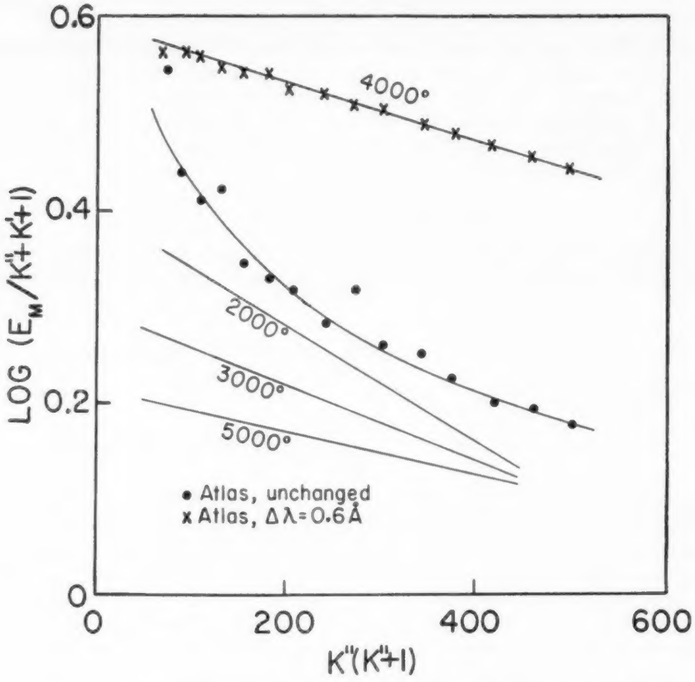

FIG. 4.—Rotation temperature from photospheric absorption band, λ 3883

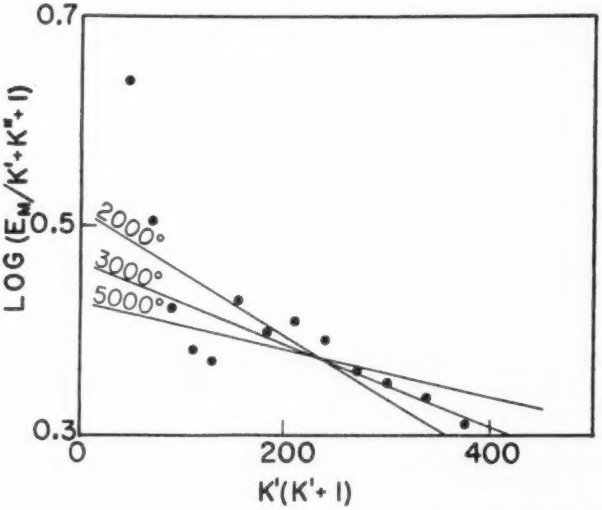

FIG. 5.—Rotation temperature from chromospheric emission band, λ 3883

obtained as a function of T_r from equation (1) (provided that the effects of the resolving power are taken into account). However, these computations give the change of $\Delta \log E_m/A$ with T_r more accurately than do the actual values of $\Delta \log E_m/A$.

The values of $\Delta \log E_m/A$ in Table 1 show a slight tendency to increase with height. A least-squares fit of a straight line to $\Delta \log E_m/A$ versus height gives an increase in $\Delta \log E_m/A$ of $+0.04 \pm 0.02$ per 1000 km. This corresponds to an increase in T_r of 500° ± 250° per 100 km increase in height Again, the data are small in number, and the probable errors are most likely underestimated. From a realistic point of view, it is safe to conclude only that $dT_r/dh > 0$.

The accuracy of the foregoing results is, of course, affected by blends with metallic lines. Further inaccuracies arise from errors in the location of the continuum, upon which the emission band is superimposed.

ABSOLUTE INTENSITY OF *CN* EMISSION

The observed intensity at the head of the *CN* band is

$$E_H = 3.5 \times 10^{14} e^{-4.7\times10^{-8}h} = \int_h^{\infty} \int_{-\infty}^{\infty} \mathfrak{E}_H dy\,dx\,, \tag{3}$$

where E_H is measured in ergs $\sec^{-1}$ angstrom^{-1} over the total radial angle and $\mathfrak{E}_H$ is the emission per unit volume. From equation (3) we obtain

$$\mathfrak{E}_H = 5.4 \times 10^{-3} e^{-4.7\times10^{-8}h}\,. \tag{4}$$

If we assume local thermodynamic equilibrium and let

T_e = the kinetic temperature ;

$\theta = \dfrac{5040}{T_e}$;

B_λ = the Planck function ;

ρ = the density in gm cm^{-3} ,

κ_H = the absorption coefficient per gram ,

P = the total gas pressure ,

n_c, n_N = the numbers of free carbon and nitrogen atoms per cubic centimeter , and

n'_c, n'_N = the total number of carbon and nitrogen atoms per cubic centimeter ,

we can write

$$\mathfrak{E}_H = B_\lambda(\theta)\ \kappa_H \rho \tag{5}$$

and

$$\kappa_H = k_H 10^{6\theta} p\,(\theta)^{1/2} \frac{n_c n_N}{n'_c n'_N}\,, \tag{6}$$

where we have used 6 volts as the dissociation energy of *CN* and where k_H contains the factor $n'_c\, n'_N$. Thus if we know κ_H, we can check the consistency of equations (4) and (5) with models of the low chromosphere.

The constant k_H in equation (6) is very poorly determined by existing laboratory data. The most accurate evaluation of this constant and, hence, of κ_H can be made by using the photospheric spectrum. However, even this determination is very poor because of the uncertainties in molecular dissociation energies and relative solar abundances of the elements. The quantity $n_c n_N/n'_c n'_N$ was computed as a function of P and θ, using Russell's (1934) dissociation coefficients and Aller's (1953) compiled values of relative abundances. We assumed that CO, OH, NH, H_2, and N_2 were the only important compounds affecting n_c and n_N. In the photospheric spectrum, we have

$$r_H = \frac{E_H}{E_c} = \frac{\int_0^\infty B_\lambda(\tau) \exp - \left[\tau + \int_0^\tau (\kappa_H/\kappa_c)\, d\tau\right] (1 + \kappa_H/\kappa_c)\, d\tau}{\int_0^\infty B_\lambda(\tau)\, e^{-\tau} d\tau}, \tag{7}$$

where τ is the optical depth in the continuum and $\kappa_H = k_H f(\tau)$. Using Minnaert's (1953) model for the photosphere, we can compute r_H as a function of k_H. The observed value of r_H, corrected to a resolving power of $\Delta\lambda = 0.5$ A, gives $k_H = 1.1 \times 10^4$. The estimated accuracy of k_H, based on uncertainties in the model, relative abundances, and dissociation energies (especially CO), is a factor of 200 in either sense.

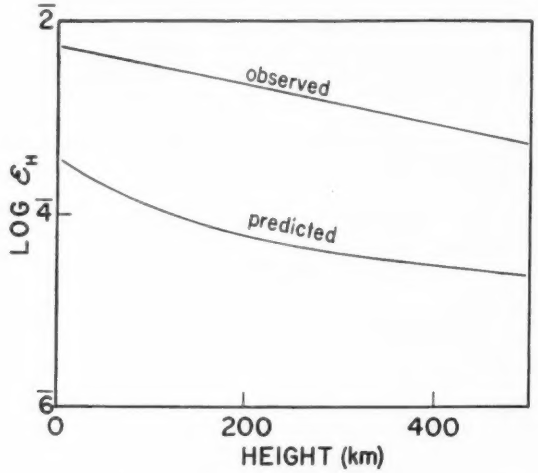

FIG. 6—Predicted and observed values of absolute intensity of emission at CN band head, λ 3883

The inaccuracy of κ_H for the chromosphere, arising from inaccuracies in k_H determined from the photosphere, are too large to allow a good check on a chromospheric model. Nevertheless, a rough check on consistency can be made. From equations (4) and (5), we can write

$$\mathfrak{E}_H = 1.16 \times 10^{-35} k_H \frac{n_c n_N}{n'_c n'_N} \theta^{-1/2} 10^{D\theta} B_\lambda(\theta)\, N^2 \mu\, (p, \theta)\,, \tag{8}$$

where μ is the mean molecular weight, D is the dissociation energy of CN, and N is the total particle density. Using the above-determined k_H and the chromospheric model of Athay, Pecker, and Thomas (1955), we computed values of $\mathfrak{E}_H$ as a function of height. The predicted values and the observed values (eq. [4]) are plotted in Figure 6. The predicted values (based on the models, dissociation energies, and our evaluation of k_H) are too low by a factor of about 20. Our estimated range of errors in k_H is much larger than this value. The discrepancy would disappear if we increased k_H by a factor of 20. Errors of this size are easily possible. We used Russell's value of 10 volts for the dissociation energy of CO. However, a value of 11.1 volts was adopted by Gaydon (1947) and Brewer, Gilles, and Jenkins (1948), whereas Herzberg (1942) used 9.1 volts and Hagstrum (1947) used 9.6 volts. The larger value of 11.1 volts would increase k_H by about a factor of 10. Errors in the dissociation energy of *CN* do not seriously affect the results, because the resultant change in k_H is balanced by an opposite change in the exponential factor in equation (6). A further source of error, however, comes from the errors in the relative abundances. We used the relative abundances compiled by Aller (1953), which are intermediate to those given by Claas (1952) and Unsöld (1948). Appreciable errors could easily arise from this source.

An alternative explanation of the discrepancy between computed and observed values of $\mathfrak{E}_H$ is a heterogeneous chromosphere consisting of local fluctuations in temperature and density. In this case the models derived from continuum data could not be expected to agree with models based on molecular emission, because of the differences in the way molecular and continuous emission vary with θ and N. Since the discrepancies can easily be accounted for by other means, there is no need to assume a heterogeneous structure. A more accurate evaluation of the molecular constants and relative abundances, however, would allow a rather critical check on whether or not a heterogeneous structure exists.

The predicted emission gradient (Fig. 6) agrees very well with the observed emission gradient. This lends support to the validity of the chromospheric model of Athay, Pecker, and Thomas (1955) in these height ranges.

The authors are indebted to W. O. Roberts, J. W. Evans, D. H. Menzel, and R. N. Thomas for discussions during the analysis of the data.

REFERENCES

Aller, L. H. 1953, *The Atmosphere of Sun and Stars* (New York: Ronald Press).
Athay, R. G., Billings, D. E., Evans, J. W., and Roberts, W. O. 1954, *Ap. J.*, **120**, 94.
Athay, R. G., Pecker, J. C., and Thomas, R. N. 1955, *Ap. J., Supplement* (in press).
Brewer, L., Gilles, P. W., and Jenkins, F. A. 1948, *J. Chem. Phys.*, **16**, 797.
Canavaggia, R., Chalonge, D., Egger Moreau, M., Oziol Peltey, H. 1950, *Ann. astr.*, **13**, 355.
Claas, W. J. 1951, *Recht. Obs. Utrecht*, **12**, 13.
Gaydon, A. G. 1947, *Dissociation Energies and Spectra of Diatomic Molecules* (London: Chapman-Hall).
Hagstrum, P. R. 1947, *Phys. Rev.*, **72**, 947.
Herzberg, G. 1942, *J. Chem. Phys.*, **10**, 306.
———. 1950, *Spectra of Diatomic Molecules* (2d ed.; New York: D. Van Nostrand Co.).
Houtgast, J. 1953, *Convegno Volta 1952, Roma, Accd. Nat. Lincei*, p. 68.
Minnaert, M. 1953, *The Sun*, ed. G. P. Kuiper (Chicago: University of Chicago Press).
Minnaert, M., Mulders, G. E. W., and Houtgast, J. 1940, *Photometric Atlas of Solar Spectrum* (Utrecht).
Pecker, C., Billings, D. E., and Roberts, W. O. 1955, *Ap. J.* **120**, 509.
Pecker, J. C., and Regemorter, H. van. 1952, *Ann. astr.*, **15**, 364.
Russell, H. N. 1934, *Ap. J.*, **79**, 317.
Unsöld, A. 1948, *Zs. f. Ap.*, **24**, 306.

INVESTIGATION OF TURBULENCE IN THE SOLAR ATMOSPHERE

MAHINDER S. UBEROI
Department of Aeronautical Engineering, University of Michigan

Received August 6, 1954; revised November 3, 1954

ABSTRACT

The correlation and the spectrum of solar granules are measured by a simple technique, and the results are compared with data obtained by orthodox methods. Published data are analyzed to give a direct evidence of convective heat transfer in the solar atmosphere.

INTRODUCTION

Recent advances in the statistical theory of turbulence have given an impetus to the study of turbulence in the solar atmosphere. However, very little useful data are available on the subject. One source of information is the direct solar photograph, which clearly shows the granules or the random variation of light received from the sun. The first problem is the statistical description of the random brightness fluctuations. One such description is the correlation or spectrum of the brightness fluctuations. The spectrum is the Fourier transform of the correlation and gives an indication of the distribution of fluctuations of different scales. The second problem is to relate the spectrum of the solar "picture" with that of turbulence in the solar atmosphere. It is not certain that the observed brightness fluctuations are entirely due to fluctuating emission in the turbulent solar atmosphere. We shall first show that the correlation or the spectrum of the granules can be obtained without making a detailed measurement of the solar brightness fluctuations.

CORRELATION AND SPECTRUM OF THE SOLAR "PICTURE"

Direct photographs of the sun are taken daily at solar observatories as a part of the routine program, and these can be used to measure the correlation of brightness fluctuations. An enlarged portion of such a photograph taken through a filter of effective wave length λ 5800 is shown in Figure 1. This photograph (courtesy of Dr. R. S. Richardson, Mount Wilson Observatory) has been used for the present investigation. The pertinent data are given there.

For the measurement of the correlation of the solar "picture," two enlarged identical positives of the original are made on photographic plates (Fig. 1). Mount Wilson photographs are taken on high-contrast plates, but it is possible to adjust the contrast of the positives so that the transparency of the positive is linearly proportional to solar brightness. In the present measurement no such adjustment has been made. We have assumed that for small fluctuations the brightness is linearly proportional to the transparency.

Let $t = t_0 + \Delta t(x, y)$ be the transparency of either positive plate, where t_0 is the average transparency of the region under investigation and $\Delta t(x, y)$ is the fluctuating transparency; (x, y) specify a point in this region. The combined transparency of two plates placed back to face and displaced from the matched position by distances ξ and η is

$$\text{Combined } t = \langle [t_0 + \Delta t(x, y)][t_0 + \Delta t(x + \xi, y + \eta)] \rangle_{AV},$$

FIG. 1.—Enlargement of a central portion of the solar photograph taken at Mount Wilson Observatory, June 7, 1952, G.C.T. 15:09. Original solar photograph was 17 cm in diameter.

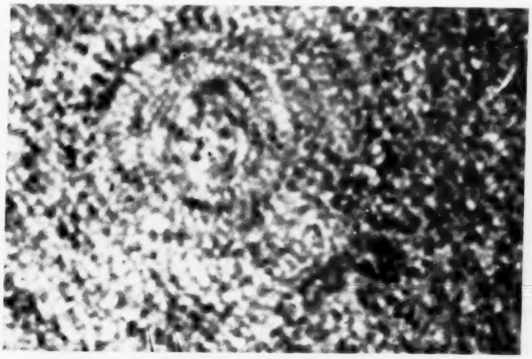

FIG. 2.—The pattern obtained by placing two plates in the matched position and turning one plate through 0.135 radians. Radius of circular pattern is 2.5–3.0 cm. Therefore, the spatial extent of the correlation = 2.5 × 0.135 × 13,000 = 4,400 km.

where the average is over x and y. The combined transparency is measured over a sufficiently large area that $\langle \Delta t(x, y)\rangle_{AV}$ and $\langle \Delta t(x+\xi, y+\eta)\rangle_{AV}$ are zero; thus

$$\text{Combined } t = t_0^2 + \langle \Delta t\,(x, y)\, \Delta t\,(x+\xi,\, y+\eta)\, \rangle_{AV}$$
$$= t_0^2 + R_t\,(\xi,\, \eta)\,,$$

where $R_t(\xi, \eta)$ is the correlation of the fluctuating transparency.[1] Visual indication of the spatial extent of the correlation can be obtained by placing the two plates back to face in the matched position and turning one plate through a small angle. The radius of the circular pattern multiplied by the angle gives the distance beyond which the correlation has dropped to an insignificant value (Fig. 2).

We have measured $R_t(\xi, \eta)$ for the central region of the solar photograph. In this region $R_t(\xi, \eta) = R_t(r)$, where $r^2 = \xi^2 + \eta^2$. The correlation of brightness fluctuations, $R(r)$, is proportional to $R_t(r)$, and the constant of proportionality can be determined from the calibration of the photographic plates. In particular, the mean-square brightness can be determined from $R_t(0)$. In this preliminary investigation we are mainly interested in the normalized brightness correlation $R(r)/R(0)$, which equals $R_t(r)/R_t(0)$. The measured correlation is shown in Figure 3. The one-dimensional spectrum of the brightness fluctuations, $E_1(k_1)$, is the Fourier transform of $R(r)$,

$$E_1\,(k_1) = \frac{2}{\pi R\,(0)} \int_0^\infty R\,(r) \cos k_1 r\, d r\,.$$

This has been computed numerically and is shown in Figure 4. There are no other measurements with which these could be compared; however, brightness fluctuations along a 111,500-km-long line in the central part of the solar surface are given by Richardson and Schwarzschild (1952). We have used these data to compute the correlation and the spectrum, and they are compared with present measurements in Figures 3 and 4.

A one-dimensional spectrum is not truly indicative of fluctuations of different scales. It is natural to define a three-dimensional spectrum, $E(k)$, which gives the mean-square contribution of all disturbances having the same wave-number magnitude k. For statistically isotropic scalar field (Uberoi and Kovasznay 1953),

$$E\,(k) = -\,k\left[\frac{dE_1\,(k_1)}{d\,k_1}\right]_{k_1=k},$$

where $E(k)$ is zero whenever E_1 has a maximum. There is continuous mixing in a turbulent fluid, and it is not very probable that $E(k)$ is zero for any finite k, while it has finite value in the neighborhood. The maximum of $E_1(k_1)$ is due either to error in measurements or to anisotropy. The results shown in Figures 3 and 4 give a statistical description of the solar "picture," and these have to be related to the fluctuating emission in the turbulent solar atmosphere. The light received at one point on the photo-

---

[1] The required measurements can be made directly from the original solar photograph. The transmitted light is reflected back onto the solar photograph by a tilted mirror, and after going through the photograph once again, it is measured by the photocell. The photocell measures the combined transparency of the solar photograph and the same photograph displaced by known distance. For the original photograph the transparency is inversely proportional to the brightness, B, so that the average transparency of the area is

$$\text{Combined } t \sim \langle\, [\,\{B_0 + \Delta B\,(x, y)\,\}\,\{B_0 + \Delta B\,(x+\xi,\, y+\eta)\,\}\,]^{-1} \rangle_{AV}$$
$$\sim 1/B_0 - \langle \Delta B\,(x, y)\, \Delta B\,(x+\xi,\, y+\eta)\, \rangle_{AV}\,,$$

since the fluctuating brightness ΔB is small compared with B_0, the mean brightness.

graphic plate is the integrated emission along the line of sight. This integrating effect and the poor resolving power of the instruments used to photograph the sun wash out the small-scale fluctuations. The light emitted from one layer of the solar atmosphere goes through the overlying turbulent solar atmosphere of fluctuating density and the transmitted light will be more or less intense according to the distortion produced by random density fluctuations acting as concave or convex lenses.[2] It appears that it is as yet premature to calculate the three-dimensional spectrum of the random emission in the turbulent solar atmosphere from the measured one-dimensional spectrum of the solar "picture."

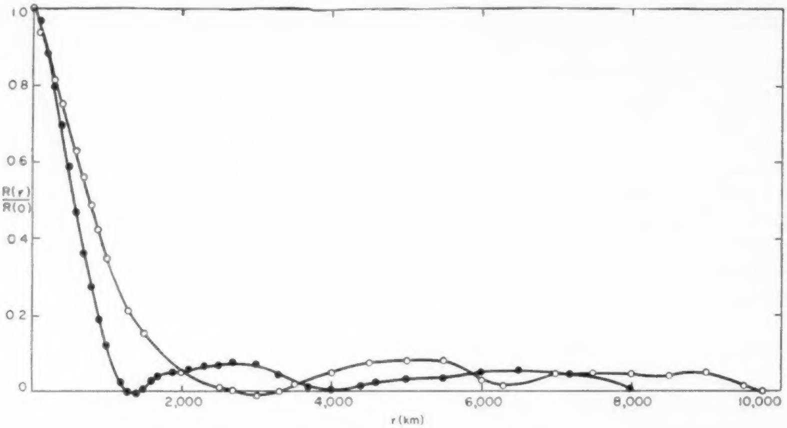

FIG. 3.—Brightness correlation; open circles are derived from data given by Richardson and Schwarzschild (1950) while the solid circles are derived from the measurements made by the author.

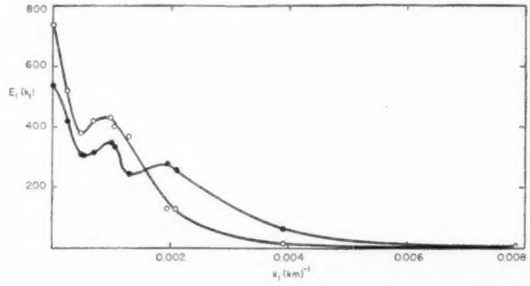

FIG. 4.—Brightness spectrum; open circles are derived from data given by Richardson and Schwarzschild (1950) while the solid circles are derived from the measurements made by the author.

TEMPERATURE-VELOCITY CORRELATION

Schwarzschild and Richardson (1950) have determined the turbulent velocity fluctuations from the Doppler shift of certain spectral lines, and the temperature fluctuations have been determined from brightness fluctuations, by assuming that the spectrum of each granule can be approximated by the equilibrium black-body spectrum. Temperature-velocity correlation at one point, using time average, gives information about the convective heat transfer. However, in the present circumstances we may replace the time average by an average over the solar surface or a line along the solar surface. Using these data, we find that $\langle T(X)U(X)\rangle_{AV}/[\langle T^2(X)\rangle_{AV}\langle U^2(X)\rangle_{AV}]^{1/2}$ has a value of -0.32, which shows that there is definite tendency for the hotter fluid to rise and the colder fluid to sink. The average is over X; T is the fluctuating temperature and U is the turbulent velocity along the line of sight and is positive toward the center of the sun. The resolving power of the instrument used is such that small-scale fluctuations are washed out (Schwarzschild and Richardson 1950; Frenkiel and Schwarzschild 1952). The Reynolds number of the turbulence is reasonably high, and we can assume that small-scale fluctuations are locally isotropic and that therefore they do not contribute much to the convective heat transfer. There is experimental evidence of the fact that, for large Reynolds number, small-scale fluctuations do not contribute much to the turbulent shear or convective momentum transfer (Corrsin and Uberoi 1951). This was demonstrated by deliberately washing out small-scale fluctuations. It is reasonable to assume that the same is true for other convective transport processes. In spite of the difficulties introduced by poor resolving power and extraneous effects, $\langle T(X)U(X)\rangle_{AV}$ can be determined more accurately than either $\langle T^2(X)\rangle_{AV}$ or $\langle U^2(X)\rangle_{AV}$. The amount of convective heat transfer is given by $-\rho C_p\langle T(X), U(X)\rangle_{AV}$ plus the effect of change in density and the work done in changing the ionization of the gas, where C_p is the heat capacity and ρ is the density. Although $\langle T(X)U(X)\rangle_{AV}$ does not give the total convective heat transfer, it is an important part of it.

---

[2] The referee points out that the effect is probably negligible because of the small index of refraction of the photosphere.

The author is indebted to Dr. Robert S. Richardson for supplying the original photograph, to Dr. Leslie S. G. Kovasznay for use of the correlation measuring equipment, and to Dr. Martin Schwarzschild for helpful criticism and useful suggestions. This work is a part of the research program supported by the Office of Naval Research under Contract NONR 1224-02.

REFERENCES

Corrsin, S., and Uberoi, M. S. 1951, *N.A.C.A. Tech. Rept.*, No. 1040.
Frenkiel, F. N., and Schwarzschild, M. 1952, *Ap. J.*, **116**, 422.
Kovasznay, L. S. G. 1949, *Heat Transfer and Fluid Mechanics Institute, ASME*, p. 211.
Richardson, R. S., and Schwarzschild, M. 1950, *Ap. J.*, **111**, 351.
Uberoi, M. S., and Kovasznay, L. S. G. 1953, *Quart. Appl. Math.*, **10**, 375.

ON BRIGHT-DARK SYMMETRY OF SOLAR GRANULATION*

ANDREW SKUMANICH
Princeton University Observatory

Received September 27, 1954

ABSTRACT

The possible existence of a statistical asymmetry between bright and dark in granulation intensities is investigated. Direct photographs of the quiet sun, taken with the 60-foot tower telescope of the Mount Wilson Observatory, were used. Two isophotes were determined, so that the total bright region (i.e., brighter than the isophote) formed 20 and 80 per cent of the total area of the field, respectively. The frequency distribution according to size of singly connected regions for both isophotes (bright on the 20 per cent and dark on the 80 per cent isophote) were obtained and intercompared. Only a very slight excess of bright regions was found, which implies a slight—if any—bright asymmetry. Further, a similar test based on the frequency distribution of granulation intensities did not show any appreciable asymmetry. Thus a strong bright-dark asymmetry, as implied by the traditional rice-grain picture of solar granulation, does not appear to exist, at least not for the granulation elements resolved on the Mount Wilson plates.

I. INTRODUCTION

The recent investigations of solar granulation in terms of correlation functions and power spectra are essentially based on quadratic operations and therefore give no information regarding the statistical symmetry between plus and minus signs, i.e., between bright and dark in the granulation intensities. The observers, on the other hand, tend to describe granulation by light rice-grains scattered on a gray background—a highly asymmetric picture. It is the purpose of this paper to investigate the possible existence of such an asymmetry by an objective criterion.

II. CRITERION OF ANALYSIS

On a direct photograph of the sun, select a rectangular field. Any isophote will divide this field into two regions—those brighter and those darker than the isophote. The total area of the bright regions will be some percentage, a, of the area of the field. Consider those two isophotes for which $a = 20$ per cent and 80 per cent (cf. Fig. 1). If the granulation is symmetric, these two isophotes will be statistically identical, i.e., both will have the same number of singly connected elements (bright on the 20 per cent isophote and dark on the 80 per cent isophote) of a given size. If there is an asymmetry, an excess will occur in the direction fixed by the sense of the asymmetry.

The advantage of this criterion is that the 20 and 80 per cent isophotes are invariant under transformations from one variable (e.g., photographic transparency on a plate) to another (intensity or temperature on the sun). Thus the presence or absence of any symmetry is not influenced by the variable chosen for study. In this paper, galvanometer deflection as obtained from microdensitometer tracings of the field was employed. In addition, the construction of both isophotes is influenced by the same measuring errors and proceeds in identical fashion, thereby excluding the introduction of fictitious asymmetries by observer selection and bias.

III. CONSTRUCTION OF ISOPHOTES

Two direct photographs of the sun were selected from the Mount Wilson Observatory files of the routine solar program. In this program two direct photographs are obtained

---

* This investigation is based on observational material made available to M. Schwarzschild as a guest investigator at the Mount Wilson and Palomar Observatories.

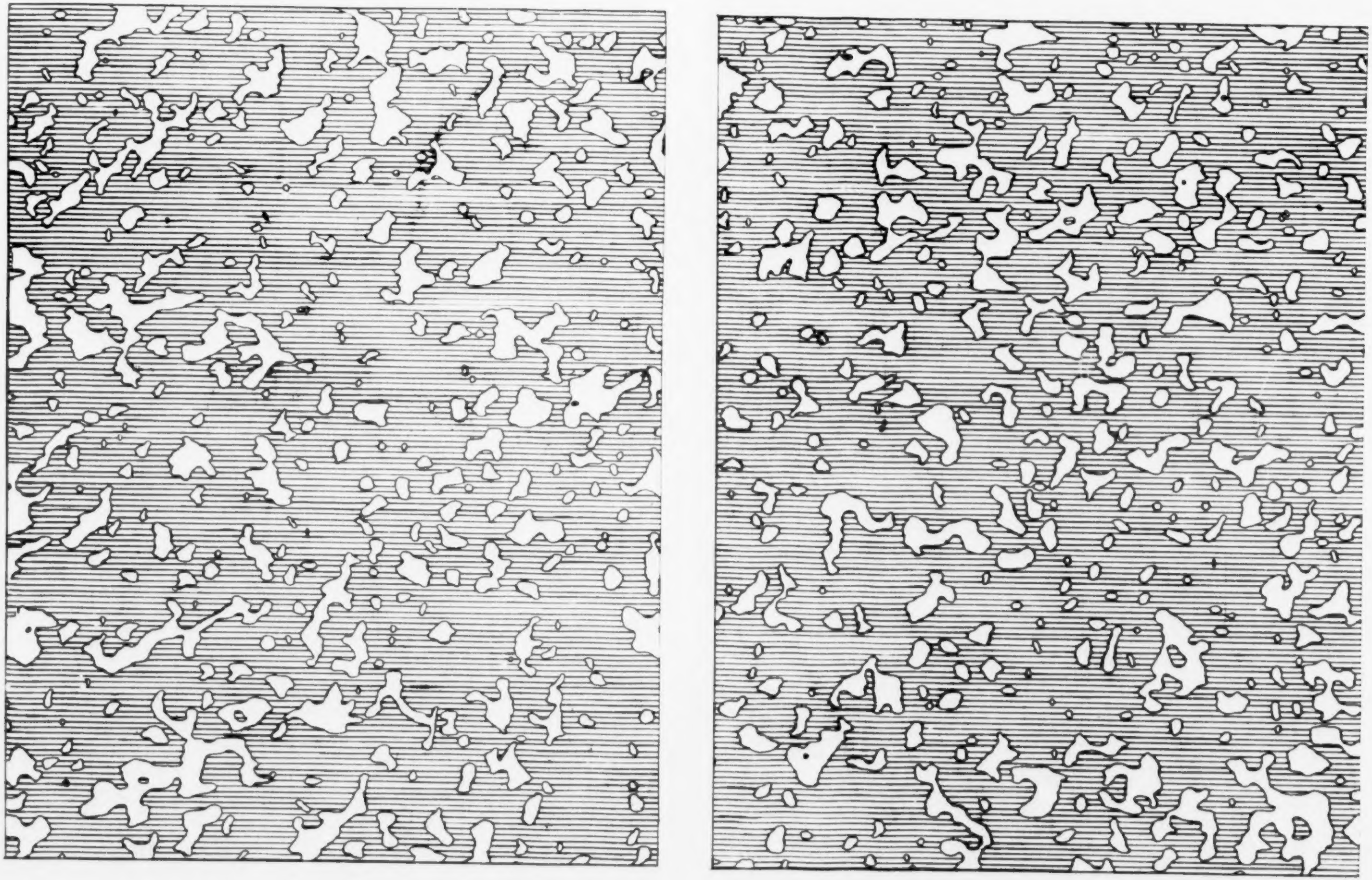

FIG. 1.—Half-field of 20 and 80 per cent isophotes for plate 13011. 20 per cent (*right*) and 80 per cent (*left*) isophotes for half of the field analyzed on plate 13011. On the right, the white elements represent the brightest features in this field; on the left, the white elements represent the darkest features in the same field. Each horizontal line corresponds to one tracing. The distance between lines corresponds to 420 km on the sun.

every clear morning with the 60-foot tower telescope diaphragmed down to 4 inches (diffraction image diameter = $1''.2$). This instrument gives a solar image 17 cm in diameter (1 mm = $11''.2$ = 8200 km on the sun). Exposures are made on Solar Green A plates with an orange filter; the effective wave length of the combination is approximately 5800 A. Plates 13011 (exposed June 9, 1949) and 13107 (exposed September 14, 1949) were judged to be excellent in definition and seeing. On each of these two plates a field 11.5 × 7.6 mm was chosen, free of, and removed from, disturbed regions, so that the quiet phenomena could be studied. In considering only the central regions of the sun, foreshortening effects were minimized.

Each field was scanned by 151 tracings made on the Mount Wilson recording microdensitometer with a linear magnification of 40. A scanning window, $50 \times 50\ \mu$, was so chosen that photographic grain was minimized and adjoining traces were independent and gave sufficient correlation to permit one to extend the isophote with a high degree of certainty. Traces were made at every $50\ \mu$ until the total field was covered.

The 20 and 80 per cent isophotes were constructed from the 151 field tracings. For this purpose, the exact galvanometer deflection which corresponds to each of the two isophotes must be determined on each tracing. This task is complicated by the circumstance that the plates used suffer from uneven shutter speed and uneven development, so that the two critical deflections are not constants but smoothly varying functions of position in the field. The procedure employed was as follows. On a particular tracing a trial 20 per cent deflection was selected and drawn as a straight horizontal on the tracing. The portions of this horizontal line cut out by the granulation-curve were summed, and the sum was compared to 20 per cent of the length of the line. If agreement was not obtained, another deflection was selected until the proper deflection was found. Each fifth tracing was thus handled, and, furthermore, the right half and left half of these tracings were handled separately.

The deflections thus obtained from the individual tracings were plotted against trace number, separately for the right and left halves. In the case of plate 13107, the plotted data could be represented satisfactorily by one straight line. No significant difference was found between halves. In the case of plate 13011, two straight segments were needed to represent the data. In addition, a difference between halves was found and allowed for under the assumption that the critical deflection was a linear function of distance along the trace direction. Altogether, the biggest changes of the critical deflections over the fields amounted to 9 per cent. The same procedure was followed for the 80 per cent isophote, and the same variations of the critical deflections were found. The final isophotes show that the gradients were satisfactorily removed (cf. Fig. 1).

To construct the 20 per cent isophote, the points of intersection of the final 20 per cent deflection line (which was drawn into each tracing) with the granulation-curve were plotted, for each successive trace, on a map. Equivalent points were identified on the map and joined. The final isophote is shown in Figure 1, where half the field of plate 13011 is illustrated. The same procedure follows for the 80 per cent isophote.

The laborious method outlined is not to be desired where many such isophotes are to be constructed. Another possible method is that of repeated high-contrast copying from the original plate. This method was tested and found feasible; however, technical complications appeared which seemed too time-consuming for the present, limited investigation.

IV. ANALYSIS OF ISOPHOTES

The areas of all bright (dark) elements—i.e., singly and doubly connected elements and elements cut by the boundary—on the 20 per cent (80 per cent) isophote were measured, and the total bright (dark) area was computed. It is a satisfactory check on the procedure described that these total areas differ rather little from the aimed-for percentages, as shown by the first line of Table 1. Corrections for the slight deviations between isophotes were found unnecessary for the following discussion.

The singly connected elements of each isophote (bright on the 20 per cent, dark on the 80 per cent) were sorted by area into five groups. Table 1 summarizes the data. This table indicates only a small degree of asymmetry, if any. For plate 13011, the bright elements exceed the dark. The excess is of the order of three times its expected statistical uncertainty. For plate 13107, a bright excess also occurs, but here it is less than its statistical uncertainty. A comparison of the mean areas in each interval and of the mean sizes of the doubly connected and boundary elements indicates that the data cannot be represented by a relative horizontal displacement (in area) of the two distributions. Thus we conclude that a slight asymmetry, in the sense of more singly connected bright elements, may exist but, if at all, not nearly so strong as the rice-grain picture implies.

TABLE 1

FREQUENCY DISTRIBUTIONS OF SIZES OF SINGLY CONNECTED ELEMENTS

ELEMENTS*		PLATE 13011 (PER CENT)					PLATE 13107 (PER CENT)				
		Bright		Dark		Diff.	Bright		Dark		Diff.
A†/A_{field}		20.6		21.7		......	20.0		20.6		......
A‡/A_{field}		2.9		5.3		......	3.1		2.8		......
A(mm²)		N§	$\bar{A}$‖	N	$\bar{A}$	ΔN	N	$\bar{A}$	N	$\bar{A}$	ΔN
Singly conn. elem.	<4	66	2.4	61	2.2	+ 5	74	2.0	66	2.3	+ 8
	4–18	252	9.4	215	10.1	+ 37	189	9.5	175	9.1	+14
	19–86	221	41.2	164	41.8	+ 57	187	41.9	178	41.4	+ 9
	87–400	80	147.9	66	158.2	+ 14	83	147.1	89	163.9	− 6
	>400	2	451.0	7	443.6	− 5	2	700.2	2	418.2	0
All singly conn. elem.		621	......	513	......	+108	535	......	510	......	+25
All doubly conn. elem.		6	202.0	6	461.8	0	9	198.7	5	217.8	+ 4
All boundary elem.		50	56.9	56	80.7	− 6	49	50.3	53	51.2	− 4

* $A_{\text{field}} = 460 \times 300$ sq mm, 1 sq mm = 42,400 sq km on sun.

† Singly and doubly connected elements and boundary elements.

‡ Doubly connected and boundary elements.

§ N = number of elements.

‖ $\bar{A}$ = mean area of elements (mm²).

Since the strong asymmetry suggested by the rice-grain picture was not verified and since the criterion used does not detect all types of asymmetry, an additional test was employed. In this test the distribution-curves of granulation intensities were analyzed in the following manner. For each distribution three intensities were determined—by linear interpolation in the numbers—so that the number of measurements brighter than these critical intensities was 20, 50, and 80 per cent of the total sample number, respectively. Thus these critical intensities are analogous to the isophotes defined by area. The interrelation of these critical intensities and the distribution-curve permit one to exclude any strong asymmetries missed by the study of the topology of these isophotes.

This test was applied to the unpublished photometric data (two distributions each of 2000 intensity measurements) kindly made available by M. Schwarzschild and F. W. Frenkiel. It was found that no strong asymmetries were present in the distributions and that the 20 and 80 per cent intensities were arranged in a symmetric fashion about the

50 per cent intensity, which fell at the mean brightness. The mean 20 and 80 per cent intensities were +0.027 and −0.026 mag., respectively. In addition, a consideration of Figure 3 of R. S. Richardson and M. Schwarzschild (1950), where 340 measurements are represented, indicated a similar symmetric arrangement; however, here the 50 per cent intensity was shifted by +0.004 mag. to the bright. The 20 and 80 per cent intensities were +0.018 and −0.012 mag., respectively. Finally, the photometric analysis of solar granulation by the Potsdam investigators—P. ten Bruggencate, W. Grotrian, and E. von der Pahlen (1938)—does not support the presence of any strong asymmetries.

One may conclude that the strong bright asymmetry suggested by the rice-grain picture of solar granulation is not corroborated by this investigation, although a slight bright asymmetry might exist. On the basis of the present data, of course, no inference on the bright-dark symmetry of element sizes smaller than those resolved on the Mount Wilson plates (i.e., $<1\overset{''}{.}2$) is justified.

REFERENCES

Bruggencate, P. ten, Grotrian, W., and Pahlen, E. von der. 1938, *Zs. f. Ap.*, **16**, 51.
Richardson, R. S., and Schwarzschild, M. 1950, *Ap. J.*, **111**, 2.

ON THERMAL CONVECTION IN A POLYTROPIC ATMOSPHERE

ANDREW SKUMANICH
Princeton University Observatory

Received September 27, 1954

ABSTRACT

Thermally induced convection is investigated in an atmosphere with a strong density variation from top to bottom, such as is found in the hydrogen convection zone of the sun. The atmosphere is assumed to be initially stratified in horizontal planes and to follow the polytrope law, $P \propto \rho^{\Gamma}$. Viscosity and heat conduction are ignored, the perturbations are assumed to be adiabatic, and the perturbation equations are linearized. It is found that in a polytropic atmosphere—in contrast to the classical case of a homogeneous atmosphere—the speed of development of a perturbation increases persistently with decreasing horizontal wave length of the perturbations, even for wave lengths shorter than the thickness of the atmosphere. Thus in the solar hydrogen convection zone small element sizes are to be expected to predominate.

I. INTRODUCTION

Rayleigh's investigation (1916) of thermally induced convection in a homogeneous, incompressible atmosphere is hardly applicable to the solar hydrogen convection zone, where the density changes from top to bottom by a factor of 10,000 or more (Vitense 1953).

In addition, solar convection is probably turbulent in character (as evidenced by nonstationary granulation and high velocities), so that theories of turbulence rather than of laminar flow should be applied. Here difficulties are encountered in finding the scale parameter which determines the characteristic eddy size. Most investigators favor the scale height (*e*-folding distance for the pressure) in preference to the zone thickness. However, where even the scale height shows strong variation through the unstable zone, as is the case in the sun—from 200 km at the surface to 20,000 km at the bottom, with a zone thickness of 70,000 km (Vitense 1953)—this selection loses much of its significance.

In view of the fact that well-developed turbulence is not likely to give larger elements than those occurring in the laminar case, the question of eddy size can be profitably investigated for the simpler laminar case, which should then give an upper limit for the actual solar case. The present investigation, consequently, seeks to evaluate the scale of the most unstable convective modes for a compressible inviscid atmosphere in which the density and scale height vary appreciably.

II. GENERAL EQUATIONS AND APPROXIMATIONS

The basic equations for the present problem are:

Conservation of momentum:

$$\rho \frac{d\boldsymbol{v}}{dt} = -\nabla p + \rho \boldsymbol{g} . \qquad (1)$$

Conservation of mass:

$$\frac{\partial \rho}{\partial t} = -\nabla \cdot (\rho \boldsymbol{v}) . \qquad (2)$$

Conservation of energy:

$$\frac{1}{P}\frac{dP}{dt} = \gamma\,\frac{1}{\rho}\frac{d\rho}{dt}. \tag{3}$$

Equation (3) holds only under the condition that heat exchanges by radiation and conduction are negligible. The problem is further simplified by considering the atmosphere to be initially uniform in horizontal planes, with a constant acceleration of gravity directed downward. The atmosphere is supported by a rigid plane and has a free surface in contact with a vacuum.

III. EQUILIBRIUM STATE

In the equilibrium state the atmosphere is assumed to be at rest and to obey the polytrope law,

$$P_0 \propto \rho_0^{\Gamma}. \tag{4}$$

Let z measure the vertical distance downward from the free surface. The general equations then require that

$$\begin{aligned} P_0 &= \frac{\Gamma-1}{\Gamma}\, g\, A\, z^{(\Gamma/\Gamma-1)}\,, \\ \rho_0 &= A\, z^{(1/\Gamma-1)}\,, \\ T_0 &= \frac{\Gamma-1}{\Gamma}\left(\frac{\mu}{k}\right) g\, z\,, \end{aligned} \tag{5}$$

where g is the acceleration of gravity, μ is the mean molecular weight (in grams), k is the Boltzmann factor, and A is a constant. In addition, the scale height has the value,

$$H = \left(\frac{d \ln P_0}{d z}\right)^{-1} = \frac{\Gamma-1}{\Gamma}\, z\,. \tag{6}$$

If $\Gamma > \gamma$, the equilibrium state is unstable and an arbitrary perturbation will grow with time. If we let

$$\epsilon = \frac{\{(dT_0/dz)_{\text{actual}} - (dT_0/dz)_{\text{adiabat}}\}}{(dT_0/dz)_{\text{adiabat}}} \tag{7}$$

measure the degree of instability, we find that

$$\epsilon = \frac{1-\gamma/\Gamma}{\gamma-1}. \tag{8}$$

IV. PERTURBED STATE

We now assume a small perturbation of the equilibrium state and seek the linearized equations which govern the perturbations. If we let $\tilde{p}$, $\tilde{\rho}$, $\boldsymbol{v} = (+u, +v, -w)$ represent the perturbations, i.e., the difference between a quantity and its value in the equilibrium state, the resulting first-order equations will then have the form

$$
\begin{aligned}
\rho_0 \frac{\partial u}{\partial t} &= -\frac{\partial \tilde{P}}{\partial x}, \\
\rho_0 \frac{\partial v}{\partial t} &= -\frac{\partial \tilde{P}}{\partial y}, \\
-\rho_0 \frac{\partial w}{\partial t} &= +\frac{\partial \tilde{P}}{\partial z} - \tilde{\rho} g, \\
\frac{\partial \tilde{\rho}}{\partial t} &= -\frac{\partial (\rho_0 u)}{\partial x} - \frac{\partial (\rho_0 v)}{\partial y} - \frac{\partial (\rho_0 w)}{\partial z}, \\
\frac{\partial \tilde{P}}{\partial t} &= \gamma \frac{P_0}{\rho_0} \frac{\partial \tilde{\rho}}{\partial t} - \left(\frac{dP_0}{dz} - \gamma \frac{P_0}{\rho_0} \frac{d\rho_0}{dz} \right) \omega,
\end{aligned}
\tag{9}
$$

where the coefficients are functions of z.

V. CHARACTERISTIC EQUATIONS

The general solution of the foregoing system of homogeneous and linear differential equations can be obtained by a superposition of elementary solutions of the form $\bar{q}(z) \exp(ik_x x + ik_y y + nt)$. Here k_x and k_y have their usual meaning, and n is the e-folding frequency.

If one introduces the nondimensional quantities,

$$
r = kz, \qquad \tau = \frac{n}{\sqrt{(kg)}}, \qquad k^2 = k_x^2 + k_y^2; \tag{10}
$$

inserts the elementary solution for each perturbation into system (9); and eliminates $\tilde{P}$, $\tilde{\rho}$, u, and v, one obtains

$$
(Ar^2 + Br) \frac{d^2 w}{dr^2} + (Cr + D) \frac{dw}{dr} + (Er^2 + Fr + G) w = 0, \tag{11}
$$

with

$$
\begin{aligned}
A &= \tau^2 \gamma \left(\frac{\Gamma - 1}{\Gamma} \right), & E &= -\tau^2 \gamma \left(\frac{\Gamma - 1}{\Gamma} \right), \\
B &= \tau^4, & F &= \left(1 - \frac{\gamma}{\Gamma} \right) - 2\tau^4, \\
C &= \tau^2 \frac{\gamma}{\Gamma}, & G &= -\tau^2 \frac{\gamma - 1}{\gamma} \frac{\Gamma}{\Gamma - 1} - \tau^6 \frac{1}{\gamma} \frac{\Gamma}{\Gamma - 1}. \\
D &= \tau^4 \frac{\Gamma}{\Gamma - 1}, & &
\end{aligned}
$$

One may note that the only term in equation (11) which does not contains a τ-factor is the first term of F, which, according to equation (8), is proportional to the measure of instability.

The boundary conditions to be applied are

$$\begin{aligned} \rho_0 w &= 0 \text{ at the free surface, } r = 0\,; \\ \rho_0 w &= 0 \text{ at the rigid base, } r = r^0 = k\,z_0\,. \end{aligned} \tag{12}$$

The first of these is obtained by requiring the kinetic energy to be finite at the surface.

Equation (11) and the boundary conditions (12) serve to specify the problem. If w and dw/dr are known throughout the atmosphere, then all other quantities can be calculated. The normalized frequence, τ, appears as an eigen-value characteristic of each mode of instability.

VI. SOLUTION OF CHARACTERISTIC EQUATION

Equation (11) was solved numerically for the case $\Gamma = \frac{20}{11}$, $\gamma = \frac{5}{3}$; hence for $\epsilon = \frac{1}{8}$. Since the coefficients of the differential equation are not regular at the surface, a power-series expansion (neglecting cubic and higher terms) was used to obtain starting values. The expansion and hence the entire solution are uniquely determined—except for an amplitude factor—by the value of τ. The explicit expression used was

$$\begin{aligned} w = 1 + \left[\frac{1}{\gamma}\,\tau^2 + \left(1 - \frac{1}{\gamma}\right)\tau^{-2}\right] r + \Bigg[& \frac{\Gamma}{2\gamma^2\,(2\Gamma - 1)}\,\tau^4 \\ & + \frac{2\Gamma^2\,(\gamma - 1/\gamma^2 + 1) - 3\Gamma + 1}{2\Gamma\,(2\Gamma - 1)} \\ & - \frac{(\gamma - 1/\gamma^2)\,(\Gamma - \gamma)\,[\gamma - (\gamma - 1)\,\Gamma] + (\Gamma - \gamma)\,(\Gamma - 1)}{2\Gamma\,(2\Gamma - 1)}\,\tau^{-4}\Bigg] r^2 + \dots . \end{aligned} \tag{13}$$

Thus the specification of τ was sufficient to start an integration.

Wherever an integration leads to a node, i.e., $w = 0$, the integration may be terminated, and the corresponding r-value can be taken as giving the depth of the zone r_0. Thus, instead of specifying r_0 and hunting by trial and error for the corresponding τ, one may specify τ and obtain, by one integration, the value of r_0.

In all, six values of τ were integrated. The resulting integrations and eigen-values are listed in Tables 1–4. In five instances the integrations have nodes before diverging. The case $\tau = 0.1846$ diverges without passing through a node and is given as an upper bound to the fundamental mode for large r_0-values. The fundamental mode for the other five cases was obtained by terminating the integration at the first node. The dependence of τ on r_0 $(= kz_0)$ for this mode is illustrated in Figure 1. The asymptotic eigen-value for infinite depth is estimated by interpolation between $\tau = 0.184$ and $\tau = 0.1846$ to be $\tau_0(\infty) = 0.1844$; this numerical value depends, of course, on the values used for γ and Γ.

Terminating the integrations at the second node, where one exists, gave the first higher mode, i.e., the solution with one internal node, and similarly for the still higher modes. The results for the higher modes are again illustrated in Figure 1. The asymptotic values for infinite depth are estimated to be approximately $\tau^1(\infty) = 0.15$ and $\tau^2(\infty) = 0.12$ for the first and second higher modes, respectively. Figure 1 shows the fundamental mode to be the most unstable.

If τ has the particular asymptotic value referring to any mode, the corresponding integration, after undergoing the requisite number of oscillations, decays for large r, as $\exp(-r)$. For all other values of τ the integrations diverge for large r as $\exp(+r)$. This behavior arises from the terms A and E in equation (11).

Figure 2 illustrates the eigen-solutions, i.e., the vertical velocity profiles, $w(r)$, of the fundamental mode reduced to the same physical depth, z_0. Curves A, B, and C are the solution for $\tau = 0.01$, 0.16, and 0.184, or $r_0 = 0.0065$, 2.12, and 5.69, respectively.

TABLE 1

INTEGRATION FOR $\tau = 0.01$

r	w	dw/dr	r	w	dw/dr
0.0000	+1.000	+4000	0.0034	+3.762	− 990
.0002	+1.742	+3440	.0036	+3.556	−1070
.0004	+2.377	+2920	.0038	+3.335	−1140
.0006	+2.912	+2440	.0040	+3.102	−1190
.0008	+3.356	+2010	.0042	+2.859	−1230
.0010	+3.716	+1610	.0044	+2.610	−1260
.0012	+4.000	+1240	.0046	+2.355	−1280
.0014	+4.215	+ 910	.0048	+2.098	−1290
.0016	+4.366	+ 610	.0050	+1.839	−1290
.0018	+4.460	+ 340	.0052	+1.580	−1290
.0020	+4.503	+ 90	.0054	+1.324	−1270
.0022	+4.499	− 120	.0056	+1.071	−1250
.0024	+4.455	− 320	.0058	+0.823	−1230
.0026	+4.373	− 490	.0060	+0.580	−1200
.0028	+4.259	− 640	.0062	+0.344	−1160
.0030	+4.117	− 780	.0064	+0.114	−1130
0.0032	+3.950	− 890	0.0066	−0.107	−1080

TABLE 2

INTEGRATION FOR $\tau = 0.1$

r	w	dw/dr	r	w	dw/dr
0.00	+1.000	+40.0	0.50	+2.005	−12.6
.02	+1.743	+34.4	0.52	+1.754	−12.6
.04	+2.378	+29.2	0.54	+1.503	−12.5
.06	+2.914	+24.5	0.56	+1.255	−12.3
.08	+3.360	+20.2	0.58	+1.010	−12.1
.10	+3.722	+16.2	0.60	+0.77	−11.8
.12	+4.010	+12.6	0.70	−0.33	−10.0
.14	+4.228	+ 9.3	0.80	−1.22	− 7.6
.16	+4.384	+ 6.4	0.90	−1.86	− 5.2
.18	+4.484	+ 3.7	1.00	−2.25	− 2.6
.20	+4.533	+ 1.3	1.20	−2.37	+ 1.3
.22	+4.537	− 0.9	1.40	−1.84	+ 3.7
.24	+4.500	− 2.8	1.60	−0.98	+ 4.7
.26	+4.427	− 4.5	1.80	−0.05	+ 4.5
.28	+4.322	− 6.0	2.00	+0.78	+ 3.7
.30	+4.189	− 7.3	2.20	+1.40	+ 2.4
.32	+4.032	− 8.4	2.40	+1.75	+ 1.1
.34	+3.854	− 9.4	2.60	+1.85	− 0.1
.36	+3.659	−10.2	2.80	+1.72	− 1.1
.38	+3.448	−10.8	3.00	+1.43	− 1.8
.40	+3.225	−11.4	3.20	+1.01	− 2.2
.42	+2.993	−11.8	3.40	+0.54	− 2.4
.44	+2.752	−12.2	3.60	+0.05	− 2.4
.46	+2.506	−12.4	3.80	−0.41	− 2.2
0.48	+2.257	−12.5			

TABLE 3

INTEGRATIONS FOR τ = 0.14, 0.16, 0.184, 0.1846

r	$\tau=0.14$		$\tau=0.16$		$\tau=0.184$		$\tau=0.1846$	
	w	dw/dr	w	dw/dr	w	dw/dr	w	dw/dr
0.00	+1.000	+20.42	+1.000	+15.64	+1.000	+11.84	+1.000	+11.76
0.10	+2.692	+13.66	+2.357	+11.62	+2.066	+ 9.54	+2.060	+ 9.50
0.20	+3.780	+ 8.32	+3.348	+ 8.30	+2.918	+ 7.56	+2.909	+ 7.54
0.30	+4.396	+ 4.16	+4.036	+ 5.56	+3.589	+ 5.98	+3.578	+ 5.88
0.40	+4.645	+ 0.96	+4.476	+ 3.32	+4.105	+ 4.46	+4.095	+ 4.48
0.50	+4.616	− 1.44	+4.714	+ 1.52	+4.489	+ 3.26	+4.481	+ 3.28
0.60	+4.380	− 3.18	+4.790	+ 0.06	+4.762	+ 2.24	+4.757	+ 2.26
0.70	+3.999	− 4.38	+4.736	− 1.08	+4.941	+ 1.38	+4.940	+ 1.42
0.80	+3.517	− 5.18	+4.580	− 1.98	+5.042	+ 0.66	+5.046	+ 0.72
0.90	+2.974	− 5.64	+4.347	− 2.66	+5.079	+ 0.08	+5.087	+ 0.13
1.00	+2.400	− 5.82	+4.056	− 3.16	+5.062	− 0.40	+5.075	− 0.35
1.10	+1.818	− 5.80	+3.721	− 3.52	+5.001	− 0.80	+5.020	− 0.74
1.20	+1.245	− 5.64	+3.358	− 3.74	+4.905	− 1.11	+4.930	− 1.05
1.30	+0.695	− 5.34	+2.977	− 3.88	+4.781	− 1.35	+4.813	− 1.30
1.40	+0.178	− 4.98	+2.586	− 3.92	+4.636	− 1.54	+4.673	− 1.48
1.50	−0.299	− 4.56	+2.194	− 3.91	+4.474	− 1.68	+4.517	− 1.63
1.60	−0.732	− 4.10	+1.806	− 3.84	+4.300	− 1.78	+4.349	− 1.73
1.70	−1.119	− 3.64	+1.427	− 3.74	+4.118	− 1.85	+4.173	− 1.80
1.80	−1.459	− 3.16	+1.059	− 3.61	+3.931	− 1.89	+3.991	− 1.84
1.90	−1.752	− 2.70	+0.706	− 3.46	+3.741	− 1.90	+3.806	− 1.85
2.00	−1.999	− 2.24	+0.368	− 3.29	+3.551	− 1.90	+3.622	− 1.84
2.20	−2.364	− 1.42	−0.254	− 2.93	+3.176	− 1.85	+3.257	− 1.79
2.40	−2.576	− 0.72	....	....	+2.814	− 1.75	+2.908	− 1.70
2.60	−2.658	− 0.12	....	....	+2.475	− 1.63	+2.580	− 1.58
2.80	−2.634	+ 0.34	....	....	+2.163	− 1.50	+2.279	− 1.44
3.00	−2.527	+ 0.71	....	....	+1.878	− 1.36	+2.004	− 1.30
3.40	−2.142	+ 1.16	....	....	+1.388	− 1.09	+1.536	− 1.04
3.80	−1.632	+ 1.35	....	....	+0.998	− 0.86	+1.169	− 0.80
4.20	−1.086	+ 1.36	....	....	+0.692	− 0.68	+0.890	− 0.60
4.60	−0.553	+ 1.29	....	....	+0.451	− 0.54	+0.683	− 0.44
5.00	−0.058	+ 1.18	....	....	+0.258	− 0.43	+0.535	− 0.31
5.20	+0.173	+ 1.13	....	....	+0.176	− 0.39	+0.479	− 0.25
5.60	....	....	....	....	+0.030	− 0.34	+0.398	− 0.16
5.80	....	....	....	....	−0.038	− 0.33	+0.371	− 0.11

TABLE 4

CHARACTERISTIC VALUES

τ	r_0			τ	r_0		
	Fund. Mode	First Mode	Second Mode		Fund. Mode	First Mode	Second Mode
0.01	0.0065	?	?	0.16	2.12	....	....
.10	0.67	1.81	3.62	0.184	5.69	....	....
0.14	1.44	5.05	....				

Curve *D* was obtained by linear interpolation between the solutions for $\tau = 0.184$ and $\tau = 0.1846$ appropriate for $r_0 = 10$.

VII. COMPARISON WITH HOMOGENEOUS ATMOSPHERE

Rayleigh (1916) considers an incompressible atmosphere which is characterized by a thermal coefficient of expansion, α, and a temperature gradient, β'. He assumes that the density variations "modify the action of gravity" only and that hence the atmosphere

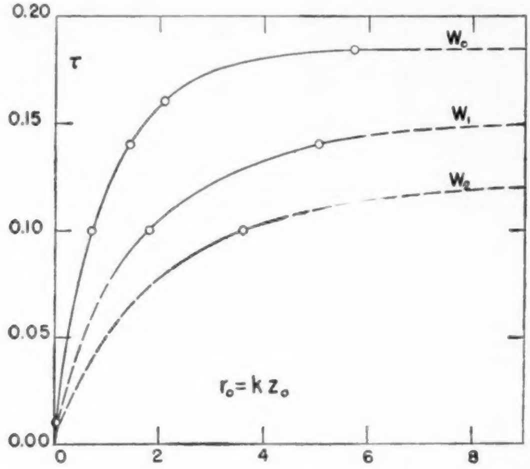

FIG. 1.—Dependence of the rate of instability, τ, on the zone depth, r_0, for fundamental mode, w_0; first mode, w_1; and second mode, w_2.

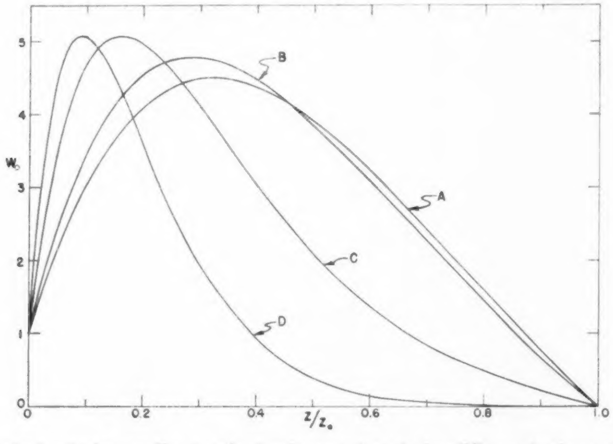

FIG. 2.—Vertical velocity profiles for the fundamental mode for different horizontal wave lengths: $\lambda_A = 970\ z_0$; $\lambda_B = 3.0\ z_0$; $\lambda_C = 1.12\ z_0$; $\lambda_D = 0.63\ z_0$.

can be considered homogeneous. He finds the eigen-value for the fundamental mode (which is the most unstable) to be

$$\frac{n^2 z_0}{g} = \alpha\beta' z_0 \left(\frac{k^2 z_0^2}{k^2 z_0^2 + \pi^2}\right), \tag{14}$$

where, as before, n is the e-folding frequency, z_0 is the depth of the unstable zone, and k is the horizontal wave number. The coefficient $\alpha\beta' z_0$ can be transfered into the present terms by a comparison of the system of perturbation equations for both problems. One finds that

$$\alpha\beta' z_0 = g\left(\frac{1}{\gamma} - \frac{1}{\Gamma}\right)\frac{z_0}{P_0/\rho_0} = \epsilon\,\frac{\gamma - 1}{\gamma}\,\frac{\Gamma}{\Gamma - 1}\,\frac{z_0}{z} = \frac{2}{9}, \tag{15}$$

where, in the last form, we have used our particular values for γ, Γ, and ϵ and have set $z = \frac{1}{2} z_0$. This latter choice corresponds to comparing the average temperature of the polytropic atmosphere with the uniform temperature of the homogeneous atmosphere.

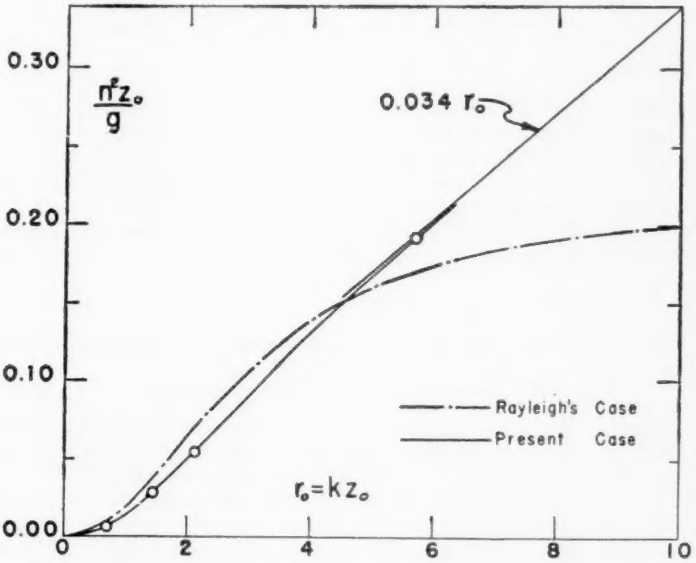

FIG. 3.—Comparison of rate of instability of the fundamental mode for present polytropic atmosphere with Rayleigh's homogeneous atmosphere.

Equation (14) is plotted in Figure 3, where a comparison of the rate of instability, $n^2 z_0/g$ (dimensionless), for the fundamental mode of the homogeneous and polytropic atmospheres is presented. The curve for the polytropic atmosphere is a simple transformation of the w_0-curve in Figure 1, with $\tau^2 r_0 = n^2 z_0/g$.

It is seen that, for horizontal wave lengths ($\lambda = 2\pi/k$) greater than the depth of the unstable zone, $kz_0 < 2\pi$, the two problems give comparable results. The asymptotic behavior for small kz_0 is

$$n^2 \simeq 0.022\, g\, z_0 k^2 \tag{16}$$

for the homogeneous atmosphere and

$$n^2 \simeq 0.015\, g\, z_0 k^2 \tag{17}$$

for the polytropic atmosphere, as discerned from the power-series expansion (eq. [13]), the constant being obtained by fitting at $\tau = 0.01$.

However, for horizontal wave lengths smaller than the zone thickness, $kz_0 > 2\pi$, the two problems differ. The homogeneous atmosphere gives a rate of instability which approaches the asymptotic value,

$$n^2 = \frac{0.222\, g}{z_0}, \tag{18}$$

whereas the polytropic atmosphere gives ever increasing instability with decreasing wave length, in accordance with

$$n^2 = 0.034\, g k\ . \tag{19}$$

The velocity profiles also indicate the changed character of the instability. In the homogeneous atmosphere the velocity profiles are given by

$$w(z) = A \sin\left(\frac{\pi z}{z_0}\right) \tag{20}$$

and are independent of the horizontal wave length. In the polytropic atmosphere a similar independence exists, but only for horizontal wave lengths larger than the thickness of the unstable zone. This independence is illustrated by curves A and B in Figure 2, where the wave length varies from $\lambda = 970\, z_0$ for A to $\lambda = 3.0\, z_0$ for B. For horizontal wave lengths less than the zone thickness, the velocity profiles show a marked dependence on the wave length in the sense that the depth of penetration, z_p, defined so that $w(z_p) = 0.10$ ($\simeq 2$ per cent $w_{\max}$), varies in accordance with

$$z_p = \lambda\ . \tag{21}$$

Curves C and D, where $\lambda = 1.1\, z_0$ and $0.63\, z_0$, respectively, illustrate this change in penetration.

VIII. NUMERICAL METHOD FOR VISCID CASE

To determine to what extent physical complications, such as viscosity (or heat conduction), would increase the numerical work involved, the linear perturbation equations governing the viscid case for the atmosphere considered here were derived. A characteristic system of two second-order simultaneous homogeneous differential equations was obtained, in which, in addition to the eigen-parameter, τ, another parameter, V—a dimensionless measure of the viscosity—appears. Only two of the four linearly independent solutions of this system are permitted by the surface boundary conditions (which follow from the vanishing of the stress components across the free surface), and, as in the inviscid case, their series developments at the surface are uniquely determined, except for amplitude factors, by a specification of both parameters τ and V (γ and Γ initially specified). Again, the trial-and-error method of hunting for the eigen-value is unnecessary, and the two linearly independent solutions can be integrated numerically inward until the lower boundary conditions are satisfied. Hence the introduction of viscosity only doubles the numerical work necessary to find a specific solution.

IX. SUMMARY

We conclude that in a polytropic atmosphere with a strong density variation from top to bottom, in the absence of viscosity and heat conduction, the smaller the convective cells, the more unstable they are. The square of the speed of development grows inversely as the eddy size. This is unlike thermal convection in a nearly homogeneous atmosphere, where the speed of development approaches a constant value for smaller and smaller sizes. Regarding the solar hydrogen convection zone, these results imply that small element sizes are to be expected to predominate. The most predominant size is presumably fixed by the effect of radiative conduction[1] rather than viscosity.

The author wishes to express his gratitude to Dr. M. Schwarzschild for his generous help and advice. Thanks are also due to Dr. A. Schlüter for the many valuable discussions, and to Mr. R. Härm for his help with the integrations.

REFERENCES

Rayleigh, Lord. 1916, *Phil. Mag.*, **32**, No. 6, 529.
Vitense, E. 1953, *Zs. f. Ap.*, **32**, 135.

---

[1] I am indebted to Dr. L. Spitzer, Jr., for calling attention to this fact.

NONCOHERENT SCATTERING DUE TO COLLISIONS. I. ZANSTRA'S RATIO OF COHERENT TO UNCORRELATED NONCOHERENT SCATTERING

Frank N. Edmonds, Jr.
Department of Mathematics and Astronomy, University of Texas, Austin, Texas

Received October 6, 1954; revised November 27, 1954

ABSTRACT

A quantum-theory formulation of the problem of noncoherent scattering due to collisions is presented in a general form and then made equivalent to Zanstra's classical oscillator formulation by a set of assumptions. These assumptions are examined critically as an indirect method of determining whether Zanstra's results are correct for statistical broadening. It would seem that Zanstra's ratio of coherent to uncorrelated noncoherent scattering is too large by at least a factor of 20, and the coherent component is not strictly coherent. The validity of evaluating Zanstra's results for impact broadening by this method is briefly discussed.

I. INTRODUCTION

Several recent investigations have advanced the theory of line formation, in which account is taken of noncoherent scattering arising from collisions, to the point of obtaining useful solutions of the equation of transfer. However, the validity of these solutions is based on highly simplifying assumptions regarding the noncoherent nature of the scattering process as represented by the source function of the equation of transfer. In certain of the investigations (Sobolev 1949; Savedoff 1952; Busbridge 1953) uncorrelated noncoherent scattering has been assumed, while for the others (Münch 1949; Stibbs 1953) a certain fraction of the scattering has been assumed to be of this type, the remainder being coherent. The term "uncorrelated noncoherent scattering" has been used to designate scattering involving not only a change in frequency but also a complete redistribution in frequency, that is, scattering in which the frequency of re-emission is uncorrelated with the frequency absorbed. This type of scattering is sometimes referred to as "completely noncoherent scattering," but this designation has not been used, because it seems somewhat misleading. The definition of noncoherent or coherent scattering as scattering in which the frequency is or is not changed would indicate that all noncoherent scattering is complete. Since strictly coherent scattering does not exist in astrophysics, these terms actually designate the accuracy with which a scattering problem is analyzed—that is, whether frequency changes will be accounted for or neglected. If frequency changes are considered, then the dependence of the scattered frequency on the absorbed frequency becomes an important property of the scattering process. This dependence can range from complete dependence, as is the case of Doppler shifts where the incident frequency and the geometry of the scattering determine the scattered frequency, to complete independence, which is possible for shifts due to collisions. Hence the designations "correlated," "partially correlated," and "uncorrelated" noncoherent scattering seem to classify more appropriately the essential features of the scattering process.

As pointed out by Spitzer (1944), the fact that noncoherent scattering due to collisions can be described approximately but quite simply in terms of coherent and uncorrelated noncoherent scattering is what allows the effects of such scattering to be analyzed in problems of radiative-transfer theory. This raises the question of the adequacy of this approximate description. A simplified quantum-theory formulation of the problem of noncoherent scattering by collisions provides criteria for answering this question. When an atomic structure undergoes a transition while being acted upon by an external perturbing force, the frequency of radiation involved in the transition will be changed, since, in effect, the perturbation shifts by different amounts the energy levels between which the transition takes place. If the perturbing force acting on a given structure is different at the times of absorption and subsequent re-emission, the scattering will be noncoherent. This is the case for noncoherent scattering by collisions when the force is due to the complex of surrounding structures and hence fluctuates in a random fashion, corresponding to changes in the complex. If the time interval between absorption and subsequent re-emission is much smaller than the time required for the perturbing force to change appreciably, the scattering will closely approximate coherent scattering. If, on the other hand, the time interval is much larger, the scattering will closely approximate uncorrelated noncoherent scattering, because the random nature of changes in the perturbing force means that the forces, and hence the frequencies, at the times of absorption and re-emission will become uncorrelated as the interval between these times increases. The question of the adequacy of the simplified description then takes the following form: Can noncoherent scattering, in which the entire range of time intervals is involved, be adequately described in terms of the two limits of this range?

An affirmative answer to this question was proposed by Zanstra (1941), whose remarkable analysis of the problem of noncoherent scattering by collisions for a spectral line has been used as theoretical justification for the simplifying assumptions by which solutions to the equation of transfer were obtained. Analyzing the emission of a classical oscillator subject to phase displacements, as postulated in the Lorentz-Weisskopf theory of collision broadening, Zanstra concluded that scattering by such an oscillator would consist of a coherent component and an uncorrelated noncoherent component, the ratio of their intensities being that of the half-width for natural broadening to that for collision broadening. In his analysis Zanstra made mathematical simplifications which left the quantitative correctness of his conclusions unproved except for absorption in the wings of the line. The validity of Zanstra's results can be demonstrated only by showing them to be consistent with the predictions of a quantum-theory formulation of the problem of noncoherent scattering by collisions; in view of the important current use made of his results, such justification seems to be in order.

A simple quantum-theory formulation appears to be prevented, however, by the incomplete status of the various theories of collision broadening. The unified theory of Lindholm (1946), which is the best available to date, and the Lorentz-Weisskopf theories for impact broadening (Weisskopf 1932; Lindholm 1942), which are most commonly used in astrophysics, analyze the wave trains of classical oscillators. These analyses have been shown to be roughly equivalent to the quantum-mechanical matrix element (Weisskopf 1932; Lindholm 1941); but the physical nature of impact broadening, though incompletely understood, seems to be a total effect of collision which cannot be expressed in terms of the notion of a time interval between absorption and subsequent re-emission. So the simplified quantum-theory formulation described earlier appears to be inadequate. On the other hand, theories of statistical broadening (Margenau and Watson 1938) are formulated in terms of such a simplified quantum theory, because the static nature of the theories allows the notion of a time interval.

In this paper a simplified quantum-theory formulation of the problem of noncoherent scattering due to collisions will be presented in a general form which is not restricted to any particular theory of collision broadening but which can be stated as valid only for statistical broadening. A set of assumptions is then applied which makes this formulation equivalent to Zanstra's classical oscillator formulation and which produces results identical with Zanstra's. These assumptions are examined critically as an indirect method of determining whether Zanstra's results, formulated for impact broadening, also apply to statistical broadening. It would seem that Zanstra's ratio of coherent to uncorrelated noncoherent scattering is too large in most cases by at least a factor of 20 and, further, that the coherent component is not strictly coherent. Improvements suggested by this evaluation will be the subject of future investigations.

II. QUANTUM-THEORY FORMULATION OF THE PROBLEM

Normally, the effects of noncoherent scattering are introduced into radiative-transfer problems by the probability function $p(\nu, \nu')$, which expresses the probability that absorption of the frequency ν' will be followed by re-emission of the frequency ν. For spectral lines three causes of noncoherent scattering are pertinent—Doppler shifts, which will be omitted from this discussion; collisions, which produce shifts of the energy levels involved; and natural broadening or radiation damping, where the width of the energy levels allows the absorbed and re-emitted frequencies to differ. The latter two causes may be separated by isolating effects of energy-level width from those of energy-level shifts. Let ν_c' represent the frequency of the line center for absorption, that is, the frequency corresponding to a transition between the centers of the energy levels. Let ν_c represent the same frequency for re-emission. Then the probability function $q(\nu_c, \nu_c')$, the probability that absorption involving ν_c' will be followed by re-emission involving ν_c, accounts only for noncoherent scattering due to collisions. Similarly, noncoherent scattering due only to natural broadening can be accounted for by the probability function $Q(\nu - \nu_c, \nu' - \nu_c')$, which gives the probability that if absorption occurs at the frequency interval $\nu' - \nu_c$ from the line center, re-emission will occur at the frequency interval $\nu - \nu_c$. Furthermore,

$$p(\nu, \nu') = \int_0^\infty d\nu_c \int_0^\infty d\nu_c' Q(\nu - \nu_c, \nu' - \nu_c')\, q(\nu_c, \nu_c') , \tag{1}$$

where all probability functions are normalized to unity.

The function $Q(\nu - \nu_c, \nu' - \nu_c')$ is discussed by Woolley and Stibbs (1953) and lies outside the scope of this discussion, which is concerned primarily with the function $q(\nu_c, \nu_c')$. The simplified quantum-theory picture of essentially instantaneous absorption and re-emission at times $t = 0$ and t, respectively, allows this probability to be expressed as

$$q(\nu_c, \nu_c') = \int_0^\infty P(t)\, W(\nu_c'; t, \nu_c)\, dt , \tag{2}$$

where $P(t)dt$ is the probability of re-emission occurring in the time interval t to $t + dt$, and $W(\nu_c'; t, \nu_c)$ is the probability that if ν_c' is the frequency absorbed, re-emission at time t will be at frequency ν_c. Assuming that the perturbations of collisions do not influence the probability of re-emission, then Dirac's theory of radiation gives

$$P(t) = \tau_s^{-1} e^{-t/\tau_s} = \tfrac{1}{2}\gamma_n e^{-\gamma_n t/2} , \tag{3}$$

where τ_s is the mean life and γ_n is the half-width for natural broadening or radiation damping of the upper level, for the transition involving re-emission only.

Equations (1)–(3) constitute a general quantum-theory formulation of the problem of noncoherent scattering due to collisions. It merely expresses one unknown probability function in terms of another, but it has accomplished some clarification of the problem. If effects of statistical broadening only are considered, then the problem has been reduced to one concerned only with the statistical properties of the perturbing force, since that is what $W(\nu_c'; t, \nu_c)$ represents. Since the fluctuations of the force are random and since the effects of collision during absorption and re-emission depend on the value of the perturbing force only at the instants that these transitions occur, $W(\nu_c'; t, \nu_c)$ represents not only a stochastic process but also a Markoff process. Hence the powerful methods for analyzing such processes (Chandrasekhar 1943) can be used to determine $W(\nu_c'; t, \nu_c)$. The fact that the scattering is coherent for $t \rightarrow 0$ places the requirement that

$$W(\nu_c'; t \rightarrow 0, \nu_c) \rightarrow \delta(\nu_c - \nu_c') , \tag{4}$$

where $\delta(\nu_c - \nu_c')$ is the Dirac delta function. The other limiting case of uncorrelated noncoherent scattering for large t requires that

$$W(\nu_c'; t \to \infty, \nu_c) \to g(\nu_c) , \tag{5}$$

where $g(\nu_c)$ represents the probability of re-emission at a frequency ν_c which is completely uncorrelated with the frequency absorbed. This means that $g(\nu_c)$ is the profile function, normalized to unity, for the line-absorption coefficient as given by the particular theory of collision broadening under consideration. Even if $W(\nu_c'; t, \nu_c)$ is not interpreted as describing the statistics of the perturbing force, this quantum-theory formulation cannot be extended to the effects of impact broadening, unless the notion of a time interval between absorption and subsequent re-emission can be shown to be a valid one.

III. DISCUSSION OF ZANSTRA'S RESULTS

The problem discussed by Zanstra (1941) can be analyzed in terms of the simplified quantum-theory formulation, provided that two restrictions are placed on equations (1)–(5). First, Zanstra dealt only with absorptions from the ground state. This means that the scattering must be coherent with respect to natural broadening or radiation damping, because, for the infinitely narrow ground state,

$$\nu_c - \nu = \nu_c' - \nu' , \tag{6}$$

and hence

$$\nu - \nu' = \nu_c - \nu_c' . \tag{7}$$

Also, as indicated by Woolley and Stibbs (1953),

$$Q(\nu - \nu_c, \nu' - \nu_c') = \frac{\gamma_n \delta(\nu' - \nu_c' - \nu + \nu_c)}{4\pi^2 (\nu - \nu_c)^2 + (\frac{1}{2}\gamma_n)^2} . \tag{8}$$

Second, Zanstra considered only the effects of impact broadening as predicted by the Lorentz-Weisskopf theory. This means that

$$g(\nu_c) = \frac{\gamma_c}{4\pi^2 (\nu_c - \nu_0)^2 + (\frac{1}{2}\gamma_c)^2} , \tag{9}$$

where γ_c is the half-width for collision broadening and ν_0 is the central frequency of the line when no perturbations occur.

The form of $W(\nu_c'; t, \nu_c)$ can be stipulated by making three assumptions which have their counterpart in Zanstra's classical oscillator formulation of the problem. First, it will be assumed that the function can be stated in terms of its two limiting forms, coherent and uncorrelated noncoherent scattering, as given by equations (4), (5), and (9). Second, it will be assumed that the variation with time of $W(\nu_c'; t, \nu_c)$ can be represented by an exponential decay of coherent scattering, with its replacement by uncorrelated noncoherent scattering. And, third, it will be assumed that the mean time for this decay is the mean time between collisions used in the Lorentz-Weisskopf theory,

$$\tau_c = \frac{2}{\gamma_c} . \tag{10}$$

These three assumptions give

$$W(\nu_c'; t, \nu_c) = \delta(\nu_c - \nu_c')\, e^{-\gamma_c t/2} + \frac{\gamma_c (1 - e^{-\gamma_c t/2})}{4\pi^2 (\nu_c - \nu_0)^2 + (\frac{1}{2}\gamma_c)^2} . \tag{11}$$

Substitution of equations (3) and (11) in equation (2) gives

$$q\,(\nu_c, \nu_c') = \frac{\gamma_n}{\gamma_n+\gamma_c}\,\delta\,(\nu_c-\nu_c') + \frac{\gamma_c}{\gamma_n+\gamma_c}\left[\frac{\gamma_c}{4\pi^2\,(\nu_c-\nu_0)^2+(\tfrac{1}{2}\gamma_c)^2}\right], \tag{12}$$

which, on substitution along with equation (8) in equation (1), gives

$$p\,(\nu, \nu') = \frac{\gamma_n}{\gamma_n+\gamma_c}\,\delta\,(\nu-\nu') + \frac{\gamma_c}{\gamma_n+\gamma_c}\left[\frac{\gamma_n+\gamma_c}{4\pi^2\,(\nu-\nu_0)^2+\tfrac{1}{4}\,(\gamma_n+\gamma_c)^2}\right]. \tag{13}$$

The delta function appearing in equation (13) follows from equation (7). This expression for $p(\nu, \nu')$ is identical with that proposed by Zanstra in equations (14) and (17) and the discussion following these equations in his paper (Zanstra 1941).

Zanstra's results are for impact broadening, for which the validity of this analysis must still be demonstrated. Whether his results also apply to statistical broadening, for which this analysis is valid, can be determined by evaluating the results obtained when $g(\nu_c)$ is the expression for the appropriate theory of statistical broadening instead of equation (9), and γ_c in equation (10) represents the half-width for statistical broadening. The assumptions made concerning the form of $W(\nu_c'; t, \nu_c)$ remain unchanged, and the $p(\nu, \nu')$ obtained will differ from equation (13) only in that the expression in brackets would be replaced by a similar one for statistical broadening.

Some evaluation of the application of Zanstra's results to statistical broadening is possible by critically examining the three assumptions made with regard to $W(\nu_c'; t, \nu_c)$. The first assumption, that $W(\nu_c'; t, \nu_c)$ can be expressed in terms of its limiting forms, is quite restrictive and difficult to evaluate without a less arbitrary and more exact determination of the probability function. For most problems in which noncoherent scattering by collisions is considered, γ_n is not appreciably larger than γ_c. This means that the portion of re-emissions occurring at times when uncorrelated noncoherent scattering is well approximated cannot be neglected. Therefore, the use of the limiting form for large times seems reasonable. On the other hand, the use of the limiting form for coherent scattering seems open to question. As indicated by equation (3), re-emission for small values of t cannot be neglected, but that it will be strictly coherent seems to be a very arbitrary restriction. The perturbing force is fluctuating rapidly, and even in very short time intervals some noncoherence should appear. So scattering with a frequency distribution around the frequency absorbed seems more reasonable than coherent scattering.

The second assumption of exponential decay and replacement has provided accurate approximations in other analyses of stochastic processes, where the function decaying with time expressed correlation and that replacing it expressed randomness. The most questionable aspect of this assumption is the use of the Dirac delta function to express correlation, which really constitutes a further objection to the first assumption.

The third assumption, as given by equation (10), now lacks the justification normally provided by the nearest-neighbor approximation used in the theories of impact broadening. For statistical broadening, the decay of coherent scattering is the decay of correlation between the perturbing forces which act at the time of absorption and re-emission. Because the fluctuations of the perturbing force represent a stochastic process of the Markoff type, this decay of correlation can be considered exponential, with a mean time called the "mean life of the initial force." Chandrasekhar and von Neumann (1942) have computed an approximate mean life for a gravitational field arising from a random distribution of stars. Their result, as given by equations (172) and (173) of their paper, can be immediately extended to the problem of linear Stark broadening by a surrounding complex of charged particles. An upper limit for this mean time, as indicated by Figure 4 of their paper, is

$$T_{\max} = \frac{0.38}{n^{1/3}\bar{V}}, \tag{14}$$

where n is the number of perturbing particles per cubic centimeter and $\bar{V}$ is their root-mean-square velocity. Corresponding mean times have not been determined for the cases of resonance, quadratic Stark, or van der Waals broadening, but one may expect only the numerical factor in equation (14) to be changed. Because of the more critical dependence of these forces on distances to the perturbing particles, this numerical factor would probably be reduced slightly, and so equation (14) should give an acceptable value of $T_{\max}$ for all types of collisions. In most astrophysical problems in which statistical broadening is important (Margenau and Watson 1938; Unsöld 1938),

$$\frac{T_{\max}}{\tau_c} < 0.05 \quad . \tag{15}$$

This would indicate that appreciable changes in the perturbing force occur far more rapidly than in the time interval τ_c, and so the coherent part of noncoherent scattering by collisions can be neglected to an accuracy of 5 per cent when statistical broadening is important.

IV. ZANSTRA'S RESULTS FOR IMPACT BROADENING

Were the simplified quantum-theory analysis used to evaluate the results that Zanstra obtained for impact broadening, as given by equation (13), by similar arguments similar conclusions would be obtained, namely, Zanstra's ratio is too high (in this case by at least a factor of 10), and the coherent component is not strictly coherent. However, before such conclusions can be accepted, the analysis must be shown to be valid for impact broadening. Some evidence for such validity is provided by the equivalence between the quantum-mechanical matrix element, which is evaluated for a specified transition time, and the classical oscillator wave-train analysis (Lindholm 1941). However, the matrix element is for a time-independent perturbation, which is not assumed in impact-broadening theories. This question of validity must be answered by a less simplified use of the quantum theory of radiation, probably employing recent advances in time-dependent perturbation theory.

Regardless of this question of validity, there is reason to believe that Zanstra's coherent component of scattered radiation is not strictly coherent, since his argument for coherent scattering is open to question. The classical oscillator which he considers is driven into forced oscillation by the surrounding radiation which is absorbed, these oscillations being at the frequency absorbed but with a constant phase lag, as indicated by equations (4), (5), and (5*b*) in his paper (Zanstra 1941). This component of the emitted wave train suffers no radiation damping and no phase displacements due to collisions, as treated by the Lorentz-Weisskopf theory. Zanstra maintains, therefore, that this component wave train is coherent, since it may be considered of infinite length and of constant amplitude, giving rise to no appreciable distribution of frequencies about the frequency absorbed. Now phase displacements are introduced into the Lorentz-Weisskopf theory as a mathematically convenient way of describing amplitude changes suggested by quenching experiments, but they have no physical reality. So the fact that these component wave trains suffer no phase displacements does not exclude amplitude changes during a collision, which normally would be expected. In fact, their existence must follow from the assumption of no field during collisions, which Zanstra introduces into his formulation. And, of course, changes in amplitude would introduce a distribution of scattered frequencies about the absorbed frequency. If collisions are assumed to quench these component wave trains, this distribution of frequencies will be a dispersion profile of half-width γ_c. Such quenching would reduce Zanstra's ratio of coherent to uncorrelated noncoherent scattering by a negligible amount, and hence Zanstra's results, as modified by this assumption, would be given by

$$
\begin{aligned}
p(\nu, \nu') = {} & \frac{\gamma_n}{\gamma_n + \gamma_c}\left[\frac{\gamma_c}{4\pi^2(\nu - \nu')^2 + (\frac{1}{2}\gamma_c)^2}\right] \\
& + \frac{\gamma_c}{\gamma_n + \gamma_c}\left[\frac{\gamma_n + \gamma_c}{4\pi^2(\nu - \nu_0)^2 + \frac{1}{4}(\gamma_n + \gamma_c)^2}\right].
\end{aligned}
\tag{16}
$$

REFERENCES

Busbridge, I. W. 1953, *M.N.*, **113**, 52.
Chandrasekhar, S. 1943, *Rev. Mod. Phys.*, **15**, 1.
Chandrasekhar, S., and von Neumann, J. 1942, *Ap. J.*, **95**, 489.
Lindholm, E. 1941, *Ark. Mat. Astr. och Fys.*, Vol. **28B**, No. 3.
———. 1942, "Über die Verbreiterung und Verschiebung von Spektrallinien" (thesis, Uppsala).
———. 1946, *Ark. Mat. Astr. och Fys.*, Vol. **32A**, No. 17.
Margenau, H., and Watson, W. W. 1938, *Rev. Mod. Phys.*, **8**, 22, § 8.
Münch, G. 1949, *Ap. J.*, **109**, 275.
Savedoff, M. P. 1952, *Ap. J.*, **115**, 509.
Sobolev, V. V. 1949, *Russian A.J.*, **26**, 129.
Spitzer, L. 1944, *Ap. J.*, **99**, 1.
Stibbs, D. W. N. 1953, *M.N.*, **113**, 493.
Unsöld, A. 1938, *Physik der Sternatmosphären* (Berlin: J. Springer), § 47.
Weisskopf, V. 1932, *Zs. f. Phys.*, **75**, 287.
Woolley, R. v. d. R., and Stibbs, D. W. N. 1953, *The Outer Layer of a Star* (Oxford: Clarendon Press), chap. viii, § 3.1. The discussion of $Q(\nu - \nu_c, \nu' - \nu_c')$, which the authors label $p(\nu, \nu')$, is restricted to the case of no shifts in energy levels; but the generalization is straightforward.
Zanstra, H. 1941, *M.N.*, **101**, 273.

THE GAUSSIAN QUADRATURE FORMULA FOR AN ELSASSER BAND-ABSORPTION MODEL

Jean I. F. King
Air Force Cambridge Research Center, Air Research and Development Command,
Cambridge 39, Massachusetts

Received November 8, 1954

ABSTRACT

Under radiative equilibrium the emission coefficient of a narrow band-absorbing gas is equal to the frequency integral of the average intensity and the band-absorption coefficient. A two-point Gaussian quadrature formula is developed for this frequency integration, by using the Elsasser band of equally spaced, equally intense, Lorentz-broadened lines as the absorption model. By the use of this formula, the Chandrasekhar method of discrete ordinates can be extended to include an integration over frequency space as well as μ-space. Thus the effect of deviations from "grayness" in an atmosphere can be included directly in the radiative equilibrium formalism, without recourse to iterative procedures.

I. INTRODUCTION

The method of discrete ordinates devised by Wick (1943) and Chandrasekhar (1944) for the solution of the radiative-equilibrium problem involves a systematic replacement of an integral term with a numerical quadrature formula. Through this substitution the integrodifferential equation is transformed into a set of linear simultaneous differential equations, more amenable to solution. Whereas their method replaced only the integration over μ-space with an appropriate finite-sum quadrature, it proves possible in the case of a narrow band-absorbing gas to extend this replacement procedure to frequency space as well.

II. THE QUADRATURE FORMULA

As the first step, it is necessary to construct a quadrature formula for a frequency integral of the type

$$\frac{1}{\bar{\kappa}_\nu \Delta\nu} \int_{\Delta\nu} J_\nu (P, \nu)\ \kappa_\nu (P, \nu)\, d\nu\,, \tag{1}$$

where J_ν is the monochromatic radiant intensity averaged over all directions about P and κ_ν is the mass-absorption coefficient. The band width $\Delta\nu$ is chosen large enough to include several spectral lines, yet sufficiently narrow that the Planck intensity will be constant over the interval.

We have chosen Gauss's method for the construction of the quadrature formula both for its analytic beauty and to facilitate comparison with Chandrasekhar's (1950) results. As an appropriate model for a far-infrared absorption band, the Elsasser (1938) array of equally spaced, equally intense, Lorentz-broadened lines suggests itself,

$$\kappa_\nu = \frac{S}{d}\,\frac{\sinh \beta}{\cosh \beta - \cos 2\pi\nu/d}\,, \qquad \bar{\kappa}_\nu = \int_{\Delta\nu} \frac{\kappa_\nu d\nu}{\Delta\nu} = \frac{S}{d}\,, \tag{2}$$

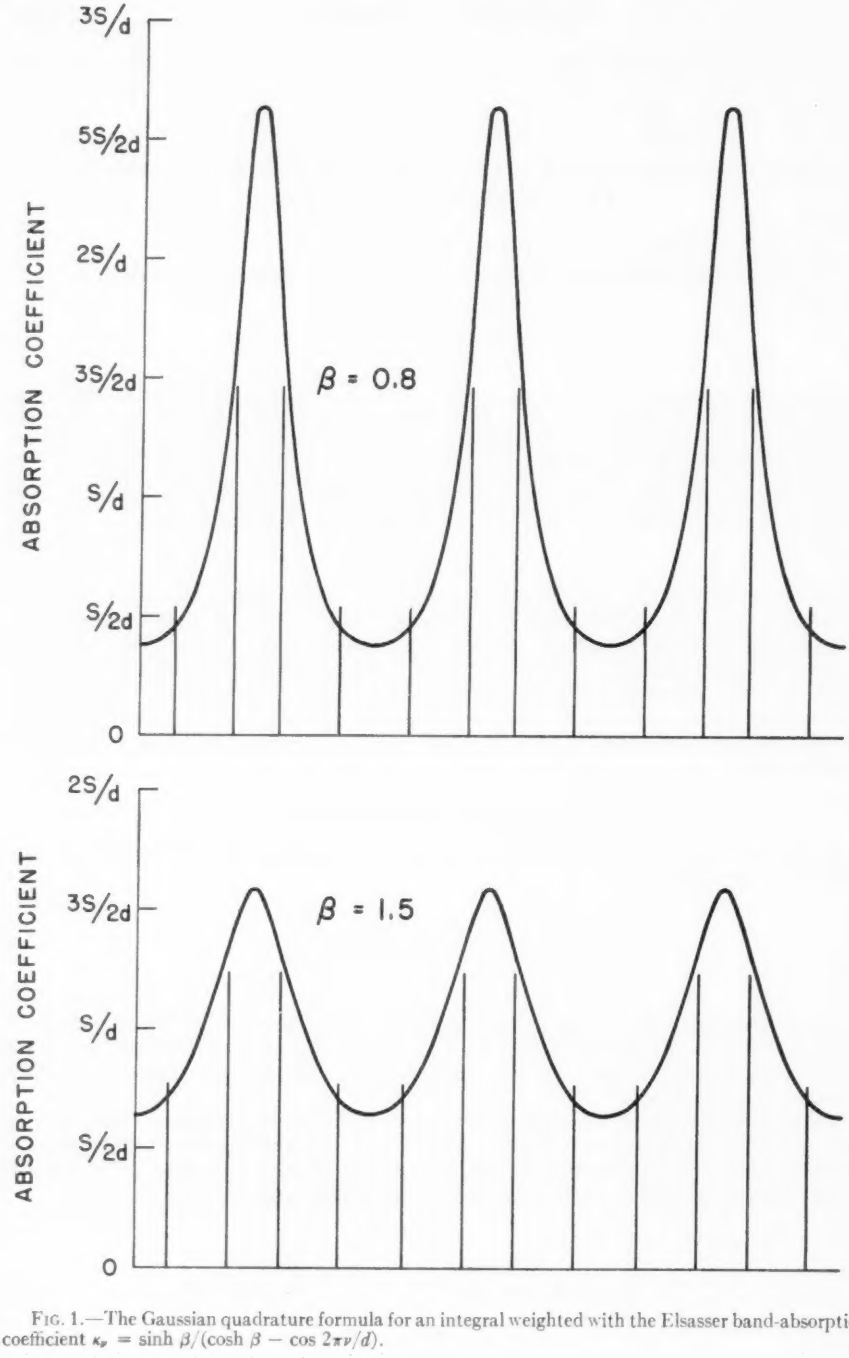

FIG. 1.—The Gaussian quadrature formula for an integral weighted with the Elsasser band-absorption coefficient $\kappa_\nu = \sinh \beta / (\cosh \beta - \cos 2\pi\nu/d)$.

where S and d are the line intensity and spacing and the line-overlap parameter, $\beta = 2\pi\alpha/d$, is the ratio of line half-width to spacing. In addition to its analytical simplicity and physical validity, the Elsasser model has the advantage of incorporating in a single parameter, β, the entire range from complete line separation to complete overlapping. For $\beta \ll 1$, the lines partake of a narrow, intense, and discrete δ-function representation, while for $\beta \gg 1$, the overlapping becomes complete and approaches the "gray" model atmosphere of constant absorption coefficient.

Since the Elsasser model is an infinite periodic array, we avoid redundancy by integrating over a single line in equation (1),

$$\frac{1}{d}\int_{-d/2}^{d/2} J_\nu (P, \nu) \; \frac{\sinh \beta \; d\nu}{\cosh \beta - \cos 2\pi\nu \;\; d}\,. \tag{3}$$

With the substitution $x = \sin \pi\nu/d$, the integral is converted into the form treated by Chandrasekhar (1950, pp. 57–60),

$$\frac{1}{2}\int_{-1}^{1} J_\nu (P, x) \frac{2 \sinh \beta d x}{\pi (\cosh \beta - 1 + 2x^2)(1 + x^2)^{1/2}}, \tag{4}$$

where the weight function is given by

$$w(x) = \frac{2 \sinh \beta}{\pi (\cosh \beta - 1 + 2x^2)(1 - x^2)^{1/2}}\,. \tag{5}$$

Our problem is to determine the Gaussian divisions x_i and weights b_i of the finite sum quadrature,

$$\frac{1}{2}\int_{-1}^{1} J_\nu (P, x)\, w(x)\, dx = \frac{1}{2}\sum_i b_i J_\nu (P, x_i) \quad (i = \pm 1, \ldots, \pm n)\,. \tag{6}$$

To obtain the best fit, we must first determine the auxiliary constants α_l, defined by

$$\alpha_l = \int_{-1}^{1} x^l w(x)\, dx \qquad (l = 0, 1, \ldots, 4n - 1)\,. \tag{7}$$

Since $w(x)$ is an even function, α_l vanishes for odd values of l. Using the substitution

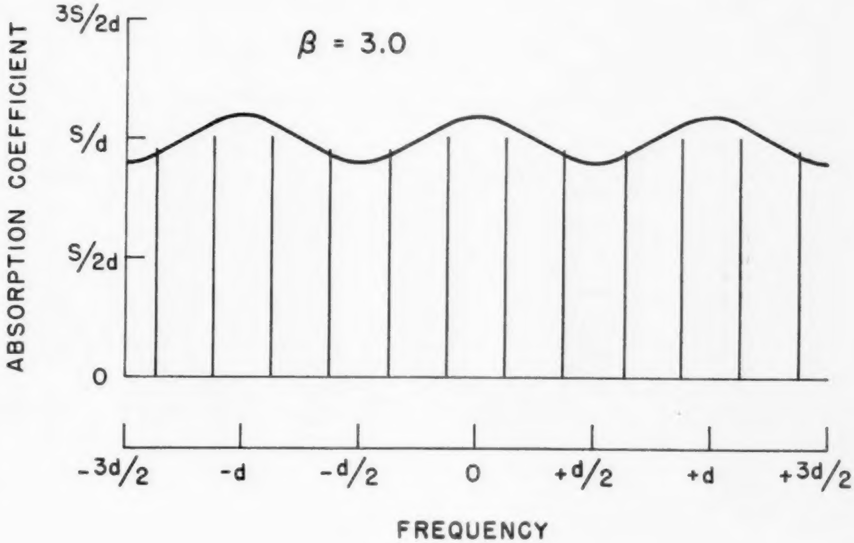

FIG. 1.—*Continued*

$z = \exp(2i \arcsin x)$, we can evaluate equation (7) by means of a contour integration about the unit circle (C) in the complex plane:

$$\alpha_l = \frac{\sinh \beta}{2^{l-1}\pi i}\int_C \frac{(2z - 1 - z^2)^{l/2} dz}{(2z \cosh \beta - 1 - z^2)\, z^{l/2}} \tag{8}$$

$$= \frac{\sinh \beta}{2^{l-2}} \left[\frac{2^{(l/2)-1}(1-\cosh \beta)^{l/2}}{\sinh \beta} + \frac{(-1)^{l/2}}{(l/2-1)!} \left| \frac{d^{(l/2)-1}}{dz^{(l/2)-1}} \frac{(z-1)^l}{(2z\cosh\beta - z^2 - 1)} \right|_{z=0} \right], \tag{9}$$

where the poles are at $z_1 = \cosh \beta - \sinh \beta$ and $z_2 = 0$. Evaluating equation (9) and collecting terms, we find that

$$\alpha_l = \frac{1}{2^{(l/2)+2}} [8 (1 - \cosh \beta)^{l/2} + A_l \sinh \beta] , \tag{10}$$

where A_l is given by a Pascal-type array:

$$\begin{aligned}
A_2 &= +8 , \\
A_4 &= -8 \cosh \beta + 16 , \\
A_6 &= +8 \cosh^2 \beta - 24 \cosh \beta + 28 , \\
A_8 &= -8 \cosh^3 \beta + 32 \cosh^2 \beta - 52 \cosh \beta + 48 , \\
A_{10} &= +8\cosh^4 \beta - 40 \cosh^3 \beta + 84 \cosh^2 \beta - 100 \cosh \beta + 83 .
\end{aligned}$$

TABLE 1

THE GAUSSIAN DIVISIONS AND WEIGHTS OF THE FREQUENCY INTEGRAL

$$\frac{1}{d}\int_{-d/2}^{d/2} J_\nu(P, \nu)\, \frac{\kappa_\nu}{\bar{\kappa}_\nu}\, d\nu = \sum_j b_j J_\nu(P, \nu_j)$$

β	$\pm 2\nu_1/d$	$\pm 2\nu_2/d$	$b_1 = b_{-1}$	$b_2 = b_{-2}$
$\ll 1$	$(2\beta/3\pi^2)^{1/2}$	$(2/3)+(\beta/3\sqrt{3\pi})$	$1-4\beta/9$	$4\beta/9$
0.1	0.0799553	0.6726536	0.9570448	0.0429552
0.2	.1100592	.6783536	.9170756	.0829244
0.3	.1312695	.6837568	.8800582	.1199418
0.4	.1476931	.6888583	.8459094	.1540906
0.6	.1720179	.6981573	.7857224	.2142776
0.8	.1893049	.7062842	.7353415	.2646585
1.0	.2021478	.7133111	.6934680	.3065320
1.5	.2226963	.7267090	.6179661	.3820339
2.0	.2339964	.7354580	.5716904	.4283096
3.0	.2442962	.7444936	.5263994	.4736006
∞	0.25	0.75	0.5	0.5

Each coefficient a_i is the absolute sum of those two lying immediately above. The last coefficient of each A_l is found from the relation

$$\Sigma a_i = \frac{(l-2)\,!}{2^{(l/2)-4}\,[\,(l/2-1)\,!]^2}\,. \tag{11}$$

The limiting values of α_l, which can be found easily from equation (7) are

$$\alpha_l = \frac{1\cdot 3\cdot 5\,\ldots\,(l-3)}{2\cdot 4\cdot 6\,\ldots\,(l-2)}\,\beta \qquad (\beta \ll 1)\,, \tag{12}$$

$$\alpha_l = 2\,\frac{1\cdot 3\cdot 5\,\ldots\,(l-1)}{2\cdot 4\cdot 6\,\ldots\,l} \qquad (\beta \gg 1)\,. \tag{13}$$

Proceeding with the method, we have obtained the divisions and weights of the quadrature formula to the second approximation ($n = 2$) for twelve values of β. These are listed in Table 1, along with representative plots in Figure 1. The tendency of the divisions and weights to conform to the Elsasser band is apparent. In a forthcoming paper these quadrature formulas will be used for the calculation of the radiative-equilibrium configuration of various nongray model atmospheres.

I acknowledge with gratitude the computational help of John S. Garing.

REFERENCES

Chandrasekhar, S. 1944, *Ap. J.*, **100**, 76.
———. 1950, *Radiative Transfer* (Oxford: Clarendon Press).
Elsasser, W. M. 1938, *Phys. Rev.*, **54**, 126.
Wick, G. C. 1943, *Zs. f. Phys.*, **121**, 702.

A MODEL FOR THE INTERNAL STRUCTURE OF THE SUN

G. Ogden Abell
Mount Wilson and Palomar Observatories
Carnegie Institution of Washington, California Institute of Technology

Received August 27, 1954; revised October 21, 1954

ABSTRACT

A model for the structure of the sun is given, in which the proton-proton nuclear process is assumed to be the source of all the sun's energy. Homogeneity of chemical composition and an envelope in radiative equilibrium are assumed, and interpolation formulae for opacity are adopted. The calculations show that a model based on these assumptions and interpolation formulae does not permit possible chemical abundances of the elements. It is suggested that this difficulty arises from the neglect of the consumption of hydrogen in the center of the sun and the possibility of an outer convection zone.

It now appears likely that the proton-proton reaction rather than the carbon cycle is the dominant nuclear process contributing to the sun's energy production (Epstein 1951; Epstein and Motz 1953, 1954; Naur 1954). The less sensitive temperature dependence of the proton-proton reaction as compared with the carbon cycle implies that the energy production is spread out over a fairly large volume of the sun. Therefore, it cannot even approximately be assumed that the total luminosity is generated within a central convective core, as it is in the case of models in which only the carbon cycle is presumed to be of importance.

This has been borne out in the computations of several theoretical solar models published recently (Epstein 1951; Epstein and Motz 1953, 1954; Naur 1954). In the present paper the results are given of an integration of another such model, in which the latest value for the nuclear cross-section for the proton-proton process is used, and interpolation formulae are adopted for opacity which include the effect of free-free transitions of hydrogen and helium.

I. PHYSICAL ASSUMPTIONS AND INTERPOLATION FORMULAE

In computing this model of the sun's interior, the following physical assumptions were made:

A. The opacity is due to (1) photoelectric ionization of heavy elements (Kramers' opacity), (2) free-free transitions of hydrogen and helium, and (3) scattering by free electrons. To take into account these three sources of opacity, interpolation formulae have been established by computing, first, the opacity on the basis of each of two existing solar models (Epstein 1951; Harrison 1952). Harrison's tables for 60 per cent oxygen and 40 per cent Russell mixture (1948) were used with an assumed Gaunt factor of 0.9 to obtain the opacity arising from photoionization. In computing the opacity arising from free-free transitions of hydrogen and helium, the Gaunt factor was taken as 0.75. The combined opacity was computed by the approximate rule of multiplying the smaller components by $\frac{3}{2}$ and adding them to the largest component (Strömgren 1933). The Kramers' component was found to be dominant throughout most of the solar interior. The total opacity was assumed to be given by an expression of the form

$$\kappa = \frac{1}{\tau} K \frac{\rho}{T^{3.5}} + 0.30 \, (1 + X) \; , \tag{1}$$

where τ' is an appropriate guillotine factor for combined Kramers' and free-free absorptions defined by equation (1) and

$$K = 3.9 \times 10^{25} (1 + X) \, (1 - X - Y) + 4.10 \times 10^{22} (1 + X) \, (X + Y) \, , \tag{2}$$

X and Y being the fractional abundances by weight of hydrogen and helium, respectively. In both Epstein's and Harrison's models, for which the opacity was computed, it was found that τ' could be well represented by

$$\tau' \propto \rho^0 \text{ for } \rho < 1$$

and

$$\tau' \propto \rho^{1/3} \text{ for } \rho \geqslant 1 \,. \tag{3}$$

B. The energy sources are derived completely from the proton-proton nuclear reactions. Dr. W. A. Fowler, by private communication, has kindly supplied the following expression for ϵ_{pp}, the energy generated per gram of stellar material by the proton-proton process:

$$\epsilon_{pp} = 3.54\,\rho X^2 \left(\frac{13}{T}\right)^{2/3} \exp\left\{-14.38\left(\frac{13}{T}\right)^{1/3}\right\} \times 10^6 \text{ ergs gm}^{-1}\text{ sec}^{-1} . \tag{4}$$

The value of the constant in this expression for ϵ_{pp} differs by about 30 per cent from the value published earlier by Fowler (1954), because of recent measurements on beta-decay energies and lifetimes by S. A. Moszkowski. For the range of temperatures in which we are interested, a good approximation to ϵ_{pp} is given by

$$\epsilon_{pp} \approx 0.20\,\rho X^2 \left(\frac{T}{13}\right)^{4.1} ; \tag{5}$$

and this expression was actually used in the calculations.

C. The parameters X and Y describing the chemical composition are constant throughout the sun.

D. The sun is in a state of radiative equilibrium, except possibly for a central convective core.

II. BASIC EQUATIONS

In terms of physical variables, the equations governing the structure of the sun are (Chandrasekhar 1951)

$$\frac{dM(r)}{dr} = 4\pi r^2 \rho \,, \tag{6}$$

$$\frac{dP(r)}{dr} = -\frac{GM(r)\,\rho}{r^2} \,, \tag{7}$$

$$\frac{dL(r)}{dr} = 4\pi r^2 \rho \epsilon_{pp} \,, \tag{8}$$

and, in the case of radiative equilibrium,

$$\frac{dT}{dr} = -\frac{3\,\kappa \rho L(r)}{16\pi a c r^2 T^3} . \tag{9}$$

The following homology invariant variables (h-variables) were used (Bondi and Bondi 1949):

$$S = -\frac{d \log M(r)}{d \log P} = 4\pi \frac{P r^4}{G M^2(r)} \,, \qquad Q = -\frac{d \log r}{d \log P} = \frac{P r}{G M \rho} \,,$$

$$N = \frac{d \log T}{d \log P} \,, \qquad W = \frac{d \log L(r)}{d \log r} . \tag{10}$$

The boundary conditions at the center are

$$W \rightarrow 3 \text{ and } \frac{S}{Q} \rightarrow 3 \text{ as } S \rightarrow \infty \,. \tag{11}$$

The relations between the Bondi variables (S, Q, and N) and the more familiar *h*-variables, U, V, and n, used by Schwarzschild and Richardson (1948), are

$$S = \frac{U}{V}, \qquad Q = \frac{1}{V}, \qquad N = \frac{1}{n+1}. \tag{12}$$

Equations (6), (7), and (8), transformed by equations (10), become

$$\frac{dQ}{dS} = \frac{Q}{S} \frac{S + N - Q}{1 + 2S - 4Q} \tag{13}$$

and

$$\frac{dW}{dS} = \frac{W}{S} \frac{(2 + 2.1\,N) - (3 - W)\,Q}{1 + 2S - 4Q}. \tag{14}$$

Equation (9) becomes

$$\begin{aligned} \frac{dN}{dS} &= \frac{N}{S} \frac{S + 1 - 4N - \omega\,(4.5\,N - 1)}{1 + 2S - 4Q} \qquad (\text{for } \rho < 1)\,, \\ \frac{dN}{dS} &= \frac{N}{S} \frac{S + 1 - 4N - \omega\,(25/6\,N - 2/3) - QW}{1 + 2S - 4Q} \qquad (\text{for } \rho \geqslant 1)\,, \end{aligned} \tag{15}$$

where

$$\omega \equiv \frac{\kappa(\text{Kramers}) + \kappa(\text{free-free})}{\kappa(\text{total})} = \frac{1/\tau' K \rho / T^{3.5}}{1/\tau' K \rho / T^{3.5} + 0.3\,(1 + X)} \tag{16}$$

is a slowly varying quantity, which can be evaluated from

$$\begin{aligned} \frac{\omega^6}{(1-\omega)^{11}} &= \frac{(4\pi)^4 \{K/0.3\,(1+X)\}^6 k/\mu H}{L^5(r)\, G \{0.9/4ac\,(1+X)\}^5} \frac{S N^5}{Q^7} r^3 \quad (\text{for } \rho < 1)\,, \\ \frac{\omega^{18}}{(1-\omega)^{35}} &= \frac{(4\pi)^{22} G^5 \{K/0.3\,(1+X)\}^{18}}{(k/\mu H)^5 L^{12}(r) \{0.9/4ac\,(1+X)\}^{17}} \frac{N^{17}}{S^5 Q^7} r^{27} \quad (\text{for } \rho \geqslant 1)\,. \end{aligned} \tag{17}$$

If a region in convective equilibrium exists at the center of the sun, the temperature gradient may be assumed to have the adiabatic gradient (Chandrasekhar 1951), in which case N has the constant value 0.4.

The physical variables, r/R, $M(r)/M$, ρ, and T/μ, are obtained from the *h*-variables by (Bondi and Bondi 1949)

$$\begin{aligned} \log \frac{r}{R} &= -\int_0^S \frac{Q\,dS}{S\,(1 + 2S - 4Q)} = -\int_0^Q \frac{dQ}{S + N - Q}, \\ \log \frac{M(r)}{M} &= -\int_0^S \frac{dS}{1 + 2S - 4Q}, \\ \rho &= \frac{M}{4\pi R^3} \frac{S}{Q} \frac{M(r)}{M} \left(\frac{R}{r}\right)^3 = 0.471\, \frac{S}{Q} \frac{M(r)}{M} \left(\frac{R}{r}\right)^3, \\ \frac{T}{\mu} &= \frac{M}{R} \frac{GH}{k} \frac{QR}{r} \frac{M(r)}{M} = 2.31 \times 10^7 \frac{QR}{r} \frac{M(r)}{M}. \end{aligned} \tag{18}$$

III. METHOD OF SOLUTION

Equations (13), (14), and (15) were integrated numerically to obtain the final model. To determine ω from equations (17), it was assumed, as a zero approximation, that $X = 0.76$ and $\mu = 0.59$, and $L(r)$ was estimated from two existing models (Epstein 1951; Harrison 1952). The value of r was determined from the first of equations (18) at each step during the integration. Then ω was evaluated, graphically, from equations (17), now expressed in the form: $F(\omega) = F(r, N, S, Q)$.

A starting point at $r/R = 0.650$ was obtained from the solutions of equations (6), (7) and (9) for the case $M(r)/M = 1.00$, and $L(r) = L$ (Chandrasekhar 1951). In terms of h-variables, this starting point is

$$Q = 0.0823\,, \qquad N = 0.236\,, \qquad S = \frac{1.32 \times 10^{-5}}{C^{1/2}}\,, \qquad W = W_0\,. \tag{19}$$

The first eigenvalue, C, is a function of the mass, luminosity, radius, and chemical composition of the sun. The second eigenvalue, W_0, is so near zero at the starting point that in practice a starting value of W—W_1—was assumed at $S = 0.150$. The correct choice of C and W_1 determines the solution which satisfies the two boundary conditions (11).

TABLE 1

VALUES OF PHYSICAL VARIABLES AT INTERFACE OF CONVECTIVE CORE AND RADIATIVE ENVELOPE IN SCHWARZSCHILD MODEL COMPARED FOR TWO INTEGRATIONS

	Schwarzschild's Solution	From Bondi's Semigraphical Method
r/R	0.1217	0.1219
ρ/ρ_c	.728	.736
T/T_c	0.809	0.808

The integration was largely simplified by the use of graphs of Emden's equation (13) prepared by Bondi and Bondi (1949) for several values of N and distributed by the Royal Astronomical Society.

To test the accuracy of this semigraphical method, Bondi's graphs were used to recompute the radiative portion of a model computed earlier by Schwarzschild (1946; Chandrasekhar 1951)—a point-source model with homogeneous chemical composition and assuming Kramers' opacity with $\tau = \rho^{0.25}$. Values of r/R, ρ/ρ_c, and T/T_c at the interface of the radiative envelope and the convective core, as determined by the two integrations, are given in Table 1. The good agreement suggests that the use of Bondi's graphs of equation (13) is justified for the accuracy required here.

IV. SOLUTION

The results of the integrations are tabulated in Table 2. The values of N for $S \geqslant 15$ are approximate only. Clearly, however, the condition for convection ($N = 0.4$) is never fulfilled; thus, on the basis of this model, there is no convective core.

In principle, the chemical composition (X and Y) can be determined from the eigenvalues, C and W_1. However, it can be shown that no possible choice of X and Y can

TABLE 2

FINAL SOLUTION

r/R	$M(r)/M$	ρ	$T/\mu\times10^6$	$L(r)/L$	S	Q	N
1.000	1.000	0.0	0.00	1.000	....	....	0.236
0.900	1.000	9.05×10^{-4}	0.605	1.000	....	....	.236
0.800	1.000	1.26×10^{-2}	1.362	1.000	....	....	.236
0.750	1.000	3.21×10^{-2}	1.816	1.000	....	....	.236
0.700	1.000	7.25×10^{-2}	2.333	1.000	....	....	.236
0.650	1.000	0.153	2.92	1.000	0.0074	0.0823	.236
0.622	0.995	0.218	3.29	1.000	0.010	0.089	.236
0.550	0.980	0.514	4.43	1.000	0.020	0.108	.238
0.505	0.964	0.873	5.34	1.000	0.030	0.121	.238
0.477	0.949	1.27	5.92	1.000	0.040	0.129	.225
0.428	0.914	2.30	7.05	1.000	0.060	0.143	.211
0.395	0.881	3.49	7.93	1.000	0.080	0.154	.213
0.373	0.851	4.76	8.53	1.000	0.100	0.162	.215
0.326	0.778	8.57	10.20	1.000	0.150	0.185	.221
0.302	0.712	12.16	10.96	1.000	0.200	0.201	.226
0.282	0.657	15.8	11.67	0.999	0.250	0.217	.231
0.265	0.610	19.6	12.5	0.995	0.300	0.235	.235
0.242	0.529	26.4	13.4	0.989	0.400	0.266	.243
0.222	0.464	32.8	14.5	0.977	0.500	0.302	.250
0.207	0.410	38.8	15.4	0.963	0.600	0.336	.257
0.184	0.331	49.4	16.9	0.920	0.800	0.406	.268
0.167	0.273	58.4	18.0	0.873	1.000	0.476	.278
0.155	0.230	64.5	18.3	0.824	1.200	0.536	.286
0.147	0.197	68.5	18.4	0.790	1.400	0.594	.292
0.139	0.172	73.0	18.9	0.753	1.600	0.660	.298
0.133	0.153	76.5	19.1	0.720	1.800	0.720	.302
0.127	0.136	80.0	19.5	0.684	2.000	0.786	.306
0.116	0.107	85.7	20.3	0.619	2.500	0.950	.314
0.107	0.0867	90.4	20.9	0.555	3.000	1.114	.320
0.0935	0.0614	97.9	22.0	0.455	4.000	1.45	.329
0.0773	0.0365	105.8	23.0	0.322	6.00	2.11	.338
0.0677	0.0250	109.7	23.6	0.240	8.00	2.77	.343
0.0608	0.0184	111.9	24.0	0.202	10.00	3.44	.346
0.0501	0.0105	115.4	24.7	0.133	15.00	5.11	.35
0.0435	0.00698	118.1	25.1	0.098	20.0	6.77	.35
0.0358	0.00391	119.6	25.6	0.060	30.0	10.11	.36
0.0254	0.00142	122	25.9	0.026	60.0	20.1	.37
0.0197	0.000669	123	26.2	0.015	100	33.4	.37
0.0140	0.000241	123	26.4	0.007	200	66.8	.37
0.00890	0.0000617	123	26.7	0.002	500	167	.37
0.00	0.00	124	27.0	0.00	$\rightarrow\infty$	$\rightarrow S/3$	0.37

satisfy the model computed with the given assumptions and interpolation formulae. Note that

$$L = 3.78 \times 10^{33} = \int_0^R 4\pi r^2 \rho\epsilon d r$$

$$= R^3 4\pi \,(0.20)\, X^2 \left(\frac{\mu}{13}\right)^{4.1} \int_0^1 \left(\frac{r}{R}\right)^2 \rho^2 \left(\frac{T}{\mu}\right)^{4.1} d\left(\frac{r}{R}\right) \quad (20)$$

$$= k \int_0^1 \left(\frac{r}{R}\right)^2 \rho^2 \left(\frac{T}{\mu}\right)^{4.1} d\left(\frac{r}{R}\right);$$

$$k = 4\pi R^3 \,(0.20)\, X^2 \left(\frac{\mu}{13}\right)^{4.1}. \quad (21)$$

The integral in equation (20) was numerically evaluated from the final model, and it was found that

$$\int_0^1 \left(\frac{r}{R}\right)^2 \rho^2 \left(\frac{T}{\mu}\right)^{4.1} d\left(\frac{r}{R}\right) = 3.28 \times 10^6 . \quad (22)$$

The constant *k*, then, is

$$k = \frac{3.78 \times 10^{33}}{3.28 \times 10^{10}} = 1.152 \times 10^{27} . \quad (23)$$

Evaluating the constants in equation (21), we obtain

$$\frac{k}{X^2 \mu^{4.1}} = 2.29 \times 10^{28} \quad (24)$$

and

$$X^2 \mu^{4.1} = 0.0504 . \quad (25)$$

As a consequence of equation (25), even if $1 - X - Y = Y = 0$, X would have to have the value 1.14—that is, more than 100 per cent of the sun's matter would have to be hydrogen!

It should be pointed out that these results are in substantial disagreement with those obtained by Naur (1954). He obtained a chemical composition of $X \approx 0.75$ and $Y \approx 0.24$ for the sun. The nuclear cross-section constant used by Naur is about 30 per cent larger than that used here. However, increasing the cross-section used here by 30 per cent would increase the disagreement in X to a factor of 2. It remains to be determined whether or not the discrepancy can be due to a very high sensitivity of the model to rather slight changes in opacity interpolation formulae. Finally, the possibility of a numerical error must not be overlooked.

V. CHECK ON ASSUMPTIONS AND INTERPOLATION FORMULAE

A. *Opacity.*—The opacity can be recomputed from the finished model. However, it would obviously make no sense to compute opacity on the basis of 114 per cent hydrogen. Therefore, the opacity and guillotine factor were evaluated for the run of temperature and density given by the model and each of the three hypothetical compositions:

(1) $X = 0.76$, $Y = 0.22$, $\mu = 0.590$;

(2) $X = 0.98$, $Y = 0.00$, $\mu = 0.508$;

(3) $X = 0.99$, $Y = 0.00$, $\mu = 0.504$.

In Figure 1 is shown the plot of log τ' versus log ρ for each of the three compositions. Also in Figure 1 is shown a heavy line with the slopes zero and $\frac{1}{3}$, corresponding to the assumed density-power law used for the guillotine factor in computing the model. The agreement is seen to be reasonably good, the greatest deviations between assumed and recomputed guillotine factors occurring in the central regions of the sun, where the solution is least sensitive to the opacity law.

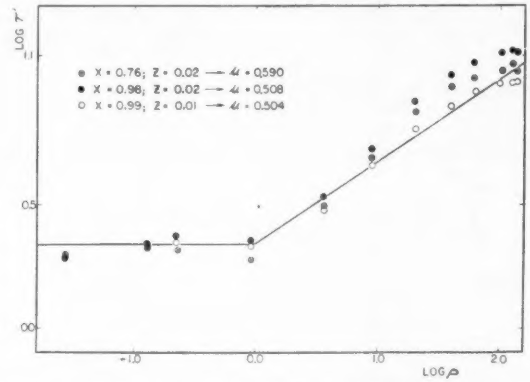

FIG. 1.—Log effective guillotine factor (τ) versus log ρ. The opacity was computed from final model and each of three assumed chemical compositions. Heavy line has slopes zero and $\frac{1}{3}$, for ρ less than 1 and for ρ greater than 1, respectively, corresponding to the assumed density-power law used for the guillotine factor in computing the model.

TABLE 3

$\omega = (\kappa_{\text{Kramers}} + \kappa_{\text{free-free}})/\kappa_{\text{total}}$

COMPUTED STEP BY STEP DURING INTEGRATION AND FROM FINISHED MODEL, WITH EACH OF THREE ASSUMED CHEMICAL ABUNDANCES (DENOTED WITH SUBSCRIPTS 1, 2, AND 3) FOR SEVERAL VALUES OF S

S	ω	ω_1	ω_2	ω_3
0.010	0.96	0.96	0.97	0.95
0.030	.95	.96	.97	.94
0.080	.93	.93	.96	.93
0.150	.91	.90	.93	.90
0.300	.88	.87	.91	.88
0.600	.84	.83	.88	.84
1.000	.80	.80	.85	.80
4.00	0.71	0.76	0.82	0.76

To determine the reliability of the value of ω, evaluated at each step in the integration (as described in Sec. II), ω was also computed from the model for each of the three assumed abundances. Table 3 lists these values of ω and also the corresponding ω's evaluated during the integration for several values of S. It has been verified that any of the four sets of values of ω could have been used without affecting the solution to the accuracy recorded in Table 2. The model is particularly insensitive to changes of ω near the center (large S).

It must be emphasized that this model is incompatible with *any* possible abundances of the elements. The three cases for which the opacity was recomputed here serve to establish that the opacity interpolation formulae adopted are not radically in error, since it happens that the opacity gradient computed throughout the sun is relatively insensitive to the run of temperature and density.

However, the computed opacity gradient can be highly sensitive to the assumed abundance of the heavy elements $(1 - X - Y)$. Epstein and Motz (1954) were able to find a self-consistent solar model by adopting opacity interpolation formulae compatible with a very low abundance of heavy elements (0.2 per cent by weight). This is much lower than the 1 per cent abundance indicated from spectroscopic observations of the solar atmosphere (Greenstein 1954). This value obtained from the atmosphere of the sun is believed by the writer to be more reliable than the values obtained from models of the interior.

B. *Energy generation*.—Since in this model a possible value for the molecular weight, and hence for the central temperature, is not determined, it is not possible to compute the relative importance of the carbon cycle. However, the addition of another energy source would require an even lower molecular weight, in order to produce the observed solar luminosity, further increasing the composition discrepancy.

Dr. Fowler estimates the uncertainty in the proton-proton cross-section constant to be about 10 per cent. If the cross-section were lowered from its present accepted value by 25 per cent, a luminosity fit could be obtained with $X \approx 0.9$.

C. *Uniform chemical composition.*—The assumption of uniform chemical composition is clearly incorrect. The conversion of hydrogen into helium results in an increase of μ in the central region of the sun. However, the introduction of such an inhomogeneity of molecular weight would result in an increase in the generated energy, again further increasing the composition inconsistency.

D. *Radiative equilibrium.*—In the case of red dwarfs, Osterbrock (1953) has shown that, in a model taking account of an outer convection zone extending down into the envelope to a depth where the temperature becomes about two to two and a half million degrees, the central temperature is substantially reduced from that of a pure radiative model. In this way a discrepancy (Aller 1950; Aller, Chamberlain, Lewis, Liller, McDonald, Potter, and Weber 1952) similar to that encountered in the present work was eliminated. Recent studies by Greenstein and Richardson (1951) and by Greenstein and Tandberg-Hanssen (1954) of the solar abundances of beryllium and lithium suggest that the sun also may have a convective zone, extending to layers at temperatures of three to three and a half million degrees.

VI. CONCLUSIONS

It is seen that this model of the sun, computed on the assumptions of homogeneous chemical composition and that the outer layers are in radiative equilibrium, requires an impossible percentage of hydrogen. Improbable modifications in opacity formulae and nuclear cross-sections or an assumed abundance of heavy elements radically different from that in the solar atmosphere could conceivably result in possible chemical abundances in this model. However, considering the spectroscopic evidence for mixing in the outer layers of the sun and the effect of an outer convection zone on models of red dwarfs, it seems far more likely that the assumption of radiative equilibrium throughout the envelope is the principal source of error.

The writer wishes to thank Drs. Guido Münch and Donald Osterbrock for their helpful discussions with him during this work, and Dr. W. A. Fowler for supplying the latest data on the proton-proton cross-sections.

REFERENCES

Aller, L. H. 1950, *Ap. J.*, **111**, 173.

Aller, L. H., Chamberlain, J. W., Lewis, E. M., Liller, W. C., McDonald, J. K., Potter, W. H., and Weber, N. E. 1952, *Ap. J.*, **115**, 328.

Bondi, C. M. and H. 1949, *M.N.*, **109**, 62.

Chandrasekhar, S. 1951, *Astrophysics: A Topical Symposium*, ed. J. A. Hynek (1st ed.; New York: McGraw-Hill Book Co., Inc.), pp. 598–674.

Epstein, I. 1951, *Ap. J.*, **114**, 438.

Epstein, I., and Motz, L. 1953, *Ap. J.*, **117**, 311.

———. 1954, *ibid.*, **120**, 156.

Fowler, W. A. 1954, *Mém. Soc. r. sci. de Liège*, 4th ser., **13**, 88.

Greenstein, J. L. 1954, *Mém. Soc. r. sci. de Liège*, 4th ser., **13**, 310.

Greenstein, J. L., and Richardson, R. S. 1951, *Ap. J.*, **113**, 536.

Greenstein, J. L., and Tandberg-Hanssen, E. 1954, *Ap. J.*, **119**, 113.

Harrison, M. H. 1948, *Ap. J.*, **108**, 310.

———. 1952, unpublished.

Naur, P. 1954, *Ap. J.*, **119**, 365.

Osterbrock, D. E. 1953, *Ap. J.*, **118**, 529.

Schwarzschild, M. 1946, *Ap. J.*, **104**, 203.

Schwarzschild, M., and Richardson, R. S. 1948, *Ap. J.*, **108**, 373.

Strömgren, B. 1933, *Zs. f. Ap.*, **7**, 222.

APSIDAL MOTION FOR AN EARLY MAIN-SEQUENCE MODEL

R. Härm and J. Rogerson
Princeton University Observatory

Received August 4, 1954; revised September 27, 1954

ABSTRACT

The effective polytropic index, which determines the rate of advance of the line of apsides, is computed for a Cowling-type stellar model with pure electron-scattering opacity in the envelope. The low value of $n = 2.63$ found for this model strongly suggests that the onset of electron scattering as an opacity factor in early B-star binaries may be reponsible for their observed low effective polytropic indices. For comparison, the analysis was also carried out for a Cowling-type model with Kramers' opacity.

I. INTRODUCTION

The observations on apsidal motions in double stars have recently been summarized by Keller (1948). His Figure 1 has to be corrected because the latest data for YY Sgr (Keller and Limber 1951) give $n = 3.55$ for this star. The corrected figure shows that the late B and A stars have an apsidal motion in satisfactory agreement with the theoretical computations for middle main-sequence models. The earliest B stars, however, show an apsidal motion corresponding to an appreciably lower effective polytropic index—as was recently re-emphasized by van Wijk's work on GL Car (1954). This is presumably caused by the large role played by electron scattering in early-type stars.

It is the purpose of this paper to check this supposition by computing the apsidal motion constant for a Cowling model with pure electron scattering in the enevlope. For comparison, the computations are also carried through for a Cowling model with Kramers' opacity law in the envelope.

II. UNPERTURBED MODELS

The following assumptions were made in computing the models: (1) all energy generation takes place in the core, (2) radiation pressure and degeneracy are negligible, (3) the opacity is due only to electron scattering in one model and only to photoionization in the other model, and (4) μ is constant throughout the star.

A. *Subscripts*

Those quantities which differ between the two models are distinguished by the subscripts e for electron scattering and k for Kramers' absorption.

B. *Absorption coefficients*

$$\kappa_e = 0.19\,(1+X)\,, \tag{1a}$$

$$\kappa_k = 10^{25}\,(1+X)\,Z\rho T^{-3.5} = \kappa_0 \rho T^{-3.5}\,. \tag{1b}$$

C. *Dimensionless variables*

$$P = p\,\frac{GM^2}{4\pi R^4}\,, \qquad T = t\,\frac{\mu H}{k}\,\frac{GM}{R}\,,$$

$$M_r = qM\,, \qquad r = xR \tag{2}$$

D. *Basic equations for envelopes*

$$\frac{dp}{dx} = -\frac{pq}{tx^2}, \qquad \frac{dq}{dx} = \frac{px^2}{t},$$

$$\left(\frac{dt}{dx}\right)_e = -\frac{C_e p}{x^2 t^4}, \qquad \left(\frac{dt}{dx}\right)_k = -\frac{C_k p^2}{x^2 t^{8.5}}, \tag{3}$$

with

$$C_e = \frac{3}{4ac}\,\frac{\kappa_e}{(4\pi)^2}\left(\frac{k}{\mu HG}\right)^4 \frac{L}{M^3}$$

and

$$C_k = \frac{3\,\kappa_0}{4ac}\left(\frac{k}{\mu HG}\right)^{7.5}\left(\frac{1}{4\pi}\right)^3 \frac{LR^{0.5}}{M^{5.5}}. \tag{4}$$

E. *Emden variables for convective core*

$$t = \theta t_c, \qquad p = \theta^{n+1} p_c \qquad x = \xi\sqrt{\frac{t_c^2\,(n+1)}{p_c}}, \tag{5}$$

with n taken to be 1.5 in the core.

F. *Homology invariants*

$$U = \frac{x^3 p}{qt}, \qquad V = \frac{q}{xt},$$

$$(n+1)_e = \frac{qt^4}{C_e p}, \qquad (n+1)_k = \frac{qt^{8.5}}{C_k p^2}. \tag{6}$$

G. *Fitting conditions between the envelope and core*

$$U_{\text{env}} = U_{\text{core}}, \qquad V_{\text{env}} = V_{\text{core}} \quad \text{when} \quad (n+1)_{\text{env}} = 2.5\,. \tag{7}$$

These equations were solved by the usual methods. Three trial values had to be integrated through for C_e and three for C_k. The final eigen-values found are

$$\log C_e = -3.2985\,, \qquad \log C_k = -5.9887\,.$$

The latter value agrees well with the more accurate computation by Gardiner (1951), which gives $\log C_k = -5.98879$. The corresponding eigen-solutions are given in Tables 1 and 2. At the fitting point of the envelope to the core, the relevant quantities for the electron-scattering model are

$$\begin{aligned} x_f &= 0.2833\,, & \log t_f &= -0.2994\,, & \xi_f &= 1.5732\,; \\ \log p_f &= 1.1970\,, & \log q_f &= -0.5058\,, & \theta_f &= 0.6546 \end{aligned} \tag{8}$$

and, for the Kramers opacity model,

$$\begin{aligned} x_f &= 0.1700\,, & \log t_f &= -0.1514\,, & \xi_f &= 1.1914\,; \\ \log p_f &= 1.7347\,, & \log q_f &= -0.8346\,, & \theta_f &= 0.7867\,. \end{aligned} \tag{9}$$

A first comparison shows the core to include 17 per cent of the radius in the Kramers opacity model, while it includes 28 per cent of the radius in the electron-scattering model.

III. APSIDAL PERTURBATION

The perturbation equation used here is that given by Sterne (1939) in his equation (4). With $n = 2$, $Y_n^m = y$, and our definitions for x and U, the perturbation equation may be cast into the form

$$\frac{d^2 y}{d x^2}+\frac{2\,U}{x}\,\frac{d y}{d x}+\frac{2}{x^2}\,(U-3)\,y=0\,. \tag{10}$$

Here U as a function of x is to be taken from the unperturbed model. In terms of y, the apsidal-motion constant has the definition

$$k_2=\frac{3y_1-(dy/dx)_1}{4y_1+2\,(dy/dx)_1}\,, \tag{11}$$

TABLE 1

MODEL WITH ELECTRON SCATTERING

log (1/[x−1])	+log q	log t	log p	U	V	n+1
−1.05	0.0000	−1.6521	−3.9118	0.004256	48.881	4.000
−1.00	.0000	−1.6021	−3.7118	0.005836	44.000	4.000
−0.95	− .0001	−1.5521	−3.5118	0.007975	39.646	4.000
−0.90	− .0001	−1.5021	−3.3119	0.01086	35.764	3.999
−0.85	− .0002	−1.4521	−3.1120	0.01473	32.305	3.999
−0.80	− .0003	−1.4021	−2.9121	0.01989	29.221	3.999
−0.75	− .0005	−1.3521	−2.7122	0.02674	26.467	3.998
−0.70	− .0007	−1.3021	−2.5125	0.03576	24.012	3.997
−0.65	− .0011	−1.2522	−2.3128	0.04756	21.818	3.995
−0.60	− .0016	−1.2022	−2.1134	0.06288	19.859	3.993
−0.55	− .0024	−1.1523	−1.9142	0.08261	18.105	3.990
−0.50	− .0035	−1.1025	−1.7154	0.1078	16.533	3.986
−0.45	− .0050	−1.0527	−1.5170	0.1396	15.120	3.979
−0.40	− .0072	−1.0030	−1.3195	0.1795	13.846	3.970
−0.35	− .0102	−0.9534	−1.1229	0.2289	12.693	3.959
−0.30	− .0144	−0.9040	−0.9277	0.2893	11.643	3.943
−0.25	− .0200	−0.8548	−0.7344	0.3624	10.681	3.922
−0.20	− .0276	−0.8060	−0.5435	0.4495	9.792	3.894
−0.15	− .0376	−0.7576	−0.3559	0.5519	8.963	3.858
−0.10	− .0507	−0.7098	−0.1723	0.6705	8.184	3.812
−0.05	− .0675	−0.6626	+0.0061	0.8053	7.444	3.754
0.00	− .0889	−0.6164	+0.1781	0.9555	6.737	3.682
+0.05	− .1156	−0.5712	+0.3425	1.1195	6.058	3.594
+0.10	− .1484	−0.5273	+0.4980	1.2940	5.406	3.491
+0.15	− .1879	−0.4850	+0.6434	1.4750	4.781	3.368
+0.20	− .2349	−0.4443	+0.7776	1.6574	4.187	3.228
+0.25	− .2896	−0.4055	+0.8999	1.8350	3.628	3.070
+0.30	− .3523	−0.3687	+1.0097	2.0019	3.110	2.895
+0.35	− .4229	−0.3339	+1.1071	2.1518	2.639	2.709
+0.40	− .5009	−0.3013	+1.1923	2.2797	2.218	2.512
+0.45	−0.5857	−0.2708	+1.2660	2.3811	1.849	2.311

with the subscript 1 indicating the value of the quantity at $x = 1$. The boundary conditions of equation (10) are $y = 1$, $dy/dx = 0$ at $x = 0$. To start the solution at $x = 0$, U was developed in a series of even powers of x and then introduced into equation (10) to permit a series development of y near $x = 0$. The numerical methods then took over, with U being supplied from the model integrations. The results of the integrations are given in Table 3 with an accuracy of one unit in the last place tabulated.

The electron-scattering model yields a value of $k_2 = 0.0284$, which corresponds to an effective polytropic index of 2.63. For the Kramers opacity model, $k_2 = 0.0146$, which corresponds to an effective polytropic index of 2.99.

TABLE 2

MODEL WITH KRAMERS' OPACITY

$\log (1/[x-1])$	$+\log q$	$\log t$	$\log p$	U	V	$n+1$
−1.05	0.0000	−1.67839	−4.4530	0.001301	51.936	4.250
−1.00	.0000	−1.62839	−4.2405	0.001835	46.750	4.250
−0.95	.0000	−1.57839	−4.0280	0.002581	42.128	4.250
−0.90	.0000	−1.52839	−3.8155	0.003626	38.007	4.250
−0.85	− .0001	−1.47839	−3.6030	0.005050	34.334	4.250
−0.80	− .0001	−1.42839	−3.3906	0.007018	31.063	4.250
−0.75	− .0001	−1.37840	−3.1781	0.009709	28.142	4.250
−0.70	− .0002	−1.32841	−2.9657	0.01336	25.539	4.249
−0.65	− .0003	−1.27843	−2.7533	0.01829	23.218	4.249
−0.60	− .0006	−1.22846	−2.5410	0.02489	21.147	4.248
−0.55	− .0009	−1.17851	−2.3288	0.03366	19.297	4.247
−0.50	− .0013	−1.12857	−2.1167	0.04520	17.642	4.246
−0.45	− .0020	−1.07868	−1.9049	0.06027	16.166	4.244
−0.40	− .0029	−1.02883	−1.6934	0.07975	14.841	4.242
−0.35	− .0043	−0.97906	−1.4824	0.1047	13.650	4.238
−0.30	− .0062	−0.92940	−1.2720	0.1362	12.578	4.233
−0.25	− .0089	−0.87988	−1.0626	0.1758	11.607	4.226
−0.20	− .0127	−0.83057	−0.8544	0.2246	10.724	4.217
−0.15	− .0178	−0.78153	−0.6479	0.2844	9.914	4.205
−0.10	− .0246	−0.73287	−0.4437	0.3565	9.166	4.188
−0.05	− .0337	−0.68470	−0.2424	0.4424	8.467	4.167
0.00	− .0457	−0.63717	−0.0450	0.5430	7.808	4.140
+0.05	− .0611	−0.59047	+0.1476	0.6591	7.180	4.106
+0.10	− .0808	−0.54478	+0.3342	0.7908	6.575	4.063
+0.15	− .1054	−0.50035	+0.5136	0.9373	5.989	4.009
+0.20	− .1359	−0.45740	+0.6845	1.0976	5.419	3.944
+0.25	− .1730	−0.41618	+0.8455	1.2686	4.864	3.866
+0.30	− .2173	−0.37694	+0.9954	1.4467	4.326	3.772
+0.35	− .2695	−0.33986	+1.1333	1.6278	3.808	3.662
+0.40	− .3300	−0.30510	+1.2585	1.8068	3.317	3.535
+0.45	− .3988	−0.27278	+1.3705	1.9788	2.857	3.391
+0.50	− .4760	−0.24292	+1.4694	2.1392	2.434	3.229
+0.55	− .5612	−0.21550	+1.5556	2.2843	2.052	3.052
+0.60	− .6540	−0.19044	+1.6297	2.4109	1.713	2.861
+0.65	− .7536	−0.16760	+1.6928	2.5170	1.418	2.660
+0.70	− .8594	−0.14681	+1.7460	2.6011	1.166	2.452
+0.75	−0.9702	−0.12790	+1.7904	2.6621	.952	2.242

TABLE 3

APSIDAL PERTURBATIONS FOR TWO MODELS

x	ELECTRON SCATTERING			KRAMERS' OPACITY		
	U	y	y'	U	y	y'
0.00	3.0000	1.0000	0.0000	3.0000	1.0000	0.0000
0.02	2.9963	1.0005	0.0528	2.9941	1.0008	0.0841
0.04	2.9852	1.0021	0.1059	2.9765	1.0034	0.1692
0.06	2.9668	1.0048	0.1599	2.9471	1.0076	0.2563
0.08	2.9410	1.0085	0.2150	2.9062	1.0136	0.3462
0.10	2.9080	1.0134	0.2715	2.8539	1.0215	0.4398
0.12	2.8678	1.0194	0.3299	2.7903	1.0313	0.5376
0.14	2.8205	1.0266	0.3903	2.7158	1.0430	0.6409
0.16	2.7663	1.0350	0.4532	2.6305	1.0569	0.7522
0.18	2.7052	1.0447	0.5190	2.5329	1.0732	0.8731
0.20	2.6374	1.0558	0.5890	2.4158	1.0920	1.010
0.22	2.5631	1.0683	0.6635	2.2835	1.1138	1.171
0.24	2.4824	1.0824	0.7425	2.1410	1.1390	1.356
0.26	2.3955	1.0981	0.8270	1.9931	1.1682	1.562
0.28	2.3025	1.1155	0.9180	1.8426	1.2016	1.790
0.30	2.2004	1.1348	1.018	1.6924	1.2399	2.039
0.32	2.0864	1.1563	1.128	1.5460	1.2834	2.311
0.34	1.9628	1.1801	1.254	1.4039	1.3325	2.604
0.36	1.8346	1.2066	1.396	1.2686	1.3877	2.922
0.38	1.7028	1.2360	1.554	1.1398	1.4495	3.264
0.40	1.5704	1.2688	1.728	1.0194	1.5184	3.633
0.42	1.4408	1.3052	1.918	0.9075	1.5950	4.028
0.44	1.3108	1.3456	2.125	0.8040	1.6797	4.450
0.46	1.1870	1.3904	2.350	0.7090	1.7732	4.902
0.48	1.0682	1.4398	2.593	0.6220	1.8760	5.382
0.50	0.9555	1.4942	2.854	0.5430	1.9886	5.893
0.52	0.8495	1.5541	3.134	0.4714	2.1119	6.434
0.54	0.7507	1.6197	3.433	0.4070	2.2462	7.006
0.56	0.6591	1.6915	3.752	0.3492	2.3923	7.609
0.58	0.5743	1.7699	4.090	0.2976	2.5508	8.244
0.60	0.4965	1.8552	4.448	0.2518	2.7223	8.910
0.62	0.4263	1.9480	4.828	0.2114	2.9074	9.607
0.64	0.3624	2.0485	5.226	0.1758	3.1068	10.336
0.66	0.3056	2.1572	5.646	0.1449	3.3210	11.094
0.68	0.2546	2.2744	6.085	0.1180	3.5507	11.882
0.70	0.2099	2.4007	6.544	0.09505	3.7965	12.699
0.72	0.1708	2.5363	7.022	0.07537	4.0589	13.544
0.74	0.1364	2.6817	7.518	0.05881	4.3384	14.417
0.76	0.1075	2.8377	8.032	0.04504	4.6358	15.317
0.78	0.08283	3.0036	8.564	0.03372	4.9513	16.242
0.80	0.06219	3.1803	9.112	0.02457	5.2856	17.192
0.82	0.04533	3.3682	9.674	0.01735	5.6391	18.165
0.84	0.03185	3.5674	10.252	0.01175	6.0123	19.162
0.86	0.02130	3.7784	10.844	0.007570	6.4057	20.181
0.88	0.01341	4.0012	11.448	0.004564	6.8197	21.221
0.90	0.007779	4.2364	12.064	0.002508	7.2547	22.282
0.92	0.003977	4.4839	12.692	0.001208	7.7111	23.364
0.94	0.001678	4.7441	13.330	0.000472	8.1894	24.465
0.96	0.000497	5.0172	13.978	0.000126	8.6899	25.587
0.98	0.000062	5.3033	14.636	0.000013	9.2130	26.728
1.00	0.000000	5.6026	15.304	0.000000	9.7591	27.889

IV. SUMMARY

A comparison of the two models shows the electron-scattering opacity to give rise to larger cores, thus allowing a greater portion of the star to act like a polytrope of index $n = 1.5$, and hence strongly reducing the effective polytropic index of the whole star. The low effective polytropic index for the pure electron-scattering model ($n = 2.6$) suggests that electron scattering does play some part in producing the relatively low value of $n \approx 3.0$ for the early B stars. That, in fact, electron scattering is effective in these stars can be seen by computing the opacity due to the two mechanisms at different points in an early B-type binary, such as GL Carinae. Letting $M = 8.5\ M_{\odot}$, $R = 5.25\ R_{\odot}$, $X = 0.90$, and $Y = 0.08$, it can be computed from the electron-scattering model that $\kappa_e = 0.361$ cm²/gm throughout the envelope, while at the fitting point and at $x = 0.5$ and $x = 0.75$, $\kappa_k = 0.211$, 0.538, and 1.031 cm²/gm, respectively. This suggests that, whereas the Kramers absorption is dominant in the outer layers of the envelope, near the core electron scattering must play a substantial role in the total opacity.

By applying the present models to GL Carinae, it may be verified that assumptions 1 and 2 of Section II are fair first approximations for early B-type stars, though the radiation pressure may approach 20 per cent of the gas pressure at the center, which will have to be taken account of in more accurate computations.

The relatively low value of $n = 3.0$ for the Kramers opacity model serves to emphasize that Kramers absorption, without regard for the guillotine factor, is not a satisfactory representation of the absorption in A-type main-sequence stars ($n \approx 3.7$).

The authors would like to thank Dr. Martin Schwarzschild for his advice and suggestions and Mr. John N. Pike for pointing out a numerical error in their original computations.

REFERENCES

Gardiner, J. G. 1951, *M.N.*, **111**, 94.
Keller, G. 1948, *Ap. J.*, **108**, 347.
Keller, G., and Limber, D. N. 1951, *Ap. J.*, **113**, 637.
Sterne, T. E. 1939, *M.N.*, **99**, 451.
Van Wijk, U., Rogerson, J. B., and Skumanich, A. 1954, *A.J.*, **59** (in press).

INHOMOGENEOUS STELLAR MODELS. IV. MODELS WITH CONTINUOUSLY VARYING CHEMICAL COMPOSITION*

R. HÄRM AND M. SCHWARZSCHILD
Princeton University Observatory

Received November 3, 1954

ABSTRACT

Nine sample models are constructed in which the mean molecular weight varies from the center to the surface by a factor of 2.5 and in which this variation occurs continuously inside an intermediate zone. These models are compared with simpler models in which the same composition variation occurs discontinuously at an interface. The comparison shows that the simpler, discontinuous models may be used to compute the luminosity with satisfactory accuracy but that they tend to exaggerate the radii—in certain cases by an order of magnitude.

I. INTRODUCTION

In recent investigations about the internal structure of red giants, several series of stellar models have been constructed with inhomogeneities in the chemical composition. In nearly all cases these inhomogeneities were represented by an abrupt change of the composition at one particular place in the stellar interior, so that the models derived consisted of a homogeneous interior and a homogeneous envelope with a discontinuous change in the molecular weight at the interface. On the other hand, in real stars any inhomogeneities would presumably occur without sharp discontinuities. Thus the question arises how far models with continuous variation of composition might differ from those in which the inhomogeneity is limited to one discontinuous jump.

In an attempt to answer this question, nine sample models with continuously varying molecular weight have been constructed. Each of these models consists of three parts—a homogeneous envelope, with the molecular weight μ_e; a homogeneous core, with the molecular weight μ_i; and an intermediate zone in which the molecular weight varies continuously from μ_i at the inner interface to μ_e at the outer interface. For the ratio of μ_i to μ_e, the large value of 2.5 was used here throughout, in order to make the effects looked for as large as possible. Finally, the variation of the composition in the intermediate zone was arbitrarily chosen so that the molecular weight changes proportional to M_r (see eq. [11]). The nine models thus selected are obviously only a feeble sample of all the possible models with continuously varying composition. It is nevertheless hoped that the results obtained with these sample models can be generalized with some assurance.

II. ASSUMPTIONS AND BASIC EQUATIONS

The following simplifying assumptions have been used for the computations: (*a*) The variation of the chemical composition affects only the hydrogen and helium content; the fraction Z of the heavy elements is constant throughout the star. (*b*) The absorption coefficient follows Kramers' law with a constant guillotine factor. (*c*) Radiation pressure and degeneracy are negligible. (*d*) In the first four models, which have convective cores, the entire energy generation occurs within the convective core. (*e*) In the last five models, which have isothermal cores, the entire energy generation occurs within an infinitely thin shell at the boundary of the core.

For the present purpose it does not appear too important whether the foregoing assumptions closely approximate real stars. It will, however, be important that these

---

* This research was supported in part by funds of the Eugene Higgins Trust allocated to Princeton University and in part by contract with the Office of Naval Research.

models with continuously varying composition be compared only with such discontinuous models as were computed under the same physical assumptions. The computations have been carried out with the help of the following definition and equations:

Nomenclature, equations, etc.

Identical with equations (1)–(9) in Paper I of this series (Oke and Schwarzschild 1952). (1)–(9)

Here, however, $\alpha = 0$ throughout.

Emden variables for isothermal core

$$t = \text{Const.} = t_e\,, \qquad p = e^{-\psi_e} p_e\,, \qquad x = \xi\,\frac{x_1}{\xi_1}\,. \tag{10}$$

Composition variation in intermediate zone

$$l = \left(\frac{q}{q_2}\right)^{-\nu}, \qquad j = l^{0.30}\,. \tag{11}$$

Logarithmic variables for intermediate zone

$$\lambda = \log\frac{p}{p_0}, \qquad \tau = \log\frac{t}{t_0}, \qquad \psi = \log\frac{q}{q_0}, \qquad y = \log\frac{x}{x_0}, \tag{12}$$

with

$$q_2^{\nu}\,\frac{q_0^{1-\nu}}{x_0 t_0} = 1\,, \qquad q_2^{\nu}\,\frac{p_0 x_0^3}{q_0^{1+\nu} t_0} = 1, \qquad q_2^{1.3\nu} C\,\frac{q_0^{-1.3\nu} p_0^2}{x_0 t_0^{9.5}} = 1\,, \qquad x_0 = x_1\,. \tag{13}$$

Basic equations in logarithmic variables

$$\begin{aligned}
\log\left(-\frac{d\lambda}{dy}\right) &= -\tau + (1-\nu)\,\psi - y && [= \log V]\,,\\
\log\left(-\frac{d\tau}{dy}\right) &= +2\lambda - 9.5\tau - 1.3\nu\psi - y && \left[= \log\frac{V}{n+1}\right],\\
\log\left(+\frac{d\psi}{dy}\right) &= +\lambda - \tau - (1+\nu)\,\psi + 3y && [= \log U]\,.
\end{aligned} \tag{14}$$

Fitting condition at outer interface

$$U,\ V, \text{ and } (n+1) \text{ continuous}\,. \tag{15}$$

Fitting condition at inner interface

For all models: U and V continuous, (16)

For models with isothermal core: no fitting condition for $(n + 1)$, (17)

For models with convective core: $(n + 1)$ continuous and equal to 2.5 . (18)

The last of the foregoing conditions may be derived as follows: For a layer in which the molecular weight varies with height, one finds, by the usual perturbation arguments, the condition for stability against convection to be

$$\left(-\frac{1}{T}\frac{dT}{dr}\right) < \frac{\gamma-1}{\gamma}\left(-\frac{1}{p}\frac{dP}{dr}\right) + \left(-\frac{1}{\mu}\frac{d\mu}{dr}\right). \tag{19}$$

In the derivation of this condition, it is assumed that the molecular weight of a given element of matter does not vary as a consequence of pressure or temperature variations, an assumption valid in the deep interior. If the molecular weight decreases with height, as is the case in the present models, condition (19) is much less stringent for the temperature gradient then the usual stability condition,

$$\left(-\frac{1}{T}\frac{dT}{dr}\right)<\frac{\gamma-1}{\gamma}\left(-\frac{1}{p}\frac{dP}{dr}\right). \tag{20}$$

This is understandable because the temperature gradient, to cause instability under the conditions here considered, would have to be appreciably steeper than the adiabatic temperature gradient, to overcome the greater average weight of the particles at the bottom of the zone as compared with those at the top of the zone. Nevertheless, it appears unlikely that the fulfilment of the weak condition (19) suffices for stability. If a layer fulfils condition (19) but not the stronger condition (20), one may—assuming energy to be available—introduce a perturbation which, in a given volume element, completely mixes up the material and thus, in this volume element, eliminates the gradient of μ. Now, because equation (20) is not fulfilled, the interior of the element will be unstable against turbulent motions of subelements. This turbulence would presumably eat into the neighboring region and thus eventually turn the entire zone from a layer in radiative equilibrium with a μ-gradient into a layer in convective equilibrium with a constant μ. Hence it appears fairly certain that the usual condition (20) must be fulfilled for stability against convection, even in zones in which the molecular weight decreases with height.

In the particular case here under consideration, the foregoing argument seems very certain. If condition (19) were to be employed in the intermediate zone, so that, at the inner boundary of this zone, just the equal sign would hold in this equation, then the temperature gradient would have to drop at the interface from the value given by this equation to the value given by condition (20) in the convective core. This finite drop of the temperature gradient would produce a finite drop of the radiative flux. To compensate for this drop, the convective flux in the core would have to be finite to the very limit of the core. Up to the core surface, therefore, the turbulence, in Öpik's terms, would be active and hence would be sure to eat into the neighboring intermediate zone, eliminate its μ-gradient by mixing, and thus make the zone unstable. Hence it seems certain that the stronger condition (20) must be fulfilled in the intermediate zone, from which follows the fitting condition (18).

III. CONSTRUCTION OF MODELS

To construct the models here considered, numerical solutions were needed for all three portions—the envelopes, the intermediate zones, and the cores. For the envelopes, the one-parameter family of solutions (characterized by the parameter C) was available, since it had already been used in the preceding papers of this series. Similarly, for the cores, the unique solution for a convective core (for models 1–4) and the unique solution for a nondegenerate isothermal core (for models 5–9) are available in tabular form (Comrie 1932; Wares and Chandrasekhar 1949). Only for the intermediate zone with continuously varying composition, did new numerical integrations have to be computed. These numerical integrations were performed in terms of the logarithmic variables according to definitions (12) with the basic equations (14). For each model, a definite value of ν was arbitrarily chosen which fixed the rate of change of the molecular weight in the intermediate zone according to equation (11).

The numerical integrations for the intermediate zone of each of the first four models were started at the edge of the convective core and at the end were fitted to the inner boundary of the envelope as follows. A trial value was chosen for ξ_1 which represents the termination point of the convective core. At this point the values of U_1 and V_1 were read from the tabulation of the core solution. These two values, together with $(n+1)_1 = 2.5$, give, according to the bracketed expressions in equations (14), three conditions for the four starting values λ_1, τ_1, ψ_1, and y_1. Since, in addition, $y_1 = 0$ according to the last equation (13), all the starting values can be determined from these relations, and a unique solution for every trial value of ξ_1 can be obtained by numerical integration outward. Each integration was terminated when the change in ψ, i.e., in q, corresponded to a change in l, according to equation (11), of exactly a factor of 2.5. Thus such an integration represented a zone in which the molecular weight decreased by a factor of 2.5. At the end-point, sharply defined by this condition, the values of U_2, V_2, and $(n+1)_2$ were read from the integration. These values had to be fitted to the envelope solutions according to condition (15). Since the one-parameter family of envelope solutions covers the U–V plane, one can determine by graphical interpolation the value of $(n+1)$ given by the envelope solutions for the point U_2, V_2, representing the end-point of the intermediate zone integration. In general, the value of $(n+1)$ thus obtained from the envelopes will differ from the value reached at the end of the intermediate zone integration. However, by changing the trial value for ξ_1 and reintegrating, a value of ξ_1 could be determined for each model such that the corresponding integration gave a terminal value of $(n+1)$ in agreement with the value from the envelope solutions for the same U, V point. This completed the fitting of the entire model.

Exactly the same method of integrating and fitting here described for the models with convective cores was also used for the models with isothermal cores, but with one change. According to equation (17), the polytropic index at the start of the intermediate zone at the inner interface is free for models with isothermal cores. This extra freedom arises physically from the circumstance that the core for models with convective cores is determined in size and mass by the equilibrium conditions, whereas for models with isothermal cores the past evolution rather than the equilibrium conditions determines the size of the core. Each model with an isothermal core is then characterized by two arbitrary parameters, for which we may choose ν as before and ξ_1, which gives the termination point of the core. Now $(n+1)_1$ is used as eigen parameter which has to be determined by trial and error to fulfil the fitting conditions at the outer interface.

The characteristics thus obtained are listed in Table 1 for the models with convective cores and in Table 2 for the models with isothermal cores. The cores and intermediate zones of all these models are represented in Figure 1 in terms of the U–V plane.

It may be noted that in all the models here computed the fraction of the mass contained in the core is rather small (q_1 at most 13 per cent) but that the mass fraction contained in the inhomogeneous intermediate zones varies greatly from model to model ($q_2 - q_1$ ranging from 9 to 70 per cent).

IV. COMPARISON WITH DISCONTINUOUS MODELS

The hydrogen content of the present model varies continuously from a high value in the envelope to a low value in the core. These continuous models are to be compared with discontinuous models in which the hydrogen content jumps discontinuously from a high and constant value in the outer parts to a low and constant value in the inner parts. Each continuous model should be compared with a discontinuous model which has the same over-all hydrogen content (the heavy-element content, Z, is here taken constant throughout each model as well as from model to model). It is therefore necessary to compute, first, the over-all or mean hydrogen content, which is given by

$$X_m = \int_0^1 X\,d\,q\,. \tag{21}$$

The quadrature can be performed for the present continuous models with the help of equations (4) and (11). The result is

$$X_m = X_e - \frac{\nu}{1+\nu} \frac{4}{5} \left(\frac{q_2}{\mu_e} - \frac{q_1}{\mu_i} \right). \tag{22}$$

If we define the over-all mean molecular weight of a star as that mean molecular weight which corresponds to the over-all hydrogen content, we obtain, from equation (22),

$$\frac{\mu_e}{\mu_m} = 1 - \frac{\nu}{1+\nu} \left(q_2 - \frac{\mu_e}{\mu_i} q_1 \right). \tag{23}$$

TABLE 1

CHARACTERISTICS OF MODELS WITH CONVECTIVE CORES

	I	II	III	IV
ν	1.0	0.5	0.4	0.38
ξ_1	1.422	1.319	1.294	1.290
U_1	2.412	2.493	2.511	2.514
V_1	1.764	1.506	1.448	1.436
$(n+1)_1$	2.500	2.500	2.500	2.500
U_2	1.230	1.081	0.687	0.504
V_2	1.378	2.493	3.857	4.561
$(n+1)_2$	3.014	3.572	3.947	4.059
$\log C$	−5.55	−5.18	−4.75	−4.60
$\log x_2$	−0.992	−0.860	−0.729	−0.646
$\log q_2$	−0.815	−0.438	−0.188	−0.114
$\log t_2$	+0.038	+0.025	−0.045	−0.127
$\log p_2$	+2.289	+2.200	+1.791	+1.400
$\log x_1$	−1.244	−1.379	−1.469	−1.487
$\log q_1$	−1.213	−1.234	−1.183	−1.161
$\log t_1$	+0.183	+0.365	+0.524	+0.566
$\log p_1$	+2.688	+3.267	+3.752	+3.870
$\log t_c$	+0.332	+0.493	+0.647	+0.689
$\log p_c$	+3.060	+3.587	+4.060	+4.178
$q_1 = M_1/M$	0.0612	0.0583	0.0656	0.0690
$q_2 = M_2/M$	0.153	0.365	0.649	0.769
q_d	0.107	0.190	0.297	0.340
μ_e/μ_m	0.936	0.886	0.822	0.796

Similarly, for a discontinuous comparison model, in which the composition jump occurs at a mass fraction q_d, the over-all hydrogen content is given by

$$X_m = X_e (1 - q_d) + X_i q_d . \tag{24}$$

If one now equates that over-all hydrogen content of a continuous model as given by equation (22) with that of a discontinuous model as given by equation (24), one obtains

$$q_d = \frac{\nu}{1+\nu} \left(\frac{\mu_i}{\mu_i - \mu_e} q_2 - \frac{\mu_e}{\mu_i - \mu_e} q_1 \right). \tag{25}$$

This relation gives the q_d-value, which a discontinuous comparison model must have, in terms of the characteristics of the continuous model. The values of q_d according to equation (25) and of μ_e/μ_m according to equation (23) for the present nine models are given in the last two lines of Tables 1 and 2.

Discontinuous models with convective cores exactly equivalent to the first four of the present continuous models have been given by Oke and Schwarzschild (1952). Interpolation into their Table 1 according to the q_d-values given at the foot of the present Table 1 (with q_d being equivalent to their q_2) gives exactly the needed comparison models. No discontinuous comparison models were available for the present continuous models with isothermal cores. Therefore, discontinuous comparison models were here computed for the rather extreme cases VII and IX of Table 2. The two comparison models were adjusted to models VII and IX, respectively, according to the q_d-values, insuring equality in total hydrogen content, and the q_1-values, insuring equality in the mass fraction contained in the isothermal core.

TABLE 2

CHARACTERISTICS OF MODELS WITH ISOTHERMAL CORES

	V	VI	VII	VIII	IX
ν	1.0	0.5	0.49	0.50	0.42
ξ_1	9.0	9.0	9.0	25.0	25.0
U_1	1.000	1.000	1.000	0.794	0.795
V_1	2.518	2.517	2.517	2.161	2.161
$(n+1)_1$	3.402	3.510	3.512	3.488	3.506
U_2	0.831	0.310	0.227	0.807	0.444
V_2	1.677	4.182	4.648	2.683	4.038
$(n+1)_2$	3.379	4.111	4.160	3.730	4.051
log C	−5.30	−3.78	−3.66	−4.83	−4.18
log x_2	−1.101	−0.879	−0.769	−0.960	−0.817
log q_2	−0.732	−0.106	−0.068	−0.389	−0.136
log t_2	+0.145	+0.151	+0.033	+0.143	+0.075
log p_2	+2.636	+2.173	+1.628	+2.541	+2.038
log x_1	−1.574	−2.139	−2.145	−1.881	−2.069
log q_1	−1.130	−0.902	−0.880	−1.185	−1.083
log t_1	+0.441	+1.233	+1.262	+0.760	+1.049
log p_1	+3.637	+6.350	+6.420	+4.719	+5.677
log t_c	+0.441	+1.233	+1.262	+0.760	+1.049
log p_c	+5.145	+7.858	+7.928	+7.280	+8.238
$q_1=M_1/M$	0.0741	0.125	0.132	0.0653	0.0826
$q_2=M_2/M$	0.185	0.783	0.855	0.408	0.731
q_d	0.129	0.407	0.440	0.212	0.344
μ_e/μ_m	0.922	0.756	0.736	0.873	0.794

Among all the characteristics in terms of which the continuous and discontinuous models may be compared, the two most directly related to observations are the luminosity and the radius. The luminosity may be computed from equation (7), which gives

$$L=\left[\frac{4ac}{3}(4\pi)^3\left(\frac{HG}{k}\right)^7\right]\left[M^5\mu_m^7\,\frac{(t/\bar{g})_0}{\kappa_{0m}}\,T_c^{1/2}\right]\left[\frac{C}{t_c^{1/2}}\left(\frac{\mu_e}{\mu_m}\right)^{7.7}\right]. \tag{26}$$

Here the first bracket contains only universal constants. The second bracket contains the mass and central temperature of the star and its over-all composition, which affects both the mean molecular weight and the constant in the opacity law. The last bracket contains the relevant nondimensional characteristics of the models in which the continuous models may differ from the discontinuous ones. The radius may be computed by applying the second of equations (3) to the center of the star, which gives

$$R=\left[\frac{HG}{k}\right]\left[\frac{M\mu_m}{T_c}\right]\left[t_c\,\frac{\mu_e}{\mu_m}\right]. \tag{27}$$

Here the three brackets have the same characteristics as those in equation (26). The last brackets of equations (26) and (27), which give the dependence of the luminosity and radius on the stellar model, are listed in Table 3 for all the models here considered.

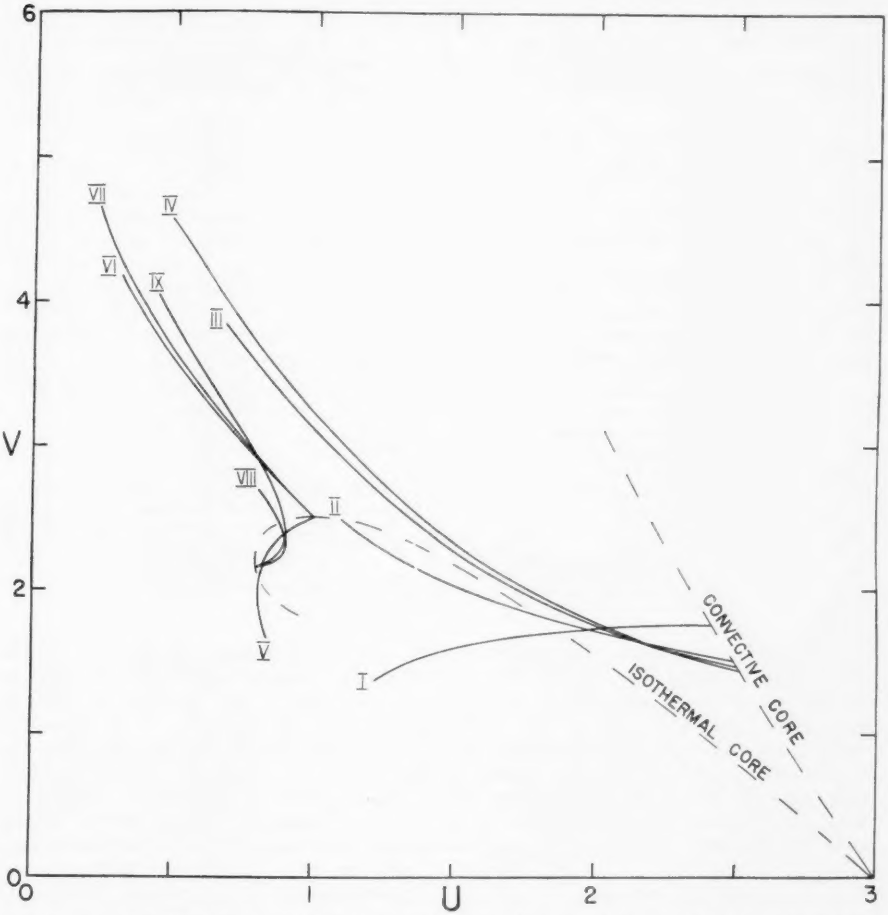

FIG. 1.—Representation of models in terms of the homology invariants U and V. The intermediate zones of models I–IV start at the convective core, those of models V–IX at the isothermal core. The envelopes are not shown.

V. RESULTS

Consider a star of a given mass, central temperature, and over-all chemical composition. The second column of Table 3 gives for such a star substantially the logarithm of the luminosity in its dependence on the model, i.e., on the distribution of the hydrogen content throughout the star. The table shows that the present continuous models differ in luminosity from the equivalent discontinuous models only little. In fact, even the extreme cases IV and VII, in which the variation of the composition is spread over 70 per cent of the stellar mass, differ from the discontinuous models only by 0.11 in the logarithm of the luminosity or 0.28 in bolometric magnitude. We may then conclude that we can compute the luminosity of a chemically inhomogeneous star with good accuracy by idealizing the inhomogeneity in terms of a discontinuous jump in composition, if we place the discontinuity so that the over-all composition remains unchanged.

TABLE 3*

COMPARISON OF CONTINUOUS AND DISCONTINUOUS MODELS

Model	log $C/t_c^{1/2}(\mu_e/\mu_m)^{7.7}$	log $(t_e\ \mu_e/\mu_m)$
I cont. model	−5.93	+0.30
discont. compar.	−5.90	+0.30
II cont. model	−5.82	+0.44
discont. compar.	−5.80	+0.54
III cont. model	−5.73	+0.56
discont. compar.	−5.66	+0.87
IV cont. model	−5.70	+0.59
discont. compar.	−5.59	+1.02
V cont. model	−5.79	+0.40
VI cont. model	−5.34	+1.11
VII cont. model	−5.31	+1.13
discont. compar.	−5.20	+5.22
VIII cont. model	−5.66	+0.70
IX cont. model	−5.47	+0.95
discont. compar.	−5.45	+2.26
Cowling model	−5.97	−0.05

* For stars of the same mass, central temperature, and mean hydrogen content, but with different distributions of the hydrogen through the interior, luminosities and radii are proportional to the antilogs of the first and second tabulated quantities, respectively.

An even rougher idealization appears permitted if only an approximate value of the luminosity is needed. The last line of Table 3 gives the relevant material for the Cowling model, which has a completely homogeneous composition but is otherwise exactly equivalent to all the models here considered (Härm and Rogerson, 1955). Consider again stars with a given mass, central temperature, and over-all composition. Then the second column of Table 3 shows that all the inhomogeneous models give higher luminosities than the homogeneous Cowling model. The differences, in terms of bolometric magnitude, however, generally amount to less than 1 mag. and do not exceed 2 mag. even in the most extreme cases among the samples here considered. These differences—though not negligible in accurate computations—are only a moderate fraction of the 5–7 mag. by which the star will brighten up during its evolution because of the increase in over-all molecular weight caused by the nuclear transmutations. Thus one sees again that the luminosity of a star is greatly affected by the over-all composition (second bracket in eq. [26]) but depends relatively little on the distribution of the composition throughout the star, i.e., on the model (last bracket in eq. [26]), as was emphasized long ago by Eddington.

The last column of Table 3 gives the logarithm of the radius in its dependence on the model. Comparing, first, all the inhomogeneous models with the homogeneous Cowling model, one sees again the well-known effect that chemical inhomogeneities (with a mean molecular weight decreasing outward) tend to enlarge the stellar radius, often by big factors. A homogeneous model can obviously not be used to compute the radius of a distinctly inhomogeneous star.

Finally, one may compare in Table 3 the radii of the present models of continuously varying composition with those of the discontinuous models. It is seen that the simpler discontinuous models well represent the tendency of inhomogeneous stars to have increased radii; and even the amount of the increase is represented by the discontinuous models with some accuracy as long as this increase over the Cowling model is not more than a factor of 3. For the more extended stars, however, the discontinuous models appear to exaggerate the radius. In fact, for extreme cases like the present model VII, in which the inhomogeneity is spread over 70 per cent of the stellar mass, the equivalent discontinuous model cannot be used for the computation of the radius in any approximation.

In summarizing the results regarding the radius, one may conclude from the present sample of models that the radius of a star depends delicately on the variation of the chemical composition throughout the star, i.e., on the model (third bracket of eq. [27]), while it depends only moderately on the over-all composition (second bracket of eq. [27]). This has two consequences. First, the observed radius of the star can be used for the determination of the over-all composition of the star only if the star is sufficiently young that the nuclear processes cannot yet have produced large inhomogeneities. Second, for inhomogeneous stars the variation of the composition throughout the interior has to be determined in fair detail by considerations of the evolution, before the radius can be computed with sufficient accuracy to warrant comparison with observed radii or effective temperatures.

REFERENCES

Comrie, L. J. 1932, *British A. Adv. Sci. Math Tables*, Vol. **2**.
Härm, R., and Rogerson, J. 1955, *Ap. J.*, **121**, 439.
Oke, J. B., and Schwarzschild, M. 1952, *Ap. J.*, **116**, 317.
Wares, G. W., and Chandrasekhar, S. 1949, *Ap. J.*, **109**, 551.

THE SPECTRUM-LUMINOSITY DIAGRAM FOR NGC 752*

NANCY G. ROMAN
Yerkes and McDonald Observatories

Received October 1, 1954; revised November 4, 1954

ABSTRACT

Spectra of 52 members of the galactic cluster NGC 752 have been classified. The main sequence in the cluster is observed from F2 to G0. In addition, there are one A0 dwarf, numerous subgiants of types F2–F6, and eight red giants. Spectroscopically, the stars belong to the weak-line group observed among the bright stars near the sun but do not resemble the extreme high-velocity stars or the globular cluster giants. The distance modulus derived for the cluster is 8.2 mag. corresponding to a distance of 435 parsecs. A comparison of the observed H-R diagram with theoretical H-R diagrams computed on the basis of the generalized Cowling model indicates a minimum age of about 1.5×10^9 years for the cluster.

The galactic cluster NGC 752 is particularly interesting because of its unusual H-R diagram. According to Trumpler (1930), the dwarf branch starts at F0, as compared to A3 for the latest of the other clusters in his catalogue. Thus this cluster plays an important role in discussions of stellar evolution. In addition, since, as in other galactic clusters, there is an appreciable range in luminosity among the stars at the early edge of the main sequence, this cluster provides an excellent set of F-type standard stars somewhat above the main sequence.

Ebbighausen (1939) measured the proper motions of all the stars in the region brighter than 14.0 mag. He divided these into five groups: (1) stars which have a high probability of being cluster members; (2) stars for which the probability is lower but which have a reasonable chance of being members; (3) stars which are probably not members; (4) stars which are definitely not members; (5) fainter stars whose proper motions are less accurate. Johnson (1953) published photoelectric colors and magnitudes on the B, V, U system for 94 of these stars. Among the latter, all the stars in Ebbighausen's classes 1 and 2 and one star in his class 5 (No. 157) were observed spectroscopically with the 110-mm camera on the Cassegrain spectrograph attached to the McDonald 82-inch telescope.

The large number of stars between spectral types F2 and F5 permits an intercomparison of these stars and a separation into five groups according to the increasing strength and development of the G band and the increasing weakness of the hydrogen lines. Since the colors seem to indicate that, at least systematically, this separation is significant, type F3 and the division of type F5 into two groups are retained. The faintest stars in each class are dwarfs; the brighter ones are class IV stars, with the exception of No. 108 at F5, which is closer to class III. Table 1 summarizes the data for the various spectral types; the F3 stars are included at F4, and the G7 and G9 giants are combined at G8 III. The table contains, for each spectral type, the number of stars presumed to be of the indicated luminosity class, their mean visual magnitude, the derived distance modulus, the mean observed and predicted blue-yellow color for all stars in each spectral type, and the mean observed and predicted ultraviolet-blue color for the main-sequence stars and the red giants (Johnson 1953; Johnson and Morgan 1953). The average of the distance moduli is 8.24, as is the mean for the F5–G0 stars for which the calibration is probably best determined. A comparison of the observed and predicted $B-V$ colors for the F-type stars indicates a reddening of about 0.024 mag. or a total visual absorption of about 0.07 mag. Thus the true distance modulus of the cluster is probably near 8.2 mag., corresponding to a parallax of 0".0023 and a distance of 435 parsecs. This table also shows the

---

* *Contributions from the McDonald Observatory, University of Texas*, No. 249.

small ultraviolet excess noticed by Johnson for the F dwarfs and apparently also present in the late-type giants.

Table 2 lists the observational data for the individual stars in the cluster. The columns contain, in order, the number of the star in Heinemann's catalogue (1926), the visual magnitude and two colors according to Johnson (1953), the spectral type on the MK system, and the absolute magnitude of the star based on the distance modulus 8.2 for the

TABLE 1

SUMMARY OF DATA

Type	No.	V	m − M	$(B-V)_{\rm obs}$	$(B-V)_{\rm pred}$	$(U-B)_{\rm obs}$	$(U-B)_{\rm pred}$
F2 V	3	10.9	+7.7	+0.39	+0.37	+0.01	0.00
F4 V	4	11.2	+7.9	+0.42	+0.40	− .03	.00
F5 V	6	11.5	+8.2	+0.46	+0.44	− .03	.00
F8 V	1	12.3	+8.4	+0.62	+0.53	+ .02	+ .02
G0 V	1	12.6	+8.3	+0.60	+0.60	− .04	+ .06
G8 III	2	9.1	+9.1	+0.90	+0.95	+ .55	+ .72
K0 III	5	9.2	+8.5	+1.00	+1.01	+0.76	+0.86

TABLE 2

OBSERVATIONAL DATA

Heinemann	V	$B-V$	$U-B$	Sp. Type	M_v
209	9.70	+0.05	−0.01	A0	+1.5
193	10.17	+ .39	+ .09	F2	+2.0
196	10.24	+ .42	+ .04	F2	+2.0
96	10.35	+ .38	+ .06	F2	+2.2
254	10.90	+ .39	+ .01	F2	+2.7
263	10.91	+ .38	+ .02	F2	+2.7
222	10.94	+ .38	.00	F2	+2.7
300	9.58	+ .41	+ .02	F3	+1.4
61	10.02	+ .40	+ .04	F3	+1.8
126	10.08	+ .43	+ .04	F3	+1.9
105	10.22	+ .42	+ .06	F3	+2.0
219	10.52	+ .41	.00	F3	+2.3
74	10.73	+ .42	+ .01	F3	+2.5
189	11.26	+ .42	− .03	F3	+3.1
205	9.88	+ .42	+ .01	F4	+1.7
238	9.95	+ .45	+ .04	F4	+1.8
171	10.16	+ .44	+ .05	F4	+2.0
187	10.41	+ .42	.00	F4	+2.2
217	10.41	+ .43	+ .04	F4	+2.2
214	10.44	+ .38	+ .04	F4	+2.2
58	10.46	+ .40	+ .02	F4	+2.3
64	10.52	+ .38	+ .04	F4	+2.3
62	11.19	+ .42	− .04	F4	+3.0
135	11.20	+ .45	− .02	F4	+3.0
266	11.21	+ .43	− .03	F4	+3.0
108	9.14	+ .45	+ .07	F5	+0.9
41	9.80	+ .49	+ .07	F5	+1.6
206	10.01	+0.47	+0.05	F5	+1.8
10	10.12	+0.42	+0.02	F5	+1.9
117	10.23	+0.44	+ .05	F5	+2.0
234	10.66	+0.43	.00	F5	+2.5
259	11.38	+0.44	− .03	F5	+3.2
235	11.43	+0.48	− .04	F5	+3.2
197	11.58	+0.45	− .05	F5	+3.4
12	9.91	+0.48	+ .03	F5	+1.7
69	10.04	+0.51	+ .10	F5	+1.8
218	10.06	+0.46	+ .04	F5	+1.9
177	10.15	+0.48	+ .04	F5	+2.0
66	10.89	+0.45	− .04	F5	+2.7
55	11.40	+0.44	− .02	F5	+3.2
139	11.72	+0.47	− .05	F5	+3.5
88	11.73	+0.49	− .02	F5	+3.5
261	11.14	+0.49	− .03	F6	+2.9
237	12.31	+0.62	+ .02	F8	+4.1
157	12.56	+0.60	− .04	G0	+4.4
110	8.94	+0.84	+ .45	G7 III	+0.7
295	9.29	+0.96	+ .66	G9 III	+1.1
75	8.95	+1.01	+ .77	K0 III	+0.8
213	9.01	+0.99	+ .74	K0 III	+0.8
311	9.04	+1.03	+ .82	K0 III	+0.8
77	9.35	+1.02	+ .79	K0 III	+1.2
1	9.47	+0.96	+ .67	K0 III	+1.3
186	10.19	+0.94	+ .59	K0 III–IV	+2.0
208	8.94	+1.08	+0.83	K1 IV	+0.7

cluster. The increase in the $U-B$ color with increasing luminosity, noticed by Johnson (1953), is clearly evident. The H-R diagram of the cluster is illustrated in Figure 1. Particular attention should be called to two stars on this diagram. The A0 star may be an interloper, although its spectroscopic parallax and proper motion are consistent with cluster membership. In addition, according to Trumpler (private communication), the radial velocity of the star agrees well with the mean for the cluster. As the space motion of the cluster is small, the agreement of the motions is not conclusive but does seem to make membership in the cluster highly probable. If velocity is not considered, there is about a 10 per cent chance that an early A-type star would be found within a half-magnitude of this star and within the circle 25′ in radius encompassing the cluster. Unlike such clusters as the Hyades, in which the yellow giants form a compact group, in this cluster star No. 186 lies 1 mag. below the other stars at K0. Since it shows its faintness spectroscopically as well as photometrically, there is no reason to assume that it is not a member.

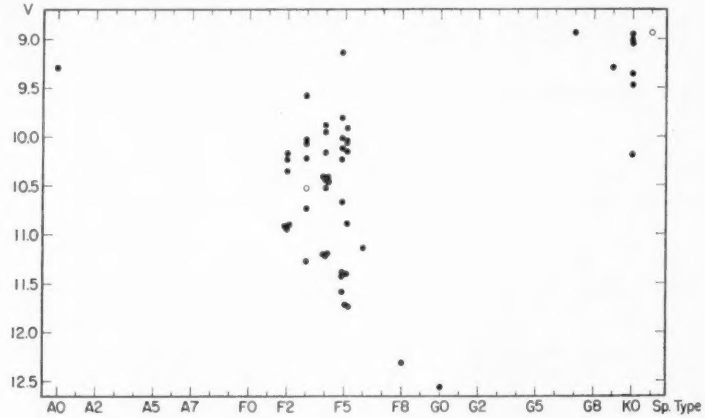

FIG. 1.—The H-R diagram of the cluster. Two stars which are probably not members are indicated by open circles.

Although the spectra, with a dispersion of 113 A/mm at $H\gamma$, were taken primarily for classification and no attempt was made to obtain more than one properly exposed plate of each star, the radial velocities were measured for most of the cluster members. These velocities have a mean error per plate of about 15 km/sec and hence are of little use individually. However, they do lead to a determination of the radial velocity of the cluster as -4.4 ± 2.5 km/sec. Moreover, they cast serious doubts on the membership in the cluster of two stars—No. 208, with a velocity of -52 km/sec from three plates, and No. 219, with a velocity of $+55$ km/sec from two plates. Star No. 208 appears to be nearer than the cluster, according to the spectroscopic parallax also.

There has been some speculation as to whether such clusters as NGC 752 and M67 are normal galactic clusters or are, perhaps, more closely related to the globular clusters. Various data seem to indicate that these clusters must be included with the galactic clusters as a peculiar type. For NGC 752 possibly the most convincing evidence is the relatively small membership and the low central condensation. Although the cluster is about 160 parsecs south of the galactic plane, its low space velocity definitely puts it in the class of galactic clusters. Except for the absence of A-type stars, the shape of the H-R diagram is typical of that for galactic clusters. Finally, the appearance of the spectra of the members establishes them as similar to the majority of stars near the sun rather than to the high-velocity stars or the globular-cluster giants.

However, there are features which distinguish NGC 752 from the more typical galactic clusters, such as the Hyades. Most striking, of course, is the almost complete absence of stars earlier than F2 and the presence of numerous F-type subgiants. The slope of the main sequence differs from that in other clusters to the extent that if the sequences are matched in the range F5–G0, the F2 stars are too bright by 0.6 mag. Spectroscopically, the members of the cluster belong to the weak-line group of stars; as an example, No. 213 is very similar to 19 Pup. The K0 giants definitely have stronger *CH* and stronger *Ca* I than do the Hyades giants, while the *CN* is probably somewhat weaker in the NGC 752 stars. Like the appearance of the spectra, the ultraviolet excess observed by Johnson (1953) is in the same sense, although much smaller in amount, as the effects observed in very high-velocity stars (Roman 1954; also unpublished).

It is interesting to investigate whether the unusual shape of the NGC 752 H-R diagram can be explained on the basis of the evolution of stars which originally occupied a main sequence similar to that found in more typical clusters. The assumption is usually made that young stars are built on the Cowling model with uniform composition throughout; as they age, the mean molecular weight of the core becomes greater, while that of the envelope remains constant until all hydrogen in the core is exhausted and the core becomes isothermal with a surrounding, energy-producing envelope; finally, the isothermal core grows until the Schönberg-Chandrasekhar (1942) limit is reached and further growth is prevented by the lack of stability of the resulting star. A rough calculation indicates that most of the stars in NGC 752 have not yet reached this limit.

Ledoux (1949) has tabulated the fraction of the stellar mass in the core, the fraction of this mass in a transition zone between the core and the envelope, and the radius and luminosity of the star in terms of the solar values for a model similar to the sun originally for various ratios of the mean molecular weight in the core to that in the envelope. It seems reasonable to assume, within the accuracy of the present comparison, that, for stars of other masses not differing from the solar mass by more than 70 per cent, the evolutionary tracks will be similar to that of the sun, although stars of larger mass (and luminosity) will proceed along their tracks more rapidly than stars of smaller mass. By comparing the instantaneous mass of hydrogen in the core with the mass of hydrogen which must be burned to sustain the instantaneous luminosity of the star, we can compute the mean molecular weight in the core and hence the position of the star on its evolutionary track as a function of time.

In order to determine the locus of stars of different mass at any time, it is necessary to know their locus at a particular time, such as $T = 0$. For the sake of consistency, it was assumed that originally the main sequence of the cluster stars was that predicted by the Cowling model,

$$L = C \kappa_0^{-1} M^{5.5} R^{-0.5} \mu^{7.5} ,$$

where C is a numerical constant, κ_0 is chosen to give the correct value of L, M, and R for the sun, $\mu = 0.55$, and M and R are assumed to obey the empirical mass-radius relation (Kuiper 1938*b*). This theoretical main sequence for stars in the range A5–G2 is shown in Figure 2, together with the locus of these stars after 1.5×10^9 years according to Ledoux's models. The same figure also illustrates the normal main sequence for stars near the sun and the observed main sequence for NGC 752. The latter is assumed to be defined by the fifteen faintest stars, omitting No. 261 at F6. The other observed quantities are derived from data given by Keenan and Morgan (1951) and by Kuiper (1938*a*, *b*). The vertical position of NGC 752 is entirely arbitrary. It is seen from this figure that while the normal and the theoretical main sequences do not coincide for $T = 0$, the difference between the normal and the NGC 752 main sequences is very similar to the change of the theoretical main sequence with time.

To obtain a more accurate indication of the extent to which the H-R diagram of NGC 752 can be explained by evolution, the detailed evolutionary tracks are shown attached to the empirical normal main sequence in Figure 3. This means that the rate of evolution is based on the theoretical luminosity for $T = 0$, while the actual luminosity plotted is based on the observed luminosity for normal stars of the same mass. Figure 3 also shows the computed locus of the same stars after various time intervals and the observed shape of the NGC 752 sequence. From this illustration it is apparent that we can explain both the unusual slope of the NGC 752 main sequence and the lack of stars earlier than F2 (the existence of the A0 star presents another problem) as a result of the evolution of stars built on the generalized Cowling model in a time of the order of 1.5×10^9 years. Since the main sequence to which the theoretical evolutionary tracks have been fitted may not be the true one for the time $T = 0$, the cluster must be at least this old, according to these considerations. Finally, it should be noted that these curves

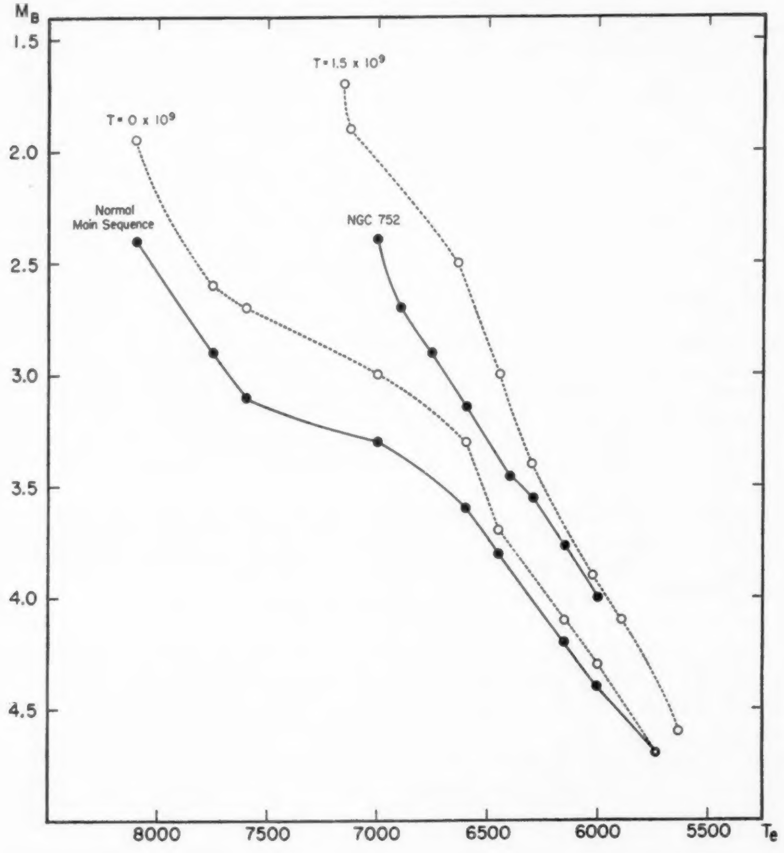

FIG. 2.—The theoretical main sequence predicted by the Cowling model for $T = 0$ and its predicted position after 1.5×10^9 years are shown by the dashed curves. The solid curves show the normal observed main sequence and the NGC 752 main sequence. The vertical position of the latter is arbitrary.

show that the stars between F5 and G0 are already 0.4 mag. brighter than they were originally. Hence this should lead us to underestimate the distance modulus of the cluster by this amount. This may explain the fact that the distance modulus derived from the late-type giants is 0.3 mag. larger than the one derived from the mean of all of the stars or from the F5–G0 dwarfs. On the other hand, these giants have undoubtedly changed also with time.

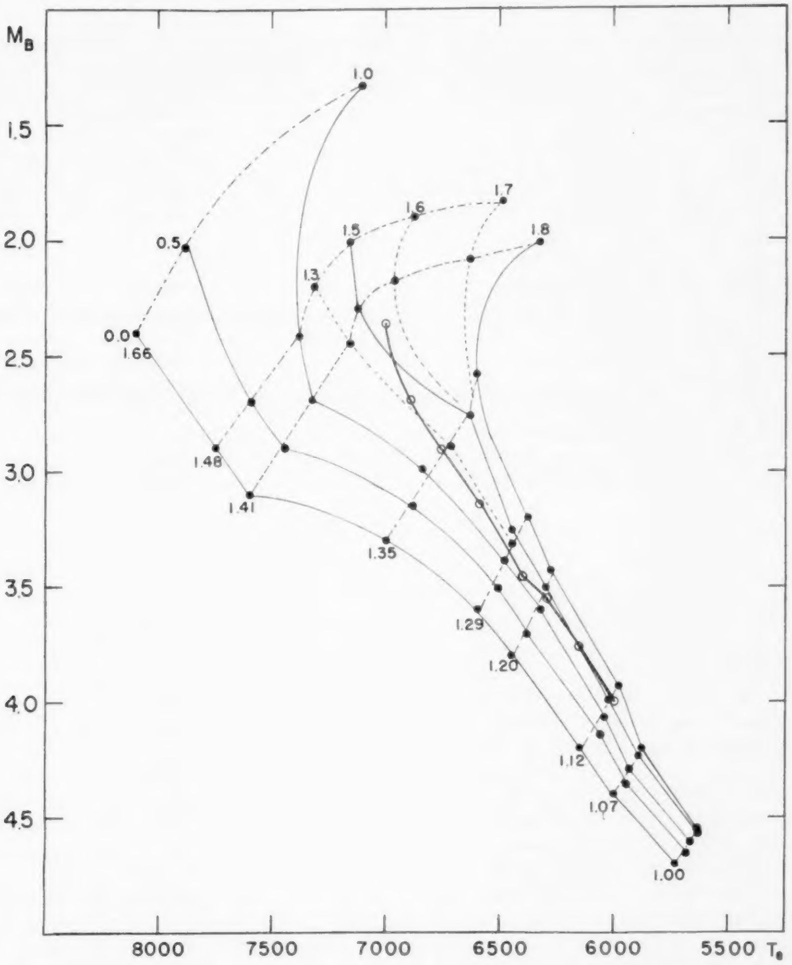

FIG. 3.—The theoretical evolutionary tracks for stars of various masses (*dashed curves*) and the locus of the main sequence after various time intervals (*solid* or *dotted curves*). In addition, the heavy curve connecting the open circles indicates the position of the main sequence observed for NGC 752. The zero point of the bolometric magnitudes is arbitrary for the observed curve. The theoretical curves are labeled according to the time elapsed in units of 10^9 years or according to the mass of the star in units of the solar mass.

These considerations of the evolution of the H-R diagram in this cluster are similar to the ideas Sandage and Schwarzschild (1952) applied to the H-R diagrams of globular clusters. However, because of the much greater age of the latter, Sandage and Schwarzschild could ignore the path by which the stars reached the Schönberg-Chandrasekhar limit, assuming only that the stars had passed this limit. In NGC 752 we see that the shape of the H-R diagram changes noticeably well before this limit is reached and that evolutionary models such as those computed by Ledoux are important to the understanding of the development of galactic clusters.

I am indebted to Dr. Harold Johnson for the use of his charts and his photometric results before publication and to Dr. R. J. Trumpler for the radial velocity of the A0 star. I also wish to thank Dr. S. Chandrasekhar for several valuable discussions of the evolution of the cluster.

REFERENCES

Cowling, T. G. 1935, *M.N.*, **96,** 42.
Ebbighausen, E. G. 1939, *Ap. J.*, **89,** 431.
Heinemann, Karl. 1926, *A.N.*, **227,** 193.
Johnson, H. L. 1953, *Ap. J.*, **117,** 356.
Johnson, H. L., and Morgan, W. W. 1953, *Ap. J.*, **117,** 313.
Keenan, P. C., and Morgan, W. W. 1951, in J. A. Hynek (ed.), *Astrophysics* (New York: McGraw-Hill Book Co.), p. 12.
Kuiper, G. P. 1938*a*, *Ap. J.*, **88,** 429.
———. 1938*b*, *ibid.*, p. 472.
Ledoux, P. 1949, *Contribution à l'étude de la structure interne des étoiles et de leur stabilité.* Liége, Belgium.
Roman, N. G. 1954, *A.J.*, **59,** 307.
Sandage, A. R., and Schwarzschild, M. 1952, *Ap. J.*, **116,** 463.
Schönberg, M., and Chandrasekhar, S. 1942, *Ap. J.*, **96,** 161.
Trumpler, R. J. 1930, *Lick Obs. Bull.*, **14,** 154.

EFFECT OF MAGNETIC FIELDS ON GENERATION OF NOISE BY ISOTROPIC TURBULENCE*

RUSSELL M. KULSRUD
Yerkes Observatory

Received August 30, 1954

ABSTRACT

Lighthill's (1952) and Proudman's (1952) results on the generation of aerodynamic noise by isotropic turbulence are generalized to include magnetic effects. It is found that if there are only turbulent magnetic fields present and no constant magnetic field, the magnetic turbulence generates sound very efficiently and increases considerably the generation of sound by kinetic turbulence. If there is a constant magnetic field, hydromagnetic waves are generated instead. For the modified sound mode of the hydromagnetic waves, a result similar to the case of no general field is obtained. No energy is generated into the Alfvén and modified Alfvén waves unless the energy density of the magnetic field is greater than the energy density of the kinetic turbulence. Expressions are found for the rate of noise generated per unit mass, and these results are applied to the problem of heating the chromosphere and the corona.

I. INTRODUCTION

Since Schwarzschild (1948) suggested that the solar corona may be supported by sound waves generated by turbulence in the solar granules, there has been considerable interest in the amount of aerodynamic noise generated by turbulent flow fields. Lighthill (1952) derived the basic equation for aerodynamic sound production, and Proudman (1952) applied this equation to the case of isotropic turbulence and obtained an explicit expression for the amount of sound generated. Since there very likely are turbulent magnetic fields in the solar granules, it seemed of interest to consider the effect on Lighthill's and Proudman's results of a magnetic field being present.

Lighthill's method consists in writing the equations of motion in the form

$$\frac{\partial^2 \rho}{\partial t^2} - a_0^2 \nabla^2 \rho = \frac{\partial^2 T_{ij}}{\partial x_i \partial x_j}, \tag{1}$$

where

$$T_{ij} = \rho v_i v_j , \tag{2}$$

a_0 is the velocity of sound, ρ is the density of the medium, and $\boldsymbol{v}$ is the velocity. The foregoing equation is valid if viscous forces and other dissipative effects are neglected. It is seen on comparing this equation with the retarded potential equation of electromagnetic theory, that the velocity stresses T_{ij} will generate sound waves. Furthermore, because of the double derivative in the source terms, the turbulent medium generating sound will have only a quadrupole moment; and Lighthill finds that the rate of production of sound is proportional to the fifth power of the Mach number v/a_0, $P = \alpha \epsilon M^5$.

However, one comment must be made on this procedure. In carrying out the integral over the sources, Lighthill neglects T_{ij} outside the turbulent region, since it is small, of the second order in the velocities. Although these terms are small, they might very well accumulate to a large sum when integrated over all space. Lighthill points out that they do not modify the energy output but merely change the shape of the waves and thus may be included in the normal nonlinear effects of sound waves. But this is a consequence of the quadrupole nature of these terms, which enables any large effects to cancel out.

In fact, if the equation of motion is written for $\boldsymbol{v}$ instead of ρ, the equation of motion becomes

$$\frac{\partial^2 \boldsymbol{v}}{\partial t^2} - a_0^2 \nabla^2 \boldsymbol{v} = \boldsymbol{P} .$$

---

* This work was done as a thesis in fulfilment of the requirements for a Ph.D. degree from the Physics Department of the University of Chicago.

The source terms $\boldsymbol{P}$ no longer have a quadrupole nature but are of second order in the velocities. If the $\boldsymbol{P}$ terms are integrated only over the turbulent region and are neglected outside, a different answer is obtained for the amount of acoustic energy generated than is obtained when the terms $\partial^2 T_{ij}/\partial x_i \partial x_j$ are integrated over the turbulent region. This can be due only to the modification of the energy generation by the sound waves themselves. Hence some care must be exercised in picking the correct dependent variable to describe the waves, when the energy generation is computed. The importance of these remarks will become evident in the second part of this paper, when the generation of hydromagnetic waves is considered.

Using Lighthill's equations, Proudman evaluated α, the proportionality constant, for the case when the turbulence is isotropic. Making the assumption of a normal distribution for the fourth correlations of the velocities, he was able to express α in terms of the longitudinal correlation of the velocities $f = \langle v_1 v_1' \rangle_{av}$, and to evaluate α for certain assumed forms of f.

If a general magnetic field is present in the neighborhood of the turbulent medium and the fluid is electrically conducting, hydromagnetic sound waves will be generated by nonlinear magnetic terms analogous to the velocity shearing terms, T_{ij}. Again it is found that sources of hydromagnetic waves are quadrupole sources. There are three modes of propagation of hydromagnetic waves: a longitudinal mode, which becomes a sound wave as H approaches zero, and two transverse waves, which disappear when H vanishes. The energy emitted in the first mode is nearly proportional to $M^5 = v^5/a_0^5$, while the energies emitted in the other two modes are proportional to $1/H^5$ and diverge as H goes to zero. However, since the condition for the nonlinear terms to be small is $v/V_H \ll 1$ where $V_H = H/(4\pi\rho)^{1/2}$, a theory which neglects them breaks down as H goes to zero.

In the first sections of this paper we shall assume that H, the general constant magnetic field, is zero and that only turbulent magnetic fields are present. In later sections we shall investigate the case of a nonzero magnetic field and calculate the energy emitted into each mode. If $H = 0$, only the sound mode of the hydromagnetic waves remains, and we calculate the sound energy generated into this mode by turbulence, by using Proudman's method. It is found under assumptions similar to Proudman that $P = \alpha\epsilon M^5$, where ϵ is the dissipation per unit mass, α is expressed in terms of f, $rg = \langle v_1 h_2' \rangle_{av}$, the transverse correlation between $\boldsymbol{v}$ and $\boldsymbol{h}$, and $h(r) = \langle h_1 h_1' \rangle_{av}$, the longitudinal correlation of $\boldsymbol{h}$ with itself. Assuming exponential forms for f and h and neglecting g, we find that α may be written as

$$\alpha = 13.47 + A_1(\beta)\gamma^2 + 12.29\beta\gamma^4 , \tag{3}$$

where $A_1(\beta)$ is an algebraic function of β, which lies between 100 and 200 when $1 < \beta < 4$, and is proportional to β for β large; β is the ratio of the scale length for $f(r)$ to that for $h(r)$, and γ is the ratio $\langle h^2 \rangle / \langle v^2 \rangle$. A plot of $A_1(\beta)$ is given in Figure 1.

II. DERIVATION OF LIGHTHILL'S FORMULA WHEN MAGNETIC TURBULENCE IS PRESENT

The equations of motion for a magnetic fluid are (Chandrasekhar 1950)

$$\frac{\partial(\rho v_i)}{\partial t} + \frac{\partial}{\partial x_j}\rho(v_i v_j - h_i h_j) = -\frac{\partial P}{\partial x_i} + \rho\nu\nabla^2 v_i , \tag{4}$$

$$\frac{\partial h_i}{\partial t} + \frac{\partial}{\partial x_j}(v_j h_i - v_i h_j) = \lambda\nabla^2 h_i , \tag{5}$$

$$\frac{\partial \rho}{\partial t} + \frac{\partial}{\partial x_i}(\rho v_i) = 0 , \tag{6}$$

where

$$\lambda = \frac{1}{4\pi\sigma}, \qquad h = \frac{H}{\sqrt{4\pi\rho}}, \qquad P = p + \rho\frac{h^2}{2},$$

σ is the electrical conductivity, ν is the kinematic viscosity, and p is the gas pressure.

To find $\partial P/\partial x_i$, we assume only adiabatic compressions and expansions. The changes in the magnetic pressure $h^2/2$ are balanced by changes in the magnetic energy. Hence, for a perfect gas,

$$\delta p = a_0^2 \delta\rho\,. \tag{7}$$

Any error arising from the assumption of equation (7) is shown by Lighthill to be small when the Mach number M is small.

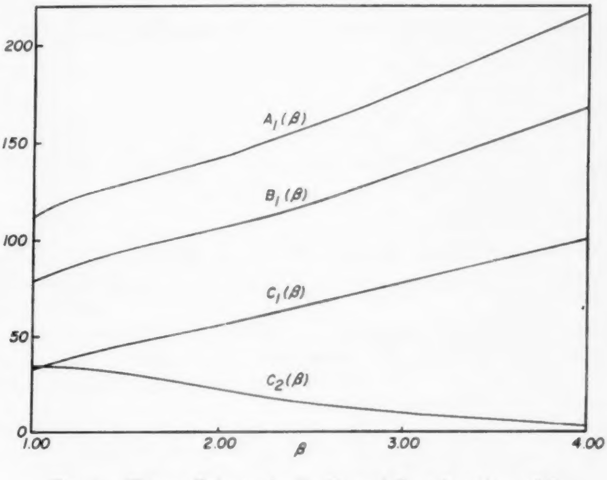

FIG. 1.—The coefficients A_1, B_1, C_1, and C_2 as functions of β

Differentiating equation (4) with respect to x_i, equation (6) with respect to t, and using equation (7), we obtain

$$\frac{\partial^2\rho}{\partial t^2} - a_0^2\nabla^2\rho = \frac{\partial^2 W_{ij}}{\partial x_i \partial x_j}, \tag{8}$$

where

$$W_{ij} = \rho v_i v_j + \rho\left(\delta_{ij}\frac{h^2}{2} - h_i h_j\right), \tag{9}$$

and δ_{ij} is the Kronecker symbol. This is analogous to Lighthill's equation (1), where the source term T_{ij} is replaced by W_{ij}. That is to say, sound is generated both by velocity shears and by magnetic-field shears.

The acoustic energy production may be obtained for isotropic homogeneous turbulence by replacing the tensor T_{ij} by W_{ij} in Lighthill's and Proudman's calculation. The retarded potential solution of equation (8) for ρ at the point $\boldsymbol{x}$ is

$$\rho - \rho_0 = \frac{1}{4\pi a_0^2}\int \frac{\partial^2 W_{ij}(\boldsymbol{y}, t - \xi/a_0)}{\partial x_i \partial x_j}\frac{d\boldsymbol{y}}{\xi} \qquad (\xi = |\boldsymbol{x} - \boldsymbol{y}|)\,.$$

Integrating by parts, taking $\mathbf{x}$ in the x-direction, and using the isotropy of the turbulence, we find

$$\rho - \rho_0 = \frac{1}{4\pi a_0^4 |\mathbf{x}|} \int \frac{\partial^2 W_{11}(\mathbf{y}, t - \xi/a_0)}{\partial^2 t} \, d\mathbf{y} .$$

To obtain the intensity of the sound produced, we multiply the mean square of the density fluctuations by a_0^3/ρ_0,

$$I(\mathbf{x}, t) = \frac{a_0^3}{\rho_0} \langle (\rho - \rho_0)^2 \rangle_{av} .$$

The total acoustic energy output is obtained by integrating $I(\mathbf{x}, t)$ over the surface of a sphere of radius x:

$$\int I(\mathbf{x}, t)\, x^2 dx$$

$$= \frac{1}{4\pi a_0^5 \rho_0} \int\!\!\int \frac{\partial^2}{\partial t^2} (W_{11} - \langle W_{11} \rangle) \Big|_{t-\xi/a_0} \frac{\partial^2}{\partial t^2} (W'_{11} - \langle W'_{11} \rangle) \Big|_{t-\xi'/a_0} d\mathbf{y} d\mathbf{y} .$$

Neglecting the retarded times, we can write the acoustic energy production per unit mass in the form

$$P = \frac{1}{4\pi a_0^5} \int U(\mathbf{r})\, d\mathbf{r} , \tag{10}$$

where

$$U = \left\langle \frac{\partial^2 W_{11}}{\partial t^2} \frac{\partial^2 W'_{11}}{\partial t^2} \right\rangle_{av} = \left\langle \frac{\partial^2 v_x^2}{\partial t^2} \frac{\partial^2 v_x'^2}{\partial t^2} \right\rangle + \frac{3}{4} \left\langle \frac{\partial^2 h_x^2}{\partial t^2} \frac{\partial^2 h_x'^2}{\partial t^2} \right\rangle$$
$$+ 2 \left\langle \frac{\partial^2 v_x^2}{\partial t^2} \frac{\partial^2 h_y'^2}{\partial t^2} \right\rangle - \frac{1}{2} \left\langle \frac{\partial^2 h_x^2}{\partial t^2} \frac{\partial^2 h_y'^2}{\partial t^2} \right\rangle , \tag{11}$$

where v_x is the value of v_x at P; v'_x is its value at P'; and $\mathbf{r}$ is the vector from P to P'.

To evaluate these fourth-order correlations, Proudman makes the assumption that fourth-order correlations are normal and may be written

$$\overline{ABC'D'} = \langle AC' \rangle \langle BD' \rangle + \langle AD' \rangle \langle BC' \rangle + \langle AB \rangle \langle C'D' \rangle , \tag{12}$$

where A and B are quantities at P and C' and D' are quantities at P'. This assumption is justified to some extent by Batchelor (1951).

Using these expansions, Proudman calculates P by taking into account the decay of turbulence (that is, the variation of the correlation coefficients with time). He finds results which differ very little from the results obtained by assuming steady turbulence (i.e., the correlation coefficients are constant in time). Hence, for simplicity, we shall assume that the turbulence is steady and that fourth-order correlations are normal. Under these assumptions we find

$$\left\langle \frac{\partial^2 v_x^2}{\partial t^2}\frac{\partial^2 v_x'^2}{\partial t^2}\right\rangle = 12\left(\left\langle \frac{\partial v_x}{\partial t}\frac{\partial v_x'}{\partial t}\right\rangle\right)^2 + 4\,\langle v_x v_x'\rangle \left\langle \frac{\partial^2 v_x}{\partial t^2}\frac{\partial^2 v_x'}{\partial t^2}\right\rangle,$$

$$\left\langle \frac{\partial^2 h_x^2}{\partial t^2}\frac{\partial^2 h_x'}{\partial t^2}\right\rangle = 12\left(\left\langle \frac{\partial h_x}{\partial t}\frac{\partial h_x'}{\partial t}\right\rangle\right)^2 + 4\,\langle h_x h_x'\rangle \left\langle \frac{\partial^2 h_x}{\partial t^2}\frac{\partial^2 h_x'}{\partial t^2}\right\rangle,$$

$$\begin{aligned}\left\langle \frac{\partial^2 h_x^2}{\partial t^2}\frac{\partial^2 h_y'^2}{\partial t^2}\right\rangle = 12\left(\left\langle \frac{\partial h_x}{\partial t}\frac{\partial h_y'}{\partial t}\right\rangle\right)^2 &+ 4\,\langle h_x h_y'\rangle \left\langle \frac{\partial^2 h_x}{\partial t^2}\frac{\partial^2 h_y'}{\partial t^2}\right\rangle \\ &+ 16\left\langle \frac{\partial h_x}{\partial t}\,h_y'\right\rangle\left\langle \frac{\partial h_x}{\partial t}\frac{\partial^2 h_y'}{\partial t^2}\right\rangle,\end{aligned} \tag{13}$$

$$\begin{aligned}\left\langle \frac{\partial^2 v_x^2}{\partial t^2}\frac{\partial^2 h_y'^2}{\partial t^2}\right\rangle = 12\left(\left\langle \frac{\partial v_x}{\partial t}\frac{\partial h_y'}{\partial t}\right\rangle\right)^2 &+ 4\,\langle v_x h_y'\rangle \left\langle \frac{\partial^2 v_x}{\partial t^2}\frac{\partial^2 h_y'}{\partial t^2}\right\rangle \\ &+ 16\left\langle \frac{\partial v_x}{\partial t}\,h_y'\right\rangle\left\langle \frac{\partial v_x}{\partial t}\frac{\partial^2 h_y'}{\partial t^2}\right\rangle.\end{aligned}$$

In this equation $\langle(\partial h_x/\partial t)h_y'\rangle$ and $\langle(\partial v_x/\partial t)h_y'\rangle$ vanish, since $\langle h_x(0)h_y'(t)\rangle$ and $\langle v_x(0)h_y'(t)\rangle$ are even functions of time.

It is known from the theory of isotropic turbulence that the correlation $\langle\phi_i\phi_j'\rangle$ of the values of a polar solenoidal vector ϕ_i at two points separated by a distance r can be expressed in terms of a single scalar $\phi(r)$ in the form

$$\langle\phi_i\phi_j'\rangle = -\frac{r_i r_j}{2r}\frac{d\phi(r)}{dr} + \left(\tfrac{1}{2}r\phi' + \phi\right)\delta_{ij}. \tag{14}$$

Let the correlations $\langle v_i/v_j'\rangle$, $\langle(\partial v_i/\partial t)(\partial v_j'/\partial t)\rangle$, and $\langle(\partial^2 v_i/\partial t^2)(\partial^2 v_j'/\partial t^2)\rangle$ be associated by equation (14) with the scalars $f(r)$, $\phi(r)$, and $\psi(r)$, respectively.

Similarly the correlations $\langle\theta_i\theta_j'\rangle$ of an axial solenoidal vector θ_i may be expressed in terms of a single scalar $\theta(r)$ in the form

$$\langle\theta_i\theta_j'\rangle = -\frac{r_i r_j}{2r}\frac{d\theta(r)}{dr} + \left(\tfrac{1}{2}r\theta' + \theta\right)\delta_{ij}. \tag{15}$$

Let the correlations $\langle h_i h_j'\rangle$, $\langle(\partial h_i/\partial t)(\partial h_j'/\partial t)\rangle$, and $\langle(\partial^2 h_i/\partial t)(\partial^2 h_j'/\partial t^2)\rangle$ be associated by equation (15) with the scalars $h(r)$, $\theta(r)$, and $\chi(r)$.

Finally, the correlation $\langle\phi_i\theta_j'\rangle$ between the values of a polar solenoidal vector ϕ_i and an axial solenoidal vector θ_j may be expressed in terms of a single scalar $\pi(r)$ in the form

$$\langle\phi_i\theta_j'\rangle = \pi(r)\,\epsilon_{ijk}r_k\,, \tag{16}$$

where ϵ_{ijk} is the symbol which equals 1 or -1 as ijk is an even or odd permutation of 1, 2, 3. Let $\langle v_i h_j'\rangle$, $\langle(\partial v_i/\partial t)(\partial h_j'/\partial t)\rangle$, and $\langle(\partial^2 v_i/\partial t^2)(\partial^2 h_j'/\partial t^2)\rangle$ be associated by equation (16) with the scalars $g(r)$, $\pi(r)$, and $\zeta(r)$.

Substituting the foregoing expressions in equation (13), and this result in equation (11), we find, from equation (10), that

$$P=\frac{2}{15a_0^5}\int_0^\infty r^4\{12\phi'^2+9\theta'^2+4f'\psi'+3h'\chi'\}\,dr$$
$$-\frac{1}{120a_0^5}\int_0^\infty r^4\{12\theta'^2+4h'\chi'\}\,dr+\frac{1}{3a_0^5}\int_0^\infty r^4\{12\pi^2+4g\zeta\}\,dr\,,$$

or

$$P=\frac{1}{15a_0^5}\int_0^\infty r^4\{24\phi'^2+17\tfrac{1}{2}\theta'^2+8f'\psi'+5\tfrac{1}{2}h'\chi'+60\pi^2+20g\zeta\}\,dr\,. \tag{17}$$

This equation gives the acoustic power generated per unit mass in terms of the above-defined correlation coefficients. It agrees with Proudman's equation (5.3), except for the neglect of terms due to the decaying turbulence and the addition of terms due to the magnetic field. Following Proudman's method, we may use the equations of motion to express the correlation coefficients ϕ, ψ, π, ζ, θ, and χ in terms of f, g, and h. It will appear that magnetic terms occur in ϕ and ψ, introducing a further modification of P. Thus the effect of the magnetic field is twofold. First, it introduces extra terms in the expression for P, equation (17), and, second, it modifies the correlation coefficients ϕ and ψ.

III. REDUCTION OF CORRELATION COEFFICIENTS TO THREE SCALARS, f, g, AND h

To evaluate ϕ, we contract equation (14) with respect to i and j and obtain

$$3\phi+r\phi'=\frac{1}{r^2}\frac{d}{dr}(r^3\phi)=\left\langle\frac{\partial v_i}{\partial t}\frac{\partial v_i'}{\partial t}\right\rangle. \tag{18}$$

From the equation of motion (4), neglecting viscosity, we have

$$\left\langle\frac{\partial v_i}{\partial t}\frac{\partial v_i'}{\partial t}\right\rangle=-\frac{\partial^2}{\partial x_j\partial x_k}\langle v_iv_jv_i'v_k'\rangle-\frac{\partial^2}{\partial x_j\partial x_k}\langle h_ih_jh_i'h_k'\rangle$$
$$-2\frac{\partial^2}{\partial x_j\partial x_k}\langle v_iv_jh_i'h_k'\rangle-\frac{1}{\rho^2}\frac{\partial^2}{\partial x_i\partial x_i}\langle PP'\rangle-\frac{2}{\rho}\frac{\partial^2}{\partial x_i\partial x_j}P(v_i'v_j'-h_i'h_j')\,, \tag{19}$$

where the density ρ is assumed incompressible. Differentiating equation (4) with respect to x_i, we can replace the last term of equation (19) by $(2/\rho)\partial^2(\langle PP'\rangle)/\partial x_i\partial x_i$, and $\langle(\partial v_i/\partial t)(\partial v_i'/\partial t)\rangle$ becomes

$$\left\langle\frac{\partial v_i}{\partial t}\frac{\partial v_i'}{\partial t}\right\rangle=\frac{1}{\rho^2}\nabla^2\langle PP'\rangle-\frac{\partial^2}{\partial x_j\partial x_k}\langle v_iv_jv_i'v_k\rangle$$
$$-\frac{\partial^2}{\partial x_j\partial x_k}\langle h_ih_jh_i'h_k'\rangle-2\frac{\partial}{\partial x_j\partial x_k}\langle v_iv_jh_i'h_k'\rangle\,. \tag{20}$$

The second term is evaluated by Proudman and is

$$\frac{\partial^2}{\partial x_j\partial x_k}\langle v_iv_jv_i'v_k'\rangle=\frac{1}{r^2}\frac{d}{dr}\,r^3\left(ff''-\tfrac{1}{2}f'^2+\frac{4}{r}ff'\right).$$

The third term is the same, with v replaced by h:

$$\frac{\partial^2}{\partial x_j \partial x_k} \langle h_i h_j h_i' h_k' \rangle = \frac{1}{r^2} \frac{d}{dr} r^3 \left(h h'' - \tfrac{1}{2} h'^2 + \frac{4}{r} h h' \right).$$

The pressure coefficient is obtained by using a result of Chandrasekhar (1951)·

$$\frac{1}{\rho^2} \langle PP' \rangle = 2 \int_r^\infty (f'^2 + h'^2) \left(y - \frac{r^2}{y} \right) dy \,, \tag{21}$$

that

$$\begin{aligned} \frac{1}{\rho^2} \nabla^2 \langle PP' \rangle &= \frac{1}{r^2} \frac{d}{dr} r^3 \left(\frac{1}{r} \frac{d}{dr} \frac{\langle PP' \rangle}{\rho^2} \right) \\ &= \frac{1}{r^2} \frac{d}{dr} r^3 \left\{ -4 \int_r^\infty \frac{dy}{y} (f'^2 + h'^2) \right\}. \end{aligned} \tag{22}$$

The last term may be written

$$\begin{aligned} \frac{\partial}{\partial x_j \partial x_k} \langle v_i v_j h_i' h_k' \rangle &= \frac{\partial^2}{\partial x_j \partial x_k} (\langle v_i h_k' \rangle \langle v_j h_i' \rangle) \\ &= -\frac{1}{r^2} \frac{d}{dr} (2 r^3 g) \end{aligned} \tag{23}$$

Combining these results, we find

$$\begin{aligned} \frac{1}{r^2} \frac{d}{dr} (r^3 \phi) = \frac{1}{r^2} \frac{d}{dr} r^3 \Big\{ -4 \int_r^\infty \frac{dy}{y} (f'^2 + h'^2) - f f'' + \frac{f'^2}{2} - \frac{4}{r} f f' \\ - h h'' + \frac{h'^2}{2} - \frac{4}{r} h h' + 4 g^2 \Big\}. \end{aligned} \tag{24}$$

Since, at infinity, all correlation coefficients vanish with their derivatives, we may write

$$\phi = -4 \int_r^\infty \frac{dy}{y} (f'^2 + h'^2) - f f'' + \frac{f'^2}{2} - \frac{4}{r} f f' - h h'' + \frac{h'^2}{2} - \frac{4}{r} h h' + 4 g^2 . \tag{25}$$

Also

$$\phi' = - f \left\{ f''' + \frac{4}{r} f'' - \frac{4}{r^2} f' \right\} - h \left\{ h''' + \frac{4}{r} h'' - \frac{4}{r^2} h' \right\} + 8 g g' . \tag{26}$$

This expresses ϕ in terms of f, g, and h.

To obtain a similar expression for ψ, we again contract equation (14) with respect to i and j and use the equation of motion (4) differentiated with respect to time. It is found that the calculation may be carried out by differentiating ϕ operationally. That is, we differentiate each term in equation (25) with respect to time and then replace df/dt by ϕ, and dh/dt by θ. Applying this to equation (26), we find

$$\psi' = -\phi G(f) - f G(\phi) - h G(\theta) - \theta G(h) + 8 g \pi' + 8 g' \pi \,, \tag{27}$$

where

$$G(f) = f''' + \frac{4}{r} f'' - \frac{4}{r^2} f' . \tag{28}$$

In an exactly analogous fashion, θ and χ are found, using the equation of motion (5) and its derivative with respect to time:

$$\theta = -H(f, h) - 4g^2 , \tag{29}$$

$$\chi = -H(f, \phi) - H(\phi, h) - 8g\pi , \tag{30}$$

$$H(f, h) = f''h + fh'' + \frac{4}{r}(f'h + fh') + f'h' . \tag{31}$$

To obtain π, we re-write equation (16) in the form

$$\left\langle \frac{\partial v_i}{\partial t} \frac{\partial h_j'}{\partial t} \right\rangle = \pi \epsilon_{ijl} x_l ,$$

and take the curl with respect to i,

$$\epsilon_{kmi} \frac{\partial}{\partial x_m} (\epsilon_{ijl} x_l) = \epsilon_{kmi} \frac{\partial}{\partial x_m} \left\{ \left\langle \frac{\partial v_i}{\partial t} \frac{\partial h_j'}{\partial t} \right\rangle \right\} .$$

Then, contracting j and k and using equations (4) and (5), we obtain

$$\begin{aligned} \frac{2}{r^2} \frac{d}{dr} (r^3 \pi) &= \epsilon_{ijk} \frac{\partial^3}{\partial x_k \partial x_l \partial x_m} \{ \langle (v_i v_l - h_i h_l)(v_m' h_j' - v_j' h_m') \rangle \} \\ &= \epsilon_{ijk} \frac{\partial^3}{\partial x_k \partial x_l \partial x_m} \{ \langle v_i v_m' \rangle \langle v_l h_j' \rangle + \langle v_i h_j' \rangle \langle v_l v_m' \rangle \\ &\qquad - \langle v_i v_j' \rangle \langle v_l h_m' \rangle - \langle v_i h_m' \rangle \langle v_l v_j' \rangle - (v \longleftrightarrow h) \} , \end{aligned} \tag{32}$$

where the symbol $(v \leftrightarrow h)$ means that v and h are to be interchanged in the first terms. The third term vanishes by symmetry, and the others may be evaluated by remembering that $\partial v_i / \partial x_i = 0$. Using a result of Batchelor (1951, equation following his eq. [5.2]), we find

$$\begin{aligned} \frac{\partial}{\partial x_l} \langle v_i v_j' \rangle = -\frac{1}{2r} \frac{d}{dr} \left(\frac{f'}{r} \right) r_i x_j x_l - \frac{f'}{2r} (x_i \delta_{jl} + x_j \delta_{il}) \\ + \frac{1}{2r} \frac{d}{dr} (r f' + 2f) x_l \delta_{ij} . \end{aligned}$$

After some further reductions, we obtain

$$\pi(r) = -K(f, g) - K(h, g) , \tag{33}$$

$$\zeta(r) = -K(\phi, g) - K(f, \pi) - K(\theta, g) - K(h, \pi) , \tag{34}$$

where

$$K(f, g) = f g'' - f'' g . \tag{35}$$

Equations (25), (26), (27), (29), (30), (33), and (34) with definitions (28), (31), and (35) express all the correlation coefficients in terms of the three scalars f, g, and h. These may be substituted in P to get an explicit expression in terms of f, g, and h.

IV. THE EVALUATION OF P

Proudman (1952) has shown that the value of P does not depend critically on the shape assumed for the longitudinal velocity correlation f. Hence it is more feasible to assume some shapes for f, g, and h and to investigate how the noise generation depends on certain parameters: $\langle v^2 \rangle$, $\langle h^2 \rangle$, the scale length of h, etc., than to derive P in terms of f, g, and h explicitly. We shall assume that

$$f = \langle v^2 \rangle e^{-(\pi/4)(r^2/L^2)} , \tag{36}$$

$$h = \langle h^2 \rangle e^{-(\pi/4)\beta^2(r^2/L^2)} , \tag{37}$$

$$g = 0 . \tag{38}$$

Where $\langle v^2 \rangle$ and $\langle h^2 \rangle$ are the mean-square values for one component, L is the scale length of the turbulence defined by the equation

$$L = \frac{(\langle v^2 \rangle)^{3/2}}{\epsilon} ,$$

and ϵ is the mean rate of dissipation of energy per unit mass. To simplify the calculation, we make the transformation $(\pi/4)(r^2/L^2) = x^2/2$ and set $\langle h^2 \rangle = \gamma \langle v^2 \rangle$. Using equations (26), (27), (29), and (30), we find

$$f' = -u^2 x e^{-x^2/2} , \tag{39a}$$

$$h' = -u^2 \beta^2 x e^{-x^2/2} , \tag{39b}$$

$$\phi' = u^4 \{ (x^3 - 7x) e^{-x^2} + \gamma^2 (\beta^6 x^3 - \beta^4 x) e^{-\beta^2 x^2} \} , \tag{40}$$

$$\theta' = \gamma u^4 \{ (\beta^6 + 2\beta^4 + 2\beta^2 + 1) x^3 - (7\beta^4 + 12\beta^2 + 7) x \} \exp - \left[\frac{(1+\beta^2)}{2} \right] x^2 , \tag{41}$$

$$\begin{aligned} \psi' = -u^6 \Big\{ & [4\tfrac{1}{2} x^5 - 56\tfrac{1}{2} x^3 + 133x] e^{-3x^2/2} \\ & + \gamma^2 [(6\beta^{10} + 5\beta^8 + 8\beta^6 + 7\tfrac{1}{2}\beta^4 + 4\beta^2 + 1) x^5 \\ & - (80\beta^8 + 71\beta^6 + 92\tfrac{1}{2}\beta^4 + 62\beta^2 + 18) x^3 \\ & + (210\beta^6 + 196\beta^4 + 182\beta^2 + 63) x] \exp - \left[\frac{(1+2\beta^2)}{2} \right] x^2 \Big\} , \end{aligned} \tag{42}$$

$$\begin{aligned} \chi' = -\gamma u^6 \{ & (\beta^{10} + 6\beta^8 + 15\tfrac{1}{2}\beta^6 + 22\beta^4 + 19\beta^2 + 10) x^5 \\ & - (18\beta^8 + 92\beta^6 + 190\tfrac{1}{2}\beta^4 + 209\beta^2 + 124) x^3 \\ & + (63\beta^6 + 266\beta^4 + 424\beta^2 + 294) x \} \exp - \left[\frac{(2+\beta^2)}{2} \right] x^2 \\ & - \gamma^3 u^6 \{ 10\tfrac{1}{2}\beta^{10} x^5 - 114\tfrac{1}{2}\beta^8 x^3 + 217\beta^6 x \} e^{-(3/2)\beta^2 x^2} , \end{aligned} \tag{43}$$

where $u^2 = \langle v^2 \rangle$.

Substituting these expressions in equation (17) and carrying out the integrations, we finally obtain

$$P = \alpha \epsilon M^5 ,$$

where

$$\begin{aligned} \alpha = 13.47 + 12.29\beta\gamma^4 + \gamma^2 \left(\frac{1+\beta^2}{2} \right)^{-11/2} \{ & 1.1114\beta^{12} + 7.576\beta^{10} + 26.06\beta^8 \\ & + 42.49\beta^6 + 24.73\beta^4 + 7.790\beta^2 + 1.232 \} \end{aligned} \tag{44}$$

We shall write this equation as follows:

$$a = 13.47 + A_1(\beta)\,\gamma^2 + 12.29\beta\gamma^4 .$$

It is seen that as β becomes large, $A_1(\beta) \rightarrow 1.114\beta$ and $A_1(\beta) \rightarrow \infty$ as β goes to infinity (i.e., the scale length of the magnetic field goes to zero), which might be expected, since a zero scale length implies infinitely strong turbulence. Values for $A'(\beta)$ are given in Table 1 and $A_1(\beta)$ is plotted in Figure 1.

V. DISCUSSION OF THE VALIDITY OF EQUATION (44)

Apart from the assumption of homogeneous isotropic turbulence, the most serious assumption which is made in deriving equation (44) is the assumption that the fourth-order correlations are normal (i.e., eq. [12]). A normal distribution implies that the third-order correlations are negligible, which is incompatible with the nonlinear character of turbulence. However, there are distributions with nonzero third-order correlations which satisfy equation (12), and we may consider our assumption to correspond to the less restrictive one in statistics of neglecting fourth-order cumulants. Thus the question of third-order cumulants need not arise. Batchelor (1951), by assuming relation (12) for the fourth-order correlations of the velocities, was able to compute pressure correlation coefficients, which agreed well with experimental values. This result justifies to some extent our neglect of the fourth-order cumulants in our calculation.

TABLE 1

THE COEFFICIENTS $A_1(\beta)$, $B_1(\beta)$, $C_1(\beta)$, AND $C_2(\beta)$

β	β^2	$A_1(\beta)$	$B_1(\beta)$	$C_1(\beta)$	$C_2(\beta)$
1.00	1	111.0	78.56	34.36	33.79
1.40	2	127.6	92.15	31.92	43.65
1.73	3	136.0	100.0	26.92	50.35
2.00	4	143.3	106.7	22.08	55.98
2.24	5	150.4	112.2	18.07	61.02
2.45	6	157.4	118.9	14.86	65.69
2.65	7	164.3	124.7	12.33	69.90
4.00	16	220.1	170.2	3.37	100.7

The assumption of particular shapes for the unknown longitudinal correlations f and h is not so serious, since the amount of sound does not depend strongly on the shapes assumed (Proudman 1952). Also the slow dependence on β of $A_1(\beta)$ shows that the value assumed for the scale length of the magnetic field is not critical. Furthermore, the neglect of g cannot change the order of magnitude of the result. It is true that Proudman does obtain a result nearly three times as large for a, by assuming the Heisenberg correlation in place of the Gaussian one, but it might reasonably be expected that the generation of sound by the magnetic terms might correspondingly increase. This has not been investigated.

Hence from equation (44) we may be certain that when the magnetic energy density is comparable with the turbulent energy density ($\gamma = 1$), the magnetic terms dominate the kinetic terms by a factor of 10 in the generation of acoustic noise.

VI. THE CASE OF A NONZERO CONSTANT MAGNETIC FIELD

If there is a finite constant magnetic field $\boldsymbol{H}$ present, the fluid motions will interact with it, producing hydromagnetic waves instead of sound waves. The methods of the first part of this paper may be generalized to find the energy generated in these hydromagnetic waves by isotropic turbulence. However, since the hydromagnetic waves are considerably more complicated, it is better first to analyze them into plane waves and to calculate separately the energy generated in each plane mode, and, finally, to add these contributions together. One difficulty remains. The velocities of two modes of the hydromagnetic waves go to zero in a direction perpendicular to the magnetic field $\boldsymbol{H}$, and this leads to divergent results. As pointed out before, a vanishing velocity makes the nonlinear terms appreciable, and so a theory which neglects these terms breaks down. However, this difficulty may be overcome somewhat by noticing that the effect of the nonlinear terms being appreciable is to increase the dissipation of the waves. If we take this into account by a rapidly increasing viscosity, for example, the results can be made to converge. Using these results, we may make a guess as to the order of magnitude of the energy generated by isotropic turbulence in the form of hydromagnetic waves.

VII. THE HYDROMAGNETIC WAVES

The derivation which follows is patterned after that of van de Hulst (1951), who first derived the three modes of the hydromagnetic waves. The equations of motion are

$$\frac{\partial(\rho v_i)}{\partial t}+\frac{\partial(\rho v_i v_j)}{\partial x_i}=\frac{1}{c}\boldsymbol{I}\times(\boldsymbol{H}'+\boldsymbol{h}')-a_0^2\,\mathrm{grad}\,\rho+\frac{\mu}{3}\,\mathrm{grad}\,\mathrm{div}\,\boldsymbol{v}+\rho\nabla^2\boldsymbol{v}\,, \tag{45}$$

$$\frac{\partial\rho}{\partial t}+\frac{\partial(\rho v_i)}{\partial x_i}=0\,, \tag{46}$$

$$\frac{\boldsymbol{I}}{\sigma}=\boldsymbol{E}+\frac{1}{c}\boldsymbol{v}\times(\boldsymbol{H}'+\boldsymbol{h}')\,, \tag{47}$$

$$\mathrm{curl}\,\boldsymbol{E}=-\frac{1}{c}\frac{\partial(\boldsymbol{H}'+\boldsymbol{h}')}{\partial t}=-\frac{1}{c}\frac{\partial\boldsymbol{h}'}{\partial t}\,, \tag{48}$$

$$\mathrm{curl}\,\boldsymbol{h}'=\frac{4\pi}{c}\boldsymbol{I}\,, \tag{49}$$

where $\boldsymbol{H}'+\boldsymbol{h}'$ is the magnetic field, $\boldsymbol{H}'$ is the constant magnetic field, $\boldsymbol{I}$ is the current, σ is the conductivity, $\boldsymbol{E}$ is the electric field, and μ is the viscosity. We will neglect the viscous terms (i.e., $\sigma\to\infty$, $\mu\to 0$). As before, we have replaced grad p by a_0^2 grad ρ. Replacing $\boldsymbol{I}$ by $4\pi/c$ curl $\boldsymbol{h}'$ in equation (45) and differentiating with respect to time, one finds, by equation (46),

$$\frac{\partial^2(\rho\boldsymbol{v})}{\partial t^2}-a_0^2\,\mathrm{grad}\,\mathrm{div}\,(\rho\boldsymbol{v})-\frac{1}{4\pi}\,\mathrm{curl}\left(\frac{\partial\boldsymbol{h}'}{\partial t}\right)\times\boldsymbol{H}'=-\frac{\partial^2(\rho v_i v_j)}{\partial x_i\partial x_j}+\frac{1}{4\pi}\frac{\partial}{\partial t}(\mathrm{curl}\,\boldsymbol{h}'\times\boldsymbol{h}')\,. \tag{50}$$

The second-order terms have been written on the right-hand side and will be considered as generating terms for the hydromagnetic waves. From equations (48) and (47) we obtain

$$\frac{\partial\boldsymbol{h}'}{\partial t}=-c\,\mathrm{curl}\,\boldsymbol{E}=\mathrm{curl}\,(\boldsymbol{v}\times\boldsymbol{H}')+\mathrm{curl}\,(\boldsymbol{v}\times\boldsymbol{h}')\,.$$

Substituting this in equation (50), we find

$$\frac{\partial^2(\rho \boldsymbol{v})}{\partial t^2}+\frac{\partial(\rho v_i v_j)}{\partial x_j}-a_0^2 \operatorname{grad} \operatorname{div}(\rho \boldsymbol{v})-\frac{1}{4\pi}[\operatorname{curl}\operatorname{curl}(\boldsymbol{v}\times\boldsymbol{H}')]\times\boldsymbol{H}'$$
$$=\frac{1}{4\pi}\frac{\partial}{\partial t}(\operatorname{curl}\boldsymbol{h}'\times\boldsymbol{h}')+\frac{1}{4\pi}[\operatorname{curl}\operatorname{curl}(\boldsymbol{v}\times\boldsymbol{h}')]\times\boldsymbol{H}'. \tag{51}$$

If we use either $(\rho \boldsymbol{v})$ or $\boldsymbol{v}$ as the dependent variable and eliminate ρ by equation (46), we will obtain second-order terms which cannot be neglected outside the turbulent region. Hence neither variable is the correct one to use. However, if we assume that ρ is constant in equation (51), the generating terms assume a quadrupole nature, and it should be possible to neglect them outside the turbulent region. This should give the correct answer. Taking ρ as constant, equation (51) becomes the usual equation for hydromagnetic waves:

$$\frac{\partial^2\boldsymbol{v}}{\partial t^2}-a_0^2 \operatorname{grad}\operatorname{div}\boldsymbol{v}-[\operatorname{curl}\operatorname{curl}(\boldsymbol{v}\times\boldsymbol{H})]\times\boldsymbol{H}=\boldsymbol{P}, \tag{52}$$

$$\boldsymbol{P}=-\frac{\partial^2(v_i v_j)}{\partial t_i \partial x_j}+\frac{\partial}{\partial t}(\operatorname{curl}\boldsymbol{h}\times\boldsymbol{h})+[\operatorname{curl}\operatorname{curl}(\boldsymbol{v}\times\boldsymbol{h})]\times\boldsymbol{H}, \tag{53}$$

and

$$\boldsymbol{h}=\frac{\boldsymbol{h}'}{\sqrt{(4\pi\rho)}}, \qquad \boldsymbol{H}=\frac{\boldsymbol{H}'}{\sqrt{(4\pi\rho)}}. \tag{54}$$

Analyzing equation (52) into plane waves,

$$\boldsymbol{v}=\int \boldsymbol{a}_k e^{-i\boldsymbol{k}\cdot\boldsymbol{r}}d\boldsymbol{k}, \qquad a_k=\int\frac{\boldsymbol{v}\,e^{i\boldsymbol{k}\cdot\boldsymbol{r}}}{(2\pi)^3}d\boldsymbol{r}, \tag{55a}$$

$$\boldsymbol{P}=\int \boldsymbol{p}_k e^{-i\boldsymbol{k}\cdot\boldsymbol{r}}d\boldsymbol{k}, \qquad \boldsymbol{p}_k=\int\frac{\boldsymbol{P}\,e^{i\boldsymbol{k}\cdot\boldsymbol{r}}}{(2\pi)^3}d\boldsymbol{r}, \tag{55b}$$

it becomes

$$\frac{\partial^2\boldsymbol{a}_k}{\partial t^2}+[a_0^2(\boldsymbol{k}\cdot\boldsymbol{a}_k)+H^2\{(\boldsymbol{k}\cdot\boldsymbol{a}_k)-(\boldsymbol{k}\cdot\boldsymbol{n})(\boldsymbol{a}_k\cdot\boldsymbol{n})\}]\boldsymbol{k}-H^2(\boldsymbol{k}\cdot\boldsymbol{n})(\boldsymbol{k}\cdot\boldsymbol{a})\boldsymbol{n}$$
$$+(\boldsymbol{k}\cdot\boldsymbol{H})^2\boldsymbol{a}_k=\boldsymbol{p}_k. \tag{56}$$

We introduce the following co-ordinates: the z-axis is taken in the direction of $\boldsymbol{k}$, and the y-axis in the plane of $\boldsymbol{k}$ and $\boldsymbol{H}$, so that $\boldsymbol{H}$ lies in the first or second quadrant of the yz-plane. In components, equation (56) breaks up into three equations:

$$(x \text{ component}): \ddot{a}_x+H^2n_z^2k^2a_x=p_x, \tag{57a}$$

$$(y \text{ component}): \ddot{a}_y+H^2n_z^2k^2a_y-n_yn_zH^2k^2a_z=p_y, \tag{57b}$$

$$(z \text{ component}): \ddot{a}_z-H^2n_yn_zk^2a_y+\{H^2(1-n_z^2)k^2+a_0^2k^2\}a_z=p_z. \tag{57c}$$

The first equation represents the ordinary Alfvén mode of hydromagnetic waves with velocity $c_x=H_z$. The last two equations are coupled and, when analyzed into normal modes, yield the modified Alfvén and the modified sound waves. Introducing the normal co-ordinates A_1 and A_2 by

$$a_y=A_1\cos\beta-A_2\sin\beta, \tag{58a}$$

$$a_z=A_1\sin\beta+A_2\cos\beta, \tag{58b}$$

equations (57*b*) and (57*c*) become

$$\ddot{A}_1+w_1^2A_1=p_y\cos\beta+p_z\sin\beta=p_1\,, \tag{59a}$$

$$A_2+w_2^2A_2=-p_y\sin\beta+p_z\cos\beta=p_2\,, \tag{59b}$$

where

$$w_1=c_1k\,,\qquad w_2=c_2k\,,\qquad \tan\,\beta=\frac{n_z}{n_y}\left(1-\frac{c_1^2}{H_z^2}\right), \tag{60}$$

and c_1 and c_2 are roots of the equation

$$c^4-(H^2+a_0^2)\;c^2+n_z^2H^2a_0^2=0\,. \tag{61}$$

As $H \rightarrow 0$, c_1 becomes the Alfvén velocity, and c_2 the sound velocity. It must be noted that if $\boldsymbol{k}$ is perpendicular to $\boldsymbol{H}$, the velocities of the Alfvén and modified Alfvén modes vanish, and these modes disappear. The significance of this will become evident.

VIII. ENERGY GENERATED INTO THE WAVES

The total energy in the acoustic and hydromagnetic fields is

$$\begin{aligned}\frac{\rho}{2}\int\left[v^2+\frac{1}{\rho^2a_0^2}(\delta p)^2+h^2\right]d\boldsymbol{r}=(2\pi)^3\,\frac{\rho}{2}\int\Big\{\frac{|\,a_{k_x}|^2}{w_x^2}+|\,a_{k_x}|^2+\frac{|\,\dot{A}_1|^2}{w_1^2}+|\,A_1|^2\\+\frac{|\,\dot{A}_2|^2}{w_2^2}+|\,A_2|^2\Big\}\,d\boldsymbol{k}\,,\end{aligned} \tag{62}$$

$$w_x=c_xk\,,$$

so that we may calculate the rate of increase in each mode separately. Consider the Alfvén mode first. Multiplying equation (57*a*) by p_x^* and adding the complex conjugate, we obtain

$$\frac{dE_{k_x}}{dt}=\frac{\rho}{2w_x^2}\frac{d}{dt}\{\,|\,\dot{a}_x|^2+w_x^2|\,a_x|^2\}=p_x^*a_x+p_xa_x^*\,. \tag{63}$$

But we may write

$$a_x(t)=\int_{-\infty}^{t}\frac{p_x(t_0)}{w_x}\sin w_x(t-t_0)\,dt_0$$

or

$$\dot{a}_x(t)=\int_{-\infty}^{t}p_x(t_0)\cos w_x(t-t_0)\,dt_0\,. \tag{64}$$

Substituting in equation (63) and taking a time average, we obtain

$$\begin{aligned}\left\langle\frac{dE_{k,x}}{dt}\right\rangle&=\lim_{T\to\infty}\frac{1}{2T}\int_{-T}^{+T}\frac{dE_{k,x}\,dt}{dt}=\lim_{T\to\infty}\frac{1}{2T}\int_{-T}^{+T}dt\int_{-\infty}^{t}\\&\quad\times\Big\{\frac{\rho}{2w_x^2}\,[p_x^*(t)\,p_x(t_0)+p_x(t)\,p_x^*(t_0)\,]\cos w\,(t-t_0)\Big\}\,dt_0\\&=\frac{\rho}{2w_x^2}\lim\frac{1}{2T}\int_{-T}^{+T}dt\int_{-\infty}^{\infty}p_x^*(t)\,p_x(t-s)\cos w\,s\,d\,s\,.\end{aligned} \tag{65}$$

In equation (55*b*) the exponential exp(*i**k*·*r*) may be expanded in a power series in ***ik*·*r***, and higher terms may be neglected. This is the usual assumption that highermultipole terms are small and is satisfied in our case if the wave length is much greater than the scale length of the turbulence. This is true for small Mach numbers. Thus

$$p^{*}_{k,\,x}\,(t)=\frac{1}{(2\pi)^{3}}\int\Big\{1-i\boldsymbol{k}\cdot\boldsymbol{r}-\frac{(\boldsymbol{k}\cdot\boldsymbol{r})^{2}}{2}+\ldots\Big\}P_{x}\,(t)\,d\boldsymbol{r}\;; \tag{66}$$

and, using equation (53), we find, after integration by parts,

$$p^{*}_{k,\,x}\,(t)=\frac{1}{(2\pi)^{3}}\int\Big\{-ik\,\frac{\partial}{\partial t}\,(v_{z}v_{x}-h_{z}h_{x})+k^{2}H_{z}\,(v_{z}h_{x}-v_{x}h_{z})\Big\}\,d\boldsymbol{r}\;. \tag{67}$$

To illustrate the calculation, we will consider only the first term. Summing equation (65) over all wave numbers $\boldsymbol{k}$ and introducing $W_{x}=kc_{x}$ as the integration variable, we have

$$\Big\langle\frac{dE_{x}}{dt}\Big\rangle=\frac{\rho}{4\,(2\pi)^{3}}\int d\Omega\lim_{T\to\infty}\frac{1}{2T}\int_{-T}^{T}dt\int d\boldsymbol{r}\int d\boldsymbol{r}'\int\frac{w^{2}dw}{c_{x}^{5}}\int_{-\infty}^{\infty}ds \\ \Big\{\frac{\partial}{\partial t}\,[\,v_{z}v_{x}\,(\boldsymbol{r}',\,t)\,]\,\frac{\partial}{\partial t}\,[\,v_{z}v_{x}\,(\boldsymbol{r},\,t-s)\,]\Big\}\,. \tag{68}$$

But

$$\int_{-\infty}^{\infty}w^{2}\,e^{iws}dw=2\pi\,\frac{\partial^{2}}{\partial s^{2}}\,\delta\,(s)\;, \tag{69}$$

where $\delta(s)$ is the Dirac delta function; hence

$$\Big\langle\frac{dE_{x}}{dt}\Big\rangle=\frac{\rho}{4\pi}\,\frac{1}{4\pi}\int\frac{d\Omega}{c_{x}^{5}}\int d\boldsymbol{r}\int d\boldsymbol{r}'\Big\langle\frac{\partial^{2}}{\partial t^{2}}\Big\{-i\,[\,v_{z}v_{x}\,(\boldsymbol{r}',\,t)\,-h_{z}h_{x}] \\ +\frac{H_{z}}{w}\,(v_{z}h_{x}-v_{x}h_{z})\Big\}\frac{\partial^{2}}{\partial t^{2}}\Big\{i\,[\,v_{z}v_{x}\,(\boldsymbol{r},\,t)\,-h_{z}h_{x}]+\frac{H_{z}}{w}\,(v_{z}h_{x}-v_{x}h_{z})\Big\}\Big\rangle_{t}\,, \tag{70}$$

where the average is over t. This is the energy emitted in the Alfvén mode. In an exactly similar way the energy emitted in the other two modes may be found. The energy emitted in the modified Alfvén waves is

$$\frac{\rho}{4\pi}\,\frac{1}{4\pi}\int\frac{d\Omega}{c_{1}^{5}}\int d\boldsymbol{r}\int d\boldsymbol{r}'\Big\langle\frac{\partial^{2}}{\partial t^{2}}\Big\{\Big[-i\,(v_{z}v_{y}-h_{z}h_{y})\,-\frac{H_{z}}{c_{1}}\,(\boldsymbol{v}\times\boldsymbol{h})_{x}\Big]\cos\beta \\ +\Big[-i\Big(v_{z}^{2}-h_{z}^{2}+\frac{h^{2}}{2}\Big)+\frac{H_{y}}{c_{1}}\,(\boldsymbol{v}\times\boldsymbol{h})_{x}\Big]\sin\beta\Big\}_{\boldsymbol{r}=\boldsymbol{r}'}\,\frac{\partial^{2}}{\partial t^{2}}\Big\{\Big[i\,(v_{z}v_{y}-h_{z}h_{y}) \\ -\frac{H_{z}}{c_{1}}\,(\boldsymbol{v}\times\boldsymbol{h})_{x}\Big]\cos\beta+\Big[i\Big(v_{z}^{2}-h_{z}^{2}+\frac{h^{2}}{2}\Big)+\frac{H_{y}}{c_{1}}\,(\boldsymbol{v}\times\boldsymbol{h})_{x}\Big]\sin\beta\Big\}_{\boldsymbol{r}=\boldsymbol{r}}\Big\rangle_{t}\,. \tag{71}$$

The energy emitted in the modified sound wave is

$$\frac{\rho}{4\pi}\,\frac{1}{4\pi}\int\frac{d\Omega}{c_{2}^{5}}\int d\boldsymbol{r}\int d\boldsymbol{r}'\Big\langle\frac{\partial^{2}}{\partial t^{2}}\Big\{\Big[-i\,(v_{z}v_{y}-h_{z}h_{y})\,-\frac{H_{z}}{c_{2}}\,(\boldsymbol{v}\times\boldsymbol{h})_{x}\Big]\sin\beta \\ -\Big[-i\Big(v_{z}^{2}-h_{z}^{2}+\frac{h^{2}}{2}\Big)+\frac{H_{y}}{c_{2}}\,(\boldsymbol{v}\times\boldsymbol{h})_{x}\Big]\cos\beta\Big\}_{\boldsymbol{r}=\boldsymbol{r}'}\,\frac{\partial^{2}}{\partial t^{2}}\Big\{\Big[i\,(v_{z}v_{y}-h_{z}h_{y}) \\ -\frac{H_{z}}{c_{2}}\,(\boldsymbol{v}\times\boldsymbol{h})_{x}\Big]\sin\beta-\Big[i\Big(v_{z}^{2}-h_{z}^{2}+\frac{h^{2}}{2}\Big)+\frac{H_{y}}{c_{2}}\,(\boldsymbol{v}\times\boldsymbol{h})_{x}\Big]\cos\beta\Big\}_{\boldsymbol{r}=\boldsymbol{r}}\Big\rangle_{t}\,. \tag{72}$$

IX. NUMERICAL EVALUATION OF THE ENERGY

The expressions for the energies generated into the three modes are given by equations (70), (71), and (72). However, the co-ordinates x, y, and z depend upon the direction of the wave vector $\boldsymbol{k}$. Since the direction of $\boldsymbol{k}$ is to be integrated over in these expressions, the components of $\boldsymbol{v}$, $\boldsymbol{h}$, and $\boldsymbol{H}$ with respect to these axes must be transformed to components with respect to fixed co-ordinate axes before the integration over Ω may be performed. Then, since axisymmetric turbulence with the axis in the direction of $\boldsymbol{H}$ must be assumed, the theory developed in the first part of this paper for isotropic turbulence must be redeveloped for axisymmetric correlation coefficients.

However, if H^2 is not too large compared to the energy density of the turbulence, it is reasonable to expect that results obtained by assuming isotropic turbulence would give the correct order of magnitude. Furthermore, under this assumption, the correlation coefficients may be computed with respect to the movable axes, thus saving much work. Using the correlation coefficients developed in equations (39)(43), the energy rates are given by the following expressions: (1) The rate of energy to the Alfvén mode is

$$\int_0^{\pi/2} \frac{\sin\theta}{c_x^5} \Big\} B(\beta) + C(\beta) \frac{H_z^2}{c_x^2} \Big\{ d\theta\,; \tag{73}$$

(2) the rate of energy to the modified Alfvén mode is

$$\int_0^{\pi/2} \frac{\sin\theta}{c_1^5} \Big[\Big\} B(\beta) + C(\beta) \frac{H_z^2}{c_1^2} \Big\{ \cos^2\beta + \Big\} A(\beta) + C(\beta) \frac{H_y^2}{c_1^2} \Big\{ \sin^2\beta \\ + 2C(\beta) \frac{H_y H_z}{c_1^2} \sin\beta\cos\beta \Big] d\theta\,; \tag{74}$$

(3) the rate of energy to the modified sound mode is

$$\int_0^{\pi/2} \frac{\sin\theta}{c_2^5} \Big[\Big\} B(\beta) + C(\beta) \frac{H_z^2}{c_2^2} \Big\{ \sin^2\beta + \Big\} A(\beta) + C(\beta) \frac{H_y^2}{c_2^2} \Big\{ \cos^2\beta \\ - 2C(\beta) \frac{H_y H_z}{c_2^2} \sin\beta\cos\beta \Big] d\theta\,, \tag{75}$$

where θ is the angle between $\boldsymbol{H}$ and $\boldsymbol{k}$,

$$\begin{aligned} A(\beta) &= \frac{1}{15}\int_0^\infty r^4 \{24\phi'^2 + 8f'\psi' + 17\tfrac{1}{2}\theta'^2 + 5\tfrac{1}{2}h\chi'\}\,dr\,, \\ A(\beta) &= [13.54 + A_1(\beta)\gamma^2 + 12.25\beta\gamma^4]\frac{u^8}{L}\,, \\ \dot{A}_1(\beta) &= \left(\frac{2}{1+\beta^2}\right)^{11/2} \{1.1114\beta^{12} + 7.575\beta^{10} + 26.08\beta^8 \\ &\qquad + 42.49\beta^6 + 24.73\beta^4 + 7.789\beta^2 + 1.232\}\,; \end{aligned} \tag{76}$$

$$
\begin{aligned}
B(\beta) &= \frac{1}{15}\int_0^\infty r^4\{13^{1/2}\phi'^2 + 4\tfrac{1}{2}f'\psi' + 13\tfrac{1}{2}\theta'^2 + 4\tfrac{1}{2}h'\chi'\}\,dr\,,\\
B(\beta) &= [7.621 + B_1(\beta)\,\gamma^2 + 7.878\beta\gamma^4]\,\frac{u^8}{L}\,,\\
B_1(\beta) &= \left(\frac{2}{1+\beta^2}\right)^{11/2}\{0.8698\beta^{12} + 5.798\beta^{10} + 18.72\beta^8\\
&\qquad + 29.34\beta^6 + 17.41\beta^4 + 5.556\beta^2 + 0.86977\}\,; \qquad (77)\\
C(\beta) &= \frac{1}{15}\int_0^\infty r^4\{21\theta'\phi' + 3\tfrac{1}{2}h'\psi + 3\tfrac{1}{2}f'\chi'\}\,dr\,,\\
C(\beta) &= [C_1(\beta)\,\gamma + C_2(\beta)\,\gamma^3]\,\frac{u^8}{L}\,,\\
C_1(\beta) &= \left(\frac{4}{3+\beta^2}\right)^{11/2}\{3.525\beta^6 + 12.18\beta^4 + 13.44\beta^2 + 5.186\}\,,\\
C_2(\beta) &= \left(\frac{4}{1+3\beta^2}\right)^{11/2}\{4.960\beta^{12} + 12.62\beta^{10} + 12.28\beta^8 + 3.965\beta^6\}\,. \qquad (78)
\end{aligned}
$$

Values for $B_1(\beta)$, $C_1(\beta)$, and $C_2(\beta)$ are given in Table 1, and they are plotted in Figure 1.

X. THE AVERAGE OVER THE DIRECTION OF THE WAVE VECTOR $\boldsymbol{k}$

Since $c_x = H\cos\theta \to 0$ as θ goes to $\pi/2$ and c_1 likewise goes to zero, we see that the integrals in equations (73) and (74) are divergent. However, as has been mentioned before, a consequence of small wave velocities is that the nonlinear terms become important. For a plane sound wave, the effect of the nonlinear terms is to push the compression part of the wave forward, steepening the gradient, and to flatten out the rarefaction part. Since the viscous dissipation depends on $\nu\nabla^2\boldsymbol{v}$, an effect of the nonlinear terms is to increase the dissipation of the sound wave. It is plausible that the nonlinear terms in hydromagnetic waves would have a similar effect. Taking these terms into account by assuming a variable coefficient of viscosity and including this viscosity in the equations of motion of the waves, one obtains convergence of these integrals.

This may be made plausible as follows: For a plane wave a viscous term $\nu_{\text{eff}}k^2\dot{a}_x$ appears in equations (57*a*), (59*a*), and (59*b*). Although these viscous terms produce a modification in the definition of the normal modes, it is not significant, and we shall ignore it. Thus

$$
\dot{a}_{k_x} = \int_{-\infty}^{t} e^{-\nu k^2(t-t_0)}\,p_x(t_0)\cos\left[w\sqrt{\left(1-\frac{\nu k^2}{c^2}\right)}\,(t-t_0)\right]dt_0\,.
$$

The main effect of the viscosity lies in the exponential factor, so we will ignore the square root in the cosine argument. Equation (68) becomes

$$
\left\langle\frac{dE}{dt}\right\rangle_t = \frac{\rho}{2(2\pi)^3}\int\frac{d\Omega}{c_x^5}\int dr\int dr'\int_{-\infty}^{\infty}w^2dw\int_0^\infty ds\,e^{-\nu k^2|s|}\cos ws
$$
$$
\times\left\{\lim_{T\to\infty}\frac{1}{2T}\int_{-T}^{+T}\frac{\partial}{\partial t}(v_xv_z)\,\Big|_{\substack{r=r'\\ t=t}}\,\frac{\partial}{\partial t}(v_xv_z)\,\Big|_{\substack{r=r\\ t=t-s}}\right\}.
$$

Although there is some trouble in the integration by parts to get rid of w^2, we may, for our purposes, neglect it here. Proceeding as before, we obtain

$$
\left\langle\frac{dE}{dt}\right\rangle = \frac{\rho}{2(2\pi)^3}\int\frac{d\Omega}{c_x^5}\int dr\int dr'\int_{-\infty}^{\infty}dw\int_0^\infty ds\,e^{-(\nu s w^2/c_x^2)}\cos ws\,e^{-\gamma^2s^2}
$$
$$
\times\left\langle\frac{\partial^2}{\partial t^2}\,v_zv_x\,\Big|_{\substack{t=t\\ r=r}},\,\frac{\partial^2}{\partial t^2}(v_zv_x)\,\Big|_{\substack{t=t\\ r=r}}\right\rangle,
$$

where we have assumed

$$\left\langle \frac{\partial^2}{\partial t^2}(v_z v_x)\Big|_{\substack{t=t,\\ r=r}}\, \frac{\partial^2}{\partial t^2}(v_z v_x)\Big|_{\substack{t=t-s\\ r=r}} \right\rangle = \left\langle \frac{\partial^2(v_z v_x)}{\partial t^2}\Big|_{\substack{t=t,\\ r=r}}\, \frac{\partial^2(v_z v_x)}{\partial t^2}\Big|_{\substack{t=t\\ r=r}} \right\rangle e^{-\gamma^2 s^2} .$$

Carrying out the integration first over w, we have

$$\int_{-\infty}^{\infty} dw \int_0^{\infty} d\,s\, e^{-(\nu s w^2/c_x^2)} e^{-\gamma^2 s^2} \cos w s = 2\sqrt{\pi}\int_0^{\infty} e^{-u^4 x^2 - u^2} du$$

$$\left\{ \begin{array}{ll} \rightarrow \dfrac{1}{\sqrt{x}} & \text{as } x \rightarrow \infty \\ \rightarrow \pi & \text{as } x \rightarrow 0 \end{array} \right\} , \tag{79}$$

where $x = \gamma\nu/c_x^2$. Thus we obtain a convergence factor $c_x/\sqrt{\nu}$ as $c \rightarrow 0$. Since ν goes to infinity rapidly as $c \rightarrow 0$, our results remain finite. It remains to guess approximate values for the integrals in equations (73) and (74).

As is seen from the foregoing considerations, the nonlinear terms give a cutoff to the divergent integrals. It would be expected that the nonlinear terms first become important when u is comparable with the velocity c of the waves. If we introduce this as a limit in our integrals in place of $\pi/2$, we should get a result of the correct order of magnitude. Thus in equation (73) we may write

$$\begin{gathered} u^5 \int_0^{H_z = u} \frac{\sin\theta}{H_z^5}\, d\theta = \tfrac{1}{4}(M_H - M_H^5) = f_1(M_H) , \\ u = \sqrt{\langle v^2 \rangle} , \qquad M_H = \frac{u}{H} . \end{gathered} \tag{80}$$

If $H < u$, ($M_H > 1$), we have $f_1(M_H) = 0$.

If u is small compared to a_0, we may assume $H \ll a_0$ and set $c_1 \approx \boldsymbol{H_z}$ and make use of the approximations

$$\sin\beta \approx \tan\beta \approx \frac{H^2}{a_0^2}\tan\theta ,$$

$$\cos\beta \approx 1 .$$

Substituting these results in the integrals of equation (74), we get

$$u^5 \int_0^{u=c_1} \frac{\sin^2\beta \sin\theta}{c_1^5}\, d\theta \approx \frac{1}{4}\frac{H^4}{a_0^4}\{M_H - 2M_H^3 + M_H^5\} = \frac{H^4}{a_0^4} f_2(M_H) ,$$

$$\begin{aligned} u^5 \int_0^{u=c_1} \frac{\sin^2\beta\, H_y^2 \sin\theta\, d\theta}{c_1^7} &\approx \frac{1}{4}\frac{H^2}{a_0^2}\{M_H - 4M_H^3 + 3M_H^5 - 4M_H^5 \log_e M_H\} \\ &= \frac{H^2}{a_0^2} f_3(M_H) , \end{aligned}$$

$$u^5 \int \frac{\sin\beta\cos\beta}{c_1^7} H_y H_z \sin\theta\, d\theta \approx \frac{H^2}{a_0^2} f_2(M_H) .$$

The functions f_1, f_2, and f_3 are of the order of magnitude of 0.1 if $M_H < 1$ ($H > u$), and drop to zero rapidly as H becomes smaller than u. Thus no energy is delivered to the Alfvén or the modified Alfvén modes until H becomes comparable to u.

Since c_2 always remains finite and nonzero, there are no divergencies present in equation (75). As $H \rightarrow 0$, the result goes into the result obtained in equation (44). For finite H we may carry out the integrals numerically.

Thus the energy rates are now given by the following equations. The rate of energy emitted in the Alfvén mode is

$$f_1(M_H)\,\{B(\beta)+C(\beta)\}\epsilon\,; \tag{81}$$

the rate of energy emitted in the modified Alfvén mode is

$$\left\{\frac{H^4}{a_0^4}f_2(M_H)\,A(\beta)+f_1(M_H)B(\beta)+\left[f_1(M_H)+\frac{H^2}{a_0^2}f_3(M_H)\right.\right.$$
$$\left.\left.+\frac{2H^2}{a_0^2}f_2(M_H)\right]C(\beta)\right\}\epsilon\,; \tag{82}$$

the rate of energy emitted in the modified sound mode is

$$M^5\left\{f_5\left(\frac{H}{a_0}\right)A(\beta)+f_4\left(\frac{H}{a_0}\right)B(\beta)+\frac{H^2}{a_0^2}f_6\left(\frac{H}{a_0}\right)C(\beta)\right\}\epsilon\,. \tag{83}$$

Here f_1, f_2, and f_3 are plotted in Figure 2, and f_4, f_5, and f_6 are given in Table 2.

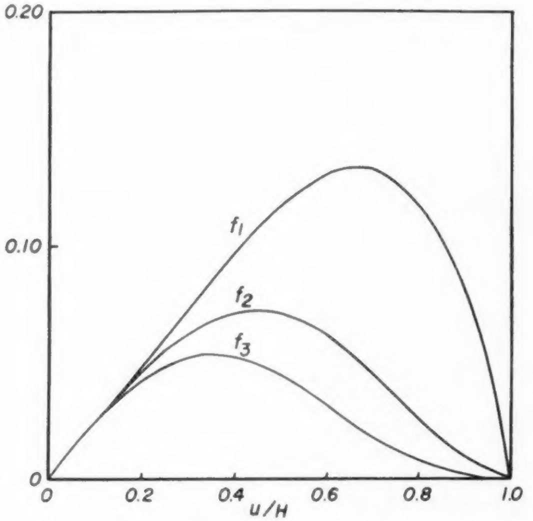

FIG. 2.—A plot of the functions f_1, f_2, and f_3 as functions of u/H

XI. DISCUSSION OF THE VALIDITY OF THE RESULTS

The same assumptions are made in deriving equations (81)–(83) as in the derivation of the results in the first part of this paper. The two assumptions made in the numerical calculation are incompatible, so there is no region where the results of equations (81), (82), and (83) are completely valid. The assumption of isotropic turbulence fails if H is comparable to u, so that the coefficients A, B, and C are given incorrectly when $H > u$. On the other hand, the expressions for f_1, f_2, and f_3 are accurate only if $H > u$. However, the essential results—the vanishing of the Alfvén modes for $H < u$ and the expression for the amount of energy into the sound mode—remain valid. Also $A_1(\beta)$, $B_1(\beta)$, $C_1(\beta)$, and $C_2(\beta)$ should be of the correct magnitude, even when H exceeds u.

One more comment may be made as to the assumptions about the nature of the turbulence. The size of our answers is due mainly to the large number of terms which arise from our assumptions. As these are the simplest ones that could be made for solving this problem, other more correct assumptions should lead to still more terms. It is unlikely that these terms would cancel one another, so that our answer probably errs on the side of being too small.

XII. APPLICATION TO THE THEORY OF THE SUPPORT OF THE CORONA

To account for the inverse temperature gradient in the solar chromosphere and the high temperatures (one million degrees) in the corona, Schwarzschild (1948) postulated that the chromosphere and the corona were heated by acoustic waves generated in the solar granulation. These waves are originally of small amplitude in the lower chromosphere and hence are not easily absorbed. As they proceed outward, the density decreases, and their amplitude increases. Since the velocity of sound is decreasing, the dissipation increases, and the inverse temperature gradient may be explained. Using our results, we may calculate the amount of acoustic energy generated in the solar granulation and compare this value with the radiation of the chromosphere and the corona, which it must balance. We will use the following figures in the calculation: the density in the photosphere, 10^{-7} gm/cm^3; velocity of sound, $a_0 = 7$ km/sec; mean turbulent velocity (of one component) in the solar granulation, 1.2 km/sec (Richardson and Schwarzschild 1953); energy radiated by the corona and the chromosphere, 10^{26}–10^{27} ergs/sec (van de Hulst 1953); surface area of the sun, 6×10^{22} cm^2.

TABLE 2

THE FUNCTIONS $f_4(a_0/H), f_5(a_0/H), f_6(a_0/H)$

H/a_0	a_0^2/H^2	f_4	f_5	f_6
0.316	10.0	0.0008	0.9992	0.6438
.447	5.0	.0027	.9973	.6183
.632	2.5	.0087	.9913	.5723
0.816	1.5	0.0183	0.9817	0.5264

Imagine the granulation to exist all over the surface of the photosphere and assume that the turbulence will be effective in generating acoustic noise to a certain depth which is comparable with the scale length of the turbulence L:

$$L = \frac{(\langle v_1^2 \rangle)^{3/2}}{\epsilon} .$$

Then the total noise generated per second is

$$L_{\text{noise}} = \alpha \epsilon M^5 \rho S L ,$$

$$= \frac{\alpha (\langle v_1^2 \rangle)^4}{a_0^5} \rho S ,$$

$$L_{\text{noise}} = 1.0 \times 10^{28} \text{ ergs/sec} .$$

Now consider the possibility of turbulent magnetic fields being present. In this case $\gamma = 1$ corresponds to a field strength of 40 gauss; and, if we take $\beta = 2$, we find $A' = 150$. The acoustic energy output in this case is 1.3×10^{29} ergs/sec. These values for a fluctuating magnetic field are compatible with values found by Kiepenheuer (1953).

For hydromagnetic waves to be generated, a general field of 40 gauss extending over a considerable region is needed. Such a field does not seem to be present, so that we must conclude that the solar granulation does not generate hydromagnetic waves.

The foregoing calculations indicate that there is abundant energy generated in the form of acoustic waves, available for heating the corona. In spite of large losses of this energy due to refraction and reflection of the outgoing waves by the decreasing density, there is still ample energy left to heat the chromosphere and the corona, if the figures used earlier are correct.

Whether there is actually magnetic turbulence in the granulations and whether the increased amount of noise due to the presence of magnetic turbulence is needed cannot be decided here. The origin of such magnetic turbulence is obscure. According to Batchelor (1950), the criteria for magnetic turbulence to arise spontaneously is that $4\pi\sigma\nu > 1$, in which σ is the electrical conductivity and ν is the kinematic viscosity. In the solar photosphere $4\pi\sigma\nu$ is of the order of 0.1, and hence magnetic turbulence would not be expected. However, if instead of kinematic viscosity the eddy viscosity of the smaller eddies is used, a factor of 10^6 is gained in ν, and magnetic turbulence is extremely likely.

Furthermore, in giant stars $4\pi\sigma\nu$ is much larger than in the sun, so that spontaneous magnetic fields are almost certainly present in their atmospheres. Hence the phenomenon of the generation of acoustic waves by hydromagnetic turbulence may be important in the theory of their atmospheres.

In conclusion, I wish to express my gratitude to Professor S. Chandrasekhar for suggesting this problem to me. I am indebted to him for many helpful discussions concerning it. I am also grateful to Professor M. Schwarzschild for discussions concerning the application of my results to the heating of the solar chromosphere. I would like to thank Miss H. Steinman for helping with the typing and Mr. Dan Schulte for making the diagrams.

REFERENCES

Batchelor, G. K. 1950, *Proc. R. Soc. London, A*, **201**, 405.
———. 1951, *Proc. Cambridge Phil. Soc.*, **47**, 359.
Chandrasekhar, S. 1950, *Proc. R. Soc. London, A*, **204**, 435.
———. 1951, *ibid.*, **207**, 301.
van de Hulst, H. C. 1951, *Problems of Cosmical Aerodynamics* (Symposium held by the I.U.T.A.M. and I.A.U., Paris, 1949) (Dayton, Ohio), chap. vi.
———. 1953, *The Sun*, ed. Gerard P. Kuiper (Chicago, 1953), chap. v.
Kiepenheuer, K. O. 1953, *Ap. J.*, **117**, 447.
Lighthill, M. J. 1952, *Proc. R. Soc. London, A*, **211**, 564.
Proudman, I. 1952, *Proc. R. Soc. London, A*, **214**, 119.
Richardson and Schwarzschild, M. 1953, *Ap. J.*, **117**, 447.
Schwarzschild, M. 1948, *Ap. J.*, **107**, 1.

MAGNETOHYDRODYNAMIC WAVES UNDER THE ACTION OF THE CORIOLIS FORCE. II

B. LEHNERT
Royal Institute of Technology, Stockholm, Sweden

Received September 16, 1954

ABSTRACT

The phase velocity of a single plane magnetohydrodynamic wave in a rotating liquid is independent of the amplitude. The nonlinear interactions between the components of the spectrum of a complex traveling disturbance vanish only in a nonrotating fluid without dissipation. A criterion for the approximate validity of the principle of superposition is given for small values of the Coriolis force and the dissipation. In a rotating medium in a magnetic field a disturbance will not necessarily travel along the magnetic field lines. The anisotropic group velocity for a wave packet is given. In solar physics the effects of anisotropic dispersion and nonlinearity are significant for disturbances with wave lengths of the order of a hundredth of the solar radius, if a dipole field with a polar strength of less than 25 gauss is assumed.

I. INTRODUCTION

In a previous paper (Lehnert 1954) magnetohydrodynamic waves in a rotating incompressible liquid were studied for small amplitudes. It was shown that the Coriolis force splits a plane-polarized Alfvén wave into two circularly polarized waves with different wave velocities. Probably this modification of the Alfvén velocity cannot be neglected in solar physics for disturbances of sunspot size. In solar physics and in many other applications of magnetohydrodynamics, disturbances may occur with amplitudes large enough to introduce nonlinear phenomena. The main purpose of this paper is to investigate the limitations of the linear theory of magnetohydrodynamic waves in a rotating, incompressible liquid. The solutions for a single plane wave are re-examined in Section II under the assumption of arbitrary amplitudes. The conclusions lead to a discussion of the superposition of plane waves in Section III, and a criterion of the approximative validity of the principle of superposition is given in Section IV. Finally, an analysis of the group velocity is carried out for small amplitudes in Section V.

II. THE PLANE WAVE

The magnetohydrodynamic equations of an incompressible liquid with electrical conductivity σ, viscosity ν, and density ρ in a homogeneous magnetic field, $\boldsymbol{B} = \mu \boldsymbol{H}$, are[1]

$$\operatorname{curl} \boldsymbol{h} = \boldsymbol{i} \,; \qquad \operatorname{curl} \boldsymbol{E} = -\mu \frac{\partial \boldsymbol{h}}{\partial t} , \tag{1}$$

$$\boldsymbol{i} = \sigma \left[\boldsymbol{E} + \mu \boldsymbol{v} \times (\boldsymbol{H} + \boldsymbol{h}) \right] , \tag{2}$$

$$\operatorname{div} \boldsymbol{h} = \operatorname{div} \boldsymbol{v} = 0 , \tag{3}$$

and

$$\rho \left[\frac{\partial \boldsymbol{v}}{\partial t} + (\boldsymbol{v} \cdot \boldsymbol{\nabla}) \boldsymbol{v} + 2 \boldsymbol{\Omega} \times \boldsymbol{v} + \boldsymbol{\Omega} \times (\boldsymbol{\Omega} \times \boldsymbol{r}) \right] = \mu \boldsymbol{i} \times (\boldsymbol{H} + \boldsymbol{h}) - \boldsymbol{\nabla} p + \nu \rho \boldsymbol{\nabla}^2 \boldsymbol{v} , \tag{4}$$

where $\boldsymbol{\Omega}$ is the angular velocity and the other symbols have their usual meaning. The eliminations of $\boldsymbol{i}$ and $\boldsymbol{E}$ are analogous to the deductions by Walén (1944) and Lundquist (1952), giving

---

[1] MKSA units are used throughout this paper.

$$\left(\frac{\partial}{\partial t} - \lambda \nabla^2\right) \boldsymbol{h} = (\boldsymbol{H} \cdot \nabla)\, \boldsymbol{v} + \operatorname{curl}\, (\boldsymbol{v} \times \boldsymbol{h})\, ; \qquad \lambda = \frac{1}{\mu \sigma}, \tag{5}$$

$$\left(\frac{\partial}{\partial t} - \nu \nabla^2\right) \boldsymbol{v} = \frac{\mu}{\rho} (\boldsymbol{H} \cdot \nabla)\, \boldsymbol{h} + 2\boldsymbol{v} \times \boldsymbol{\Omega} - \nabla \Phi - \frac{\mu}{\rho}\, \boldsymbol{h} \times \operatorname{curl} \boldsymbol{h} + \boldsymbol{v} \times \operatorname{curl} \boldsymbol{v}\, , \tag{6}$$

and

$$\Phi = \frac{p}{\rho} + \phi_c + \frac{\mu}{\rho} (\boldsymbol{H} \cdot \boldsymbol{h}) + \frac{v^2}{2}. \tag{7}$$

Just as in the previous work (Lehnert 1954), we study plane waves where the particle velocity and the induced magnetic field (but not necessarily the pressure) vary as $\exp\, [i(\kappa z + \omega t)]$. Equations (5) and (6) reduce to

$$(i\omega + \lambda \kappa^2)\, (h_x,\ h_y) = i\, \kappa H_z\, (v_x,\ v_y)\, ; \qquad h_z = v_z = 0\, , \tag{8}$$

$$(i\omega + \nu \kappa^2)\, (v_x,\ v_y) = i\, \frac{\mu}{\rho}\, \kappa H_z\, (h_x,\ h_y) + 2\Omega_z\, (v_y, - v_x)\, , \tag{9}$$

and

$$0 = 2\, (\Omega_y v_x - \Omega_x v_y) - \frac{\partial}{\partial z} \Phi - \frac{1}{2} \frac{\partial}{\partial z} \left[\frac{\mu}{\rho} (h_x^2 + h_y^2) - (v_x^2 + v_y^2) \right]. \tag{10}$$

The determinant of equations (8) and (9) vanishes if

$$[\, (i\omega + \lambda \kappa^2)\, (i\omega + \nu \kappa^2) + \kappa^2 V_\kappa^2]^{\,2} = - 4\Omega_\kappa^2\, (i\omega + \lambda \kappa^2)^{\,2}, \tag{11}$$

where

$$V_\kappa \equiv V_z = V \cos \psi\, ; \qquad V = H \left(\frac{\mu}{\rho}\right)^{1/2}; \qquad \Omega_\kappa \equiv \Omega_z = \Omega \cos \varphi\, . \tag{12}$$

Equation (11), which is also given in an earlier paper (Lehnert 1955), has the solutions

$$\pm\, \omega = \kappa V_\kappa \{ \pm \{ 1 + [\chi \mp i\, (\zeta - \eta)\,]^{\,2} \}^{1/2} \pm \chi + i\, (\zeta + \eta)\, \}\, ; \tag{13}$$

$$\chi = \frac{\Omega_\kappa}{\kappa V_\kappa}; \qquad \zeta = \frac{\lambda \kappa}{2 V_\kappa}; \qquad \eta = \frac{\nu \kappa}{2 V_\kappa}, \tag{14}$$

where the right-hand side of equation (13) corresponds to four different types of waves and the notation on the left-hand side of the same equation is used to indicate the two possible, opposite, directions of motion of the wave front for each type of wave.

For small values of χ, ζ, and η, equations (12), (13), and (14) show that we may write

$$|\, \chi\, | \approx \left| \frac{\Omega_\kappa}{\omega} \right| = \frac{\tau}{T} |\cos \varphi\, |\, , \tag{15}$$

which indicates that the Coriolis force is usually significant for a wave with a period, τ, comparable to the period of revolution, T, of the medium.

When equations (8) and (9) are satisfied, the pressure may be determined by equations (7) and (10), giving

$$\frac{1}{\rho} \frac{\partial p}{\partial z} = - \frac{\partial \phi_c}{\partial z} - \frac{\mu}{\rho} \frac{\partial}{\partial z} (\boldsymbol{H} \cdot \boldsymbol{h}) + 2\, (\Omega_y v_x - \Omega_x v_y) - \frac{1}{2} \frac{\mu}{\rho} \frac{\partial}{\partial z} (h_x^2 + h_y^2)\, , \tag{16}$$

in about the same way as in the waves studied by Alfvén (1950, see pp. 78–81) in a nonrotating liquid. Thus the solutions (13) for a single plane wave are valid for arbitrary amplitudes.

From equations (8) and (12) we have

$$\boldsymbol{v} = A\boldsymbol{h}\,, \qquad \text{where} \qquad A = \left(\frac{\mu}{\rho}\right)^{1/2}\left(\frac{\omega}{\kappa V_\kappa} - 2i\zeta\right). \tag{17}$$

Expressions (13), (14), and (17) are still valid if the frame of reference is rotated arbitrarily; V_κ and Ω_κ are the projections of $\boldsymbol{V}$ and $\boldsymbol{\Omega}$ on the wave number $\boldsymbol{\kappa}$.

III. SUPERPOSITION OF PLANE WAVES

a) CONDITIONS FOR THE VALIDITY OF THE PRINCIPLE OF SUPERPOSITION

In the previous section a solution was found for a single plane wave, valid for arbitrary amplitudes. In several physical applications, complex disturbances are of interest, and it is not obvious that such problems can be discussed in terms of plane waves. We start with a disturbance,

$$\boldsymbol{h}(\boldsymbol{r}, t) = \sum_{n=1}^{N} \boldsymbol{h}^{(n)}\,, \qquad \boldsymbol{v}(\boldsymbol{r}, t) = \sum_{n=1}^{N} \boldsymbol{v}^{(n)}\,, \tag{18}$$

composed of a finite number, N, of plane waves

$$\boldsymbol{h}^{(n)} = \boldsymbol{h}_0^{(n)} \exp\left[i\left(\boldsymbol{\kappa}_n \cdot \boldsymbol{r} + \omega_n t\right)\right] \tag{19}$$

and

$$\boldsymbol{v}^{(n)} = \boldsymbol{v}_0^{(n)} \exp\left[i\left(\boldsymbol{\kappa}_n \cdot \boldsymbol{r} + \omega_n t\right)\right] = A_n \boldsymbol{h}^{(n)}\,, \tag{20}$$

each of which satisfies the fundamental equations (5) and (6). Disturbance (18) also satisfies these equations if the following conditions are fulfilled:

$$\sum_{n=1}^{N} \left(i\omega_n + \lambda\kappa_n^2\right) \boldsymbol{h}^{(n)} = \sum_{n=1}^{N} i\left(\boldsymbol{\kappa}_n \cdot \boldsymbol{H}\right) \boldsymbol{v}^{(n)} + \sum_{n \neq m} \operatorname{curl}\left(\boldsymbol{v}^{(n)} \times \boldsymbol{h}^{(m)}\right) \tag{21}$$

$$\begin{aligned} \sum_{n=1}^{N} \left(i\omega_n + \nu\kappa_n^2\right) \boldsymbol{v}^{(n)} = {} & \sum_{n=1}^{N} \left[i\frac{\mu}{\rho}\left(\boldsymbol{\kappa}_n \cdot \boldsymbol{H}\right) \boldsymbol{h}^{(n)} + 2\boldsymbol{v}^{(n)} \times \boldsymbol{\Omega}\right] \\ & - \boldsymbol{\nabla}\Psi + \sum_{n \neq m} \left[\boldsymbol{v}^{(n)} \times \operatorname{curl} \boldsymbol{v}^{(m)} - \frac{\mu}{\rho} \boldsymbol{h}^{(n)} \times \operatorname{curl} \boldsymbol{h}^{(m)}\right], \end{aligned} \tag{22}$$

and

$$\begin{aligned} \Psi = {} & \sum_{n=1}^{N} \Phi^{(n)} + \frac{1}{\rho}\left[p - \sum_{n=1}^{N} p^{(n)}\right] + \frac{1}{2}\sum_{n=1}^{N}{}' \sum_{m=1}^{N} \boldsymbol{v}^{(n)} \cdot \boldsymbol{v}^{(m)} \\ & - \frac{1}{2}\sum_{n=1}^{N}\left[\left(\boldsymbol{v}^{(n)}\right)^2 - \frac{\mu}{\rho}\left(\boldsymbol{h}^{(n)}\right)^2\right], \end{aligned} \tag{23}$$

where $\Phi^{(n)}$ and $p^{(n)}$ are associated with the nth partial wave and use has been made of relations (3), from which

$$\boldsymbol{\kappa}_n \cdot \boldsymbol{v}^{(n)} = 0\,, \qquad \boldsymbol{\kappa}_n \cdot \boldsymbol{h}^{(n)} = 0\,, \tag{24}$$

and

$$\boldsymbol{v}^{(n)} \times \operatorname{curl} \boldsymbol{v}^{(n)} = \tfrac{1}{2}\boldsymbol{\nabla}\left(\boldsymbol{v}^{(n)}\right)^2. \tag{25}$$

The terms with $n = m$ drop out, since waves (19) and (20) are solutions of the fundamental equations. If the curl is taken of equation (22), the conditions reduce to

$$\boldsymbol{s}_1 = \sum_{n \neq m} \operatorname{curl}\,(\boldsymbol{v}^{(n)} \times \boldsymbol{h}^{(m)}) = 0 \tag{26}$$

and

$$\operatorname{curl}\,\boldsymbol{s}_2 = \operatorname{curl} \sum_{n \neq m} \left[\boldsymbol{v}^{(n)} \times \operatorname{curl}\,\boldsymbol{v}^{(m)} - \frac{\mu}{\rho}\,\boldsymbol{h}^{(n)} \times \operatorname{curl}\,\boldsymbol{h}^{(m)} \right] = 0\,. \tag{27}$$

The gradient term in equation (22) is balanced by the pressure.

Now, with the notation of equation (20),

$$\boldsymbol{s}_1 = \frac{1}{2} \sum_{n=1}^{N}{}' \sum_{m=1}^{N} [(A_n - A_m)\operatorname{curl}\,(\boldsymbol{h}^{(n)} \times \boldsymbol{h}^{(m)})] \tag{28}$$

and

$$\boldsymbol{s}_2 = \frac{1}{2} \sum_{n=1}^{N}{}' \sum_{m=1}^{N} \left[\left(A_n A_m - \frac{\mu}{\rho} \right) (\boldsymbol{h}^{(n)} \times \operatorname{curl}\,\boldsymbol{h}^{(m)} + \boldsymbol{h}^{(m)} \times \operatorname{curl}\,\boldsymbol{h}^{(n)}) \right], \tag{29}$$

where the summation has to be carried out over values $n \neq m$. Relations (26) and (27) have to be satisfied for any disturbance of the form (18), i.e., the terms of the series (28) and the series formed by the curl of equation (29) may be chosen independently of each other and have to vanish separately. We also ignore the special cases when the right-hand factors of these terms vanish, e.g., when $\boldsymbol{\kappa}_n$, $\boldsymbol{\kappa}_m$, and $\boldsymbol{h}^{(n)}$, $\boldsymbol{h}^{(m)}$ are parallel. Thus the conditions for superposition become

$$A_n = A_m \qquad \text{and} \qquad A_n A_m = \frac{\mu}{\rho}, \tag{30}$$

giving

$$A_n = A_m = \pm \left(\frac{\mu}{\rho} \right)^{1/2} \tag{31}$$

for all values of n and m. If these conditions are satisfied, equation (20) shows that we also have

$$\tfrac{1}{2} \rho\, (\boldsymbol{v}^{(n)})^2 = \tfrac{1}{2} \mu\, (\boldsymbol{h}^{(n)})^2\,. \tag{32}$$

Results (13) and (17) indicate that conditions (31) may be satisfied for a traveling disturbance in an ideal, nonrotating liquid, which also agrees with the conclusions drawn by Walén (1944) and Lundquist (1952). In a situation where equations (21), (22), and (23) are satisfied, the pressure $p^{(n)}$ of a single wave is not additive, and the total pressure p differs from $\Sigma p^{(n)}$ (cf. also the paper by Lundquist 1952). The signs of A_n for all the partial waves have to be equal, which requires that all the "intersection points" of the elementary wave fronts with the magnetic-field lines of $\boldsymbol{H}$ have to travel in the same direction along $\boldsymbol{H}$. That the conditions are violated for waves traveling in opposite directions is also seen from an example given by Walén (1944), where the induced magnetic fields of two disturbances traveling in opposite directions cancel during the time of coincidence and the balance between magnetic and inertia forces is destroyed.

Finally, we conclude from expressions (13), (17), and (31) that the principle of superposition is generally not valid if the Coriolis force or the losses cannot be neglected. In such a case, relations (32) also become invalid.

b) AN OBJECTION TO THE VALIDITY OF THE PRINCIPLE OF SUPERPOSITION

From the physical point of view it is rather surprising that a superposition of partial waves should be possible in an ideal, nonrotating liquid.[2] In particular, it is necessary to discuss to what extent the local magnetic field due to the waves enters into the expression for the wave velocity. A disturbance composed of elementary waves, which travels in the external magnetic field $\boldsymbol{H}$, generates an induced magnetic field added to the external field. At first glance, it seems plausible to assume that the wave velocity of a particular elementary wave being observed in the laboratory system will be modified by the contributions from the induced field quantities of the rest of the waves. That this is actually not true has just been proved for such a liquid, where all interactions (26) and (27) between the waves vanish and there remain only the direct interactions between each wave and the external field $\boldsymbol{H}$, this effect being represented by the first terms in the right-hand members of equations (21) and (22).

We may also make the situation clear with a simple example. Suppose that a plane wave

$$\boldsymbol{h}^{(1)} = \boldsymbol{h}_0^{(1)} \exp\left[i\left(\boldsymbol{\kappa}_1 \cdot \boldsymbol{r} - \omega_1 t\right)\right], \qquad \boldsymbol{v}^{(1)} = -\left(\frac{\mu}{\rho}\right)^{1/2} \boldsymbol{h}^{(1)}, \tag{33}$$

with a large amplitude $h_0^{(1)}$, travels in the homogeneous field $\boldsymbol{H}$ with a velocity $+\boldsymbol{V} = \boldsymbol{H}(\mu/\rho)^{1/2}$. If we now superpose another wave $\boldsymbol{h}^{(2)}$, $\boldsymbol{v}^{(2)} = -(\mu/\rho)^{1/2}\boldsymbol{h}^{(2)}$ on the configuration composed of $\boldsymbol{H}$ and $\boldsymbol{h}^{(1)}$, we may ask whether this new wave will move in a stronger field than $\boldsymbol{H}$ with a velocity larger than V, or, in other words: Will the configuration $\boldsymbol{h}^{(2)}$, $\boldsymbol{v}^{(2)}$ move with respect to the configuration $\boldsymbol{h}^{(1)}$, $\boldsymbol{v}^{(1)}$?

Since the conductivity of the liquid is assumed to be infinite, the electric field, $\boldsymbol{E}'$, in a frame of reference following the liquid with the velocity $\boldsymbol{v}^{(1)}(\boldsymbol{r}, t) + \boldsymbol{v}^{(2)}(\boldsymbol{r}, t)$ has to vanish for all points $\boldsymbol{r}$ and times t:

$$\boldsymbol{E}' = \boldsymbol{E} + \mu\left(\boldsymbol{v}^{(1)} + \boldsymbol{v}^{(2)}\right) \times \left(\boldsymbol{H} + \boldsymbol{h}^{(1)} + \boldsymbol{h}^{(2)}\right) = 0\,; \qquad v \ll c\,, \tag{34}$$

where the unprimed quantities are measured in the laboratory system. In the same way we obtain the electric field

$$\boldsymbol{E}'' = \boldsymbol{E} + \mu\boldsymbol{V} \times \left(\boldsymbol{H} + \boldsymbol{h}^{(1)} + \boldsymbol{h}^{(2)}\right) \tag{35}$$

for a co-ordinate system moving with velocity $+\boldsymbol{V}$, i.e., a system which follows wave (33). From equation (34) we get

$$\boldsymbol{E}'' = \mu\left(\frac{\mu}{\rho}\right)^{1/2}\left[\left(\boldsymbol{h}^{(1)} + \boldsymbol{h}^{(2)}\right) \times \left(\boldsymbol{H} + \boldsymbol{h}^{(1)} + \boldsymbol{h}^{(2)}\right) + \boldsymbol{H} \times \left(\boldsymbol{H} + \boldsymbol{h}^{(1)} + \boldsymbol{h}^{(2)}\right)\right] = 0\,. \tag{36}$$

Further, according to the Lorentz invariance of Maxwell's equations, we have

$$\operatorname{curl}'' \boldsymbol{E}'' = -\mu\frac{\partial}{\partial t}\left(\boldsymbol{h}^{(1)\prime\prime} + \boldsymbol{h}^{(2)\prime\prime}\right) \tag{37}$$

in the co-ordinate system, where the configuration $\boldsymbol{h}^{(1)\prime\prime}$, $\boldsymbol{v}^{(1)\prime\prime}$ is stationary, i.e., $(\partial/\partial t)(\boldsymbol{h}^{(1)\prime\prime}) = 0$. From equations (36) and (37) we get

$$\frac{\partial}{\partial t}\left(\boldsymbol{h}^{(2)\prime\prime}\right) = \frac{\partial}{\partial t}\left(\boldsymbol{v}^{(2)\prime\prime}\right) = 0\,, \tag{38}$$

and the wave $\boldsymbol{h}^{(2)}$, $\boldsymbol{v}^{(2)}$ also moves with velocity V in the laboratory system in agreement with the foregoing discussions.

---

[2] I am indebted to Professor H. Alfvén for pointing this out to me.

IV. THE APPROXIMATIVE VALIDITY OF THE PRINCIPLE OF SUPERPOSITION

a) A CRITERION FOR A ROTATING LIQUID WITH DISSIPATION

It has been shown in the previous discussion that the nonlinear interactions between the partial waves composing a complex traveling disturbance vanish only in an ideal nonrotating liquid. However, in reality, we often meet the problem of a rotating medium with losses, and conditions (31) cannot be satisfied generally. This raises the question to what extent the principle of superposition may still be approximately valid for a complex disturbance, i.e., the conditions under which the nonlinear terms in equations (21) and (22) become small compared to the linear terms.

We rewrite the left-hand member of equation (21) in the form

$$\boldsymbol{S}_1 = \frac{1}{2}\sum_{n=1}^{N}\sum_{m=1}^{N}\left[(i\omega_n + \lambda\kappa_n^2)\,\boldsymbol{h}^{(n)} + (i\omega_m + \lambda\kappa_m^2)\,\boldsymbol{h}^{(m)}\right] \tag{39}$$

and use a similar expression for the left-hand member, $\boldsymbol{S}_2$, of equation (22). Using the vector identities,

$$\operatorname{curl}(\boldsymbol{a}\times\boldsymbol{b}) = (\boldsymbol{b}\cdot\boldsymbol{\nabla})\,\boldsymbol{a} - (\boldsymbol{a}\cdot\boldsymbol{\nabla})\,\boldsymbol{b} + \boldsymbol{a}\operatorname{div}\boldsymbol{b} - \boldsymbol{b}\operatorname{div}\boldsymbol{a}\,, \tag{40}$$

$$\operatorname{grad}(\boldsymbol{a}\cdot\boldsymbol{b}) = (\boldsymbol{a}\cdot\boldsymbol{\nabla})\,\boldsymbol{b} + (\boldsymbol{b}\cdot\boldsymbol{\nabla})\,\boldsymbol{a} + \boldsymbol{a}\times\operatorname{curl}\boldsymbol{b} + \boldsymbol{b}\times\operatorname{curl}\boldsymbol{a}\,, \tag{41}$$

and equation (24), series (28) and (29) may be written as follows:

$$\boldsymbol{s}_1 = \frac{1}{2}\sum_{n=1}^{N}\sum_{m=1}^{N}\left\{i(A_n - A_m)\left[(\boldsymbol{\kappa}_n\cdot\boldsymbol{h}^{(m)})\,\boldsymbol{h}^{(n)} - (\boldsymbol{\kappa}_m\cdot\boldsymbol{h}^{(n)})\,\boldsymbol{h}^{(m)}\right]\right\} \tag{42}$$

and

$$\begin{aligned}\boldsymbol{s}_2 = \frac{1}{2}\sum_{n=1}^{N}\sum_{m=1}^{N}\Big\{\Big(\frac{\mu}{\rho} - A_n A_m\Big)&\big[i(\boldsymbol{\kappa}_n\cdot\boldsymbol{h}^{(m)})\,\boldsymbol{h}^{(n)} + i(\boldsymbol{\kappa}_m\cdot\boldsymbol{h}^{(n)})\,\boldsymbol{h}^{(m)}\\ &- \boldsymbol{\nabla}(\boldsymbol{h}^{(n)}\cdot\boldsymbol{h}^{(m)})\big]\Big\} + \frac{1}{2}\sum_{n=1}^{N}\Big(\frac{\mu}{\rho} - A_n^2\Big)\,\boldsymbol{\nabla}(\boldsymbol{h}^{(n)})^2\,.\end{aligned} \tag{43}$$

The nonlinear interactions can be neglected if

$$|\boldsymbol{s}_1| \ll |\boldsymbol{S}_1| \qquad \text{and} \qquad |\operatorname{curl}\boldsymbol{s}_2| \ll |\operatorname{curl}|\boldsymbol{S}_2|\,. \tag{44}$$

The left members of these inequalities can be made arbitrarily small compared to the right members if the modulus of every term in the series $\boldsymbol{s}_1$ and curl $\boldsymbol{s}_2$ is made small enough compared to the modulus of the corresponding term in the series $\boldsymbol{S}_1$ and curl $\boldsymbol{S}_2$. Thus we arrive roughly at the following conditions:

$$|i\omega_n + \lambda\kappa_n^2| \gg |(A_n - A_m)\,\boldsymbol{\kappa}_n\cdot\boldsymbol{h}^{(m)}| \tag{45}$$

and

$$|A_n(i\omega_n + \nu\kappa_n^2)| \gg \Big|\Big(A_n A_m - \frac{\mu}{\rho}\Big)\,\boldsymbol{\kappa}_n\cdot\boldsymbol{h}^{(m)}\Big| \tag{46}$$

for all values of n and m. This is, of course, of use only when A_n and A_m deviate slightly from their "ideal" values (31), and we may introduce

$$A_n = \pm\Big(\frac{\mu}{\rho}\Big)^{1/2}(1 + \epsilon_n)\,; \qquad |\epsilon_n| \ll 1\,. \tag{47}$$

A traveling disturbance, where all the coefficients A_n have the same sign, gives

$$|A_n - A_m| = \left(\frac{\mu}{\rho}\right)^{1/2} |\epsilon_n - \epsilon_m| \tag{48}$$

and

$$\left|\frac{(A_n A_m - \mu/\rho)}{A_n}\right| \approx \left(\frac{\mu}{\rho}\right)^{1/2} |\epsilon_n + \epsilon_m| \,. \tag{49}$$

Further, the approximation $|\omega_n/\kappa_n| \approx V$ may be used because of the assumption of small losses. The values from equations (48) and (49) are introduced into conditions (45) and (46), which are satisfied if

$$\vartheta \equiv \left|\frac{h_0^{(m)}}{H}\right| \ll |\epsilon_n + \epsilon_m|_{\max}^{-1} \tag{50}$$

for all partial waves n and m composing the disturbance. The nonlinear effects are significant as soon as the amplitudes of the partial waves become large enough to invalidate this condition.

The discussion of a disturbance formed by a limited discrete spectrum may be extended to a disturbance of the form

$$\boldsymbol{h}(\boldsymbol{r}, t) = \iiint_{-\infty}^{+\infty} \boldsymbol{h}(\boldsymbol{\kappa})\, e^{i[\boldsymbol{\kappa}\cdot\boldsymbol{r} + \omega(\boldsymbol{\kappa})t]} d\kappa_x d\kappa_y d\kappa_z \,. \tag{51}$$

We choose a disturbance which can be represented by this form and for which the transition into integral representation of the series (39), (42), and (43) is possible. It may be assumed that, for a given value of $\boldsymbol{\kappa}$, the integrands of the expressions $\boldsymbol{s}_1$ and curl $\boldsymbol{s}_2$ will have moduli much less than the moduli of the integrands of the expressions $\boldsymbol{S}_1$ and curl $\boldsymbol{S}_2$. In cases where this integral representation is valid, we thus arrive at the same criterion expressed by equation (50), ϵ_n and ϵ_m now being continuous functions of $\boldsymbol{\kappa}_n$ and $\boldsymbol{\kappa}_m$, and $h_0^{(m)}$ the maximum amplitude within the region of the disturbance.

b) APPLICATIONS TO SOLAR PHYSICS

In order to estimate the importance of the nonlinear effects for a traveling disturbance in the sun, two special cases will be examined.

1. If the Coriolis force is neglected and the influence of the finite conductivity is taken into consideration, coefficients (17) reduce to

$$A_n \approx \left(\frac{\mu}{\rho}\right)^{1/2} (1 - i\zeta_n) \tag{52}$$

for small values of $\zeta_n = \lambda\kappa_n/(2V_\kappa)_n$, i.e.,

$$|\epsilon_n| \approx |\zeta_n| \approx \left|\frac{\lambda\kappa_n}{2V\cos\psi_n}\right| \,. \tag{53}$$

Formula (50) now becomes

$$\vartheta \ll \frac{2V}{\lambda}\left[\left|\frac{\kappa_n}{\cos\psi_n}\right| + \left|\frac{\kappa_m}{\cos\psi_m}\right|\right]_{\max}^{-1} . \tag{54}$$

With values of ψ_n and ψ_m not too close to $\pi/2$, we get

$$\vartheta \ll \frac{V}{\lambda\kappa^*} \,. \tag{55}$$

where the spectrum of the disturbance has been cut off at a wave number, κ^*, large enough for the main part to be situated within the region $\kappa \leq \kappa^*$ and to justify neglecting the rest of the spectrum for $\kappa > \kappa^*$.

We apply the results to a disturbance of the ordinary size of sunspots and assume that it can be represented by partial waves in the range of wave lengths from 10^{-3} to 2×10^{-2} of the solar radius $R_0 = 6.96 \times 10^8$ meters with sufficient accuracy. This gives $\kappa^* = 10^{-5}$ meters^{-1}. If the values (Alfvén 1950) $V = 1$ meter/sec, corresponding to a dipole field with a polar strength of about 25 gauss, $\sigma \geq 10^5$ ohms^{-1} meters^{-1}, and $\lambda = 1/(\mu\sigma) \leq 8$ meters/sec are used, the result becomes

$$\vartheta \ll 10^4 \,. \tag{56}$$

This indicates that the nonlinear phenomena arising from the finite conductivity can probably be neglected, even for an induced field of the same strength as that of a sunspot.

2. Since the dissipation may be neglected, the discussion will now be limited to an ideal nonrotating liquid, where

$$A_n = \frac{(\mu/\rho)^{1/2}\omega_n}{(\kappa V_\kappa)_n} \,. \tag{57}$$

For $|\chi| \ll 1$, equations (13), (14), (15), and (47) give

$$|\epsilon_n| \approx |\chi_n| \approx \left|\frac{\Omega}{\omega_n}\cos\varphi_n\right| \,, \tag{58}$$

and condition (50) becomes

$$\vartheta \ll \left|\frac{\omega_n\omega_m}{\Omega}(\omega_n\cos\varphi_n + \omega_m\cos\varphi_m)^{-1}\right|_{\min} \,. \tag{59}$$

For a disturbance composed of wave lengths not larger than $10^{-3}R_0$ corresponding to $|\omega| \approx |\boldsymbol{\kappa}\cdot \boldsymbol{V}| \geq 10^{-5}$ sec^{-1} for $V = 1$ meter/sec, we find

$$\vartheta \ll 3 \,, \tag{60}$$

where the value $\Omega = 3 \times 10^{-6}$ sec^{-1} has been used.

From this result it is plausible to conclude that the nonlinear interactions cannot be neglected for a traveling disturbance with magnitudes of the induced field and size comparable to those of an ordinary sunspot.

V. THE GROUP VELOCITY FOR SMALL AMPLITUDES

Up to this stage the Coriolis force has been shown to modify the phase velocity of magnetohydrodynamic waves and to introduce nonlinear effects. It is natural to extend the discussion to the motion of a wave packet and to the influence of the Coriolis force on the direction and magnitude of its group velocity.

In a homogeneous, isotropic medium the frequency $\omega = \omega(\kappa)$ of plane waves depends only on the modulus of the wave number $\boldsymbol{\kappa}$. A wave packet built up of waves with wave numbers situated in a small region of wave-number space, i.e., waves with slightly inclined normals and slightly different moduli of their wave numbers, will be propagated with a group velocity $d\omega/d\kappa$ along the direction of the mean wave number $\bar{\boldsymbol{\kappa}}$.

However, in an anisotropic, homogeneous medium the frequency $\omega = \omega(\boldsymbol{\kappa})$ depends not only on the modulus of the wave number but also on its direction. This is the situation in magnetohydrodynamics where expression (13) indicates anisotropic properties introduced by the magnetic field and the Coriolis force.

To be able to study the motion of a magnetohydrodynamic wave packet, composed of a narrow spectrum of plane waves, the following investigations will be limited to the state of small amplitudes. It is easily seen that the fundamental equations (5) and (6) cannot be satisfied generally by a disturbance traveling only along the magnetic field, as soon as the Coriolis force is taken into account. For negligible losses and small amplitudes the fundamental equations (5) and (6) reduce to

$$\frac{\partial}{\partial t}\boldsymbol{h} = (\boldsymbol{H}\cdot\boldsymbol{\nabla})\,\boldsymbol{v} \tag{61}$$

and

$$\frac{\partial}{\partial t}\boldsymbol{v} = \frac{\mu}{\rho}(\boldsymbol{H}\cdot\boldsymbol{\nabla})\,\boldsymbol{h} + 2\boldsymbol{v}\times\boldsymbol{\Omega} - \boldsymbol{\nabla}\Phi\,. \tag{62}$$

Using relations (3), a divergence operation on equation (62) gives

$$\boldsymbol{\nabla}^2\Phi = 2\,\mathrm{div}\,(\boldsymbol{v}\times\boldsymbol{\Omega})\,, \tag{63}$$

which shows that Φ is not a harmonic function in the case of a rotating liquid. Now $\boldsymbol{h}$ and Φ are eliminated on applying the operator $\partial/\partial t$ curl to equation (62):

$$\left[\frac{\partial^2}{\partial t^2} - (\boldsymbol{V}\cdot\boldsymbol{\nabla})^2\right]\mathrm{curl}\,\boldsymbol{v} = 2\,\frac{\partial}{\partial t}\,\mathrm{curl}\,(\boldsymbol{v}\times\boldsymbol{\Omega})\,. \tag{64}$$

Writing $\boldsymbol{v}$ in terms of components, we obtain, after some straightforward deductions,

$$\frac{\partial}{\partial t}(\boldsymbol{\Omega}\cdot\boldsymbol{\nabla})\left\{\boldsymbol{\nabla}^2\left[\frac{\partial^2}{\partial t^2} - (\boldsymbol{V}\cdot\boldsymbol{\nabla})^2\right]^2 + 4\,\frac{\partial^2}{\partial t^2}(\boldsymbol{\Omega}\cdot\boldsymbol{\nabla})^2\right\}\boldsymbol{v} = 0\,. \tag{65}$$

If, for simplicity, the frame of reference is chosen with the z-axis along $\boldsymbol{V}$, it is seen that this expression is not satisfied generally by a disturbance of the form

$$\boldsymbol{v} = \boldsymbol{v}\,(x,\ y,\ z \pm ut)\,. \tag{66}$$

To calculate the motion of a wave packet of the form (51), with a spectrum limited to a narrow region around the mean $\bar{\boldsymbol{\kappa}}$, we introduce the group velocity in an anisotropic, homogeneous medium,

$$\boldsymbol{u} = \left(\frac{\partial\omega}{\partial\kappa_x},\quad \frac{\partial\omega}{\partial\kappa_y},\quad \frac{\partial\omega}{\partial\kappa_z}\right)_{\boldsymbol{\kappa}=\bar{\boldsymbol{\kappa}}}, \tag{67}$$

given by Madelung (1950), among others. If this formula is applied to an ideal, nonrotating liquid, where

$$\omega = \pm\,\boldsymbol{\kappa}\cdot\boldsymbol{V}\,, \tag{68}$$

the group velocity becomes

$$\boldsymbol{u} = \pm\boldsymbol{V}\,, \tag{69}$$

and any wave packet will travel only along the magnetic lines of force in agreement with earlier conclusions by Alfvén (1942) and Walén (1944).

Now, if a slow rotation is introduced, we obtain, from equations (13) and (67),

$$\omega \approx \pm\left[\boldsymbol{\kappa}\cdot\boldsymbol{V} \pm \frac{\boldsymbol{\kappa}\cdot\boldsymbol{\Omega}}{\kappa}\right] \tag{70}$$

and

$$\boldsymbol{u}_{1,\,2} = \pm\left\{\boldsymbol{V} \pm \frac{[\bar{\boldsymbol{\kappa}}\times(\boldsymbol{\Omega}\times\bar{\boldsymbol{\kappa}})]}{\bar{\kappa}^3}\right\}. \tag{71}$$

This indicates that a wave packet which travels only along the magnetic field in a nonrotating liquid moves for a given mean, $\bar{\boldsymbol{\kappa}}$, in a slowly rotating liquid in two possible directions, forming small angles $\Theta_{1,2}$ with the magnetic field. Solutions (71) have opposite directions of polarization. The largest deflection occurs when the two terms of the group velocity (71) are perpendicular to each other;

$$|\Theta_{1,2}|_{\max} = \frac{\Omega}{\bar{\kappa} V} = \bar{\chi} . \tag{72}$$

From this result we may conclude that, at least for small amplitudes, the deflection from the direction of propagation along the magnetic field cannot be neglected as soon as the Coriolis force becomes comparable to the electromagnetic force.

VI. CONCLUSIONS

The investigations of this paper and the previous discussion (Lehnert 1954) on magnetohydrodynamic waves in a rotating liquid have shown that the Coriolis force introduces at least three effects which modify the properties of magnetohydrodynamic waves: (1) The phase velocity of plane waves is modified. A plane-polarized Alfvén wave is split up into two circularly polarized waves, one traveling with a larger phase velocity and one with a smaller phase velocity than the Alfvén wave. (2) To the group velocity of a wave packet for small amplitudes is added an increment which depends on both the modulus and the direction of the mean wave number. A complex disturbance will not necessarily travel along the external magnetic field and will be distorted because of anisotropic dispersion. (3) For large amplitudes, nonlinear interactions arise between the components of the spectrum of a traveling disturbance.

All these three effects appear when the Coriolis force becomes comparable to the electromagnetic force. In solar physics this is the case for wave lengths of the order of a hundredth of the solar radius, if a general solar field is assumed with a dipole component less than 25 gauss at the poles.

It is probably a good approximation to neglect the losses for disturbances with an induced field and a size comparable to those of ordinary sunspots. In case of a twisted solar field the numerical results of Section IV.2 have to be changed, but this probably does not influence the conclusions drawn in this section, as long as the twisting does not assume extremely high values.

The author is greatly indebted to Professor H. Alfvén and to Dr. N. Herlofson, Dr. S. Lundquist and Dr. E. Åström for many valuable and stimulating discussions on this paper. The investigation was supported by grants from Statens Naturvetenskapliga Forskningsråd.

REFERENCES

Alfvén, H. 1942, *Ark. f. mat., astr. o. fys.*, Vol. **29B**, No. 2.
———. 1950, *Cosmical Electrodynamics* (Oxford: Clarendon Press), chap. v.
Lehnert, B. 1954, *Ap. J.*, **119**, 647.
———. 1955, *Quart. Appl. Math.*, **XII**, No. 4, 321.
Lundquist, S. 1952, *Ark. f. fys.*, **5**, 338.
Madelung, E. 1950, *Die Mathematischen Hilfsmittel des Physikers* (4th ed.; Berlin: Springer-Verlag), p. 189.
Walén, C. 1944, *Ark. f. mat., astr. o. fys.*, Vol. **30A**, No. 15.

THE FORMATION OF SUNSPOTS FROM THE SOLAR TOROIDAL FIELD*

Eugene N. Parker
Department of Physics, University of Utah, Salt Lake City, Utah

Received October 18, 1954

ABSTRACT

It is shown that a horizontal magnetic flux tube in an electrically conducting atmosphere is buoyant and will tend to rise. This magnetic buoyancy is large enough to bring an occasional strand of flux from the general solar toroidal field up into the photosphere, if we assume general field densities of a few hundred gauss farther down. Identifying the intersection of such ropes with the photosphere as the source of sunspots, we may deduce several general characteristics of the spots, e.g., east-west orientation, bipolarity, appearance only in low latitudes, migration, reversal of polarity, etc. The linearized static equilibrium equations for a flux tube are developed. With a cooling mechanism, such as that suggested by Biermann (1941), we find from the equilibrium equations that a sunspot group should consist of a diffuse flux tube of 10–100 gauss and 10^5 km extent in the photosphere, forming eventually a number of cool intense cores of several thousand gauss.

I. INTRODUCTION

Hydromagnetic dynamo theory suggests that we should expect dynamo waves just under the surface of the sun in the convective zone migrating from the polar to the equatorial regions. The waves are prevented from diffusing out of the convective zone by the high conductivity of the medium. The waves consist in part of bands of toroidal magnetic field; the sense of the field alternates from one band to the next. The poloidal field is $\pi/2$ out of phase with the toroidal field, essentially occupying the regions between the intense toroidal bands. This is shown schematically in Figure 1. Observations of secondary magnetic phenomena such as sunspots indicate that there are two (or at most three) toroidal bands in each hemisphere at any one time and that about 22 (or 33) years are required for the migration of each band from the pole to the equator. Dynamical considerations indicate that the initial amplification of the relatively weak wave starting at the pole is primarily of the poloidal components; by the time that middle latitudes are reached, the decrease of cyclonic motions and the increase of the nonuniform rotation of the sun shift the amplification to the toroidal field. Thus the poloidal component of the traveling wave predominates from the pole to the middle latitudes; in low latitudes the toroidal field predominates until both the poloidal and toroidal fields finally vanish at the magnetic equator.

The problem before us now is the question of what secondary magnetic effects might be expected around the fringes of the solar dynamo. We have in mind, of course, the obviously magnetic phenomena, such as sunspots and prominences, as well as those occurrences such as spicules, flares, etc., which one suspects must be of magnetic origin because no purely hydrodynamic explanation seems to exist.

In this paper we discuss what we shall call "magnetic buoyancy." Consider a magnetic flux tube running horizontally through a gaseous electrically conducting medium such as one finds in the sun. It is well known that the tensile stress in the tube is $B^2/2\mu$ in mks units, where B is the magnetic-field density. The magnetic field also exerts an outward pressure, and, were the tube not impeded by the surrounding matter, it would expand. As it is, B satisfies the diffusion equation

$$\frac{\partial \boldsymbol{B}}{\partial t} = \nu_m \nabla^2 \boldsymbol{B} ,$$

---

* This work was supported by the U.S. Office of Naval Research.

where ν_m is the magnetic viscosity. If the medium is a sufficiently good conductor, ν_m becomes small enough that

$$\frac{\partial B}{\partial t} \cong 0 ,$$

and the field does not diffuse through the medium. Hydrostatic equilibrium requires that the magnetic pressure p_m be balanced by the gas pressure p_e outside the tube. Thus, if p_i is the gas pressure inside the tube, we must have

$$p_e = p_i + p_m . \tag{1}$$

Now

$$p_m = \frac{B^2}{2\mu} \tag{2}$$

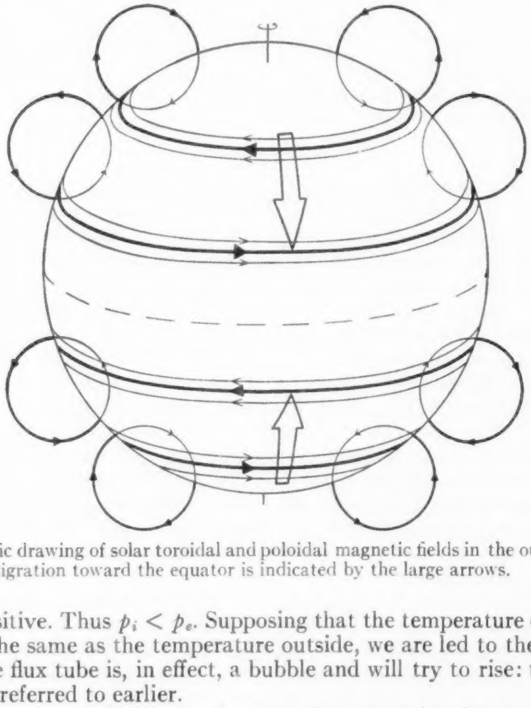

Fig. 1—Schematic drawing of solar toroidal and poloidal magnetic fields in the outer half of the convective zone. The migration toward the equator is indicated by the large arrows.

and is always positive. Thus $p_i < p_e$. Supposing that the temperature of the gas within the flux tube is the same as the temperature outside, we are led to the conclusion that $\rho_i < \rho_e$. Thus the flux tube is, in effect, a bubble and will try to rise: this is the "magnetic buoyancy" referred to earlier.

The buoyant force per unit length of a tube of cross-sectional area A is $g(\rho_e - \rho_i)A$. The tension is $AB^2/2\mu$. Consider a length L of the flux tube clamped at both ends. If the tube is to be able to rise, we must require that the buoyant forces exceed the tension at the ends of the length, which will try to hold the length in place. Thus we must satisfy an approximate relation of the form

$$Lg\,(\rho_e - \rho_i)\,A > \frac{2\,AB^2}{2\mu} . \tag{3}$$

Now

$$p = \frac{kT\rho}{m} , \tag{4}$$

where k is Boltzmann's constant and m is the mass of an individual gas molecule. Using equation (4) for p_e and p_i, equation (1) may be rewritten as

$$\rho_e = \rho_i + \frac{m}{kT}\frac{B^2}{2\mu}; \tag{5}$$

and equation (3) becomes

$$L > \frac{2kT}{mg}. \tag{6}$$

Thus magnetic buoyancy is effective over any length of flux tube exceeding twice the scale height of the medium.

It should be emphasized that magnetic buoyancy is not an instability in the usual sense. The buoyant force per unit volume is the quantity

$$F_b = \frac{mg}{kT}\frac{B^2}{2\mu}, \tag{7}$$

and a long horizontal flux tube can never be in static equilibrium. So long as F_b is large enough not to be overwhelmed by other motions, such as convection and turbulence, the tube will rise.

Conditions within a flux tube that has undergone vertical displacement are investigated at some length in Appendixes II and III; it is found that raising a length of a long flux tube results in a flow of fluid along the tube which enhances the magnetic buoyancy in the raised portion. Thus, once the tube has begun to rise, it will not generally stop.

To obtain a quantitative estimate of the buoyancy force, consider a flux tube of 100 gauss at a depth of 2×10^4 km in the sun. At this level $\rho_e \simeq 2.5 \times 10^{-4}$ gm/cm^3, $T_e \simeq 2\overset{\circ}{.}5 \times 10^5$ K. Equation (5) gives $\rho_e - \rho_i \simeq 2 \times 10^{-11}$ gm/cm^3, which is only 10^{-7} of the density ρ_e. A temperature variation of $0\overset{\circ}{.}02$ K would produce the same fluctuation in the density. We see, then, that magnetic buoyancy will be negligible for the general solar field. Consider, however, a relatively intense strand of field of, say, 10^3 gauss, produced by an abrupt shearing in the turbulent convective motions at a depth of only 10^3 km. Now $\rho_e \simeq 0.8 \times 10^{-8}$ gm/cm^3 and $T_e \simeq 1\overset{\circ}{.}5 \times 10^4$ K; equation (5) gives $\rho_e - \rho_i \simeq 3 \times 10^{-8}$ gm/cm^3. Hence $\rho_e - \rho_i$ is now $0.04\ \rho_e$ and is equivalent to heating the region by 600° K; if the rope is not swept back down into the convective zone by some violent convective flow, it will rise to the surface of the sun.

In the sun, then, we expect to find an occasional strand from the toroidal or poloidal fields bobbing up to the surface of the sun; the main field will be essentially unaffected. We expect these strands to come up where the buoyant force F_b is strongest and can overcome the random velocity and magnetic fields present in the convective zone. Thus strands of the toroidal field are expected to appear only below the middle latitudes. This leads us to a suggestion by Elsasser[1] that sunspots seem most naturally explained as a portion of the toroidal field which has been heaved up to the surface of the sun by some dynamic mechanism. The mechanism here assumed is magnetic buoyancy, supplemented to an unknown extent by the convective forces existing in the convective zone. Strands of the poloidal field may appear much nearer the pole than strands of the toroidal field, because, as was pointed out earlier, the poloidal field is amplified at higher latitudes than the toroidal field. Ropes of flux floating up from the poloidal field may be responsible for the prominence activity observed (Menzel 1953) in the middle latitudes shortly before the onset of a new sunspot cycle.

If we identify sunspots with the strands of the toroidal field breaking through the photosphere, several of the general properties of sunspots follow immediately. The bipolar character of the spots is due to the two passages of the flux tube through the photosphere, one exit and one entrance; the near east-west orientation of an individual group of spots results from the initial east-west direction of the flux tube; the appearance of the spots only below middle latitudes is due to the fact that the toroidal field is not intensely amplified until low latitudes are reached; the migration toward the equator of the region of spot formation is a result of the migration of the underlying toroidal field; the reversal of polarity every half-cycle occurs as a consequence of the alternation of sign of successive bands of toroidal field.

---

[1] Unpublished.

II. FORMATION OF A SUNSPOT

Having shown that several of the general characteristics of sunspots follow from the assumption that the magnetic buoyancy occasionally brings a strand of the solar toroidal field up to the surface, let us now investigate the configuration of such a strand upon reaching the surface.

The flux tube forming a real sunspot is not at all slender but diverges abruptly. To take into account the resulting curvature of the lines of force results in nonlinear equations, which have not yet been solved except for very special cases (Schlüter and St. Temesvary 1953). In this paper we shall confine our attention to slender flux tubes, neglecting the curvature of the lines in force, and so obtain linear equations which are easily solved. In this way we are able to determine how a flux tube will deviate from uniformity, but our quantitative description of the extent to which the tube will taper can be only preliminary. Our purpose is merely to demonstrate that flux tubes do tend toward configurations suggestive of sunspots. A quantitative description of sunspots could follow only from extension of the nonlinear calculations of Schlüter and St. Temesvary.

The relatively long life of a sunspot group suggests that the flux producing each group is near static equilibrium. Now consider a *vertical* flux tube (along the z-axis), with the assumption that, after the tube has broken through the surface, the part located in the upper convective zone has a sufficiently steep inclination to be considered vertical. We shall also assume that, to begin with, the tube does not taper off rapidly. Let the field B be homogeneous across the tube. We shall denote the state of the gas inside the flux tube by p_i, ρ_i, and T_i; outside by p_e, ρ_e, and T_e. For static equilibrium of the gas within the flux tube, we must satisfy equation (1). In addition, we must now require that the net force in the z-direction be zero or at least approximately so. Thus, in mks units,

$$0 = -\frac{d p_i}{d z} - g \rho_i + \frac{1}{\mu} [(\nabla \times \boldsymbol{B}) \times \boldsymbol{B}]_z . \tag{8}$$

Now

$$[(\nabla \times \boldsymbol{B}) \times \boldsymbol{B}]_z = \left[\frac{\partial B_z}{\partial y} - \frac{\partial B_y}{\partial z}\right] B_y - \left[\frac{\partial B_x}{\partial z} - \frac{\partial B_z}{\partial x}\right] B_x . \tag{9}$$

Our assumption that B is homogeneous across the tube means that

$$\frac{\partial B_z}{\partial y} = \frac{\partial B_z}{\partial x} = 0 ,$$

and equation (9) reduces to

$$[(\nabla \times \boldsymbol{B}) \times \boldsymbol{B}]_z = -\frac{\partial}{\partial z} \frac{B_x^2 + B_y^2}{2} . \tag{10}$$

Hence equation (8) becomes

$$\frac{d p_i}{d z} = -g \rho_i - \frac{\partial}{\partial z} \frac{B_x^2 + B_y^2}{2 \mu} . \tag{11}$$

We assume that the gas outside the tube is in equilibrium, so that

$$\frac{dp_e}{dz} = -g\rho_e . \tag{12}$$

Differentiating equation (1) with respect to z and using equations (11) and (12), we obtain

$$\frac{\partial}{\partial z}\left(\frac{B^2}{2\mu}\right) = g(\rho_i - \rho_e) + \frac{\partial}{\partial z}\frac{B_x^2 + B_y^2}{2\mu}$$

or

$$\frac{\partial}{\partial z}\frac{B^2}{2\mu} = g(\rho_i - \rho_e) . \tag{13}$$

Equation (13) is the equation for longitudinal equilibrium of a vertical flux tube; it states that any change in the longitudinal magnetic stress must be balanced by the local buoyancy.

The assumption of a slowly tapering flux tube implies that B_x, $B_y \ll B_z$; so that, if B is the magnitude of $\boldsymbol{B}$, equations (11) and (13) may be rewritten as follows:

$$\frac{dp_i}{dz} = -g\rho_i + O^2(B_x, B_y) , \qquad \frac{\partial}{\partial z}\frac{B^2}{2\mu} = g(\rho_i - \rho_e) + O^2(B_x, B_y) . \tag{14}$$

Equation (14) applies to an oblique, as well as to a vertical, flux tube, as is shown more generally in Appendix I.

Let us use the static equilibrium equation (14) to investigate the portion of the flux tube rising up from the convective zone through the photosphere. Assume that, as a consequence of the slowness of the rise up to the photosphere, the tube is in thermal equilibrium with its surroundings, $T_i = T_e$. The sunspot which ultimately results from the flux tube is independent of whether $T_i = T_e$ initially; and so we shall not investigate the rate of rise and of radiative transfer to see whether the assumption is entirely justified; observation indicates that it is. Given that $T_i = T_e$, equation (1) may be rewritten to give

$$\rho_e - \rho_i = \frac{m}{kT_e}\frac{B^2}{2\mu} , \tag{15}$$

where m is the mass of a gas molecule in grams and k is Boltzmann's constant. Using equation (15), equation (14) becomes

$$\frac{\partial}{\partial z}\frac{B^2}{2\mu} = -\frac{mg}{kT_e}\frac{B^2}{2\mu} \qquad \text{or} \qquad \frac{\partial B}{\partial z} = -\frac{mg}{2kT_e}B .$$

Integrating, we have

$$B(z) = B(0)\exp\left[-\int_0^z dz\,\frac{mg}{kT_e}\right] . \tag{16}$$

We see that the magnetic field decreases with height, with a characteristic length of twice the scale height of the atmosphere. In other words, $B \propto p_e^{1/2}$. The width w of the flux tube varies as $p_e^{-1/4}$.

Between the base of the vertical flux tube in the convective zone and the upper end of the tube in the photosphere p_e decreases by one or two powers of 10. Thus, if the flux tube had an initial field density of 100 or 1000 gauss before rising up to the photosphere, $B \propto p_e^{1/2}$ implies that we will find fields of only 10 or 100 gauss at the photosphere. This diffuse field will appear over a region of the order of 10^5 km. The configuration of the field is illustrated in Figure 2, *a;* the line PP' represents the level of the photosphere.

The diameter of the flux tube at the photosphere determines how close together the exit and re-entrance of the tube may be; we expect the halves of the bipolar pair forming a sunspot group to be separated by a distance of the order of 10^5 km. At this stage of development of the flux tube we introduce a cooling postulate (Biermann 1941; Kuiper 1953). We assume that the presence of a magnetic field of the order of 100 gauss or more produces a cooling of the region occupied by the flux tube. Biermann's assumption that the cooling follows as a result of the magnetic field's inhibiting effect on convection seems the most stranghtforward explanation, though our conclusions do not depend critically on details.

We find that the field intensity at the photosphere in a flux tube is remarkably sensitive to the temperature difference between the inside and the outside of the tube. Consider a vertical flux tube in static and thermal equilibrium with its surroundings. Suppose that, at the base of the flux tube, the field intensity is 100 gauss and that $\rho_e = 10^{-5}$ gm/cm^3, $T_e = 4 \times 10^{-4}$ ° K. Then, from equation (1), we find that $(\rho_e - \rho_i)/\rho_e = 10^{-5}$ and $\rho_e - \rho_i = 10^{-10}$ gm/cm^3. The important fact is that $\rho_e - \rho_i$ is a very small quantity.

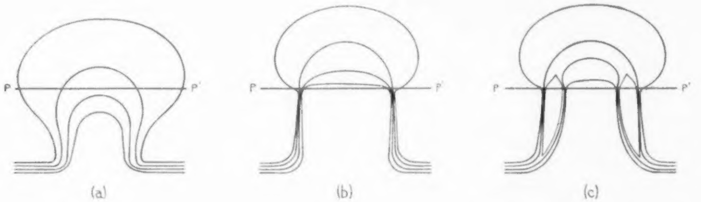

(a) (b) (c)

FIG. 2.—The development of a toroidal flux tube into a sunspot. *a*, indicates in a rough way how the tube might look after being borne to the surface by the magnetic bouyancy; *b*, shows the concentration just under the photosphere due to cooling; *c*, indicates splitting of the tube as a consequence of the abrupt tapering above the cool region.

If we decrease the temperature T_i inside the flux tube by 1° K, about two parts in 10^5, then ρ_i, in order to maintain the static equilibrium condition (1), must increase by 2 parts in 10^5. Then $\rho_e - \rho_i$ changes from $+10^{-10}$ gm/cm^3 to -10^{-10} gm/cm^3; from equation (21) we see that $(\partial/\partial z)[B^2/2\mu]$ also reverses its sign without changing its magnitude. Thus, instead of the divergence of the flux tube with height, as indicated in equation (16), where we find that $B_e \propto p_e^{1/2}$, the cooling by 1° K of the interior of the tube results in the tube's converging with height and $B \propto p_e^{-1/2}$. Hence a slight cooling effect in a vertical flux tube can result in a tremendous increase in field intensity at the upper end of the tube, as shown in Figure 2, *b;* this change of the static equilibrium configuration of the tube involves a large change in the volume of the tube, as may be seen by comparing Figure 2, *a* and *b*. The decrease in volume results in considerable flow of gas along the tube and is discussed in Section IV.

To investigate the matter a little further, we write equation (1) in terms of temperature and density. The resulting expression may be rearranged as follows:

$$\rho_i - \rho_e = \frac{\rho_e}{T_i}(T_e - T_i) - \frac{m}{kT_i}\frac{B^2}{2\mu}. \tag{17}$$

For vertical equilibrium we put equation (17) into equation (14) and obtain

$$\frac{d}{dz}\frac{B^2}{2\mu} = \frac{\rho_e g}{T_i}(T_e - T_i) - \frac{mg}{kT_i}\frac{B^2}{2\mu}. \tag{18}$$

As a first approximation, let us assume that the cooling effect $(T_e - T_i)$ is simply proportional to the magnetic stresses. Then we write

$$T_e - T_i = \kappa\left[\frac{B^2}{2\mu}\right], \tag{19}$$

where κ is a constant. Equation (18) becomes

$$\frac{d}{dz}\frac{B^2}{2\mu} = \frac{B^2}{2\mu}\frac{mg}{kT_i}\left[\frac{k\rho_e\kappa}{m} - 1\right]. \tag{20}$$

Upon integration, we obtain

$$\frac{B^2}{2\mu} = \left(\frac{B^2}{2\mu}\right)_0 \exp\left[\int_0^z dz\,\frac{mg}{kT_i}\left(\frac{k\rho_e\kappa}{m} - 1\right)\right]. \tag{21}$$

Then $(k\rho_e\kappa/m) - 1$ is integrated over distances several times the scale height kT_i/mg and appears in the exponent. Thus fields of the order of 2000 gauss are easily obtained from a field of 100 gauss at the base of the flux tube, even though $(k\rho_e\kappa/m) - 1$ may be only slightly greater than zero. We do not need the intense fields throughout the outer layers of the sun that have been postulated by Gurvich and Lebedinsky (1946).

In conclusion, then, we see that our calculations from the local lateral equilibrium equation (1) and the longitudinal equilibrium equation (14) have shown that the cooling and the intense magnetic field of a sunspot are mutually dependent; before cooling becomes effective, we have at the level of the photosphere a diffuse flux tube of 10–100 gauss over 10^5 km diameter. Giving a cooling effect, however, the diffuse tube forms a dense core. In our greatly oversimplified model the density of the core increases up to the level where the cooling is no longer effective; at higher levels $T_i = T_e$, and the flux tube diverges according to equation (16), as is discussed in the next section. We need not assume that the entire cross-section of the flux tube goes into the core, because there is undoubtedly a transition region near the surface of the flux tube where the cooling is not very effective. Thus we may expect a spot to be surrounded by a region of diffuse field.

III. THE EVOLUTION OF A SPOT GROUP

Now consider the field over a sunspot. If Biermann's mechanism is correct, we expect no cooling because there is no convection above the photosphere; observation indicates that the gas in the chromosphere and the corona over a sunspot are at least not cooler than gas at the same level elsewhere in the solar atmosphere. Thus we are led back to $T_i = T_e$ and the resulting divergence with height (eq. [16]) of a flux tube in equilibrium. The diameter of such a tube increases with height as $p_e^{-1/4}$. Thus in a region $T = 6000°$ K, yielding a scale height of 200 km, the flux tube increases its width by a factor of e every 800 km; a spot with a diameter of 2×10^4 km at a height z will have a diameter of 5.5×10^4 km at $z + 800$ km. The walls of the flux tube will make an angle of only 1°.7 with the horizontal. It must be remembered that this result is only approximate, because it was computed from equation (16), which was derived by assuming that the rate of divergence is small. But it serves to show how rapidly the tube is diverging and how the horizontal velocities of the Evershed effect may indeed be gas flowing along the lines of force rather than across them.

The rapid divergence of the tube has interesting dynamic implications. Consider a tube which tapers off abruptly, as shown in Figure 3, *a*. The lines of force have no tendency to stick together and, because of the tension along the lines, will try to separate into several branches at the restriction, as shown in Figure 3, *b*.

The tendency for such a breakup is readily demonstrated by showing that the energy of the field is less after breakup has occurred than before. If we assume that the cooling within the flux tube is not affected seriously or large quantities of matter elevated, it will be sufficient to consider the energy of the two-dimensional periodic field given by

$$B_x = 0\,, \qquad B_y = \left[\frac{2B_1}{ak}\right]\sin ky\left(\frac{z}{a}\right)\exp-\frac{z^2}{a^2}\,, \qquad B_z = B_0 + B_1\cos ky\exp-\frac{z^2}{a^2}\,. \tag{22}$$

This represents an initial uniform field B_0 extending in the z-direction. The periodic disturbing field, characterized by B_1, has the effect of bunching the initial field into bundles at intervals of $2\pi/k$ along the y-axis. The field at the center of each bundle is $B_0 + B_1$. These bundles merge into a uniform field a distance of the order of a on each side of the y-axis.

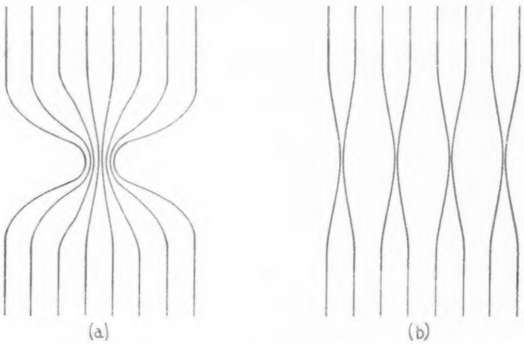

FIG. 3.—Schematic drawing of the splitting of a flux tube at a constricted region

The energy of the bundle lying in $-\pi/k \leqq y \leqq +\pi/k$ is

$$E = \frac{1}{2\mu}\int_{-\infty}^{+\infty} dz \int_{-\pi/k}^{+\pi/k} dy\,(B_y^2 + B_z^2)$$

$$= E_0 + \frac{B^2}{2\mu}\int_{-\infty}^{+\infty} dz \int_{-\pi/k}^{+\pi/k} dy\left[\frac{4}{a^2k^2}\left(\frac{z^2}{a^2}\right)\sin^2 ky + \cos^2 ky\right]\exp\left(-2\,\frac{z^2}{a^2}\right),$$

where E_0 is the energy of the homogeneous component of the field. The first-order term in B_1 drops out because of the integration over y. We finally obtain the energy due to the bunching as

$$E - E_0 = \frac{\pi^{3/2}}{2^{1/2}}\frac{B_1^2}{2\mu}\frac{a}{k}\left(1 + \frac{2}{a^2k^2}\right).$$

The energy per unit y is

$$\epsilon = \frac{k}{2\pi}(E - E_0) = \frac{\pi^{1/2}}{2^{3/2}}\frac{B_1^2}{2\mu}\,a\left(1 + \frac{2}{a^2k^2}\right). \tag{23}$$

For given values of a and B_1, ϵ is a monotonically decreasing function of k. This demonstrates the tendency for flux tubes to split up where the tube changes size abruptly.

The magnetic stresses at the surface of the sun are of the order of 0.2 times the gas pressure; we conclude that, unless some other effect is of large magnitude and opposite in sense to the magnetic stresses, the flux tube has sufficient potential energy to carry out the branching, pushing the gas out of its way as it does so. Therefore, at the surface of the sun we expect to find, after a time, not one, but several, flux tubes, each producing a small spot. Initially, the field from the spot was of the general configuration shown in Figure 2, *b;* branching results in something like Figure 2, *c*.

Each branch of a flux tube in a spot group extends, on the order of 10^4 km or more, down into the convective zone and so is pushed around by the convective motions there. We should expect the portion of the branch above the surface of the sun to show some of this random motion, with the result that the spots of a group spread out from their initial position. Besides this branching process, one would expect the magnetic buoyancy, which was initially successful in heaving a region of relatively intense field up to the surface, to continue to operate, though more slowly than at first, to pull up more of the toroidal field. The process will not go far, because, as was shown in the first section, the magnetic buoyancy becomes unimportant as one goes to weaker fields and deeper layers. But, in so far as the process operates, it should result in a progressively larger region of the toroidal field rising to the surface, with a subsequent increase in the separation of the two parts of the spot group. We conclude from the two effects discussed in this paragraph that each half of a spot group should slowly diverge within itself and from the other half.

The eventual expiration of a given spot group follows from the fact that a flux tube rising from the convective zone up to the photosphere and descending again to the convective zone, to form an inverted **U**, does not constitute a regenerative portion of the solar hydromagnetic dynamo; in this prodigal state it dies from diffusion. We must remember that it is not the molecular diffusion, which is negligible, but the eddy diffusivity of the convective zone that is responsible for the decay of the spot; vertical convective velocities of 10 m/sec in the region of the convective zone under the spot give a decay time of only a few months.

I should like to express my gratitude to Dr. Arnulf Schlüter for critical discussion of the linearized sunspot model presented in this paper.

APPENDIX I

KINEMATICS OF A FLUX TUBE

To supplement the rather brief discussion in Section II of the equilibrium of a flux tube, let us consider the stresses within a tube of flux which may not be in equilibrium. Let us idealize the flux tube to be of square cross-section of side w and to contain a magnetic field B uniform over the cross-section. Let us confine the tube to the yz-plane. We assume a gravitational field of acceleration g in the negative z-direction. We let s represent distance measured along the axis of the tube from left to right, and θ the inclination of the tube. We shall take the tube to be sufficiently slender compared to the characteristic lengths of the medium in which it is suspended that

$$\frac{dw}{ds} \ll 1\,, \qquad \frac{d\theta}{ds} \ll \frac{1}{w}. \tag{24}$$

Let p_i, ρ_i, T_i, and p_e, ρ_e, T_e represent the state of the material medium inside and outside the flux tube, respectively. Assuming the molecular weight of the medium to be uniform throughout, we write

$$p_i = \frac{k}{m} T_i \rho_i\,, \qquad p_e = \frac{k}{m} T_e \rho_e\,. \tag{25}$$

We shall assume that equation (1) is satisfied, which puts the flux tube in local lateral equilibrium. Finally, we shall assume that the medium outside is in equilibrium, satisfying the barometric relation,

$$\frac{\partial p_e}{\partial z} = -\rho_e g\,, \qquad \frac{\partial p_e}{\partial x} = \frac{\partial p_e}{\partial y} = 0\,. \tag{26}$$

Consider the element $w^2 ds$ of the flux tube shown in elevation and plan view in Figure 4, *a* and *b*, respectively. The angle between the sides and the axis of the flux tube is

$$\alpha = \frac{1}{2}\frac{dw}{ds}\,. \tag{27}$$

Consider the force $F_s ds$ in the s-direction on the element. The weight of the element is $g\rho_i w^2 ds$. On the left-hand end there is a net pressure $p_i - B^2/2\mu$ on the area w^2; a corresponding

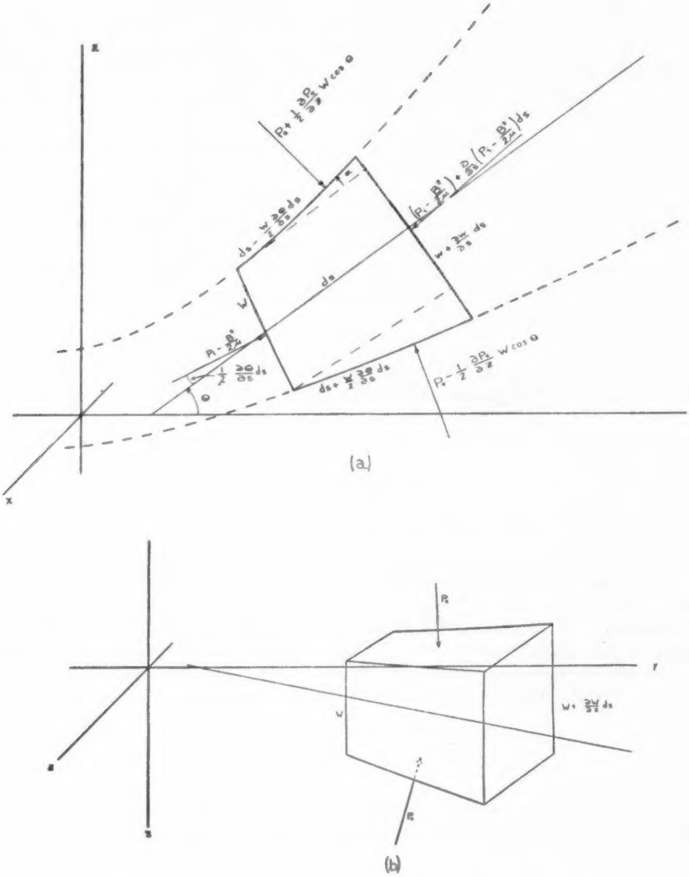
z
$P_e + \frac{1}{2}\frac{\partial P_e}{\partial z} W\cos\theta$
α
$(P_i - \frac{B^2}{2\mu}) + \frac{\partial}{\partial s}(P_i - \frac{B^2}{2\mu})ds$
$ds - \frac{W}{2}\frac{\partial\theta}{\partial s}ds$
$w + \frac{\partial w}{\partial s}ds$
ds
W
$P_i - \frac{B^2}{2\mu}$
$\frac{1}{2}\frac{\partial\theta}{\partial s}ds$
θ
$ds + \frac{W}{2}\frac{\partial\theta}{\partial s}ds$
$P_e - \frac{1}{2}\frac{\partial P_e}{\partial z} W\cos\theta$
y
x
(a)
P_e
y
w
$w + \frac{\partial w}{\partial s}ds$
z
x
P_e
(b)

FIG. 4.—*a*, elevation of flux tube. *b*, plan view of flux tube

force is exerted on the opposite end of the element. The sides of the element parallel to the yz-plane experience a pressure p_e inclined at an angle $(\pi/2 - \alpha)$ to the axis of the element. Finally, the remaining pair of sides experience pressures $p_e \pm \frac{1}{2}(\partial p_e/\partial z)w \cos\theta$. Multiplying the foregoing pressures by their respective areas and taking the s component, we obtain

$$\begin{aligned} F_s d s = {} & - g \rho_i w^2 \sin\theta d s + 2 p_e w \alpha d s \\ & + \left(p_i - \frac{B^2}{2\mu}\right) w^2 - \left[\left(p_i - \frac{B^2}{2\mu}\right) + \frac{\partial}{\partial s}\left(p_i - \frac{B^2}{2\mu}\right) d s\right]\left(w^2 + \frac{\partial w^2}{\partial s} d s\right) \\ & + \left(p_e + \frac{1}{2}\frac{\partial p_e}{\partial z} w \cos\theta\right) w \left(1 - \frac{w}{2}\frac{d\theta}{d s}\right) \alpha d s \\ & + \left(p_e - \frac{1}{2}\frac{\partial p_e}{\partial z} w \cos\theta\right) w \left(1 + \frac{w}{2}\frac{d\theta}{d s}\right) \alpha d s . \end{aligned} \tag{28}$$

Using equation (1) to eliminate p_i, equations (26) to eliminate $\partial p_e/\partial z$, and equation (27) to eliminate α, we may simplify equation (28) to

$$F_s = \frac{d}{d s}\left(w^2 \frac{B^2}{\mu}\right) + g w^2 \sin\theta\, (\rho_e - \rho_i) , \tag{29}$$

neglecting terms of second and higher order in dw/ds and $d\theta/ds$.

Since we are considering a flux tube, it follows that the total flux Φ is independent of s. Then

$$B = \frac{\Phi}{w^2} , \tag{30}$$

and

$$\frac{d}{d s}\left(w^2 \frac{B^2}{\mu}\right) = \frac{\Phi^2}{\mu}\frac{d}{d s}\left(\frac{1}{w^2}\right) = \frac{\Phi^2}{2\mu} w^2 \frac{d}{d s}\left(\frac{1}{w^4}\right) = w^2 \frac{d}{d s}\frac{B^2}{2\mu} .$$

Thus we may write equation (29) as

$$F_s = w^2\left[\frac{d}{d s}\frac{B^2}{2\mu} + g \sin\theta\, (\rho_e - \rho_i)\right] . \tag{31}$$

Consider the forces normal to the axis of the tube. Similar to equation (28), we write

$$\begin{aligned} F_n d s = {} & - g \rho_i w^2 \cos\theta d s - 2\left(p_i - \frac{B^2}{2\mu}\right) w^2 \frac{1}{2}\frac{d\theta}{d s} d s \\ & - \left(p_e + \frac{1}{2}\frac{\partial p_e}{\partial z} w \cos\theta\right) w \left(1 - \frac{w}{2}\frac{d\theta}{d s}\right) d s + \left(p_e - \frac{1}{2}\frac{\partial p_e}{\partial z} w \cos\theta\right) w \left(1 - \frac{w}{2}\frac{d\theta}{d s}\right) d s , \end{aligned}$$

which reduces to

$$F_n = w^2\left[\frac{B^2}{\mu}\frac{d\theta}{d s} + g \cos\theta\, (\rho_e - \rho_i)\right] . \tag{32}$$

Consider the special case where the tube is in longitudinal equilibrium. Then $F_s = 0$, and equation (31) reduces to

$$0 = \frac{d}{d s}\frac{B^2}{2\mu} + g \sin\theta\, (\rho_e - \rho_i) . \tag{33}$$

Now

$$\frac{d}{d s} = \frac{d z}{d s}\frac{d}{d z} = \sin\theta \frac{d}{d z} . \tag{34}$$

Hence, for any inclination of the tube, we obtain

$$0=\frac{d}{dz}\frac{B^2}{2\mu}+g\left(\rho_e-\rho_i\right), \tag{35}$$

which was obtained in equation (14) for a vertical tube. If we differentiate equation (1) with respect to z and use equation (26), we obtain

$$0=\frac{d}{dz}\frac{B^2}{2\mu}+g\rho_e+\frac{dp_i}{dz}. \tag{36}$$

Comparing equations (35) and (36), we find that equilibrium requires that p_i obey the barometric law,

$$\frac{dp_i}{dz}=-\rho_i g. \tag{37}$$

The physically obvious fact that a flux tube is stable against a local constriction or expansion is readily demonstrated from equation (31). Consider a horizontal flux tube of uniform cross-section. Let us pinch the tube over a finite extent of its length. B is increased in the restriction. Approaching the restriction from the left, we have $(d/ds)(B^2/\mu) > 0$. Equation (31) gives $F_s > 0$, causing the fluid to flow into the restricted region and restoring the tube to its initial uniformity.

APPENDIX II

FLUX TUBE IN THERMAL EQUILIBRIUM

Consider a flux tube in thermal equilibrium with its surroundings. The static equilibrium of such a tube was investigated briefly in Section II. There we found that $B \propto p_e^{1/2}$, so that $p_m \propto p_e$. From equation (1) it follows that $p_i \propto p_e$. Since Bw^2 is the total flux through the tube and is constant, we have $w \propto p_e^{-1/4}$. We note that the mass per unit length $w^2\rho_i$ decreases with height for a tube in either an isothermal or an adiabatic atmosphere.

We shall now inquire into the longitudinal motions within a flux tube and the variation of the magnetic buoyancy as a segment of an initially horizontal flux tube is displaced vertically by the magnetic buoyancy. We should like to know whether the tube can be expected to tend toward the static equilibrium configuration discussed in the foregoing paragraph and whether the magnetic buoyancy continues to function even after large displacement; the fact that $w^2\rho_i$ decreases with height implies that there must be a longitudinal flow away from the elevated portion of the tube. We shall find just such a flow from the following calculations; the flow allows an approach to $B \propto p_e^{1/2}$ and guarantees that the magnetic buoyancy will not fail after some finite displacement.

Consider how conditions will vary when a flux tube, initially horizontal and of uniform cross-section, is displaced vertically by some small but varying amount $\delta z(y)$. We are particularly interested in finding whether an upward bulging of the tube will result in fluid flowing along the tube away from the bulge or toward the bulge. Thus we shall assume that $T_i = T_e = T$ and constrain the fluid within the tube to move only in the z-direction, allowing no flow along the tube; we then investigate the longitudinal force F_s, to see which way along the tube the fluid would flow if the constraints were removed. The tube will have to be held in place, of course, by external forces, because of the magnetic buoyancy and longitudinal stresses.

We shall assume that $d\delta z/ds \ll 1$. Then

$$\sin\theta \simeq \frac{d\delta z}{ds}, \qquad ds \simeq dy. \tag{38}$$

Using equations (5), (30), and (36), we may write equation (29)

$$F_s=\frac{\Phi^2}{\mu w^2}\frac{d\delta z}{dy}\left[\frac{mg}{2kT}-\frac{2}{w}\frac{dw}{d\delta z}\right].$$

Consider $(2/w)(dw/d\delta z)$. With the constraint that there be no longitudinal flow within the tube, it follows that

$$\rho_i = \rho_{i0}\left(\frac{w_0}{w}\right)^2, \qquad B = B_0\left(\frac{w_0}{w}\right)^2. \tag{39}$$

Then equation (5) may be written

$$\rho_e\left(\frac{w}{w_0}\right)^4 - \rho_{i0}\left(\frac{w}{w_0}\right)^2 - \frac{mB_0^2}{2\mu kT} = 0. \tag{40}$$

Because we are considering only a small vertical displacement, $\delta z(y)$, we may introduce the approximation

$$\begin{gathered}\left(\frac{w}{w_0}\right)^2 = 1 + \left[\frac{d}{dz}\left(\frac{w}{w_0}\right)^2\right]_0 \delta z + O^2(\delta z), \qquad T = T_0 + \left(\frac{dT}{dz}\right)_0 \delta z + O^2(\delta z), \\ \rho_e = \rho_{e0} + \left(\frac{d\rho_e}{dz}\right)_0 \delta z + O^2(\delta z).\end{gathered} \tag{41}$$

Solving equation (25) for ρ_e, differentiating with respect to z, dividing by ρ_e, and using equation (26) to eliminate $\partial p_e/\partial z$, we obtain

$$\frac{1}{\rho_e}\frac{d\rho_e}{dz} = -\frac{mg}{kT_e} - \frac{1}{T_e}\frac{dT_e}{dz}. \tag{42}$$

Putting equations (41) and (42) into equation (40), we finally obtain

$$\begin{aligned}\frac{d}{d\delta z}\left(\frac{w}{w_0}\right)^2 &= \left[\frac{mg}{kT} + \frac{1}{T}\frac{dT}{dz}\left(1 - \frac{p_{m0}}{p_{e0}}\right)\right]\left(1 + \frac{p_{m0}}{p_{e0}}\right)^{-1} + O(\delta z) \\ &= \left[\frac{mg}{kT}p_{e0} + \frac{1}{T}\frac{dT}{dz}p_{i0}\right](p_{e0} + p_{m0})^{-1} + O(\delta z).\end{aligned} \tag{43}$$

But

$$\frac{2}{w}\frac{dw}{d\delta z} = \frac{1}{w_0^2}\frac{dw^2}{d\delta z} + O(\delta z).$$

Thus, to the degree of approximation used in equation (41), equation (43) gives $(2/w)(dw/d\delta z)$; the equation for F_s may be rewritten as

$$F_s = \frac{d\delta z}{dy}\frac{\Phi^2}{\mu w^2}\left\{\frac{mg}{2kT} - \left[\frac{mg}{kT}p_{e0} + \frac{1}{T}\frac{dT}{dz}p_{i0}\right](p_{e0} + p_{m0})^{-1} + O^2(\delta z)\right\}. \tag{44}$$

If the medium through which the flux tube passes is of uniform temperature, so that dT/dz vanishes, then

$$F_s = -\frac{d\delta z}{dy}\frac{\Phi^2}{\mu w^2}\frac{mg}{2kT}\frac{p_{e0} - p_{m0}}{p_{e0} + p_{m0}}. \tag{45}$$

If, on the other hand, it is an adiabatic atmosphere, then

$$\frac{1}{T}\frac{dT}{dz} = \frac{\gamma - 1}{\gamma}\frac{1}{p_e}\frac{dp_e}{dz} = -\frac{(\gamma - 1)}{\gamma}\frac{mg}{kT},$$

and

$$F_s = -\frac{d\delta z}{dy}\frac{\Phi^2}{\mu w^2}\left(\frac{2 - \gamma}{\gamma}\right)\left(\frac{mg}{2kT}\right)\left(\frac{p_{e0} - p_{m0}}{p_{e0} + p_{m0}}\right). \tag{46}$$

We see from equations (45) and (46) that, for both an isothermal and an adiabatic atmosphere, $d\delta z/dy > 0$ implies that $F_s < 0$, resulting in a flow of fluid out of the raised portions of the flux tube. This has the effect of increasing p_m relative to p_i and *enhances* the magnetic buoyancy in the upward bulges. Only when dT/dz is sufficiently negative to reverse the sign of F_s, will the longitudinal flow degenerate the magnetic buoyancy; certainly in any large-scale region, T never decreases at a rate significantly greater than the adiabatic rate because of the extreme convective instability that would result from a more rapid decrease.

APPENDIX III

ADIABATIC FLUX TUBE

Consider a flux with an adiabatic interior. Here T_i no longer need be equal to T_e, and many physical relations which are taken for granted in Appendix II are no longer obvious. We have in mind the same questions as when $T_i = T_e$, viz., whether a flux tube displaced vertically by the magnetic buoyancy tends toward the static equlibrium configuration and whether the magnetic buoyancy vanishes after some finite displacement. The latter question no longer has the unambiguous answer it had when $T_i = T_e$.

Consider the static equilibrium of a flux tube with an adiabatic interior; the relation between p_i and ρ_i is, accordingly,

$$p_i = p_{i0}\left(\frac{\rho_i}{\rho_{i0}}\right)^{\gamma}. \tag{47}$$

If the flux tube is in equilibrium, we may combine equation (47) with equation (37). We obtain the familiar relations for an adiabatic atmosphere:

$$\rho_i = \rho_{i0}\left[1 - \frac{\gamma-1}{\gamma}\frac{mg}{kT_{i0}}z\right]^{1/(\gamma-1)}, \qquad p_i = p_{i0}\left[1 - \frac{\gamma-1}{\gamma}\frac{mg}{kT_{i0}}z\right]^{\gamma/(\gamma-1)}. \tag{48}$$

ρ_{i0}, p_{i0}, and T_{i0} are the values of ρ_i, p_i, and T_i at $z = 0$. Using equation (1), the magnetic pressure for static equilibrium is

$$p_m = p_e - p_i = p_e - p_{i0}\left[1 - \frac{\gamma-1}{\gamma}\frac{mg}{kT_{i0}}z\right]^{\gamma/(\gamma-1)}. \tag{49}$$

The width w of the tube may be computed from the fact that it varies as $p_m^{-1/4}$.

Consider the special case that the atmosphere outside the tube is an adiabatic atmosphere and, further, that $T_i = T_e$ at $z = 0$. Now, independently of the latter condition, T_i and T_e vary linearly with height, according to

$$T_i = T_{i0}\left[1 - \frac{\gamma-1}{\gamma}\frac{mg}{kT_{i0}}z\right], \qquad T_e = T_{e0}\left[1 - \frac{\gamma-1}{\gamma}\frac{mg}{kT_{e0}}z\right].$$

Thus, setting $T_i = T_e$ at $z = 0$ implies that $T_i = T_e$ at all heights in the atmosphere; the tube is in thermal equilibrium with its surroundings, even though insulated from them, and the relations worked out in the previous section for thermal equilibrium in an adiabatic atmosphere are valid.

The magnetic buoyancy depends on the sign of $\rho_i - \rho_e$, which must be investigated quantitatively, because, in an adiabatic atmosphere, it depends critically on the initial conditions. Consider, then, a long horizontal uniform flux tube. There will be no longitudinal flow under these conditions, and $B \propto \rho_i$. Thus

$$p_m = p_{m0}\left(\frac{\rho_i}{\rho_{i0}}\right)^2. \tag{50}$$

The zero subscript denotes initial values. Comparing equation (50) with equation (47), it follows that p_m varies more rapidly with the density than does p_i, since $\gamma < 2$. A vertical displacement of the flux tube, with the resulting change in ρ_e, results in ρ_m taking up more than its share of the pressure change. Thus p_i does not have to vary so rapidly, and we conclude that

$$\frac{1}{p_i}\frac{dp_i}{dz} < \frac{1}{p_e}\frac{dp_e}{dz}. \tag{51}$$

The slower rate of variation of p_i may be deduced quantitatively from equation (1). Differentiating with respect to z, we obtain

$$\frac{dp_i}{dz} = \frac{dp_e}{dz} - \frac{B^2}{\mu}\frac{1}{B}\frac{dB}{dz}. \tag{52}$$

But, from equations (39) and (48), it follows that

$$\frac{1}{B}\frac{dB}{dz} = \frac{1}{\rho_i}\frac{d\rho_i}{dz} = \frac{1}{\gamma}\frac{1}{p_i}\frac{dp_i}{dz}. \tag{53}$$

Putting equation (53) into equation (52) and solving for $(1/p_i)(dp_i/dz)$, we obtain

$$\frac{1}{p_i}\frac{dp_i}{dz} = \frac{dp_e}{dz}\left[p_i + \frac{B^2}{\gamma\mu}\right]^{-1} = \frac{1}{p_e}\frac{dp_e}{dz}\left[1 + \frac{2-\gamma}{\gamma}\frac{p_m}{p_e}\right]^{-1}. \tag{54}$$

Thus, with $\gamma < 2$, we obtain equation (51).

If the medium outside the flux tube varies adiabatically with height z, then, besides equation (51), we have

$$\frac{1}{\rho_i}\frac{d\rho_i}{dz} < \frac{1}{\rho_e}\frac{d\rho_e}{dz}, \qquad \frac{1}{T_i}\frac{dT_i}{dz} < \frac{1}{T_e}\frac{dT_e}{dz}. \tag{55}$$

To obtain relations between ρ_e and ρ_i, etc., rather than just their derivatives, we put equations (47) and (50) into equation (1), obtaining

$$p_e = p_{i0}\left(\frac{\rho_i}{\rho_{i0}}\right)^{\gamma} + p_{m0}\left(\frac{\rho_i}{\rho_{i0}}\right)^{2}. \tag{56}$$

Equation (56) gives ρ_i in terms of p_e; and p_i, p_m, and w may then be computed, using equations (47), (50), and (39), respectively.

If the external medium is an adiabatic atmosphere, then

$$p_e = p_{e0}\left(\frac{\rho_e}{\rho_{e0}}\right)^{\gamma}, \tag{57}$$

and equation (56) may be written as

$$p_{e0}\left(\frac{\rho_e}{\rho_{e0}}\right)^{\gamma} = p_{i0}\left(\frac{\rho_i}{\rho_{i0}}\right)^{\gamma} + p_{m0}\left(\frac{\rho_i}{\rho_{i0}}\right)^{2}. \tag{58}$$

Consider how ρ_i and ρ_e compare near the top of the atmosphere, where ρ_e approaches zero. Here ρ_i also approaches zero, so that $\rho_i/\rho_{i0} \ll 1$. Equation (58) reduces to

$$p_{e0}\left(\frac{\rho_e}{\rho_{e0}}\right)^{\gamma} = p_{i0}\left(\frac{\rho_i}{\rho_{i0}}\right)^{\gamma}.$$

Thus

$$\frac{\rho_e}{\rho_i} = \frac{\rho_{e0}}{\rho_{i0}}\left(\frac{p_{i0}}{p_{e0}}\right)^{1/\gamma} = \left(\frac{\rho_{e0}}{\rho_{i0}}\right)^{(\gamma-1)/\gamma}\left(\frac{T_{i0}}{T_{e0}}\right)^{1/\gamma}. \tag{59}$$

For the special case that $T_{i0} = T_{e0}$, we have $\rho_{e0} > \rho_{i0}$; equation (59) implies that $\rho_e/\rho_i > 1$ as ρ_e approaches zero. If, on the other hand, $\rho_{e0} = \rho_{i0}$, then $T_{e0} > T_{i0}$, and equation (59) tells us that $\rho_e/\rho_i < 1$, which also follows from equation (55). Thus we have demonstrated that, beginning with a flux tube initially in thermal equilibrium with its surroundings, the magnetic buoyancy is operative at all heights in an adiabatic atmosphere to which the flux tube may be displaced; the presence of flux tubes induces convection in an adiabatic atmosphere. If, on the other hand, the flux tube initially satisfies equation (1) by virtue of $T_{i0} < T_{e0}$ rather than $\rho_{i0} < \rho_{e0}$, then the flux tube is stable against vertical displacement; the presence of flux tubes inhibits convection in an adiabatic atmosphere.

The critical condition giving an initial magnetic buoyancy which vanishes as $\rho_e/\rho_i \rightarrow 1$ at the top of the atmosphere may be obtained from equation (59) by putting $\rho_e = \rho_i$. We obtain the relation

$$\rho_{i0} = \rho_{e0}\left(\frac{T_{i0}}{T_{e0}}\right)^{1/(\gamma-1)} . \tag{60}$$

This is the condition that the variation of the matter within the flux tube is adiabatic during the generation of the magnetic field.

To determine p_e/p_i as $\rho_e \rightarrow 0$, we note from equations (47) and (50) that p_m decreases more rapidly with decreasing ρ_i than does p_i. Thus p_m/p_i approaches zero as the top of the atmosphere is approached, and equation (1) becomes

$$\frac{p_e}{p_i} = 1 + \frac{p_m}{p_i} \sim 1 . \tag{61}$$

To compute T_e/T_i as $\rho_e \rightarrow 0$, we use equations (25), (59), and (61). We find

$$\frac{T_e}{T_i} = \left(\frac{T_{e0}}{T_{i0}}\right)^{1/\gamma}\left(\frac{\rho_{i0}}{\rho_{e0}}\right)^{(\gamma-1)/\gamma} . \tag{62}$$

If, initially, $T_{e0} = T_{i0}$, we have $\rho_{i0} < \rho_{e0}$ and conclude from equation (62) that $T_i > T_e$, the interior of the flux tube becomes hotter than its surroundings, which also follows from equation (55). If, on the other hand, $\rho_{i0} = \rho_{e0}$, then $T_{i0} < T_{e0}$, and we conclude that $T_i < T_e$. Again the critical case leading to $T_i = T_e$ at the top of the atmosphere yields the adiabatic relation (60).

As in the previous section, where $T_i = T_e$, let us investigate F_s as a result of a small vertical adiabatic displacement of an initially horizontal and uniform flux tube in thermal equilibrium with its surroundings. We shall again introduce the constraint that there be no longitudinal flow; the resulting F_s will tell us whether the fluid would flow toward or away from an upward bulge of the tube if the constraint were removed.

From equations (29), (30), and (38) we obtain

$$F_s = \frac{d\delta z}{ds}\left[\frac{\Phi^2}{\mu w_0^2}\frac{1}{\rho_{i0}}\frac{d\rho_i}{d\delta z} + g w^2(\rho_e - \rho_i)\right] . \tag{63}$$

We shall compute the quantity in brackets, omitting terms $O(\delta z)$, and obtain F_s omitting terms $O^2(\delta z)$. Thus, using initial values, we obtain, from equation (5),

$$w^2(\rho_e - \rho_i) = w_0^2(\rho_{e0} - \rho_{i0}) + O(\delta z) = \frac{mg}{kT_0}\left(\frac{\Phi^2}{2\mu w_0^2}\right) + O(\delta z) . \tag{64}$$

Since the fluid inside the flux tube varies adiabatically, we obtain

$$\frac{1}{\rho_i}\frac{d\rho_i}{dz} = \frac{1}{\gamma}\frac{1}{p_i}\frac{dp_i}{dz} = \frac{1}{\gamma}\frac{1}{p_e}\frac{dp_e}{dz}\left[1 + \frac{2-\gamma}{\gamma}\frac{p_m}{p_e}\right]^{-1} ,$$

the latter by equation (54). Using equations (25) and (26), we finally obtain

$$\frac{1}{\rho_{i0}}\frac{d\rho_i}{dz} = -\frac{1}{\gamma}\frac{mg}{kT_0}\left[1 + \frac{2-\gamma}{\gamma}\frac{p_m}{p_e}\right]^{-1} + O(\delta z) . \tag{65}$$

Substituting equations (64) and (65) in equation (63), we obtain

$$F_s = -\frac{d\,\delta z}{d s}\,\frac{m g}{k T_0}\,\frac{\Phi^2}{2\mu w^2}\,\frac{\gamma-2}{\gamma}\,\frac{p_{e0}-p_{m0}}{p_{e0}+(2-\gamma/\gamma)\,p_m}+O^2(\delta z)\,, \tag{66}$$

which is to be compared with equation (56). Now $d\delta z/ds > 0$ implies that $F_s < 0$, indicating a longitudinal flow along the tube away from an upward bulge, as in the case worked out previously where $T_e = T_i$. The transport of matter from the raised, and therefore expanded, portion of the tube enhances p_m relative to p_i by removing part of the fluid producing p_i and compressing B. This *enhances* the magnetic bouyancy and explains why ρ_e/ρ_i is greater than unity, as shown by equation (59), at the top of the atmosphere, even though p_m, on which the magnetic buoyancy depends, drops off with ρ_i more rapidly than does p_i.

REFERENCES

Biermann, L. 1941, *Vierteljahrsschr. Astr. Gesellsch.*, **76**, 194.
Gurevich, L., and Lebedinsky, A. 1946, *J. Phys.*, **10**, 327.
Kuiper, G. P. 1953, *The Sun* (Chicago: University of Chicago Press), p. 570.
Menzel, D. H., and Bell, B. 1953, *Trans. 11th Volta Cong., 1952* (Rome: Acad. Lincei).
Schlüter, A., and St. Temesvary. *Zs. f. Ap.* (in press).

THE CHARACTER OF THE INSTABILITY OF AN INCOMPRESSIBLE FLUID OF CONSTANT KINEMATIC VISCOSITY AND EXPONENTIALLY VARYING DENSITY

T. Y. Teng Fan

Received September 17, 1954

ABSTRACT

The equations determining the rate of growth of a horizontal periodic disturbance (of a given wave number k) in an incompressible fluid of constant kinematic viscosity (ν) and exponentially varying density ($\rho = \rho_0 \exp [\beta z]$) are obtained. It is shown that this rate of growth depends on the two dimensionless parameters $L = l\beta$ and $G = g/\nu^2\beta^3$, where l is the depth of the fluid layer considered and g is the value of gravity. For a number of assigned values of L and G, the dependence of the growth rate on $\kappa (= k/\beta)$ is established, and the mode of maximum instability ($\kappa = \kappa_{\max}$) is determined. For large or small values of G, simple asymptotic formulas for $\kappa_{\max}$ are derived.

1. *Introduction.*—The character of the equilibrium of an incompressible fluid of variable density stratified in horizontal planes was first investigated by Lord Rayleigh (1883). He considered the case of two uniform fluids of different densities separated by a horizontal boundary and also the case of an exponentially varying density. In all cases Rayleigh showed that the situation is unstable if the stratification is one in which a layer of higher density overlies a layer of lower density, also that the instability (as measured by the rate at which a disturbance grows) is greatest when the wave number, k, of the disturbance in the horizontal plane is greatest.

More recently Rayleigh's discussion has been extended by Chandrasekhar (1955) to include the effect of viscosity; and the case of two uniform fluids separated by a horizontal boundary was considered in detail by him. Making use of a general variational principle established in Chandrasekhar's paper, Hide (1955) has obtained approximate solutions for the problem under more general conditions. In this paper we shall obtain the exact solution for the case of a layer of fluid of constant kinematic viscosity and exponentially varying density confined between two rigid planes, i.e., the second case of Rayleigh, including viscosity.

2. *The characteristic equation.*—Considering the effect of a horizontal disturbance characterized by a wave number k on a horizontally stratified fluid of varying density and viscosity, Chandrasekhar has derived the following equation for determining the initial growth of the disturbance, according to e^{nt}:

$$D\left\{\left[\rho-\frac{\mu}{n}(D^2-k^2)\right]Dw-\frac{1}{n}(D\mu)(D^2+k^2)w\right\}$$

$$=k^2\left\{-\frac{g}{n^2}(D\rho)w+\left[\rho-\frac{\mu}{n}(D^2-k^2)\right]w-\frac{2}{n}(D\mu)(Dw)\right\}. \tag{1}$$

In this equation w is the vertical component of the velocity, ρ is the density, and μ is the coefficient of viscosity, both assumed to be functions of the vertical co-ordinate, z, only, and D stands for d/dz.

We shall consider equation (1) for the case when the density varies with z as

$$\rho = \rho_0 e^{\beta z}, \tag{2}$$

where ρ_0 is a constant. If the coefficient of viscosity is assumed to have the same dependence on z, so that

$$\mu = \mu_0 e^{\beta z} , \tag{3}$$

then equation (1) reduces to a linear equation with constant coefficients and can be treated by standard methods. Thus, with ρ and μ given by equations (2) and (3), equation (1) becomes

$$\begin{aligned} D\left\{ e^{\beta z}\left[1 - \frac{\nu}{n}(D^2 - k^2)\right] Dw - \frac{\beta\nu}{n} e^{\beta z}(D^2 + k^2) w \right\} & \\ = k^2 \left\{ -\frac{g\beta}{n^2} e^{\beta z} w + e^{\beta z}\left[1 - \frac{\nu}{n}(D^2 - k^2)\right] w - \frac{2\beta\nu}{n} e^{\beta z} Dw \right\} , & \end{aligned} \tag{4}$$

where ν is the coefficient of kinematic viscosity, which is a constant on assumptions (2) and (3).

On further simplification equation (4) can be reduced to the form

$$[D^4 + 2\beta D^3 + (\beta^2 - b^2) D^2 - \beta b^2 D + a] w = 0 \tag{5}$$

where

$$b^2 = 2k^2 + \frac{n}{\nu} \tag{6}$$

and

$$a = k^2\left[(\beta^2 + b^2) - \left(\frac{g\beta}{n} - n\right)\frac{1}{\nu}\right] . \tag{7}$$

The general solution of equation (5) is clearly of the form

$$W = \sum_{i=1}^{4} c_i \exp(q_i z) , \tag{8}$$

where the c_i's are constants of integration and the q_i's are the roots of the equation (cf. eq. [5])

$$q^4 + 2\beta q^3 + (\beta^2 - b^2) q^2 - \beta b^2 q + a = 0 . \tag{9}$$

This equation for q can be factored in the following manner:

$$\{ q^2 + \beta q + \tfrac{1}{2} [b^2 - \sqrt{(b^4 - 4a)}] \} \{ q^2 + \beta q - \tfrac{1}{2} [b^2 + \sqrt{(b^4 - 4a)}] \} = 0 . \tag{10}$$

The required roots, q_i, can therefore be expressed in the following forms:

$$\begin{aligned} q_1 &= \tfrac{1}{2}(-\beta + A - B) , & q_3 &= \tfrac{1}{2}(-\beta + A + B) , \\ q_2 &= \tfrac{1}{2}(-\beta - A + B) , & q_4 &= \tfrac{1}{2}(-\beta - A - B) , \end{aligned} \tag{11}$$

where

$$A + B = [\beta^2 + 2b^2 + 2\sqrt{(b^2 - 4a)}]^{1/2} \tag{12a}$$

and

$$A - B = [\beta^2 + 2b^2 - 2\sqrt{(b^2 - 4a)}]^{1/2} . \tag{12b}$$

These last equations can be solved for A and B, to give

$$A = [\tfrac{1}{2}(\beta^2 + 2b^2) + \tfrac{1}{2}(\beta^4 + 4b^2\beta^2 + 16a)^{1/2}]^{1/2}$$

and

$$B = [\tfrac{1}{2}(\beta^2 + 2b^2) - \tfrac{1}{2}(\beta^4 + 4b^2\beta^2 + 16a)^{1/2}]^{1/2} . \tag{12c}$$

Relations among the q_i's which follow from equation (11) are

$$q_2 - q_1 = B - A\,, \qquad q_3 - q_1 = B\,, \qquad \text{and} \qquad q_4 - q_1 = -A\,. \tag{13}$$

These relations are useful in the subsequent analysis.

We shall now suppose that the fluid is confined between two rigid planes at $z = 0$ and $z = l$. On these confining surfaces we should impose the boundary conditions (cf. Chandrasekhar 1955, eqs. [23] and [24]),

$$w = 0 \quad \text{and} \quad Dw = 0 \qquad (z = 0 \quad \text{and} \quad z = l)\,. \tag{14}$$

Applying the foregoing conditions to solution (8), we can express the resulting conditions on the coefficients c_i's in matrix notation in the form

$$\begin{vmatrix} 1 & 1 & 1 & 1 \\ q_1 & q_2 & q_3 & q_4 \\ e^{q_1 l} & e^{q_2 l} & e^{q_3 l} & e^{q_4 l} \\ q_1 e^{q_1 l} & q_2 e^{q_2 l} & q_3 e^{q_3 l} & q_4 e^{q_4 l} \end{vmatrix} \begin{vmatrix} c_1 \\ c_2 \\ c_3 \\ c_4 \end{vmatrix} = 0\,. \tag{15}$$

It is clear that for a nontrivial solution we must require that the determinant of the matrix on the left-hand side of equation (15) must vanish. By subtracting the first column from each of the remaining columns and making use of relations (13), we readily deduce that the vanishing of the determinant is equivalent to

$$\begin{vmatrix} B - A & B & -A \\ e^{(B-A)l} - 1 & e^{Bl} - 1 & e^{-Al} - 1 \\ (B - A)\, e^{(B-A)l} & B e^{Bl} & -A e^{-Al} \end{vmatrix} = 0\,. \tag{16}$$

By adding and subtracting suitable multiples of the different rows of the foregoing determinant, we can reduce it still further to

$$\begin{vmatrix} B - A & B & -A \\ e^{(B-A)l} - 1 & e^{Bl} - 1 & e^{-Al} - 1 \\ 0 & A\,(e^{Bl} - 1) & -B\,(e^{-Al} - 1) \end{vmatrix} = 0\,. \tag{17}$$

On expanding this last determinant and simplifying, we find

$$e^{-Al} A^2 (e^{2Bl} - 2e^{Bl} + 1) - e^{Bl} B^2 (e^{-2Al} - 2e^{-Al} + 1) = 0 \tag{18}$$

or

$$A^2 e^{-Al} (e^{Bl} - 1)^2 = B^2 e^{Bl} (e^{-Al} - 1)^2 = 0\,. \tag{19}$$

Hence, finally, we have

$$\frac{\sinh \frac{1}{2} Al}{\sinh \frac{1}{2} Bl} = \pm \frac{A}{B}\,. \tag{20}$$

This is the required characteristic equation for determining n.

3. *The case of zero viscosity.*—It is of interest to verify that in the case of zero viscosity we can recover Rayleigh's result as a special case of the charasteristic equation (20).

$$\text{When} \quad \nu \to 0\,, \quad b \to \infty\,,$$

$$\frac{A}{B} \to 1\,, \quad \text{while } A \text{ and } B \text{ both tend to infinity}\,; \tag{21}$$

further, from equation (12*b*) we find, on substituting for a and b according to equations (6) and (7), that

$$(A-B)\rightarrow\left[\beta^2+4k^2-\frac{4g\beta k^2}{n^2}\right]^{1/2}. \tag{22}$$

Hence the limiting form of equation (20) is

$$1=\lim_{\nu\to0} e^{(A-B)l}=\exp\left\{\left(\beta^2+4k^2-\frac{4g\beta k^2}{n^2}\right)^{1/2} l\right\}. \tag{23}$$

Hence

$$\left(\beta^2+4k^2-\frac{4g\beta k^2}{n^2}\right)^{1/2} l=2\alpha\pi i, \tag{24}$$

where α is an integer; or, alternatively,

$$\frac{g\beta}{n^2}=\frac{1}{k^2l^2}\left(\tfrac{1}{4}\beta^2l^2+k^2l^2+\alpha^2\pi^2\right); \tag{25}$$

this is equivalent to the equation given by Rayleigh (1883, eq. [27]).

4. *The solution of the characteristic equation and the results of numerical calculation.*—Returning to equation (20), we first observe that A and B cannot both be real. For, if A and B are real and the positive sign in equation (20) is taken, then $A = B$, which is impossible. On the other hand, if A and B are real and the negative sign is taken, then the equation cannot be satisfied. Thus A and B must both be complex.

In the further discussion of equation (20) it is convenient to measure length and time in the units l/β and $l/\nu\beta^2$, respectively. Let κ and G denote the wave number, k, the time constant, n, and the value of gravity, g, in these units, i.e.,

$$\kappa=\frac{k}{\beta},\qquad \sigma=\frac{n}{\nu\beta^2},\qquad\text{and}\qquad G=\frac{g}{\nu^2\beta^3}. \tag{26}$$

Also, let L be the thickness of the layer in the same units:

$$L=l\beta. \tag{27}$$

In terms of these new variables we can rewrite equations (12) in the forms

$$\tfrac{1}{2}Al=\frac{L}{2^{3/2}}\left\{1+4\kappa^2+2\sigma+\left[1+24\kappa^2+16\kappa^4+4\sigma\left(1+4\kappa^2-\frac{4G\kappa^2}{\sigma^2}\right)\right]^{1/2}\right\}^{1/2}, \tag{28}$$

$$\tfrac{1}{2}Bl=\frac{L}{2^{3/2}}\left\{1+4\kappa^2+2\sigma-\left[1+24\kappa^2+16\kappa^4+4\sigma\left(1+4\kappa^2-\frac{4G\kappa^2}{\sigma^2}\right)\right]^{1/2}\right\}^{1/2}, \tag{29}$$

where we have further substituted for a and b in accordance with equations (6) and (7). With A and B given by these equations, we must satisfy the equation

$$\frac{\sinh\frac{1}{2}Al}{\sinh\frac{1}{2}Bl}=\pm\frac{A}{B}. \tag{30}$$

In seeking solutions of this equation, we can, under the circumstances of the problem ($\beta > 0$), assume that σ is real. This entails no loss of generality, since Chandrasekhar has shown (1955, p. 9) that if σ is complex, then the real part, $R(\sigma)$, of σ should be negative; and we are not interested in such solutions so long as a solution with σ real and positive exists. (Note that for the case on hand $D^2\mu > 0$, and the possibility that $R[\sigma]$ can be positive if $D^2\mu < 0$ does not arise.)

Letting

$$\xi = \frac{L^2}{8}(1 + 4\kappa^2 + 2\sigma) \tag{31}$$

and

$$\eta^2 = -\frac{L^2}{8}\left[1 + 24\kappa^2 + 16\kappa^4 + 4\sigma\left(1 + 4\kappa^2 - \frac{4G\kappa^2}{\sigma^2}\right)\right], \tag{32}$$

we can write

$$\tfrac{1}{2}Al = \sqrt{}(\xi + \eta i) = x + yi \qquad \text{(say)} \tag{33}$$

and

$$\tfrac{1}{2}Bl = \sqrt{}(\xi \eta i) = x - yi\,, \tag{34}$$

where

$$\xi = x^2 - y^2\,(> 0) \qquad \text{and} \qquad \eta = 2xy\,. \tag{35}$$

In these variables, equation (30) becomes

$$\frac{\sinh(x + yi)}{x + yi} = \pm\frac{\sinh(x - yi)}{x - yi}\,; \tag{36}$$

with the positive sign on the right-hand side, equation (36) is equivalent to

$$\frac{\tanh x}{x} = \frac{\tan y}{y}\,, \tag{37}$$

while with the negative sign it is equivalent to

$$x \tanh x = -y \tan y\,. \tag{38}$$

For any assigned x, equations (37) and (38) allow infinitely many solutions for y. In the case of equation (37), there exists one root in each of the intervals $(\pi, 3\pi/2)$, $(2\pi, 5\pi/2)$, $(3\pi, 7\pi/2)$, $\ldots$, $[m\pi, (m + \frac{1}{2})\pi]$. In the case of equation (38) the corresponding intervals are $(\pi/2, \pi)$, $(3\pi/2, 2\pi)$, $(5\pi/2, 3\pi)$ $\ldots$, $([\mathrm{m} - \frac{1}{2}]\pi, \mathrm{m}\pi)$. Now it can be shown that the mode of maximum instability corresponds with the smallest allowed value of $|y|$. This can be seen most readily by considering the case $\nu \to 0$.

Now, from equations (33) and (34) we have

$$\tfrac{1}{2}(A - B)\,l = 2yi\,, \tag{39}$$

while, according to equations (23) and (24),

$$\operatorname*{limit}_{\nu \to 0}\,(A - B)\,l = 2a\pi i\,. \tag{40}$$

Hence

$$\operatorname*{limit}_{\nu \to 0}\, y = \tfrac{1}{2}a\pi\,. \tag{41}$$

But from Rayleigh's result (1883, eq. [27]) for this case we know that the mode of maximum instability occurs when $a = 1$. Hence, in the general case, we must for a given x seek for y that root of equation (36) which occurs in the interval $(\pi/2, \pi)$. In other words, it will suffice for our purposes to seek solutions of equation (38) which allow roots in the interval $(\pi/2, \pi)$ (eq. [37] does not allow roots in this interval).

We shall now show how, in terms of the solutions of equation (38) in the interval $(\pi/2, \pi)$, we can specify the complete (k, n) relation for assigned values of L and G.

Let x and y $(\pi/2 < y < \pi)$ represent a pair of values which satisfy equation (38). This defines a corresponding pair of (ξ, η) values (cf. eq. [35]), which, in turn, determines a corresponding pair of (κ, σ) values in accordance with equations (31) and (32). Thus, rewriting equation (31) in the form

$$\kappa^2 = \frac{1}{4}\left(\frac{8\xi}{L^2} - 1 - 2\sigma\right) \tag{42}$$

and eliminating κ between this equation and equation (32), we obtain the following cubic equation for σ:

$$\sigma^3 + 2\sigma^2 - \left[2G + \frac{8\xi}{L^2} - 1 + \frac{16}{L^4}(\xi^2 + \eta^2)\right]\sigma + \left(\frac{8\xi}{L^2} - 1\right)G = 0 . \tag{43}$$

For given L and G, equation (43) allows two positive and one negative roots for σ. But only the smaller of the two positive roots for σ leads to a real value of κ. Thus, for a given pair of (ξ, η) values, equations (42) and (43) (for given G and L) lead to a unique pair of (κ, σ) values. In this manner the (κ, σ) relations were determined for the following sets of values of L and G:

$L = 1$ and $G = 1, 10, 10^2, 10^3, 10^4, 10^5$, and 10^{10}

$L = \frac{1}{2}$ and $G = 10, 10^3$, and 10^5 ,

$L = 2$ and $G = 10, 10^3$, and 10^5 .

The results of these calculations are given in Tables 1, 2, 3, and 4 and are further illustrated in Figures 1, 2, 3, 4, and 5. The modes of maximum instability determined for the various cases are listed in Table 5 and exhibited in Figure 6.

TABLE 1

THE (κ, σ) RELATIONS FOR $L = 1$

$G=1$		$G=10^2$		$G=10^4$		$G=10^{10}$	
κ	σ	κ	σ	κ	σ	κ	σ
2.318	0.00837	2.231	0.7921	1.582	26.67	1.224	10799
3.979	.01365	3.897	1.3094	2.967	47.87	1.414	40332
4.486	.01410	4.542	1.3708	4.579	60.46	3.324	71955
4.874	.01417	4.804	1.3767	5.200	62.26	5.310	85768
5.176	.01405	5.110	1.3701	5.913	62.97	9.282	94578
5.721	.01359	5.663	1.3322	6.767	62.47	12.85	98113
7.155	.01161	6.480	1.2369	9.216	56.05	26.42	98919
12.167	0.00571	7.115	1.1478	12.59	45.56	40.92	98855
		7.849	1.0416	19.58	23.16	53.46	98396
						137.96	90904

5. *The asymptotic dependence of the mode of maximum instability on the parameters for large or small G.*—Substituting equation (35) in equations (42) and (43), we obtain the following equations:

$$\sigma^3 + 2\sigma^2 - \left[2G + \frac{8(x^2 - y^2)}{L^2} - 1 + \frac{16(x^2 + y^2)^2}{L^4}\right]\sigma + \left[\frac{8(x^2 - y^2)}{L^2} - 1\right]G = 0 \tag{44}$$

and

$$\kappa^2 = \frac{1}{4}\left[\frac{8(x^2 - y^2)}{L^2} - 1 - 2\sigma\right] . \tag{45}$$

TABLE 2

THE (κ, σ) RELATIONS FOR $G = 10$

$L=\frac{1}{2}$		$L=1$		$L=2$	
κ	σ	κ	σ	κ	σ
4.715	0.02222	2.309	0.08477	1.012	0.2638
8.752	.03579	3.971	.1361	1.881	.4713
9.541	.03610	4.476	.1406	2.346	.5059
10.099	.03594	4.867	.1413	2.427	.5051
11.475	.03453	5.170	.1401	2.504	.5033
13.083	.03174	5.715	.1357	3.520	.4351
14.336	.02937	6.522	.1253	4.329	.3543
17.503	.02342	7.150	.1159	5.284	.2740
21.274	0.01781	7.878	.1050	6.059	0.2227
		12.068	0.0570		

TABLE 3

THE (κ, σ) RELATIONS FOR $G = 10^3$

$L=\frac{1}{2}$		$L=1$		$L=2$	
κ	σ	κ	σ	κ	σ
4.604	2.119	1.726	4.795	1.875	18.19
7.903	3.308	3.315	9.703	2.327	19.86
9.449	3.541	4.368	11.107	2.921	20.77
9.698	3.544	4.765	11.325	3.153	20.84
10.305	3.518	5.200	11.406	3.401	20.78
13.024	3.146	5.480	11.345	4.255	19.90
15.745	2.641	6.779	10.494	5.281	17.87
18.842	2.119	8.487	8.768	6.055	16.96
		10.465	6.866	7.834	12.23
				8.758	10.52
				9.698	9.04

TABLE 4

THE (κ, σ) RELATIONS FOR $G = 10^5$

$L=\frac{1}{2}$		$L=1$		$L=2$	
κ	σ	κ	σ	κ	σ
3.992	96.35	0.912	63.81	0.8478	133.6
7.159	160.9	2.067	144.3	2.3412	248.9
10.64	184.6	3.350	203.5	3.2072	271.0
11.55	185.1	5.199	242.1	4.4601	283.0
12.54	184.2	6.192	249.7	5.0704	285.5
14.76	177.1	8.032	253.3	7.6000	278.3
19.41	151.7	8.722	252.6		
22.99	129.2	12.44	232.1		
25.82	119.1	17.30	191.2		
32.29	81.57				
35.79	69.06				
39.38	58.64				

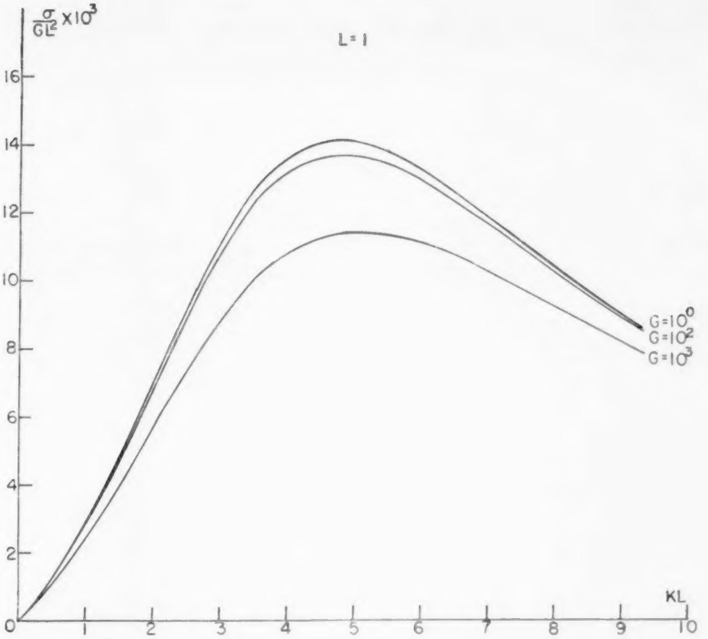

FIG. 1.—The (κ, σ) relation for $L = 1$ and $G = 10^0$, 10^2, and 10^3

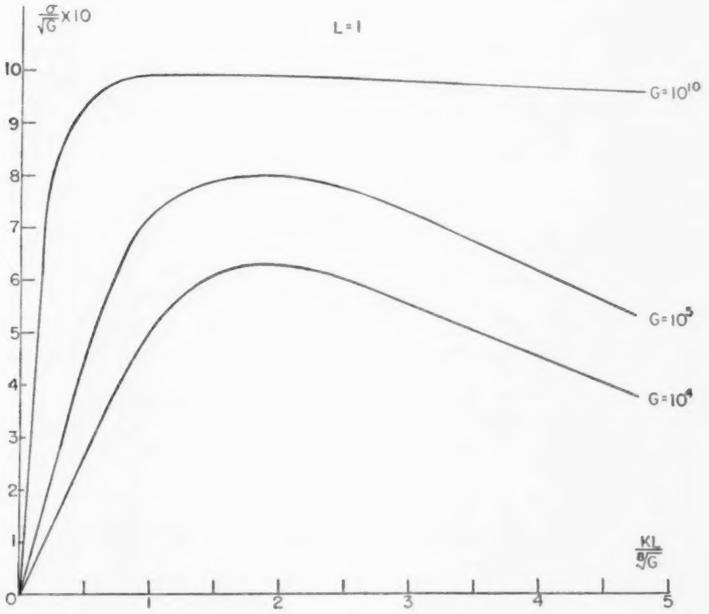

FIG. 2.—The (κ, σ) relation for $L = 1$ and $G = 10^4$, 10^5, and 10^{10}

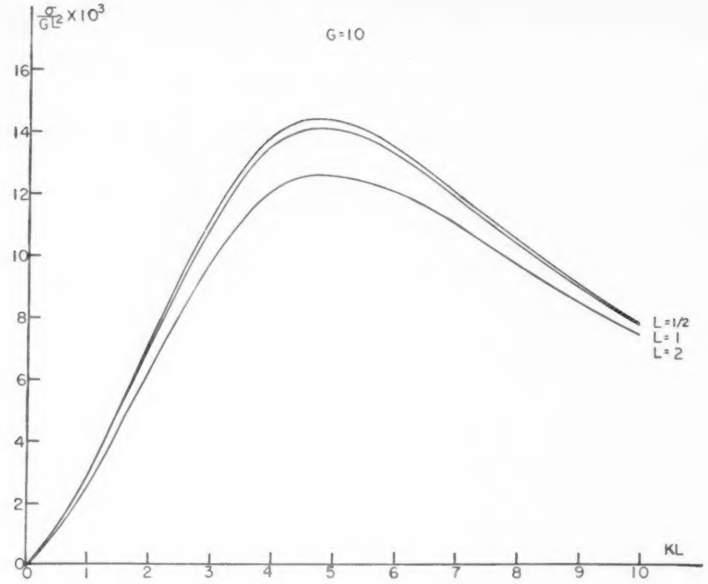

FIG. 3.—The (κ, σ) relation for $G = 10$ and $L = \frac{1}{2}$, 1, and 2

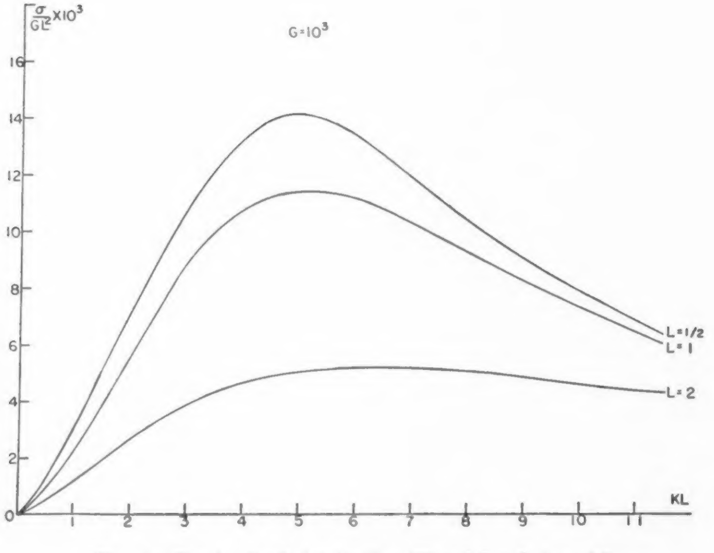

FIG. 4.—The (κ, σ) relation for $G = 10^3$ and $L = \frac{1}{2}$, 1, and 2

Eliminating x from equations (44) and (45), we find

$$\left(4\kappa^2+16\frac{y^2}{L^2}+1\right)\sigma^2+\left[4\kappa^4+\left(6+32\frac{y^2}{L^2}\right)\kappa^2+\tfrac{1}{4}+8\frac{y^2}{L^2}+64\frac{y^4}{L^4}\right]\sigma-4\kappa^2G=0. \tag{46}$$

In equation (46) κ and y cannot be considered as independent quantities: they are, in fact, related by equation (45). Nevertheless, it appears that for both $G \to \infty$ and

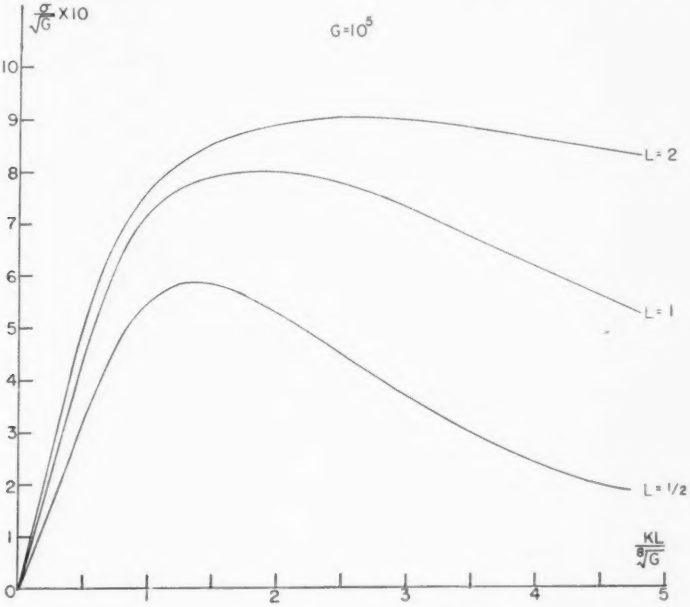

FIG. 5.—The (κ, σ) relation for $G = 10^5$ and $L = \frac{1}{2}$, 1, and 2

TABLE 5

THE MODES OF MAXIMUM INSTABILITY

G	$L=1$		$L=\frac{1}{2}$		$L=2$	
	κ (Exact)	κ (App.)	κ (Exact)	κ (App.)	κ (Exact)	κ (App.)
1	4.778	4.23	....	....	....	....
10	4.778	4.23	9.512	8.415	2.334	2.159
10^2	4.811	....	....	....	....	....
10^3	5.133	....	9.659	....	3.165	....
10^4	5.980	....	....	....	....	....
10^5	7.870	7.24	11.42	9.953	5.914	5.31
10^{10}	32.18	31.64	....	....	....	....

$G \rightarrow 0$ the variation of y is relatively small compared to the other quantities in the domain where σ attains its maximum. Thus y is very nearly $\pi/2$ for $G \rightarrow \infty$ (cf. remarks in paragraph below); similarly $y \sim 2.1$ for $G \rightarrow 0$ (cf. remarks following eq. [59], below). Consequently, in determining the mode of maximum instability for large (or small) G, we may treat y in equation (46) as a sutiably chosen constant. Assuming, then, that y is a constant, and differentiating equation (46) with respect to κ, and setting $d\sigma/d\kappa = 0$, we obtain,

$$\sigma^2 + \left(2\kappa^2 + \tfrac{3}{2} + 8\frac{y^2}{L^2}\right)\sigma - G = 0 \tag{47}$$

or

$$\sigma = \frac{1}{2}\left\{-\left(2\kappa^2 + \tfrac{3}{2} + 8\frac{y^2}{L^2}\right) + \left[\left(2\kappa^2 + 8\frac{y^2}{L^2} + \tfrac{3}{2}\right)^2 + 4G\right]^{1/2}\right\}. \tag{48}$$

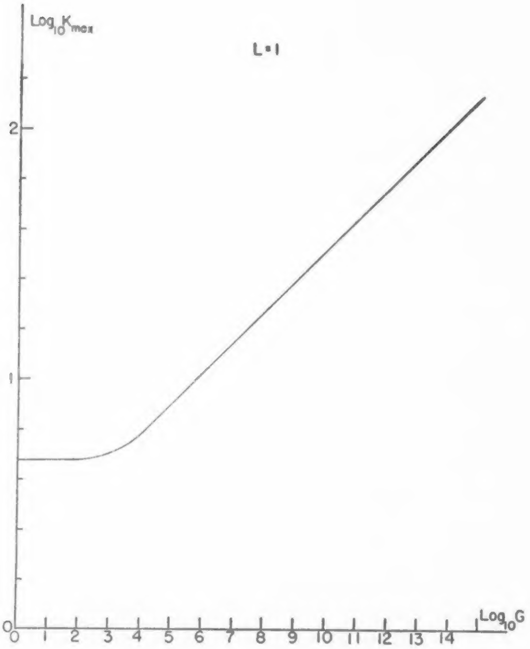

FIG. 6.—The modes of maximum instability

Substituting equation (48) in equation (46), we find that it reduces to

$$\begin{aligned}\left(1+16\frac{y^2}{L^2}\right)^2 G^2 + \left(1+16\frac{y^2}{L^2}\right)\left[\left(2\kappa^2+8\frac{y^2}{L^2}\right)^2 + 2\kappa^2 + 24\frac{y^2}{L^2} + \tfrac{5}{4}\right]& \\ \times\left(2\kappa^2 + 8\frac{y^2}{L^2} + \tfrac{3}{2}\right)G = \left\{\left(2\kappa^2+8\frac{y^2}{L^2}\right)^2 + 2\kappa^2 + 24\frac{y^2}{L^2} + \tfrac{5}{4}\right\}^2 G.&\end{aligned} \tag{49}$$

Solving this quadratic equation in G, we obtain

$$G = \frac{[(2\kappa^2+8y^2/L^2)^2+2\kappa^2+24y^2/L^2+\frac{5}{4}](2\kappa^2+\frac{1}{2}+8y^2/L^2)(2\kappa^2-\frac{1}{2}-8y^2/L^2)}{(1+16y^2/L^2)^2}\,. \tag{50}$$

a) Asymptotic form for large G.—If G is very large, κ^2 must be large, since the value of y must lie in the range $(\pi/2, \pi)$. In this case $\kappa^2 \backsim G^{1/4}$ (cf. eq. [50]); hence $\sigma \sim G^{1/2}$ (cf. eq. [48]) and $x \sim G^{1/4}$. Consequently, for $G \rightarrow \infty$, $x \rightarrow \infty$ and $y \rightarrow \pi/2$. Therefore, putting $y = \pi/2$ in equation (50) and neglecting terms such as $2\kappa^2 + 24y^2/L^2 + \frac{5}{4}$ compared to $(2\kappa^2 + 8\,y^2/L^2)^2$ and $\frac{1}{2}$ compared to $2\kappa^2 + 8\,y^2/L^2$, we find that equation (50) reduces to

$$G = \frac{16\,(\kappa^2+\pi^2/L^2)^3\,(\kappa^2-\pi^2/L^2)}{(1+4\pi^2/L^2)^2}\,. \tag{51}$$

The values of $\kappa_{\max}$ derived from this formula are listed in Table 5. Comparing them with the exact values (also listed in this table), we observe that formula (51) provides $\kappa_{\max}$ with and accuracy of 10 per cent and better for $G > 10^5$.

b) Asymptotic form for very small G.—Since $2\kappa^2 > \frac{1}{2} + 8\,y^2/L^2$ (cf. eq. [50]), it follows that

$$\left(2\kappa^2+8\frac{y^2}{L^2}\right)^2+2\kappa^2+24\frac{y^2}{L^2}+\tfrac{5}{4} > \left(1+16\frac{y^2}{L^2}\right)^2 \tag{52}$$

and

$$G > \left(1+16\,\frac{y^2}{L^2}\right)\left(2\kappa^2-\tfrac{1}{2}-8\,\frac{y^2}{L^2}\right). \tag{53}$$

Therefore, if

$$G < 1+16\,\frac{y^2}{L^2}, \tag{54}$$

$$\kappa^2 \doteq \tfrac{1}{4}+4\,\frac{y^2}{L^2}. \tag{55}$$

The proper value of y can now be determined as follows. We have

$$\begin{aligned} 4\kappa^2 &= \frac{8\,(x^2-y^2)}{L^2} - 2\sigma - 1 \\ &\doteq \frac{8\,(x^2-y^2)}{L^2} - 1 \end{aligned} \tag{56}$$

since as $G \rightarrow 0$, $\sigma \rightarrow 0$. Substituting equation (55) in equation (56), we obtain

$$1+16\,\frac{y^2}{L^2} = \frac{8\,(x^2-y^2)}{L^2} - 1\,; \tag{57}$$

and solving equation (57) for x, we find

$$x = \left(3y^2+\frac{L^2}{4}\right)^{1/2}. \tag{58}$$

Substituting for x from equation (58) in equation (38), we have, in the framework of these approximations,

$$-\tan\,y = \left(3+\frac{L^2}{4y^2}\right)^{1/2}. \tag{59}$$

A numerical solution of this equation gives $y \sim 2.1$. With this value of y, equation (55) becomes

$$\kappa^2 = \tfrac{1}{4} + \frac{4\,(2.1)^2}{L^2} = 0.25 + \frac{17.64}{L^2}. \tag{60}$$

The value of $\kappa_{\max}$ derived from this formula are also listed in Table 5 for comparison with results of the exact calculations. We see that the formula predicts $\kappa_{\max}$ with an error not exceeding 15 per cent for $G < 10^2$.

In conclusion, I wish to thank Professor S. Chandrasekhar for suggesting this problem and for his continuous interest and guidance. My thanks are also due to Dr. C. Y. Fan, who gave valuable assistance.

REFERENCES

Chandrasekhar, S. 1955, *Proc. Cambridge Phil. Soc.*, **51**, 162.
Hide, R. 1955, *Proc. Cambridge Phil. Soc.*, **51**, 179.
Rayleigh, Lord. 1883, *Proc. London Math. Soc.*, **14**, 170–177.

THE PHYSICAL THEORY OF METEORS. VIII. FRAGMENTATION AS CAUSE OF THE FAINT-METEOR ANOMALY*

Luigi G. Jacchia
Harvard College Observatory

Received August 16, 1954

ABSTRACT

The observed decelerations and light-curves of bright meteors are in good agreement with the simple ballistic theory, while fainter meteors photographed with the Super-Schmidt cameras in New Mexico show startling anomalies. In particular, the durations of faint meteors are shorter and the decelerations increase faster than predicted by the theory, when the mass is computed from the integration of the luminous-intensity-curve, in the same fashion as for bright meteors. Extreme fragility and progressive fragmentation seem to account for these and other anomalies. The concept of pellet-like meteors must be replaced with that of a cluster of breaking fragments in the case of most smaller bodies.

I. OBSERVED ANOMALIES

The observed decelerations of bright photographic meteors are in good agreement with the simple ballistic theory of meteors. Atmospheric densities computed by the Harvard Meteor Project from bright meteors photographed in Massachusetts and New Mexico show considerable scatter around a mean curve, but the slope of this curve agrees quite well with that of the density profile derived from White Sands rocket launchings (Jacchia 1952). Whenever several independent decelerations can be determined in the course of a single meteor trajectory, these give, on the average, the right density gradient. Theoretical light-curves and velocity-curves computed by feeding the Rocket Panel (1952) atmospheric data into the basic differential equations governing the motion and the loss of mass of the meteor (Jacchia 1949*a*), agree remarkably well with observations (Jacchia 1949*a*).

The situation is quite different for the fainter meteors, which, in the course of the last two years, have been photographed in New Mexico with the aid of the new 12-inch, *F*/0.8 Super-Schmidt cameras designed by J. G. Baker. In most of the fainter meteors the observed deceleration increases much too fast in the course of the trajectory to be explained by the corresponding change in atmospheric density and by the loss of mass as determined from the integrated light-intensity; the anomaly increases with decreasing brightness of the meteor. Decelerations observed near the beginning of meteor trails still give reasonably correct atmospheric densities, but densities derived from later portions of the trail are too large. Unless we assume that the drag equation changes unexpectedly, we have to postulate that the mass which enters this equation is only a fraction of the mass as determined from the meteor light-curve and, further, that this fraction decreases steadily as the meteor progresses in its trajectory. For some of the fainter meteors this fraction changes from 1 at the beginning to 1/1000 near the end of the trajectory, although a change by a factor of 1/100 is more representative of the general situation.

Meteors that exhibit deceleration anomalies invariably have anomalous light-curves also. Apart from special incidental features, peculiar only to faint meteors, which we shall presently discuss in detail, meteors with anomalous decelerations are of shorter duration than those with normal decelerations. In other words, they go through the

---

* This research has been carried out through the sponsorship of the U.S. Army Office of Ordnance Research from observations supported by the U.S. Office of Naval Research.

same range of light-variation as bright meteors in a shorter time. In particular, the slope of the early portion of the light-curve is, for these meteors, systematically larger than the theoretical value, $dM/dt = 2.5\ (d \log_{10} \rho/dH)V \cos Z_R$, which was successfully used by the writer to obtain atmospheric density gradients from bright meteors (Jacchia 1949*b*). Here M is the photographic magnitude of the meteor at time t, V its velocity, Z_R the zenith distance of the apparent radiant, and ρ the atmospheric density at height H above sea-level. A few meteors, particularly most of the members of the Taurid shower, do not conform to this pattern and, although faint, do not show any deceleration anomaly. For such meteors the light-curves are also regular, in agreement with theory.

Other peculiarities are occasionally observed in faint meteors:

a) While the initial part of the light-curve is normally very smooth in bright meteors, small and sometimes not so small irregularities are often present in fainter meteors. Major flares are noticeably absent in faint meteors.

b) In a number of cases the meteor appears quite suddenly, increasing in brightness by a couple of magnitudes in less than 0.1 second, and then goes over to a slower rise to a maximum. In a few exceptional meteors maximum light is reached almost at once, during the first twentieth of the trajectory, and is followed by a relatively steady decline. Nothing of the sort is ever observed among brighter meteors.

c) The exposed segments of the meteor trail (the rotating shutters cut off the meteor three-fourths of the time) often become progressively elongated and fuzzy until, near the end of the trajectory, they nearly fuse together in an almost continuous trail ("terminal blending"). In some cases the transition is gradual, in others more abrupt; the latter case is always accompanied by a sudden drop in velocity. A few bright meteors also show a trace of terminal blending at the very end of their trails, but in faint meteors the phenomenon is more frequent and involves a greater portion of the trajectory.

II. FRAGMENTATION THEORY

All the phenomena we have described can be explained by progressive fragmentation. The average meteor may be visualized as having a very porous and fragile structure, as might be expected on the basis of Whipple's icy-comet model (1950, 1951). Fragments can be detached from the surface of larger meteor bodies without destroying their unity; but if fragments of similar size are detached from small bodies, this may mean their complete disruption into a cluster of fragments. Larger meteors, then, will disintegrate only toward the end of their trajectories, while among fainter meteors the breakup may occur at earlier stages, even at the very beginning of the visible trail.

What we obtain by integrating the brightness of a faint meteor is not the mass of a single body but a function of the total mass of all the fragments. The observed meteor deceleration, on the other hand, is the average deceleration of the brighter fragments and therefore larger than the deceleration of a single, unfragmented body. Irregularities in the fragmentation process easily explain points *a* and *b*, while differential deceleration among fragments of unequal sizes accounts for point *c*. The presence of a few non-fragmenting (or less-fragmenting) bodies must be expected if we assume irregular structure within the original meteor bodies and different structure, or even composition, for meteors born from different comets with a great variety of orbital characteristics, especially "age," size, and perihelion distance.

That fragmentation occurs in meteors has been recognized for a long time, since split meteor trails have been recognized with a certain frequency. The writer's conclusion (1949*a*) that flares in meteors arise from quick losses of material certainly pointed in that direction, although flares probably represent a more violent type of fragmentation than the progressive crumbling postulated in this paper. According to a recent study by Henry J. Smith (1954), the masses of the individual fragments which contribute to the light of a flare must be of the order of 10^{-3}–10^{-4} times the mass lost by the meteors in the flare process, and therefore 10^{-4}–10^{-5} times the mass of the original meteor. That meteors are bodies of low density (0.2–1.0 gm/cm^3), probably porous and fragile, had been inferred by F. L. Whipple (1952) from the comparison of photographic meteor results with experimental data on high-speed pellets obtained at Inyokern. The present paper simply suggests that fragmentation is not a sporadic phenomenon, but rather the rule, and that for faint meteors the classical concept of a single-body meteor must be replaced with that of a cluster of breaking fragments.

III. QUANTITATIVE ANALYSIS

As a result of geometric reductions, the measured positions of trail segments yield a series of observed distances D on the meteor trajectory in function of time t. The velocity v and the acceleration dv/dt are obtained for the center of a trail portion by fitting to the observed D's an equation of the form

$$D = a + bt + c\,e^{kt}\,, \tag{1}$$

where the coefficients a, b, and c are determined by least squares; the constant k is computed in advance from four points, equidistant in time, on a graph.

Atmospheric densities, ρ, are computed from the drag equation,

$$\frac{dv}{dt} = -\Gamma A\,\delta^{-2/3} m^{-1/3} \rho\, v^2\,, \tag{2}$$

in which the mass m is obtained by integration from the luminosity equation,

$$\frac{dm}{dt} = -\frac{2}{\tau_0}\frac{I}{v^3}\,dt\,. \tag{3}$$

Here Γ is the drag coefficient, A the shape factor, and δ the density of the meteor body; a single constant $\Gamma A \delta^{-2/3} = 1$ is used in all the reductions. In the luminosity equation, τ_0 is the luminous efficiency coefficient; when the photographic intensity I of the meteor is expressed in units of a zero-magnitude star and v in cm/sec, $2/\tau_0$ is assumed to be equal to 3.1×10^{18}.

Let the atmospheric density as determined from equation (1) be ρ_{obs} and the Rocket Panel density for the same height H be ρ_T and let us write $\Delta \log \rho = \log \rho_{\text{obs}} - \log \rho_T$. A preliminary analysis had shown that $d/dH(\Delta \log \rho)$, as determined from multiple-deceleration meteors, was statistically correlated with the magnitude reached at maximum by the meteor. A better correlation was found when the integrated meteor brightness was used instead of the maximum magnitude, which is often affected by irregularities in the light-curve. As a consequence, the parameter

$$\epsilon = \log\left(m_\infty v_\infty^3\right) \approx \log\left(\frac{2}{\tau_0}\int_{-\infty}^{\infty} I\,dt\right),$$

was used to divide meteors into different classes of brightness; m_∞ stands for the initial mass and v_∞ for the initial velocity of the meteor outside the atmosphere. It was found, moreover, that the correlation improved if the derivative d/dD of $\Delta \log \rho$ was used instead of d/dH (a logical consequence of fragmentation) and that an even greater improvement was obtained if the derivative was taken with respect to a parameter $s = \log_{10}([m_\infty/m] - 1)$, which measures the amount of mass lost by ablation (see Fig. 1). The quantity $\chi = d/ds(\Delta \log \rho)$ thus emerged as a good measure of the deceleration anomaly. Table 1 gives the coefficient of correlation r between χ and $\log(mv^n)$ for $n = 0, 1, 2, \ldots, 6$ and shows that the choice of the third power of v in ϵ—prompted only for reasons of simplicity—was a good choice. The relative insensitivity of r to n indicates, however, that the choice of any other low power of v would not substantially alter the present results.

Although only multiple-deceleration meteors give reliable values of χ, some indication of its order of magnitude can be derived from the determination of k in equation (1). It is easy to see that $k = (d^2v/dt^2)/(dv/dt)$. Differentiating equation (2) logarithmically, we obtain, after substitution,

$$\chi = \frac{1 - (m/m_\infty)}{-\dot{m}/m}\left[k + \frac{1}{3}\frac{\dot{m}}{m} - 2\frac{\dot{v}}{v} + (\ln 10)\frac{d\log_{10}\rho_T}{dH}\,v\cos Z_R\right]. \tag{4}$$

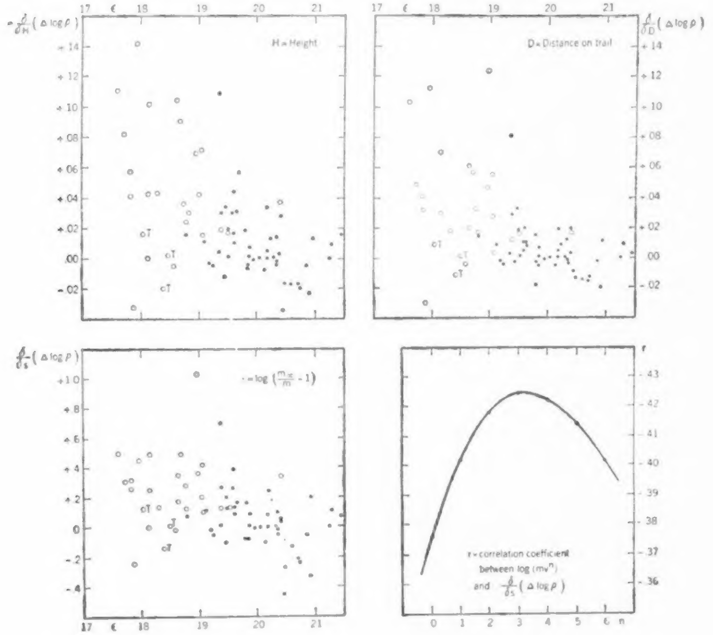

FIG. 1.—Data from multiple-deceleration meteors. The rates of change in $\Delta\log\rho$ with H, D, and s are plotted against $\epsilon = \log_{10}(mv^3)$. Dots are small-camera meteors; open circles are Super-Schmidt meteors. The last diagram shows that the best correlation between $\delta/\delta s$ $(\Delta\log\rho)$ and $\log(mv^n)$ is achieved when $n = 3$.

TABLE 1

n	r	n	r
0	−0.366	4	−0.412
1	− .392	5	− .404
2	− .408	6	−0.392
3	−0.415		

Here $\dot m$ and $\dot v$ indicate *dm/dt* and *dv/dt*, respectively. According to equation (3),

$$\frac{\dot m}{m} = \frac{I}{v^3}\left(\int_t^\infty \frac{I}{v^3}\,dt\right)^{-1},$$

i.e., $\dot m/m$ can be obtained directly from photometric data.

In Figure 2, where $\Delta \log \rho$ is plotted against *s* for seven groups of ϵ, values of $\Delta \log \rho$ pertaining to the same meteor were connected with straight lines. For single-deceleration meteors, a short, straight line was drawn through each point, with slope equal to χ, as computed from equation (4). No attempt was made to derive χ for single-deceleration meteors photographed with small cameras and reduced in earlier years, because in most cases the small number of shutter breaks would have made such a computation meaningless; an empirical formula of the type suggested by Whipple (1938) was used instead.

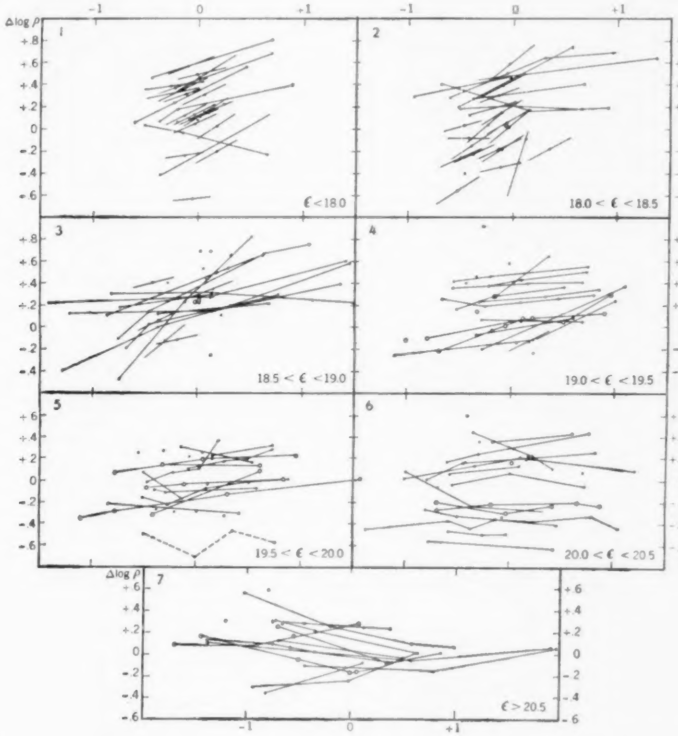

FIG. 2.—Trends in $\Delta \log \rho$ for seven groups of ϵ. Values of $\Delta \log \rho$ computed from different points on the same meteor trail are joined by straight lines. For single-deceleration meteors the slope was computed from equation (4). Geminids, for which a constant correction +0.20 in $\Delta \log \rho$ was applied to bring them in line with other meteors, are shown as open circles.

Mean values of χ obtained from all the available material for eight groups of ϵ are given in Table 2. In Figure 2 groups 7 and 8, which were sparsely populated, were condensed into a single diagram. Straight lines with slopes equal to χ from Table 2 were drawn through the scattered points of the individual group diagrams and are shown in Figure 3. The length of each segment represents the section covered by observations. An inspection of the diagram shows that both bright and faint meteors give similar atmospheric densities for $s < -0.6$, i.e., for points where the meteor has lost not more than 20 per cent of its original mass. As we proceed to later portions of the trail, the fainter meteors diverge more and more from the bright meteors. At $s = +1.0$, which corresponds to the center of the last section into which long meteor trails could be safely subdivided to obtain decelerations, meteors of group 1 show residuals $\Delta \log \rho$ averaging $+0.60$, compared to zero for brighter meteors.

TABLE 2

Group	ϵ	χ	Group	ϵ	χ
1.........	17.5	+0.35	5.........	19.75	+0.06
2.........	18.25	+ .32	6.........	20.25	.00
3.........	18.75	+ .24	7.........	20.75	− .03
4.........	19.25	+0.16	8.........	21.5	0.00

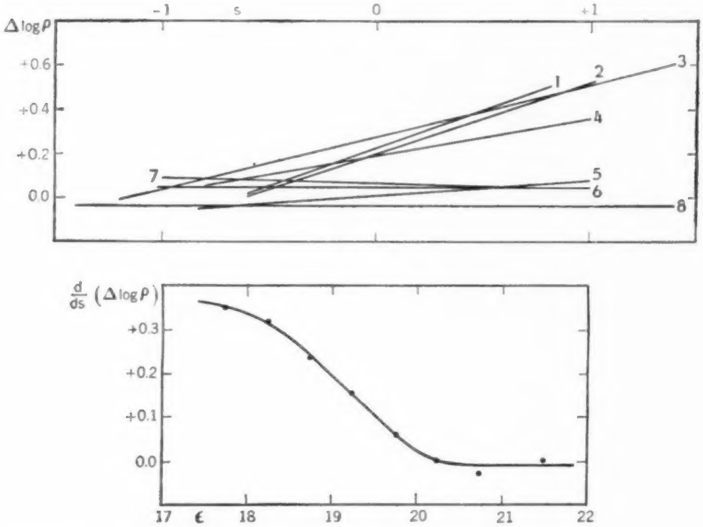

FIG. 3.—Schematic assembly of results from Fig. 2. In the upper diagrams are collected the best linear correlations between $\Delta \log \rho$ and s for eight groups of ϵ (groups 7 and 8 are fused together in Fig. 2 for graphic reasons). The slopes (χ) of these lines are plotted against ϵ in the lower diagram.

No sensible explanation can be found for such a large discrepancy if we try to consider the meteor as a single body. Only equations (2) and (3) were used to compute ρ, and the form of the drag equation (2) can be considered to be well established. We are then left with only two alternatives.

1. To accept equation (3) as correct. Then the product $\Gamma A\delta^{-2/3}$ must vary by a factor of at least 4 in the course of the trajectory of fainter meteors. We can exclude a

systematic variation of δ. On the other hand, we can think of no apparent cause for a similar variation in the drag coefficient Γ: any conceivable agent (such as Öpik's "reverse rocket action") would equally affect bright and faint meteors. This leaves us with the shape factor A, whose variation by a factor of 4 would require a systematic change in the body of faint meteors from a sphere to a thin disk with a cross-section eight times its thickness (and for some meteors ten to twenty times its thickness).

2. To reject equation (3) and determine the mass from the drag equation, taking ρ from the Rocket Panel atmosphere. If we still want to represent the mass with equation (3), we must assume that τ_0 varies in the course of the trajectory, and the variation required becomes enormous. A change in τ_0 by a factor of 10^3 is necessary for most faint meteors, and in some cases the factor reaches 10^6. It is hardly conceivable that τ_0 could change so drastically without a parallel change in the wave length of the emitted light—but such a probability is precluded by the observed color indices of fainter meteors, which are just about the same as for bright meteors.[1] In addition, for some meteors with large χ the "mass" determined in such a manner decreases faster in the first portion of the trail than at the end, where the atmospheric density is higher, in contradiction with known physical experience.

In conclusion, progressive fragmentation offers a simple explanation of all the anomalies observed in faint meteors without any obvious contradiction. Observational details about the individual meteors which formed the basis for the present investigation will be published in a forthcoming Technical Report of the Harvard Meteor Project.

REFERENCES

Jacchia, L. G. 1948, *Harvard Reprint Series II*, No. 30.
———. 1949*a*, *ibid.* No. 31.
———. 1949*b*, *ibid.*, No. 32.
———. 1952, *ibid.*, No. 44.
Rocket Panel. 1952, *Phys. Rev.*, **88**, 1027.
Smith, H. J. 1954, *Ap. J.*, **119**, 438.
Whipple, F. L., 1938, *Proc. Amer. Phil. Soc.*, **79**, 499–548.
———. 1950, *Ap. J.*, **111**, 375.
———. 1951, *ibid.*, **113**, 464.
———. 1952, *A.J.*, **58**, 28.

---

[1] The mean color index from 70 Super-Schmidt meteors which were also observed visually is -1.5. This compares with the previously obtained value of -1.8 for small-camera meteors.

SPIN-ORBIT PARAMETERS FOR THE p^2 CONFIGURATION, WITH SPECIAL REFERENCE TO THE YELLOW CORONAL LINE*

HAROLD ZIRIN
Harvard College Observatory

Received August 16, 1954; revised November 1, 1954

ABSTRACT

Parameters of variational wave functions for the $1s^2 2s^2 2p^2$ configuration with $Z = 6$–15 and 20 are given. These are used to calculate the spin-orbit parameter ζ, as well as the spin-spin parameter η, for this isoelectronic sequence. The theoretical values so obtained are found to agree closely with empirical values. The theoretical value of ζ for *Ca* XV is 24,900 cm^{-1}, close to Garstang's extrapolated value.

Despite several attempts to predict theoretically the spin-orbit energy in the p^2 isoelectronic sequence, the atomic wave functions hitherto available have not made this possible with any accuracy. It has been necessary instead, in cases where the spin-orbit splitting was not measurable experimentally, to extrapolate observed values for other atoms. Garstang (1951), for instance, finds poor agreement for values of ζ (the spin-orbit radial integral parameter) derived from Hartree wave functions compared with empirical values.

In the present work we have used the variational wave functions described by Morse, Young, and Haurwitz (1935) to obtain the spin-orbit energy. These wave functions are simple and hydrogenic in form. The trial functions for the minimization of the energy are as follows:

$$1s\colon u_1(r) = \left(\frac{\mu^3 a^3}{\pi}\right)^{1/2} e^{-\mu a r},$$

$$2s\colon u_2(r) = \left(\frac{\mu^5}{3\pi N}\right)^{1/2} \left[r\, e^{-\mu r} - \left(\frac{3A}{\mu}\right) e^{-\mu b r} \right];$$

$$2p\colon u_3(r) = \left(\frac{\mu^5 c^5}{\pi}\right)^{1/2} r \cos\vartheta \cdot e^{-\mu c r},$$

$$u_4(r) = \left(\frac{\mu^5 c^5}{2\pi}\right)^{1/2} r \sin\vartheta \cdot e^{i\varphi - \mu c r},$$

$$u_5(r) = \left(\frac{\mu^5 c^5}{2\pi}\right)^{1/2} r \sin\vartheta \cdot e^{-i\varphi - \mu c r}.$$

The parameters a, b, and c are to be determined by the minimization. The quantity μ is a scale factor, and N and A are normalization constants, all of which are determined from a, b, and c.

In the description of Morse, Young, and Haurwitz, the potential energy of the $1s^2 2s^2 2p^2$ configuration is given by

$$V = -2Z(V_1 + V_2 + V_3) + 4(V_{12} + V_{23} + V_{13}) + V_{11} + V_{22} + V_{34} - 2(X_{12} + X_{23} + X_{13}) - X_{34},$$

---

* The work reported herein was accomplished under the sponsorship of the Air Force Cambridge Research Center, Geophysics Research Directorate, through Contract AF19(604)-146 with Harvard University.

where the subscripts of the V's refer to the subscripts of the 1-electron wave functions $u_i(r)$. The X's participating in each integral are exchange integrals. The total kinetic energy T is the sum of that of all six electrons:

$$T = 2\,(T_1 + T_2 + T_3)\,.$$

The total energy $W(a, b, c)$ for each set of parameters is found from the relation

$$W = -\frac{V^2}{4T}\,.$$

The original table of V's, T's, and X's, calculated by Morse, Young, and Haurwitz, has recently been revised and expanded by Morse and Yilmaz (1954). These were kindly made available to me by the authors in punched-card form, and the energies $W(a, b, c)$ for a range of each parameter were obtained on the card-programmed electronic calculator at the Office of Statistical Services at the Massachusetts Institute of Technology. The energies were only printed out for $Z = 13$, 14, 15, and 20; but quantities for easy calculation of the energy for the other atoms of the isoelectronic sequence were also printed out. It remained only to minimize graphically $W(a, b, c)$ with respect to a, b, and c for each atom of the isoelectronic sequence. The parameters and energies for the $1s^2 2s^2 2p^2$ configuration are given in Table 1. Note that W is the total energy, referred to a completely stripped nucleus. The minimizations for $Z = 6$–9 had been carried out by Mr. Yilmaz. The wave function for neutral carbon is shown in Figure 1, compared with that obtained by Jucys (1939) from the Hartree-Fock method.

TABLE 1

VARIATIONAL PARAMETERS FOR THE p^2 ISOELECTRONIC SEQUENCE

Z	a	b	c	μ	$-W(a, b, c)$*
6	3.51	3.11	0.965	1.62	75.256
7	3.25	2.89	1.03	2.06	107.655
8	3.02	2.58	1.01	2.53	146.080
9	2.98	2.61	1.09	2.90	190.501
10	2.83	2.36	1.06	3.43	240.985
11	2.77	2.30	1.05	3.88	297.43
12	2.70	2.21	1.09	4.33	358.75
13	2.62	2.10	1.07	4.85	428.43
14	2.54	2.00	1.06	5.38	502.82
15	2.49	1.90	1.06	5.90	583.31
20	2.38	1.75	1.06	8.28	1077.22

* In atomic units; 1 a.u. = 13.54 ev.

With the wave functions in hand, the calculation of spin-orbit constants is relatively simple. The spin-orbit energy is (Condon and Shortley 1951)

$$H' = \frac{1}{2\mu^2 c^2}\left(\frac{1}{r}\,\frac{\partial U(r)}{\partial r}\right)\boldsymbol{L}\cdot\boldsymbol{S} = \xi(r)\,\boldsymbol{L}\cdot\boldsymbol{S} \tag{1}$$

and can be expressed in terms of the parameters ζ, given by

$$\zeta_{nl} = \left(\frac{h}{2\pi}\right)^2 \int_0^\infty R^2(nl)\,\xi(r)\,r^2 dr\,. \tag{2}$$

We shall concern ourselves with evaluation of ξ and ζ.

The potential $U(r)$ in equation (1) can be split into the contribution of the nucleus plus that of each of the 5 electrons acting on the 2p electron whose spin-orbit energy we compute. Since the density of i-type electrons at any point is given by $\rho_i(r, \vartheta, \varphi) = |u_i(r, \vartheta, \varphi)|^2$, the value of $\xi(r)$ due to this electron is

$$\begin{aligned}\xi_i(r) &= \frac{1}{2\mu^2 c^2}\frac{1}{r}\frac{\partial}{\partial r}\left[\frac{1}{r}\int_0^r\int_0^\pi\int_0^{2\pi} u_i^2(r', \vartheta, \varphi)\, r'^2 dr' \sin\vartheta d\vartheta d\varphi\right. \\ &\qquad\qquad + \int_r^\infty\int_0^\pi\int_0^{2\pi} u_i^2(r')\, r' dr' \sin\vartheta d\vartheta d\varphi \\ &= -\frac{1}{2\mu^2 c^2}\frac{1}{r^2}\int_0^r\int_0^\pi\int_0^{2\pi} u_i^2(r', \vartheta, \varphi)\, r'^2 dr' \sin\vartheta d\vartheta d\varphi .\end{aligned} \tag{3}$$

The total ξ is $\xi_{\text{nucleus}} + 2\xi_{1s} + 2\xi_{2s} + \xi_{2p}$, where, of course, the interelectronic ξ's will turn up with different sign from ξ_{nucleus}. All these quantities are easily evaluated by using the variational wave functions, with the parameters of Table 1. We then insert $\xi(r)$ in equation (2) and integrate, using, of course, u_3 for R_{nl}. The values of ζ thus obtained are set forth in Table 2, along with those obtained empirically by Garstang (1951).

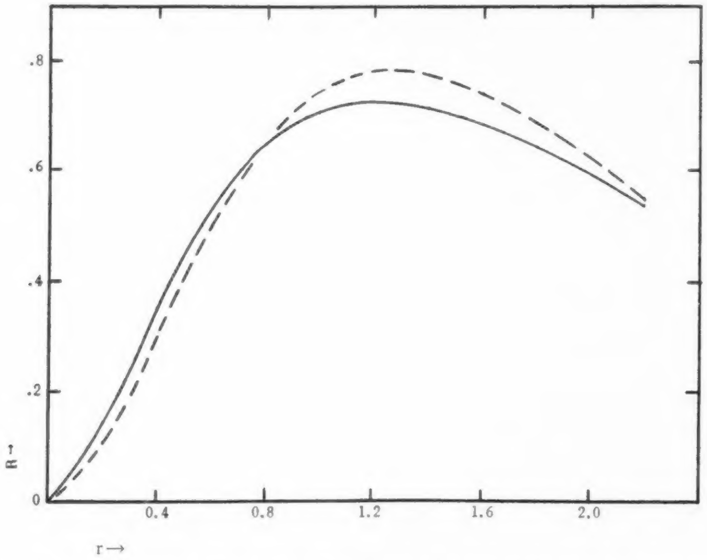

FIG. 1.—Variational (dashed curve) and Hartree-Fock (full line curve) wave functions for *C* I

The spin-spin parameter η is given by the integral

$$\eta = \frac{e^2 h^2}{16\pi^2 m^2 c^2}\int_0^\infty dr_2 \int_0^{r_2} dr_1 \int_0^\pi\int_0^{2\pi} r_2^{-3} u_3^2(r_2, \vartheta, \varphi)\, u_3^2(r_1, \vartheta, \varphi) \sin\vartheta d\vartheta d\varphi , \tag{4}$$

and the result of this integration is simplicity itself, namely,

$$\eta = \frac{e^2 h^2}{16\pi^2 m^2 c^2} \frac{7}{192} \mu^3 c^3 = 0.1084 \mu^3 c^3 \text{ cm}^{-1} . \tag{5}$$

The values of η are consequently listed in Table 2.

We see that the agreement between theoretical and empirical parameters is quite good. The theoretical values of ζ are, on the average, 2 or 3 per cent higher than the empirical. Compare this with the result of Garstang (1951), using Hartree wave functions. He obtains $\zeta = 42.8$ for *C* I and $\zeta = 268.7$ for *O* III. The only poor agreement is in the case of *P* X, which is the highest degree of ionization in this sequence for which measures are available. Because all the experimental measures for this ion are somewhat out of line with the rest of the isoelectronic sequence and the data are in the form of unpublished results, it seems not unreasonable to attach low weight to this disagreement.

TABLE 2

SPIN-ORBIT PARAMETERS ζ AND SPIN-SPIN PARAMETERS η FOR THE p^2 ISOELECTRONIC SEQUENCE

Z	ζ_{calc}	ζ_{emp}	η_{calc}	η_{emp}
6	30.9 cm^{-1}	32.6 cm^{-1}	0.41 cm^{-1}	0.38 cm^{-1}
7	97.4	97.0	1.02	1.01
8	212	222	1.78	1.90
9	459	436	3.43	3.06
10	803	789	5.25	5.6
11	1250	1300	7.32	8.3
12	2150	2060	11.31	12.9
13	3170	3080	15.2	18
14	4600	4440	19.6	24
15	6500	5700	26.9	13
20	24,900	24,210*	73.7	91*

* Extrapolated values of Garstang.

We are particularly interested in the result for *Ca* XV. Garstang (1952) obtains the empirical value 24,210 cm^{-1}, from which he further obtains a wave length of 5480 A for the transition $^3P_1 - {}^3P_0$. We obtain the theoretical value $\zeta = 24{,}895$ cm^{-1}, close to the extrapolated empirical quantity and corresponding to an even shorter wave length. However, if we allow for the fact that our theoretical spin-orbit parameters for $Z = 12$–15 are systematically higher than the empirical values, then it seems reasonable to accept Garstang's values as the likely ones. Layzer (1955) has calculated the energy levels of *Ca* XV taking into account explicitly the effects of configuration mixing. Using the value of ζ as chosen above, he finds predicted wave lengths of 5650 A and 5456 A for the $^3P_1 - {}^3P_0$ and $^3P_2 - {}^3P_1$ transitions, respectively. Since the value of ζ is now fairly well fixed by two independent methods, Layzer's analysis leads to the conclusion that we do indeed observe lines of *Ca* XV in the solar corona.

It should be noted that we do not directly predict the wave lengths theoretically or, more accurately, that the empirical values of ζ are not directly observed. It is necessary first to solve the secular equation for the p^2 configuration. This usually involves an expansion in terms of $\zeta/(S - P)$ or $\zeta/(D - P)$. It is not possible to predict theoretically the values of $(S - P)$ and $(D - P)$ to include the deviation from Slater's rule; it is instead necessary to use empirical values of the quantities and, in the case of *Ca* XV, to extrapolate these quantities. Thus it is not possible to predict the term splittings purely theoretically. On the other hand, errors in (S − P) and (P − D) affect only higher energies in the energy expansions and should therefore not produce serious errors in the predicted wave lengths.

It seems therefore quite feasible to predict the spin-orbit splitting for light atoms with rather good accuracy, using simple analytic variational wave functions and empirical intermultiplet separations. Using the theoretical spin-orbit parameters together with the Slater energies should give reasonably good estimates of the term intervals.

I should like to thank Professor P. M. Morse and Mr. Hussein Yilmaz for making available their unpublished calculations and for numerous discussions, and Dr. David Layzer for several stimulating conversations on this subject.

REFERENCES

Condon, E. U., and Shortley, G. H. 1951, *The Theory of Atomic Spectra* (Cambridge: At the University Press), p. 120.
Garstang, R. H. 1951, *M.N.*, **111,** 115.
———. 1952, *Ap. J.*, **115,** 569.
Jucys, A. 1939, *Proc. R. Soc. London, A*, **173,** 59.
Layzer, D. 1955 (unpublished.)
Morse, P. M., and Yilmaz, H. Unpublished.
Morse, P. M., Young, L. A., and Haurwitz, E. S. 1935, *Phys. Rev.*, **48,** 948.

INFLUENCE OF VIBRATION-ROTATION INTERACTION ON LINE INTENSITIES IN VIBRATION-ROTATION BANDS OF A ROTATING MORSE OSCILLATOR*

Robert Herman and Robert J. Rubin
Applied Physics Laboratory, The Johns Hopkins University, Silver Spring, Maryland

Received August 6, 1954

ABSTRACT

The effect of vibration-rotation interaction on line intensities in vibration-rotation bands of diatomic molecules is investigated for a diatomic molecule treated as a rotating Morse oscillator with fixed electronic angular momentum. The matrix element of the electric dipole moment is calculated for the transition $v, J, \lambda \rightarrow v', J', \lambda$, using Morse-Pekeris wave functions, where the electric dipole moment is written as a Taylor series expansion about the equilibrium internuclear separation. The matrix element of the nth-order term in the dipole-moment expansion can be simply derived from the matrix element of the zeroth-order term. The matrix elements of the first four terms are given explicitly. These results greatly extend those of the perturbed harmonic oscillator treatment of Herman and Wallis, since they apply to all v, v' to within the accuracy of the expansion of the rotational energy. The matrix elements obtained when $J \rightarrow 0$ and $\lambda \rightarrow 0$ generalize the results obtained by Heaps and Herzberg, since they include all the terms in the electric dipole-moment expansion.

I. INTRODUCTION

There has been a great deal of interest recently in studying the intensities of individual lines as well as integrated intensities of lines in vibration-rotation bands of diatomic molecules. This information is of importance in the spectroscopic determinations of population distributions, of rotational and vibrational temperatures, and in the fundamental study of line shape and width.

It was recognized quite early that the intensity of a vibration-rotation line of a diatomic molecule is influenced by vibration-rotation interaction (Kemble 1925). With the advent of quantum mechanics, Oppenheimer (1926) obtained the J-dependent correction factor to the intensity of a line in the fundamental band of a diatomic molecule treated as a harmonic oscillator consisting of point charges. Recently this problem was investigated by Herman and Wallis (1955) by means of a perturbation treatment for a more refined model consisting of an anharmonic oscillator whose electric dipole moment is represented by a power-series expansion about the equilibrium internuclear separation. It should be emphasized that a J-dependent correction for the 0–1 transition occurs for the rotating harmonic oscillator and that higher correction terms may be obtained which involve the influence of anharmonicity. The perturbation treatment was carried out specifically for the 0–1, 1–2, and 0–2 transitions, since this type of treatment fails for large transitions in v and for high-lying initial states. The results obtained for the molecules CO and HCl on the basis of this theory are in essential agreement with experiment. The theory permits a determination of the sign of the effective charge relative to that of the permanent electric moment.

It was felt that it was highly desirable to extend the work to describe line intensities for transitions between higher vibrational levels, since this is of particular importance in astrophysics and in the currently active domain of high-temperature phenomena in flames and other combustion processes. For example, an understanding of the details of the vibration-rotation spectrum of OH would be of great importance in studying night-sky phenomena and chemical kinetic processes. For these reasons an attempt was made to obtain a more general treatment of the vibrational matrix elements of a diatomic molecule described by a more general potential function. The results of this investigation for a rotating Morse oscillator with fixed electronic angular momentum which are applicable to all transitions to within the accuracy of the approximation in the treatment are presented here. It is hoped that these results will be of use to other investigators.

---

* A portion of this work was presented at the Symposium on Molecular Structure and Spectroscopy at Ohio State University, Columbus, Ohio, June 14–18, 1954. The work reported in this paper was supported by the Bureau of Ordnance, Department of the Navy, under Contract NOrd-7386.

II. THEORY

The problem of calculating the intensity of a line associated with the transition v, J, $\lambda \rightarrow v'$, J', λ in a vibration-rotation band of a diatomic molecule with a fixed electronic angular momentum λ requires the evaluation of the squares of the matrix elements:

$$\sum_{M,\,M'} \sum_{\tau} \left| \, [v, J, M, \lambda \,|\, M_\tau (r, \theta, \phi) \,|\, v', J', M', \lambda] \, \right|^2 , \tag{1}$$

where v, J, and M are the vibrational, rotational, and magnetic quantum numbers, respectively, and M_τ is the τth Cartesian component of the electric dipole moment $M(r, \theta, \phi)$. The Schrödinger equation for the diatomic molecule is separable, so that this expression can be written as (Hönl and London 1925; Dennison 1926; Reiche and Rademacher 1927; Crawford and Dinsmore 1950; Herzberg 1950)

$$\begin{aligned} \left| \, [v, J, \lambda \,|\, M(r) \,|\, v', J', \lambda] \, \right|^2 \sum_{M,\,M'} \sum_{\tau} \left| \, [J, M, \lambda \,|\, f_\tau (\theta, \phi) \,|\, J', M', \lambda] \, \right|^2 \\ = \left| \, \mathfrak{M}_{v,J,\lambda}^{v',J',\lambda} \right|^2 S_{J,\lambda}^{J',\lambda} , \end{aligned} \tag{2}$$

where the vibrational matrix element is

$$\mathfrak{M}_{v,J,\lambda}^{v',J',\lambda} = [v, J, \lambda \,|\, M(r) \,|\, v', J'\lambda] , \tag{2a}$$

with

$$M(r) = \sum_{i=0} M_i (r - r_e)^i , \tag{2b}$$

$$\begin{aligned} S_{J,\lambda}^{J',\lambda} = \frac{\lambda^2 (2J+1)}{J(J+1)} \delta_{J',J} + \frac{(J+\lambda)(J-\lambda)}{J} \delta_{J',J-1} \\ + \frac{(J+1+\lambda)(J+1-\lambda)}{(J+1)} \delta_{J',J+1} \end{aligned} \tag{2c}$$

and $\delta_{i,j}$ is the Kronecker delta. For the cases $\Delta\lambda = \pm 1$, the quantity $S_{J,\lambda}^{J',\lambda'}$ is given in the references cited earlier.

In the present paper the vibrational matrix elements are determined for a diatomic molecule treated as a Morse oscillator with both J and λ different from zero. If the complete wave function is written as

$$\Phi (x, r) \left[\frac{R(r)}{r} \right] \Theta (\theta, \phi) ,$$

where x represents all the electronic co-ordinates, then the radial wave equation obtained by the separation of variables in Schrödinger's equation is (Pekeris 1934)

$$\frac{d^2 R}{d r^2} - [J(J+1) - \lambda^2] \frac{R}{r^2} + \frac{8\pi^2 \mu}{h^2} [E - U(r)] R = 0 , \tag{3}$$

where

$$U(r) = E_{el} + D_e\,[1 - e^{-\beta(r-r_e)}]^2\,. \tag{3a}$$

In equation (*3a*), E_{el} is the electronic energy at $r = r_e$ and D_e and β are the Morse potential constants. Following Morse (1929) and Pekeris (1934), we let

$$W = E - E_{el} - D_e\,, \tag{4a}$$

$$y = e^{-\beta(r-r_e)}\,, \tag{4b}$$

$$A = B_e\,[J\,(J+1) - \lambda^2]\,, \tag{4c}$$

where

$$B_e = \frac{h^2}{8\pi^2\mu r_e^2}\,, \tag{4d}$$

and expand $(r_e/r)^2$, letting $\epsilon = (r_e\beta)^{-1}$, as follows:

$$\begin{aligned}\left(\frac{r_e}{r}\right)^2 &= [1 - \ln(\epsilon y)]^{-2}\\ &= 1 + 2\epsilon\,(y-1) + (-\epsilon + 3\epsilon^2)\,(y-1)^2\\ &\quad + \left(\frac{2\epsilon}{3} - 3\epsilon^2 + 4\epsilon^3\right)(y-1)^3 + \ldots\,.\end{aligned} \tag{4e}$$

Using equations (*4a–4d*) and the first three terms of equation (*4e*) in equation (3) and assuming that

$$R\,(y) = N\,e^{-z/2}z^{b/2}F\,(z)\,, \tag{5a}$$

where

$$z = 2d_0 y\,, \tag{5b}$$

$$d_0^2 = \left[\frac{8\pi^2\mu}{\beta^2h^2}\right][D_e + A\,(-\epsilon + 3\epsilon^2)]\,, \tag{5c}$$

and

$$b^2 = -\left[\frac{32\pi^2\mu}{\beta^2h^2}\right]\left[W - A\,(1 - 3\epsilon + 3\epsilon^2)\right]\,, \tag{5d}$$

one finds that $F(z)$ must satisfy the confluent hypergeometric equation,

$$z\,\frac{d^2F}{dz^2} + (b + 1 - z)\,\frac{dF}{dz} + vF = 0\,, \tag{6}$$

where the quantity v, identified with the vibrational quantum number, is an integer and is related to the other parameters by

$$v = \left[\frac{4\pi^2\mu}{\beta^2h^2d_0}\right][2\,D_e - A\,(4\epsilon - 6\epsilon^2)] - \frac{b+1}{2}\,. \tag{6a}$$

The normalized radial wave function $R(r)$ for the state v, J, λ is given by[1]

$$R_{v,J,\lambda}(r) = N_0\,e^{-d_0y}\,(2d_0y)^{b/2}\,{}_1F_1\,(-v;\; b+1;\; 2d_0y)\,, \tag{7}$$

---

[1] It should be noted that we have taken the limits of integration on r to be $-\infty$ to $+\infty$ instead of 0 to $+\infty$. The error involved in this approximation is small, as discussed in D. ter Haar, *Phys. Rev.*, **70,** 222, 1946.

where the normalization factor is

$$N_0 = \beta^{1/2}\left[\Gamma(b)\binom{v+b}{v}\right]^{-1/2}. \tag{7a}$$

The function F in equation (6) is designated by ${}_1F_1(-v; b+1; 2d_0y)$, the standard symbol for the confluent hypergeometric function, whose representation is

$${}_1F_1(-v;\ b+1;\ 2d_0y) = \frac{1}{2\pi i}\int_C e^{-2d_0yt}t^{-(1+v)}(1+t)^{v+b}dt, \tag{7b}$$

where the closed contour C is a counterclockwise path which includes the origin and excludes the point $t = -1$.

The vibrational matrix element for the transition $v, J, \lambda \rightarrow v', J', \lambda$ is given by

$$\mathfrak{M}^{v', J', \lambda}_{v, J, \lambda} = \frac{N_0N_0'}{\beta}\int_0^\infty y^{-1}R_{v,J,\lambda}(y)R_{v',J',\lambda}(y)\sum_{i=0} M_i(-\beta^{-1}\ln y)^i dy. \tag{8}$$

In equation (8) and in what follows, primes are employed to designate the final state. Using equations (7) and (7*b*), equation (8) becomes

$$\mathfrak{M}^{v', J', \lambda}_{v, J, \lambda} = \frac{N_0N_0'}{\beta}(2d_0)^{b/2}(2d_0')^{b'/2}\int_C\int_C\frac{(1+t)^{v+b}}{2\pi i t^{1+v}}\frac{(1+s)^{v'+b'}}{2\pi i s^{1+v'}}$$
$$\times\int_0^\infty \exp[-y(d_0+d_0'+2d_0t+2d_0's)]\,y^{(b+b'-2)/2}\sum_{i=0} M_i(-\beta^{-1}\ln y)^i dy\,ds\,dt. \tag{9}$$

It should be noted that the coefficient C_i of $(-1)^iM_i\beta^{-i}$ in equation (9) can be obtained as follows:

$$C = \frac{\partial^i C_0}{\partial([b+b']/2)^i}. \tag{10}$$

For this reason the problem is now one of finding C_0. Performing the integration on y in equation (9), one obtains

$$C_0 = \frac{N_0N_0'}{\beta}(2d_0)^{b/2}(2d_0')^{b'/2}\Gamma\left(\frac{b+b'}{2}\right)$$
$$\times\int_C\int_C\frac{(1+t)^{v+b}}{2\pi i t^{1+v}}\frac{(1+s)^{v'+b'}}{2\pi i s^{1+v'}}(d_0+d_0'+2d_0t+2d_0's)^{-(b+b')/2}d\,s\,dt. \tag{11}$$

The value of the contour integral in t is given by the residue of

$$(1+t)^{v+b}t^{-v}(d_0+d_0'+2d_0t+2d_0's)^{-(b+b')/2}$$

at $t = 0$. One is led to

$$C_0 = \frac{N_0N_0'}{\beta}(2d_0)^{b/2}(2d_0')^{b'/2}\Gamma\left(\frac{b+b'}{2}\right)\sum_{i=0}^{v}\binom{-\frac{b+b'}{2}}{i}\binom{v+b}{v-i}(2d)^i$$
$$\times\int_C\frac{(1+s)^{v'+b'}}{2\pi i s^{1+v'}}(d_0+d_0'+2d_0's)^{-[(b+b')/2]-i}d\,s, \tag{12}$$

where

$$\binom{m}{n} = \frac{\Gamma(m+1)}{\Gamma(m-n+1)\Gamma(n+1)}.$$

Upon repeating this procedure for the contour integral in s, one obtains

$$C_0 = \frac{N_0 N_0'}{\beta} \frac{(2d_0)^{b/2} (2d_0')^{b'/2}}{(d_0 + d_0')^{(b+b')/2}} \times \sum_{i=0}^{v} \sum_{j=0}^{v'} \binom{v+b}{v-i} \binom{v'+b'}{v'-j} \binom{-\frac{b+b'}{2}}{i} \binom{-\frac{b+b'}{2} - i}{j} \frac{(2d_0)^i (2d_0')^j}{(d_0 + d_0')^{i+j}} . \tag{13}$$

Remembering that $\Gamma(x)\Gamma(1-x) = \pi/\sin \pi x$, the following group of factors in equation (13) can be written as

$$\Gamma\left(\frac{b+b'}{2}\right) \binom{-\frac{b+b'}{2}}{i} \binom{-\frac{b+b'}{2} - i}{j}$$

$$= \Gamma\left(\frac{b+b'}{2}\right) \frac{\Gamma[1 - \frac{1}{2}(b+b')]}{i!\Gamma[1 - \frac{1}{2}(b+b') - i]} \frac{\Gamma[1 - \frac{1}{2}(b+b') - i]}{j!\Gamma[-\frac{1}{2}(b+b') - j - i + 1]}$$

$$= \frac{\pi}{\sin \pi [(b+b')/2]} \frac{1}{i!j!} \frac{\Gamma[\frac{1}{2}(b+b') + i + j] \sin \pi [\frac{1}{2}(b+b') + i + j]}{\pi} ,$$

and, finally,

$$= (-1)^{i+j} \frac{\Gamma[\frac{1}{2}(b+b') + i + j]}{i!j!} . \tag{13a}$$

Inserting equation (13*a*) in equation (13), we have

$$C_0 = \left[\Gamma(b)\Gamma(b')\binom{v+b}{v}\binom{v'+b'}{v'}\right]^{-1/2} \frac{(2d_0)^{b/2}(2d_0')^{b'/2}}{(d_0 + d_0')^{(b+b')/2}} \times \sum_{i=0}^{v} \sum_{j=0}^{v'} (-1)^{i+j} \binom{v+b}{v-i} \binom{v'+b'}{v'-j} \frac{\Gamma[\frac{1}{2}(b+b') + i + j]}{i!j!} \frac{(2d_0)^i (2d_0')^i}{(d_0 + d_0)^{i+j}} . \tag{14}$$

The coefficients C_1, C_2, and C_3 obtained from equation (10) are given below:

$$C_1 = q_0 \sum_{i=0}^{v} \sum_{j=0}^{v'} Q_{ij} [\psi(\xi_{ij}) - \ln(d_0 + d_0')] , \tag{15a}$$

$$C_2 = q_0 \sum_{i=0}^{v} \sum_{j=0}^{v'} Q_{ij} \left[\ln^2(d_0 + d_0') - 2 \ln(d_0 + d_0')\psi(\xi_{ij}) + \left.\frac{d\psi}{dx}\right|_{x=\xi_{ij}} + \psi^2(\xi_{ij}) \right] , \tag{15b}$$

and

$$\begin{aligned} C_3 = q_0 \sum_{i=0}^{v} \sum_{j=0}^{v'} Q_{ij} \Big\{ & - \ln^3(d_0 + d_0') + 3 \ln^2(d_0 + d_0')\psi(\xi_{ij}) \\ & - 3 \ln(d_0 + d_0') \left[\left.\frac{d\psi}{dx}\right|_{x=\xi_{ij}} + \psi^2(\xi_{ij}) \right] + \left.\frac{d^2\psi}{dx^2}\right|_{x=\xi_{ij}} \\ & + 2 \left[\left.\frac{d\psi}{dx}\right|_{x=\xi_{ij}} \right]^2 + \psi(\xi_{ij}) \left.\frac{d\psi}{dx}\right|_{x=\xi_{ij}} + \psi^3(\xi_{ij}) \Big\} , \end{aligned} \tag{15c}$$

where

$$q_0 = \left[\Gamma(b)\,\Gamma(b')\binom{v+b}{v}\binom{v'+b'}{v'}\right]^{-1/2} \frac{(2d_0)^{b/2}\,(2d_0')^{b'/2}}{(d_0+d_0)^{(b+b')/2}}, \tag{15d}$$

$$Q_{ij} = (-1)^{i+j}\binom{v+b}{v-i}\binom{v'+b'}{v'-j}\frac{\Gamma[\frac{1}{2}(b+b')+i+j]}{i!\,j!}\,\frac{(2d_0)^{i}\,(2d_0')^{j}}{(d_0+d_0')^{i+j}}, \tag{15e}$$

and

$$\xi_{ij} = \tfrac{1}{2}(b+b') + i + j\,.$$

The function $\psi(x)$, which is the logarithmic derivate of the Γ-function (Whittaker and Watson 1952) or psi function, namely,

$$\psi(x) = \frac{1}{\Gamma(x)}\,\frac{d\Gamma(x)}{dx}, \tag{16}$$

is given in series form as[2]

$$\psi(x) = -C + \sum_{n=0}^{\infty}\left(\frac{1}{n+1} - \frac{1}{x+n}\right), \tag{16a}$$

where C is Euler's constant. The ith derivative of $\psi(x)$ is

$$\frac{d^i\psi(x)}{dx^i} = i!\sum_{n=1}^{\infty}(-1)^{i+1}(x+n)^{-i-1}. \tag{16b}$$

The final expression for the vibrational matrix element can be written as follows:

$$\mathfrak{M}_{v,J,\lambda}^{v',J',\lambda} = \sum_{i=0}(-1)^{i}\beta^{-i}C_iM_i\,, \tag{17}$$

where the C_i have been given in equation (15) and the M_i are the coefficients in the expansion for the electric dipole moment given in equation (2*b*). The intensity of the absorption line corresponding to the transition $v, J, \lambda \rightarrow v', J', \lambda$ is given, according to the foregoing treatment, by

$$I_{v,J,\lambda}^{v',J',\lambda} = \frac{8\pi^3 N_{v,J,\lambda}}{3hc(2J+1)}\,\omega_{v,J,\lambda}^{v',J',\lambda}\,S_{J,\lambda}^{J',\lambda}\,|\mathfrak{M}_{v,J,\lambda}^{v',J',\lambda}|^2, \tag{18}$$

where $N_{v,J,\lambda}$ is the number of molecules in the initial state and $\omega_{v,J',\lambda}^{v',J',\lambda}$ is the frequency for the transition in wave numbers.

III. DISCUSSION

The problem of determining the vibrational transition probabilities of a diatomic molecule using Morse wave functions, neglecting rotation, has been treated by several

---

[2] The representation of $\psi(x)$ most suitable for computation for the range of $x \sim 50$ which is encountered is

$$\psi(x) \sim \tfrac{1}{2}\ln x(x+1) + \frac{1}{6}\left(\frac{1}{x} - \frac{1}{x+1}\right) - \dots .$$

The following relation is also useful to note, namely,

$$\psi(x+n) = \psi(x) + \frac{1}{x} + \frac{1}{x+1} + \dots + \frac{1}{x+n-1}.$$

investigators (Scholz 1932; Rosenthal 1935; Infeld and Hull 1951; Heaps and Herzberg 1952). Most recently Heaps and Herzberg (1952) obtained expressions for $[v|(r - r_e)|v']$ and $[v|(r - r_e)^2|v']$. It should be noted that our results for $\mathfrak{M}_{v,J,\lambda}^{v',J',\lambda}$ yield the results of Heaps and Herzberg if one allows $J \rightarrow 0$ and $\lambda \rightarrow 0$. Furthermore, the matrix elements of all powers of $(r - r_e)$ can be obtained, if desired, by this procedure from the coefficients C_i.

The expressions for the matrix elements $\mathfrak{M}$ for the transition $v, J, \lambda \rightarrow v', J', \lambda$ given in equation (17) by using equation (15), are not in a form which readily displays the dependence on the physical parameters and quantum numbers. For this reason we have obtained an approximate form for the fundamental transition 0–1 by expanding the appropriate coefficients C_0 and C_1, assuming that the rotational corrections to the parameters d_0 and b are small. The result, given in the form of the vibrational matrix element for $J = 0$ and $\lambda = 0$ multiplied by the F-factor taken up through the leading correction, is as follows:

$$|\mathfrak{M}_{0,J,\lambda}^{1,J',\lambda}|^2 = \frac{M_1^2}{2a} \frac{(1 - 3x_e)}{(1 - 2x_e)^2} F_{0-1}, \tag{19}$$

where

$$a = \frac{4\pi^2 \mu c \omega_e}{h}.$$

The F-factor is given by

$$F_{0-1} \cong 1 - 4 a_0 \gamma \theta m + \ldots, \tag{19a}$$

with

$$\gamma = \frac{2B_e}{\omega_e}, \qquad \theta = \frac{M_0}{M_1 r_e}, \qquad a_0 = 3\left(1 - \frac{1}{\beta r_e}\right), \tag{19b}$$

and

$$m = \begin{cases} J + 1, & R\text{-branch}, \\ -J, & P\text{-branch}, \\ 0, & Q\text{-branch}. \end{cases} \tag{19c}$$

This result is similar in form to that obtained by Herman and Wallis (1955) for the perturbed harmonic oscillator, which is

$$|\mathfrak{M}_{0,J}^{1,J'}|^2 \cong \frac{M_1^2}{2a}(1 - 4\gamma\theta m + \ldots), \tag{20}$$

where the parameters are defined above. The parameter a_0 in equation (19a) for most molecules is slightly larger than unity ($1 \gtrsim a_0 \gtrsim 2$). The full influence of this difference on the intensity depends on the evaluation of the complete expression in equation (17).

It should be recalled that the wave functions given in equation (7) are not exact, in that they involve the expansion of the rotational energy term. The expansion of $(r_e/r)^2$ in equation (4e) up to and including the term in $(y - 1)^2$ was used to solve the radial wave equation. This approximation is best for small J and not too large vibrational quantum number v, since the complete contributions of $(r - r_e)^p$ for $p > 2$ in the expansion in equation (4e) are not taken into account. The accuracy of the results given for the vibrational matrix elements could perhaps be examined for a molecule such as CO. Goldberg and Müller (1953) have determined line intensities in vibration-rotation bands of CO in the solar limb for transitions between high-lying states. Another test would involve the use of higher terms in the expansion in equation (4d) in a perturbation calculation to improve the wave functions if experimental data were sufficiently accurate.

REFERENCES

Crawford, B. L., and Dinsmore, H. L. 1950, *J. Chem. Phys.*, **18**, 983.
Dennison, D. M. 1926, *Phys. Rev.*, **28**, 318.
Goldberg, L., and Müller, E. A. 1953, *Ap. J.*, **118**, 397.
Heaps, H. S., and Herzberg, G. 1952, *Zs. f. Phys.*, **133**, 48.
Herman, R. C., and Wallis, R. F. 1955, *J. Chem. Phys.* (in press).
Herzberg, G. 1950, *Spectra of Diatomic Molecules* (New York: D. Van Nostrand Co., Inc.).
Hönl, H., and London, F. 1925, *Zs. f. Phys.*, **33**, 803.
Infeld, L., and Hull, T. E. 1951, *Rev. Mod. Phys.*, **23**, 21.
Kemble, E. C. 1925, *Hhys. Rev.*, **25**, 1.
Morse, P. M. 1929, *Phys. Rev.*, **34**, 57.
Oppenheimer, J. R. 1926, *Proc. Cambridge Phil. Soc.*, **23**, 327.
Pekeris, C. L. 1934, *Phys. Rev.*, **45**, 98.
Reiche, F., and Rademacher, H. 1927, *Zs. f. Phys.*, **41**, 453.
Rosenthal, J. E. 1935, *Proc. Nat. Acad. Washington*, **21**, 281.
Scholz, K. 1932, *Zs. f. Phys.*, **78**, 751.
Whittaker, E. T., and Watson, G. N. 1952, *Modern Analysis* (Cambridge: At the University Press).

THE *OH* BANDS IN THE INFRARED AIRGLOW*

Joseph W. Chamberlain and Frederick L. Roesler
Yerkes Observatory

Received August 31, 1954

ABSTRACT

A series of infrared airglow spectra have been made at 70 A/mm, in order to obtain accurate wave lengths of the high-excitation ($v' = 8$ and 9) Meinel *OH* bands. Band origins have been measured with a very small probable error, and the agreement between the airglow 6–2 and 5–1 bands with earlier high-dispersion measurements in the laboratory indicates that there are no appreciable systematic errors such as plagued previous airglow measurements. In order to represent accurately all energy levels up to $v = 9$, it is necessary to use five terms in the usual power series involving ω_e, $\omega_e x_e$, etc. These vibrational levels are discussed, and a possible blending of airglow lines with [*O* II] in the infrared auroral spectrum is pointed out.

INTRODUCTION

Since the identification of the Meinel (rotation-vibration) bands of *OH* in the infrared spectrum of the airglow (Meinel 1950*a*), there has been considerable uncertainty in the wave lengths of the lines and consequently in the vibrational constants for the molecule. Although his absolute wave lengths were quite uncertain, Meinel (1950*b*) pointed out that even his more accurate relative wave lengths for neighboring bands did not agree with the predicted values as well as one might expect. At that time, values of the vibrational constants ω_e and $\omega_e x_e$ had been determined from studies of the ultraviolet electronic bands (Dieke and Crosswhite 1948; cf. Herzberg 1950, Table 39), but Meinel emphasized that several higher-order terms (cf. eq. [1]) would be required to represent adequately the levels up to $v = 9$.

So far, 12 bands have been identified between 5500 and 9000 A, and additional bands have been found in the photoelectric infrared (e.g., Jones and Gush 1953). The wave lengths of most of these bands have remained uncertain, however, because of the low dispersion and resolution required in working with the faint airglow.

The production of the Meinel bands in oxyacetylene flames has enabled the 6–2, 5–1, and 4–0 bands to be studied under high resolution (Herman and Hornbeck 1953; Déjardin, Janin, and Peyron 1953). However, even four vibrational constants (ω_e, $\omega_e x_e$, $\omega_e y_e$, and $\omega_e z_e$), as determined from these accurate infrared measurements combined with the ultraviolet data of Dieke and Crosswhite (1948), led to predicted wave lengths of the bands with $v' = 8$ and 9 that were considerably different from those observed in the airglow (Chamberlain and Oliver 1953). On the other hand, the airglow wave lengths were not sufficiently precise to yield vibrational constants that were consistent with the laboratory data. Indeed, Déjardin, Janin, and Peyron (1953, Table 7) have drawn attention to the fact that there was a systematic difference of several angstroms between their laboratory wave lengths and the airglow wave lengths as measured by several observers.[1]

In view of these uncertainties in wave lengths and vibrational constants, we have attempted improved wave-length determinations on some of the stronger airglow bands.

---

* The research reported in this paper was supported in part by the Geophysics Research Directorate of the Air Force Cambridge Research Center, Air Research and Development Command, under Contract AF 19(122)-480.

[1] The systematic error in Meinel's measurements changes approximately linearly with wave length. His measurements are about +7 A too large at 7300 A and decrease to about +3 A at 8500 A. There seems to be no appreciable systematic difference between the measurements of Meinel and the later ones of Dufay and Dufay (1951) and Small and Petrie (1952).

Four well-exposed plates with *Ne* and/or *A* comparison spectra have been obtained in the region 7000–9000 A on hypersensitized Eastman I-N emulsion with exposures ranging up to 20 hours. The spectrograph utilizes a grating with 600 lines/mm and a 23-cm, *F*/0.8 camera. The resulting dispersion in the first-order infrared was 70 A/mm, and the slit width projected onto the plate was 36 μ ($=2.5$ A). A microphotometer tracing of the spectrum is shown in Figures 1 and 2.

ANALYSIS

In Table 1 are presented our measurements of the well-defined *P*-branch lines in the 8–3, 9–4, 5–1, and 6–2 bands. Other bands in this region (see Figs. 1 and 2) are the 4–0 and 7–3, which did not show enough strong *P* lines on our plates for an accurate determination of the band origins. The alternating intensities between the strong P_1 lines (originating from the lower, $^2\Pi_{3/2}$ state) and weak P_2 lines (upper, $^2\Pi_{1/2}$ state) are not observed in flame spectra and are probably a peculiarity of the airglow excitation mechanism. The rotational constants, B_v and D_v, and the spin-coupling constant, Y_v, given by Herman and Hornbeck (1953, Tables 8 and 9), have been adopted, along with the Hill and Van Vleck (1928) formula for spin doubling, to derive the band origins from the rotational lines.

In Table 2 are listed band origins, ν_0, as derived from the airglow bands and from laboratory measurements. It will be noticed that the origins of the 5–1 and 6–2 bands agree closely in the two sources; hence it seems probable that there is no appreciable systematic error in our wave lengths, as appeared in the earlier measurements. The probable errors in our values of ν_0 arise from the small differences in ν_0 as derived from one rotational line to the next, as well as from the variations in measurements from plate to plate.

Combining our data with the laboratory measurements of Dieke and Crosswhite (for the lowest vibrational levels) and of Herman and Hornbeck (for $v = 4$, 5, and 6), we obtain the energy levels, $G_0(v)$, listed in Table 3. We have used the laboratory measurements of Herman and Hornbeck rather than the slightly different ones of Déjardin, Janin, and Peyron (1953), since the former were made with somewhat better dispersion and resolution and agree slightly better with our airglow data for the 5–1 and 6–2 bands (cf. Table 2).[2]

With these adopted energy levels, we have derived, by the method of least squares. a set of four vibrational constants according to the formula

$$G(v) = \omega_e\left(v+\tfrac{1}{2}\right) - \omega_e x_e\left(v+\tfrac{1}{2}\right)^2 + \omega_e y_e\left(v+\tfrac{1}{2}\right)^3 - \omega_e z_e\left(v+\tfrac{1}{2}\right)^4 + \dots \quad (1)$$

Here $G(v)$ is the energy value (measured in cm^{-1}) of the vth vibrational level (for details, cf. Herzberg 1950). In Table 4 we compare the vibrational constants determined by several authors with our own (last column), and in Tables 2 and 3 we have listed the values of ν_0 and $G_0(v) \equiv G(v) - G(0)$, respectively, computed from the four-term constants derived in this paper.

The computed values of $G_0(v)$ in Table 3 are in fair agreement with the observed values. If we omit $v = 8$, with its larger probable error, the mean residual between observed and computed levels, averaged without regard to sign, is 0.14 cm^{-1}. The new constants (last column of Table 4) are all appreciably different from the earlier determinations. Herman and Hornbeck (1953) and Déjardin, Janin, and Peyron (1953) derived their constants to reproduce the levels up to $v = 6$, and their predicted $v = 9$ levels were in error by as much as 9 and 5 cm^{-1}, respectively (cf. Table 2).

[2] The differences in $G_0(v)$ obtained from the two sets of laboratory data are greater, however, than can be explained in terms of differences in measurements of the individual lines. A more important factor seems to be the rotational constant, B_v, used to derive ν_0 from the line measurements. Whereas Herman and Hornbeck derived B_v from their own data by a least-squares solution, Déjardin, Janin, and Peyron extrapolated the constants from Dieke and Crosswhite's (1948) ultraviolet data.

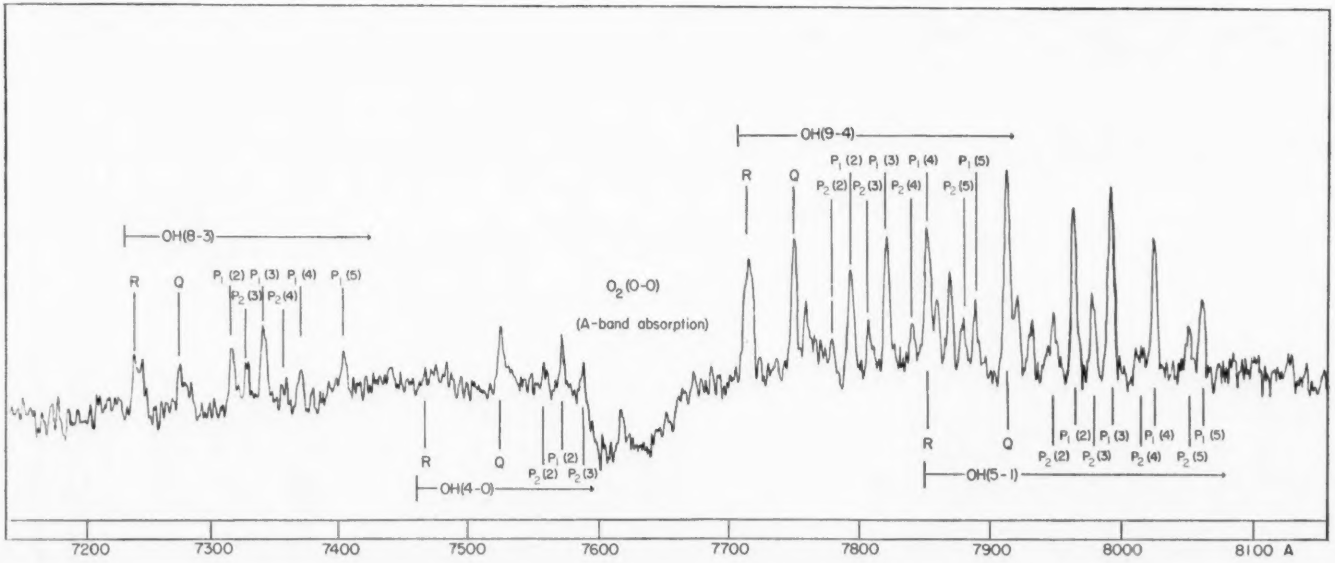

FIG. 1.—Microphotometer tracing of the infrared airglow spectrum, 7100–8150 A

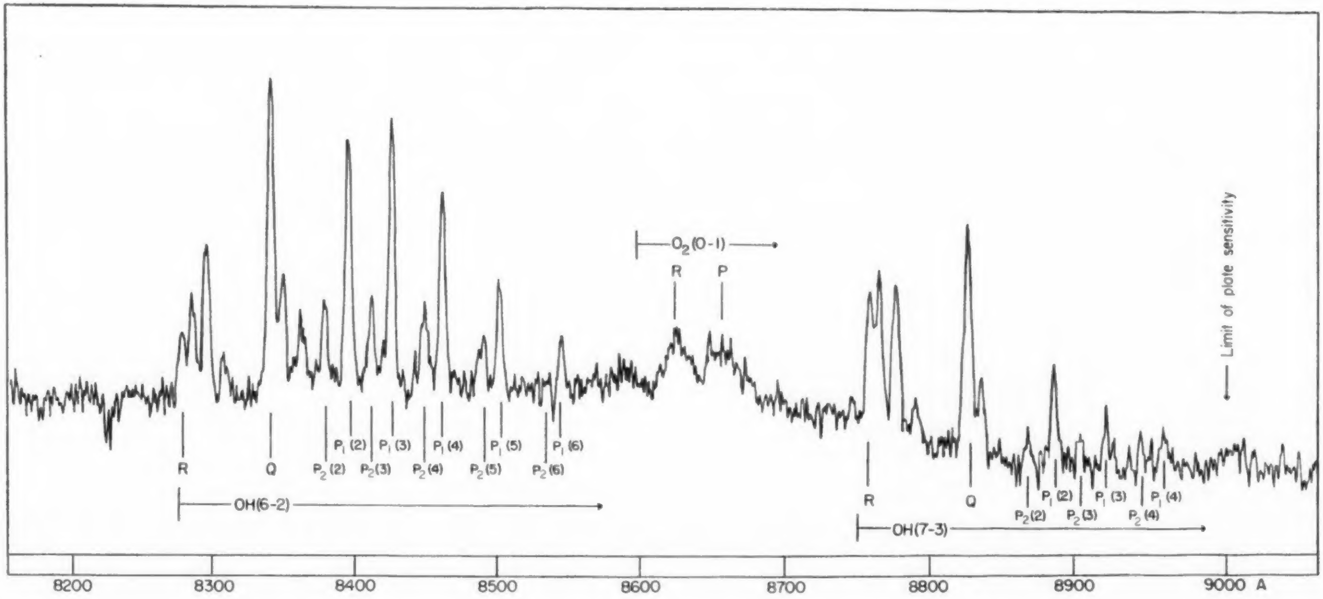

FIG. 2.—Microphotometer tracing of the infrared airglow spectrum, 8150–9000 A

TABLE 1

MEASUREMENTS OF STRONG *P*-BRANCH LINES OF *OH* IN THE INFRARED AIRGLOW

Band (v'–v'')	Line (K'')	λ_{air} (A)	ν_{vac} (Cm^{-1})	Band (v'–v'')	Line (K'')	λ_{air} (A)	ν_{vac} (Cm^{-1})
8–3	P_1 (2)	7316.2	13664.5	5–1	P_1 (3)	7993.6	12506.6
	P_2 (3)	7330.0	13638.8		P_1 (4)	8025.8	12456.4
	P_1 (3)	7341.1	13618.2		P_1 (5)	8062.6	12399.5
9–4	P_1 (2)	7794.0	12826.8	6–2	P_2 (2)	8382.0	11927.0
	P_2 (3)	7809.0	12802.2		P_1 (2)	8399.7	11901.9
	P_1 (3)	7821.9	12781.1		P_2 (3)	8415.1	11880.1
	P_2 (4)	7841.4	12749.0		P_1 (3)	8430.7	11858.2
	P_1 (4)	7853.3	12730.0		P_2 (4)	8452.4	11827.7
	P_1 (5)	7889.8	12671.1		P_1 (4)	8465.3	11809.7
					P_2 (5)	8493.8	11770.0
5–1	P_1 (2)	7964.9	12551.6		P_1 (5)	8505.0	11754.6
	P_2 (3)	7979.5	12528.7		P_1 (6)	8549.2	11693.8

TABLE 2

OBSERVED AND COMPUTED ORIGINS OF MEINEL *OH* BANDS

BAND (v'–v'')	ν_0 (OBSERVED)			ν_0 (COMPUTED)		
	Herman and Hornbeck (1953)	Déjardin, Janin, Peyron (1953)	Airglow	Herman and Hornbeck (1953)	Déjardin, Janin, Peyron (1953)	Combined Laboratory and Airglow Constants
4–0	13291.50	13291.5	. . . .	13291.5	13291.5	13291.5
5–1	12637.11	12636.8	12637.3±0.12	12637.0	12636.8	12637.0
6–2	11984.59	11983.5	11984.4±0.11	11984.5	11983.6	11984.8
8–3	. . . .	. . . .	13743.7±0.33	13746.2	13743.0	13743.3
9–4	. . . .	. . . .	12902.4±0.15	12911.3	12907.0	12902.6

TABLE 3

OH VIBRATIONAL ENERGY LEVELS, $G_0(v) = G(v) - G(0)$

v	Observed*	Computed†	v	Observed*	Computed†
1	3569.63	3569.89	6	18958.17	18958.38
2	6973.58	6973.56	7	. . . .	21543.20
3	10213.83	10213.65	8	23957.5	23956.92
4	13291.50	13291.45	9	26193.9	26194.03
5	16206.74	16206.86			

* Based on Dieke and Crosswhite's (1948) measures of the ultraviolet bands, Herman and Hornbeck's (1953) measures of the laboratory infrared bands (for $v = 4$, 5, and 6), and the present airglow measures (for $v = 8$ and 9).

† Obtained from the combined laboratory and airglow constants in the last column of Table 4.

Assuming that the data are of sufficient accuracy to warrant it, we may obtain considerably better agreement between the observed and computed quantities by adding another term to the power series in equation (1). Thus

$$G(v) = 3737.90\left(v+\tfrac{1}{2}\right) - 84.965\left(v+\tfrac{1}{2}\right)^2 + 0.5398\left(v+\tfrac{1}{2}\right)^3 - 0.01674\left(v+\tfrac{1}{2}\right)^4 - 0.001637\left(v+\tfrac{1}{2}\right)^5, \tag{2}$$

where the coefficients have been derived without regard to the less accurate $v = 8$. The mean of the absolute values of the residuals obtained from equation (2) is only 0.01 cm^{-1}.

DISCUSSION

Vibrational energy levels.—Although the energy levels with $v \leq 9$ have been represented here by four constants in Table 4 and five constants in equation (2), it is doubtful whether one could, on the basis of these data, make an accurate prediction of higher energy levels. For $v \leq 9$, the contribution of higher terms in the power series has been neglected, because an adequate fit could be obtained without them. For higher levels these terms will become more important, however, with the result that any use of the present constants outside the range for which they were derived is of questionable validity.

TABLE 4

DETERMINATIONS OF VIBRATIONAL CONSTANTS FOR X $^2\Pi$ STATE OF *OH* (IN CM^{-1})

Term	Dieke and Crosswhite (1948)	Herman and Hornbeck (1953)	Déjardin, Janin, and Peyron (1953)	Laboratory plus Airglow*
ω_e	3735.21	3738.48	3738.1	3739.94
$\omega_e x_e$	82.81	85.482	85.230	86.350
$\omega_e y_e$	. . . .	+ 0.7232	+ 0.6783	+ 0.9046
$\omega_e z_e$	. . . .	+ 0.04544	+ 0.0436	+ 0.05763

* These constants are based on the present airglow data combined with laboratory measurements of the infrared and ultraviolet spectra as explained in the text.

Another point of some importance here is that the vibrational "constants" are dependent on the number of terms used in equation (1). For example, $\omega_e z_e$ changes from +0.058 to +0.017 when we add the next highest term to the power series. Thus when so many terms are required, the coefficients lose much of their physical significance as well as practical usefulness.

The deviations of the X $^2\Pi$ potential curve from a Morse function (in which only ω_e and $\omega_e x_e$ are considered) are likely to be important and cause the vibrational transition probabilities of Heaps and Herzberg (1952) to be somewhat in error. A representation of the *OH* potential curve should be based directly on the individual observed levels rather than on a few vibrational and rotational constants (cf. Herzberg 1950, p. 102).

It is not likely that the higher-order terms in equation (1) are made necessary merely by one or two perturbed levels. The increase of the vibrational energy is quite regular and smooth; moreover, no undiscovered electronic states are expected at low enough energy to perturb these levels (cf. Mulliken 1932, Fig. 38). Other cases wherein numerous terms are required have been discussed by Coolidge, James, and Vernon (1938).

Blending of the airglow with the infrared auroral spectrum.—Often the infrared airglow spectrum is faintly superimposed on auroral spectra (e.g., cf. Chamberlain, Fan, and

Meinel 1954, Fig. 2), and certain features in the airglow may be confused with auroral emissions. In this respect it is of interest that our measurements give the $P_1(2)$ and $P_2(3)$ lines of the 8–3 band at 7316 and 7330 A (Table 1), which are extremely close to λ 7319 and λ 7330 [*O* II], suspected of being in auroral spectra. In view of this fact, it is not likely that these [*O* II] lines would be easily and unambiguously detected in aurorae unless they were quite strong. Hence Petrie's (1952) failure to observe these lines, in spite of a special search for them, cannot be regarded as strong evidence for their absence.

REFERENCES

Chamberlain, J. W., Fan, C. Y., and Meinel, A. B. 1954, *Ap. J.*, **120**, 560.
Chamberlain, J. W., and Oliver, N. J. 1953, *Phys. Rev.*, **90**, 1118.
Coolidge, A. S., James, H. M., and Vernon, E. L. 1938, *Phys. Rev.*, **54**, 726.
Déjardin, G., Janin, J., and Peyron, M. 1953, *Cahiers de phys.*, No. 46, p. 3.
Dieke, G. H., and Crosswhite, H. M. 1948, *Bumblebee Series Rept. No. 87* (Johns Hopkins University).
Dufay, J. and M. 1951, *C.R. Acad. Sci.*, **232**, 426.
Heaps, H. S., and Herzberg, G. 1952, *Zs. f. Phys.*, **133**, 48.
Herman, R. C., and Hornbeck, G. A. 1953, *Ap. J.*, **118**, 214.
Herzberg, G. 1950, *Spectra of Diatomic Molecules* (2d ed.; New York, Toronto, London: D. Van Nostrand Co.).
Hill, E. L., and Van Vleck, J. H. 1928, *Phys. Rev.*, **32**, 250.
Jones, A. V., and Gush, H. 1953, *Nature*, **172**, 496.
Meinel, A. B. 1950*a*, *Ap. J.*, **111**, 555.
———. 1950*b*, *ibid.*, **112**, 120.
Mulliken, R. S. 1932, *Rev. Mod. Phys.*, **4**, 1.
Petrie, W. 1952, *Phys. Rev.*, **87**, 1002.
Small, R., and Petrie, W. 1952, *Scientific Report No. AR-8* (University of Saskatchewan).

THE CONCENTRATION OF CARBON DIOXIDE IN THE ATMOSPHERE OF MARS

J. GRANDJEAN* AND R. M. GOODY
Imperial College, London

Received September 9, 1954

ABSTRACT

From observations of carbon dioxide bands in the spectrum of Mars made by G. P. Kuiper, we have redetermined the fraction by volume of this gas in the planet's atmosphere, taking into account the fine structure of the band and the shape of the rotation lines. If the ground-level pressure on Mars is 100 mb, we find that the fraction by volume of carbon dioxide is 50 times greater than in the earth's atmosphere.

INTRODUCTION

On October 7 and 8, 1947, G. P. Kuiper (1952) observed the 1.575 and 1.605 μ vibration-rotation bands of carbon dioxide in the spectrum of Mars under low resolution and found them to be stronger than could be accounted for by terrestrial absorption. From solar calibration spectra he determined the approximate CO_2 content of the Martian atmosphere but noted that his results were, so far, uncorrected for differential pressure effects between Mars and the earth. These bands arise from transitions from the ground state to the $2\,2^0\,1$ and $1\,4^0\,1$ states, respectively (cf. Herzberg 1945), and the rotational fine structure consists of simple P and R branches, with nearly equally spaced lines, separated, on the average, by 1.56 cm^{-1} (Goldberg 1950).

At the time of observation, the radial velocity of Mars with respect to the earth was about -13 km/sec. The absorption lines due to the Martian atmosphere were therefore shifted toward the violet by 0.27 cm^{-1} as compared with those arising in the terrestrial atmosphere. This shift is small compared with the mean line spacing but large compared with the half-widths of the lines, which are about 0.06 cm^{-1} for the earth's atmosphere[1] (for a mean pressure of 500 mb), and 0.006 cm^{-1} for the Martian atmosphere (for a mean pressure of 50 mb). The only unusual problem involved in interpreting Kuiper's spectrum is that of disentangling the superimposed absorptions due to the two atmospheres.

THE SUPERPOSITION OF DOPPLER-SHIFTED SPECTRA

Consider radiation which has passed through both the terrestrial and the Martian atmospheres, giving rise to a single pair of lines caused by the same transition. If the lines do not overlap at all, then the equivalent widths are additive, and

$$\int_{E+M} A_\nu d\nu = \int_E A_\nu d\nu + \int_M A_\nu d\nu ,$$

where A_ν is the absorption at frequency ν. Since the line spacing is roughly constant and greater than the Doppler shift, this proposition will also be true for the sum over an array of lines. The average absorption recorded by a low-resolution spectrometer will therefore be given by

$$\bar{A}_{E+M} = \bar{A}_E + \bar{A}_M . \tag{1}$$

---

* On leave from the Institut Royal Météorologique Belgique with the aid of a studentship from the British Council.

[1] We will use the only measured line width in a carbon dioxide band; 0.12 cm^{-1} at 1 atm. pressure for a line in the 15 μ band (see Adel 1953).

However, the terrestrial lines have some influence on the Martian lines, and vice versa. Since the Doppler shift is large compared with the line width, we may assume, as a second approximation, that the terrestrial lines produce a uniform absorption,

$$A_{E\to M} = 1 - e^{-\tau_{E\to M}} ,$$

in the vicinity of a Martian line, where $\tau_{E\to M}$ is the optical depth caused by all terrestrial lines at the center of a Martian line. The equivalent width of the Martian line will therefore be decreased by a factor $\exp - \tau_{E\to M}$, which we may take to be constant for all lines embraced by the spectrometer slits. Therefore, we find as a second approximation that

$$\bar{A}_{E+M} = \bar{A}_E \exp(-\tau_{M\to E}) + \bar{A}_M \exp(-\tau_{E\to M}) . \qquad (2)$$

If rotation lines have the Lorentz shape, the absorption coefficient is given by

$$k_\nu = \frac{k a}{\pi (\nu^2 + a^2)} ,$$

where k is the line intensity, a is the line width (proportional to the total pressure), and ν is the distance from the line center. It can be shown that, if $a \ll \nu_D \ll \delta$,

$$k_{E\to M} \simeq \frac{k a_E}{\pi \nu_D^2} ,$$

$$k_{M\to E} \simeq \frac{k a_M}{\pi \nu_D} ,$$

where ν_D is the Doppler shift and δ is the mean line spacing.

We must now assume that the carbon dioxide in both atmospheres is intimately mixed with the main gas responsible for the collision broadening. This is sufficiently near the truth for the earth's atmosphere, but it is hypothetical for the Martian atmosphere. The optical depth is given by

$$\tau_\nu = \int_0^{m_0} k_\nu \, d m ,$$

where m is the total amount of absorbing matter in the path of the beam and the subscript $_0$ denotes ground level. For a mixed atmosphere,

$$m = \frac{p}{p_0} m_0 = \frac{a}{a_0} m_0 ,$$

where p is the pressure at the level concerned. It follows that

$$\tau_{E\to M} = \gamma_E \left[\frac{a_{0E}}{\nu_D} \right]^2 ,$$

$$\tau_{M\to E} = \gamma_M \left[\frac{a_{0M}}{\nu_D} \right]^2 ,$$

where

$$\gamma = \frac{k m_0}{2\pi a_0} ,$$

so that

$$\bar{A}_{E+M} = \bar{A}_E \exp\left\{ -\gamma_M \left(\frac{a_{0M}}{\nu_D} \right)^2 \right\} + \bar{A}_M \exp\left\{ -\gamma_E \left(\frac{a_{0E}}{\nu_D} \right)^2 \right\} . \qquad (3)$$

Equation (3) will be a good approximation, provided that it does not differ greatly from 1. Inserting values for the parameters as found in the next section, we find $\tau_{M\rightarrow E} \leq 0.008$ and $\tau_{E\rightarrow M} \leq 0.035$. This shows that equation (3) is a good approximation and also that errors in the estimates of $\tau_{M\rightarrow E}$ and $\tau_{E\rightarrow M}$ are of little consequence.

RESULTS

On the records published by Kuiper the absorption at the center of the 1.575 μ band is about 9 per cent, caused by two traversals of the Martian atmosphere and one traversal of the earth's atmosphere at a zenith angle ψ such that $\sec \psi = 1.1$.

According to Kuiper, this record is matched by a solar spectrum through 10 terrestrial air masses. We have made use of this fact to determine the parameters required for estimating the concentration of Martian carbon dioxide.

The mean absorption for a dilute gas, intimately mixed with the atmosphere, for a ray passing from outer space to the surface, has been computed for a model consisting of an infinite array of equally spaced Lorentz lines of equal intensity (Kaplan 1952; Goody 1954). This model would be appropriate for the *P*- and *R*-branch maxima; but, as might be expected from the slight overlap between terrestrial and Martian lines, it is sufficient for this problem to use an asymptotic form which applies in the limit of no overlap between lines (Strong and Plass 1950):

$$\bar{A} = 2\pi^{1/2} y \frac{\Gamma(\gamma + \frac{1}{2})}{\Gamma(\gamma)}, \tag{4}$$

where $y = \alpha/\delta$. All parameters are known except k, which can be found to be 0.035 cm gm^{-1} if the absorption is 9 per cent for 10 terrestrial air masses containing 3.2×10^{-4} parts by volume of carbon dioxide (Glueckauf 1951).

Using this value of k, we may compute $\bar{A}_E$ for $\sec \psi = 1.1$. If, as a first approximation, we adopt the same value of k for Mars (in fact, k is temperature-dependent; see below), we may calculate the concentration of CO_2 on Mars required to give $\bar{A}_{E+M} = 0.09$ from equation (3) if we know the pressure at the surface of the planet. More precisely, we require to know the product of the pressure and the square of the ratio of the collision diameter in the Martian atmosphere to that in the terrestrial atmosphere. If we assume that most of the Martian atmosphere is nitrogen, this distinction disappears; if it is later found that it is mainly some other gas, then it will be necessary to use different values of α/p for Mars and the earth; but this presents no new difficulties. To allow for some future change in the opinions held about the pressure of the Martian atmosphere, we have assumed the ground-level pressure to be 50, 100, and 150 mb.[2]

When computing the value of γ for Mars, the total amount of carbon dioxide was doubled to allow for the two traversals of the atmosphere. A mean value for $\sec \psi = \frac{4}{3}$ was adopted; this is the square of the mean value of $(\sec \psi)^{1/2}$ integrated over the hemisphere. The grounds for adopting this value were that equation (4) gives close proportionality between absorption and the square root of the amount of absorbing matter and that, for lack of other information, we had to assume that radiation from the whole sunlit hemisphere passed the spectrometer slits. This latter assumption clearly cannot be very precise, since Mars was not in opposition at the time of observation.

Results of computations are shown in Table 1. Since the absorption of 9 per cent is rather difficult to measure accurately, we have also made computations for absorptions of 5 and 13 per cent, although it is very unlikely that the value could be as far out as these figures suggest. The results may be summarized by the relation,

$$p_{0M}^2 C_M = 1.6 \pm 0.5 \times 10^2 \text{ mb}^2,$$

---

[2] "The pressure on Mars is still uncertainly known but appears to be in the region of 90 mb near the ground" (de Vaucouleurs 1950).

where C_M is the fraction by volume of carbon dioxide in the Martian atmosphere. Thus, if $p_{0M} = 100$ mb, the Martian concentration is 50 times greater than the terrestrial concentration, and the total amount of carbon dioxide in gm cm^{-2} is about 13 times greater.

The probable error which we have assigned is largely due to uncertainties in the correct value of sec ψ to use for Mars and in the value of the mean absorption at the center of the absorption bands. Both these sources of uncertainty could be decreased. A number of other possible sources of error are discussed in the next section.

DISCUSSION OF ERRORS

There are several sources of error which do not seem to be very important but which require consideration. We have assumed the same value of k to hold on Mars as on the earth. Temperature affects the population of the rotational levels and hence changes k. Near the P- and R-branch maxima it can be shown that a change in temperature $\Delta\theta$ will give rise to a change in k, represented by

TABLE 1

CONCENTRATIONS BY VOLUME OF CARBON DIOXIDE IN THE ATMOSPHERE OF MARS FOR VARIOUS HYPOTHESES ABOUT TOTAL PRESSURE AND MEAN ABSORPTION

TOTAL PRESSURE (MB)	MEAN ABSORPTION		
	0.13	0.09	0.05
50	8.16×10^{-2}	6.35×10^{-2}	3.97×10^{-2}
100	2.06×10^{-2}	1.62×10^{-2}	1.05×10^{-2}
150	9.32×10^{-3}	7.51×10^{-3}	5.11×10^{-3}

$$\frac{\Delta k}{k} \simeq -\tfrac{1}{2}\frac{\Delta\theta}{\theta}\,.$$

If the mean temperature on Mars differs by 30° K from that of the earth, the value of k will change by 5 per cent and the computed C_M by 4.5 per cent, a difference which we may neglect. The population of the ground state also varies with temperature, and line intensities are directly proportional to it. The partition function has been computed, and we find that the effect is very small.

Throughout, we have made use of the Lorentz line shape. The Doppler width on Mars is about equal to the mean Lorentz width; nevertheless, the effect of Doppler broadening can be ignored. To establish this, we made use of an expression for the equivalent width of a single "strong line" in a mixed atmosphere of combined Doppler and Lorentz line shape (Plass and Fivel 1953). For zero Doppler width we found that the results of Table 1 were unaltered, except for a mean absorption of 0.05 and a total pressure of 150 mb, thus establishing that, for most conditions, the "strong-line" approximation is sufficient. Concentrations were then recalculated by using the correct value of the Doppler width, and we found the values to be the same as for the previous computation to better than 2 per cent.

The Lorentz shape is a poor approximation to the shape of a pressure-broadened line. However, it has been shown that the effect of pressure shift on the equivalent width of "strong lines" is small (Plass and Warner 1952). Moreover, if rotation lines had the

Lindholm rather than the Lorentz shape, the mean absorption near a band center would scarcely be altered except for very large absorptions (Curtis and Goody 1954). Since the absorptions concerned here are very small and since there will be some cancellation of errors due to making the same assumption for both planetary and solar spectra, it is unlikely that the assumption of the Lorentz shape will cause any very serious errors.

OBSERVATIONS DURING AN OPPOSITION OF MARS

It is of interest to note that spectra can also be interpreted if there is no Doppler shift, by using an approximation (Curtis 1952), whereby the problem can be reduced to one involving constant-pressure paths. Assuming no Doppler shift and with the data used here, the results given in Table 2 are obtained for a mean absorption of 9 per cent.

TABLE 2

Total Pressure	C_M
50 mb	6.94×10^{-2}
100 mb	1.65×10^{-2}
150 mb	7.60×10^{-3}

The differences between Tables 1 and 2 are small, so that unless the Martian pressure is very much less than 50 mb, there should be no observable difference between spectra recorded in or out of opposition, apart from those arising from changes in the various zenith angles.

REFERENCES

Adel, A. 1953, *Phys. Rev.*, **90**, 1024.
Curtis, A. R. 1952, *Quart. J. R. Meteorol. Soc.*, **78**, 638.
Curtis, A. R., and Goody, R. M. 1954, *Quart. J. R. Meteorol. Soc.*, **80**, 58.
Glueckauf, E. 1951, *Compendium of Meteorology* (Boston: American Meteorological Society), p. 3.
Goldberg, L. 1950, *Rept. Prog. Phys.*, **13**, 24.
Goody, R. M. 1954, *The Physics of the Stratosphere* (London: Cambridge University Press,) p. 164.
Herzberg, G. 1945, *Infrared and Raman Spectra of Polyatomic Molecules* (New York: D. Van Nostrand Co.), p. 274.
Kaplan, L. D. 1952, *J. Meteorol.*, **9**, 1.
Kuiper, G. P. 1952, *The Atmospheres of the Earth and Planets* (2d ed.; Chicago: University of Chicago Press), p. 360.
Plass, G. N., and Fivel, D. I. 1953, *Ap. J.*, **117**, 227.
Plass, G. N., and Warner, D. 1952, *J. Meteorol.*, **9**, 333.
Strong, J., and Plass, G. N. 1950, *Ap. J.*, **112**, 365.
Vaucouleurs, G. de. 1950, *The Planet Mars* (London: Faber & Faber).

NOTES

WIDE-ANGLE INFRARED PHOTOGRAPH OF THE SOUTHERN MILKY WAY

During the course of observations of the southern Milky Way, several infrared exposures were obtained with the Greenstein-Henyey wide-angle camera (Struve 1951). The camera, on loan from the Yerkes Observatory, was installed at the Boyden Station of the Harvard College Observatory at Bloemfontein, South Africa. The exceptionally high quality of the sky at this site made it an ideal location for the $f/2$ camera. Since the galactic center culminates near the zenith at this latitude, it was felt that an extension of the observations of Osterbrock and Sharpless (1952) would be profitable.

Figure 1 is a reproduction of a 2-hour exposure of the southern Milky Way in the infrared. The filter and plate combination is the same as that used by Osterbrock and Sharpless; an Eastman I-N emulsion behind Corning 5850 and 2403 filters, giving an effective wave length of about 7900 A. A 20-minute exposure on a 103*a*-O plate without filter is shown in Figure 2 for comparison.

The most striking feature of the infrared photograph is its similarity to typical edge-on spirals of early type. The photograph shows a narrowing of the general surface brightness toward the galactic plane, as well as a more clearly defined belt of obscuration. North of the dark rift through the galactic center is the infrared star cloud observed by Dufay (1951). The dark obscuration starting about galactic longitude 285°, near α Centauri, and running along the galactic equator to about longitude 300°, near γ Normae, is quite as prominent in both the blue and the infrared and may be partly responsible for the decrease in number of spiral-arm features in this region of the Milky Way. The Coal Sack east of Crux is, however, less conspicuous in the infrared.

McGee and Bolton (1954) have observed a bright radio source at 400 Mc/sec which they have identified as probably being the galactic nucleus. Haddock, Mayer, and Sloanaker (1954), observing at 9.4 cm, have given the position of this source as $l = 327\overset{\circ}{.}6$, $b = -1\overset{\circ}{.}46$ (Lund pole), with an estimated accuracy of $5'$. In Figure 3, two concentric circles centered on this position have been indicated. The inner circle represents the extent of the minor axis of the galactic bulge apparent on the infrared exposure, while the outer circle delineates the major axis, with diameters of 18° and 28°, respectively. The identification of the radio source with the galactic nucleus is wholly consistent with the distribution of surface brightness in the infrared. The linear diameter of the bright galactic bulge would be 4.1 kpc, based on the presently accepted value of 8.2 kpc (van de Hulst, Muller, and Oort 1954) for the distance from the sun to the galactic center.

The probable extension of the nearest inner spiral arm is indicated by the arcs in Figure 3 near Carina and Aquila. This is based upon results obtained for the distribution of the bright OB stars by Morgan, Whitford, and Code (1953), and by Weaver (1953). The decrease in the general surface brightness of the Milky Way beyond these limits is clearly shown on all the wide-angle photographs taken of these regions.

This research was supported in part by the National Science Foundation and partly by the Wisconsin Alumni Research Foundation. We are grateful to Drs. B. Strömgren

and W. W. Morgan for making the wide-angle camera available and to the staff of the Boyden Station for the co-operation and generosity in installing and maintaining the instrument at Bloemfontein.

A. D. CODE
T. E. HOUCK

WASHBURN OBSERVATORY
September 27, 1954

REFERENCES

Dufay, J. 1951, *Sky and Telescope*, **12**, 41.
Haddock, F. T., Mayer, C. H., and Sloanaker, R. M. 1954, *Nature*, **174**, 176.
van de Hulst, H. C., Muller, C. A., and Oort, J. H. 1954, *B.A.N.*, **452**, 117.
McGee, R. X., and Bolton, J. G. 1954, *Nature*, **173**, 985.
Morgan, W. W., Whitford, A. E., and Code, A. D. 1953, *Ap. J.*, **118**, 318.
Osterbrock, D., and Sharpless, S. 1952, *Ap. J.*, **115**, 140.
Struve, O. 1951, *Sky and Telescope*, **10**, 215.
Weaver, H. 1953, *A.J.*, **58**, 177.

PHOTOMETRY OF THE LACERTA AGGREGATE*

The group of early-type stars in Lacerta, forming one of the nearer OB aggregates, is of special interest because of its apparent expansion (Blaauw and Morgan 1953), which leads to an age of 4.2×10^6 years. To obtain improved photometric data for the aggregate, the stars were observed at the McDonald Observatory in the fall of 1952.

The magnitudes and colors in Table 1 are based on at least one observation with the 82-inch reflector and on at least three observations with the 13-inch reflector. The uncertainty in the zero points of the magnitudes and colors should be quite small, as the observations were made relative to the fundamental standards 10 Lacr and BS 8832 (Johnson and Morgan 1953). The mean errors of the magnitudes and colors, as determined from the ranges, are 0.010 and 0.005 mag. The relatively large mean error of the visual magnitudes is due to the retention of several stars which show evidence of being variables of small range. Before these are announced, further observations must be made to guarantee their being variable.

The color excesses, E, are based entirely on the photometric data, according to the method outlined by Morgan and Harris (1954). The total absorption, $3.0E$, applied to V, gives the corrected apparent magnitudes, V_0.

The color excess of 0.11 mag. for 10 Lacr determined photometrically agrees with the value determined from the intrinsic color of an O9V star (Morgan, Harris, and Johnson 1953). This color excess is supported by the color excesses of the other stars in the neighborhood.

The photometric method of determining color excesses fails in the case of some emission-line stars; therefore, we have not used the values of E given in parentheses but have adopted the values derived from the spectral types and intrinsic colors. The values of E_{sp} for HD 211835 and 215227 are 0.19 and 0.25 mag., while that for HD 214168 is 0.11 mag. The differences between the photometric and spectral color excesses can be interpreted as being caused by the ultraviolet being too bright by 0.27 and 0.38 mag. for the first two stars, as compared to normal main-sequence stars. The third star has a difference of only 0.02 mag., which is not significant when the variation among the main-sequence stars is considered.

The values of V_0 can be reduced to absolute magnitudes when a value for the distance modulus of the aggregate is assumed. The distance modulus given by Blaauw and

---

* *Contributions from the McDonald Observatory, University of Texas,* No. 250.

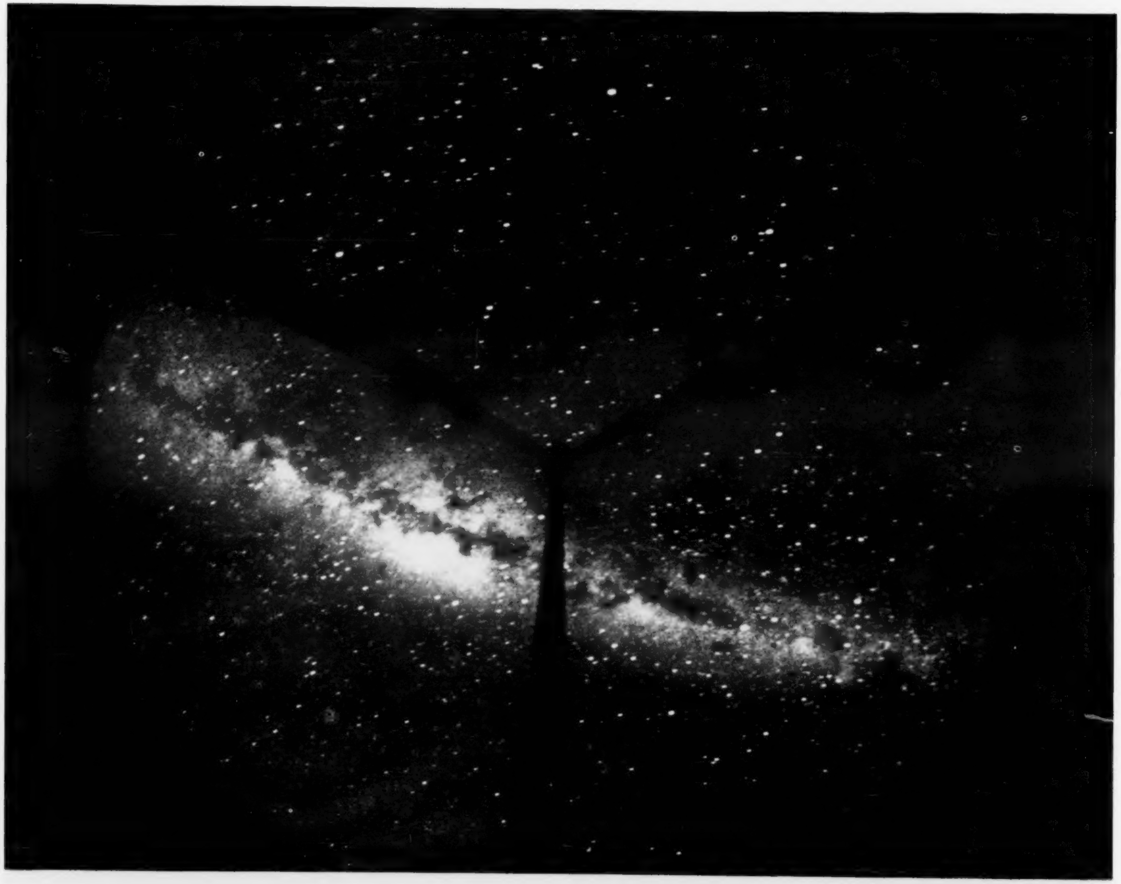

FIG. 1.—The Milky Way from Aquila to Carina in the infrared

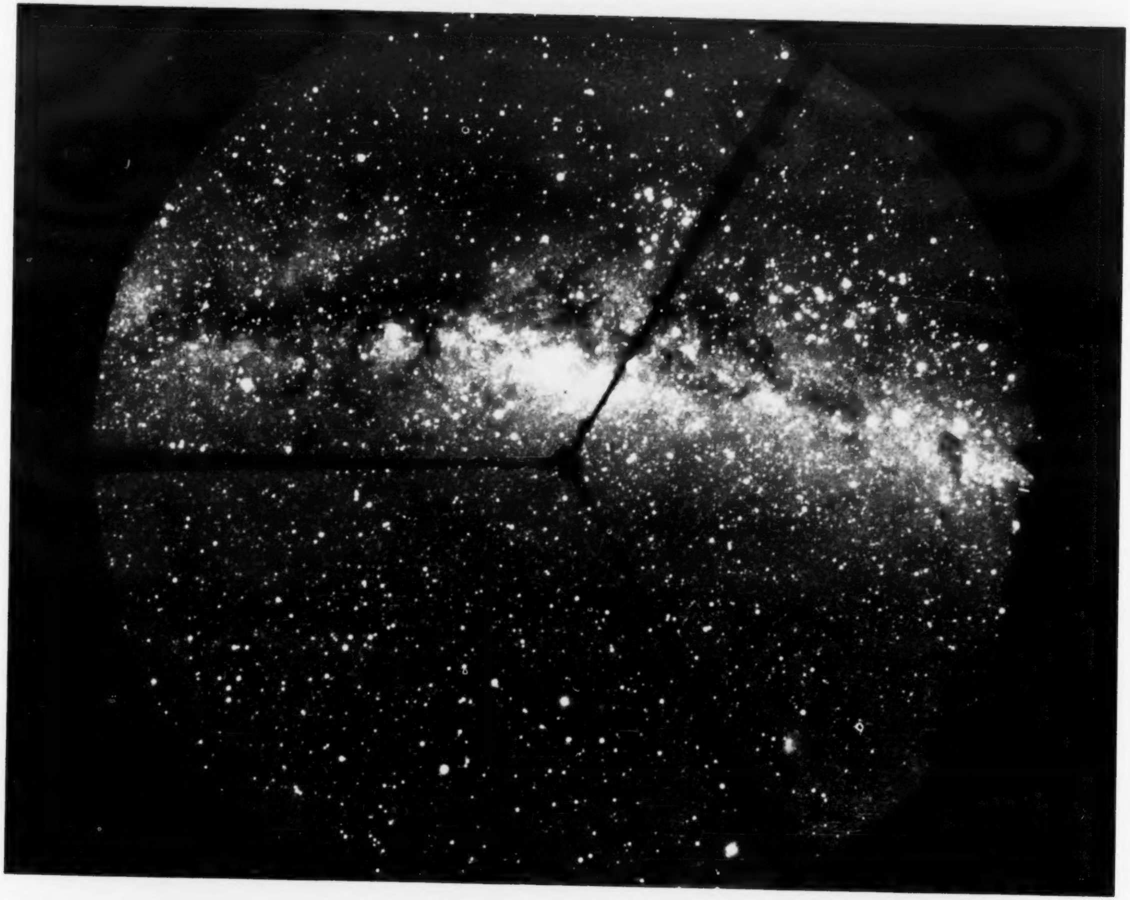

FIG. 2.—The Milky Way from Sagitta to Crux in the blue

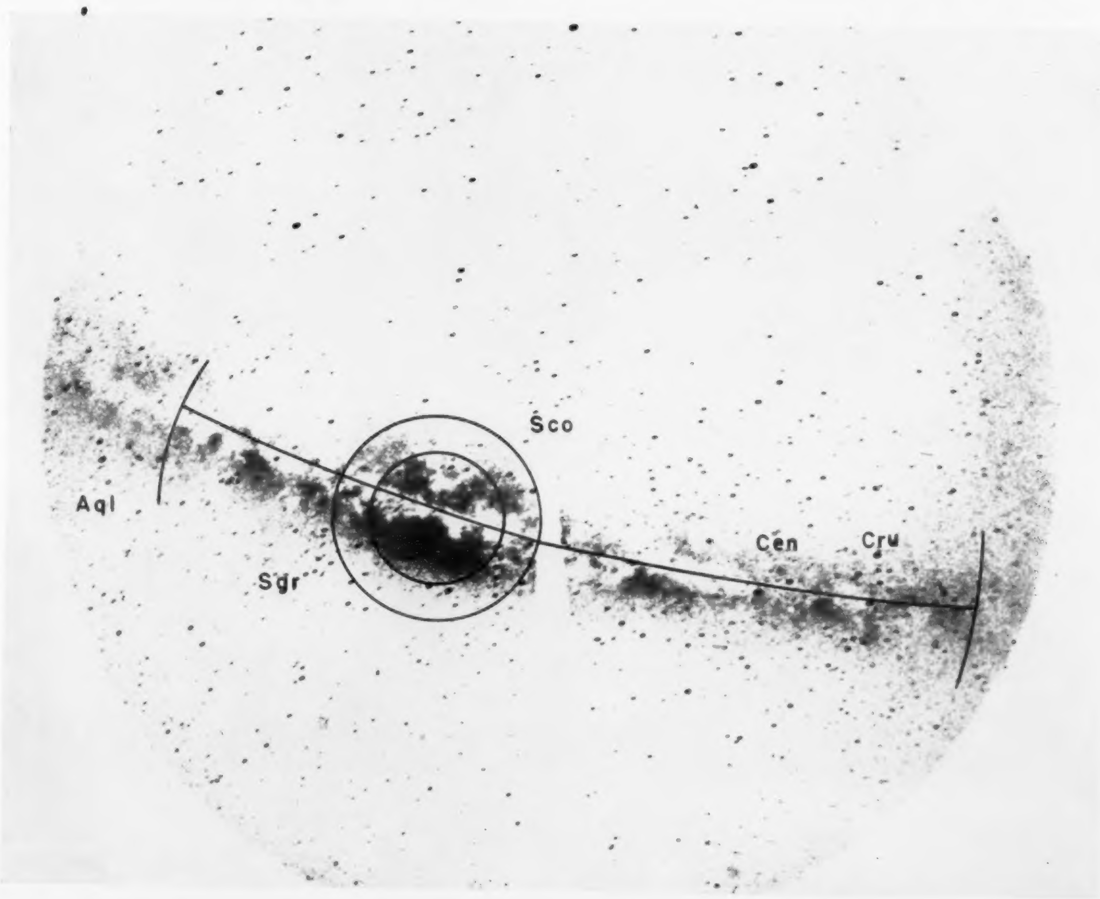

FIG. 3.—Infrared exposure of the southern Milky Way, indicating the position of the galactic center, the galactic equator, and the extent of the inner spiral structure.

Morgan (1953) is 8.3, while four stars in Petrie's lists (1953, 1954) make it 7.9. However, the values of V_0 for the B2 V and B3 V stars, combined with the absolute magnitudes −2.6 and −2.0 given by Johnson and Morgan (1953), would lead to a distance modulus of the order of 9.0. It is apparent that the reduction to absolute magnitudes will have to await the final calibration of luminosity classes now in progress (Blaauw and Morgan 1952).

TABLE 1

MAGNITUDES AND COLORS OF THE LACERTA AGGREGATE

HD No.	MKK	V	$B-V$	$U-B$	n	E	V_0	Notes
209961	B2 V	6.27	−0.06	−0.71	5	0.17	5.8	1
211835	B3:Ve	8.48	.00	−0.80	6	(.28)	7.9	
212883	B2 V	6.45	− .13	−0.75	5	.09	6.2	2
212978	B2 V	6.14	− .14	−0.77	5	.09	5.9	2
213420	B2 IV	4.50	− .08	−0.73	5	.15	4.0	
213976	B1.5 V	7.02	− .11	−0.80	6	.14	6.6	
214167	B2 V	6.46	− .15	−0.82	4	.10	6.2	
214168	B1 Vne	5.73	− .15	−0.90	4	(.12)	5.4	
214240	B3 V	6.29	− .05	−0.54	4	.12	5.9	1
214263	B2 V	6.85	− .13	−0.78	5	.08	6.6	
214432	B3 V	7.59	− .11	−0.67	6	.09	7.3	
214652	B2:V	6.84	− .11	−0.74	5	.12	6.5	1
214680	O9 V	4.87	− .20	−1.04	S	.11	4.5	
214993	B2 III	5.25	− .14	−0.87	5	.13	4.9	3
215191	B1 V	6.43	− .09	−0.81	5	.16	5.9	
216092	B1:V	7.85	− .07	−0.70	6	.16	7.4	4
216200	B3 IV:	5.91	.08	−0.51	4	.29	5.0	5
216534	B3 V	8.50	− .01	−0.58	5	.19	7.9	
216684	B3 V	7.76	− .02	−0.60	4	.19	7.0	
216851	B3 V:n	8.02	.04	−0.50	4	.24	7.3	
216916	B2 IV	5.58	− .14	−0.83	4	.11	5.3	3
217101	B2 IV–V	6.17	− .15	−0.80	4	.09	5.9	
217227	B2:V	7.16	− .06	−0.61	4	.14	6.7	
217543	B3	6.54	− .11	−0.64	4	.09	6.3	
217811	B2 V	6.38	.00	−0.58	4	.20	5.8	
218325	B3 V	7.71	.06	−0.61	4	.29	6.8	
218344	B2 V	7.42	− .11	−0.72	8	.11	7.1	
218407	B2 V	6.66	− .05	−0.68	4	.18	6.1	1
218674	B3 IV	6.73	− .01	−0.57	5	.19	6.2	
215227	B5:ne	8.75	0.09	−0.77	6	(0.39)	8.0	6, 4

NOTES TO TABLE 1

1. Spectroscopic binary: V_0 is for combined light.
2. Possible field stars (Blaauw and Morgan 1953).
3. Beta Canis Majoris variable.
4. Possible field star.
5. Variable announced by Walker (1952).
6. Not included by Blaauw and Morgan (1953).

DANIEL L. HARRIS III

YERKES AND MCDONALD OBSERVATORIES

REFERENCES

Blaauw, A., and Morgan, W. W. 1952, *A.J.*, **57**, 199.
———. 1953, *Ap. J.*, **117**, 256.
Johnson, H. L., and Morgan, W. W. 1953, *Ap. J.*, **117**, 313.
Morgan, W. W., and Harris, D. L. 1954, *Vistas in Astronomy* (in press).
Morgan, W. W., Harris, D. L., and Johnson, H. L. 1953, *Ap. J.*, **118**, 92.
Petrie, R. M. 1953, *Pub. Dom. Ap. Obs. Victoria*, **9**, 251.
———. 1954, *J.R.A.S. Canada*, **48**, 169.
Walker, M. F. 1952, *Ap. J.*, **116**, 106.

FOUR FAINT WOLF-RAYET STARS*

In the routine observational program of early-type stars for interstellar polarization, color, and spectra, four faint Wolf-Rayet stars were included in the program of the last observing period (August). The four stars were found by B. Iriarte and E. Chavira to show Wolf-Rayet characteristics at the Observatorio Astrofisico Nacional with the 26-inch Schmidt. Two, however, had been discovered previously, as indicated in the footnote of the accompanying table. The photometric and spectroscopic data are given in this table. The available spectrograms are reproduced in Figure 1. Some of the stronger features are identified in the figure for orientation purposes. The four stars are typical Wolf-Rayets, three of the carbon and one of the nitrogen sequence. The photographic magnitudes are all 13.0 or fainter, and the stars are greatly reddened. The distance moduli are, of course, not well determined because of the absence of known intrinsic colors and absolute magnitudes. However, their distance moduli must be of the order of 12.5–14.5. At the present time, no data are available as to whether or not any of the stars exhibit a variable radial velocity.

FOUR FAINT WOLF-RAYET STARS

No.	1900		V	$B-V$	$U-B$	Sp.
	α	δ				
1	$17^{h}58^{m}9$	$-21^\circ 12'$	12.02	+1.25	+0.31	WC7+
2	18 17.6	−13 49	12.02	+0.97	+ .54	WC6
3*	18 36.0	− 4 33	11.94	+1.05	+ .11	WN7
4†	18 39.2	− 3 58	11.94	+1.40	+0.36	WC7+

* See A. N. Vyssotsky, 1942, *Pub. A.S.P.*, **54**, 152, Star No. 3.

† See Paul W. Merrill and Cora G. Burwell, 1950, *Ap. J.*, **112**, 77, Star No. 320. These authors report strong $H\alpha$ emission. Note that $H\beta$ emission is weak or absent on our spectrogram.

W. A. Hiltner
Braulio Iriarte

Yerkes and McDonald Observatories
and
Observatorio Astrofísico Nacional (México)

---

* *Contributions from the McDonald Observatory, University of Texas*, No. 251.

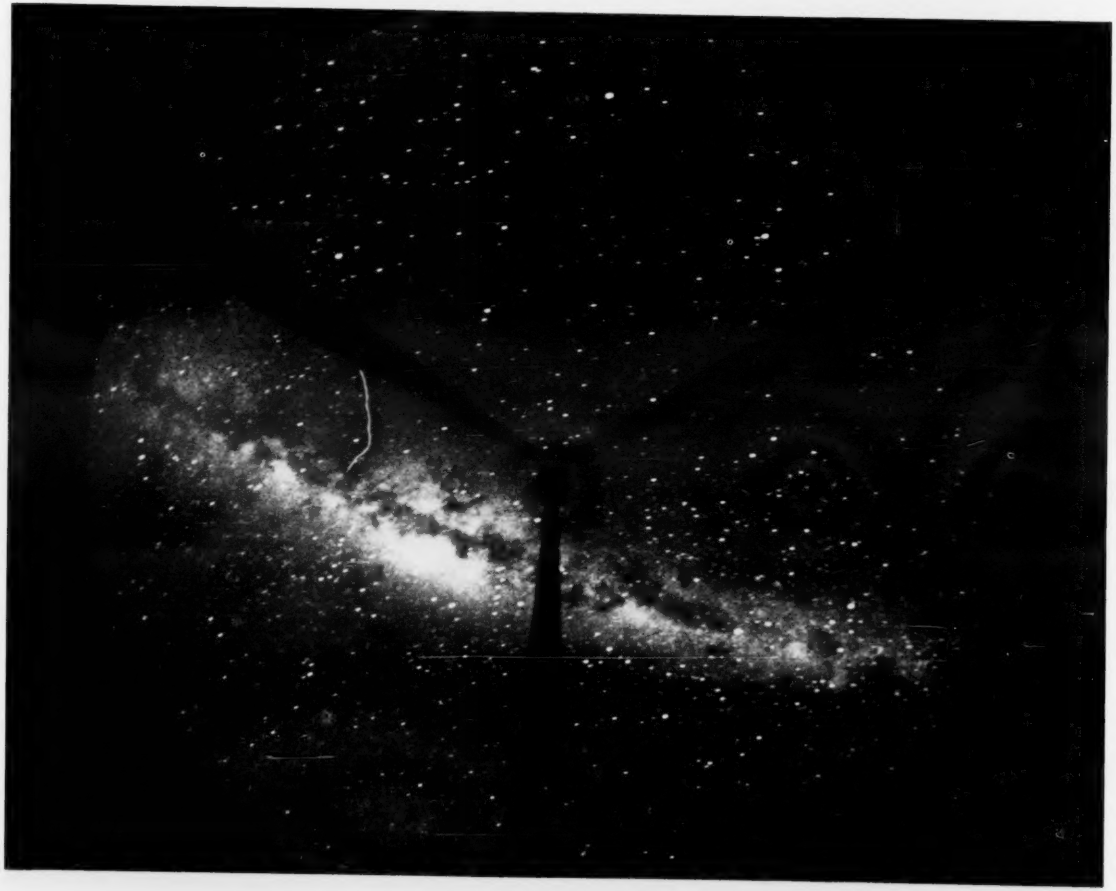

FIG. 1.—The Milky Way from Aquila to Carina in the infrared

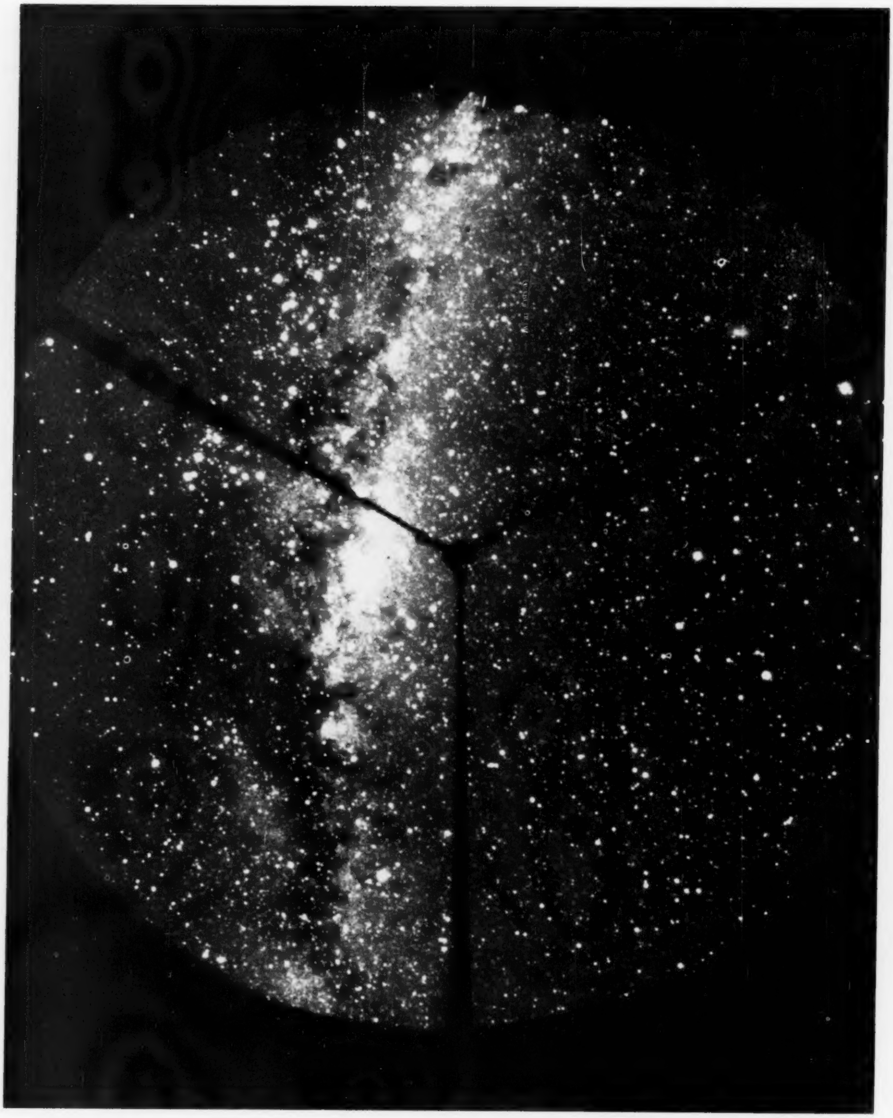

FIG. 2.—The Milky Way from Sagitta to Crux in the blue

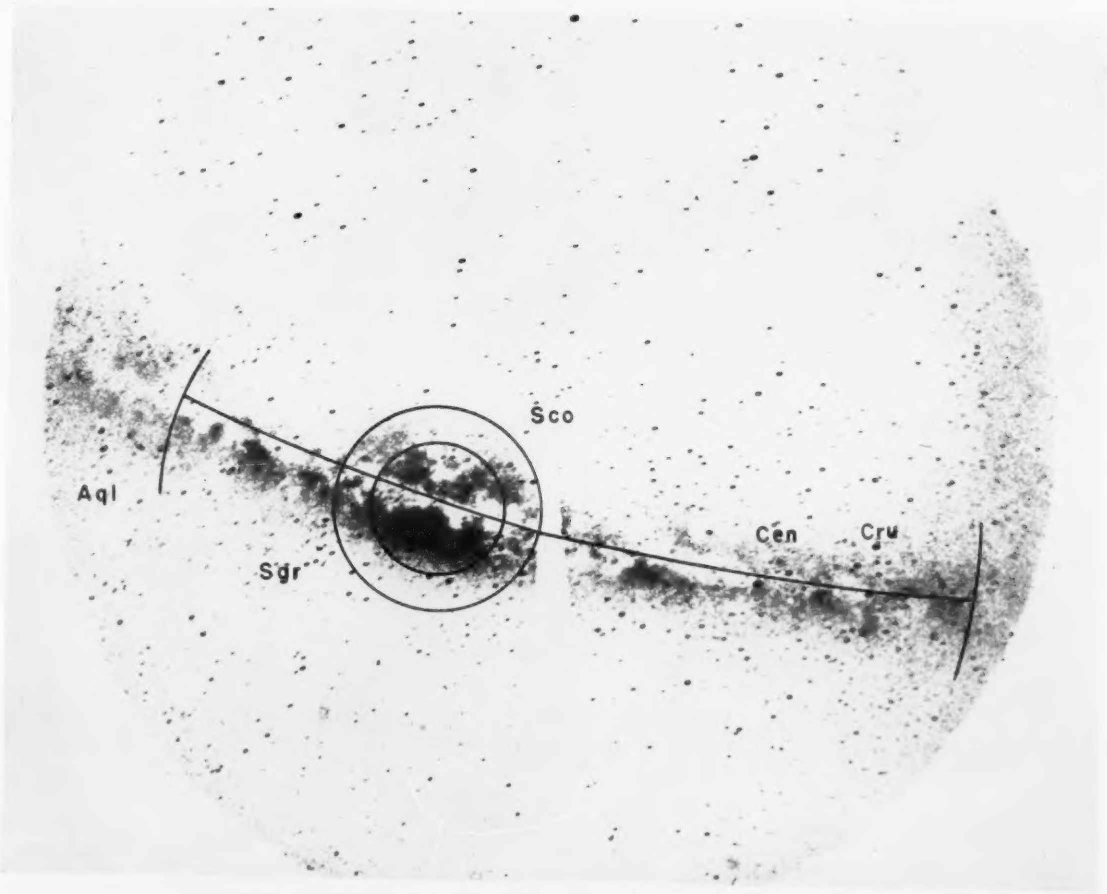

FIG. 3.—Infrared exposure of the southern Milky Way, indicating the position of the galactic center, the galactic equator, and the extent of the inner spiral structure.

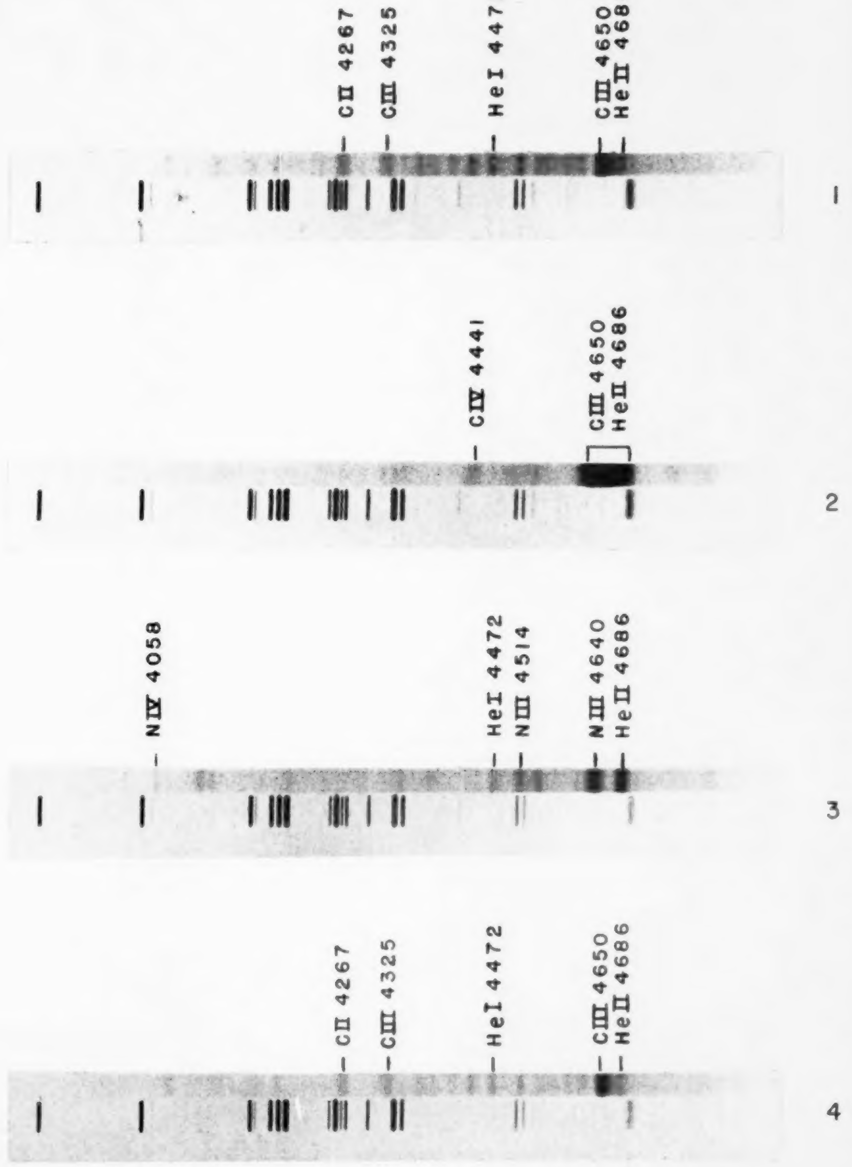

FIG. 1.—Spectrograms of four Wolf-Rayet stars. The comparison spectrum is neon

19 SCORPII, A LUMINOUS A STAR IN THE SCORPIO-CENTAURUS ASSOCIATION

19 *o* Scorpii (HD 147084, vis. mag. 4.76) has been found to be a member of the Scorpio-Centaurus association on the basis of its proper motion and its position in the sky. The accompanying table shows the positions and proper motions of 19 Sco and of stars in its immediate neighborhood, with accurate proper motions, belonging to the Scorpio-Centaurus association. The proper motions are weighted means of the values given in the *GC* and new ones derived by Bertiau from the positions at mean epoch in the *GC* and modern meridian observations. (The catalogues used were LaPl XII, Cape 2nd 25, Wash XIV, and Cape 1st 50.) They are in the system of the N30 catalogue and corrected for errors in Newcomb's precession. The radial velocities and their qualities are taken from R. E. Wilson's catalogue.

STAR	l	b	PROPER MOTION (UNIT 0″001 PER YEAR)			RAD. VEL. (KM/SEC)	QUAL.
			$\mu_l \cos b$	μ_b	p.e.		
χ Oph..........	326°0	+19°4	−24	−12	±1.5	− 5	b
ν Sco..........	322.7	+21.4	−25	−11	1.0	− 7	c
ω^1 Sco..........	320.9	+21.4	−24	−10	1.5	− 4	c
δ Sco..........	318.1	+21.2	−23	−11	0.8	−14	c
22 Sco..........	321.1	+14.5	−22	−15	1.6	− 4	b
σ Sco..........	319.3	+15.7	−20	−10	1.0	....	....
τ Sco..........	319.4	+11.5	−20	−10	1.1	− 1	a
19 Sco..........	320.1	+16.8	−24	−12	±1.8	− 8	a

19 Sco is located near the center of the most northern subgroup of the association and about 1°3 from ρ Oph. Both stars are strongly reddened. Accurate photometry of 19 Sco is given in *Cape Mimeograms*, No. 1, from which one derives $B - V = +0.78$ mag. Subtracting the intrinsic color, we find the color excess $E_{B-V} = +0.63$ mag. and the visual absorption $A_V = +1.9$. Hence the corrected apparent magnitude is 2.9.

Pending the completion of a rediscussion of the motions and distances for the Scorpio-Centaurus association, which is now under way at this observatory, we adopt for the distance modulus of 19 Sco the mean value for the stars in its surroundings given by Blaauw in *Gron. Pub.*, No. 52 (1946), Table 33. We find $m_0 - M = 6.46$, and hence the visual absolute magnitude $M_v = -3.6$. Thus 19 Sco appears to be an A-type star of intermediate luminosity. This is also shown in the appearance of the spectrum. A provisional classification in the MK system gives the type A5 II.

19 Sco and Antares are the only known luminous members of the Scorpio-Centaurus association of spectral type later than B. So far, no other case is known of the occurrence of an A-type giant in a B-star association.

We acknowledge discussion of the photometric data on 19 Sco with Dr. D. Harris.

A. BLAAUW
W. W. MORGAN
F. C. BERTIAU, S.J.

YERKES OBSERVATORY

ABSTRACTS OF ASTROPHYSICAL JOURNAL SUPPLEMENT SERIES

Supplement No. 10, Volume 1

NUMERICAL INTEGRATIONS FOR THE STELLAR INTERIOR

R. HÄRM AND M. SCHWARZSCHILD
Princeton University Observatory

During past investigations on the stellar interior, a number of solutions of the differential equations for the stellar interior have been obtained by numerical integration. These integrations generally represent not just individual eigen solutions but rather families of solutions characterized by one or more parameters. Owing to this more general nature of the integrations, they can be applied to a variety of problems beyond their original purpose. It is for this reason that they are now being published.

Of the fifteen families of integrations which are included in the present tabulation, the first thirteen were computed at this Observatory with desk calculators, the fourteenth was obtained by G. W. Wares at the Yerkes Observatory, and the last, large family was integrated with the electronic computer of the Institute for Advanced Study.

None of the tabulated integrations covers an entire star from the center to the surface. Rather, each family covers only a region, either the envelope or an intermediate zone or the core. Hence, by combining various integrations, complete stellar models can be constructed for a large variety of physical circumstances.

The main characteristics of the fifteen families of integrations are given in the accompanying table.

Family	Region	Opacity	Remarks
1	Envelope	Kramers'	....
2	Envelope	Kramers'+electron scattering	With radiative pressure
3	Envelope	Modified Kramers'	Proton-proton source
4	Envelope extension	Electron scattering	Attached to Family 1
5	Intermediate zone	Kramers'	Attached to convective core
6	Intermediate zone	Electron scattering	Attached to convective core
7	Intermediate zone	Modified Kramers'	Attached to convective core
8	Intermediate zone	Kramers'	Variable composition
9	Intermediate zone	Kramers'	Variable composition
10	Radiative core	Modified Kramers'	Proton-proton source
11	Contracting core	Modified Kramers'	Gravitation energy source
12	Contracting core	Electron scattering	Gravitation energy source
13	Intermediate zone	....	Isothermal, nondegenerate
14	Exhausted core	....	Isothermal, partially degenerate
15	Convective envelope	....	Adiabatic

The 98 pages of tabulations give for each integration the pressure, the temperature, the mass fraction, and the luminosity fraction as a function of the distance from the center. All these variables are given in nondimensional, logarithmic form. The tabulations also give the homology invariants U, V, and $(n+1)$.

THE ASTROPHYSICAL JOURNAL SUPPLEMENT SERIES

These *Supplements* are intended to provide a medium for the publication of extensive investigations, such as wave-length lists of stars of special interest, photometric data, results of numerical integrations pertaining to stellar interiors, model stellar atmosphere calculations, and original memoirs. The following twelve *Supplements* are in Volume I.

1. "Chromospheric Structure of the K-type Component of Zeta Aurigae." O. C. WILSON and HELMUT A. ABT. $1.25
2. "Spectroscopic Observations of Mira Ceti, 1934–1952." ALFRED H. JOY. $1.25
3. "An Analysis of W Virginis." HELMUT A. ABT. $1.25
4. "Photometric Investigation of the Eclipsing Binary UX Ursae Majoris." H. L. JOHNSON, BARBARA PERKINS, and W. A. HILTNER. $1.25
5. "On Nuclear Reactions Occurring in Very Hot Stars. I. The Synthesis of Elements from Carbon to Nickel." F. HOYLE. $1.25
6. "On the Dissipation of Gas and Volatilized Elements from Protoplanets." HAROLD C. UREY. $1.25
7. "Catalogue and Bibliography of Emission-Line Stars of Types Later than B." WILLIAM P. BIDELMAN. $3.00
8. "The Index of Clumpiness of the Distribution of Images of Galaxies." JERZY NEYMAN, ELIZABETH L. SCOTT, and C. D. SHANE. $1.25
9. "The Spectrum of the CN Molecule." A. E. DOUGLAS and P. M. ROUTLY. $1.25
10. "Numerical Integrations for the Stellar Interior." R. HÄRM and M. SCHWARZSCHILD. $2.50
11. "An Analysis of the Magnetic Variable α^2 Canum Venaticorum." G. R. BURBIDGE and E. MARGARET BURBIDGE. $1.25
12. "The Thermodynamic Structure of the Outer Solar Atmosphere. III, IV, V." SATOSHI MATSUSHIMA; R. G. ATHAY and R. N. THOMAS; R. G. ATHAY, D. H. MENZEL, J.-C. PECKER, and R. N. THOMAS. $1.25

An abstract of each supplement is published in THE ASTROPHYSICAL JOURNAL. The *Supplements* appear irregularly, and may be purchased separately or by subscription. Each volume of *Supplements* will consist of approximately 500 pages.

Subscriptions

$8.00 per volume
Canada, $8.75. Foreign, $9.50.
To members of the American Astronomical Society, $6.00 per volume.

THE UNIVERSITY OF CHICAGO PRESS

5750 ELLIS AVENUE **CHICAGO 37, ILLINOIS**

THE ASTROPHYSICAL JOURNAL SUPPLEMENT SERIES

These *Supplements* are intended to provide a medium for the publication of extensive investigations, such as wave-length lists of stars of special interest, photometric data, results of numerical integrations pertaining to stellar interiors, model stellar atmosphere calculations, and original memoirs.

Supplement No. 11
"An Analysis of the Magnetic Variable α^2 Canum Venaticorum." G. R. BURBIDGE and E. MARGARET BURBIDGE.

A detailed spectrophotometric study of the magnetic variable α^2 CVn is described. Equivalent widths through the period are given for about 1200 lines, and the magnetic variations of the star are discussed. The anomalous abundances of the magic number and other nuclei are considered in terms of surface nuclear reactions.

(Ready April, 1955. Price $1.25)

Supplement No. 12
"The Thermodynamic Structure of the Outer Solar Atmosphere. III, IV, V." SATOSHI MATSUSHIMA; R. G. ATHAY and R. N. THOMAS; R. G. ATHAY, D. H. MENZEL, J.-C. PECKER, and R. N. THOMAS.

Observations of the 1952 eclipse are analyzed to obtain a preliminary model of the 1952 chromosphere. A discussion of the Balmer decrement from two viewpoints provides values for the self-absorption in the higher Balmer lines. Data at λ 3640 and λ 4700 combine to provide electron density and temperature as functions of height.

(Ready May, 1955. Price $1.25)

Subscriptions
$8.00 per volume
Canada, $8.75. Foreign, $9.50.
To members of the American Astronomical Society, $6.00 per volume. Orders now accepted.

THE UNIVERSITY OF CHICAGO PRESS
5750 ELLIS AVENUE CHICAGO 37, ILLINOIS

THE OBSERVATORY

FOUNDED 1877

* * *

A Magazine presenting current developments in Astronomy by means of Articles, Correspondence, Notes on discoveries and Reviews of important astronomical books. The papers read at the Meetings (Astronomical & Geophysical) of the Royal Astronomical Society and the discussions which follow are also fully reported.

* * *

Annual subscription for 6 issues, post free, £1 (U.S.A. and Canada, $3.00) should be sent to

The Editors, ROYAL GREENWICH OBSERVATORY
Herstmonceux Castle, Hailsham, Sussex, England

THE ASTROPHYSICAL JOURNAL SUPPLEMENT SERIES

These *Supplements* are intended to provide a medium for the publication of extensive investigations, such as wave-length lists of stars of special interest, photometric data, results of numerical integrations pertaining to stellar interiors, model stellar atmosphere calculations, and original memoirs.

Supplement No. 8

"The Index of Clumpiness of the Distribution of Images of Galaxies." JERZY NEYMAN, ELIZABETH L. SCOTT, and C. D. SHANE

The index K of clumpiness, a statistical characterization of the distribution of galaxies on a photographic plate, is studied. The empirical values of K (from Lick Observatory counts) agree with the theory of the authors and contradict that of Chandrasekhar-Münch-Limber. These same K-values do not require for their explanation the hypothesis of extra-galactic absorbing clouds considered by Zwicky.

(January, 1955. Price, $1.25)

Supplement No. 9

"The Spectrum of the CN Molecule." A. E. DOUGLAS and P. M. ROUTLY.

This paper gives the results of an investigation of the spectrum of the CN molecule excited in an electric discharge through C_2N_2 and photographed with a high dispersion spectrograph. Four new band systems and extensions of the two known band systems are described.

(February, 1955. Price, $1.25)

Supplement No. 10

"Numerical Integrations for the Stellar Interior." R. HÄRM and M. SCHWARZSCHILD.

This Supplement contains 98 pages of tables which represent 173 numerical integrations of the differential equations for the stellar interior. By combining the various integrations, complete stellar models can be constructed for a great variety of physical circumstances.

(March, 1955. Price, $2.50)

An abstract of each supplement will be published in THE ASTROPHYSICAL JOURNAL. The *Supplements* will appear irregularly, and may be purchased separately or by subscription. Each volume of *Supplements* will consist of approximately 500 pages.

Subscriptions

$8.00 per current volume
Canada, $8.75. Foreign, $9.50.
To members of the American Astronomical Society, $6.00 per current volume.
Price of Vol. I will be increased upon publication of Vol. II, No. 1.

Orders now accepted.

THE UNIVERSITY OF CHICAGO PRESS
5750 ELLIS AVENUE **CHICAGO 37, ILLINOIS**

Outstanding

McGRAW-HILL Books

IN PRESS

NEW FIFTH EDITION

★ **ELEMENTS of ASTRONOMY** ★

EDWARD ARTHUR FATH

Formerly Professor of Astronomy and Director of the Observatory, Carleton College

The appearance of this new edition marks a high point in building an impressive record of distribution and use for this outstanding volume. Since 1926, it has held a unique position in the field as a thorough, non-technical presentation of the facts of astronomy and the principles and methods used in modern astronomical investigations.

Since the publication of the previous edition much new observational material has been obtained and many new ideas have been developed. The author has sought to include every important discovery published up to the time of going to press.

★ **ASTROPHYSICS** ★

A TOPICAL SYMPOSIUM

674 pages **A. J. HYNEK** **$12.00**

Ohio State University

Here is a symposium of papers treating "essentially all the active fields" of astrophysics. The fifteen contributors are leaders and authorities in their respective fields. The volume commemorates the Fiftieth Anniversary of the Yerkes Observatory and reviews the progress in astrophysics during the half-century since the founding of the observatory. The book combines many of the features of a textbook, a handbook, a historical study, and a technical treatise.

Send for copies on approval

McGRAW-HILL BOOK COMPANY, Inc.

330 West 42nd Street New York 36, N.Y.